UNIVERSITAT DE BARCELONA

Simultaneous etherification of C_4 and C_5 iso-olefins with ethanol over acidic ion-exchange resins for greener fuels

Rodrigo Soto López

UNIVERSITAT DE BARCELONA

Doctoral Program

Engineering and Advanced Technologies

Simultaneous etherification of C_4 and C_5 iso-olefins with ethanol over acidic ion-exchange resins for greener fuels

Presented by

Rodrigo Soto López

Supervised and approved by

Dr. Carles Fité Piquer and **Dr. Eliana Ramírez Rangel**

Chemical Engineering and Analytical Chemistry Department,

Universitat de Barcelona

Barcelona, March 2017

LIST OF PUBLICATIONS

R. Soto, C. Fité, E. Ramírez, R. Bringué, F. Cunill. Equilibrium of the simultaneous etherification of isobutene and isoamylenes with ethanol in liquid-phase. *Chem. Eng. Res. Des.* **2014**; 92 (4): 644–656. http://dx.doi.org/10.1016/j.cherd.2013.11.012

R. Soto, C. Fité, E. Ramírez, R. Bringué, M. Iborra, Green metrics analysis applied to the simultaneous liquid-phase etherification of isobutene and isoamylenes with ethanol over Amberlyst™35. *Green Process. Synth.* **2014**; 3: 321–333. http://dx.doi.org/10.1515/gps-2014-0049

R. Soto, C. Fité, E. Ramírez, J. Tejero, F. Cunill. Effect of water addition on the simultaneous liquid-phase etherification of isobutene and isoamylenes with ethanol over Amberlyst™35. *Catal. Today.* **2015**; 256 (2): 336–346. http://dx.doi.org/10.1016/j.cattod.2014.12.031

R. Soto, C. Fité, E. Ramírez, R. Bringué, F. Cunill. Equilibrium conversion, selectivity and yield optimization of the simultaneous liquid-phase etherification of isobutene and isoamylenes with ethanol over Amberlyst™35. *Fuel Process. Technol.* **2016**; 142: 201–211. http://dx.doi.org/10.1016/j.fuproc.2015.09.032

R. Soto, C. Fité, E. Ramírez, R. Bringué, F. Cunill. Kinetic modeling of the simultaneous etherification of ethanol with C_4 and C_5 olefins over Amberlyst™35 using model averaging. *Chem Eng. J.* **2017**; 307: 122–134. http://dx.doi.org/10.1016/j.cej.2016.08.038

R. Soto, N. Oktar, C. Fité, E. Ramírez, R. Bringué, J. Tejero. Adsorption of C_1–C_4 alcohols, C_4–C_5 isoolefins and their corresponding ethers over Amberlyst™35. *Chem. Eng. Technol*. **2017**; https://doi.org/10.1002/ceat.201600592

WORK IN PROGRESS

R. Soto, C. Fité, E. Ramírez, M. Iborra, J. Tejero. Catalytic activity dependence on morphological properties of acidic ion-exchange resins for the simultaneous ETBE and TAEE liquid-phase synthesis. State: Preparing submission to *Catal. Sci. Technol.* journal.

R. Soto, C. Fité, E. Ramírez, J. Tejero, F. Cunill. Deactivation of acidic ion-exchange resins by acetonitrile in the simultaneous liquid-phase syntheses of ethyl *tert*-butyl ether and *tert*-amyl ethyl ether. State: Preparing submission to *Appl. Catal., A* journal.

R. Soto, C. Fité, E. Ramírez, R. Bringué, F. Cunill. Kinetic modeling of the simultaneous etherification of ethanol with C_4 and C_5 olefins over Amberlyst™ 35. Poster contribution submitted to the *Meeting of the Spanish Catalysis Society (SECAT'17)*. June **2017**. Oviedo (Spain).

CONFERENCE CONTRIBUTIONS

R. Soto, E. Ramírez, C. Fité, R. Bringué, F. Cunill. Simultaneous etherification of C_4 and C_5 fractions over Amberlyst™35 using bioethanol for greener fuels. Oral presentation contribution. *9th European Congress on Chemical Engineering (ECCE9)*. April **2013**. The Hague (The Netherlands).

R. Soto, C. Fité, E. Ramírez, R. Bringué, M. Iborra. Green metrics analysis applied to the simultaneous etherification of isobutene and isoamylenes with ethanol in the liquid phase over Amberlyst™35. Oral presentation contribution. *4th International Congress on Green Process Engineering (GPE)*. April **2014**. Seville (Spain).

R. Soto, C. Fité, E. Ramírez, R. Bringué, F. Cunill. Conversion, selectivity and yield optimization of the simultaneous liquid-phase synthesis of isobutene and isoamylenes with ethanol over Amberlyst™35. Oral presentation contribution. *2014 AIChE Annual Meeting*. November **2014**. Atlanta (United States of America).

R. Soto, C. Fité, E. Ramírez, J.H. Badia, R. Bringué. Empirical kinetic model for the simultaneous liquid-phase etherification of isobutene and isoamylenes with ethanol over Amberlyst™35. Poster presentation. *II International Congress of Chemical Engineering of ANQUE (II ICCE)*. July **2014**. Madrid (Spain).

R. Soto, C. Fité, E. Ramírez, J. Tejero, F. Cunill. Effect of water addition on the simultaneous liquid-phase etherification of isobutene and isoamylenes with ethanol over Amberlyst™35. Poster contribution. *21st International Congress of Chemical and Process Engineering (CHISA 2014)*. August **2014**. Prague (Czech Republic).

R. Soto, C. Fité, E. Ramírez, M. Iborra, F. Cunill. Síntesis simultánea de ETBE y TAEE en fase líquida sobre resinas ácidas de intercambio iónico. Poster presentation. *Meeting of the Spanish Catalysis Society (SECAT'15)*. July **2015**. Barcelona (Spain).

R. Soto, E. Ramírez, C. Fité, F. Cunill, J. Tejero. Deactivation of acidic ion-exchange resins by acetonitrile in the simultaneous liquid-phase synthesis of ethyl tert-butyl ether and tert-amyl ethyl ether. Poster contribution. *10th European Congress on Chemical Engineering (ECCE 10)*. September **2015**. Nice (France).

R. Soto, C. Fité, E. Ramírez, M. Iborra, J. Tejero. Catalytic activity dependence on morphological properties of ion-exchange resins for the simultaneous ETBE and TAEE synthesis. Oral presentation contribution. *IEX 2016 Ion Exchange - a continuing success story*. July **2016**. Cambridge (United Kingdom).

R. Soto, N. Oktar, C. Fité, E. Ramírez, R. Bringué, J. Tejero. Experimental liquid- and gas-phase study on adsorption of C_1-C_4 alcohols, C_4-C_5 isoolefins and their corresponding ethers over Amberlyst™35. Poster presentation. *22nd International Congress of Chemical and Process Engineering (CHISA 2016)*. August **2016**. Prague (Czech Republic).

J. H. Badia, R. Bringué, C. Fité, M. Iborra, R. Soto, F. Cunill. Kinetics of the liquid-phase synthesis of propyl tert-butyl ether (PTBE) and butyl tert-butyl ether (BTBE) over Amberlyst™35. Poster presentation. *22nd International Congress of Chemical and Process Engineering (CHISA 2016)*. August **2016**. Prague (Czech Republic).

J. Massanet, R. Bringué, E. Ramírez, M. Iborra, J. Tejero, R. Soto. Etherification of furfuryl alcohol to butyl levulinate, an oxygenate of second generation. Poster presentation. *22nd International Congress of Chemical and Process Engineering (CHISA 2016)*. August **2016**. Prague (Czech Republic).

CONTENTS

MOTIVATION

The present thesis is involved in the framework of the production of new fuels that apart from reducing the environmental impact of the combustion processes, also increase the fuels energetic efficiency. This challenge is understood as a short term measure due to the immediate necessity of improving fuels performance being fully compatible with the current vehicle fleet, which is foreseen to increase in the forthcoming years. The possibility of implementing this technology in contemporary refineries makes the present thesis a realistic alternative that can help to extend the reservoirs of fossil fuels while other technologies are fully developed and spread out in the society.

"*Research is to see what everybody else has seen and to think what nobody else has thought*".
Albert Szent-Gyorgyi

ABSTRACT

The use of tertiary alkyl ethers as gasoline components has been gaining relevance in the last decades because they can enhance the gasoline octane rating at the time that they reduce the environmental impact of combustion processes, being therefore considered as environmentally friendly additives. Methyl *tert*-butyl ether (MTBE) and ethyl *tert*-butyl ether (ETBE) are the most produced ethers at industrial scale. More recently, ETBE market is acquiring a predominant role compared to MTBE, due to environmental concerns associated with MTBE usage and because ETBE can be manufactured from bioethanol, what confers a bioether character. Apart from MTBE and ETBE, other ethers as *tert*-amyl methyl ether (TAME) and *tert*-amyl ethyl ether (TAEE) are interesting alternatives since they can be manufactured from C_5 reactive olefins present in gasoline that present drawbacks as high blending vapor pressure or high potential of tropospheric ozone formation. Similar to ETBE, TAEE can be considered as a bioether since bioethanol can be used as reactant. In this sense, ETBE and TAEE can be envisaged as the most promising alternatives as gasoline additives to fulfill the progressively stricter legislation while being compatible with current engines and therefore, a plausible solution at medium-short term.

The optimization and integration of chemical processes is an incentive for industrial plants since several benefits can be obtained as savings in operating and maintenance costs. The simultaneous production of several ethers in the same reaction unit can be a clear example of such technology. A simultaneous etherification unit yielding a mixture of ETBE and TAEE would be one of the most interesting configurations. To the best of our knowledge, such a process has not been yet studied at bench scale. The present Ph.D. thesis is focused on the study of the feasibility of producing ETBE and TAEE as one pot synthesis in the same reaction unit since the industrial interest of such ethers implies a realistic possibility of implementation in the near future.

The main topics covered and assessed throughout the present manuscript are: the comparison of different chemical pathways to evaluate the process feasibility, the optimization of experimental conditions that maximize etherification yields, the study of the effect of water presence on the ethanol used as reactant, the characterization of potential byproducts and how to avoid side reactions, the study of the chemical equilibrium and the implicit thermodynamics of involved reactions, the assessment of several catalysts in order to find the best catalyst and the catalytic properties influencing the observed catalytic activity, the study of the intrinsic kinetics of the main reactions involved in order to find a reliable kinetic model, the study of the adsorption equilibrium of involved species in a potential catalytic surface and finally, the study of the catalyst deactivation process caused by the presence of acetonitrile in the feed stream.

1. GENERAL INTRODUCTION

1.1 OIL AND FUELS FOR TRANSPORTATION, AIR QUALITY AND SOCIETY

The development of new oil reserves and extraction technologies is changing the geopolitical trends and prospects of fossil fuels. Oil accounts for a large percentage of the worldwide energy consumption, ranging from 32% in Europe and Asia, to 53% in the Middle East. For other regions: 44% in South and Central America, 41% in Africa, and 40% in North America. An important part of the consumed oil is dedicated to the manufacture of transportation fuels as gasoline, diesel, fuel oil, jet fuel or kerosene.

The global oil consumption has been increasing in the last decades together with the world population (Fig. 1.1), as well as the consumption of transportation fuels as gasoline and diesel. By 2007 there were 468 urban areas with more than one million inhabitants. Fourteen of these are classified as megacities, with the largest metropolitan complexes centered at Tokyo and Mexico City c. If this trend continues, the world's urban population will double every 38 years, and during the next 10–15 years it is expected that there will be more than 30 megacities. These megacities suffer from high levels of pollution and degraded air quality due to the high demand for energy and the associated combustion for transportation that end up in huge sources of air pollutants into the surrounding areas. For example, Mexico City with a population 30 million people emits 1.1 megatons of ozone and 15 megatons of particulate matter of less than 2.5 microns per year. In addition, the transport of primary pollutants leads to the substantial formation of ozone and other oxidants in the surrounding regions. These megacities drive the modification of climate on regional scales. The current number of cars is approximately one car for every two people and it is expected to increase in countries like China and India in the near future. The ensuing increase of emitted pollutants is taking a heavy poll on the atmosphere, especially in urban areas where the air quality has shown a sharp deterioration. For instance, the emissions of carbon dioxide (CO_2) from petroleum consumption are nowadays above 30% higher than in 1990 [2] and they are expected to increase in the forthcoming years, see Fig. 1.1. Also, the average temperature on Earth is increasing what can lead to catastrophic consequences.

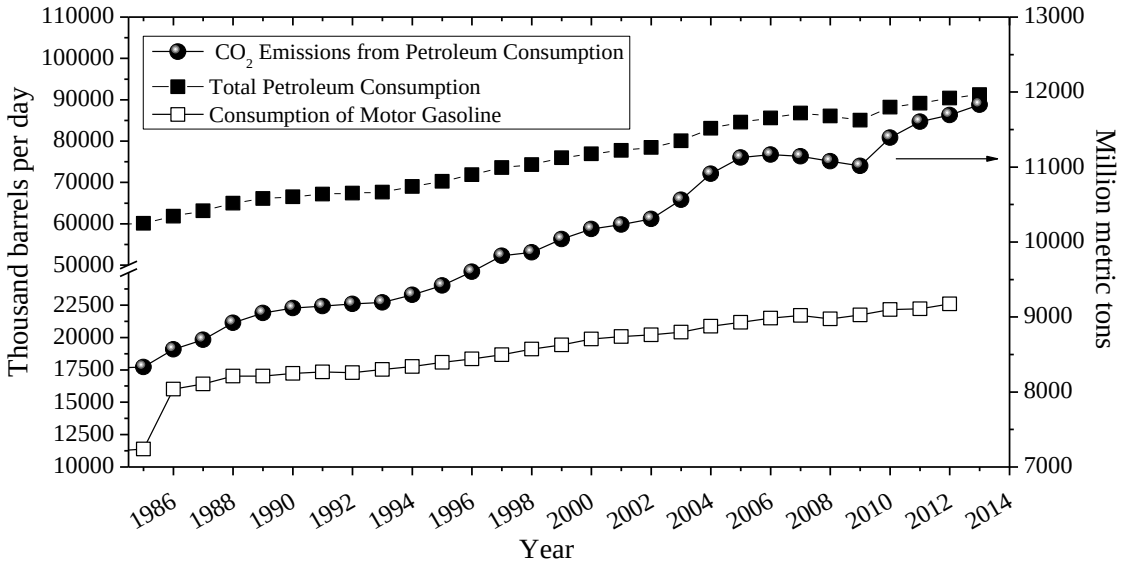

Figure 1.1. Annual consumption of petroleum and gasoline (left Y axis). Annual CO_2 emissions from petroleum consumption (right Y axis) [2].

As a result of the increasing level of pollutants in the atmosphere, emission of harmful compounds, as greenhouse gases (GHG), has been considered as a worldwide concern of

paramount importance. New trends support the idea of fossil fuel free vehicles based on renewable energies. This sort of technology is attractive but still needs to be further developed in order to be installed at industrial scale and spread out in the society at competitive price and with high energetic yield. Besides, it is obvious that the whole vehicle fleet and the way in which actual refineries produce fuels cannot suddenly disappear. Instead of one or another alternative, a gradual change from existing fuels toward vehicles working with both renewable energy and more efficient fuels (reformulated fuels) would result, at short term, in a more interesting chance for the forthcoming future. As a consequence, gasoline and diesel are still expected to play an important role for transportation in the present century.

The preferred use of gasoline or diesel depends on the world region. Gasoline is more widely used in US, Brazil, Japan, Australia, and the Middle East, whereas diesel consumption has been favored in Asia and Europe during the last decades, where the gasoline surplus was mainly palliated by exportation to the US. Although diesel produces 15% less CO_2 than petrol, its combustion emits four times more nitrogen dioxide (NO_2) and 22 times more particulate matter (PM). The first consequences of the overextended use of diesel are appearing, for instance, Paris suffered in March 2016 a pollution alarm becoming temporary the most polluted city in the world. The government response was to ban diesel vehicles and half its average number of cars on alternate days. A similar approach was used in Beijing in the run up to the 2008's Olympic Games. In fact, some European cities are considering the banning of diesel vehicles circulation by 2021. This scenario could end up in an increasing demand of gasoline fueled engines in the near future.

1.1.1 GASOLINE

Gasoline is a transparent liquid obtained from fractional distillation of petroleum used primarily as a fuel in internal combustion engines. The main components of a base gasoline can be separated into paraffins/iso-paraffins, olefins/iso-olefins, naphthenes, and aromatics [3]. Besides, a wide variety of additives are used to give some specific properties to final fuel, as oxygenates or detergents. Fig. 1.2 plots a chromatogram obtained for a commercial gasoline from a petrol station in Barcelona (Spain). Despite gasoline is produced worldwide, its base composition is quite similar independently of the country. The usual boiling point of gasoline ranges from 261.5 K (isobutane) to 491.2 K (naphthalene).

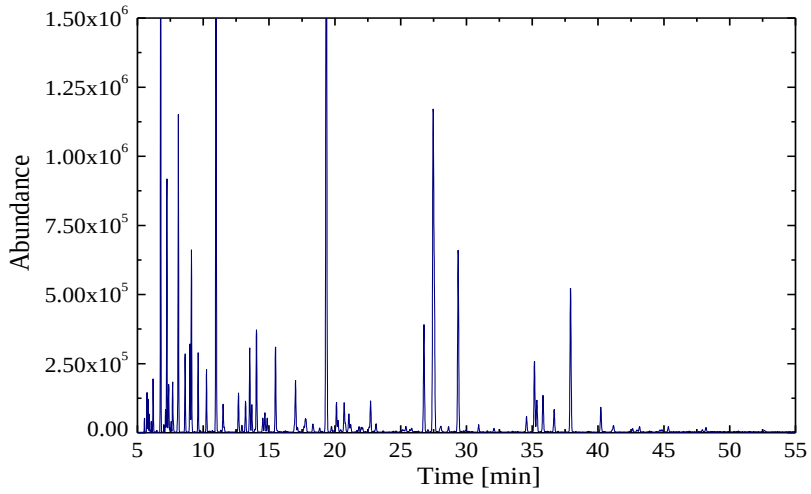

Figure 1.2. Chromatogram obtained for a commercial gasoline from Barcelona (Spain).

As it can be deduced, gasoline is a complex mixture of hydrocarbons containing more than 100 different compounds. The peaks detected in Fig. 1.2 by gas-chromatography (GC) were identified by mass spectrometry (MS). The analysis results and the GC-MS parameters used are detailed in Tables 7.1.1 and 7.1.2 of *Appendix 7.1*. The results in terms of chromatographic area revealed that such gasoline is composed of 37.6% of paraffins and isoparaffins, 4.4% of olefins and iso-olefins, 48.1 % of aromatics, 0.1 % of naphtalenes, and 9.8% of additives as oxygenates, among which 9.0 % are ethers (mainly ethyl *tert*-butyl ether) and 0.8% are alcohols.

1.1.2 GASOLINE ENGINE BEHAVIOR (KNOCKING)

The fuel´s composition, the advance of the ignition, compression rate, quality of the spark, type of valves and design of the combustion chamber influence the obtained power from combustion [4]. In typical combustion, the air/fuel mixture produces homogeneous combustion in each of the engine's cylinders after sparking. When the front of the flame sweeps the combustion chamber, the as yet unburned part of the fuel undergoes an increase in temperature due to the compression, causing detonation in the mixture with the ensuing brusque increase in pressure. The piston, instead of being pushed down uniformly, is subjected to a momentary dry strike, in which it does not respond since it is connected to the crankshaft, which in turn, is connected to other pistons. This sudden release of detonation energy in the area of the residual gas causes high frequency pressure fluctuations in the combustion chamber that are perceived by the ear as a strong metallic noise known as "detonation" or "knocking". In other words, fuel energy that could be converted into useful work is dissipated as pressure waves increasing radiant heat within the engine. Besides producing a metallic sound and wasting energy, prolonged knocking overheats the valves, spark-plugs and piston, reducing the engine's lifespan. Knocking is understood as the end result of chemical reactions of the air/fuel mixture in the cylinder as a consequence of the spontaneous burning of this mixture. As the temperature of the mixture rises through the cylinder during combustion, the residual gas is involved in a series of oxidation and cracking reactions that result in unstable compounds susceptible to self-ignition and instantaneous detonation [4].

The efficiency of a gasoline fueled engine is highly dependent upon the fuel's antiknock characteristics, which depends mainly on the fuels chemical composition. The quality of gasoline is typically measured by its octane number (ON) or antiknocking strength. For normalizing, isooctane is given an ON=100, while for *n*-heptane ON=0. ON is determined experimentally in an engine with variable compression rates as Motor Octane Number (MON) or Research Octane Number (RON). The MON evaluates the gasoline's antiknocking strength when the engine is operating under severe conditions as driving uphill and its determination is made by ASTM D 2700 standard. The RON evaluates the gasoline's antiknocking strength when the engine operates under milder conditions as driving condition on a highway. Its evaluation is described in ASTM D 2699 standard. The average of MON and RON is known as the Antiknock Index (AKI=(MON+RON)/2). The octane number is directly related to the resistance of a gasoline to autoignition and it is influenced by the type and content of hydrocarbons, oxygenates and sulfurs in final gasoline. A gasoline produced by direct distillation, rich in mid and long chain hydrocarbons, shows the greatest tendency to self-ignite and presents low octane number values. On the other hand, a gasoline from catalytic reform with high olefin content shows a low tendency for self-ignition and high octane number.

1.1.3 EMISSIONS FROM GASOLINE

The gasoline composition determines the emission of organic compounds. A gasoline with a high content of olefins and aromatic hydrocarbons has a great tendency to emit unburned hydrocarbons, which are not easily oxidized in catalytic converters and are precursors of photochemical contamination. The vapor pressure is a fundamental physicochemical property accounting for the level of emission of volatile organic compounds (VOC's) of the gasoline supply system and combustions processes, especially in starting the engine on cold days and in continuous operation in hot days. The fuel´s volatility can be expressed by several characteristics as the Reid vapor pressure (RVP), distillation curves, vapor pressure, vaporization enthalpy, and the vapor/liquid ratio. It has been confirmed that a vehicle's satisfactory performance is related to a minimal volatility of the fuel [5].

The main pollutants emitted from gasoline engines are carbon monoxide (CO), CO_2, PM, nitrogen oxides (NO_x's) and VOC's [4]. CO_2, though traditionally not considered a pollutant, accumulates in the atmosphere, contributing to global warming. NO_x's and VOC's emissions react in the presence of sunlight by means of a series of photochemical reactions involving hydroxyl-, peroxy-, and alkoxy radicals, to form ozone, a secondary and hazardous pollutant in the troposphere [6]. PM are harmful not only because they can reach the respiratory system of humans and animals, but also because most of them are carcinogenic and can accumulate in the atmosphere acting as catalysts for other secondary reactions. High levels of PM are especially dangerous in presence of SO_2 and NO_2. Of course, ozone is not the only oxidant formed from the reactions of NO_2 and the VOC's in the atmosphere. Other atmospheric oxidants are also formed such as hydrogen peroxide (H_2O_2), which can react with SO_2 to form sulfuric acid aerosol, aldehydes, organic acids, nitric acid, and the peroxyacyl nitrates (PAN's).

1.1.4 THE PROBLEMATIC OF C_5 ISO-OLEFINS OR ISOAMYLENES

Apart from the most reactive VOC's, isoprene and alphapinene, it is well known that olefins from the C_5 fraction from Fluid Catalytic Cracking (FCC), mainly the reactive isoamylenes (IA) 2-methyl-1-butene (2M1B) and 2-methyl-2-butene (2M2B), present some disadvantages from an environmental point of view as components of gasoline, specifically in tropical zones. The AKI index of such olefins is notably high and they are nowadays directly added to the gasoline pool. The relative potential of tropospheric ozone formation of a gasoline component (P_{OF}) can be evaluated as the product of its vapor pressure, its distribution in volume and its atmospheric reactivity. As it can be seen in Fig. 1.3a, C_5 olefins show the highest atmospheric reactivity of the olefins from a gasoline. From Fig. 1.3b, it can be deduced that C_5 olefins present the highest vapor pressure and the largest proportion in volume in a gasoline (around 40 vol.% of the C_5 fraction from FCC). Thus, accordingly with the above definition, these olefins show the highest potential (around 90%) of tropospheric ozone formation of a gasoline, see Fig. 1.3c. Consequently, the reduction or substitution of the C_5 olefins content in gasoline is environmentally advisable. On that purpose, several alternatives coexist such as etherification, oligomerization and/or alkylation. Besides that, other advantages of the reduction of IA content in gasoline are: i) the reduction of the olefins content, which can open the margin for using other larger olefins, ii) increasing the gasoline pool by the introduction of alcohol molecules as ethers and, iii) a significant reduction of the gasoline volatility.

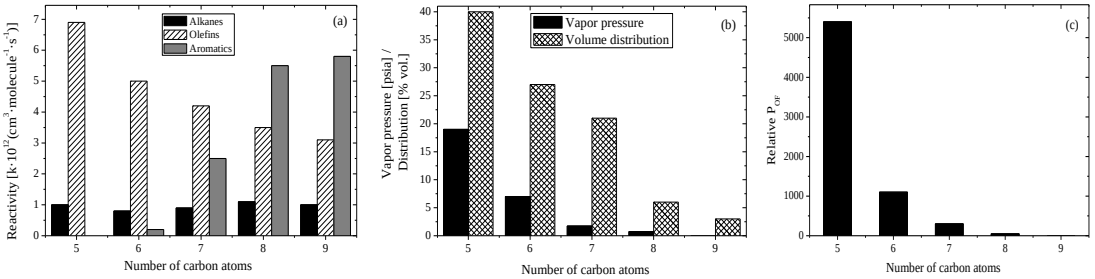

Figure 1.3. Relation between the number of carbon atoms and (a) atmospheric reactivity of alkanes, olefins and aromatics, (b) olefins vapor pressure and distribution in volume, and (c) olefins relative potential of tropospheric ozone formation. Data source [7].

1.2 GASOLINE REFORMULATION

To mitigate and prevent the mentioned detrimental effects of gasoline combustion and evaporative ones on the environment, major efforts and new more restrictive legislation have been devoted to fuel reformulation. The new generation of fuels has been developed by decreasing the olefin content, increasing oxygenates content and reducing the blending Reid vapor pressure (bRVP) of fuel. In the United States, the Clean Air Act Amendments (C.A.A.A.) elaborated by the Environmental Protection Agency (E.P.A.) in 1990 increased the severity of legislation concerning emissions limits of vehicles and required the manufacture of high quality fuels through reformulation of diesel and gasoline. In Europe, the Directives 2009/28/EC, 2009/30/EC and 2015/1513/EC establish the main guidelines. They take into account some prevention measures in order to deliver cleaner fuels and toward the greenhouse gas emission reduction goals at the time that promote the increasing use of renewable energies. For instance, they limit the composition of olefins, oxygen, aromatics and sulfur, and fix the minimum RON of a gasoline (Table 1.1). One reference value established is that, by 2020, renewable energy must account for the 20% of total energy used for transportation and the emissions of GHG must be reduced by a minimum of 6%. Moreover, the European Directive 2003/96 allow to member states to apply a total or partial tax exemption to biofuels, making thus biofuel production more competitive than classical fossil fuels. Finally, refiners have significant incentive to produce increasing amounts of reformulated gasoline and to reduce the production of conventional gasoline [8] because of gasoline distribution and segregation problems.

Table 1.1. Gasoline composition requirements established in the Directive 2009/30/EC.

Parameter	Unit	Limit	
		Minimum	Maximum
RON	-	95	-
MON	-	85	-
Vapor pressure (summer)	kPa	-	60
Evaporated at 100 °C	Vol.%	46	-
Evaporated at 150 °C	Vol.%	75	-
Olefins	Vol.%	-	18
Aromatics	Vol.%	-	35
Benzene	Vol.%	-	1
Methanol	Vol.%	-	3
Ethanol	Vol.%	-	10
Isopropyl alcohol	Vol.%	-	12
Isobutyl alcohol	Vol.%	-	15
tert-Butyl alcohol	Vol.%	-	15
5 or more carbon atom ethers	Vol.%	-	22
Other oxygenates	Vol.%	-	15
Total oxygen content	Wt.%	-	3.7
Sulfur content	mg/kg [ppm]	-	10
Lead content	g/L	-	0.005

1.2.1 OXYGENATES (ALCOHOLS AND ETHERS)

Examples of oxygenate compounds are alcohols, carboxylic acids, ketones, ethers, esters and phenols. Since lead compounds were banned as octane enhancers, oxygenated compounds have been gradually gaining importance in the gasoline market. However, only alcohols and ethers are used for gasoline and esters for diesel [9]. With regards to gasoline, oxygenates increase the octane index and incorporate oxygen in their composition, what contributes to a more complete combustion in the engine and reduces the exhaust emissions. Based on studies with vehicles [10,11], it has been shown that oxygenates addition to gasoline reduce the formation of CO up to 46 wt.% with respect to a typical gasoline. Significant savings in emissions of CO_2, VOC's and irregular emissions as benzene and 1,3-butadiene can also be achieved [12,13]. In addition, they can be considered ideal substitutes for aromatics in high performance gasoline [14]. Apart from being carcinogenic, aromatics, as toluene, increase the formation of PM and the emission of unburned hydrocarbons which are responsible for photochemical contamination and, as shown in *Section 1.1.1*, they represent about a 48% GC of the gasoline composition.

Among alcohols, the most widely used is ethanol (EtOH) since it is considered a renewable resource. EtOH can be produced by fermentation of biomass [15], such as corn, grain and even agricultural waste [16] and renewable stock can be then introduced to biofuels. In renewable fuels, the carbon originates from biomass and does not add to CO_2 emissions in the way that fossil fuels do. Since CO_2 is a GHG, such carbon cycle of renewable fuels helps in preventing the accumulation of CO_2 in the atmosphere that leads to the greenhouse effect. EtOH fuel mixtures denoted by "E" numbers that indicate the volumetric percentage of alcohol added to the fuel mixture. For example, E85 is 85% anhydrous ethanol and 15% gasoline. Low-ethanol blends, from E5 to E25, are also known as gasohol. Blends of E10 or less are used in more than 20 countries around the world, led by the United States (U.S.). Blends from E20 to E25 have been used in Brazil since the late 1970s. E85 is commonly used in the U.S. and Europe for flexible-fuel vehicles. Hydrous ethanol or E100 is used in Brazilian neat ethanol vehicles and flex-fuel light vehicles and hydrous E15 (called E15) for modern petrol cars in the Netherlands. More recently, higher alcohols as butanol (BuOH) have also been considered as potential additives for direct blending to gasoline, since they can be produced by fermentation technology that can be applied to various carbohydrate substrates [17].

The main tertiary ethers, in terms of worldwide production, are methyl *tert*-butyl ether (MTBE), ethyl *tert*-butyl ether (ETBE), *tert*-amyl methyl ether (TAME), and, in less extent, *tert*-amyl ethyl ether (TAEE). These ethers can be obtained by means of the addition of primary alcohols to tertiary olefins over acid catalysts [18]. MTBE and TAME are produced by the reaction of methanol (MeOH) with isobutene (IB) and IA (2M1B and 2M2B), respectively. Analogous reactions of these olefins with EtOH lead to ETBE and TAEE production. In the last decades, other ethers as propyl *tert*-butyl ether (PTBE) and butyl *tert*-butyl ether (BTBE) have attracted the attention of researches [19–21] due to the possibility of heavier alcohols etherification, propanol (PrOH) and BuOH, with IB. However, their relatively low ON and the lower availability of heavier alcohols at global scale compared to the dominant role of EtOH as biofuel, are still matter of discussion.

Some relevant properties of alcohols, olefins, their corresponding ethers, and other interesting additives are listed in Table 1.2. Ethers are generally preferred rather than alcohols due to their blending characteristics since they are more similar to conventional constituents hydrocarbons of a gasoline [22]. Despite the choice of some countries like the US and Brazil for EtOH or

bioethanol direct blending (gasohol) mainly for economic advantages, alcohols direct blending has some drawbacks such as: high vapor pressure owing to minimum boiling azeotropes formation, high latent heat of vaporization, possibility of introducing water into the system (risk of phase separation), less energetic content and less enthalpy of combustion compared to ethers. In addition, alcohol presents corrosion problems and the overall evaporative and exhaust pollutant emissions to air from gasohol usage are higher than those of conventional gasoline due to its high bRVP [12,23,24]. Likewise, its high oxygen content can promote NO_x's formation or limit the amount of blended additive in order to fulfill the maximum legislated oxygen content [25], which constitutes an important industrial constraint. Furthermore, the specific fuel consumption induced by direct blending of EtOH is around 40% higher than that induced by tertiary ethers blending (mainly ETBE and TAEE) [26]. Thus, a better utilization of bioethanol is by means of its incorporation as fatty acid esters to biodiesel, and as ETBE and TAEE to reformulated gasoline.

Table 1.2. Relevant properties of potential gasoline additives [17,18,27–35].

Compound	(RON+MON)/2	Water Solubility [mg/L water]	Oxygen Content [wt.%]	bRVP [psi]	b_p [K]	Reactivity[a]
MTBE	110	48,500	18.2	8	328	2.6
ETBE	112	26,000	15.7	4	345	8.1
TAME	105	20,000	15.7	2	361	7.9
TAEE	100	4,000	13.8	2	375	-
PTBE	100.5	-	13.8	-	379[e]	-
BTBE	81[b]	-	12.2	-	402[e]	-
Methanol	116	∞	50	60	338	1
Ethanol	115	∞	34.8	18	351	3.4
Propanol	108	∞	26.7	-	371	-
Butanol	87	73,000	21.6	6.4	391	-
IB	Low	388	0	66	266	55
2M2B	91	190	0	15	304	85
2M1B	92	130	0	19	312	70
TBA	101	∞	21.6	10	356	1.1
TAA	97[c]	120,000	18.2	0.32[d]	375	-
TMP-1 and TMP-2	~100	0	0	1.56[d]	375	-
Hydrogenated C_5 dimer	95	-	0	0.5	420	-

[a]Hydroxyl reaction rate coefficient: $k \cdot 10^{12}$ $cm^3 \cdot molecule^{-1} \cdot s^{-1}$. [b]As (RON+MON)/2 was not available, MON is given instead. [c]Since (RON+MON)/2 was not available, RON is given instead. [d]Since blending Reid vapor Pressure was not available, vapor pressure at 293 K is given instead. [e]Estimated by Joback method.

Apart from overcoming the drawbacks of alcohols direct blending, the use of ethers as ETBE and TAEE presents many advantages. For instance, the ON of the gasoline pool increases by 2.0 RON octane points when blending 5.0 vol.% of EtOH, while it increases by 4.3 octane points when blending 15 vol.% ETBE and by 2.3 octane points when blending 15 vol.% of TAEE [36]. Besides, as bioethers do not contain aromatics, the heavy bioethers have a dilution effect on the amount of aromatic hydrocarbons in the gasoline/bioether mixture. Assuming that the mixture contains 35 vol.% in aromatics, when ETBE or TAEE are blended to gasoline in 15 vol.%, the total aromatics content drops to 30%. Moreover, using the problematic C_5 iso-olefins of a gasoline to produce TAEE, can result in a reduction of the olefin content of a gasoline from 32 to less than 18 vol.% [36]. Since ethers present lower oxygen content, they can be incorporated to gasoline in a higher proportion than alcohols without exceeding the maximum ruled oxygen content, what also contributes to extending the gasoline pool. In addition, it has been stated that ETBE and TAEE are also useful as cosolvents to make EtOH compatible with diesel, thereby making the range of application of ethylic ethers wider [14]. Finally, ethers present a higher

added value since they are quite unreactive and can be therefore used as efficient solvents for oils, paints, resins, dyes and hydrocarbons, and ethers with high boiling points can also be used as solvents in chemical reactions [15].

1.2.2 OTHER INTERESTING ADDITIVES

1.2.2.1 Tertiary alcohols

tert-Butyl alcohol (TBA) and *tert*-amyl alcohol (TAA) are produced by hydration of C_4 and C_5 iso-olefins. Apart from ethers and primary alcohols, these tertiary alcohols are also considered suitable additives for gasoline due to their low volatility and low atmospheric reactivity [37]. This is because the carbon linked to the oxygen atom does not contain any hydrogen, which is required to produce aldehydes during combustion. Besides, aldehyde emissions from ether combustion are lower in the presence of these alcohols [37], which makes these byproducts interesting up to a point since they can reduce harmful emissions from the combustion of gasoline-ether mixtures. Furthermore, solubility in water of both TBA and TAA is lower than that of lighter alcohols as well as their volatility and oxygen content, which are desirable attributes. As a result, a gasoline blended with a proper mixture of ethers and tertiary alcohols could improve the "cold driveability", in which aldehydes are produced, by making easier the vaporization and combustion of higher boiling point hydrocarbons of gasoline. In fact, as seen in Table 1.1, the European Directive 2009/30/EC allows gasoline with up to 15 and 22 vol.% content of TBA and ethers with 5 or more carbon atoms per molecule, respectively; the maximum oxygen content being up to 3 wt.%. In the U.S., the E.P.A. limits the maximum oxygen content to 2.1 wt.% for reformulated gasoline.

Summarizing, the option of adding tertiary alcohols to tertiary ethers for producing reformulated gasoline would entail the advantages of lower emissions and the prospect of using hydrated EtOH as a raw material. The main drawback would arise from the remaining water, since tertiary alcohols are synthesized in equilibrium-limited reactions and the etherification rates (catalytic activity) of industrial reactors would be strongly decreased by the presence of water.

1.2.2.2 C_4 and C_5 olefins dimerization products

As abovementioned, an interesting alternative to reduce the olefins content of a gasoline is via oligomerization. Propylene and butenes can be oligomerized to form high octane (RON up to 97) products in the gasoline boiling point range [38]. Despite not being oxygenates, hydrogenated dimers of IB and IA are also interesting chances as fuel additives because of their high octane rating and low water solubility [29,39,40]. For instance, 2,4,4-trimethyl-1-pentene (TMP-1) and 2,4,4-trimethyl-2-pentene (TMP-2), could be used as a feedstock to produce other high-octane gasoline components such as isooctane (2,2,4-trimethyl pentane) by means of the dimer hydrogenation or ethers like 2-methoxy-2,4,4-trimethyl pentane and 2-ethoxy-2,4,4-trimethyl pentane. However, the main market for isooctenes until now is the production of nonyl alcohol, which is used for synthesizing plasticizers [41]. In addition, dimers of IA present wide applications in the perfumery and flavor industry which makes these side products valuable [42]. The main drawback of oligomerization reactions is the control of selectivity toward products due to the high exothermicity of the process [43]. Moreover, an increase in the reaction temperature due to hotspots can easily lead to the formation of higher oligomers or waxes that eventually deactivate the catalyst.

1.2.3 FRAMEWORK OF TERTIARY ALKYL ETHERS PRODUCTION

Some tertiary alkyl ethers are already produced worldwide, namely MTBE, TAME and ETBE. Countries like China are opting for MTBE as the main oxygenate for being added to gasoline, whereas, in Europe, the production trends are different and they are expected to change in the forthcoming years. Table 1.3 summarizes the European fuel-ethers production capacities. Despite being currently the tertiary ether most widely produced, MTBE usage was banned in some states of the U.S., such as California, due to its toxicity, its water solubility and consequently, its potential danger of polluting freatic waters [44]. Besides, methanol and its derivative ethers (MTBE and TAME) are mostly derived from natural gas, contributing to global warming [45].

Table 1.3. European fuel-ethers production capacities 2011 (kT/y) [46]

	Production [kT/y]					
Country	MTBE	ETBE	TAME	TAEE	Planned	Total
Austria	65	0	0	0	0	65
Belarus	41	0	0	0	106	41
Belgium	270	183	0	0	0	453
Bulgaria	82	0	0	0	0	82
Croatia	0	0	0	0	24	0
Czech Republic	92	0	0	0	0	92
Finland	0	115	110	0	0	225
France	0	836	56	0	0	892
Germany	108	835	0	160	0	1103
Greece	110	0	128	0	0	238
Hungary	86	0	0	0	53	86
Italy	192	150	292	0	0	634
Lithuania	80	0	0	0	0	80
Netherlands	842	138	0	0	0	980
Poland	0	120	0	0	204	120
Portugal	0	50	0	0	0	50
Romania	220	0	0	0	0	220
Serbia	35	0	0	0	0	35
Slovakia	52	0	0	0	0	52
Spain	0	422	0	0	0	422
Sweden	0	50	0	0	0	50
Ukraine	24	0	0	0	0	24
United Kingdom	304	0	0	0	0	304

Ethanol derivative ethers as ETBE and TAEE, are considered bioethers and are the most promising fuel additives. ETBE production has experienced fast global growth in the last two decades, especially in Europe, due to the ease of revamping of existing MTBE plants. The cost of revamping an MTBE plant to ETBE is very low [36]. Most of unconverted MTBE and TAME units are located in Eastern Europe, United Kingdom and Italy. Nowadays, TAEE is not produced industrially at large scale, being only produced in Germany. Nevertheless, it could become an interesting alternative, since, as ETBE, TAEE can be obtained from bioethanol, and existing TAME plants can be easily revamped to TAEE. In fact, as the production of biofuels is expected to increase in the following years due to legislation constraints, it is likely that non-converted MTBE and TAME units will eventually be revamped to ETBE and TAEE, respectively. This will result in an important number of current TAME plants that will produce TAEE.

1.2.4 INDUSTRIAL PRODUCTION OF TERTIARY ALKYL ETHERS

There are several chemical pathways to produce tertiary alkyl ethers, namely tertiary olefins addition to primary alcohols and dehydration between primary and tertiary alcohols. ETBE is mainly synthesized at industrial scale through the liquid-phase reaction of IB present in C_4 streams from FCC or steam cracking (SC), with EtOH. This process is usually catalyzed by macroporous sulfonic acid resins at a temperature below 353 K under pressurized conditions [47]. Similar processes using the corresponding alcohol and source of olefins can be applied for producing MTBE, TAME and TAEE. Fig. 1.4 illustrates a typical integration of refinery MTBE/ETBE and TAME units. Another configuration for ethers production is the so-called "world-scale unit", with a typical capacity of 10 times that of a typical refinery MTBE unit. So far MTBE is the only ether manufactured in that huge scale plants [48].

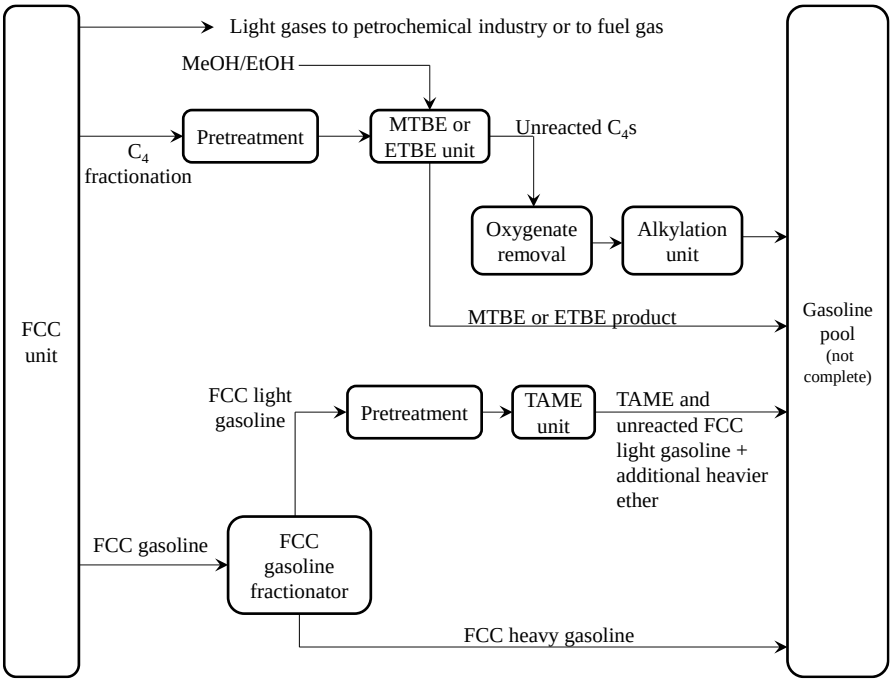

Figure 1.4. MTBE/ETBE and TAME processes in refinery connection [48].

The first MTBE units were built in the late 1970s and, since then, the basic configuration has not changed substantially. Fig. 1.5 illustrates a conventional unit, which has typically two reactors, a product distillation and a MeOH recovery section. Nevertheless, almost always a pretreatment section and an oxygenate removal unit for unreacted C_4 hydrocarbon are required. Such a configuration allows obtaining up to 96% of IB conversion, reflecting the equilibrium concentration between IB and MTBE. Since lower temperatures favor MTBE yield, such drawback is overcome by using two or three reactors in series. Most commonly used reactors are fixed bed catalytic reactors but tubular reactors with cooling water jackets are also extensively used [48]. The feedstock to these units is a C_4 fraction from the FCC unit. In world scale units, the feedstock usually come from SC process and it is more concentrated in IB, what implies the necessity of a higher accuracy in the control of the temperature in the reaction zone. MeOH and C_4 hydrocarbons form an azeotropic mixture in which MeOH concentration is 4%. As MeOH cannot be present in the subsequent units, a MeOH recovery unit is required. MeOH is separated from C_4 hydrocarbons in an extraction column where water is fed in the top section. Practically MeOH free hydrocarbon stream is obtained as the bottom product. Then, MeOH is separated from water by distillation and led back to the MTBE reactor whereas water is recycled

to the extraction column. As unreacted C_4s go to alkylation units where oxygenated must be avoided even in trace amounts, another purification section is required in which oxygenates are separated from C_4s via distillation or adsorption. The main disadvantage of using this process for ETBE production is that, since IB conversion in ETBE process is lower than in MTBE process, a larger water wash extraction unit is required and, therefore, an extra EtOH purification section is required. Water and EtOH cannot be separated by conventional distillation and recirculation of EtOH with water to the prereactor would increase the yield to byproducts, namely TBA.

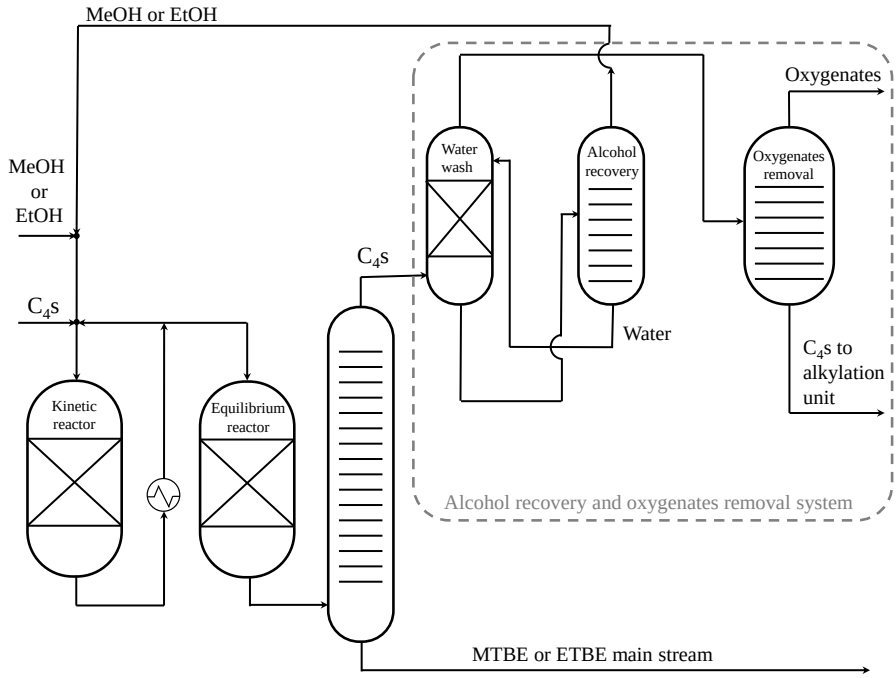

Figure 1.5. Conventional MTBE or ETBE process with integrated alcohol recovery and oxygenates removal system. Adapted from [48].

Reactive distillation or catalytic distillation can be used in processes in which selectivity and conversion are high enough that an additional separation step is not required, as MTBE or ETBE processes. However, the fixed bed prereactors have not been possible to eliminate so far. Fig. 1.6 illustrates a typical configuration of a reactive distillation plant. Reactive distillation technology units are interesting since, by means of assembling the catalyst in the product distillation column, the equilibrium limitations can be overcome and IB conversion can be increased up to 99%. However, most of MTBE plants integrated in refineries use the conventional process and the unreacted IB is fed to the alkylation units where it reacts with isobutane to form alkylates. On the contrary, reactive distillation technology is widely profitable in world scale units because they recycle unreacted IB in order to increase production and revenue. In addition to higher conversion, reactive distillation also provides energy savings because of the exothermic nature of etherification reactions. The released heat reduces the reboiler duty and thus the steam consumption, whereas it needs to be removed from fixed bed catalytic reactors. On the other hand, reactive distillation disadvantages are: i) the extra cost when adding the catalyst to the distillation column, since the column has to be specially designed for such purpose, ii) the need to maintain the desired alcohol to olefin molar ratio in the reaction zone to avoid large proportions of formed byproducts, and iii) the control of pressure in the column, which can also be a source of operational problems.

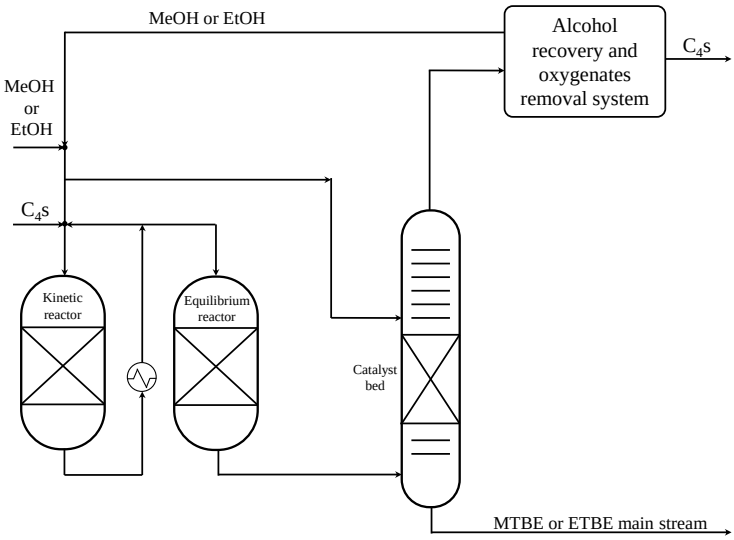

Figure 1.6. Reactive distillation MTBE or ETBE process

Reactive distillation has been widely used for MTBE process, nonetheless it can be applicable to ETBE or TAME processes but these are not as good candidates for reactive distillation. Despite equilibrium limitations of isoamylenes etherification reactions can be overcome by reactive distillation, catalyst contamination in TAME columns due to a larger presence of nitriles is a much bigger problem than in MTBE units. Combination of reactors and distillation units in series is a way to solve this problem, which is called reaction with distillation technology (Fig. 1.7). The main advantage is that this configuration does not require an extra alcohol recovery section. High conversion can be achieved by redirecting a side draw from the distillation column to the prereactor. Distillation column is not used to separate ether from unreacted hydrocarbons and MeOH, but to concentrate MeOH in the prereactor. This process cannot produce pure TAME without an additional distillation step, but as TAME is always produced for being used as gasoline component the bottom product can be considered a valuable product. In addition, nitriles, the main poison of the catalyst, are also concentrated in the bottom of the column so they are effectively removed from the process.

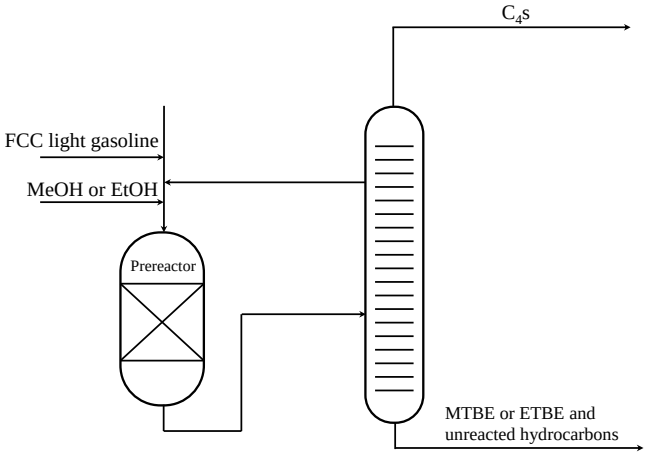

Figure 1.7. Reaction with distillation TAME process.

Based upon the described configurations, a number of commercial processes for MTBE or ETBE are available nowadays. Among them, Oxene (Hüls) process for ETBE, Institute Français du Pétrole (IFP) process for MTBE, Snamprogetti process for MTBE and TAME, ETHERMAX process, Texaco Process, Philips etherification process, NExTAME and NExETHERS processes, CDTECH process, CDMTBE, CDETHEROL [34,36,49] are the most important ones.

1.2.5 THE C_4 AND C_5 FRACTIONS FROM REFINERIES

C_4 and C_5 streams from SC and FCC units are significantly different in composition [41], see Table 1.4. In the processing of such streams, in particular for etherification, the first step is the recovery of dienes, which is carried out by selective hydrogenation. Afterwards, the streams are fed to several process units with the aim of recovering some components or producing new ones, e.g. distillation, adsorption or etherification. It is important that the olefinic fractions that are fed to etherification reactors do not contain dienes, because oligomerization of such very reactive compounds can lead to a swift catalyst deactivation via fouling [36].

Table 1.4. Typical composition wt.% of C_4 and C_5 fractions from FCC and SC [41].

C_4 Stream			C_5 Stream		
Component	FCC	SC	Component	FCC	SC
C_3s	0.5	0.3	C_4s	2.0	1.0
Isobutane	33.0	1.3	*n*-Pentane	5.5	26.0
Isobutene	18.0	27.4	Isopentane	31.5	24.0
1-Butene	12.0	16.0	*n*-Pentenes	22.5	4.5
1,3-Butadiene	-	37.0	Methyl-butenes	37.5	12.0
2-Butenes (cis & trans)	25.0	11.9	Cyclopentene	-	1.5
n-Butane	11.0	5.2	Isoprene	-	13.5
Acetylenics	-	0.4	Pentadiene and cyclopentadiene	-	16.5
C_5s	0.5	0.5	C_6s	1.0	1.0

In the etherification of industrial diolefins-free C_4 fraction over acid ion-exchange resins, IB is the most reactive component at the temperature range 323–353 K. The 1-butene, *cis*-2-butene and *trans*-2-butene react at higher temperatures and molar ratios alcohol to olefin lower than 1.3, whereas C_4 paraffins (butanes) do not react [50]. Concerning the C_5 fraction, only tertiary olefins react in the etherification reactions under the usual process conditions. The rest of olefins from the C_5 fraction, as well as paraffins or naphtenes, remain unreactive [51]. The typical composition of methylbutenes in a light C_5 cut from FCC comprises 12.5 wt.% of 2M1B, 3.5 wt.% of 3-methyl-1-butene (3M1B) and 21.5 wt.% of 2M2B. Among the three methylbutene isomers, 2M1B gives the fastest reaction, and 2M2B reacts 2-5 times more slowly depending on the alcohol. 3M1B does not react via carbocation formation because it does not have tertiary carbon and therefore no reaction take place with alcohol in the presence of resin catalyst.

Most of the IB used in Europe comes from FCC units (50%), from TBA dehydration units (20%) and from SC units (30%). Very few TBA dehydration and SC units are planned in the near future, so IB availability can be limited if the biofuels production increases. Though not currently, IA necessary for TAEE production could undergo similar constraints [8]. In order to counteract it, there are several proposals for increasing the C_4 and C_5 iso-olefins availability as skeletal isomerization of linear olefins using zeolite catalyst. Recent processes have shown that up to 44% of linear butenes can be converted to IB and up to 66% of linear pentenes can be transformed into IA [36]. However, special care must be taken with such technology since skeletal isomerization suffers from severe competition with cracking. A general scheme of such process is depicted in Fig. 1.8.

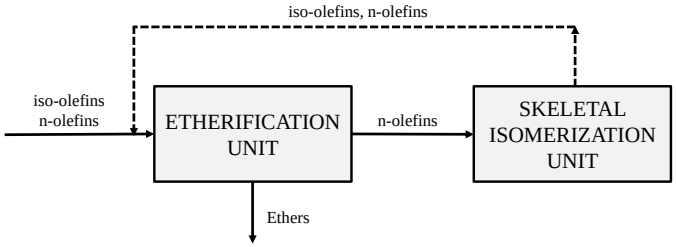

Figure 1.8. Configuration for increasing the C_4 and C_5 iso-olefins stock. Adapted from [36].

1.2.6 SIMULTANEOUS SYNTHESIS OF ETBE AND TAEE

Depending on technology, it is possible to combine MTBE and TAME units in a single unit, but that has not been done on a commercial scale so far [48]. Analogously, ETBE and TAEE production could be integrated in the same plant being therefore produced in the same reactor unit. As mentioned, gasoline oxygenated with ETBE and TAEE presents a low volatility that is certainly appropriate to be used in summer time or in tropical zones. Even in the cold season, C_4 hydrocarbons can be blended with such oxy-gasoline to get an easy startup of the engine. This flexibility offers a top position in any choice of a gasoline producer, particularly compared to direct blending of alcohols [52,53]. Simultaneous production of ETBE and TAEE can be regarded as an interesting one-pot synthesis from an environmental point of view, because it is a versatile process that allows processing the excesses of C_4 and C_5 fractions in the separation units from refineries. Indeed, many refineries have FCC or SC units, which produce mixed C_4 and C_5 olefinic streams that would be useful as direct feed stream to the simultaneous etherification unit. Fig. 1.9 represents a possible scheme for the simultaneous production of ETBE and TAEE. Apart from using bioethanol and reducing the harmful C_5 isolefins content in fuel, the simultaneous production of ETBE and TAEE brings about the versatility to adapt production targets depending on either the desired final fuel volatility or the refinery needs [46]. Moreover, the simultaneous process could constitute the integration of two etherification processes at industrial scale with the advantages derived from process optimization, integration and intensification such as savings at installation, operation and maintenance costs.

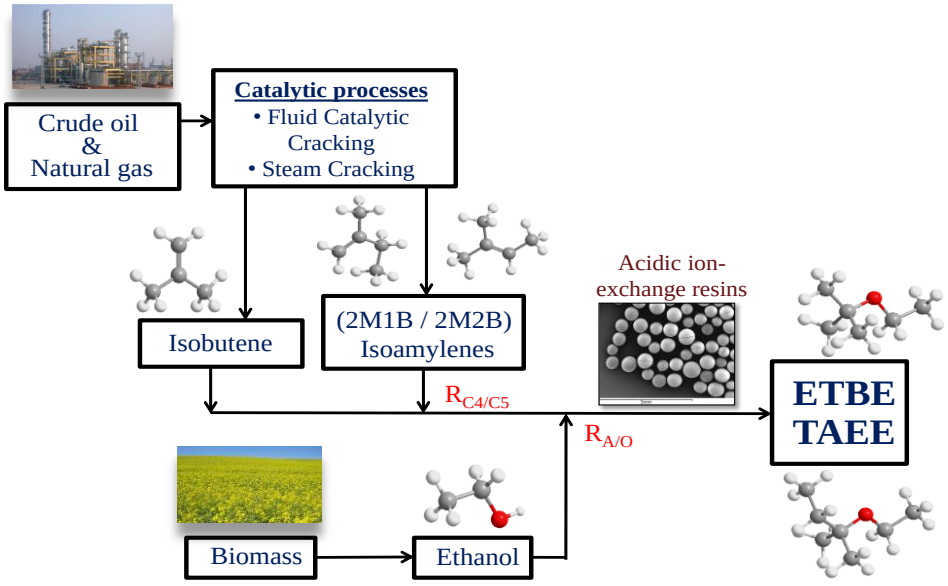

Figure 1.9. Schematic representation of a possible industrial pathway for the simultaneous production of ETBE and TAEE. $R_{A/O}$=alcohol to olefins molar ratio. $R_{C4/C5}$=IB to IA molar ratio.

As the availability of IB in refineries is limited, it can be a constraint for increasing biofuels production. On the other hand, C_5 iso-olefins are available in most of refineries with an FCC unit. In this sense, when the IB supplying is threatened, the possibility of increasing the production of TAEE within the same plant, adapting therefore the production targets to particular circumstances, will be advantageous for refiners [36]. Furthermore, MTBE, TAME and ETBE existing plants could be easily readapted toward a new simultaneous production target by revamping. Another potential of such etherification plant, resides in the possibility of using ETBE, TAEE and EtOH (in lower extent than ethers) together for direct blending with gasoline what would reduce the number of downstream required separation units.

1.3 GREEN CHEMISTRY AND CATALYSIS

The next phase of the process for designing a more efficient and sustainable chemical industry will be the successful application of green catalytic technologies in the synthesis of organic chemicals, such as fuels and other commodities, from renewable resources. The challenge in heterogeneously catalyzed processes is driven by the need for selective chemistry, with high reaction yield and few side reactions. The existence of competing routes makes the choice of the catalyst, raw materials and experimental conditions crucial steps to design and develop chemical processes as efficiently as possible. Many environmental and chemical factors must be considered simultaneously when selecting a synthetic route [10,11]. At the first step of development, the so-called "Green Chemistry Metrics", is a very useful tool to properly lead decisions about the process design [12,13]. The metrics can be used during route (chemical pathway) selection, to compare between several options according to green principles, chemical and energetic efficiencies, since much deeper insights are gleaned about synthesis strategy if metrics are used. The Green Metrics Analysis (GMA) constitutes itself a quantitative methodology to test the material and strategy efficiencies of a proposed plan against prior published plans at the chemical route selection design stage [58].

The concept of green chemistry metrics and methodology actually deals with reaction optimization with respect to materials and energy use, waste reduction from all sources and overall cost minimization [59]. There are also included aspects on minimization of toxicity, hazards, corrosion and the maximization of safety practices. When analyzing the Green Metrics related to a process, there are several graphical methodologies to evaluate the metrics as a visual display of the analysis results. For instance, the percentage kernel and the percentage total waste distribution profiles, the reaction yield profile, the reaction mass efficiency profile, the synthesis tree diagram and the radial pentagons (see Fig. 1.10) related to each step of the process [14].

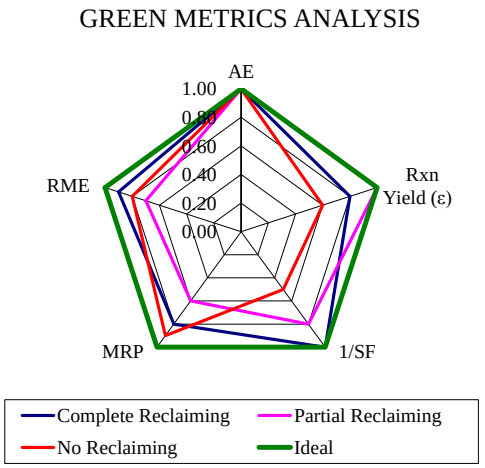

Figure 1.10. Example of the radial pentagons obtained from the analyses of different situations for a given process.

The GMA presents some important applications, such as to compare a new synthesis with other published plans with respect to material efficiency and cost, to highlight, to compare, and to

contrast strategy and material efficiencies of various approaches. It is also a useful methodology to optimize a procedure or an entire synthesis plan and as a way of tracking progress for industrial chemists and, to know the best route according to material efficiency, cost, and safety. By their application, chemists can improve their awareness of environmental issues related to new products as well as to existing ones. In this purpose, the radial pentagon analysis that leads to calculations of green metrics is of invaluable help in assessing reaction "greenness". This methodology is extremely important and educational for scientists as it is instructive in teaching chemistry students how to critique plans and in ultimately choosing the best possible synthetic approach [58].

The GMA results therefore in a useful technique to identify the best chemical pathway. It is also a tool to evaluate whether the process needs to reduce reaction solvent usage, to avoid using excess reagents, except when there is a chemical reason (as in driving equilibria toward product), to select lower-mass reagents or to select a different catalyst. It also allows determining whether the process needs to optimize the reaction yield by tweaking such parameters as reaction time, reaction temperature, reaction pressure or the use of catalyst.

So far, there are no evidences of studies comparing the inherent green chemistry of the different options that emerge from bioethers synthesis, more specifically regarding the simultaneous production of several ethers in the same process. This is interesting and necessary, not only to obtain numerically pondered information about the greenest pathways, but also to compare processes, feedstocks and toward the design of new technologies that improve the process efficiency.

1.4 HETEROGENEOUS CATALYSIS FOR ETHERIFICATION

1.4.1 FUNDAMENTALS

The main function of a catalyst is to decrease the activation energy of a chemical process. The use of catalytic materials plays a fundamental role in the production of many chemical products as methanol, sulfuric acid, ammonia, polymers, plastics, fuels, paintings, etc. It is estimated that approximately 50% of current industrial chemical production processes are based on catalytic reactions. Among them, heterogeneous catalysis represents the 80%. The importance of reactions catalyzed by solids is huge since it accounts for the 90% of the heterogeneously catalyzed processes. Tertiary alkyl ethers production using ion-exchange resins is an important example of industrial heterogeneous catalysis, because it is a widely applied process to obtain high performance additives for fuels.

The first catalyst used for tertiary alkyl ethers production was sulfuric acid [60]. However, the use of solid catalysts was rapidly imposed. Besides the undoubtable economic factor that justifies the use of solid catalyst instead of liquids, the main advantages of using solid catalyst are:

- To diminish the corrosion of the different parts of the industrial plants.
- Ease for separating products from the catalyst.
- Less pollution potential of waste streams.
- Ease for recycling the catalyst.
- Reaction rates and selectivity can increase by the use of solid catalysts.

The design of a solid catalyst constitutes a wide and crucial part of the field of heterogeneous catalysis. The aim is to optimize the catalytic, chemical, physical and mechanical properties of the solid catalyst [61]. Among catalytic properties, activity, selectivity and catalyst lifespan are the most relevant. Chemical composition, actives sites concentration and acidity are examples of chemical properties. Finally, a good catalyst must present mechanical and thermal resistance, suitable pore volume, pore distribution, particle size and shape.

1.4.2 KINETICS AND THERMODYNAMICS OF SOLID SURFACES

The most common type of heterogeneous catalysis entails reactants in liquid or gas-phase, which are in contact with the solid catalyst. It is mandatory that at least one reactant or fluid phase interact with the catalytic surface. To achieve it, the specific surface area and pore volume distribution must be suitable to allow diffusion of reactants and products within the catalyst matrix. Accordingly, several steps are involved in the catalytic process. Fig. 1.11 illustrates one of the most used physical models to represent the catalytic process for the reversible reaction A ⇄ B, in which the following stages can be distinguished:

I) External mass transfer (EMT) of reactants from bulk fluid phase to the external catalyst surface through the external film layer.
II) Internal mass transfer (IMT) or diffusion of reactants through the catalyst pores.
III) Adsorption of reactants on the active sites.
IV) Chemical reaction between adsorbed species or between adsorbed species and those in the fluid phase. The adsorbed chemical product is obtained in this step.
V) Desorption of products.
VI) Internal mass transfer (IMT) or diffusion of products through the catalyst pores to the external catalytic surface.
VII) External mass transfer (EMT) of products from the external catalyst surface to the bulk phase through the external film layer.

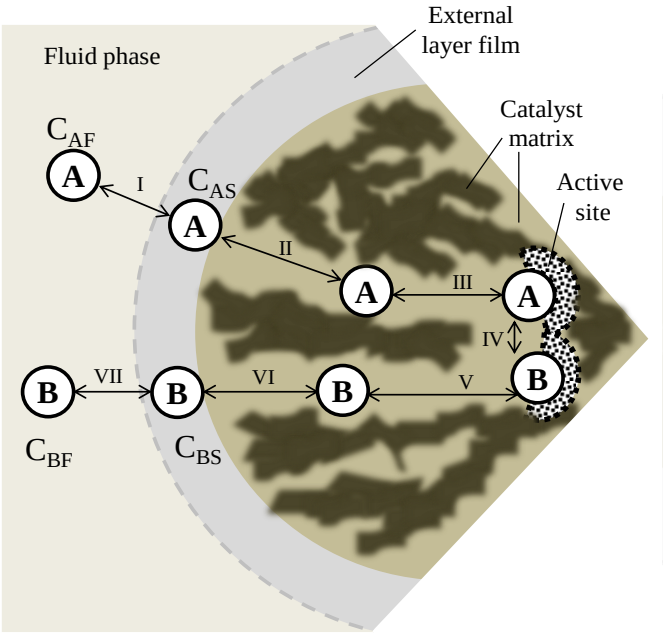

Figure 1.11. Steps of the catalytic process for reaction A ⇄ B in a porous solid. C_{AF} and C_{AS} are the concentrations of A in the fluid phase and on the catalyst surface, respectively. Analogous meaning for C_{BF} and C_{BS}.

In the described catalytic model for a porous solid, steps III, IV and V are of chemical nature, whereas steps I, II, VI and VII are of physical nature and they include IMT and EMT effects. In a kinetic model, it must be considered that steps I, III, IV, V and VII take place in series and steps II and VI take place in series parallel with the previous ones. Besides, it must be taken into account that diffusion of involved chemical species in steps II and VI, being known as intraparticle mass transfer phenomena, whose rates are usually expressed in terms of effective diffusivities of involved species. As diffusivity of reactants within the catalyst pores is different, some molecules may be reacting while other are still diffusing what makes the catalytic process a complex problem of simultaneous chemical reaction and diffusion.

As for the implicit kinetics of the elementary steps III, IV and V of chemical nature previously described for a reversible reaction A ⇄ B, they can be treated by the thermodynamic transition state theory (TTST) [48]. The conventional transition state theory is based on the potential energy surface for a reaction and involves the following postulates: (i) the reacting system in traversing from the initial to the final state passes through a region called the transition state corresponding to the highest potential energy surface in its path; (ii) the species corresponding to the transition state, the transition state complex (TSC), is assumed to be in dynamic equilibrium with the reactants; and (iii) the rate of product formation is proportional to the product of a universal frequency and the concentration of the TSC. According to this, each step is assumed to possess its own TSC.

Adsorption of reactants (Eq. 1.1) and desorption of formed products (Eq. 1.3) are usually assumed to be rapid compared to the surface reaction step (Eq. 1.2). The adsorption and desorption equilibrium constants $K_a=k'_a/k_a$ and $K_d= k'_d/k_d$ can be expressed by means of the standard Gibbs free energy change associated with each process, which indeed are of similar nature based on the principle of microscopic reversibility. As for surface reaction, it can be as well expressed by the equilibrium constant of reaction $K_r=k'_r/k_r$, which is a function of the standard Gibbs free energy change of the reaction. Fig. 1.12. illustrates the reaction coordinate diagram for such elementary steps in the example reaction A ⇄ B (exothermic).

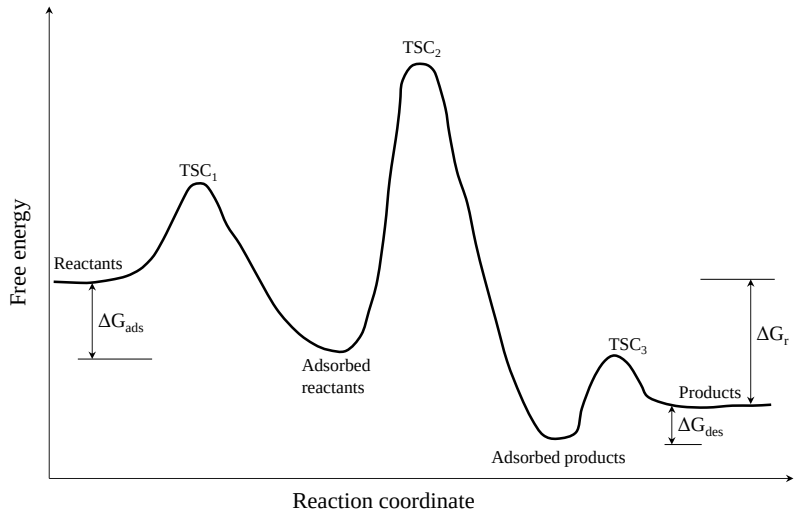

Figure 1.12. Reaction coordinate diagram for a chemical catalytic reaction involving elementary steps of adsorption, surface reaction and desorption, each involving a transition-state complex (TSC) at the point of highest free energy. Adapted from [48].

$$A+S \underset{k'_a}{\overset{k_a}{\rightleftharpoons}} AS \qquad (1.1)$$

$$AS \underset{k'_r}{\overset{k_r}{\rightleftharpoons}} BS \qquad (1.2)$$

$$BS \underset{k'_d}{\overset{k_d}{\rightleftharpoons}} B+S \qquad (1.3)$$

Though a catalyst affects the kinetics of a process, it does not present any influence on the chemical equilibrium or final point of a reversible reaction, since this is only related to the thermodynamic state functions of involved reactions. In other words, chemical equilibrium is independent of the catalyst used to reach it but not the time required to reach equilibrium conditions.

1.4.3 ADSORPTION AND DESORPTION PROCESSES

IUPAC defines the adsorption process as the increase in the concentration of a substance at the interface of a condensed and a liquid or gaseous layer owing to the operation of surface forces. This process is a surface phenomenon and creates a film of the adsorbate on the surface of the adsorbent. Adsorption can be physical or chemical (chemisorption). The former involves only relatively weak intermolecular forces, whereas chemisorption involves the formation of a chemical bond between the sorbate molecule and the surface of the adsorbent [62]. Though this distinction is conceptually useful, there are many intermediate cases and it is not always possible to categorize a particular system unequivocally. Table 1.5 summarizes some general features which distinguish physical adsorption from chemisorption with gases. Physical adsorption is useful in catalysis because it allows the determination of some catalytic properties as surface area, porosity and pore distribution. On the other hand, chemisorption is of paramount importance because chemical reactions taking place on solid catalytic surfaces involve the chemisorption of one or more reactants as intermediate step in the catalytic process. Usually, chemisorption rate is fast enough above a threshold temperature, so it is called activated chemisorption (non-null activation energy). Finally, both types of adsorption are exothermic processes, however, though rarely, chemisorption may be endothermic since in some systems, adsorption equilibrium constants of species may increase with temperature [63]. When adsorption equilibrium constants increase with temperature, it must be greeted suspiciously because adsorption coefficients are very likely a ratio of kinetic coefficients.

Table 1.5. Specific features for the different types of adsorption [62].

Physical adsorption	Chemisorption
• Low heat of adsorption (<2 or 3 times latent heat of evaporation)	• High heat of adsorption (>2 or 3 times latent heat of evaporation)
• Non specific	• Highly specific
• Monolayer or multilayer	• Monolayer only
• No dissociation of adsorbed species	• May involve dissociation
• Only significant at relatively low temperatures	• Possible over a wide range of temperatures and significant above a threshold temperature
• Rapid, non-activated, reversible	• Activated, may be slow and irreversible
• No electron transfer though polarization of sorbate may occur	• Electron transfer leading to bond formation between sorbate and surface

The relation at constant temperature between the amount of adsorbed compound on a solid surface and its concentration in the fluid phase is known as adsorption isotherm. Langmuir, Freundlich and Temkin isotherms are three classical isotherms usually found in the literature and they can be applied for both physical and chemical adsorptions when the process is reversible and the adsorption equilibrium can be reached. Eqs. 1.4, 1.5 and 1.6. are their respective mathematical expressions for the adsorption of the species A. Due to its simplicity, the Langmuir isotherm has been widely applied in the development of kinetic expressions for reactions catalyzed by solids. Langmuir isotherm is based upon the following assumptions [62]: i) the solid surface is energetically uniform, in other words, the free energy change is the same for all the adsorbed molecules of the same species, ii) adsorption is monolayer, iii) adsorption rate per active sites is uniform what is to say that there are no interactions between adsorbed molecules, iv) the heat of adsorption is independent of the surface coverage and, v) the extent of adsorption is lower than one complete monolayer on the surface.

$$\theta = \frac{K_A C_A}{1 + K_A C_A} \tag{1.4}$$

$$\theta = k' C_A^{1/n} \tag{1.5}$$

$$\theta = (1/f) \ln A_0 C_A \tag{1.6}$$

Langmuir isotherm, which only has the adsorption equilibrium constant of the species as the parameter to estimate, is usually accurate enough. Nonetheless, the higher number of parameters of Freundlich and Temkin isotherms usually lead to a better fit of real systems. Determination of adsorption equilibrium constants of involved species in etherification systems has been usually carried out by non-linear least square regression as the estimates of proposed kinetic equations. However, the experimental determination of such parameters is possible by means of the moment techniques [64–67] in either liquid- or gas-phase. This is important not only to assess how prone a chemical species is to be adsorbed on the catalyst surface, but also to contrast the information obtained when fitting kinetic equations. Once the adsorption equilibrium constants are known, the adsorption thermodynamic state functions, heat and entropy of adsorption, can be obtained by the van't Hoff plot. The main limitation of the adsorption parameters that can be derived from the moment techniques is that linear adsorption relation (Henry's law) between the fluid phase and adsorbed concentrations of the tracer is assumed.

1.4.4 INTERNAL AND EXTERNAL MASS TRANSFERS (EMT & IMT)

External mass transfer (EMT) is due to the existence of temperature and concentration profiles within the external film layer that surrounds the catalyst particle immersed in a fluid phase. The magnitude of these profiles and their effect on the reaction rate must be considered for designing catalytic reactors. Analogously, as reaction take places on the inner surface of catalyst pores, diffusion of reactants and products through the catalyst pores also affect the observed reaction rates. This phenomenon is known as internal mass transfer (IMT) and it is originated by temperature and concentration gradients from the catalyst surface toward the inner parts of the porous catalyst. The temperature and concentration profiles that are expected for an exothermic reaction as a consequence of the EMT and IMT are depicted in Fig.1.13.

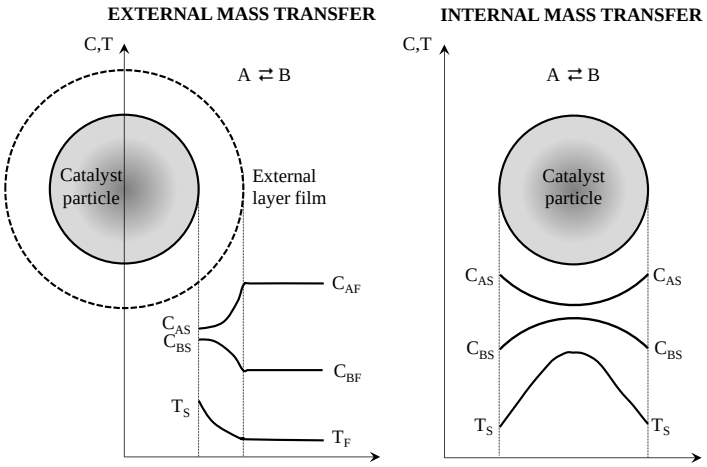

Figure 1.13. Temperature and concentration profiles along the external film surrounding the catalyst particle (left) and within a spherical particle (right) for the exothermic reaction A ⇄ B.

The study of the EMT effects on reaction rates depends upon the used device in the experimental practice. If a batch reactor is considered, these effects are inversely proportional to the stirring speed (see Fig. 1.14a). For a fixed bed reactor, the effects of EMT on reaction rates are reduced as the volumetric flow or the space velocity increases (see Fig. 1.14b). The liquid hour space velocity (LHSV), defined as the quotient of the volumetric flow to reactor volume, is often used for liquid-phase reactions. Concerning the study of the effects of IMT on observed reaction rates, it is generally assumed that the influence of IMT is less noticeable as the catalyst particle diameter decreases, since the intraparticle way that molecules have to travel is shorter (see Fig. 1.14c). Finally, it is to be noted that the effects of both IMT and EMT are more noticeable as reaction temperature increases. Ion-exchange resins used as catalyst for etherification reactions are one example of catalyst showing IMT limitations when commercial particle sizes are used.

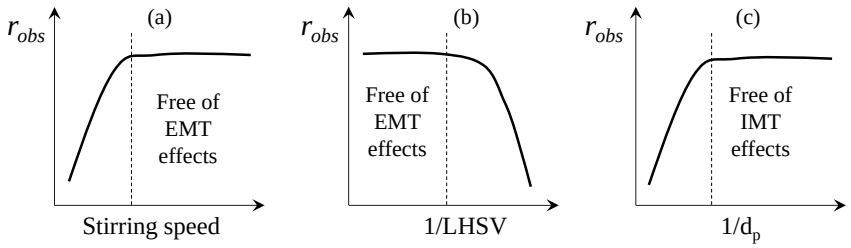

Figure 1.14. Typical reaction rate profiles in the experimental study of EMT in: (a) a stirred tank batch reactor or, (b) a fixed bed reactor. (c) Rate profile in the experimental study of IMT.

1.4.5 SURFACE REACTION

The surface reaction is often the rate determining step (RDS) in reactions taking place on solid catalysts. Proposed kinetic models and derived kinetic equations usually consider that the solid surface contains a fixed number of active sites, that all active sites are identical and that their reactivity does not depend on the quantity and nature of the rest of compounds present on the solid surface but only on temperature. Kinetics of tertiary alkyl ethers formation have been traditionally explained by means of the classical models of heterogeneous catalysis, those described by the Langmuir-Hinshelwood-Hougen-Watson (LHHW) and by Eley-Rideal (ER), see Fig. 1.15. In the former, all reactants are adsorbed on the active sites, they react with each other to produce the adsorbed product that eventually desorb from the catalytic surface. In the

ER mechanism, at least one reactant is adsorbed on the catalytic surface and it reacts with other reactant molecule present in the bulk-phase to form the adsorbed product that later desorb from the active sites [19].

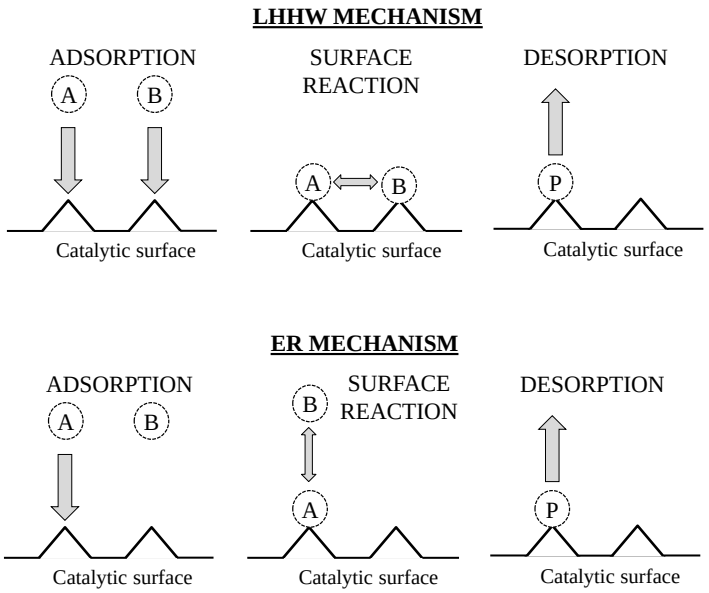

Figure 1.15. Schematic representation of LHHW and ER mechanisms for A+B⇄P reaction.

For both types of mechanisms, in the absence of IMT and EMT effects, the general procedure for obtaining a reliable kinetic equation consists in proposing a RDS (adsorption of reactants, surface reaction or desorption of products) and then developing kinetic equations that consider relevant or not the adsorption some of the involved species and the number of free active sites [63]. It is worth mentioning that several kinetic models can explain experimental data with accuracy and that all of them are usually based on the same structure: a kinetic term, a driving force term, reaction medium-catalyst affinity term, and an adsorption term. It is therefore mandatory to check all possible models that fit experimental rate data since they allow drawing conclusions about the actual mechanism taking place and about the implicit thermodynamic of the catalytic process.

1.5 STYRENE DIVINYLBENZENE RESINS AS CATALYSTS

1.5.1 SYNTHESIS OF STYRENE DIVINYLBENZENE RESINS

Ion-exchange resins (IER) are solid organic materials composed by a skeleton or polymeric matrix formed by hydrocarbon chains joined together that constitutes a tridimensional structure of hydrophobic nature in which functional groups, normally of hydrophilic nature, are anchored. As a result of the structural characteristics, resins are insoluble in solvents that do not induce the break of the carbon-carbon bonds of the matrix.

One of the most common type of ion-exchange resins are polystyrene-divinylbenze (PS-DVB) resins. But other aromatic vinyl compounds, such as vinyl toluene, vinyl naphthalene, vinyl ethylbenzene, methyl styrene, vinyl chlorobenzene, and vinyl xylene, can be used as co-monomers in the manufacture of polystyrene-based resins. PS-DVB resins are synthesized by the suspension or copolymerization of styrene (addition) and dinivylbenzene. It is carried out by

the dispersion in form of drops of a mixture of monomers insoluble in water by the introduction of a radical free generator that acts as initiator. Optimization of the suspension polymerization depends on several factors, such as the composition of the monomeric mixture, the type of initiator of radicals, the stirring speed, the reactor shape and size, the amount and nature of the emulsifier agent, the reaction time, etc. Styrene polymerization in the presence of at least a small amount (1%) of a divinylic compound, as 1,4-divinylbenzene (DVB) creates a cross-linked polymer insoluble in common organic solvents [68]. Though the crosslinking is a complex phenomenon, DVB typically acts as crosslinker between two linear chains of polystyrene.

The mechanism of copolymerization by addition, also called vinyl polymerization, is a free radical induced polymerization between reactants (monomers) carrying ethenyl (or vinyl) double bonds (-CH=CH_2). One of the reactants must contain at least two ethenyl double bonds to effect crosslinking. The extent to which the copolymer is crosslinked depends upon the proportion of crosslinking agent (DVB) used in the synthesis and has a pronounced impact upon both the mechanical and chemical behavior of the derived ion-exchange resin [68]. The miscible monomers, ethenylbenzene (styrene) and diethenylbenzene (DVB) undergo a free radical copolymerization reaction initiated by benzoyl peroxide catalyst. The exothermic reaction is carried out in an aqueous suspension whereby the mixed monomers are immiscibly dispersed as spherical droplets throughout the reacting medium resulting in discreet beads of copolymer formed. Correct reaction conditions and the use of suspension stabilizers enable the control the particle size distribution. Finally, functionalization (activation) of such supports provides catalytic activity to the resins. Fig. 1.16 depicts the usual reaction scheme for the production of a sulfonated PS-DVB resin.

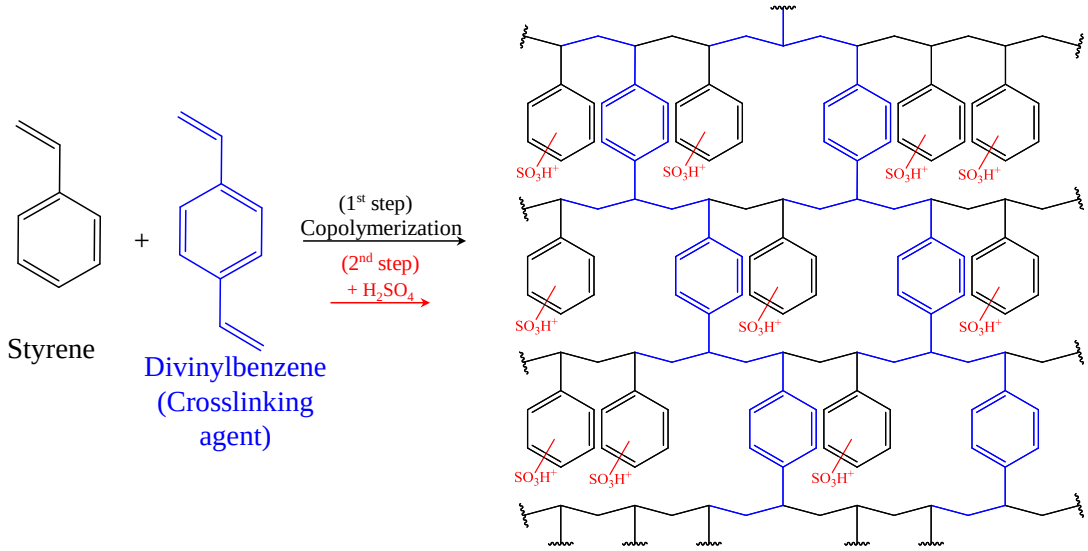

Figure 1.16. Schematic representation of the synthesis pathway and final structure of an acidic ion-exchange resin.

Depending on the foreseen application, functional groups can be acid, basic, redox or even metallic complexes (transition metals) [69]. Acidic ion-exchange resins are usually functionalized with sulfuric acid between 90 and 140 °C. Sulfonic groups (-SO_3H) are therefore the functional groups eventually incorporated to the resin backbone giving a strongly acidic cation exchange resin (see Fig. 1.16). However, different functional groups can be used to give particular properties to the catalyst, for instance, electron attracting groups such as halogens atoms can be used to enhance thermal resistance [70]. For example, perfluoritaned resins are stable up to 210 °C.

1.5.2 CLASSIFICATION OF SULFONIC STYRENE DIVINYLBENZENE RESINS

Two main types of porous structures can be created as a result of the porogens and the amount of crosslinking agent (DVB) used during polymerization: microporous and macroreticular matrixes. The former is a closed-cell, also called gel-phase, containing micropores, whereas macro-reticular resins present an open-cell with permanent macropores apart from the gel-phase [71], see Fig. 1.17. Macroporous resins consist of large agglomerates of gel microspheres with smaller nodules (10-30 nm) than microporous resins that are fussed together forming permanent meso and macropores.

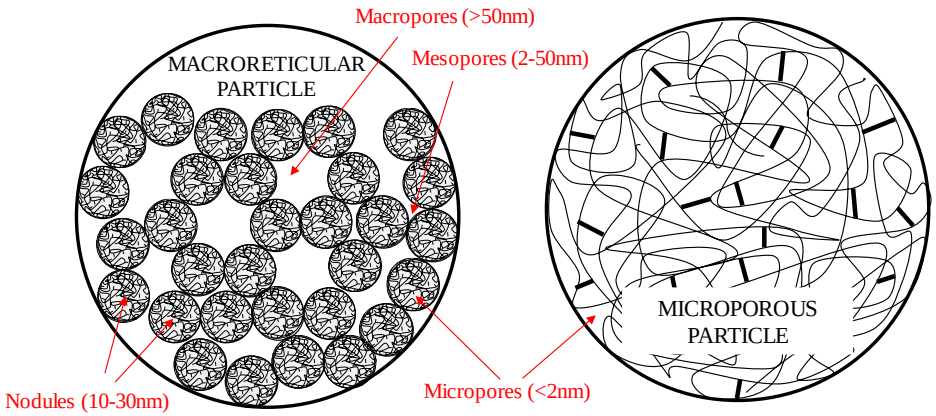

Figure 1.17. Simplified representation of macroreticular and microreticular particles of a PS-DVB resin. – Polystyrene chain. ▬ Divinylbenzene crosslink.

On one hand, microporous or gel-type resins are low crosslinked (1-8% DVB) solids with low surface areas in dry state (< 1 m^2/g) and without permanent porosity. Their pores, referred to as micropores, are very small (0.7 to 2 nm) [72] and only appear in the swollen state. On the other hand, macroporous resins are obtained when the polymerization of styrene is carried out with 5-60 %DVB and in the presence of diluents, such as *n*-heptane, acting as porogens. During the polymerization, phase separation occurs and, after the extraction of the diluent and drying, permanent pores of various sizes are created. Macropores are permanent and can be detected by adsorption-desorption of N_2 at 77 K. For this type of resins, the surface area increases with the %DVB, unlike for microporous resins [73].

1.5.3 PROPERTIES OF STYRENE DIVINYLBENZENE RESINS

As organic polymers, resins properties depend on the nature of the monomer, the polymerization method, the crosslinking degree and the nature of the functional groups anchored to the polymeric matrix that confer catalytic activity. The catalytic activity and selectivity of an IER depends upon a wide array of properties such as the acid or basic strength, the structure, active sites concentration and their accessibility, the structure of pores and distribution, the degree of swelling that eventually affect the IER structure, and the ease of diffusion of involved species. The most relevant properties of IER and how they can be determined are explained below.

- **Functionalization degree.** It represents the percentage of aromatic rings that have been functionalized.

- **Ion-exchange capacity.** It is expressed as the number of functional group that the resin is able to introduce in ion-exchange reactions. It is usually measured as miliequivalents of functional group per dry gram of resin, e.g. meqH^+/g for sulfonic IER. It can be determined by titration against a standard base for the case of acidic IER [74]. As Fig. 1.18 illustrates, the typical distribution of the sulfonic groups throughout the diameter of a resin particle suggests that the sulfonation degree proceeds from the outer parts of the polymer to the inner layers. It is accepted that the maximum exchange capacity (q_{max}) of a medium crosslinked matrix is above 4.5 meq[H^+]/g, which corresponds to one sulfonic group per styrene ring [75]. Such resins are typically known as conventionally sulfonated resins. Sulfonation below this limit produces surface sulfonated materials and sulfonation beyond this limit gives an oversulfonated material (more than one sulfonic group per styrene ring).

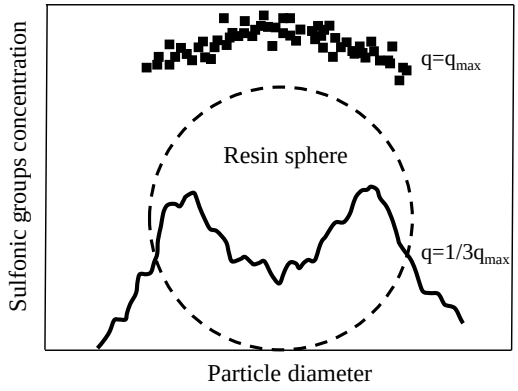

Figure 1.18. Distribution of sulfonic groups in a resin sphere for different ion-exchange capacities. q_{max}= 4.5 meq/g, q=exchange capacity. Adapted from [75].

- **Crosslinking degree.** It indicates the weight percentage of crosslinking agent respect to the total weight of monomers before carrying out the copolymerization. It is usually expressed as "%DVB". Ion-exchange capacity, moisture and swelling degree increase as the crosslinking degree decreases. Besides, it must be considered that for resins with relatively high crosslinking degree (10-15%) some mass transfer limitation can take place since the number of active sites that are accessible in non-polar media is drastically reduced. Furthermore, the resin stiffness and its mechanical resistance increase as the crosslinking degree increase.

- **Porosity (θ).** The intrinsic porosity of an IER is associated with the hollows that remain between the polymer chains forming the matrix. It depends on the crosslinking degree since more porous resins and less dense are those with low crosslinking degree. It also depends on the nature of the reaction medium, for instance, gel-type resins do not present porosity in anhydrous media but they do in polar media. On the contrary, macroreticular resins present permanent porosity even in anhydrous conditions.

- **Surface area or specific area (S_g).** It is the total surface of the particle (external and pores) per gram of dry solid. As for porosity, the surface area of a dry resin increases with the crosslinking degree for macroreticular resins up to %DVB $\leq$ 20. It is usually determined by the adsorption-desorption of N_2 at 77K by means of the Brunauer-Emmet-Teller (BET) method, however, it can be determined by other techniques as mercury intrusion porosimetry.

- **Pore Volume (V_g) and pore distribution.** It is defined as the volume of pores per gram of dry solid. Depending on the pore size or pore diameter (d_{pore}) the following pore distribution can be distinguished: micro (<2nm), meso (2nm<d_{pore}<50nm) or macropores (>50nm). Pore volume is usually determined by N_2 adsorption at 77 K and P/P_0=0.99 and the pore distribution by the Barrett-Joyner-Halenda (BJH) analysis of N_2 desorption curve.

- **Stability.** Resins stability is a property of utmost importance since as catalyst they must remain operative for long lasting periods. IER must show chemical, thermal and mechanical stability. These properties are strongly influenced by the structure, crosslinking degree, amount and nature of functional groups.

  - **Chemical stability.** At highly oxidizing conditions, as under chlorine or chromic acid presence, the resin matrix can be irreversibly affected losing ion-exchange capacity. For PS-DVB resins, these agents destroy the bonds between polystyrene chains reducing the reticulation of the resin.

  - **Thermal stability.** It depends on the resin structure and on the crosslinking degree. Macroporous resins are generally less stable than microporous ones. Besides, conventionally sulfonated IER are less thermally stable than oversulfonated ones. A suitable technique to assess the thermal stability of a resin is thermogravimetric analysis (TGA) where the thermal resistance of anchored sulfonic groups as well as of the polymeric matrix can be observed.

  - **Physical or Mechanical stability.** It is defined as the IER resistance to attrition or osmotic shock. Generally, macroreticular resins are more resistant than gel-type resins. Moreover, the less elastic resins (those with high crosslinking degree) are more fragile and they are more easily broken.

- **Density or skeletal density (ρ_s).** It is defined as the weight of dry resin per unit of volume of solid. It depends on the resin structure, crosslinking degree, nature and amount of functional groups. It can be accurately determined by Helium displacement. The density of the IER determines the fluid dynamic behavior in upward flow fixed beds or in countercurrent flow systems. For practical purposes, the apparent density (ρ_p) of a particle is commonly used being always lower than skeletal density. It can be calculated by means of Eq. 1.7. Typical values of ρ_p for IER are from 1.1 to 1.55 g/cm^3.

$$\rho_p = \rho\left(1-\theta\right) \qquad (1.7)$$

- **Moisture content.** It is defined as the ratio of the weight of water within the resin to the total weight of hydrated resin. IER contain some water linked to the structure due to the hydrophilic nature of the active sites. They can also contain non-linked water on the surface. The amount of water retained in a resin depends on the nature and amount of active sites, as well as on the density of the polymeric matrix that allows the resin capture water until osmotic forces are compensated. It is observed that the capacity of capturing water of a resin decreases as the crosslinking degree increases. One effective method for measuring the moisture of an IER is by Karl Fisher titration method.

- **Particle size.** A Gaussian-like particle size distribution is obtained when a resin is synthesized. From such distribution some interesting properties can be derived as kurtosis, mean particle size, uniformity coefficient, etc. Generally, acidic PS-DVB resins present mean particles diameters from 0.2 to 1.2 mm. One useful technique to determine the particle size distribution is by Laser diffraction in different mediums, such as in air, or in different liquid solvents as alcohols.

- **Swelling degree.** IER are known to swell, being the swelling more pronounced in polar solvents as water or alcohols. Several factors are involved in the swelling phenomenon as the temperature, the chemical nature of the solvent (polar or non-polar), the resin crosslinking degree, the nature of the functional groups and its concentration [76,77]. Generally, it can be said that the higher the crosslinking degree the lower the resin swelling. Surface area and porosity increase with swelling. In a reactor of limited volume, the advantages of loading a catalyst swelled in low extent are obvious in terms of yield. When resins are transferred from one medium to another a change in the volume of the beads is produced, caused by the difference between the osmotic pressure within the resin and the fluid pressure that tend to equalize.

As it is well known, morphology of macroreticular resins can be modified as a result of swelling in polar media with the development of non-permanent meso and macropores. Conventional porosimetric methods as mercury intrusion or nitrogen adsorption-desorption (BET technique) are seldom used since they provide information about dry catalysts [78]. A more suitable approach relies on characterization techniques that consider the variation of the morphological properties of the catalyst with the medium nature, providing more reliable information about the actual resin morphology in the working-state. A reliable description of the actual pore structure in polar media can be obtained by the analysis of data obtained by Inverse Steric Exclusion Chromatography (ISEC), which supplies morphological information about the swollen polymer using an aqueous solution, see Fig. 1.19. The technique relies on measurements of elution volumes of a series of standard solutes with known effective molecular sizes through a HPLC column filled with the investigated polymer material [79].

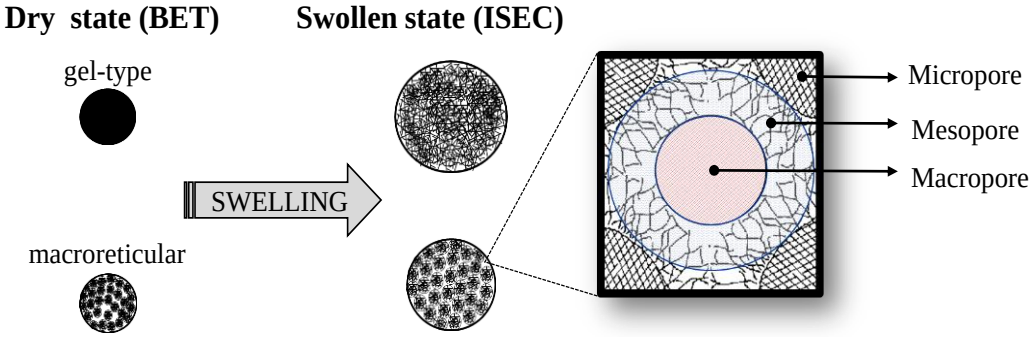

Figure 1.19. Diagrammatic representation of the structure of micro- and macroreticular resins in dry and swollen states. Adapted from [80].

Combined with the cylindrical pore model, ISEC technique allows to characterize macro and mesopores (pore diameter and volume). Besides, combined with the geometrical model developed by Ogston [81], it gives a good approach of the spaces

between polymer chains formed by aggregates and nodules swelling. The final ISEC output of the morphology of swollen resin consists of information on both, the distribution of "true pore" (meso and macropores) and the volume distribution of differently dense gel fractions of the swollen polymer.

1.5.4 APPLICATIONS OF STYRENE DIVINYLBENZENE RESINS

The catalytic use of IER also constitute a profitable market of thousands of tons per year. The most relevant applications of IER are related to the molecules to be synthesized and the type of reaction involved. Based on the use to be given, catalytic IER can be divided into anionic, cationic or resins for enzyme immobilization. The framework of application of acidic IER is quite wide [82] being excellent catalysts for the following syntheses:

- Oligomerization of C_4-C_8 iso-olefins [38].
- Alcohols dehydration for the production of symmetric ethers [76,83–85].
- Etherification of iso-olefins with primary alcohols [20,86–90].
- Olefins hydration to form tertiary alcohols [91,92].
- Alkyl phenols formation by phenol alkylation and condensation reactions. For instance, bisphenol A synthesis from phenol and acetone.
- Esterification reactions between acids and alcohols.
- Hydrolysis of ethers and esters.
- Synthesis of hydroxyl methyl furfural (HMF), production of methyl isobutyl ketone (MIBK) and mesityl oxide from acetone, synthesis of tetrahydrofuran (THF), synthesis of levulinic acid and derived alkyl levulinates, synthesis of 1,1-bisylvylbutane and other diesel precursors from 2-methyl furan.
- Supports for enzymatic catalysts.

Though several researches have been focused on the use of new sulfonated catalysts for etherification reactions such as carbon nanotubes [93], activated carbons [94,95], or zeolites [96–99], ion-exchange resins are still the most promising option for such reactions. This is because IER present very high activity and selectivity in etherification reactions at low temperature. Based on this fact, the study of the properties that confer to IER such privileged position is important not only for understanding their catalytic behavior, but also to create new IER able to improve the catalytic performance in etherification systems.

1.5.5 EFFECT OF POLAR COMPOUNDS ON ACIDIC ION-EXCHANGE RESINS

The role of polar compounds as alcohols and water in the oil industry as in the related heterogeneously catalyzed processes, such as catalysis by ion-exchange resins, is often crucial. When enough polar compound is present in a sulfonic acid resin, it can dissociate and disaggregate the network of the sulfonic acid groups, and the locus where catalysis takes place can be regarded as an aqueous solution of a strong (dissociated) acid surrounded by an inert solid polymer (quasihomogeneous catalysis). This catalysis is known as specific acid catalysis (catalysis by hydrated protons) [100]. On the contrary, when only a small amount of water (or another polar solvent, such as alcohols) is present, the $–SO_3H$ groups remain undissociated, sometimes aggregated, and the catalytic process takes place on them. This type of catalysis is known as general acid catalysis (catalysis by undissociated acid groups) [101]. The catalytic properties of undissociated $–SO_3H$ groups are much different from those of hydrated protons, in part because they differ in their acid strength. Consequently, sulfonic acid resins can be highly

active in the absence of water, but much less active in the presence of significant amounts of water [100].

The characterization of the interactions between the $–SO_3H$ groups located on the resin backbone can be performed by infrared spectroscopy [102]. In a dry resin with enough flexible polymer matrix (relatively low crosslinking degree) and sufficiently high concentration of $–SO_3H$ groups (relatively high acid capacity), these groups bond with each other. When water is present in the vicinity of the active sites, the hydrogen bonds between the acid groups are broken up, and water molecules link to the sulfonic groups network by hydrogen bonds. Even very low amounts of water at trace level can inhibit strongly some reactions, because water disrupts the sulfonic groups network and diminishes the reactants opportunities to bond it. The structure of water bonded within the resin has been determined by infrared spectroscopy and Fig. 1.20 shows a representative picture of such interaction, where water is bound tightly within this structure, and cannot be easily removed, even by heating the resin under vacuum [102]. In the presence of a sufficient amount of water (from 2 molecules per $–SO_3H$ group), resin acid groups become dissociated and almost all water can be effectively removed by heating. Both situations can take place within the resin structure and can affect the possible reaction mechanisms. Other polar molecules (e.g., alcohols) can bond to the $–SO_3H$ groups in the network similarly to water but with less strength, and such bonding may favor catalytic reactions. It has been reported that two alcohol molecules are bound per functional group by polar interaction [103].

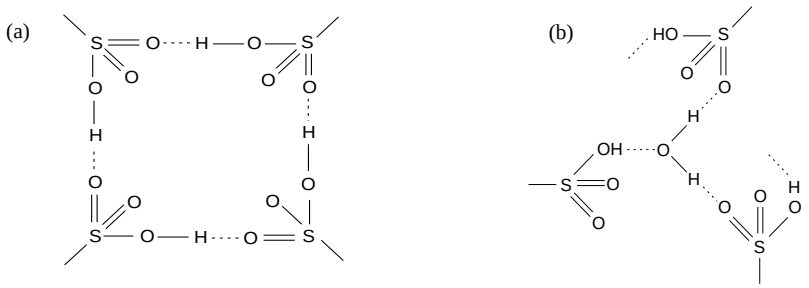

Figure 1.20. (a) Representative structure of the hydrogen-bonded network formed by the sulfonic groups of the catalyst. (b) Representative structure of one water molecule hydrogen-bonded to three undissociated $–SO_3H$ groups [100].

Obviously, in the absence of water, the $–SO_3H$ groups in the network are not generally single as isolated catalytic sites; rather, it is the network that acts as a catalytic agent by means of concerted mechanisms of proton-donor and proton-acceptor groups. The $–SO_3H$ groups can act as both proton-donor and proton-acceptor groups [100]. When the network of $–SO_3H$ groups is broken up by the presence of a large amount of polar component, such as water or alcohols, activity of the catalyst declines. Hence, alcohols –similarly to water– act as reaction inhibitors [5,6]. If alcohols are reactants, they can promote inhibition of the catalyst activity by breaking up the network of $–SO_3H$ groups and at high concentration, they can even induce dissociation of $–SO_3H$ groups. Such results have been demonstrated and illustrated in the gas-phase dehydration reactions of alcohols [106], and also in oligomerization systems [107] where alcohols were used as selectivity enhancers for the liquid-phase isoamylenes dimerization.

From an industrial point of view, an essential issue is the evaluation of the effect of water on etherification processes, which normally are carried out over sulfonic acid resins. In general, water is present in the fresh catalyst and in the alcohol feed stream. EtOH and water form an

azeotropic mixture and its distillation yields an EtOH at 95.5 wt.% [9,10], often called "hydrated ethanol". So if purer EtOH is needed, a previous azeotropic distillation process or membrane separation is required, what means a rise in the reactant price.

1.5.6 CATALYTIC ACTIVITY AND ACCESSIBILITY

Accessibility can be defined as the maximum fraction of active sites that can be reached by a substrate molecule [104]. The catalytic activity of IER depends dramatically on both the nano-environment surrounding the active sites and their accessibility [80]. Accessibility to active sites is critically affected by the extent of swelling of the polymer in contact with the reaction medium for both macroreticular and gel-type resins. As a consequence of swelling, polymer chains separate from each other, what enhances the accessibility to inner parts of the polymer network. Accessibility to the supported functional groups in the polymer chains depends on the polymer morphology at the micro and nanoscopic level. An interesting interpretation on the types of accessibility in a macroporous sulfonic acid resin was made by Buttersack (1989)[104], as illustrated in Fig. 1.21. The accessibility can be understood as sharp changes in the diffusion coefficient of a given substrate in a certain solvent or solid.

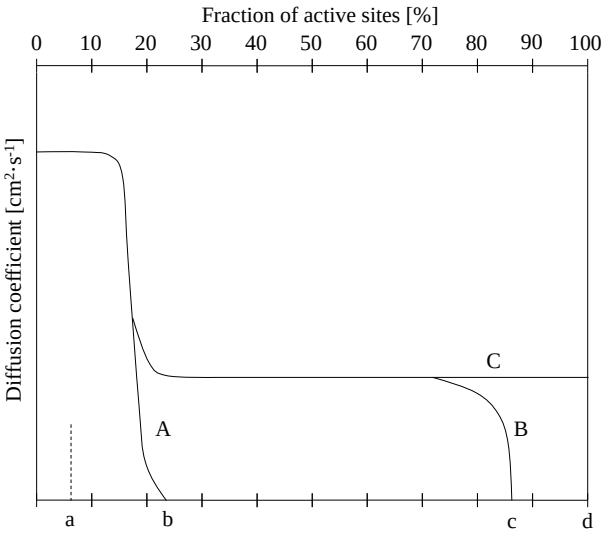

Figure 1.21. Types of accessibility in a macroporous resin: non-interaction accessibility (a), interaction accessibility of the surface (a-b), and gel-phase (b-c). Adapted from [104].

According to Fig. 1.21, the macroporous fraction of an IER is supposed to have the same diffusion coefficient as the bulk phase. The fraction "a" accounts for the non-interaction accessibility, which can be obtained by BET measurements, while the fraction a-b consider the pendent polymer chains on the macroporous surface and may be called "surface-interaction accessibility". Inside the gel-phase fraction (b-d), accessibility is expected to be considerably lower. In this last case, the corresponding diffusion coefficient is expected to be zero and the "surface interaction accessibility" is supposed to follow the curve A. In the case of swollen resins by the influence of polar components, the diffusion coefficient can be expected to follow the curve C. Moreover, the sieve effect due to the steric demand of the substrate can lead to a further reduction of the diffusion coefficient at "c" just defining the "total interaction accessibility" for the fraction "a"–"c" (curve B). These three types of accessibility are taking place at once in macroporous acidic IER and therefore they should be considered under reaction conditions. Most of resin catalyzed reactions can be placed into the following description: the solvent can cause only a partial dissociation of acid groups which, additionally, may depend on

the amount of adsorbed substrate. A low degree of swelling can lead to diffusion-controlled reactions and the accessibility, in coherence with Fig. 1.21, may show a type B. This complicated situation is true for important industrial reactions such as MTBE synthesis [104] and, it is thus expected to occur though with different magnitude in other etherification systems.

There are several methodologies to evaluate the different types of accessibility in an IER. In order to obtain non-interaction accessibility, the surface area (S_g) in [m^2 kg^{-1}] measured by adsorption-desorption of N_2 is the method of choice [104]. The corresponding fraction of accessible functional groups ζ_N is proportional to the surface area per polymer skeletal density (ρ) in [kg m^{-3}] according to:

$$\zeta_N = S_g \rho^{2/3} / ([H^+]\, N_A)^{1/3} \qquad (1.8)$$

where $[H^+]$ is the ion-exchange capacity in mole of acid groups per kg of dry resin and N_A is Avogadro's number in [mol^{-1}].

In order to assess the interaction accessibility, the Ogston distribution coefficient [110] or the comparison of random coil diameters [111] for involved species are useful approaches for evaluating the accessibility in a swollen polymer.

As a result, the study of diffusion coefficients of IER of different particle sizes under reaction conditions is essential to understand relations between accessibility, diffusion phenomena and catalytic activity. This will provide knowledge for designing catalysts with an improved morphology able to overcome the inherent drawbacks of physical nature of the functionalized polymer-based porous materials.

1.5.7 ADSORPTION ON ION-EXCHANGE RESINS

Macroreticular acidic IER as Amberlyst™35, Amberlyst™15, Purolite®CT-175 and Purolite®CT-275 are excellent catalysts for the production of tertiary alkyl ethers [19]. Adsorption equilibrium constants and adsorption related thermodynamic state functions of involved species are usually present in kinetic equations of etherification reactions and therefore they provide essential information about the catalytic process. Adsorption equilibrium constants and related thermodynamic state functions for the species participating in etherification reactions can be determined through kinetic experiments by non-linear regression or experimentally by performing specially designed adsorption experiments. In order to assess the thermodynamic coherence of adsorption related parameters, some guidelines, referred to as the Boudart rules [112,113], must be fulfilled. The rules that can be applied to IER are:

i) $\Delta_{ads}S°_j < 0$, because the adsorption process implies a loss of entropy.
ii) $|\Delta_{ads}S°_j| < S°_j$, because the loss of entropy cannot be larger than the total entropy.
iii) $\Delta_{ads}H°_j < 0$, because adsorption is an exothermic process.

As mentioned in *Section 1.5.2*, macroreticular IER catalysts can be envisaged as bidisperse catalyst consisting of agglomerates of microspherical particles with free space between them, which provides permanent porosity [114]. When these resins are immersed in a fluid medium, different concentrations of the species *j* can be distinguished as a consequence of the adsorption process. These are namely: bulk phase concentration (C_j), macropore concentration ($C_{j,a}$) and

micropore concentration ($C_{j,i}$). Gradients in such concentration profiles create extra and intraparticle transport phenomena, which can be evaluated by means of effective diffusion coefficients of the different parts of the macroporous polymer, see Fig 1.22.

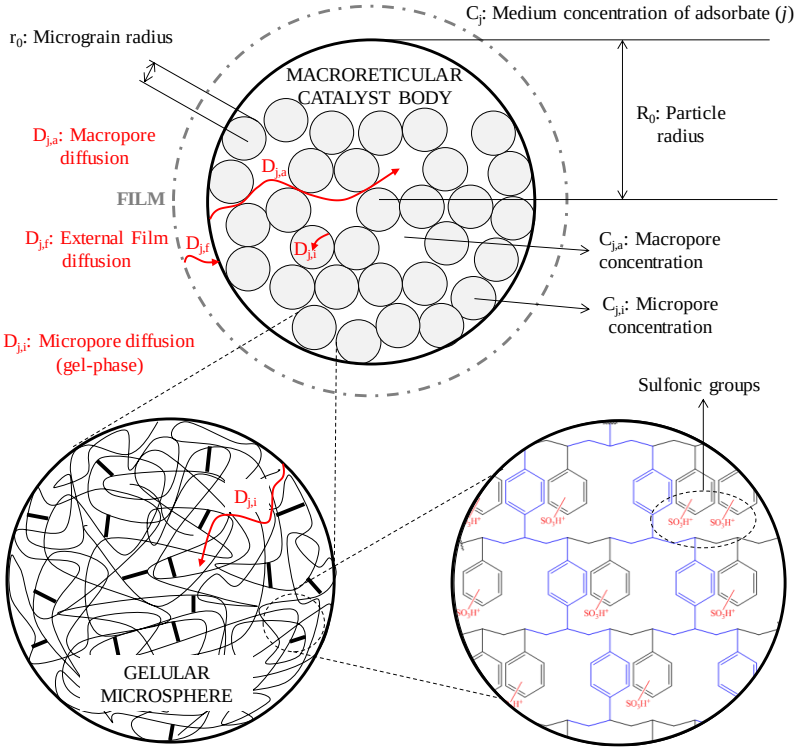

Figure 1.22. Schematic representation of a bidisperse-like macroporous catalyst consisted of sulfonated polystyrene-divinylbenzene. – Polystyrene chain. ▬ Divinylbenzene crosslink. Adapted from [48].

The functional groups of the resin (–SO_3H) can be divided into those located on the surface of the microparticles and those located within the inner polymer matrix of the microparticles. The former account for relatively easy accessibility because of the permanent pores and macropore diffusion rules the transport of the involved molecules. On the other hand, inner functional groups need the molecules to penetrate through the polymer matrix to gain accessibility and this stage of the catalytic process is driven by diffusion of molecules within the resin gel-phase (micropores). Such diffusion within the microspheres is expected to be strongly influenced by the interactions with the polymer matrix. Experimental determination of data on macro- and micropore diffusion coefficients is thus essential for modeling the catalytic process at a molecular level and for understanding the catalytic process.

The moment techniques [62,65–67] have been demonstrated to be a very useful tool to extract information on macro and micropores diffusion resistances of species within a macroreticular porous solid using previously determined adsorption equilibrium constants. As mentioned in *Section 1.4.3*, the main limitation of such a technique is the assumed linear adsorption relation (Henry's law) between the fluid phase and adsorbed concentrations of the tracer. Such an assumption may in general be justified at sufficiently low concentrations of the tracer. At higher concentrations, linearization of the adsorption isotherm is necessary at the concentration level of the experiment [65] since large divergences can be found between obtained results.

1.5.8 ION-EXCHANGE RESINS LIFESPAN

Catalyst deactivation or, alternatively, catalyst lifespan is, after selectivity, the most important catalytic feature when selecting the catalyst for a given process. Deactivation can be defined as the depletion of the total concentration of active sites accessible to reaction [115]. The catalyst lifespan is one of the most important concerns from an industrial standpoint because the change-out of the catalytic beds usually takes 20 days of production to shut down and restart reaction units, which implies increasing the operating expenses. Hence, experimental studies on catalyst deactivation are essential for scaling-up new processes and improve the current ones. Paradoxically, most of publications on the field of heterogeneous catalysis lack the study of the catalyst lifespan and the mechanisms of catalyst deactivation. The understanding of the causes of catalyst deactivation can lead to significant time and cost savings by means of the implementation of pre-treatment units and operating practices. Concerning etherification reactions, catalytic beds are usually replaced after two years of continuous production [116].

1.5.8.1 Types of deactivation

Deactivation processes that can affect to sulfonic ion-exchange can be divided into the following types:

i) **Deactivation by sintering (aging).** It is referred to the loss of catalytic activity due prolonged exposure to high temperatures. The catalyst support becomes soft and melts, resulting in pore closure. The active surface area is lost by crystal agglomeration or by narrowing/closing of the pores of the catalyst pellet. Sintering is usually negligible at temperature below 40% of the melting point temperature of the solid catalyst in the case of inorganic supports [115].

ii) **Desulfonation or thermal stress.** A specific case for ion-exchange resins exposure to high temperatures or thermal stresses is the desulfonation phenomenon. It generally occurs at temperatures above 140 °C and it causes the destruction of the C-S bond between catalyst matrix and sulfonic groups [28]. Etherification plants operating over 76 °C commonly experience desulfonation rates of the order of 10% annually [116]. Above 100 °C the rate of sulfonic groups loss increases approximately 1.8 fold per each 10 °C. As a preventive measure, temperature control in industrial etherification reactors is of paramount importance.

iii) **Decrosslinking of the resin matrix.** The exposure of the matrix to strong oxidizing agents as Fe^{3+}, O_2, chlorine or peroxides, results in decrosslinking and swelling of the resin beads. It affects diffusion of reactants and products and it ends up in irreversible damage of the catalyst.

iv) **Deactivation by coking or fouling.** This mechanism of catalyst decay is common in reactions involving hydrocarbons. It results from the deposition of carbonaceous material (coke), heavy oils, waxes, gums and polymers on the catalyst pores [115], see Fig. 1.23. It leads to the permanent loss of catalytic activity and to the reduction of surface area, pore volume, and pore diameter. Potential fouling agents of ion-exchange resins used in etherification of C_4 and C_5 olefinic fractions are typically butadienes, pentadienes, and oligomers of isobutene and isoamylenes heavier than trimers are.

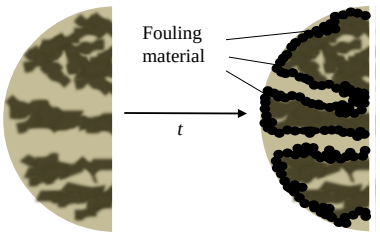

Figure 1.23. Schematic representation of deactivation by fouling.

v) **Deactivation by poisoning.** This mechanism occurs when poison molecules become irreversibly chemisorbed on active sites, thereby reducing the number of active sites available for reaction, see Fig. 1.24. The poisoning molecule may be a reactant, a product or an impurity in the feed stream. In the case of etherification reactions, IER resins poisons are typically bases that neutralize the acid sites [116]. Such mechanism is called neutralization.

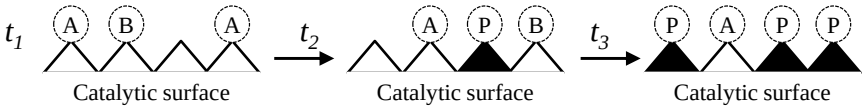

Figure 1.24. Schematic representation of deactivation via poisoning. A=reactant. B=product. P=Poison. Λ=active site. ▲= deactivated site. Adapted from [115].

1.5.8.2 Modes of neutralization

Two main modes of deactivation of etherification catalytic beds are distinguished in the mechanism of neutralization: plug flow neutralization and diffused flow neutralization [28]. Fig. 1.25 illustrates the effect of both types of neutralization on conversion along the catalytic bed length.

a) **Plug flow neutralization.** It takes place when a strong cation as sodium reacts with sulfonic acid groups on the catalyst. This neutralization starts at the catalytic bed inlet and the neutralization front slowly moves along the reactor length at a speed that depends on the amount of contaminant present in the feed [28], see Fig. 1.25. The uptake of deactivator is fast and stoichiometric. As deactivation progresses, plug flow neutralization results in a foreshortening of the active catalyst bed length [116]. Examples of plug flow deactivators are salts, amines and other Lewis and Brønsted bases.

b) **Diffused flow neutralization.** It generally occurs when a weak basic compound is present in the feed stream. The weak bases are not neutralized readily. As a consequence, active sites neutralization takes place progressively and simultaneously throughout the entire bed length, rather than a neutralization front moving from the inlet to the outlet, see Fig. 1.25. As etherification rates depend on the acid groups concentration, reaction rates decrease and the overall etherification conversion is adversely affected [28]. Diffusional deactivators are generally weak bases, which either bind weakly to active sites or generate more strongly binding species in situ. Examples of such deactivators are: amine formers as acetonitrile (ACN), propionitrile (PPN), dimethylformamide (DMF), dimethylsulfide (DMS), hydrogen sulfide (H_2S). Physical foulants as heavy oils and waxes can also act as diffused flow deactivators [116].

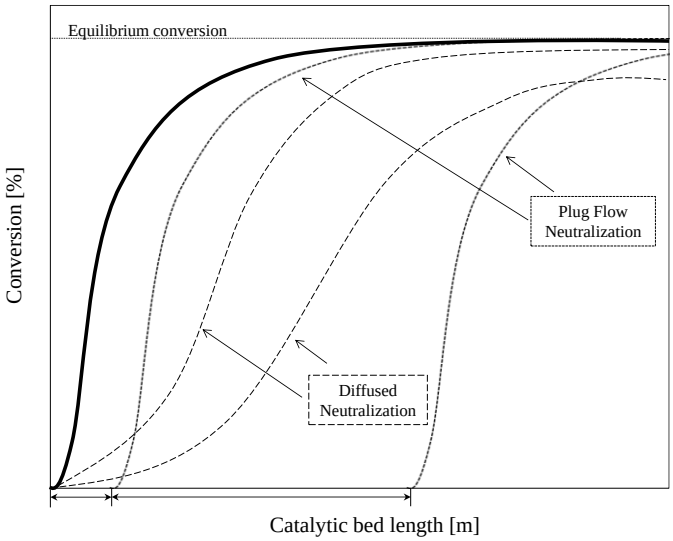

Figure 1.25. Tubular reactor performance when affected by plug-flow (⋯) or diffused (---) neutralization. Performance of ideal reactor without deactivation (▬). Adapted from [117].

1.5.8.3 Catalyst deactivation in etherification plants

A catalytic bed where around 40% of active sites have been neutralized can be considered as exhausted. ACN is, beyond doubt, the most prevalent catalyst killer in current etherification plants [116]. ACN is usually originated as a residual compound from butadienes extraction, whose typical concentration in FCC hydrocarbons streams is 100–200 ppm. Since most etherification plants have an alcohol recovery unit, ACN concentration usually increases up to 2,000 ppm in the recycle stream. With respect to TAME units, the most relevant poison is the PPN contained in the C_5 fraction [48].

Due to its detrimental effect, the effect of ACN diffused neutralization has been studied [117-119]. It has been proposed that deactivation occurs according to a two-step adsorption/reaction mechanism. In the first step, ACN, as a weak base is adsorbed on the resin and it has been observed that such adsorption is diffused through the catalyst bed. The interaction between nitriles and resin is reversible and of a prevailing acid-base nature. Therefore, adsorption is governed by a partition coefficient that depends on temperature and on the nature of the solvent where nitrile is present. Alcohols strongly decrease the partition coefficient. Consequently, ACN adsorption along the catalytic bed follows a quite complex profile due to the decreasing concentration of alcohol, the increasing concentration of ether and the operating temperature conditions. In the second step, the adsorbed ACN reacts either with water, alcohol or a carbonium ion by means of the following mechanisms [116,117]:

i) **Direct hydrolysis.** The adsorbed ACN reacts with water to form an amide that in turn reacts with another molecule of water to form acetic acid and ammonia, which eventually neutralizes the sulfonic groups of the resin.

ii) **Alcoholysis followed by hydrolysis.** The adsorbed ACN reacts with the alcohol (Pinner synthesis) to form an unstable intermediate (salt of imido ester) that in turn undergoes hydrolysis with a molecule of water to form the corresponding alkyl acetate and ammonia, which neutralizes the active sites of the resin.

iii) **Ritter reaction.** The adsorbed ACN molecule reacts with a carbonium ion (usually formed from alkanes in the petroleum refining industry in the thermal cracking units) to form other amines. The formed amine neutralizes the active sites by plug flow deactivation mechanism.

The hydrolysis reaction is much faster than the alcoholysis reaction, although the amount of water is expected to be very low compared to that of alcohol in the feed stream. Deactivation by Ritter reaction is the least common mechanism. Nitriles other than ACN follow analogous mechanisms.

Catalyst deactivation caused by ACN can be avoided with a water wash section prior to the MTBE unit, which results in a very effective solution to remove practically all ACN. TAME units are somehow more problematic, since water wash is not very effective for PPN removal. The best way for protecting a TAME or TAEE unit is to use a process that does not concentrate nitriles with the alcohol stream if it is recycled. Despite selective adsorbents have also been considered for nitriles removal, they did not reach commercial acceptance [48].

1.6 STATE OF THE ART OF ETBE AND TAEE SYNTHESES

To date, several studies have payed attention to the etherification of C_5-C_8 alkenes with C_1-C_4 alcohols [21,88,96,120]. With regards to individual ETBE and TAEE syntheses, important progresses have been achieved concerning product distribution, effect of water presence in the feed stream, relations between catalyst properties and catalytic activity, thermodynamics and kinetics of involved reactions, adsorption of involved species, and in less extent, catalyst deactivation. The main obtained conclusions set the state of the art in this field and they are summarized below.

Several studies have been focused on the performance of isolated production of ETBE and TAEE in both absence and presence of water [21,31,49,91,120–124]. Nevertheless, there is a dearth of information about equilibrium conversion and selectivity over an industrially attractive range of experimental conditions in such etherification systems. The product distribution in the synthesis of ETBE or TAEE depends mainly on reactants composition, temperature and the catalyst used. When these ethers are produced from pure olefin feedstock and EtOH at equimolar feed ratio and mild temperatures (313 to 353 K), the main products expected are the ethers. In addition, olefins can react with water present in the alcohol stream to form the corresponding hydration products: TBA from IB, and TAA from IA. An EtOH excess in the feed stream can increase olefins conversion, but at high temperatures EtOH dehydration to form diethyl ether and water gains relevance. On the contrary, with an initial stoichiometric excess of olefins, olefins oligomerization reactions can become relevant, in particular, at temperatures above 363 K [31,49,107,125].

Concerning the effect of water on the isolated tertiary ethers liquid-phase syntheses over acidic ion-exchange resins, the main remarks are: 1) water competes with the main reactants for the catalytic active sites, 2) the polar nature of water promotes resins swelling, which may promote reactants accessibility to inner active sites, and 3) water can solvate the sulfonic acid protons, which diminishes their acid strength (inhibition). It has been concluded that the third point is the predominant factor and, as a general result, water presence in etherification processes leads to

lower reaction rates. Besides, water and other polar compounds have been found to induce a moderator or inhibitory effect over olefin oligomerization reactions.

Thermodynamics of MTBE [122,126,127] and TAME [51,128–134] syntheses have been described in the literature. Likewise, thermodynamics of ETBE and TAEE isolated syntheses [22,89,91,121,122,127,129,135–138] can also be found. All studies confirm that etherification reactions are exothermic and the estimated enthalpy changes of reaction usually range from -20 to -45 kJ/mol. However, some divergences can be found in the literature with regards to the thermodynamic state functions and to the enthalpies of formation of the involved compounds. Finally, most studies confirm that TAEE formation reactions are more limited thermodynamically, which can be ascribed to the simultaneous isomerization reaction of isoamylenes [89].

With respect to the kinetics of isolated liquid-phase formation of ethanol-based tertiary ethers over acidic ion-exchange resins, Fité et al. [123] presented an Eley-Rideal mechanism for the synthesis of ETBE from IB and EtOH. Françoisse and Thyrion [139] found a change in the kinetic mechanism depending on the EtOH concentration for ETBE synthesis. Linnekoski and Krause [140] proposed a Langmuir-Hinshelwood-Hougen-Watson mechanism for the synthesis of TAEE from IA and EtOH. Further progress was made by Oktar et al. [124] and Zhang et al. [141] concerning TAEE formation reactions. The influence of the reaction media on etherification reactions was also studied [86,123,142–144], and adsorption equilibrium and also kinetic parameters were estimated [65]. More recently, reviews on ETBE [47] and TAEE [145] isolated syntheses gathered the main progresses and the future prospects for the synthesis of these ethers. Tables 1.6, 1.7 and 1.8 summarize the most reliable kinetic models that have been found in the literature for the syntheses of ETBE, TAEE and the isomerization reaction of isoamylenes, respectively.

Table 1.6. Proposed kinetic models for ETBE synthesis.

Reference	Catalyst	Equation
Françoisse and Thyrion (1991) [139]	Amberlyst™15	$r_{ETBE} = k\left[c_{IB} - \alpha\frac{c_{ETBE}}{c_{EtOH}} + \frac{\beta\left(c_{IB}c_{EtOH} - \alpha c_{ETBE}\right)}{c_{IB} + Fc_{EtOH}^2 + c_{ETBE}}\right]$
Fité et al. (1994)[123]	Lewatit K2631	$r_{ETBE} = k\left(\frac{a_{IB}a_{EtOH} - a_{ETBE}/K}{a_{EtOH}^3}\right)$
Sundmacher et al. (1995)[146]	Amberlyst™15	$r_{ETBE} = k\left(\frac{a_{IB}}{a_{EtOH}} - \frac{1}{K_a}\frac{a_{ETBE}}{a_{EtOH}^2}\right)$
Jensen and Datta [147]	Amberlyst™15	$r_{ETBE} = k\frac{a_{EtOH}^2\left[a_{IB} - a_{ETBE}/(Ka_{EtOH})\right]}{\left(1 + K_{EtOH}a_{EtOH}\right)^3}$
Solà et al. (1995)[148]	Lewatit K2631	$r_{ETBE} = k\left(\frac{a_{IB}a_{EtOH} - a_{ETBE}/K}{a_{EtOH}^2}\right)$
González (2011) [49]	Amberlyst™35	$r_{ETBE} = \frac{k\left(a_{IB}a_{EtOH} - a_{ETBE}/K\right)\exp\left(\frac{\overline{V}_M\phi_P^2}{RT}\left(\delta_M - \delta_P\right)^2\right)}{\left(a_{H2O} + K_{IB}a_{IB} + K_{ETBE}a_{ETBE} + K_{1\text{-butene}}a_{1\text{-butene}}\right)^2}$
Badia (2016) [34]	Amberlyst™35	$r_{ETBE} = \frac{k\left(a_{IB}a_{EtOH} - a_{ETBE}/K\right)\exp\left(\frac{\overline{V}_M\phi_P^2}{RT}\left(\delta_M - \delta_P\right)^2\right)}{\left(a_{EtOH} + K_{BuOH}a_{BuOH} + K_{ETBE}a_{ETBE}\right)}$

Table 1.7. Proposed kinetic models for TAEE synthesis.

Reference	Catalyst	Equation
Zhang et al. (1997) [141]	Amberlyst™15	$r_{TAEE} = k\frac{a_{EtOH}^2\left[a_{iC5} - a_{TAEE}/(Ka_{EtOH})\right]}{\left(1+K_{EtOH}a_{EtOH}\right)^3}$
Linnekoski et al. (1997) [131]	Amberlyst™16	$r_{TAEE} = \frac{k_1^{'}\left(a_{EtOH}a_{2M1B} - a_{TAEE}/K_{e1}\right)}{\left(1+K_{EtOH}a_{EtOH}\right)^2} + \frac{k_3^{'}\left(a_{EtOH}a_{2M2B} - a_{TAEE}/K_{e2}\right)}{\left(1+K_{EtOH}a_{EtOH}\right)^2}$
Linnekoski et al. (1998) [91]	Amberlyst™16	$r_{TAEE} = \frac{k^{'}\left(a_{olef}a_{EtOH} - a_{TAEE}/K_{eTAEE}\right)}{\left(1+K_{EtOH}a_{EtOH}+K_{water}a_{water}+K_{TAOH}a_{TAOH}+K_{TAEE}a_{TAEE}+K_{olef}a_{olef}\right)^2}$
Linnekoski et al. (1999) [136]	Amberlyst™16	$r_{TAEE} = \frac{k_1^{'}\left(a_{EtOH}a_{2M1B} - a_{TAEE}/K_{e1}\right)}{\left(K_0^{'}\left(a_{2M2B}+a_{2M1B}\right)+a_{TAEE}\right)\left(1+K_{EtOH}a_{EtOH}\right)} + \frac{k_3^{'}\left(a_{EtOH}a_{2M2B} - a_{TAEE}/K_{e2}\right)}{\left(K_0^{'}\left(a_{2M2B}+a_{2M1B}\right)+a_{TAEE}\right)\left(1+K_{EtOH}a_{EtOH}\right)}$
Oktar et al. (1999)[124]	Amberlyst™15	$r_{TAEE} = 17.34\exp\left(-\frac{4899}{T}\right)C_{2M1B}^{0.93} + 5.6\cdot10^5\exp\left(-\frac{8850}{T}\right)C_{2M2B}^{0.69}$ [molg^{-1}s^{-1}]
Bozga et al. (2008)[145]	Amberlyst™35	$r_{TAEE} = \frac{k\left(a_{EtOH}a_{IA} - a_{TAEE}/K\right)}{\left(1+K_{EtOH}a_{EtOH}\right)^2}$

Table 1.8. Proposed kinetic models for IA double bond isomerization reaction.

Reference	Catalyst	Equation
Zhang et al. (1997)[141]	Amberlyst™15	$r_{ISOM} = \frac{\left(a_{2M1B} - a_{2M2B}/K_3\right)}{\left(1+K_{EtOH}a_{EtOH}\right)^2}$
Linnekoski et al. (1997) [131]	Amberlyst™16	$r_{2M1B} = -\frac{k_1^{'}\left(a_{EtOH}a_{2M1B} - a_{TAEE}/K_{e1}\right)}{\left(1+K_{EtOH}a_{EtOH}\right)^2} - \frac{k_5^{'}\left(a_{2M1B} - a_{2M2B}/K_{e3}\right)}{\left(1+K_{EtOH}a_{EtOH}\right)}$
Linnekoski et al. (1999) [136]	Amberlyst™16	$r_{ISOM} = \frac{k_5^{'}\left(a_{2M1B} - a_{2M2B}/K_{e3}\right)}{\left(K_0^{'}\left(a_{2M2B}+a_{2M1B}\right)+a_{TAEE}\right)}$

As it can be seen, most of the kinetic models in Tables 1.6, 1.7 and 1.8 are based on activities due to the non-ideality of the system due to the presence of polar compounds. Besides, generally EtOH is included in the adsorption term of the kinetic equations.

Despite the great relevance of etherification processes, IER screening studies are scarce in the open literature [19,20,49,78,83,111,149], in particular those concerned to the synthesis of ETBE, and, more specifically, of TAEE. In general, it is considered that macroreticular oversulfonated ion-exchange resins are the best option for the production of these ethers. Besides, microreticular IER are also active in the synthesis of these ethers, although their catalytic activity is not comparable to that of macroreticular IER.

To the best of our knowledge, experimental studies on adsorption of tertiary olefins, alcohols and their respective ethers are very scarce in the available literature [64,65,150], and they have

been performed only on Amberlyst™15. Determination of adsorption equilibrium constants, heat of adsorption, macro- and micropore diffusion coefficients have been determined in gas-phase whereas in liquid-phase there is only information on MeOH, EtOH and 2M2B. The main findings indicate that alcohols are preferentially adsorbed on the resin rather than olefins and ethers. Estimated macropore diffusion coefficients from experimental data are in the order 10^{-10}–10^{-11} m^2/s for the liquid-phase and of the order 10^{-7}–10^{-8} m^2/s in the gas-phase. Analogously, estimated micropore diffusion coefficients for both the liquid- and gas-phase were in the order 10^{-20}–10^{-18} m^2/s.

With respect to IER lifespan, there is scarce information in the literature. The effect of ACN and monomethyl amine (MMA) presence in the feed stream in the synthesis of ETBE, and the effect of ACN in the synthesis of MTBE [118,119]. The main obtained results confirm that MMA induces a plug flow neutralization in the fixed bed, whereas ACN induces a diffused like neutralization of the bed. Besides, temperature and poison concentration were found to favor the deactivation process.

In the last decades, new interesting processes of simultaneous production of several ethers have been on the spotlight [88,122,141], and the possibility of producing several ethers in the same reaction unit could become an industrial reality in the forthcoming years. As discussed in *Section 1.2.6*, the simultaneous production of ETBE and TAEE is one of the most promising alternatives. Nevertheless, to the best to our knowledge, there is a dearth of experimental studies regarding the product distribution, the effect of the water content in EtOH to be used as reactant, kinetics, catalyst screening and catalyst lifespan on simultaneous etherification systems. Such studies are essential for selecting the optimum experimental conditions that could maximize the etherification yields, for predicting compositions when shifting from the preferred production of one ether to another, for designing tailored catalysts, and for increasing the catalyst lifespan. The present PhD thesis attempts to cope with all these issues, aiming to provide a sound study on the simultaneous etherification of IB and IA with EtOH over acidic IER that covers the significant aspects related to the performance of such complex reaction system.

2. SCOPE/GOALS OF THE WORK

The present work is focused on the study of the simultaneous liquid−phase etherification of IB and IA with EtOH over acidic ion-exchange resins. Based on the starting point that the aforementioned state of the art constitutes, the main goals to achieve are as follows:

- To analyze several batch processes and synthesis pathways for the syntheses of ETBE and TAEE under the Green Metrics Analysis aiming to find the "greenest" route for synthesizing both ethers simultaneously.

- To study the feasibility of the simultaneous liquid−phase etherification of IB and IA with EtOH under different experimental conditions, namely temperature and initial composition. The determination of equilibrium conversions and selectivity, as well as the modeling and optimization of etherification yields are main goals for their direct application at industrial scale.

- To study the chemical equilibria of the involved reactions in the simultaneous liquid-phase production of ETBE and TAEE. The experimental determination of reaction equilibrium constants and thermodynamic state functions of these reactions, and their comparison with literature data are explicit objectives.

- To study the influence of the initial water content on product distribution, chemical equilibria and etherification rates using an IER as catalyst.

- To assess the simultaneous production of ETBE and TAEE on different acidic IER. The main objective is to correlate catalytic activity with catalyst properties and to study the effect of accessibility on catalytic activity.

- To study the kinetics of the simultaneous etherification system over the most active IER catalyst found in the catalyst screening. The main goals are to find the best kinetic model, to estimate the kinetic parameters, to extract mechanistic conclusions based on LHHW or ER formalisms, and to compare it with the isolated production of both ethers.

- To perform adsorption studies on a potential IER catalyst in order to obtain information on adsorption equilibrium constants and adsorption related thermodynamic properties of C_1-C_4 alcohols, C_4-C_5 iso-olefins and their corresponding ethers. Experimental determination of effective diffusion coefficients of these species is also a main target.

- To study the effect of acetonitrile presence in the feedstream on the catalyst lifespan over sulfonic IER at different experimental conditions. The kinetic modeling of the deactivation process is the main goal to be achieved.

3. EXPERIMENTAL SECTION

3.1 MATERIALS

3.1.1 CHEMICALS

A mixture of IA containing 2M2B (96% GC) and 2M1B (4% GC, TCI Europe, Belgium), IB (>99.9% GC, Air Liquide, Spain), absolute dry EtOH (max. 0.02 wt.% of water, Panreac, Spain) and deionized water were used as the initial reaction mixture in the experimental runs of *Sections 4.3−4.8*. Also for these experiments, the following chemical standards were used for the calibration of the system: TMP-1 (>98.0% GC, Fluka, Buchs, Switzerland) and TMP-2 (>98% GC, Fluka, Buchs, Switzerland), TAA (>98.0% GC, TCI Europe, Belgium), TBA (>99.7% GC, TCI Europe, Belgium), ETBE (>99.0% GC, TCI Europe, Belgium), 2M1B (>99.0% GC, TCI Europe, Belgium) and 2M2B (>99% GC, Sigma Aldrich, Germany). TAEE was obtained in our laboratory by distillation with a minimum purity of 99% GC. Dimers C_5 were also synthetized and purified in our laboratory (>99% GC). Due to the difficulty of obtaining pure $C_{4\text{-}5}$ codimers, an intermediate response factor between C_4 and C_5 dimers was used for its calibration.

The following chemicals were used for the system calibration and for the liquid- and gas-phase adsorption experiments of *Section 4.9*: *n*-heptane (>99 %GC, Merck KGaA, Darmstadt, Germany), *n*-hexane (>99 %GC, Merck KGaA, Darmstadt, Germany), MeOH (>99.8 %GC, Merck KGaA, Darmstadt, Germany), EtOH (>99.8 %GC, Sigma Aldrich, Steinheim, Germany), PrOH (>99.8 %GC, Sigma–Aldrich, Tres Cantos, Spain), BuOH (>99.8 %GC, Sigma–Aldrich, Tres Cantos, Spain), 2M1B (>99 %GC, TCI Europe, Zwijndrecht, Belgium), 2M2B (>99 %GC, TCI Europe, Zwijndrecht, Belgium), IB (>99 %GC, Air Products, Paris, France) and MTBE (>99.5 %GC), ETBE (>99.9 %GC), PTBE (>99.5 %GC), BTBE (>99.5 %GC) and TAEE (>99.7 %GC) were synthesized in our lab and purified after successive distillations.

Finally, for the experiments of IER deactivation by ACN (*Section 4.10*), the chemicals used as reactants and for the calibration of the system: 2M2B (96% GC) and 2M1B (4% GC, TCI Europe, Belgium), IB (>99.9% GC, Air Liquide, Spain), absolute EtOH (99.9% GC, Panreac, Spain), ACN (>99.99% GC, Fischer Scientific, Loughborough, United Kingdom) and deionized water were used as reactants.

3.1.2 AUXILIARY GASES

Nitrogen (N_2, >99.995% GC, Abelló-Linde, Barcelona, Spain) was used for pressurizing the reactants injection system and the reaction system of the different setups. Reactors were pressurized to 2.0 MPa to widely exceed the vapor pressure of the reaction mixture at the maximum explored temperature, and also for impelling samples from the reaction medium to the analysis devices through the piping system. Helium (>99.998% GC Abelló-Linde, Barcelona, Spain) was used as carried gas for the different gas chromatographs used. Hydrogen (>99.99% GC) and synthetic air (>99.999% GC) were used for the chromatographic analyses performed with a FID detector.

3.1.3 CATALYSTS AND INERT

The following fifteen acidic IER were tested because they have a varied array of morphological properties: Amberlyst™15 (A-15), Amberlyst™16 (A-16), Amberlyst™35 (A-35), Amberlyst™36 (A-36), Amberlyst™39 (A-39), Amberlyst™40 (A-40), Amberlyst™45 (A-45), Amberlyst™46 (A-46), Amberlyst™48 (A-48), Amberlyst™DT (A-DT), Purolite®CT-124 (CT-124), Purolite®CT-175 (CT-175), Purolite®CT-275 (CT-275), Purolite®CT-482 (CT-482) and Purolite®MN-500 (MN-500). Table 3.1 gathers a summary of the main physical properties of the tested catalysts. A more detailed description about the resins morphology, chemical and structural properties is given in *Section 4.7*. The maximum operating temperature was considered for choosing the conditions of the experiments in order to preserve the thermal stability of the catalysts.

Table 3.1. Main physical properties of tested catalysts

Catalyst	Type	Acid Capacity [eq $H^+ \cdot kg^{-1}$] [a]	DVB [%][b]	Bead diameter, d_b [mm][c]	Moisture [%][d]	Max. Operating T [°C]	Sulfonation type[e]
A-15	macro	4.81	20	0.74	50	120	C
A-16	macro	4.80	12	0.6 - 0.85	52-57	120	C
A-35	macro	5.36	20	0.51	55	150	O
A-36	macro	5.40	15	0.63	55	140	O
A-39	macro	4.81	8	0.54	60-66	130	C
A-40	macro	5.20	high	0.58-0.80	44-53	140	O
A-45	macro	3.65	medium	0.58-0.75	49-54	170	S/Cl
A-46	macro	0.87	high	0.78	26-36	120	S
A-48	macro	5.62	high	0.95	49-56	-	O
A-DT	macro	3.94	medium	0.58-0.75	49-54	170	S/Cl
CT-482	macro	3.65	low	0.81	48-58	190	S/Cl
CT-124	micro	5.00	4	0.77	63	130	C
CT-175	macro	4.98	high	0.94	55	145	C
CT-275	macro	5.37	high	0.75	55	145	O
MN-500	macro	2.70	hyper	0.5-1	52-57	130	S

[a] Titration against a standard base. [b] Crosslinking degree classification: low (7-12%); medium (12-17%); high (17-25%); hyper (50%). [c] Determined by laser diffraction in air (Beckman Coulter LS particle size analyzer) or manufacturer values (range). [d] As shipped. [e] Conventionally sulfonated (C), oversulfonated (O), surface sulfonated (S) and sulfonated/chlorinated (S/Cl)

In order to remove the initial moisture as much as possible all IER were pretreated following the same procedure: 3 h in atmospheric oven at 383 K and then 15h (overnight) in a vacuum oven (0.01 bar) at 383K. The residual amount of water in the catalyst was measured by Karl Fisher titration method for different samples of A-35 with an average result of less than 3.5% $g_{water} \cdot g_{catalyst}^{-1}$. The residual amount of water in the rest of resins after the pretreatment was assumed to be of the same order and therefore, its influence on measured catalytic activity was ignored when comparing resins. If a specific range of particle diameter was required for the experiments, resins were grinded and sieved.

When the dilution of the catalytic bed was necessary to obtain an isothermal bed and working at conversion levels lower than 10%, Silicon Carbide (SiC, pure, Alfa Aesar, Karlsruhe, Germany) was used as inert with an average particle size 0.475 mm, similar to sieved catalyst particles. SiC has been previously proved as inert in etherification reactions [19].

3.2 EXPERIMENTAL SETUPS

3.2.1 STIRRED TANK BATCH REACTOR

Experiments referred to in the *Sections 4.2−4.7* were conducted in the experimental setup depicted in Fig. 3.1, which is composed namely by the reactants injection system, the reactor, the thermostatic bath and the analysis device (GC/MS). The reactant injection system consisted of a cylinder of N_2, a pressurized burette and a system of valves (V1-V10) for purging the system, loading and injecting the reactants. The useful volume of the stainless steel reactor used was 200 cm^3 (45 mm i.d.) and it was equipped with a six-blade magnetic stirrer (Autoclave Engineers, Pennsylvania, USA). It was operated isothermally in batch mode. The stirring speed was set to 600 rpm except for those experiments in which the effect of external mass transfer was studied. Working temperature ranged from 323 to 353 K. It was controlled within ± 0.1 K by a thermostatic bath (Lauda, MGW) mixture (33 vol.% of 1,2-propanediol, 67% of water) fed to the reactor jacket. The reactor pressure was maintained at 2.0 MPa with N_2. One of the reactor outlets was directly connected to a gas chromatograph (GC, Agilent 6890 Series) coupled to a mass selective detector (MS, Agilent 5973N). Filters of 0.5 µm were placed in the sampling pipe and before the analysis system to avoid the entrance of catalyst particles to the GC/MS. More detailed information can be found elsewhere [125].

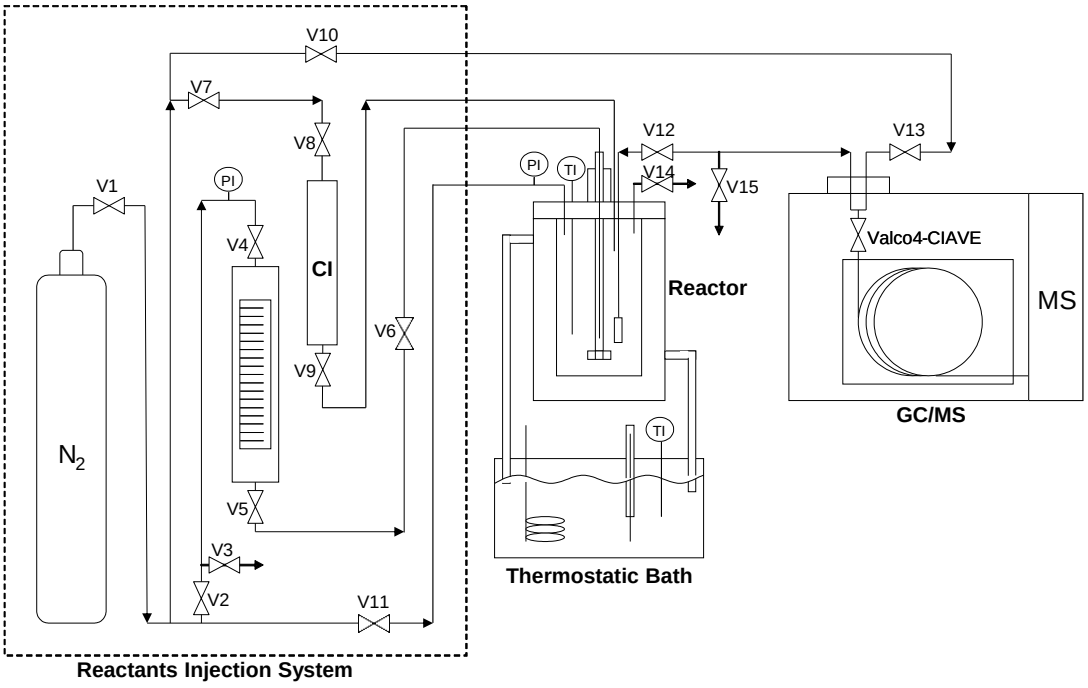

Figure 3.1. Detailed scheme of the experimental setup. V1-V15: Valves. GC/MS: Gas Chromatograph/Mass Spectrometer. CI: Catalyst Injector. PI: Pressure Indicator (Manometer). TI: Temperature Indicator (NiCr/NiAl Thermocouple).

3.2.2 CONTINUOUS FIXED-BED CATALYTIC REACTOR

The ion-exchange resins deactivation experiments by ACN (*Section 4.9*) were carried out in a continuous fixed bed catalytic reactor (Process Integral Development Eng&Tech S.L., Madrid, Spain), see Fig. 3.2. The stainless steel reactor was composed by a tubular bed zone of 180 mm length and 6.5 mm internal diameter (useful volume of 6 cm^3) and it was equipped with 0.5 µm

filters at the inlet and outlet. The bed temperature was measured by means of a thermocouple and controlled through a heating jacket. Besides, the reactor, mixers and conditioning coils were placed into a hot box whose temperature was controlled using a forced convection electric heater. The system pressure was controlled by an electronic back pressure valve (Hoke, model 1315G2Y) with a control accuracy of ±0.1 bar, placed after the gas-chromatograph. Pump P1 (Gilson 307) fed the pressurized mixture of olefins (IB/IA) whereas pump P2 (Gilson 307) fed either EtOH or EtOH and ACN depending on the position of the three ways valve placed before the pump. Two check valves were placed after each pump and before the heating coil to ensure the flow only in one direction. The outlet of the reactor was connected to a GC (Agilent, 6890N). Filters of 0.5 µm were placed along the setup to protect the analysis system from solid particles. The data acquisition software enabled the control of the temperature, pressure and flows by means of PID controllers. The parameters used for the control of the setup are summarized in Table 3.2. An example of the process control graphs obtained in-line is shown in *Appendix 7.2*.

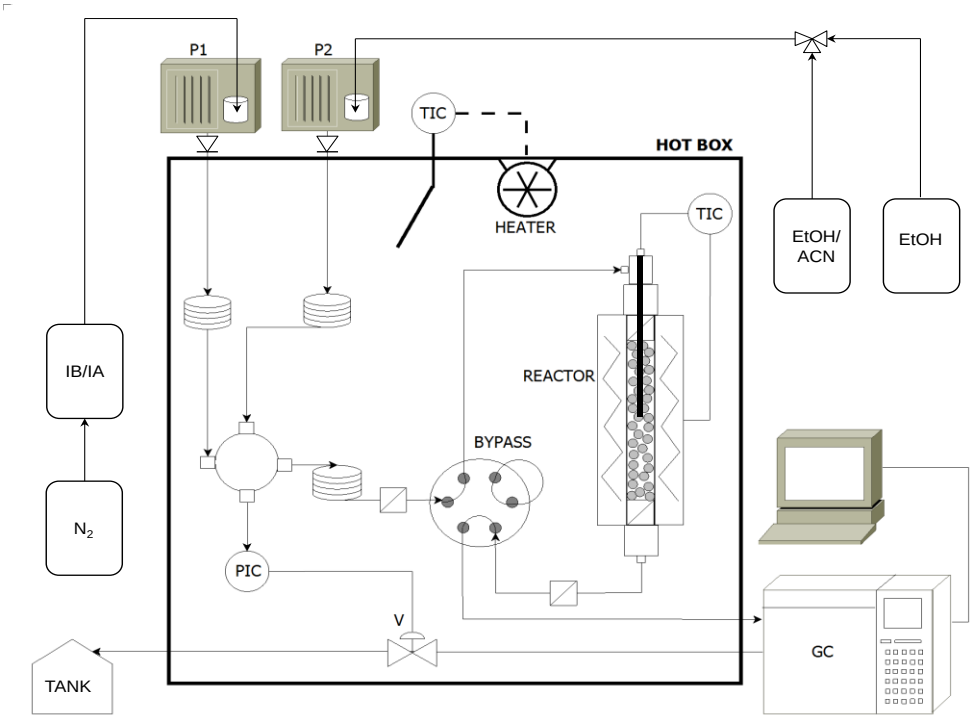

Figure 3.2. Experimental setup used for deactivation experiments. P1-P2: HPLC pumps. TIC: Temperature Indicator and Controller. PIC: Pressure indicator and Controller. GC: Gas chromatograph.

Table 3.2. Values used in the PID controller of experimental setup depicted in Fig. 3.2

Control Parameter	Proportional band [%] (P)	Integral time [s] (I)	Derivative time [s] (D)
System pressure	50	50	0
Reactor Temperature	60	400	60
Hot Box Temperature	16	120	20

3.2.3 BATCH ADSORBER

Liquid-phase adsorption experiments described in *Section 4.8* were carried out in a specially designed glass batch adsorber tightly covered by a Teflon plate to which a total reflux condenser and a sampling septum were attached, see Fig. 3.3. The inner part of the condenser was fed with water at 283 K. The temperature was controlled by means of a thermostatic bath (water) within ±1 K. The liquid mixture was stirred at 1000 rpm using a magnetic stirrer to avoid the effects of the external mass transfer caused by the external layer film in all the experiments. Samples of 2.5 µL were taken periodically from the bulk phase with a syringe and analyzed in a GC (Agilent 6890N series) equipped with a packed column.

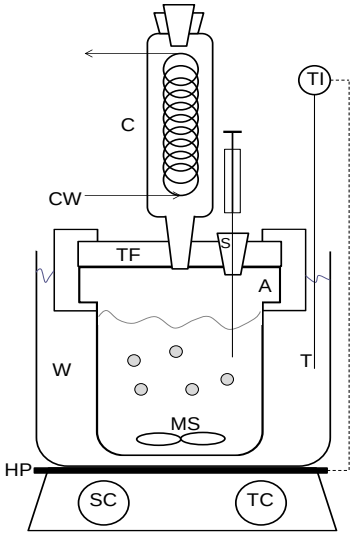

Figure 3.3. Setup used in liquid-phase adsorption experiments. A: Adsorber, C: Condenser, CW: Cold water, HP: Heating plate, MS: Magnetic stirrer, S: Sampling port (septum), SC: Stirring controller, T: Thermocouple, TC: Temperature controller, TF: Teflon plate, W: Water.

3.2.4 PACKED-BED ADSORBER

For gas-phase adsorption study, pulse response experiments were performed in a packed bed adsorber connected to the inlet and to the detector of a gas chromatograph (Agilent 6890N), see Fig. 3.4. The 20 cm length of ¼ inch i.d. stainless steel tube was placed in the GC oven and loaded with pretreated catalyst. The packed bed, consisted of pretreated catalyst that was fixed in the tube using glass wool in both sides of the bed.

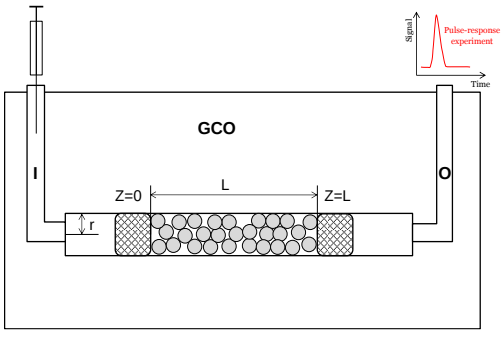

Figure 3.4. I: Inlet (Splitless), GCO: Gas chromatograph oven, L: Packed bed length, O: Outlet (FID-detector), r: Tube radius.

The average linear velocity of carrier gas (Helium) was varied from 10 to 100 mL/min. Before each experiment, the column was conditioned for 1 h at 373 K while carrier gas flowing through. The response peaks were detected using a flame ionization detector (FID). The chromatograph inlet temperature was set to 448 K and the detector temperature was set to 523 K. At the beginning of the runs, 0.2 µL of liquid were injected to the gas chromatograph for all the tracers. In the case of IB 100 µL of pure gas were injected. By means of the data acquisition software the peak high at any time was obtained.

3.3 ANALYTICAL EQUIPMENT AND METHODS

For the experiments conducted in the batch reactor (Fig. 3.1), samples were taken inline from the reaction medium through a liquid sampling valve (Valco A2CI4WE.2, VICI AG International, Schenkon, Switzerland), which injected 0.2 µL into a GC (Agilent 6890GC, Madrid, Spain) equipped with a capillary column (HP-PONA 19091S-001, Hewlett Packard, Palo Alto, USA.; 100% dimethylpolysiloxane, 50.0 m x 0.2 mm x 0.5 µm nominal). A mass selective detector (HP 5973N) coupled to the GC was used to identify and quantify the reaction system components. The oven temperature was programmed with a 10 min hold at 304 K, followed by a 20 $K \cdot min^{-1}$ ramp, from 304 to 353 K, a subsequent second hold of 5 min followed by a second temperature ramp of 60 $K \cdot min^{-1}$ from 353 to 493 K. The final temperature was held for 10 min. Since several $C_{4\text{-}5}$ and C_5 dimers were formed, $C_{4\text{-}5}$ codimers on one side and C_5 dimers on another were respectively lumped together. Neither trimers nor higher oligomers were detected under the conditions of this study. An example of the chromatograms obtained using this analytical method is plotted in Fig. 3.5. The average linear velocity of compounds, expressed as the ratio of column length to retention times, the mass spectra of involved compounds can be found in *Appendix 7.3*.

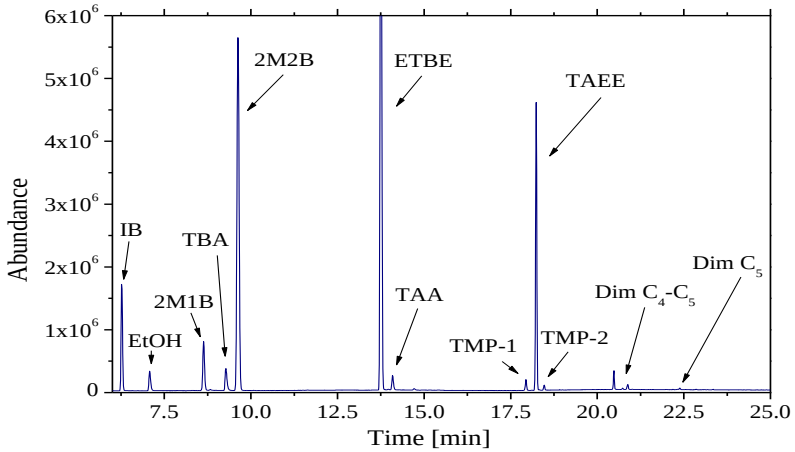

Figure 3.5. Example of a chromatogram obtained in the GC-MS system. Experimental conditions: $R°_{A/O}$=0.5, $R°_{C4/C5}$=1, 353 K, t=300 min using A-35 as catalyst.

For the experiments in the fixed-bed catalytic reactor (Fig. 3.2), 0.2 µL samples were injected inline from the reaction outlet through a liquid sampling valve (Valco A2CI4WE.2, VICI AG International, Schenkon, Switzerland) into a GC (Agilent 6890GC, Madrid, Spain) equipped with a capillary column (HP-PONA 19091S-001, Hewlett Packard, Palo Alto, USA.; 100% dimethylpolysiloxane, 50.0 m x 0.2 mm x 0.5 µm nominal) and a thermal conductivity detector (TCD). The oven temperature was maintained constant at 308 K; a He flow of 1 mL/min and a split ratio of 1/75. One example of the chromatograms obtained is depicted in Fig. 3.6.

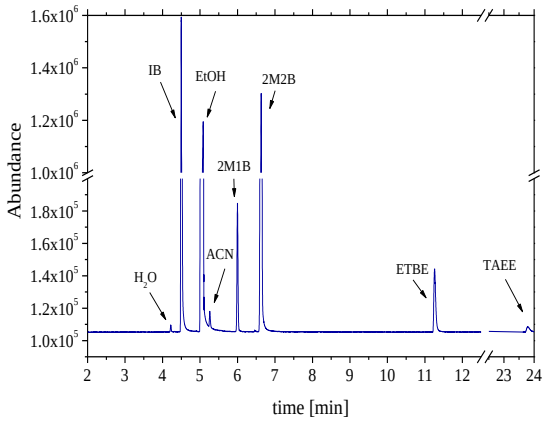

Figure 3.6. Example of the chromatograms obtained in deactivation experiments. T = 353 K, $R°_{A/O}$=1.1, $R°_{C4/C5}$=1, 4000 ppm of ACN, and 0.04 g of A-35.

For liquid-phase adsorption experiments, gas chromatograph (GC, Agilent 6890N series) which was equipped with a packed column (2m, 15% FFAP on Chromosorb AW) and a flame ionization detector (FID). The GC inlet and detector temperatures were set to 448 and 523 K, respectively. A carrier gas (He) flow of 30 mL·min^{-1} was used. Before each experiment, the column was conditioned for 1 h at 373 K. The temperature of the gas chromatographic oven was varied from 333 to 378 K depending on the tracer in order to achieve a good separation of the solvent and tracer peaks. No ramps were used in the temperature program of the chromatographic oven. An example of the chromatograms obtained in these experiments is plotted in Fig. 3.7. Gas-phase adsorption experiments were performed in the same GC, using the same set parameters for GC inlet and detector, while the oven temperature and the carrier flow were varied depending on the desired conditions for the pulse-response experiments. One example of the signals obtained is depicted in Fig. 3.8.

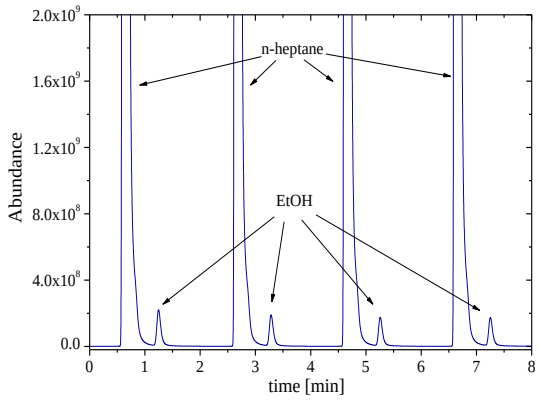

Figure 3.7. Example of chromatogram for liquid-phase adsorption runs. C^0_{EtOH}=0.125 mol L^{-1}, T=323 K.

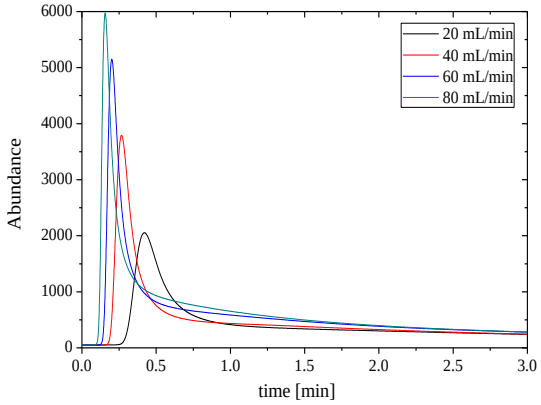

Figure 3.8. Example of gas-phase pulse response adsorption experiments for TAEE at 353 K.

3.4 EXPERIMENTAL PROCEDURE

For equilibrium experiments (*Sections 4.2−4.4*), EtOH, water and the catalyst were placed into the reactor and the stirrer was turned on. Then, the reactor was heated up by the thermostatic bath until the system reached the desired temperature. Known amounts of IA and IB were introduced in a calibrated burette and pressurized to 1.5 MPa with nitrogen. Once the working temperature was reached inside the reactor, the mixture of olefins was shifted from the burette into the reactor with N_2. Then the reactor pressure was set to 2.0 MPa with N_2, and the reactor was heated up until it reached the desired temperature again. The reactor was pressurized to widely exceed the vapor pressure of the reaction mixture at the highest assayed temperature, and to impel samples to the GC/MS through the piping. During the experimental runs the reactor operated isothermally. For the measurement of the reaction mixture composition, samples were taken and analyzed periodically until pseudo-equilibrium state was reached (typically after 6-8 h of running).

For kinetic experiments referred to in *Sections 4.5−4.7,* the initial reaction mixture of EtOH and olefins was placed into the reactor, pressurized to 1.0 MPa with N_2, and heated up to the desired reaction temperature. It was verified that no reaction takes place in the absence of catalyst. The weighted mass of previously pretreated catalyst was placed in the catalyst injector, pressurized with N_2 to 2.0 MPa and injected into the reactor by means of pressure difference. Immediately after, the reactor pressure was set to 2.0 MPa. That instant was considered the starting time.

As for adsorption experiments of *Section 4.8*, two experimental procedures were used. On one hand, for liquid-phase adsorption experiments, the batch adsorber was filled up with 60 mL of *n*-heptane, subsequently closed and placed within the previously switched on thermostatic bath. The total reflux condenser was then connected to the adsorber and the magnetic stirrer was connected. Once the desired temperature was reached in the adsorber bulk phase, the dry mass of catalyst was injected to the adsorber. Then, the desired amount of tracer was loaded into a syringe and injected to the bulk-phase containing *n*-heptane and the catalyst. That instant was considered the starting time of the adsorption experiment. Immediately after, the first sample was taken from the liquid medium and from then on, samples were taken periodically until no changes in the bulk composition were observed, indicating that adsorption equilibrium was reached. On the other hand, for gas-phase adsorption experiments, the pretreated catalyst mass was fixed in the tube with glass wool, then the tube was connected to the inlet and outlet of the GC and the system was conditioned 1 h at 373 K. When online signals of the GC were stable, the desired amount of each tracer was injected with a chromatographic syringe and the response peaks were obtained. Fresh catalyst was used in all the runs.

For deactivation experiments, *Section 4.9*, the corresponding reactants reservoirs were initially filled with the adequate mixture of olefins (IB and IA), EtOH or EtOH containing ACN. Then the reactor was connected to the setup, and the desired set points of pressure, temperature and flows were indicated in the PID controlling software. Pressure was always set to 17 MPa and the temperature was varied from 313 to 353 K. After that, Pump 2 from Fig. 3.2 was switched on and EtOH started to flow through the setup pipelines. Once the reactor temperature was the desired for the experiments, the second HPLC pump was switched on and the mixture of IB and IA was added to the reactor inlet stream. Once the system reached the steady state, etherification reactions rates were constant, the feeding of EtOH was immediately shifted to feeding EtOH poisoned with ACN at the desired concentration by means of the three ways valve. That moment was considered as the initial time of the deactivation experiment. Samples were taken at analyzed periodically at the reactor outlet. The approximate duration of a typical run was 4h.

3.5 AUXILIARY DEVICES AND TECHNIQUES

- **N_2 adsorption-desorption at 77K.** Dry state catalyst Brunauer-Emmet-Teller (BET) surface area ($S_{g,BET}$), pore volume ($V_{pore,BET}$) and pore diameter ($d_{pore,BET}$) were obtained by N_2 adsorption-desorption at 77 K (Accusorb ASAP 2020, Micrometrics). For $S_{g,BET} < 1$ m^2 g^{-1}, krypton was used. $V_{pore,BET}$ was obtained by the volume of N_2 adsorbed at relative pressure $(P/P_0)=0.99$. $d_{pore,BET}$ was computed as $4V_{pore,BET}/S_{g,BET}$. The samples were previously dried at 383 K till no mass variation was detected.

- **Mercury intrusion porosimetry.** Surface area and pore volume of previously pretreated commercial A-35 particles were also determined by mercury intrusion porosimetry (Quantachrome 60).

- **ISEC.** The morphology of IER in swollen state has been assessed by means of the ISEC technique [151]. Catalysts were crushed, sieved in swollen state ($0.250<d_p<0.125$ mm), placed overnight in the mobile phase (0.2N Na_2SO_4) and later on packed in the column. 20 μL of the standard solutes (deuterium oxide, sugars and dextranes) were injected during the chromatographic measurements. Elution volumes were determined on the basis of the first statistical moments of the chromatographic peaks. Additionally, the swollen morphology of

resin MN-500 was also characterized by ISEC measurements using THF as the mobile phase. The ISEC data treatment is based on fitting the volumes of the differently dense model fractions with the aim to minimize differences between experimental elution volumes of standard solutes and values computed on the base of the morphology model, as described elsewhere [152].

- **Scanning Electron Microscopy (SEM).** The inner morphology of A-35 resin was examined by SEM (QUANTA 400F Field Emission Instrument) using crashed and uncrashed pretreated particles of fresh A-35. Particles were crashed in order to observe with higher level of detail the inner structure of the catalyst. Before taking the images, particles were coated with gold in order to make them conductive, so electrons can easily flow around them. Also a mapping of elements present in the catalyst surface was performed in this instrument.

- **Thermogravimetric Analysis (TGA).** TGA and STDA (s*imultaneous difference thermal analysis*) curves were determined (STARe SW 8.10, Mettler Toledo) for A-35 to evaluate the thermal effects on the resin structure. A fresh catalyst mass of 0.1 g was used in such analysis with N_2 flowing at 50 mL min^{-1} in the temperature range 30-1000 ºC at 10 ºC min^{-1}.

- **Fourier Transform Infrared Spectroscopy (FTIR).** FTIR analysis (Spectrum™ 100, PerkinElmer, equipped with attenuated total reflectance accessory) of pyridine adsorption was performed for A-35 at 353 K to evaluate the acidic properties of the catalyst surface. The catalyst was pretreated before the analysis.

- **Helium displacement.** Skeletal density of all IER resins used was determined by Helium displacement (Accupic 1330) at 300.6 K. All the resins were dried under vacuum before the analyses.

- **Laser diffraction in Air.** The bead size distribution of commercially shipped resins was measured by laser diffraction in air (LS 13320 Laser Diffraction Particle Size Analyzer). Resins samples were previously pretreated.

- **Distillation columns.** A distillation column of 1m length and 0.03 m internal diameter (Fisher Scientific) packed with Pall rings was used to purify the ethers obtained in the present work. It was operated at atmospheric pressure. Afterwards a Vigreux distillation column (0.4 m length and 2.5 cm i.d.) was used for refining the etherification products obtained.

- **Karl-Fischer titration.** A Karl Fischer automatic titrator (Orion AF8, Thermo Electron Corporation, Massachusetts, USA) was used to determine the water content of resins after pretreatment. Reagents used were dry MeOH and hydranal-composite 5 (Fluka Analytical).

- **Ovens.** Atmospheric and vacuum ovens (Memmert, Beschikung Loading model 100-80) were used for the pretreatment of the catalysts.

In addition, precision balances (Denvert Instrument, SI-4002 model), micropipettes (Gilson P200, P-1000 and P-5000), electronic burettes (Brand GMHB) and other daily lab equipment were used for standard procedures of weighting, preparing solutions, titrating, etc.

3.6 GENERAL CALCULATIONS

For all the experiments carried out in the present thesis, reactants conversion, selectivity and yield toward products were calculated at each instant for each run by means of the following expressions:

$$X_j = \frac{\text{mole of } j \text{ reacted}}{\text{initial mole of } j} \quad (3.1)$$

$$S_j^k = \frac{\text{mole of } k \text{ produced}}{\text{mole of } j \text{ reacted}} \quad (3.2)$$

$$Y_j^k = X_j \cdot S_j^k \quad (3.3)$$

where *j* refers to the reactant and *k* to the considered product or byproduct.

For the calculations of the experimental reaction rates (r_i) in the batch reactor the next procedure was follow. First, the mole evolution of ethers was fitted to an exponential equation form. Then, as formation rates can be expressed by means of Eq. 3.4, deriving the fitted function of the corresponding variation of n_k versus time, it is obtained an expression from which experimental rates can be calculated as any time. W_{cat} refers to the catalyst mass in dry basis.

$$r_k^t = \frac{1}{W_{cat}}\left[\frac{dn_k}{dt}\right]_{t=t} = \upsilon_k r_i^t \quad (3.4)$$

where r^t_k is the reaction rate at the instant t for the formation reaction of *k* and n_k are the formed moles of product *k*. Initial reaction rates r^0_k were calculated for the instant at which t=0.

For a plug-flow fixed bed catalytic reactor under differential regime, the experimental etherification rates were calculated as follows:

$$\mathrm{r_{ether}} = \frac{F^0_{\mathrm{olef}}\left(X_{\mathrm{olef,inlet}} - X_{\mathrm{olef,outlet}}\right)}{W_{\mathrm{cat}}} \quad (3.5)$$

where F^0_{olef} is the IB or IA reference molar flow at null conversion, $X_{\mathrm{olef,outlet}}$ is the IB or IA conversion at the reactor outlet, and $X_{\mathrm{olef,inlet}}$ is the inlet IB or IA conversion (zero).

3.7 MASS BALANCE AND EXPERIMENTAL UNCERTAINTY

In order to evaluate the experimental error, some experiments were replicated in the different experimental designs referred to in the different sections of the present thesis. The results were found to be reproducible in all the runs. In replicated experiments, the standard error of the average equilibrium constant was always lower than 5%, except for etherifications of IB and 2M1B at 323 K, where the standard error was 9 and 7%, respectively. The main cause of this deviation is the low olefin content (IB and 2M1B) at equilibrium at the lowest temperature, which led to higher differences between calculated values. For experiments in *Sections 4.6* and *4.7*, an experimental uncertainty of 6% in mole basis was estimated for a 95% confidence level. Maximum experimental uncertainties of 6% and 12% were estimated for r_{ETBE} and r_{TAEE}, respectively, for the same confidence level. It can be assumed that the experimental error of non-replicated experiments would be of the same order. Additionally, the mass balance was fulfilled within ± 4% for all the experiments. As these values of experimental error are acceptable, experiments were considered reproducible and reliable.

3.8 SYSTEMS CALIBRATION

Prior to carry out the experiments of the different sections of the present thesis, the calibration of the gas chromatographs used for the analyses and other devices as pumps for controlling the flow in the different experimental setups was performed.

For the calibration of the GC/MS used in the batch reactor described in *Section 3.2.1*, several standard samples of known composition were prepared and injected through the chromatographic valve by means of a pressurized burette. The chromatographic responses, in terms of chromatographic area fraction ($\%A_j$) were then correlated to the mass percentage of the corresponding species ($\%M_j$) contained in each standard. The calibration equations obtained for all the involved species are gathered in Table 3.3.

In order to reduce the errors associated with the manipulation of the mixture, that is to improve the quality of the responses, as well as to increase the linearity of the response of the GC/MS system, 2M2B was used as internal standard for preparing the standard calibration samples. The composition of such standards was varied to include the expected variation of chemical species composition during the subsequent experimental runs. When necessary, additional calibration samples were prepared to gather this range. Due to the difficulty of purifying $C_{4\text{-}5}$ codimers, their chromatographic response was estimated as an intermediate response factor between C_4 and C_5 dimers as $(\%A_{DimC4\text{-}C5}/\%A_{2M2B}) = 0.4453(\%M_{DimC4\text{-}C5}/\%M_{2M2B})$. The calibration plots obtained for each chemical species are shown in *Appendix 7.4.1*.

Table 3.3. Calibration results for the GC/MS analysis system used for the batch reactor setup.

Chemical species	Calibration Equation	R^2
IB	$(\%M_{IB}/\%M_{2M2B}) = -0.138(\%A_{IB}/\%A_{2M2B})^2 + 1.6334(\%A_{IB}/\%A_{2M2B})$	0.9975
EtOH	$(\%M_{EtOH}/\%M_{2M2B}) = -0.0841(\%A_{EtOH}/\%A_{2M2B})^2 + 1.997(\%A_{EtOH}/\%A_{2M2B})$	0.9943
2M1B	$(\%M_{2M1B}/\%M_{2M2B}) = -0.0607(\%A_{2M1B}/\%A_{2M2B})^2 + 1.1635(\%A_{2M1B}/\%A_{2M2B})$	0.9954
TBA	$(\%M_{TBA}/\%M_{2M2B}) = 0.3014(\%A_{TBA}/\%A_{2M2B})^2 + 1.7171(\%A_{TBA}/\%A_{2M2B})$	0.9957
ETBE	$(\%M_{ETBE}/\%M_{2M2B}) = -0.0069(\%A_{ETBE}/\%A_{2M2B})^2 + 0.8243(\%A_{ETBE}/\%A_{2M2B})$	0.9955
TAA	$(\%M_{TAA}/\%M_{2M2B}) = -1.387(\%A_{TAA}/\%A_{2M2B})^2 + 1.4566(\%A_{TAA}/\%A_{2M2B})$	0.9949
TAEE	$(\%M_{TAEE}/\%M_{2M2B}) = -0.0114(\%A_{TAEE}/\%A_{2M2B})^2 + 0.7151(\%A_{TAEE}/\%A_{2M2B})$	0.9969
TMP-1	$(\%M_{TMP\text{-}1}/\%M_{2M2B}) = 0.6156(\%A_{TMP\text{-}1}/\%A_{2M2B})$	0.9989
TMP-2	$(\%M_{TMP\text{-}2}/\%M_{2M2B}) = 0.4868(\%A_{TMP\text{-}2}/\%A_{2M2B})$	0.9924
Dimers C_5	$(\%M_{DimC5}/\%M_{2M2B}) = 0.2749(\%A_{DimC5}/\%A_{2M2B})$	0.9985

With respect to the calibration of the GC used in the experiments performed in *Section 4.9*, the calibration equations obtained for all the involved species are gathered in Table 3.4. The corresponding experimental calibration curves can be seen in detail in *Appendix 7.4.2*. For this analysis system, the chromatographic area fractions obtained were found to follow virtually perfect linear trends for all the species, therefore, $\%A_j$ were directly correlated to $\%M_j$ and the use of an internal standard was considered unnecessary.

Table 3.4. Calibration curves obtained for the GC used in the fixed bed catalytic reactor setup.

Chemical Species	Calibration Equation	R^2
H_2O	$\%M_{H2O}=1.00325(\%A_{H2O})$	0.99861
IB	$\%M_{IB}=0.94034(\%A_{IB})$	0.99361
EtOH	$\%M_{EtOH}=0.96431(\%A_{EtOH})$	0.99081
ACN	$\%M_{ACN}=0.58428(\%A_{ACN})$	0.99882
2M1B	$\%M_{2M1B}=1.17648(\%A_{2M1B})$	0.99552
TBA	$\%M_{TBA}=1.19892(\%A_{TBA})$	0.99906
2M2B	$\%M_{2M2B}=1.00522(\%A_{2M2B})$	0.99556
ETBE	$\%M_{ETBE}=1.21476(\%A_{ETBE})$	0.99821
TAA	$\%M_{TAA}=1.33487(\%A_{TAA})$	0.99887
TAEE	$\%M_{TAEE}=1.29374(\%A_{TAEE})$	0.99963

The HPLC pumps used for feeding the reactants to the fixed bed catalytic reactor also needed a flow calibration. The nominal flow was related to the real flow by: Q_{nom} (mL s^{-1}) = a·Q_{real} (mL s^{-1}) + b. The obtained calibration equations are gathered in Table 3.5 and the experimental tests performed for the calibration are included in *Appendix 7.4.3*.

Table 3.5. Calibration of the HPLC pumps used for feeding the fixed bed catalytic reactor.

Device	a	b
Pump 1[a]	1.01528	0.00011
Pump 2[b]	1.02323	-0.00033

[a]Pump 1 was used for feeding EtOH and EtOH+ACN mixture. [b] Pump 2 was used for feeding an equimolar mixture of IB and IA.

With regards to the calibration of the GC used in liquid-phase adsorption experiments, calibration factors for each of the tracers used and *n*-heptane were obtained by preparing standards at different concentrations. The calibration factors (α) determined by means of Eq. 3.6 are summarized in Table 3.6.

Table 3.6. Calibration factors for liquid-phase adsorption experiments.

Compound	α
MeOH	9.699 ± 0.179
EtOH	3.821 ± 0.095
PrOH	2.848 ± 0.043
BuOH	2.031± 0.051
2M2B	2.167 ± 0.107

$$\alpha_A = \frac{x_A}{A_A / A_B \left(1 - x_A\right)} \qquad (3.6)$$

where x_A is the molar fraction of tracer A in the mixture of tracer and solvent, A_A is the chromatographic area of tracer *A* and A_B is the chromatographic area of the solvent (*n*-heptane). α values were computed as an average of the values obtained at five different concentrations for each tracer. More detailed description about the pairs tracer and *n*-heptane calibration factors obtained can be found in *Appendix 7.4.4*.

4. RESULTS AND DISCUSSION

4.1 DESCRIPTION OF THE REACTION SYSTEM

Tertiary alkyl ethers are manufactured in thermodynamically limited reactions and, depending on the experimental conditions, a wide variety of compounds can be formed as products of reversible and irreversible reactions. The product distribution under different experimental conditions and at chemical equilibrium is hence information of utmost importance for designing reaction units, such as industrial fixed-bed catalytic reactors or reactive distillation units. This is crucial not only to determine whether further separation units are required, but also to predict composition, properties and possible emissions from final blended gasoline. Preliminary experiments were performed at different experimental conditions to assess the product distribution and the whole reaction network involved in the studied system. Fig. 4.1.1, depicts the proposed reaction scheme for the simultaneous etherification of IB and IA with EtOH comprising all possible chemical reactions occurring at different conditions.

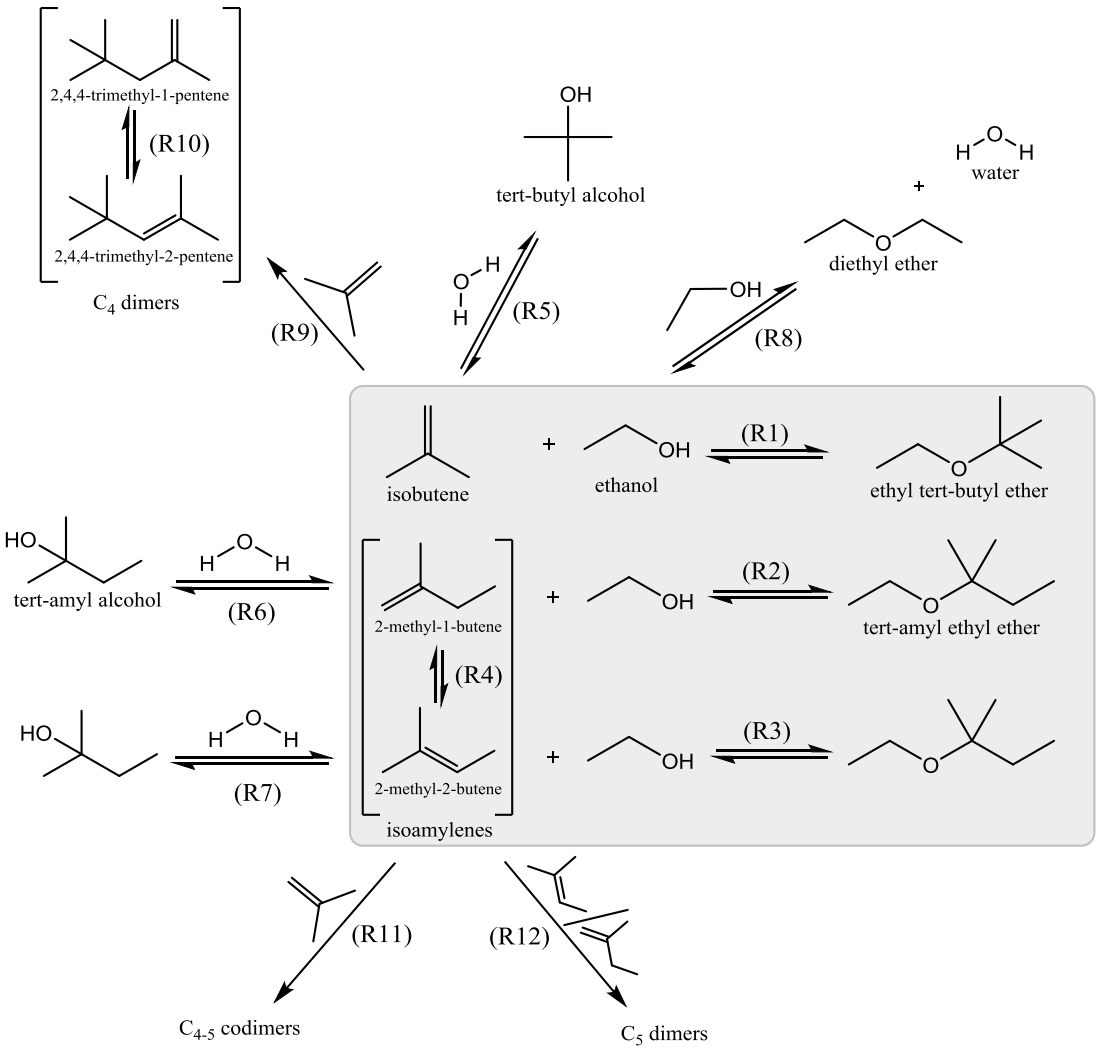

Figure 4.1.1. Full reaction network. Grey colored area gathers the main reactions from which bioethers are produced.

The main reactions in Fig. 4.1.1 are the etherification of IB (R1), 2M1B (R2) and 2M2B (R3) with EtOH that produce ETBE or TAEE. Besides, the double bond isomerization reaction (R4) between both IA (2M1B and 2M2B) also takes place. Since water was present in the initial reactant mixture of some of the experiments, hydration of IB and IA also took place (R5, R6 and R7) to form TBA and TAA (tertiary alcohols). In addition, diethyl ether (DEE) can be formed by dehydration of two EtOH molecules (R8) but it was detected only at 353K and $R°_{A/O}$=2 and at such a low amount (less than 0.06% GC) that it was included neither in the system calibration nor in further calculations. That was expected since the extension of alcohol dehydration reactions become significant at higher temperatures than those explored in the present work [153]. IB (C_4) and IA (C_5) dimers and thereof codimers (C_{4-5}) were detected under initial olefin stoichiometric excess ($R°_{A/O}$=0.5) at the higher explored temperatures (R9, R11 and R12). Only TMP-1 and TMP-2 were detected as C_4 dimers, whereas a wide variety of compounds were identified as C_{4-5} codimers and C_5 dimers. They are analyzed in detail in *Section 4.5*. Double bond isomerization reaction between TMP-1 and TMP-2 is also expected to take place (R10). According to Fig. 4.1.1, the global reaction rate of TAEE formation is expressed as $r_{TAEE}=r_{R2}+r_{R3}$, and the formation rate of 2M2B is expressed as $r_{2M2B}=r_{R4}-r_{R3}$.

4.2 GREEN METRICS ANALYSIS OF THE REACTION SYSTEM

An extended and revised version of this chapter has been published as:

R. Soto, C. Fité, E. Ramírez, R. Bringué, M. Iborra, Green metrics analysis applied to the simultaneous liquid-phase etherification of isobutene and isoamylenes with ethanol over Amberlyst™ 35. *Green Process. Synth.* **2014**; 3: 321–333.
DOI 10.1515/gps-2014-0049.

4.2.1 INTRODUCTION

Generally, ETBE and TAEE can be produced by EtOH etherification with IB and IA, respectively, over acid catalysts such as IER and zeolites. Using the same catalysts, an alternative ether synthesis route is via an intermolecular dehydration reaction between the corresponding tertiary alcohol and short chain primary alcohol; for instance, ETBE can be produced by reaction between TBA and EtOH. The analogous reaction of TAA and EtOH leads to TAEE. Besides, several reaction devices and configurations can be used in the production of these ethers, among others, stirred tank reactors, reactive distillation, reactor and membranes, etc. The aim of this work is to analyze the simultaneous etherification of IB and IA with EtOH in the liquid-phase over Amberlyst™35 under the Green Metrics Analysis (GMA) in order to compare several batch processes and synthesis pathways of isolated syntheses for both ETBE and TAEE.

4.2.2 EXPERIMENTAL AND CALCULATIONS

The stirred tank batch reactor described in *Section 3.2.1* was used to carry out the experimental work. A dried catalyst mass of 8 g within the commercial bead size distribution were used. An initial molar ratio alcohol to olefins ($R°_{A/O}$) and an initial molar ratio between IB and IA ($R°_{C4/C5}$), both equal to unity and T = 333 K, were chosen as experimental conditions in order to compare results with literature data which can be found at these conditions.

Designed as a tool to compare the material efficiency of different chemical processes, the GMA consider five parameters to be measured and optimized: Atom Economy (AE), Reaction Mass Efficiency (RME), Reaction Yield (ε), Stoichiometric Factor (SF) and Material Recovery Parameter (MRP), in order to evaluate how green a chemical process is from an environmental point of view [154]. These five parameters can be gathered in one parameter called Vector Magnitude Ratio (VMR), defined as the root mean square (also called quadratic mean). One important application of the green chemistry concepts resides in their translation into mathematical language, which easily allows the numerical comparison among different chemical routes. In general terms, five parameters are used whose values should be optimized to get unity. It has been proved to be an effective methodology to compare hundreds of organic chemical reactions [155]. AE measures how much of the starting material ends in the desired product, that is to say, how many atoms of the reactants are included in the structure of the final product. Hence, this parameter assesses the reaction stoichiometry as it does not consider either the reaction yields (ε), the side products produced, or other auxiliary materials used [57]. RME

takes into account the reaction yield (ε), the implicated masses of reactants and target product, and the actual molar quantities of reactants. SF considers the use of excess reactants and MRP considers the use of other materials in the reaction and post-reaction phases (work-up and purification), such as solvents and washings for extractions, and whether they are recovered.

Since the different metrics focus on different process scopes, for instance AE focus on reaction stage while MRP includes the downstream processing, it is important to clarify that the GMA must be performed to each step of the process, building the corresponding radial pentagons for each stage. Otherwise, the interpretation of results could be difficult and may lead to confusions when comparing different processes. It should be noticed that the scope of the present work was focused on the reaction stage, considering the material inputs and outputs of the reaction zone. The purification stage and other downstream processes were excluded in the analysis due to the differences in final composition of the evaluated approaches and due to the lack of accurate information on required work-up and purification materials.

Additionally, beyond these five metrics, other relevant environmental, health and safety issues must be considered such as the Environmental Factor (E_{factor}) and the Carbon Mass Efficiency (CME). The E_{factor} quantifies the amount of waste formed in the synthesis of chemical compounds as the weight ratio of the amount of waste created to the product formed [156,157]. It can also include all the steps in a chemical synthesis, upstream or downstream of the reaction step. Under stoichiometric conditions and assuming that all solvents and catalyst are recycled, E_{factor} and RME are related and the use of both metrics becomes unnecessary. CME or carbon efficiency measures the sustainability of a process. It is defined as the percentage of carbon in the reactants that remains in the final product [54]. Thus, the ideal reaction system corresponds to CME=100%, and a reaction with lower CME represents an amount of carbon that can eventually end in a waste stream or as emissions. Finally, other helpful metrics to assess the inherent green chemistry of a process are the Process Mass Intensity (PMI) and the Carbon Factor (C_{factor}). PMI is defined as the total mass of materials used to produce a specified mass of product and the C_{factor} quantifies the amount of CO_2 produced per mass unit of product formed. Besides, there are other metrics such as the Energy Loss Index (ELI), that is an indicator to estimate the energy-related efforts associated with the process and the Space Time Yield (STY) that assesses the speed at which reaction occurs [57].

Based on the definitions found in previous key publications [54,57,154,155,158,159], the main parameters of the Green Metric Analysis (AE, ε, RME, 1/SF, MRP, and VMR) were calculated as follow:

$$AE = \frac{MW_{product}}{\sum_j MW_{reactants}} \tag{4.2.1}$$

$$\varepsilon = \frac{mole_{product}}{mole_{j,\,reacted}} \tag{4.2.2}$$

$$RME = \frac{m_{product}}{\sum_j m_{reactants}} \tag{4.2.3}$$

$$SF = 1 + \frac{\sum m_{er}}{\sum m_{sr}} = \frac{AE \cdot \sum m_{er}}{m_{tp}} \quad (4.2.4)$$

$$MRP = \frac{RME \cdot SF}{\varepsilon \cdot AE} \quad (4.2.5)$$

$$VMR = \frac{\sqrt{AE^2 + \varepsilon^2 + (1/SF)^2 + MRP^2 + RME^2}}{\sqrt{5}} \quad (4.2.6)$$

In addition to the aforementioned metrics that constitute the core of the analysis carried out in the present study, the E_{factor}, E_{total}, CME and PMI were also evaluated by means of the following expressions:

$$E_{factor} = \frac{\sum_j m_{waste}}{m_{product}} = \frac{1}{RME} - 1 \quad (4.2.7)$$

$$E_{total} = E_{factor} + E_{aux} \quad (4.2.8)$$

$$CME = \frac{m_{C\text{-}product}}{\sum m_{C\text{-}reactants}} \cdot 100 \quad (4.2.9)$$

$$PMI = \frac{\sum_j m_j}{m_{product}} = E_{total} + 1 \quad (4.2.10)$$

where E_{aux} is the ratio of the amount of auxiliary materials used to the product formed.

All these metrics were calculated following the radial pentagon spreadsheet algorithm proposed by Andraos for linear single reactions [58,154]. In order to substantiate the algorithm calculations and procedure, *Appendix 7.5.1* includes all the metrics calculation and the radial pentagon diagram for each of the evaluated approaches. It also contents the mass data for all the ingredients (masses of reactants, catalysts, reaction solvents, any other auxiliary materials, and the mass of target product) used in each case.

4.2.3 GREEN METRICS RESULTS

The main parameters of the Green Metrics Analysis (AE, ε, RME, 1/SF and MRP) calculated by means of Eqs. 4.2.1–4.2.5 are displayed graphically as a radial pentagon depicting a "material usage footprint". Therefore, it is easy to recognize which of these factors are contributing to an attenuation of VMR (Eq. 4.2.6) and, therefore, to the total process material efficiency. This efficiency is directly related to the environmental performance since the optimum exploitation of the reaction ingredients in terms of mass allows the minimization of side products, waste and other purification materials. Each radial pentagon axis corresponds to each of the five parameters, emanates from the center and ranges in values from zero to one. Values of these parameters are depicted as dots and are connected to form a pentagonal figure. The ideal "green" situation is depicted by a regular pentagon of unit radius where each parameter is equal to one. The less "green" a reaction is, the more distorted the resultant pentagon toward the center. These diagrams can ascertain by visual inspection which reaction classes are inherently

"green" and which are not. The degree of distortion of the radial pentagon from its regular ideal shape may be directly related to which parameters are responsible for that distortion.

For the sake of comparison, GMA is performed on the experimental data of this work and to the data found in several works in the literature focusing isolated ETBE and TAEE syntheses. The resulting GMA radial pentagons for ETBE and TAEE syntheses are gathered in Figs. 4.2.1 and 4.2.2, respectively. The reactor input and output are given in terms of mass in Table 4.2.1.

Selected bibliographic references [45,137,139,160–166] refer to batch processes and include batch reactive distillation [161,164,165], stirred tank reactor (STR) [45,137,139,160,162,163,166] and also comprise two ethers synthesis pathways; from tertiary alcohols (TBA and TAA) and EtOH [45,161–163,166] and from tertiary olefins (IB and IA) and EtOH [137,139,160,164,165]. Besides the comparison of Figs. 4.2.1 and 4.2.2, obtained values for the main Green Metrics are summarized in Table 4.2.2 in order to compare them numerically. The catalyst used, temperature, E_{factor}, E_{total} and CME [57,157] calculated following the Eqs. 4.2.7–4.2.9 are also included in Table 4.2.2.

Table 4.2.1. Mass balance data for the run at 353 K, $R°_{A/O}$=$R°_{C4/C5}$=1 over A-35.

Time [min]	0	360
Component	Initial [g]	Final [g]
IB	34.50	1.57
ETOH	59.18	16.08
2M1B	2.20	1.58
TBA	-	0.44
2M2B	41.80	18.83
ETBE	-	59.50
TAA	-	0.40
TAEE	-	39.29
TOTAL	137.68	137.68

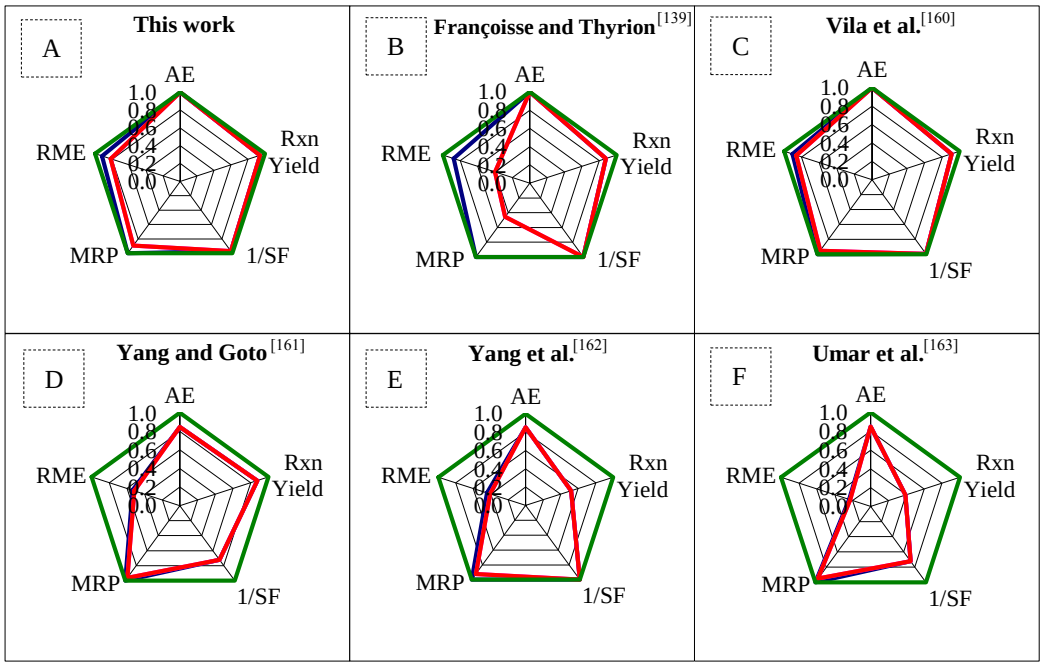

Figure 4.2.1. Evaluated cases for ETBE synthesis. (—) Complete reclaiming, (—) Partial Reclaiming, (—) No reclaiming, (—) Ideal.

Regarding ETBE synthesis, the most suitable synthesis pathway seems to be in a batch reactor (STR), under IB and EtOH stoichiometric conditions (Fig. 4.2.1, A and C). Obviously, the use of solvents (Fig. 4.2.1, B) diminishes RME and MRP and would lead to rise the overall costs of

the process, so its use is not advisable unless absolutely necessary. The synthesis of ETBE from TBA and EtOH (Fig. 4.2.1, D, E and F) leads to water formation and it reduces considerably the reaction yield, AE, and RME. Furthermore, it promotes some azeotropes formation, what increases the downstream difficulty of components separation owing to the simultaneous presence of considerable amounts of water, EtOH and ETBE. Interestingly, reactive distillation allows higher yield in the synthesis of ETBE from TBA and EtOH (Fig. 4.2.1, D), but an excess of EtOH is required and hence lower RME and SF are obtained.

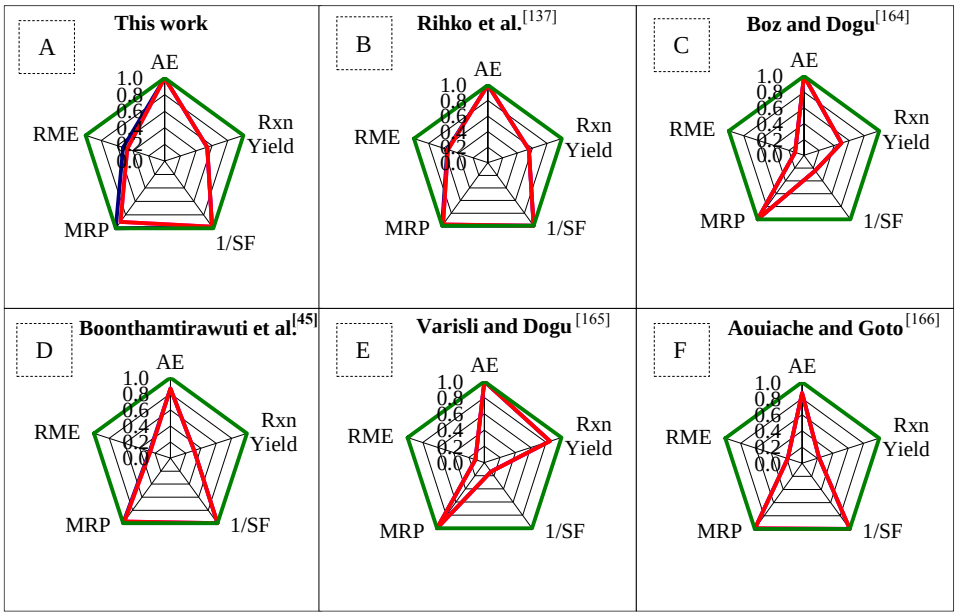

Figure 4.2.2. Evaluated cases for TAEE synthesis. (—) Complete reclaiming, (—) Partial reclaiming, (—) No reclaiming, (—) Ideal.

With respect to TAEE formation, its synthesis from tertiary olefins (IA) and EtOH yields the best results (Fig. 4.2.2, A and B), analogously to the optimum route selected for ETBE synthesis, although its synthesis is less favorable in terms of reaction yield compared to ETBE synthesis. It is due to the higher thermodynamic limitations of the reactions of IA with EtOH compared to that of IB. TAEE synthesis in a STR is more favorable from IA and EtOH than from TAA and EtOH, in terms of AE, ε and RME. A similar yield or yield improvement can be achieved by reactive distillation of IA and EtOH (Fig. 4.2.2, C and E). However, it requires an EtOH excess to promote the etherification reaction and to avoid dimerization of olefins due to the higher temperatures throughout the column compared to batch reactor process, so it becomes less efficient in terms of RME and SF. Comparing TAEE synthesis from TAA and EtOH (Fig. 4.2.2, D and F), the use of a STR under stoichiometric conditions is more suitable than the use of reactive distillation of EtOH and IA (Fig. 4.2.2, C and E) in terms of RME and SF. This is because reactive distillation requires an excess of EtOH to avoid IA dimerization, as explained above, and it consequently implies oversizing the operation units. This alcohol excess also implies that EtOH is normally obtained with ETBE in column bottoms, so additional purification steps would be necessary. Nevertheless, higher yields can be achieved by reactive distillation of IA and EtOH (Fig. 4.2.2, C and E) and this pathway avoids water formation and subsequent risk of azeotropes formation. Observed differences between obtained results in this work and those for the analogous isolated ether syntheses in STR are attributed to the experimental error and the slight excess of EtOH used ($R°_{A/O}$=1.03), which was taken into account for the calculations of both ETBE and TAEE cases.

It is noteworthy that series corresponding to partial and complete reclaiming for the evaluated cases in the GMA performed are depicted in Figs. 4.2.1 and 4.2.2 (pink and blue series, respectively), however they are overlapped by no reclaiming series (red one). This occurs because the main substances considered in this reclaiming analysis are reaction solvents, catalyst and side products [159]. As the amounts of catalyst used were relatively low, very small amounts of side products were formed and the syntheses were carried out in the absence of solvents. In most of the evaluated cases these series overlapped. Although in this study the partial and complete reclaiming series do not provide extra information compared to no reclaiming series, they can be essential in the analysis of other processes in which the amounts of catalyst, solvents and byproduct could be higher and therefore they could be optimized. Besides, it is to be highlighted that reclaiming refers to the recovering (retrieval) of solvents, side products and catalysts to repair them and to reuse them later on. Recycling refers to processing the unreacted reactants into new products in order to prevent waste of potentially useful materials and to reduce the consumption of fresh raw materials. In other words, reclaiming includes only the separation of these materials from the target product whereas recycling includes the separation and the reuse.

Table 4.2.2. Summary of main GMA parameters obtained for the evaluated processes. All Metric values for the different approaches refer to no reclaiming analysis.

Case	Plan	Catalyst	T [K]	Setup	AE	Yield	1/SF	RME	MRP	VMR	E_{total}	CME [%]
ETBE	This work	Amberlyst™35	333	Batch reactor	1	0.94	0.97	0.82	0.89	0.93	0.23	92.4
	(Françoisse and Thyrion. 1991) [139]	Amberlyst™15	333	Batch reactor	1	0.88	1	0.40	0.46	0.79	1.51	87.6
	(Vila et al. 1993) [160]	Bayer K-2431	333	Batch reactor	1	0.91	0.99	0.86	0.95	0.95	0.16	90.4
	(Yang and Goto. 1997) [161]	Amberlyst™15	343	Reactive distillation and pervaporation	0.85	0.88	0.72	0.52	0.96	0.80	0.93	65.6
	(Yang et al. 2000) [162]	S-54	338	Batch reactor	0.85	0.52	1	0.41	0.92	0.78	1.45	52.0
	(Umar et al. 2009) [163]	CT-124	343	Batch reactor	0.85	0.39	0.72	0.23	0.95	0.69	3.38	29.3
TAEE	This work	Amberlyst™35	333	Batch reactor	1	0.53	0.97	0.47	0.90	0.81	1.13	52.4
	(Rihko et al. 1994) [137]	Amberlyst™16	333	Batch reactor	1	0.55	1	0.54	0.98	0.84	0.84	55.2
	(Boz and Dogu. 2005) [164]	Amberlyst™15	377	Batch reactive distillation	1	0.50	0.24	0.12	0.99	0.68	7.44	15.2
	(Boonthamtirawuti et al. 2009) [45]	Amberlyst™16	353	Semi batch reactor	0.87	0.31	1	0.26	0.98	0.76	2.79	31.2
	(Varisli and Dogu. 2005) [165]	Amberlyst™16	383	Batch reactive distillation column	1	0.85	0.14	0.12	1	0.74	7.45	15.6
	(Aiouache and Goto. 2003) [166]	Amberlyst™15	353	Batch reactor	0.87	0.22	1	0.19	0.99	0.75	4.32	21.9

Values of VMR from Table 4.2.2 show that synthesis of both ethers from the correspondent olefin and EtOH in a STR, in the simultaneous process or the isolated ones, is the most suitable chemical route in terms of this unifying metric, especially for TAEE. The low values of E_{total} and the process temperature confirm this result. The highest values of VMR and the lowest ones of E_{total} from Table 4.2.2 were obtained for the isolated ETBE and TAEE synthesis from the corresponding tertiary olefin and EtOH. As mentioned, the difference with respect to the results obtained for the present simultaneous synthesis can be attributed to the slight excess of EtOH used, which led to slightly lower values of 1/SF, RME and MRP. The PMI values evaluated using Eq. 4.2.10 have been excluded from Table 4.2.2. Since this metric measures the total mass used in a process per mass of final product, it can be expressed as $1 + E_{total}$ for calculations

purposes in the present study [54]. Consequently, its values are easily deduced from those of E_{total}. Finally, regarding values of CME, all the evaluated cases entail chemical reactions in which, apart from the small amount of tertiary alcohols formed, all the carbon atoms in the reactants end up in the target product molecule. Hence, there is no special risk of downstream carbon emissions due to byproducts formation, provided that reactants are recycled or retrieved, because small amounts of TBA and TAA could also be blended to gasoline. Therefore, CME values for the present study mainly reflect the conversion referring to the carbon atoms within the process that end up in final product, as this metric considers stoichiometry and reaction yield. Table 4.2.2 values confirm this statement as well as the aforementioned selected chemical process and pathway. The fact that the highest CME value for ETBE synthesis was obtained for the present work can be due, as well, to the slight excess of EtOH used, that faintly favored the ETBE synthesis over the TAEE one. It is also shown in the higher yield value obtained for the simultaneous etherification compared to that for the isolated ETBE synthesis. As a consequence, the highest value of CME for TAEE synthesis was obtained for the isolated reaction of IA and EtOH and not for the simultaneous synthesis of ETBE and TAEE.

Further study on toxicity of the involved compounds and the evaluation of different options for the production of ethers in continuous operating mode (PFR, CSTR and continuous reactive distillation) becomes necessary to ascertain the most efficient process. In addition, the process evaluation in other design stages, such as early and late development, in which overall costs (installation, operation and maintenance), total emissions and a thorough evaluation of the green chemistry related to each process step from the "cradle to gate", are essential to the overall analysis of the process viability. Very valuable analysis tools for this purpose would be the Life Cycle Analysis (LCA) and other Green Metrics such as the Added Value Index (AVI), the Space Time Yield (STY), the Effective Mass Yield (EMY) and the C_{factor}, for instance. At any rate, obtained results in this work are focused on the chemical pathway selection and reflect the main shortcomings of the evaluated processes, allowing therefore the suggestion of alternatives to overcome them. On this purpose, a continuous process for the simultaneous production of ETBE and TAEE has been simulated, counteracting the main drawback found in the batch operation mode, which is to virtually achieve total reactants conversion.

4.2.4 CONTINUOUS PROCESS SIMULATION

Among several possible setups, distillation after reaction zone (reaction with distillation configuration described in *Section 1.2.4*) has been chosen because this configuration allows the separation of reaction and purification into two different units. This is important because of the different optimal temperatures for each operation and also because the pressure control throughout the column can be troublesome in reactive distillation. Based on the obtained results, the simultaneous etherification process in an equilibrium reactor and a subsequent separation unit in a distillation column has been simulated using Aspen HYSYS v. 2006.5 (AspenTech). The fluid package selected was the UNIQUAC model for the liquid phase and ideal gas for the gaseous phase, and the UNIFAC parameters were also used by setting binary coefficients for liquid-liquid equilibrium (LLE) due to the non-ideality of the system. The Poynting correction factor was also considered to take into account the effect of pressure over the reactor output equilibrium composition. The steady state simulation has been performed by using a sparse continuation solver. The resulting process flux diagram (PFD) is depicted in Fig. 4.2.3 and the material streams composition and main properties are summarized in Table 4.2.3. The initial feed molar ratios $R°_{A/O}$ and $R°_{C4/C5}$ in the equilibrium reactor input were both adjusted to unity approximately.

These are the same conditions of the experimental carried out in the first part of the present work (taking into account that a slight excess of ethanol would prevent oligomerization reactions), as it is observed in the stream 4 composition. For the simulation, it was assumed that the reactor size was large enough to reach chemical equilibrium compositions at 353 K. The equilibrium constants for main reactions (R1−R4) at 353 K were experimentally obtained, see *Section 4.4* and they were used in the simulation of the equilibrium reactor what allows to know the compositions at steady state for the reactor output. After the distillation unit, the separated unreacted olefins (IA and IB) and EtOH were recycled to the reactor inlet.

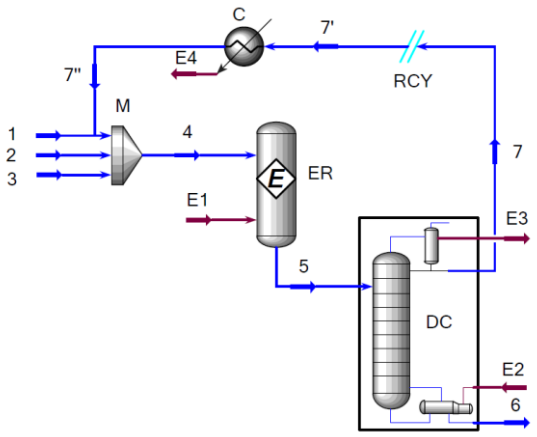

Figure 4.2.3. Simulated process PFD for ETBE and TAEE simultaneous production. (1—7'') Material streams. (E1—E4) Energy streams. (M) Mixer. (ER) Equilibrium reactor. (DC) Distillation Column. (RCY) Reactants recycle. (C) Cooler.

The column is equipped with 10 separation trays (the 10th tray being the optimum feed stage for the entry to the column), a partial reboiler and total condenser. The tray diameter obtained was 1.5 m and the space between trays was 0.55 m (total high of 5.5 m). The external reflux ratio was set to 3 and the obtained minimal reflux ratio was 0.203. A condenser temperature of 410.4 K and a reboiler temperature of 473.6 K were obtained. Only 8 iterations were needed to reach numerical convergence. The column working pressure was set to 1.5 MPa in order to avoid the limitations of the azeotropic mixture formed by ethers and EtOH at lower pressures. Higher pressures would contribute to facilitate the separation, but at the expense of increasing the column energetic requirements. The same pressure was set to all the devices from the PFD to keep the liquid phase throughout the whole reacting zone and the up—downstream piping.

Table 4.2.3. Material streams composition and conditions for the simulated PFD.

Stream/Composition [Molar fraction]	1	2	3	4	5	6	7=7'	7''
2M1B	0.07	0	0	0.016	0.012	0	0.024	0.024
2M2B	0.93	0	0	0.206	0.145	0.001	0.298	0.298
IB	0	0	1	0.235	0.036	0	0.074	0.074
ETBE	0	0	0	0.053	0.393	0.61	0.163	0.163
EtOH	0	1	0	0.487	0.237	0.05	0.434	0.434
TAEE	0	0	0	0.002	0.178	0.339	0.007	0.007
Molar flow [kmol/h]	1	2.95	1.80	8.533	5.732	2.948	2.783	2.783
T[K]	333.0	333.0	333.0	333.0	333.0	400.6	410.4	333.0
P [MPa]	1.5	1.5	1.5	1.5	1.5	1.5	1.5	1.5
Heat [MJ/h]	-63.7	-804.5	-58.96	-1478	-1552	-887.4	-511.8	-551.4

The proposed configuration for the process units was also suggested in a study concerning the possible configurations and operating conditions for *tert*-butyl ethers production [167]. A column producing ETBE as bottom product would contain a 9 mol.% (4 wt.%) of EtOH, but this is not necessarily a problem since EtOH is also an effective oxygenate. In case that a higher

ether purity is desired, another separation unit would be required. Based on this configuration and the obtained results, the distillation unit to obtain a high purity ETBE and TAEE stream has been simulated. The separation of reactants and products in the present simulation could be achieved in a simple fractionation column with low energy requirements. Nevertheless, the overhead product (stream 7) contains the unreacted olefins and a minimum boiling point azeotrope between ETBE and EtOH. Therefore, some ETBE would be recycled on recirculating EtOH (about 20 mol.% of the amount fed to the column), thereby slightly increasing investment and operating costs would be required. However, since more than 80 mol.% of ETBE and 99.9 mol.% of TAEE fed to this column would leave with the bottoms product, stream 6 (high purity ethers stream), this shortcoming is considered acceptable.

The ethers product stream (stream 6) was composed mainly of ETBE and TAEE. No further separation of ethers and EtOH was considered due to the relative difficulty in separating the formed azeotropic mixture between them. If more purity is required in stream 6, a higher pressure, a bigger column and a higher recirculation ratio with a higher ETBE and TAEE content are necessary, see *Appendix 7.5.2*. For this reason, a product stream containing a maximum of 0.05 (molar fraction) of EtOH was considered as a direct stream to be added to fuel. Molar fractions of ETBE and TAEE in this stream are 0.61 and 0.34, respectively. This additive possesses a potential application in gasoline formulations. Compared to the direct blending of EtOH, it implies far lower volatility, lower solubility in water and less emissions derived risks. Furthermore, ethers presence, especially TAEE, enhances EtOH solubility in fuels [14,26,46] reducing the possibility of phase separation [12]. In addition, the proposed PFD allows a considerably high EtOH usage as raw material (stream 2) and avoids an extra-unit for EtOH recovering.

The simulated process presents the advantage of recovering practically all the unreacted reactants, achieving overall reactant conversion of 97.4 %, what is undoubtedly a desirable improvement. To assess the upgrading that could be achieved with the simulated continuous process comparing with experimental batch results, the system has been evaluated under the GMA. Resulting radial pentagon diagrams for ETBE and TAEE are plotted in Fig. 4.2.4. As it can be seen, non-reacted reactants recycling constitutes an approach to the ideal process (depicted by a perfect pentagonal shape of unit radius) for synthesis of both ethers, especially for the TAEE case. The obtained values for the main Green Metrics and the other relevant metrics studied in this work, such as CME and E-total, are shown in Table 4.2.4 and confirm the improvement achieved with the continuous process.

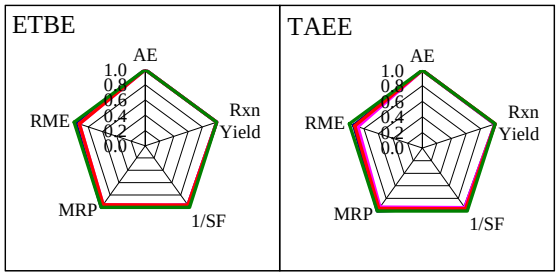

Figure 4.2.4. Radial pentagon diagrams for the simulated continuous process. (—) Complete reclaiming, (—) Partial Reclaiming, (—) No reclaiming, (—) Ideal.

Table 4.2.4. Obtained values for the green metrics evaluated for the simulated continuous process (no reclaiming).

Metric	ETBE	TAEE
AE	1.00	1.00
Rxn Yield	1.00	1.00
1/SF	0.96	0.94
RME	0.92	0.88
MRP	0.96	0.94
VMR	0.97	0.95
E-total	0.08	0.13
CME (%)	97.30	95.61

Finally, it should be noted that the STR processes from the literature mentioned earlier in this paper, particularly those corresponding to isolated ETBE and TAEE syntheses from tertiary olefins and EtOH, could achieve similar improvements when produced in continuous operation mode with a subsequent step of distillation to recycle the unreacted reactants. Also the analogous synthesis carried out in a reactive distillation setup operating in continuous mode would show a noticeable improvement. However, the processes in which ethers are produced from EtOH and tertiary alcohols would not show similar improvements, even with a different process design. This is because the considerable amounts of water formed would lead to difficulties in separating the azeotropic mixture of ethers, alcohols and water and because water, as a side product would result in a drawback to the process material efficiency.

4.2.5 PARTIAL CONCLUSIONS

The employed methodology has proved to be an efficient technique to compare numerically the inherent green chemistry of several etherification systems, such as the different ether synthesis pathways and the evaluated batch processes. In terms of the parameters obtained in the GMA, the simultaneous etherification of the correspondent tertiary olefins (IB and IA) with EtOH to produce ETBE and TAEE at 333 K is more favorable than their synthesis from the correspondent tertiary alcohols (TBA or TAA) and EtOH in batch operation mode. Batch reactive distillation presents the advantage to improve the reaction yields for both synthesis pathways. However, it implies device oversizing due to the necessity of work under non stoichiometric conditions and it results in lower values of RME and 1/SF compared to STR processes.

The simulated continuous process speaks for the feasibility of industrial application to produce high octane and low volatility fuel additives with high purity, avoiding extra separations units apart from the required distillation to recycle reactants. The process comprises an equilibrium reactor followed by a distillation column working at 1.5 MPa and represents a potential improvement of the process efficiency by means of the practically total reactants conversion (97.4%). This alternative simultaneous etherification route offers high conversion, low implementation and operating costs, and high quality fuel additives. It also preserves the advantages of syntheses of isolated ethers and represents an interesting alternative toward versatile bioethers production according to the benefits derived from process optimization, integration and intensification.

4.2.6 CHAPTER NOTATION

2M1B	2-methyl-1-butene
2M2B	2-methyl-2-butene
AE	atom economy [$MW_{product} \cdot MW_{reactants}^{-1}$]
AVI	added value index [$€_{product} \cdot €_{reactants}^{-1}$]
C_{factor}	carbon factor [$g_{CO2(cradle\ to\ gate)} \cdot kg_{product}^{-1}$]
CME	carbon mass efficiency [$g_{C\text{-}product} \cdot g_{C\text{-}reactants}^{-1}$]
CSTR	continuous stirred tank reactor
E_{factor}	environmental factor [$g_{waste} \cdot g_{product}^{-1}$]
ELI	energy loss index [dimensionless]
EMY	effective mass yield [$g_{product} \cdot g_{non\text{-}benign\ reactants}^{-1}$]
ETBE	ethyl *tert*-butyl ether
EtOH	ethanol
FCC	Fluid Catalytic Cracking

GMA	Green Metrics Analysis
IA	isoamylenes
IB	isobutene
LLE	liquid-liquid equilibria
m	mass [g]
MRP	mass recovery parameter [dimensionless]
MW	molecular weight [$g \cdot mol^{-1}$]
P	pressure [MPa]
PFD	process flux diagram
PFR	plug flow reactor
PMI	process mass intensity [$g_{\text{all reactants and products}} \cdot g_{\text{product}}^{-1}$]
$R°_{A/O}$	initial molar ratio alcohol to olefins
$R°_{C4/C5}$	initial molar ratio C_4 to C_5 olefins
RME	reaction mass efficiency [$g_{\text{product}} \cdot g_{\text{all reactants}}^{-1}$]
Rxn	reaction
SF	stoichiometric factor [$g_{er} \cdot g_{sr}^{-1}$]
STR	batch stirred tank reactor
STY	space time yield [$g_{\text{product}} \cdot L_{\text{reactor}}^{-1} \cdot h^{-1}$]
T	temperature (°C)
TAA	*tert*-amyl alcohol
TAEE	*tert*-amyl ethyl ether
TBA	*tert*-butyl alcohol
VMR	vector magnitude ratio [dimensionless]

Subscripts

j	component
er	excess reactants
sr	stoichiometric reactants or reactants with no excess
tp	target product
aux	auxiliary materials (catalyst, solvents and materials for purification)
c	carbon

Greek Letters

ε	reaction yield

4.3 EQUILIBRIUM CONVERSION, SELECTIVITY AND YIELD OPTIMIZATION OVER AMBERLYST™35

An extended and revised version of this chapter has been published as:

R. Soto, C. Fité, E. Ramírez, R. Bringué, F. Cunill. Equilibrium conversion, selectivity and yield optimization of the simultaneous liquid-phase etherification of isobutene and isoamylenes with ethanol over Amberlyst™ 35. *Fuel Process. Technol.* **2016**; 142: 201–211. http://dx.doi.org/10.1016/j.fuproc.2015.09.032.

4.3.1 INTRODUCTION

As mentioned in *Section 1.6*, several studies have been focused on the performance of isolated production of ETBE and TAEE in both absence and presence of water [31,49,91,123,124]. But there is scarce information about the simultaneous production of bioethers and more specifically concerning equilibrium conversion and selectivity [21,120,122]. Since these are important features to consider in the design of industrial reactors and downstream separation units, the aim of this work is to study the feasibility of the simultaneous etherification of IB and IA with EtOH over a wide range of experimental conditions. Modeling and optimization of etherification yields is a main goal.

4.3.2 EXPERIMENTAL AND CALCULATIONS

The stirred tank reactor working in batch mode described in *Section 3.2.1* was used to carry out the experimental work. $R°_{A/O}$ and $R°_{C4/C5}$ were both varied between 0.5 and 2. A water amount of 1 wt.% of the total reactant mixture was initially added to all experiments to monitor TBA and TAA formation and to approach industrial conditions in which the alcohol stream would contain small amounts of water. Assayed reaction temperatures were in the range of 323 to 353 K. These particular conditions were chosen because they are similar to those of industrial interest in etherification processes. The catalyst load was varied between 4 and 8 g of commercial bead size A-35 in order to reach chemical equilibrium during the experimental runs. Conversion, selectivity and yields were calculated by the expressions detailed in *Section 3.6*.

The response surface methodology (RSM) is a useful technique in the solution of many problems of the chemical industry. For instance, one important application is the modeling and optimization of industrial processes [168,169]. It is a valuable tool to determine the experimental conditions for which the throughput toward a desirable chemical product is the maximum attainable. The following second order polynomial form was used for the modeling of the experimental etherification yields:

$$y_n(z) = \beta_0 + \sum_{m=1}^{n} \beta_m z_m + \sum_{m=1}^{n} \beta_{mm} z_m^2 + \sum \sum_{l<m=2}^{n} \beta_{lm} z_l z_m \qquad n=1,2.3...r \qquad (4.3.1)$$

where z_1, z_2, …, z_k are the coded variables ([-1,1]) that refer to the experimental conditions, and β_0, β_m, β_{mm} and β_{lm} are fitting parameters. A confidence level of 95% was used to assess the statistical significance of fitted polynomial models. The number of variables of Eq.4.3.1 was reduced to the minimum statistically significant by means of the stepwise regression procedure [170] using the software Design-Expert 9. The significance level for each parameter to be either included or rejected from the final equation was set to 0.05. This technique has been demonstrated to be effective when selecting a predictive equation that comprises the fewest possible variables to determine reliable process values.

Since four different responses are obtained in the modeling of etherification yields, the simultaneous optimization of all of them results in a multi-objective optimization (MOO) problem. The conditions for which the yield to ETBE is maximum may differ from those for which the yield to TAEE is maximum and therefore, the challenge consists in find out the conditions that simultaneously maximize the yields toward both ethers. A relatively straightforward approach in MOO is to overlay the contour plots (OCP) for each target response [169]. Nonetheless, this methodology presents limitations in large systems involving several input variables and several responses. Furthermore, it is difficult to identify the optimal conditions since a region near "optimal" is obtained with such procedure [171]. On the other hand, the desirability function approach is a useful numerical technique for the analysis of experiments in which several responses have to be optimized simultaneously. Originally developed by Harrington (1965) [172] and modified by Derringer and Suich (1980) [173], the main concept of the desirability function is to transform a multiresponse problem into a single response problem. Once all the responses $Y_n(z)$ have been fitted to polynomials by RSM, an individual desirability function $d_n(Y_n(z))$ ranging between 0 and 1 is assigned for each response $Y_n(z)$. For the two sided case and considering the maximization of $Y_n(z)$, the individual desirability function is expressed by Eq.4.3.2.

$$d_n(Y_n(z)) = \begin{cases} 0 & if\ y_n(z) < L_n \\ \left(\dfrac{y_n(z) - L_n}{T_n - L_n} \right)^s & if\ L_n \geq y_n(z) \geq T_n \\ 1 & if\ y_n(z) > T_n \end{cases} \qquad (4.3.2)$$

where z are the factors, L_n is the lower acceptable value of $Y_n(z)$, T_n is the target value and s is a parameter (user specific weight factor) which defines the shape of the desirability function and it takes values either higher or lower than the unity depending on the higher or lower importance assigned to the response. The parameter s can be set to the unity for all responses when equal importance is assigned to each.

When the individual desirabilities are defined for the r responses of interest, an overall objective function, the total desirability $D(z)$, is defined as the geometric mean of each of them by means of Eq (4.3.3).

$$D(z) = \sqrt[r]{\prod_{n=1}^{r} d_n(Y_n(z))} \qquad (4.3.3)$$

4.3.3 EFFECT OF TEMPERATURE ON EQUILIBRIUM CONVERSION AND SELECTIVITY

The main products from reactions R1 to R3 (see Fig. 4.1.1), ETBE and TAEE, were detected in all runs and ETBE was the main reaction product in terms of mole followed by TAEE. The main side products were tertiary alcohols (TBA and TAA) and dimerization products. Since the main etherification reactions involved in this study are exothermic (R1-R3), reactants equilibrium conversion (X_j) is expected to decrease on increasing temperature. Reaction equilibrium constants only depend on temperature but reactants conversion at equilibrium situation is given by initial composition and operating temperature.

As depicted in Fig. 4.3.1, the higher the temperature, the lower the reactants equilibrium conversion. Compared to X_{IB}, significantly lower X_{IA} (about a half) was reached indicating that ETBE synthesis from IB and EtOH is favored thermodynamically compared to that of TAEE from IA and EtOH. Under stoichiometric conditions between alcohols and olefins ($R°_{A/O}$=1), X_{EtOH} values at equilibrium were between X_{IB} and X_{IA}. As it will be further analyzed in *Section 4.4*, equilibrium constants of ETBE formation (R1) are higher than those of TAEE formation (R2 and R3) at each temperature. A steeper decrease of X_{IA} on increasing temperature was observed at $R°_{A/O}$=2 (Figs. 4.3.1c and 4.3.1d) and it suggests that TAEE formation is more affected by temperature changes than that of ETBE. Globally, X_{IB}, X_{IA} and X_{EtOH} values ranged between 69.8 and 97.9%, between 17 and 65.6% and between 32.3 and 97.0%, respectively. The effect of temperature on X_{IA} was in good agreement with that reported for the isolated etherification IA with EtOH [89] for similar conditions.

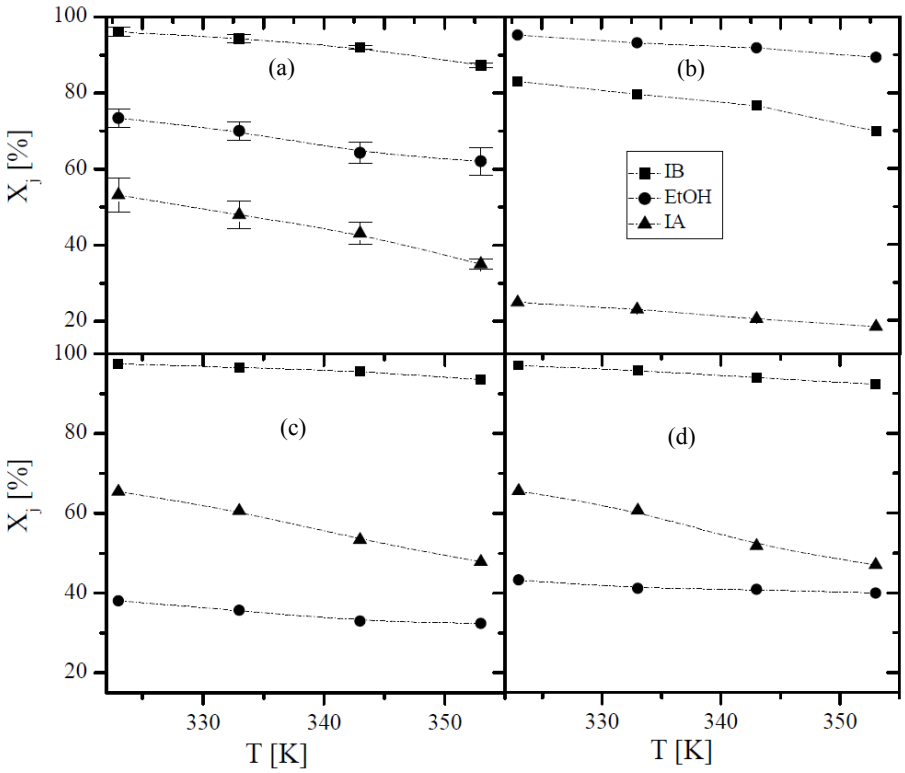

Figure 4.3.1. Reactants equilibrium conversion vs. temperature. (a) $R°_{A/O}=R°_{C4/C5}=1$. (b) $R°_{A/O}=0.5$, $R°_{C4/C5}=1$. (c) $R°_{A/O}=2$, $R°_{C4/C5}=0.5$. (d) $R°_{A/O}=R°_{C4/C5}=2$. Errors bars are referred to a 95% confidence interval.

The effect of temperature on reactants selectivity toward products is shown in Fig. 4.3.2. Remarkably high values of S_{IB}^{ETBE} and S_{IA}^{TAEE} (always >90%) were obtained which did not depend significantly on temperature. This is undoubtedly a desirable industrial performance. Both S_{IB}^{ETBE} and S_{IA}^{TAEE} decreased smoothly on rising the temperature, whereas S_{IB}^{TBA} and S_{IA}^{TAA} followed an opposite trend. S_{IB}^{ETBE} values were always slightly higher than those of S_{IA}^{TAEE} and this is related to the fact that S_{IA}^{TAA} values were slightly higher than S_{IB}^{TBA} values. Regarding products from EtOH, it was generally more selective toward ETBE than to TAEE and this difference was even more noticeable at higher temperatures. As pointed out before, equilibrium constants of ETBE formation are higher than those of TAEE formation and this is coherent with the higher selectivity of EtOH toward ETBE at initial $R°_{C4/C5}$=1. However, EtOH was equally selective toward ETBE and TAEE at $R°_{C4/C5}$=0.5 and $R°_{A/O}$=1 or 2 independently of the reaction temperature (Fig. 4.3.2b).

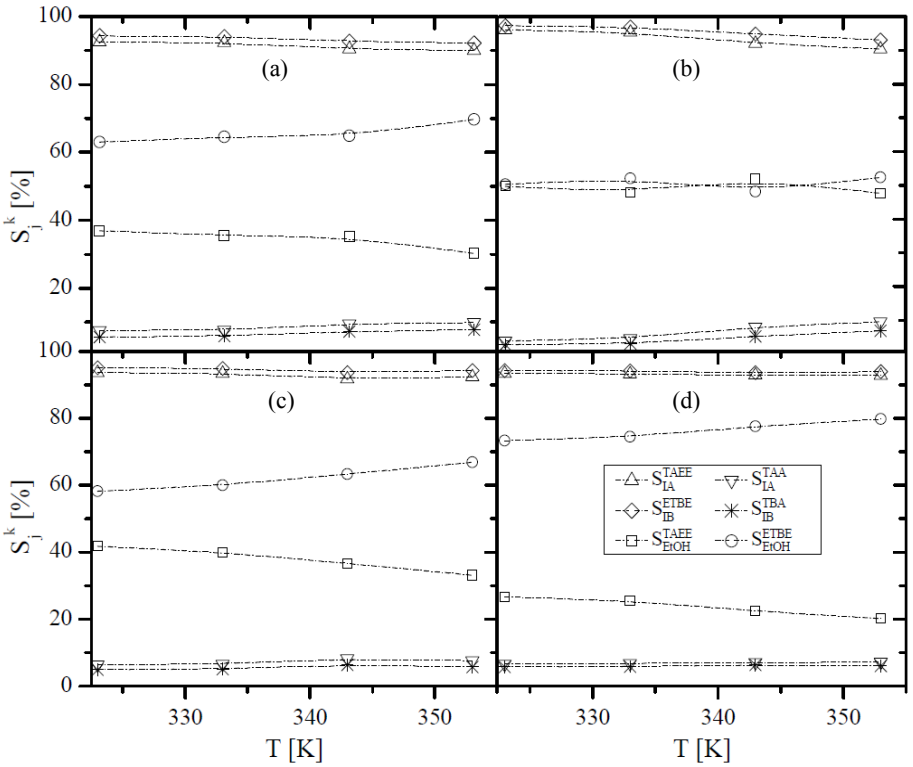

Figure 4.3.2. Reactants selectivity toward products vs. temperature at chemical equilibrium. (a) $R°_{A/O}=R°_{C4/C5}=1$. (b) $R°_{A/O}=1$, $R°_{C4/C5}=0.5$. (c) $R°_{A/O}=1$, $R°_{C4/C5}=2$. (d) $R°_{A/O}=R°_{C4/C5}=2$.

4.3.4 EFFECT OF $R°_{A/O}$ ON EQUILIBRIUM CONVERSION AND SELECTIVITY

The effect of $R°_{A/O}$ on reactants equilibrium conversion is illustrated in Fig. 4.3.3. The highest X_{EtOH} was obtained at $R°_{A/O}$=0.5 and the highest olefins equilibrium conversion were reached at initial stoichiometric excess EtOH ($R°_{A/O}$=2), but at the expense of lower X_{EtOH}. X_{IA} was more sensitive to temperature changes than X_{IB}. As shown in Fig. 4.3.3, the shape of the curves X_j vs. $R°_{A/O}$ was similar for any temperature.

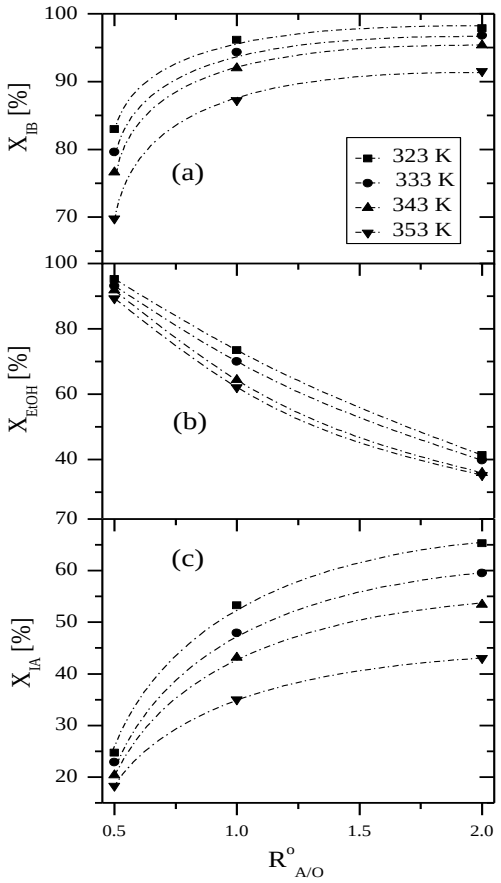

Figure 4.3.3. X_j dependence on $R°_{A/O}$ at several temperatures and $R°_{C4/C5}$=1. (a) IB, (b) EtOH, (c) IA.

The effect of $R°_{A/O}$ on reactants selectivity toward products at equilibrium is shown in Fig. 4.3.4. S_{IB}^{ETBE} and S_{IA}^{TAEE} slightly increased on increasing $R°_{A/O}$ whereas S_{IB}^{TBA} and S_{IA}^{TAA} followed an opposite trend. The highest value of S_{EtOH}^{ETBE} was obtained at $R°_{A/O}$=0.5 and the highest value of S_{EtOH}^{TAEE} was reached at $R°_{A/O}$=2. This difference between S_{EtOH}^{ETBE} and S_{EtOH}^{TAEE} was reduced on increasing $R°_{A/O}$, showing that TAEE production could be favored on increasing $R°_{A/O}$. As seen in Fig. 4.3.4, the shape of selectivity profile vs. $R°_{A/O}$ was very similar at 343 and 353 K, the main difference being the extent in which dimerization products were formed. The selectivity profiles obtained at 323 and 333 K were similar to those plotted in Fig. 4.3.4, but without noticeable formation of dimers. The effect of $R°_{A/O}$ on byproducts formation will be further discussed in the side reactions section.

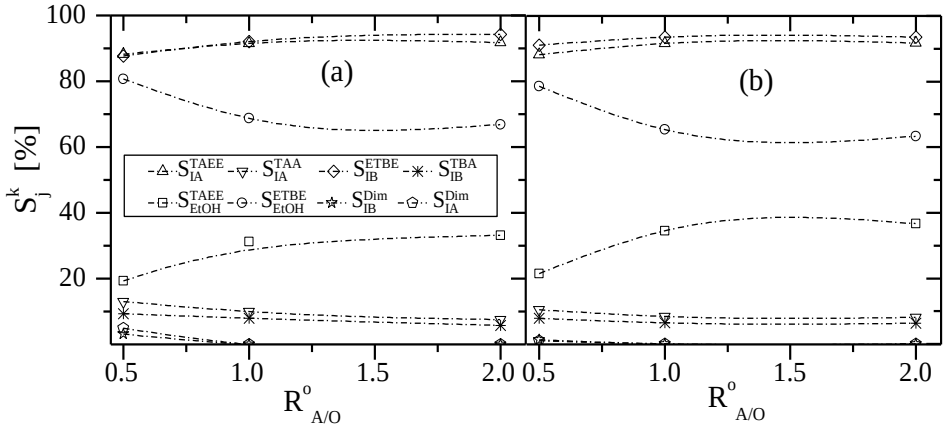

Figure 4.3.4. S_j^k at equilibrium vs. initial $R°_{A/O}$ at $R°_{C4/C5}$=1. (a) 353 K, (b) 343 K.

4.3.5 EFFECT OF $R°_{C4/C5}$ ON EQUILIBRIUM CONVERSION AND SELECTIVITY

Fig. 4.3.5 depicts the dependence of reactants conversion on $R°_{C4/C5}$. As the initial IB concentration increased, lower values of X_{IB} and X_{IA} were obtained whereas X_{EtOH} was slightly higher. The effect of $R°_{C4/C5}$ on reactants equilibrium conversion was more noticeable at $R°_{A/O}$=1 (see Fig. 4.3.5c). The overall effect of $R°_{C4/C5}$ on reactants equilibrium conversion was less pronounced than those of temperature and $R°_{A/O}$.

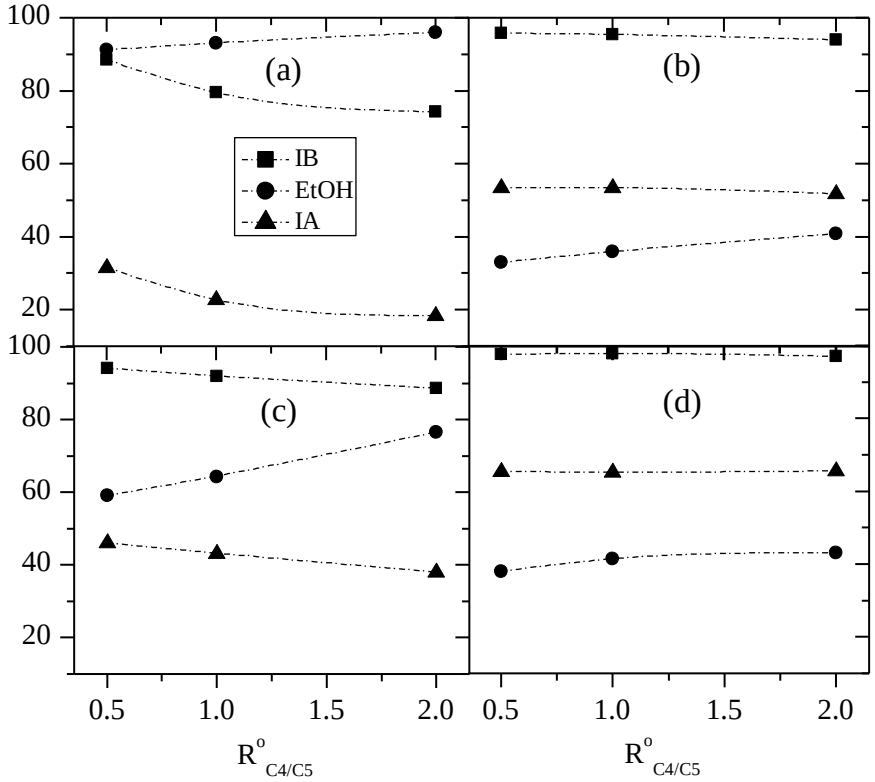

Figure 4.3.5. X_j vs. $R°_{C4/C5}$. (a) $R°_{A/O}$=0.5 and 333 K. (b) $R°_{A/O}$=2 and 343 K. (c) $R°_{A/O}$=1 and 343 K. (d) $R°_{A/O}$=2 and 323 K.

The effect of $R°_{C4/C5}$ on reactants selectivity is shown in Fig. 4.3.6. S_{IB}^{ETBE} and S_{IA}^{TAEE} values at equilibrium decreased smoothly on increasing $R°_{C4/C5}$. Concerning EtOH, S_{EtOH}^{ETBE} increased with $R°_{C4/C5}$ and accordingly S_{EtOH}^{TAEE} followed the opposite trend. Thus, it can be concluded that increasing $R°_{C4/C5}$ chiefly favors ETBE formation. Similar values of S_{EtOH}^{ETBE} and S_{EtOH}^{TAEE} were obtained at $R°_{C4/C5}$=0.5 and $R°_{A/O}$=2, see Fig. 4.3.6a. The effect of $R°_{C4/C5}$ on olefins selectivity toward dimerization products was enhanced at high temperatures and $R°_{A/O}$=0.5 (Fig. 4.3.6b).

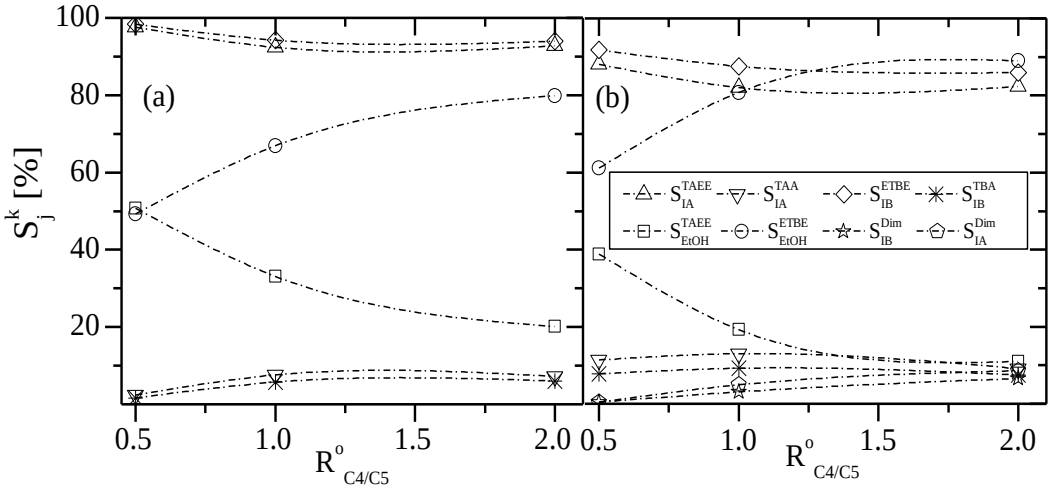

Figure 4.3.6. S_j^k vs. initial $R°_{C4/C5}$. (a) 353 K and $R°_{A/O}$ =2. (b) 353 K and $R°_{A/O}$ =0.5.

4.3.6 SIDE REACTIONS

4.3.6.1 Tertiary alcohols formation

The initial water presence (1 wt.%) drastically affected olefins selectivity to ethers. S_{IA}^{TAA} and S_{IB}^{TBA} values at equilibrium were always lower than 13 and 9%, respectively. As can be observed in Fig. 4.3.7, S_{IA}^{TAA} was always higher than S_{IB}^{TBA}. Nevertheless, mole of TBA formed were always larger than those of TAA at $R°_{C4/C5}$=1, indicating that TBA formation is favored thermodynamically compared to that of TAA. These results are also in agreement with the higher equilibrium constants values reported for TBA synthesis (R5) compared to those of TAA [126] formation from 2M1B and 2M2B (R6 and R7) [91].

The effect of the reaction temperature on tertiary alcohols formation is presented in Fig. 4.3.7a. Both S_{IB}^{TBA} and S_{IA}^{TAA} increased smoothly with temperature. This fact is in good agreement with the literature, where an increase of S_{IB}^{TBA} with temperature was observed in the synthesis of ETBE [31] and the synthesis of isopropyl *tert*-butyl ether [87]. Despite the known exothermicity of hydration reactions of olefins, there are several chemical and physical equilibria to be fulfilled at once. The selectivity at chemical equilibrium depends on the initial composition and on the relation between equilibrium constants of all reaction involved. Etherification reactions of olefins are known to present a higher value of thermodynamic equilibrium constants than hydration reactions [91,92,126] and that can explain the enhancing effect of temperature on S_{IB}^{TBA} and S_{IA}^{TAA}.

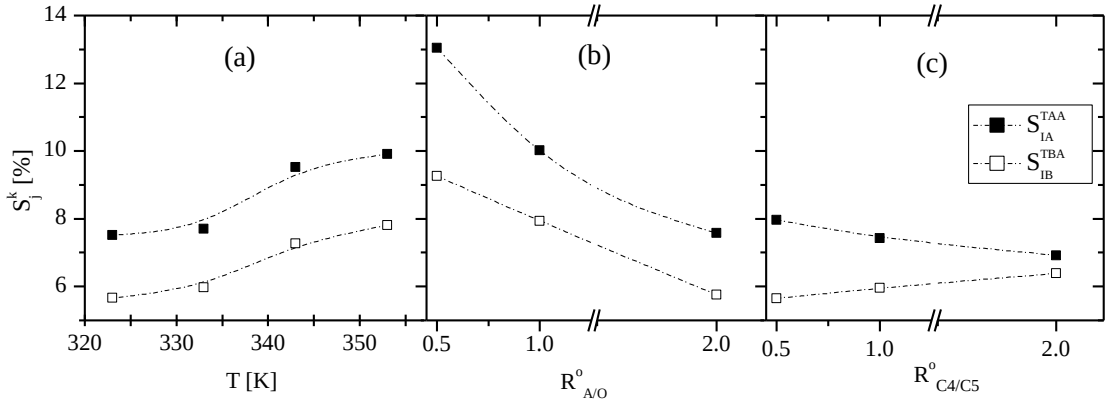

Figure 4.3.7. (a) Effect of temperature on tertiary alcohols formation at $R°_{A/O}$= $R°_{C4/C5}$=1. (b) Effect of $R°_{A/O}$ on tertiary alcohols formation at 353 K and $R°_{C4/C5}$=1. (c) Effect of $R°_{C4/C5}$ on tertiary alcohols formation at 343 K and $R°_{A/O}$=2.

Fig. 4.3.7b plots the effect of $R°_{A/O}$ on the formation of tertiary alcohols. Both S_{IB}^{TBA} and S_{IA}^{TAA} decreased on increasing $R°_{A/O}$. This is because as $R°_{A/O}$ increases, lower amount of olefins is initially present in the reaction media and therefore lower amount of tertiary alcohols is formed by olefins hydration. The effect of $R°_{C4/C5}$ on tertiary alcohols formation is depicted in Fig. 4.3.7c. S_{IB}^{TBA} increased slightly on increasing $R°_{C4/C5}$ whereas S_{IA}^{TAA} followed an opposite trend. The explanation of this fact arises from the initial IB concentration, as it increased, water was preferably consumed to form TBA rather than TAA.

4.3.6.2 Dimers and codimers formation

Irreversible formation of dimerization products was detected only at the highest temperatures (343 and 353 K), as a result of the higher sensitivity of these side reactions to temperature, and at $R°_{A/O}$=0.5, as shown in Fig. 4.3.4. This is consistent with previous studies focused on the IB and IA dimerization that concluded that polar conditions (induced namely by water and alcohol presence in the present study) inhibit oligomerization reactions [87,107].

By isobutene dimerization (R9 in Fig. 4.1.1) both TMP-1 and TMP-2 were formed. In addition, isomerization between both diisobutenes (R10 in Fig. 4.1.1) also took place and favored the formation of TMP-1, a more stable molecule than TMP-2 due to the internal repulsions caused by the large size of the *tert*-butyl group in the TMP-2 molecule [174,175]. As observed in Fig. 4.3.8a, when C_4 dimers were formed the molar ratio TMP-1/TMP-2 was around 4 at the end of the runs, consistent with published results [174] and with the thermodynamic equilibrium constants for trimethylpentenes isomerization (R10), which are in the range from 0.26 to 0.29 for the assayed temperatures [174]. From IA dimerization (R12 in Fig. 4.1.1), a wide variety of diisoamylenes can be formed [125]. Additionally, codimerization between IB and IA (R11 in Fig. 4.1.1) also occurred. Dimers formation took place so slowly that increased almost linearly with time. The formed mole of C_4 dimers and C_{4-5} codimers was very similar at $R°_{C4/C5}$=1, which suggests competitive adsorption between IB and IA. The largest amount of dimers was detected at $R°_{A/O}$= 0.5, $R°_{C4/C5}$=2 and 353 K. The obtained dimerization products that could be identified by GC/MS are described in more detail in *Section 4.5*.

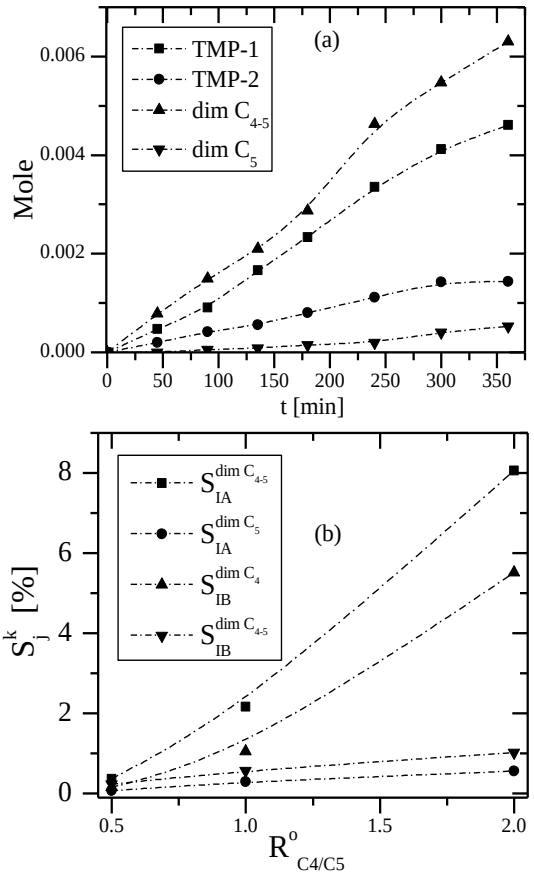

Figure 4.3.8. (a) Mole evolution of dimerization products at $R°_{A/O}$=0.5, $R°_{C4/C5}$=1 and 353 K using 4g of A-35. (b) Olefins selectivity toward dimerization products vs. $R°_{C4/C5}$ at 353 K and $R°_{A/O}$=0.5.

The effect of $R°_{C4/C5}$ on dimers formation is illustrated in Fig. 4.3.8b. The total values of IB and IA selectivities toward dimerization products (dimers and codimers) were always lower than 8% and 10%, respectively. However, IB always yielded larger amounts of dimers than IA in terms of mole, as seen in Fig. 4.3.8a. As $R°_{C4/C5}$ increased, the amount of C_4 and C_{4-5} dimers detected at the end of the runs did it as well. It is explained by the larger amount of IB available in the bulk phase. So it can be stated that IB concentration is a determinant factor for dimerization in the present system. The effect of initial IA concentration on dimers formation was less noticeable.

4.3.7 MODELING AND OPTIMIZATION OF ETHERIFICATION YIELDS

The reaction yield is a suitable parameter to measure the industrial feasibility, which considers simultaneously reactants conversion and selectivity (Eq. 3.3). Equilibrium etherification yield data were modeled using RSM to fit such responses with respect to reaction temperature and initial composition. A second order polynomial form (Eq. 4.3.1) was fitted to experimental yield data by means of the stepwise regression procedure. In order to center the variables of the experimental design, both initial molar ratios of $R°_{A/O}$ and $R°_{C4/C5}$ were translated into initial molar fractions of alcohol in the initial reactant mixture (x_A) and of IB in the initial olefins mixture (x_{C4}). The experimental yield data modeled are gathered in *Appendix 7.6*. Tables 4.3.1 and 4.3.2 show the analysis results in terms of coded variables for the regression coefficients and the models obtained.

Table 4.3.1. Data analysis for coded variables in the modelling of the olefins yield toward ETBE and TAEE after elimination of non-significant terms.

	Y_{IA}^{TAEE}			Y_{IB}^{ETBE}		
Terms	Coefficient	Standard error	*p*-value	Coefficients	Standard error	*p*-value
β_0	41.598	0.486	$3.48\cdot10^{-43}$	87.612	0.573	$1.94\cdot10^{-53}$
β_1 (T)	-7.228	0.384	$3.10\cdot10^{-20}$	-3.982	0.518	$3.56\cdot10^{-09}$
β_2 (x_A)	16.011	0.387	$5.99\cdot10^{-32}$	9.160	0.523	$1.69\cdot10^{-19}$
β_3 (x_{C4})	-2.484	0.387	$1.93\cdot10^{-07}$	-3.646	0.523	$3.10\cdot10^{-8}$
β_{22} (x_A^2)	-6.260	0.596	$1.62\cdot10^{-12}$	-6.807	0.776	$1.42\cdot10^{-10}$
β_{33} (x_{C4}^2)	1.470	0.596	$1.85\cdot10^{-02}$	-	-	-
β_{12} (T·x_A)	-2.880	0.519	$2.82\cdot10^{-06}$	1.470	0.702	$4.31\cdot10^{-2}$
β_{23} (x_A· x_{C4})	2.642	0.474	$2.59\cdot10^{-06}$	4.100	0.641	$1.80\cdot10^{-7}$
R^2 adjusted		98.14			92.51	
F model		325.66			89.47	
F critic		$1.4\cdot10^{-30}$			$1.7\cdot10^{-20}$	

Table 4.3.2. Data analysis for coded variables in the modelling of the alcohol yield toward ETBE and TAEE after elimination of non-significant terms.

	Y_{EtOH}^{TAEE}			Y_{EtOH}^{ETBE}		
Terms	Coefficient	Standard Error	*p*-value	Coefficients	Standard Error	*p*-value
β_0	23.436	0.339	$6.99\cdot10^{-40}$	45.4741	0.382	$1.38\cdot10^{-51}$
β_1 (T)	-3.509	0.267	$2.72\cdot10^{-15}$	-1.053	0.512	0.047
β_2 (x_A)	-4.173	0.270	$1.76\cdot10^{-17}$	-22.517	0.517	$1.08\cdot10^{-34}$
β_3 (x_{C4})	-8.823	0.270	$2.25\cdot10^{-28}$	12.460	0.517	$4.86\cdot10^{-25}$
β_{22} (x_A^2)	-5.292	0.415	$6.50\cdot10^{-15}$	-	-	-
β_{33} (x_{C4}^2)	0.942	0.415	$2.93\cdot10^{-2}$	-	-	-
β_{13} (T·x_{C4})	1.391	0.362	$4.75\cdot10^{-4}$	-	-	-
β_{23} (x_A·x_{C4})	4.396	0.330	$1.81\cdot10^{-15}$	-4.469	0.633	1.7710^{-8}
R^2 adjusted		97.71			98.33	
F model		262.53			633.45	
F critic		$6.33\cdot10^{-29}$			$6.73\cdot10^{-35}$	

As it can be seen, the analysis of variance (ANOVA) revealed that the proposed empirical models were adequate to express the actual relation between the responses and significant variables, with high values of adjusted R^2. The significance level for each equation variable was evaluated by its *p*-value and the significance level of each empirical model by the test of Fisher (*F*-value). Residual plots confirmed the randomness of the residuals for each model (see *Appendix 7.6*). Experimental data vs. predicted value plots also confirmed the suitability of the fitted equations (see Fig. 4.3.9). The largest deviations were found for the modeling of Y_{IB}^{ETBE} at the highest temperatures, what is attributed to the higher amount of formed dimers.

The empirical equations obtained for etherification yields in terms of non-coded variables (Eqs. 4.3.4–4.3.7), refer to the expressions with the minimum number of terms in which all parameters and the regression itself are statistically significant at a confidence level of 95%. *T* is expressed in K in these equations. With respect to the effects for each model, the linear terms *T*, x_A and x_{C4}, the quadratic effect x_A^2 and the interaction effect of $x_A \cdot x_{C4}$ showed the highest level of statistical significance for the fitted equations. The quadratic effect x_{C4}^2 was only significant for Y_{EtOH}^{TAEE}. Finally, the interaction effect $T \cdot x_A$ was only significant for the olefins yield toward ethers. Globally, increasing the temperature, decreased both Y_{IB}^{ETBE} and Y_{IA}^{TAEE}. Y_{EtOH}^{ETBE} resulted almost independent of temperature.

$$Y_{IA}^{TAEE} = -50.12 + 0.094 \cdot T + 663.21 \cdot x_A - 115.37 \cdot x_{C4} - 225.36 \cdot x_A^2 + 52.92 \cdot x_{C4}^2 - 1.15 \cdot T \cdot x_A + 95.11 \cdot x_A \cdot x_{C4} \quad (4.4.4)$$

$$Y_{IB}^{ETBE} = 235.77 - 0.559 \cdot T + 27.53 \cdot x_A - 95.68 \cdot x_{C4} - 245.07 \cdot x_A^2 + 0.588 \cdot T \cdot x_A + 147.62 \cdot x_A \cdot x_{C4} \quad (4.4.5)$$

$$Y_{EtOH}^{TAEE} = 235.91 - 0.512 \cdot T + 86.35 \cdot x_A - 354.02 \cdot x_{C4} - 190.52 \cdot x_A^2 + 33.93 \cdot x_{C4}^2 + 0.556 \cdot T \cdot x_{C4} + 158.27 \cdot x_A \cdot x_{C4} \quad (4.4.6)$$

$$Y_{EtOH}^{ETBE} = 59.15 - 0.07 \cdot T - 54.665 \cdot x_A + 155.2 \cdot x_{C4} - 160.88 \cdot x_A \cdot x_{C4} \quad (4.4.7)$$

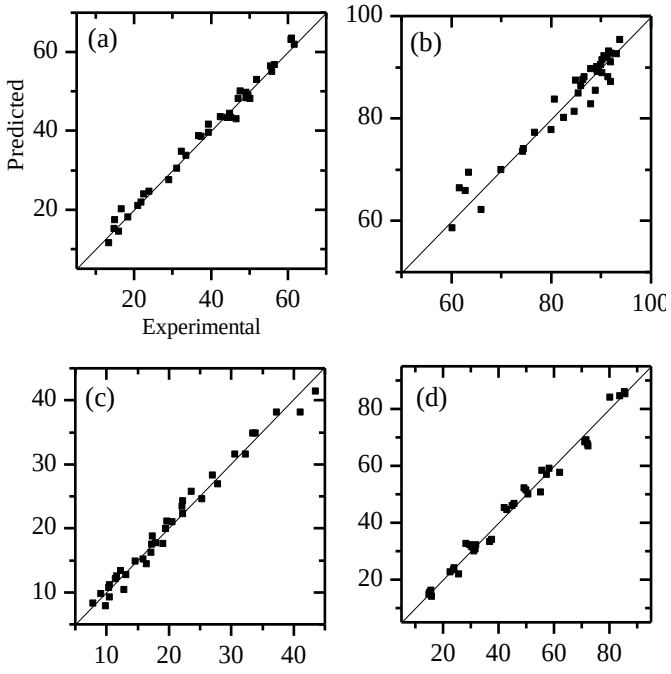

Figure 4.3.9. Predicted data vs. experimental yield data modeled at all assayed temperatures and initial compositions. (a) Y_{IA}^{TAEE}, (b) Y_{IB}^{ETBE}, (c) Y_{EtOH}^{TAEE}, (d) Y_{EtOH}^{ETBE}.

The ability of the empirical models to predict product yields has been confirmed by carrying out an additional run under slightly different conditions, but within the assayed experimental range. More specifically, the run was carried out at $R°_{A/O}$=1.5, $R°_{C4/C5}$= 1.5 and 343 K. Experimental etherification yields obtained were compared to those predicted by the empirical models (Eqs. 4.3.4–4.3.7), the largest deviation being around 5% for Y_{IA}^{TAEE}. Using the obtained models, response surfaces and their contour plots were constructed for the pair of factors T and x_A (the most influencing factors) while holding the third factor, x_{C4}, constant. An example of the response surface profiles obtained and the corresponding contour plots are shown in Fig. 4.3.10. As can be seen, the proposed models fit experimental data reasonably well.

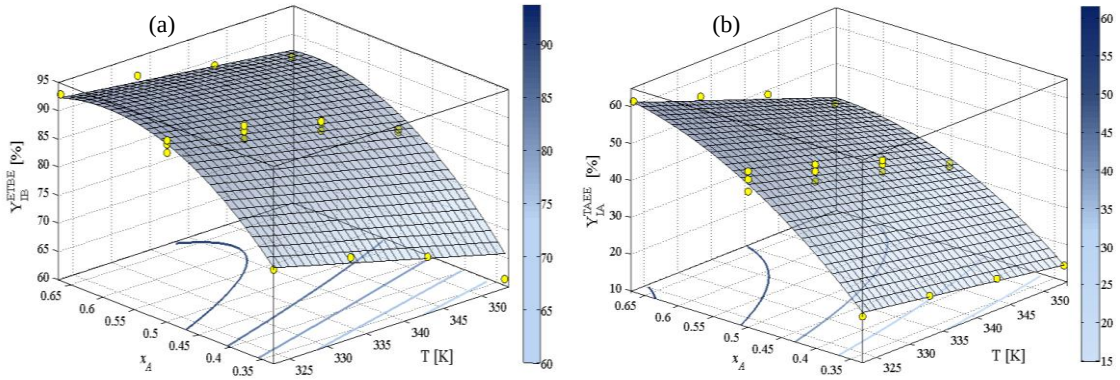

Figure 4.3.10. (a) Response surface for Y_{IB}^{ETBE} vs. x_A and T at x_{C4}=0.5. (b) Response surface for Y_{IA}^{TAEE} vs. x_A and T at x_{C4}=0.5. Symbols (○) refer to the experimental yield data.

The optimization of the experimental conditions that simultaneously maximize etherification yields was carried out graphically by the overlaid contour plots (OCP) holding constant x_{C4} at 0.333, 0.500 and 0.667. Fig. 4.3.11 represents an example of the OCP obtained. The grey shadowed area highlights the optimal experimental region that simultaneously maximizes all etherification yields.

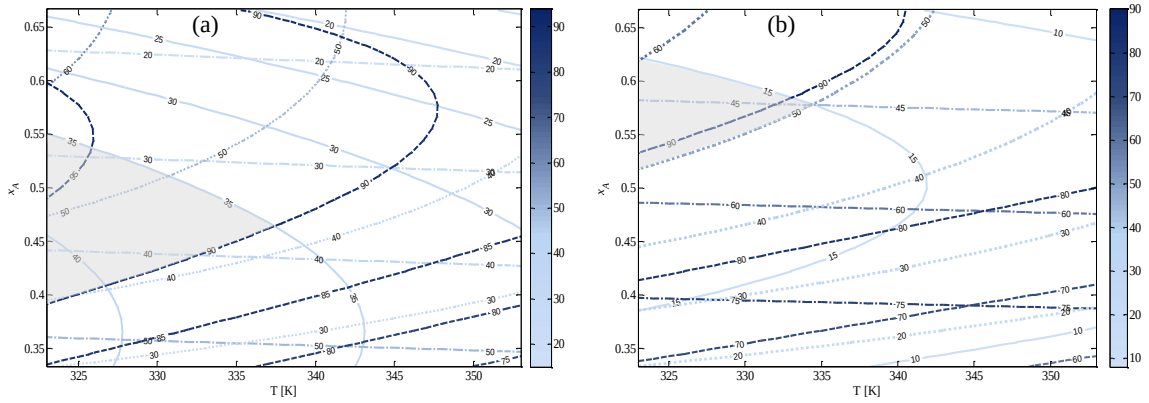

Figure 4.3.11. Overlaid Contour Plot (OCP) for etherification yields at (a) x_{C4}=0.333 and (b) x_{C4}=0.667. Grey shadowed area gathers the optimal conditions for the simultaneous production of ETBE and TAEE. (▬) Y_{EtOH}^{TAEE} ;(▪▪▪) Y_{IA}^{TAEE} ;(---) Y_{IB}^{ETBE} ;(−·−) Y_{EtOH}^{ETBE} .

It was observed that the optimum area is shifted to higher values of x_A when x_{C4} increases, which should be due to IB dimers formation. In other words, a larger initial amount of polar component (EtOH) is required to avoid expected formation of diisobutenes on increasing the initial IB concentration. This methodology reported the best results for x_{C4}=0.333, x_A ranging from 0.4 to 0.55 and temperature ranging from 323 to 337 K. However, a large grade of inaccuracy arises from these plots since the optimal region limited between the contour levels is subjected to a deal of subjectivity. Furthermore, separated analysis is required for each value of x_{C4}.

For the sake of contrasting results and obtaining more accurate data, numerical MOO was also made by solving the overall desirability *D(x)* function obtained from the individual desirability functions. After using RSM to fit appropriate polynomial models to the *r* responses $Y_n(z)$, Eqs. 4.3.4–4.3.7, individual desirability functions $d_n(Y_n(z))$ were defined for each response using Eq. 4.3.3. The value of *s* was set to the unity to assign equal weight to each response and the same priority has been therefore given to the production of ETBE and TAEE. Other criteria could be applied, such as giving priority to olefins yield toward ethers or depending on reactants price and availability. However, the present MOO has been focused from an academic standpoint and so raw materials price has not been considered. Eigenvalues analysis described in Khuri and Cornell (1987)[171] was made prior to numerical optimization in order to evaluate the linear correlation between responses showing that responses were not linearly correlated. The constraints applied to the experimental variables for the optimization of overall *D(x)* were set to obtain results within the range of assayed experimental conditions: $0.333<x_A<0.666$, $0.333<x_{C4}<0.667$ and 323 K$<T<$353 K. Obtained numerical results for each $d_n(Y_n(z))$ and *D(x)* are summarized in Table 4.3.3. Fig. 4.3.12 plots the contour plot obtained for the overall desirability *D(x)* at x_{C4}=0.333. As can be seen the shape of *D(x)* delimits as well an optimal region of x_A and *T* in which the maximum values of etherification yields are attained.

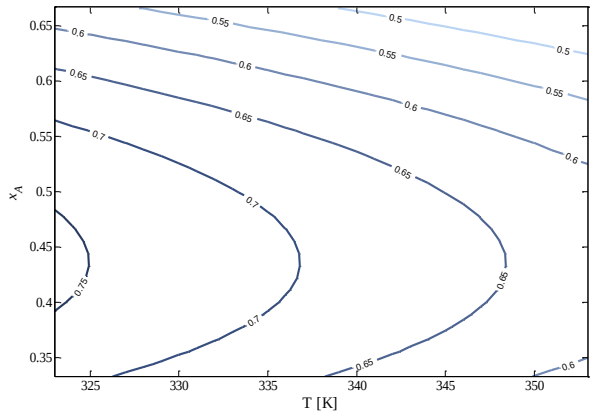

Figure 4.3.12. Contour plot for the obtained overall desirability *D(x)* at x_{C4}=0.333.

From numerical optimization values of $R°_{A/O}$=0.86, $R°_{C4/C5}$=0.5 and T=323 K were estimated as the experimental conditions that maximize the simultaneous production of ETBE and TAEE. Perhaps, the obtained value of $R°_{A/O}$=0.86 is somewhat low compared to the $R°_{A/O}$ value used in isolated production of tertiary alkyl ethers, typically 1.05 [48], because a slight excess of EtOH would prevent dimerization reactions and would enhance olefins conversion. Moreover, $R°_{A/O}$=1 represents the stoichiometric ratio of etherification reactions. Nevertheless, it is to be highlighted that an initial 1 wt.% of water was used in all the experiments of the present study, thus an additional amount of olefins was consumed in hydration reactions and that could explain

the slight excess of olefins obtained by numerical MOO. Besides, the obtained values of T=323 K and $R°_{C4/C5}$=0.5 imply a reduction of olefins dimerization production, because, as seen before, IA concentration is not as critical factor for dimerization as IB concentration. Based on these reasons, obtained results from numerical MOO are considered plausible and unbiased.

According to the optimal region determined by the OCP methodology at x_{C4}=0.333, optimal range of temperature to produce simultaneously ETBE and TAEE ranges from 323 to 337 K and $R°_{A/O}$ from 0.64 to 1.22. These values are coherent with those determined numerically by the desirability function approach. Finally, the sensitiveness of *D(x)* on varying experimental conditions, see Table 4.3.3, revealed that x_{C4} can be varied from 0.333 to 0.667 and the obtained values for *D(x)* are still higher than 0.67. Thus $R°_{C4/C5}$ could be set depending on both, the refinery necessities (preferred production of ETBE or TAEE) and the provisioning of C_4 and C_5 olefinic streams.

Table 4.3.3. Values of individual desirabilities ($d_n(Y_n(z))$), overall desirability *D(x)* and etherification yields obtained for other interesting experimental conditions.

T [K]	x_A	x_{C4}	$d(Y_{EtOH}^{TAEE})$	$d(Y_{IA}^{TAEE})$	$d(Y_{IB}^{ETBE})$	$d(Y_{EtOH}^{ETBE})$	*D(x)*	Y_{EtOH}^{TAEE}	Y_{IA}^{TAEE}	Y_{IB}^{ETBE}	Y_{EtOH}^{ETBE}
323	0.462	0.333	0.92	0.79	1	0.45	0.76	39.8	49.0	94.2	38.2
323	0.5	0.333	0.88	0.86	1	0.39	0.74	38.1	53.1	95.4	34.1
323	0.5	0.5	0.62	0.8	0.98	0.54	0.72	26.9	49.1	91.7	46.5
323	0.5	0.667	0.41	0.78	0.94	0.69	0.67	17.7	48.1	88.1	58.9
323	0.55	0.333	0.81	0.93	1	0.34	0.71	35.1	57.4	95.9	28.6
323	0.667	0.5	0.40	1	0.99	0.28	0.58	17.5	61.8	92.7	24.1

The applied methodology can be particularly useful when modeling yields in units that produce several desired products simultaneously. In that case, numerical MOO using desirability functions can help to decide how much in the yield of a certain product is the engineer willing to reduce for a gain in the yield of other products. Also to find out the experimental conditions that give priority to special production targets.

4.3.8 PARTIAL CONCLUSIONS

Experimental equilibrium data presented in this paper would represent the output composition of industrial equilibrium reactors and thus represent valuable information. Reactants equilibrium conversion decreases on increasing the temperature, as expected for exothermic reactions. Increasing $R°_{A/O}$, higher olefins equilibrium conversion can be achieved but at the expense of lower X_{EtOH}. Increasing $R°_{C4/C5}$ slightly increases X_{EtOH} and favors ETBE formation over TAEE one. As a whole, X_{IB}, X_{IA} and X_{EtOH} ranged from 69.8 to 97.9%, from 17 to 65.6% and from 32.3 to 97.0%, respectively, depending on initial composition and temperature. The simultaneous etherification performed is a feasible technique to convert up to 65% of the environmentally troublesome C_5 iso-olefins and entails large EtOH use as raw material.

High values of olefins selectivity toward target products are obtained which is certainty desirable from an industrial standpoint. Increasing temperature promotes formation of both tertiary alcohols and dimerization products whereas increasing $R°_{A/O}$ shows an opposite effect on the formation of both side products. $R°_{A/O}$ is therefore an important control variable to avoid side reactions. The effect of $R°_{C4/C5}$ on side products formation is less noticeable but an increase in IB concentration is a critical factor toward dimers formation at high temperatures.

The experimental yield data have been empirically modeled using response surface methodology and expressions able to predict etherification yields within the experimental conditions have been obtained. Two different approaches have been applied to the multiobjective optimization of the overall ether yield and obtained results from both methodologies are in reasonable agreement. For the present system, the experimental conditions that maximize the simultaneous production of both ETBE and TAEE are $R°_{A/O}$=0.86, $R°_{C4/C5}$=0.5 and a temperature of 323 K.

4.3.9 CHAPTER NOTATION

2M1B	2-methyl-1-butene
2M2B	2-methyl-2-butene
A-35	macroporous ion-exchange resin Amberlyst™35
$D(z)$	overall desirability function
$d_n(Y_n(z))$	individual desirability function for each response
ETBE	ethyl *tert*-butyl ether
EtOH	ethanol
IA	isoamylenes
IB	isobutene
MOO	multi-objective optimization
OCP	overlaid contour plots
$R°_{A/O}$	initial molar ratio of alcohols to olefins [dimensionless]
$R°_{C4/C5}$	initial molar ratio of isobutene to isoamylenes [dimensionless]
RSM	response surface methodology
t	reaction time [min]
T	temperature [K]
T_b	boiling point [K]
TAEE	*tert*-amyl ethyl ether
TAA	*tert*-amyl alcohol
TBA	*tert*-butyl alcohol
TMP-1	2,4,4-trimethyl-1-pentene
TMP-2	2,4,4-trimethyl-2-pentene
X_j	conversion of reactant *j* at chemical equilibrium
S_j^k	selectivity of reactant *j* toward product *k* at chemical equilibrium
s	user specific weight factor
$Y_n(z)$	response *n* to be optimized
Y_j^k	yield of reactant *j* toward product *k* at chemical equilibrium
x_A	molar fraction of alcohol in the initial reactant mixture
x_{C4}	molar fraction of isobutene in the initial olefin mixture

Greek letters

β *regression coefficients*

4.4 CHEMICAL EQUILIBRIUM AND THERMODYNAMIC ANALYSIS

An extended and revised version of this chapter was published as:

R. Soto, C. Fité, E. Ramírez, R. Bringué, F. Cunill. Equilibrium of the simultaneous etherification of isobutene and isoamylenes with ethanol in liquid-phase. *Chem. Eng. Res. Des.* **2014**; 92 (4): 644–656. http://dx.doi.org/10.1016/j.cherd.2013.11.012

4.4.1 INTRODUCTION

As mentioned in *Section 1.6*, the thermodynamics of isolated ETBE and TAEE syntheses [22,89,91,121,122,127,129,135–138] have been studied in the open literature. However, some divergences can be found with regards to the thermodynamic state functions obtained and well as for the enthalpies of formation of involved compounds. Since equilibrium constants of reactions are an essential part of the driving force in kinetic equations, their determination constitutes a crucial step for a subsequent kinetic study. This work aims to study the chemical equilibria of the main reactions involved in the simultaneous etherification of IB and IA with EtOH over a wide range of experimental conditions. Experimental determination of thermodynamic properties of these reactions is also a key factor in order to compare them with those reported previously in the literature for the isolated etherification systems.

4.4.2 EXPERIMENTAL AND CALCULATIONS

The experimental setup, procedure and conditions used in this section are described in *Section 4.3*. Most of the experiments were carried out using A-35, but A-15 and CT-275 were also used aiming to compare resins. With regards to the calculations, a detailed description is made while the main outcomes are described throughout this section.

4.4.3 EFFECT OF THE CATALYST LOAD

The catalyst load was varied from 4 g in experiments at 343 K and 353 K to 8 g in experiments at 333 and 323 K in order to shorten the length of the experiment at lower temperatures and being therefore able to reach equilibrium in a relatively short time. Hence, the effect of the catalyst load (using 4 g and 8 g) was studied on commercial bead size distribution for A-35 at 333 K. To allow the comparison for the different catalyst loads, the contact time $W_{cat} \cdot t \cdot n_{EtOH,0}^{-1}$ was used instead of time *t*. Fig. 4.4.1 shows the reactants conversion versus contact time for the two used catalyst loads. It can be observed that, for each reactant, conversion evolution for both catalyst loads overlaps when it is plotted versus the contact time. Hence, no significant effect of the catalyst loading was observed under these conditions within the limits of experimental error. Therefore, hereinafter both catalyst loads of 4 and 8 g will be used as appropriate for the experiment duration.

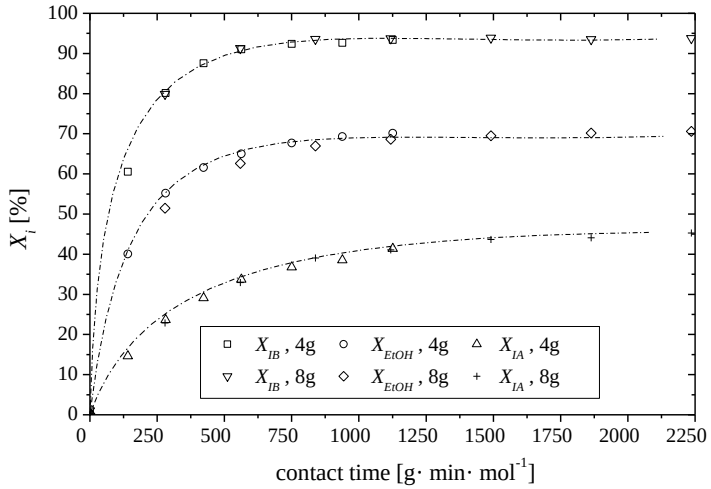

Figure 4.4.1. Evolution of reactants conversion with respect to the contact time ($W_{cat}\cdot t\cdot n_{EtOH,0}^{-1}$) for different catalyst loads of A-35 at 333K, $R°_{A/O}$=1 and $R°_{C4/C5}$=1.

4.4.4 EQUILIBRIUM CONSTANTS

Fig. 4.4.2 shows a model experiment. As seen, ETBE production reaction was practically at chemical equilibrium state after 180 min, whereas that of TAEE needed twice that period to reach equilibrium. The number of moles of tertiary alcohols formed was very similar for TBA and TAA, and both reached quickly the chemical equilibrium state, usually in less than 100 min of reaction. From the global reactions scheme presented in Fig. 4.1.1, the thermodynamic study was mainly focused on etherification reactions R1-R3 and isoamylenes isomerization reaction (R4). The rest of the reactions were not studied due to the low amount of the involved products detected, namely DEE, TBA and TAA. Though some dimers were irreversibly formed at the highest temperature and in olefin excess, it took place so slowly that reactions R1 to R4 could be considered to be at pseudo-equilibrium at the final time of each experimental run. It is worth noting that only two of reactions R2, R3 and R4 are stoichiometrically independent in the TAEE formation reaction system. For instance, addition of reactions R3 and R4 gives reaction R2. Thus, in relation with the equilibrium constants, it can be written:

$$K_2 = K_3\, K_4 \tag{4.4.1}$$

Considering the non-ideality of the mixture, mainly due to the presence of alcohols and water, activity coefficients of compounds, γ_j, were estimated by means of the UNIFAC-Dortmund predictive method [176–179], see *Appendix 7.7*. This method was chosen because it gave good results for most of the studies reported before for the isolated etherification systems and aiming to compare results properly. Activity coefficients for alcohols are normally larger than 3 (at low mole fractions), and for ethers (slightly non ideals) and olefins they are close to the unity [48]. The evolution of a model experiment in terms of activities (a_j) is plotted in Figure 4.4.2b. In general, the thermodynamic equilibrium constant K_i, for the liquid-phase reaction *i* of a nonideal system with *S* species can be expressed as follows:

$$K_i \equiv \prod_{j=1}^{s} (a'_j)_{ei}^{\nu_j} = \left(\prod_{j=1}^{s} (\gamma_j)_e^{\nu_j} \right)_i \left(\prod_{j=1}^{s} (x_j)_e^{\nu_j} \right)_i \equiv K_{\gamma_i} K_{x_i} \tag{4.4.2}$$

where K_{xi} is the equilibrium constant of reaction i in terms of molar fractions and $K_{\gamma i}$ is the related equilibrium constant in terms of activity coefficients.

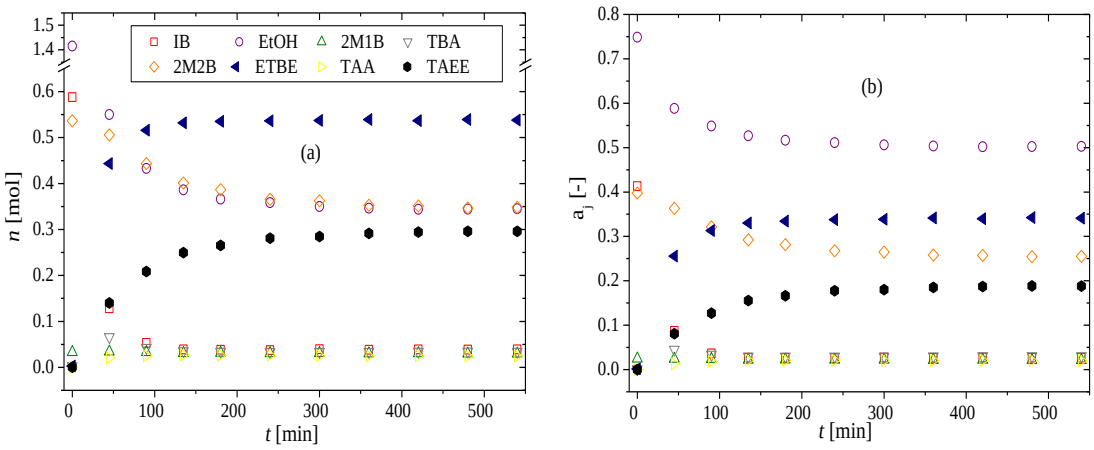

Figure 4.4.2. Model experiment carried out at 333 K, $R°_{A/O}$=1 and $R°_{C4/C5}$=1, with 8 g of A-35. (a) Evolution in terms of mole. (b) Evolution in terms of activities of compounds.

Appendix 7.8.1 shows the experimental conditions of the performed experiments, the calculated equilibrium constants and the experimentally obtained K_{xi} and $K_{\gamma i}$ for the etherification reactions of olefins with EtOH and the IA isomerization reaction. Obtained values for K_{xi} at different temperatures ranged from 236.0 to 20.4, from 183.3 to 14.4, from 15.1 to 1.6 and from 14.4 to 8.3 for R1, R2, R3 and R4, respectively. Moreover, K_{xi} was found to decrease when $R°_{C4/C5}$, $R°_{A/O}$ and temperature increased. On the other hand, $K_{\gamma i}$ showed an opposite trend in its relationship with the different initial molar ratios and temperature with the exception of R4, where it is difficult to establish a clear relationship between $K_{\gamma 4}$ and temperature, $R°_{C4/C5}$ or $R°_{A/O}$. $K_{\gamma i}$ ranged at the assayed temperatures from 0.178 to 0.636, from 0.170 to 0.611, from 0.168 to 0.608 and from 1.006 to 1.019 for R1, R2, R3 and R4, respectively. Values of $K_{\gamma i}$ for reactions R1, R2 and R3 (reactions where EtOH is a reactant) were significantly different from unity, especially at low $R°_{A/O}$, which confirms the non-ideality of the system. The values of $K_{\gamma 4}$, for the IA isomerization reaction, were very close to the unity, as expected, since in this reaction only the two olefins are involved, which are very similar and, therefore, they should present similar activity coefficient.

As mentioned above, irreversible olefins dimerization took place at $R°_{A/O}$=0.5 and at high temperatures (343–353K) which could make the study of the chemical equilibrium difficult as the actual equilibrium state composition would not be reached until reactants consumption. Notwithstanding, dimers formation was so slow compared to isomerization and etherification reactions at the assayed temperatures that equilibrium constants of the main etherification reactions could be evaluated assuming a pseudo-equilibrium state. Moreover, isomerization reactions are known to take place faster than etherification reactions. Consequently, olefins were consumed slowly to form dimers, allowing a quick readjustment of the compositions for the etherification and isomerization reactions and maintaining a pseudo-equilibrium state.

In Fig. 4.4.3 the relationship between the average values of experimentally obtained thermodynamic equilibrium constants and temperature for each reaction is plotted for A-35. Results obtained for A-15 and CT-275 were included neither to obtain the values plotted in Fig. 4.4.3 nor in the subsequent determination of thermodynamic properties. However, it was confirmed that experimentally obtained equilibrium constants for A-35, A-15 and CT-275 were

very similar under the same conditions (see *Appendix 7.8.1*), as expected considering the well-known fact that K_i value is independent of the used catalyst.

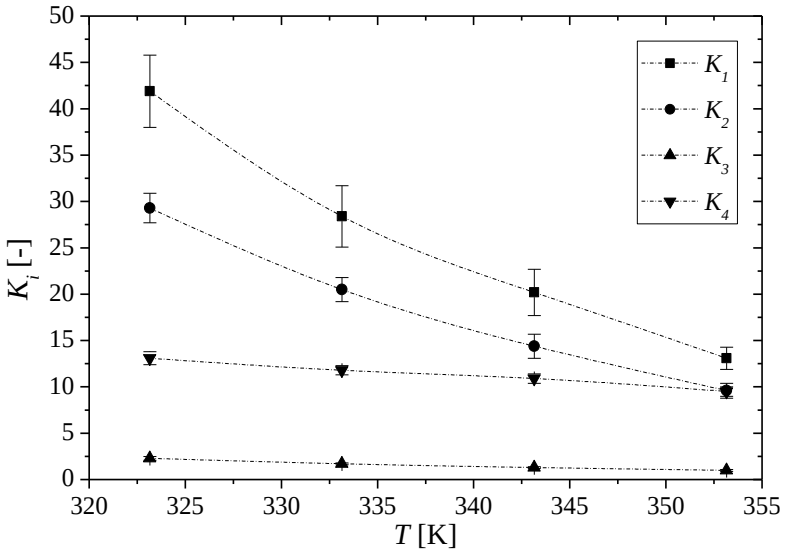

Figure 4.4.3. Temperature dependence of the thermodynamic equilibrium constants for reactions R1 to R4. Error bars refer to a 95% confidence interval.

The relatively larger error of K_1 in the ETBE formation reaction is attributed to the low IB content at equilibrium, due to the high conversion of IB at low temperatures. All four thermodynamic equilibrium constants decrease monotonically with temperature, as expected for exothermic reactions. As for kinetics, at the highest temperature, the highest reaction rate for ethers formation was observed, but also the lower amount of ethers formed at chemical equilibrium. R1 was the first reaction that reached chemical equilibrium. Concerning etherification reactions, K_1 was always higher than K_2 and K_3 at the same temperature, what suggests that the equilibrium constant decreases when the size of the olefin molecule increases. This fact is consistent with the results reported in published studies in which different alcohols were used in the reaction with isobutene [88,127]. It was concluded that the equilibrium constant value decreased when the alcohol size increased. As a consequence, it can be said that the higher the reactant molecular size, the lower the equilibrium constant value is observed for these etherification reactions.

ETBE synthesis reaction (R1) presented the highest exothermicity since K_1 showed a relatively larger decrease at increasing temperature compared to the rest of reactions. As K_1, K_2 and K_3 decreased monotonically with increasing temperature, less ETBE and TAEE were produced at higher temperatures. K_4 decreased as well with increasing temperature, but in a much lesser extent than the ethers formation reactions because of the smaller exothermicity of this reaction. Since K_4 decreased at slower rate with temperature, it can be said that isomerization conversion of C_5 iso-olefins (2M1B to 2M2B) decreases more slightly with the rise of temperature, whereas etherification conversion for both olefins, IA and IB, decreases in a significant extension. In fact, it has been already contrasted in the isolated TAEE formation system from IA that a lower temperature favors etherification reactions, whereas a higher temperature favors the isoamylenes isomerization reaction [22,91,137].

The values in *Appendix 7.8.1* and Fig. 4.4.3 show that TAEE synthesis from 2M2B was less favorable than its synthesis from 2M1B, since K_3 was always lower than K_2. This fact might be

related to the thermodynamic stabilities of both isoamylenes. The relative stability of an olefin is determined by the number of alkyl groups bonded to the carbon atoms with double bonds, the olefins being more stable as that number increases [175]. Therefore, 2M2B should be thermodynamically more stable than 2M1B. With regard to the IA isomerization reaction equilibrium constant, it was slightly dependent of temperature.

Theoretical equilibrium constants values can be estimated from the thermodynamic data available in literature using the liquid-phase standard molar enthalpy and Gibbs free energy changes of formation of the components involved in each reaction. The accuracy in the calculation of the equilibrium constants following this procedure is highly sensitive to the quality of the thermodynamic data, especially for reactions with moderate standard Gibbs free energy changes, as it is the case for reversible reactions [180]. Experimental data for the liquid-phase heat capacity, the standard enthalpy and standard Gibbs free energy of formation of EtOH, IB, 2M1B, 2M2B, ETBE and TAEE at 298 K are available in the literature, and they are listed in Table 4.4.1. Nonetheless, thermodynamic data for the formation of TAEE and ETBE are scarcely reported and in any case, the lack of agreement between sources led to a discrepancy between theoretically and experimentally obtained equilibrium constants.

Table 4.4.1. Liquid-phase thermochemical data and liquid-phase molar heat capacity equation coefficients, $C^{o}_{p_j}\left[J\ K^{-1}mol^{-1}\right] = a_j + b_j T + c_j T^2 + d_j T^3$, with T expressed in Kelvin.

Component j	Heat capacity coefficients				$\Delta_f G_j^o$ [kJ/mol]	$\Delta_f H_j^o$ [kJ/mol]
	a_j	b_j	c_j	d_j		
IB	35.44 [a]	0.802 [a]	$-3.124\cdot10^{-3}$ [a]	$5.045\cdot10^{-6}$ [a]	60.67 [a]	-37.7 [a]
EtOH	29.01 [a]	0.2697 [a]	$-5.658\cdot10^{-4}$ [a]	$2.079\cdot10^{-6}$ [a]	-174.8 [a]	-277.51 [a]
ETBE	148.48 [b]	0.09 [b]	$5.058\cdot10^{-4}$ [b]	0 [b]	-126.8 [a]	-350.8 [c]
2M1B	126.5 [d]	-0.0609 [d]	$5.084\cdot10^{-4}$ [d]	$1.692\cdot10^{-7}$ [d]	66.5 [e]	-60.96 [e]
2M2B	132.9 [d]	-0.1475 [d]	$7.511\cdot10^{-4}$ [d]	$-8.817\cdot10^{-8}$ [d]	60.0 [e]	-68.07 [e]
TAEE	180.08 [b]	0.0169 [b]	$6.95\cdot10^{-4}$ [b]	0 [b]	-119.9 [a,e]	-372.9 [a,e]

Data based on experimental values: [a] Gallant (1993) [181]; [b] Zábranský et al. (2010) [182]; [c] Sharonov et al. (1995) [138]; [d] Yaws (1992) [183]; [e] TRC (Thermodynamic Research Center) (1986) [184].

For the sake of comparison, Tables 4.4.2 and 4.4.3 provide the values of experimental equilibrium constant values reported previously for the ETBE and TAEE synthesis in isolated systems, respectively. Also the equilibrium constants determined theoretically by means of the thermodynamic data available in Table 4.4.1 and those obtained experimentally in this work as the mean values at each temperature are included in Tables 4.4.2 and 4.4.3. Errors indicated by authors in these tables are referred to a 95% confidence interval.

Table 4.4.2. Experimental equilibrium constants values for ETBE formation reaction (R1) and comparison with published results.

	T [K]	This work	Françoise and Thyrion (1991) [139]	Vila et al. (1993) [160]	Cunill et al. (1993) [37]	Izquierdo et al. (1994) [127]	Jensen and Datta (1995) [135]	Gómez et al. (1997) [122]	Determined theoretically
K_1	323	41.9 ± 3.9	46	42.1	41.5	40±7	44	34.3±0.4	54.6
	333	28.4 ± 3.3	26	26.4	26.8	26±3	27	22.3±1	36.7
	343	20.2 ± 2.5	16	18.4	18.1	18±1	17	17.1±1.8	25.3
	353	13.1 ± 1.2	11.5	12.8	12.6	13±2	11	11.3±0.7	17.7

Table 4.4.3. Experimental equilibrium constant values for TAEE formation reactions (R2 and R3) and for isoamylenes isomerization reaction (R4) and comparison with published results.

	T [K]	This work	Rihko et al. (1994)[137]	Kitchaiya and Datta (1995)[22]	Cruz et al. (2007) [185]	Fitó and Linnekoski (2008) [121]	Determined theoretically
K_2	323	29.3 ± 1.6	24.8±1.5	30.6	-	31.1	36.7
	333	20.5 ± 1.3	17.4±1.1	20.8	20.6	20.9	25.0
	343	14.4 ± 1.3	11.3±0.8	14.7	-	14.5	17.4
	353	9.6 ± 0.8	8.3±0.6	-	8	-	12.4
K_3	323	2.3 ± 0.2	2.2±0.1	2.6	-	2.6	3.4
	333	1.7 ± 0.1	1.7±0.1	1.9	2.1	1.9	2.5
	343	1.3 ± 0.1	1.2±0.1	1.5	-	1.5	1.8
	353	1.0 ± 0.1	1.0±0.1	-	1.2	-	1.4
K_4	323	13.1 ± 0.7	11±0.4	11.9	-	12	11.0
	333	11.8 ± 0.5	10.2±0.4	10.9	-	10.9	10.2
	343	10.9 ± 0.5	9.3±0.4	10	-	10.0	9.5
	353	9.5 ± 0.5	8.6±0.4	-	-	-	8.8

A good agreement is observed between experimental equilibrium constants for ETBE formation reaction (K_1) in the simultaneous synthesis and those obtained for the isolated system experimentally. Furthermore, the agreement of the equilibrium constants for TAEE synthesis reactions (K_2, K_3 and K_4) was rather good as well, which confirms the equilibrium constants to be independent of the simultaneous reactions. On the whole, it seems reasonable that the equilibrium constants obtained for the simultaneous syntheses of ETBE and TAEE were practically the same as those of isolated reactions. Hence, it can be concluded that the simultaneous etherification does not present any influence on reaction equilibrium constants when compared to the thermodynamic data of the separated ETBE and TAEE formation reactions by etherification of EtOH with the corresponding olefins. A larger difference between experimental and theoretical values was observed for R1, R2 and R3. It can be explained because the respective equilibrium constants are highly sensitive to the thermodynamic data used in the calculations. The influence of the enthalpy of formation, $\Delta_f H_j^o$, of a component *j* in the equilibrium constant is of utmost importance; for instance, a deviation of 1 kJ/mol in the enthalpy of formation of 2M1B changes the equilibrium constant of the 2M1B etherification reaction from 21 to 31, and changes the equilibrium constant of the isoamylenes isomerization reaction from 11 to 17. A similar difference in the absolute entropy of a component *j*, S_j^o or C_{pj}^o has a minor effect on the calculation of K_i.

Deviation in K_i values due to the difference between the working pressure and the pressure at the standard state was evaluated by means of the product between K_i and the Poynting correction factor $K_{\Gamma i}$, which can be estimated by the following expression [186]:

$$K_{\Gamma i} = \exp\left(\frac{P-1}{RT} \sum_{j=1}^{S} \nu_{ji} V_j \right) \tag{4.4.3}$$

where V_j is the molar volume of compound *j*.

Molar volumes were calculated by HBT method [33] and $K_{\Gamma i}$ correction factors for the main four chemical reactions were approximately equal to unity (always higher than 0.9999), see

Appendix 7.8.2. Consequently, it can be said that the effect of the working pressure on the calculated K_i was negligible and, therefore, it can be assumed that the equilibrium constant is only a function of temperature.

4.4.5 THERMODYNAMIC STATE FUNCTIONS OF REACTIONS

The temperature dependence of the thermodynamic equilibrium constant is given by:

$$\ln K_i = \frac{-\Delta_r G_i^o}{RT} = \frac{-\Delta_r H_i^o}{RT} + \frac{\Delta_r S_i^o}{R} \tag{4.4.4}$$

At this point, two alternatives can be considered: i) $\Delta_r H_i^o$ constant with temperature ($\Delta_r H_i^o \neq f(T)$), and ii) $\Delta_r H_i^o$ depends on temperature ($\Delta_r H_i^o = f(T)$). On one hand, if the enthalpy change of reaction is assumed to be constant within the assayed temperature range, fitting Eq. 4.4.4 to the experimental equilibrium constant values should produce a straight line. Fig. 4.4.4 depicts $\ln K_i$ versus $1/T$ for the four experimental equilibrium constants obtained. As it can be seen, experimental results fit quite well to a straight line.

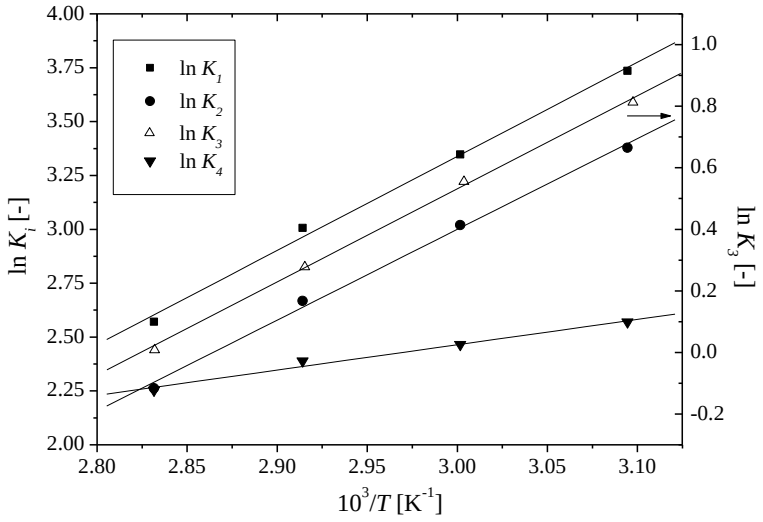

Figure 4.4.4. Van't Hoff plot for the case where the reaction enthalpy change is considered constant within the temperature range ($\Delta_r H_i^o \neq f(T)$). Solid lines refer to the values predicted by Eqs. 4.5.5–4.5.8.

The resulting fitting equations obtained by least squares regression are:

$$\ln K_1 = \left(\frac{4370.52 \pm 868.01}{T}\right) - \left(9.77 \pm 2.57\right) \tag{4.4.5}$$

$$\ln K_2 = \left(\frac{4218.21 \pm 726.33}{T}\right) - \left(9.66 \pm 2.15\right) \tag{4.4.6}$$

$$\ln K_3 = \left(\frac{3068.08 \pm 357.38}{T}\right) - \left(8.67 \pm 1.06\right) \tag{4.4.7}$$

$$\ln K_4 = \left(\frac{1168.30 \pm 459.28}{T}\right) - \left(1.04 \pm 1.36\right) \tag{4.4.8}$$

The standard molar enthalpy change of reaction ($\Delta_r H_i^o$) can be obtained from the slope and the standard molar entropy change of the reaction ($\Delta_r S_i^o$) from the intercept. From the fitted parameters, the values of $\Delta_r H_i^o$ and $\Delta_r S_i^o$ have been estimated, as presented in Table 4.4.5.

On the other hand, if $\Delta_r H_i^o$ is considered to change over the temperature range, its dependence can be expressed by the Kirchoff equation:

$$\frac{d\Delta_r H_i^o}{dT} = \sum_{j=1}^{S} \nu_{ij} C_{p_j}^o \tag{4.4.9}$$

where C_{pj}^o are the molar heat capacities in the liquid phase of the compounds *j* that take part in the reaction *i*, which can be estimated from equation and data included in Table 4.4.1 [48].

Estimated values for molar heat capacity of ETBE with parameters from Table 4.4.1 were in agreement with those obtained by Solà et al. (1995) [133], who estimated a value of 226.6 J/(mol K) at 298 K. Also the values obtained for TAEE are very similar to those reported by Kitchaiya and Datta (1995)[22] at 298 K, being 240 and 244 J/(mol K), estimated by the Rowlinson method and from TRC Thermodynamic Tables, respectively. This difference in the estimation of heat capacities is acceptable, since calculations indicate that an error in the value of heat capacity of 10 J/(mol K) introduced an error less than 1.5% into the calculated equilibrium constants for TAEE synthesis [22]. The values of molar heat capacity obtained were also very similar to those estimated at 298 K by the Missenard method [33] for ETBE and TAEE. Henceforward, the coefficients from Table 4.5.1 were used in the calculations of the thermodynamic properties showed below.

The integrated form of the Kirchoff equation, combined with equations from Table 4.4.1, gives the following expression:

$$\Delta_r H_i^o = I_k + aT + \frac{b}{2}T^2 + \frac{c}{3}T^3 + \frac{d}{4}T^4 \tag{4.4.10}$$

where:

$$a = \sum_{j=1}^{S} \nu_{ij} a_i ; \qquad b = \sum_{j=1}^{S} \nu_{ij} b_i ; \qquad c = \sum_{j=1}^{S} \nu_{ij} c_i ; \qquad d = \sum_{j=1}^{S} \nu_{ij} d_i \tag{4.4.11}$$

The dependence of the equilibrium constant on temperature is described by the van't Hoff equation:

$$\frac{d \ln K_i}{dT} = \frac{-\Delta_r H_i^o}{RT^2} \tag{4.4.12}$$

This equation, combined with Eq. 4.4.10 and integrated, leads to:

$$\ln K_i = I_H - \frac{I_K}{RT} + \frac{a}{R}\cdot\ln T + \frac{b}{2R}T + \frac{c}{6R}T^2 + \frac{d}{12R}T^3 \tag{4.4.13}$$

where I_K and I_H are the integration constants (unknown parameters).

By fitting Eq. 4.4.13 to the experimental values of the equilibrium constants at different temperatures (see Fig. 4.4.5), I_K can be obtained from the slope and I_H from the intercept. The

fitting was accurate enough for both methods, assuming $\Delta_r H_i^o$ constant or a function of temperature. The linear fitting coefficient R^2 was always higher than 0.99 for each reaction with the exception of the value of 0.983 obtained for the isomerization reaction between isoamylenes.

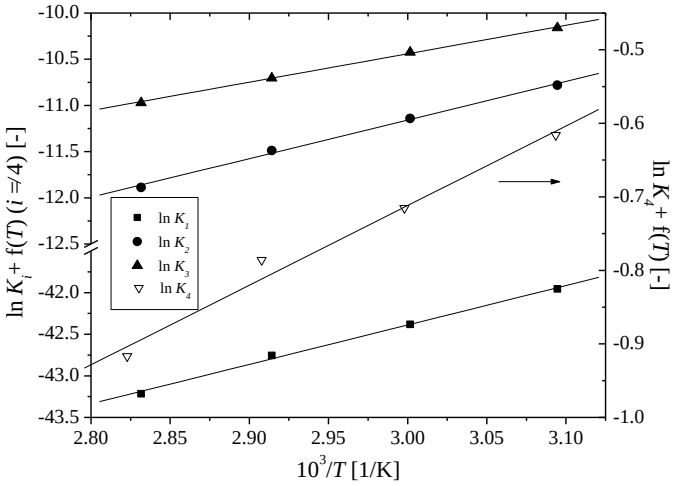

Figure 4.4.5. Van't Hoff plot for the case where the reaction enthalpy change is considered dependent on temperature ($\Delta_r H_i^o$ = f(T)).

The standard molar changes of reaction $\Delta_r S_i^o$ and $\Delta_r G_i^o$ can be evaluated, by means of Eqs. 4.4.4, 4.4.10 and 4.4.13, as follows:

$$\Delta_r S_i^o(T) = R \cdot I_H + a + a \cdot \ln T + bT + \frac{c}{2}T^2 + \frac{d}{3}T^3 \qquad (4.4.14)$$

$$\Delta_r G_i^o(T) = I_K - R \cdot I_H \cdot T - a \cdot T \cdot \ln T - \frac{b}{2}T^2 - \frac{c}{6}T^3 - \frac{d}{12}T^4 \qquad (4.4.15)$$

Parameters of equations 4.4.10─4.4.15 are shown in Table 4.4.4.

Table 4.4.4. Temperature dependence parameters of K_i, $\Delta_r H_i^o$, $\Delta_r S_i^o$ and $\Delta_r G_i^o$ for reactions R1 to R4 when $\Delta_r H_i^o$ =f(T).

Parameters	R1	R2	R3	R4
a [J/mol K]	84.0282	24.5698	18.1698	6.4
b [J/mol K^2]	-0.9817	-0.1919	-0.1053	-0.0866
c [J/mol K^3]	0.0042	0.000752	0.00051	0.000243
d [J/mol K^4]	$-7.1 \cdot 10^{-6}$	$-2.25 \cdot 10^{-6}$	$-1.99 \cdot 10^{-6}$	$-2.57 \cdot 10^{-7}$
I_k [J/mol]	-39414.5	-34760.44	-25696.08	-9215.31
I_H [-]	-56.61	-23.70	-19.71	-4.04

Finally, the thermodynamic state functions $\Delta_r H_i^o$, $\Delta_r S_i^o$ and $\Delta_r G_i^o$ can also be computed theoretically from the thermodynamic data available in Table 4.4.1 ($\Delta_f H_j^o$ and $\Delta_f G_j^o$) for the involved species by using Eq. 4.4.4 and the following expressions:

$$\Delta_r H_i^o = \sum \left(\nu_{ij} \cdot \Delta_f H_j^o \right) \qquad (4.4.16)$$

$$\Delta_r G_i^o = \sum \left(\nu_{ij} \cdot \Delta_f G_j^o \right) \qquad (4.4.17)$$

Table 4.4.5 is a summary of the experimentally and theoretically calculated thermodynamic changes for every reaction and considered hypothesis.

Table 4.4.5. Summary of thermochemical properties of reactions at 298 K and comparison with values reported in literature. Errors refer to a 95% confidence interval.

Reaction	Properties	Case $\Delta_r H_i^o \neq f(T)$	Case $\Delta_r H_i^o = f(T)$	Theoret.	Literature data			
R1	$\Delta_r H°_1$ [kJ/mol]	-36.3±7.2	-35.0±6.7	-35.6	-34.8 ±1.3 [a]	-35.5±2 [b]	-36±2 [c]	-44.3 [d]
	$\Delta_r S°_1$ [J/(mol K)]	-81.3±21.4	-77.1±20.0	-76.9	-77.3±0.6 [a]	-82.4±6 [b]	-	-
	$\Delta_r G°_1$ [kJ/mol]	-12.1±4.5	-12.0±6.7	-12.7	11.8±1.3 [a]	-	-	-
R2	$\Delta_r H°_2$ [kJ/mol]	-35.1±6.0	-33.8±5.5	-34.4	-33.6 [e]	-35.2±5.8 [f]	-34.5 [g]	-
	$\Delta_r S°_2$ [J/(mol K)]	-80.3±17.9	-76.1±16.3	-76.5	-75.4 [e]	-82.3±17.3 [f]	-80.1 [g]	-
	$\Delta_r G°_2$ [kJ/mol]	-11.1±2.7	-11.1±5.5	-11.6	-11.1 [e]	-10.7 [e]	-10.6 [g]	-
R3	$\Delta_r H°_3$ [kJ/mol]	-25.5±3.0	-24.4±2.5	-27.3	-24.2 [e]	-27.3±6.7 [f]	-27 [g]	-27.7±0.8 [h]
	$\Delta_r S°_3$ [J/(mol K)]	-72.1±8.8	-68.6±7.4	-74.5	-67 [e]	-77.8±19.8 [f]	-76.5 [g]	-
	$\Delta_r G°_3$ [kJ/mol]	-4.0±4.7	-4.0±2.5	-5.1	-4.1 [e]	-4.1 [f]	-4.2 [g]	-
R4	$\Delta_r H°_4$ [kJ/mol]	-9.7±3.8	-9.5±3.8	-7.1	-9.16 [e]	-8±1.4 [f]	-8.8±2.7 [i]	-9.5 [j]
	$\Delta_r S°_4$ [J/(mol K)]	-8.6±11.3	-8.0±11.2	-2.0	-7.48 [e]	-4.7±4.2 [f]	-4.1±7.8 [i]	-10±6.6 [k]
	$\Delta_r G°_4$ [kJ/mol]	-7.1±2.5	-7.1±3.8	-6.5	-6.93 [e]	-6.6 [f]	-7.1±11.7 [k]	-6.8 [j]

[a] Vila et al. (1993)[160]; [b] Sharonov et al. (1995)[138]; [c] Gómez et al. (1997)[122]; [d] Françoisse and Thyrion (1991)[139]; [e] Kitchaiya and Datta (1995)[22]; [f] Rihko et al. (1994)[137]; [g] Linnekoski et al. (1999)[136]; [h] Verevkin (2004)[187]; [i] Ferreira and Loureiro (2004)[180]; [j] Syed et al. (2000)[134]; [k] Mao et al. (2008)[128].

$\Delta_f H_j^o$ of TAEE obtained experimentally from equilibrium measurements by Sharonov et al. (1995)[138] was not used in the theoretical calculations because it led to a high deviation between theoretical and experimental values of the thermodynamic reaction changes. Thus, its value of -379.8 kJ/mol for TAEE was refused accordingly with the data of Table 4.4.1, but not the value of -350.8 kJ/mol obtained for $\Delta_f H_j^o$ of ETBE in the same study. It can be observed in Table 4.4.5 that the obtained experimental thermodynamic state functions values are very close or within the range of the experimental ones reported previously for the isolated ether production reactions. Since all four molar enthalpy changes of reactions are negatives, all four chemical reactions are exothermic, as it was already mentioned earlier. A fair agreement is obtained between the experimental and the theoretical data, the larger differences being found in the isoamylenes isomerization reaction, but always within the experimental error.

On the whole, it seems that the negative values $\Delta_r H_i^o$ and $\Delta_r S_i^o$ increase in absolute value when more branched is the olefin for the mentioned etherification reactions using ethanol. Thus, the most ramified the olefin, the highest the exothermicity was observed. This fact agrees with results available in the literature, where a higher enthalpy change in the production of *tert*-hexyl ethyl ether (THEE) from 2-ethyl-1-butene and EtOH than from the etherification of *cis* or *trans*-3-methyl-2-pentene with the same alcohol was reported (Zhang and Datta, 1996)[188]. Furthermore, concerning the etherification of 2M1B and 2M2B, the enthalpy of reaction was lower when the double bond is not terminal (2M2B).

Due to the lack of information, especially for TAEE (and the lack of agreement between sources for both main produced ethers ETBE and TAEE), the experimental data obtained in this work were used to estimate the standard Gibbs free energy and molar enthalpy changes of formation for both ethers. The estimated values of $\Delta_f G_j^o$ for ETBE and TAEE which were found to fit better to the experimental values were -126.3 and -119.2 kJ/mol, respectively. Analogously, the estimated $\Delta_f H_j^o$ for ETBE and TAEE were -351.5 and -372.3 kJ/mol, respectively. The difference between these proposed enthalpies of formation and those estimated by improved

Benson group additive method [189] are less than 1%. Using this data, both theoretical equilibrium constants and thermodynamic state functions are more similar to the experimental values of this study.

Considering that the molar reaction enthalpy change is not constant over the temperature range, it is interesting to see its variation with the temperature. Such values are presented in Table 4.4.6 for all four chemical equilibrium reactions. From the variation of $\Delta_r H_i^o$, it can be said that the reaction enthalpy hardly varies in the assayed temperature range. Therefore, it has been concluded that $\Delta_r H_i^o$ can be considered constant over the temperature range.

Table 4.4.6. Estimated values of the standard molar enthalpy of reaction, $\Delta_r H_i^o$, for reactions R1 to R4, when it is considered as temperature dependent.

T [K]	$\Delta_r H_1^o$ [kJ/mol]	$\Delta_r H_2^o$ [kJ/mol]	$\Delta_r H_3^o$ [kJ/mol]	$\Delta_r H_4^o$ [kJ/mol]
323	-35.8	-34.5	-25.0	-9.64
333	-36.1	-34.9	-25.3	-9.69
343	-36.6	-35.3	-25.7	-9.74
353	-37.1	-35.8	-26.1	-9.80

The values for the ETBE synthesis in Table 4.4.6 are quite close to those determined by Vila et al. (1993)[160] and by Solà et al. (1995)[148], who predicted an enthalpy variation from -34.8 to -35.9 kJ/mol and from -32 to -35.8 kJ/mol, respectively, in the temperature range from 298 to 333K. For TAEE synthesis reactions (R2, R3 and R4) between 323 to 353 K, a fair agreement is also observed with values reported previously in literature by Rihko et al. (1994)[137], who determined a variation of the molar standard enthalpy reaction between -34 and -38 kJ/mol for the TAEE synthesis from 2M1B and between -27 and -31 kJ/mol for TAEE synthesis from 2M2B.

4.4.6 TRIMETHYLPENTES ISOMERIZATION EQUILIBRIUM

The chemical equilibrium of the isomerization reaction between C_8 dimers (TMP-1 and TMP-2) is also known to take place (Karinen et al., 2001)[174]. This double bond isomerization reaction of trimethylpentenes does not follow the usual rule of the chemical equilibrium of alkenes, which typically favors the species with the double bond further from the end of the carbon chain, as is the case of the isoamylenes isomerization reaction [175]. But it follows an opposite trend owing to the size of *tert*-butyl group, which produces a highly crowded part in the molecule of TMP-2 and promotes then the elimination of the proton from the methyl group in the other part of the molecule [174]. In the case of TMP-1, the *tert*-butyl group is further away in the position β to the double bond and the largest substituent is in the *cis* position with hydrogen, which occupies much less space. The chemical equilibrium of TMP-1 and TMP-2 has not been deeply studied in this work, because the conditions of the experiments were not designed for it. However, some aspects will be further deduced from the obtained results.

In addition to reactions R1-R4, the isomerization reaction (R10 in Figure 4.1.1) between both isobutene dimers, TMP-1 and TMP-2, has also been analyzed. The equilibrium constants of this isomerization reaction were calculated at the temperature range 323–353 K under the conditions that favored the C_4 dimers formation, namely $R°_{A/O}$=0.5 and $R°_{C4/C5}$=2. Although C_4 dimers were also produced at $R°_{A/O}$=0.5, $R°_{C4/C5}$=1 and 343–353 K, the low amount at which they were detected made difficult to study the chemical equilibrium in the whole range of the assayed temperatures and with the required accuracy. For the appropriate experiments, the equilibrium

constant of R10 was estimated through the same procedure as described above for the calculations of activity coefficients. Obtained results are presented in Table 4.4.7.

Equilibrium constants from Table 4.4.7 are comparable to those reported in a specific study of the isomerization reaction between both trimethylpentenes, TMP-1 and TMP-2 [174]. K_{x10} ranged from 0.242 to 0.286 and $K_{\gamma 10}$ hardly changed in the temperature range from 1.018 to 1.019, which are very close to the unity, as expected, because only two similar olefins are involved in this reaction. K_{x10} and $K_{\gamma 10}$ increased at increasing temperature. Consequently, it can be said that this isomerization reaction is slightly endothermic.

Table 4.4.7. Experimental values of equilibrium constant for the double bond isomerization reaction of trimethylpentenes (R10).

T [K]	K_{10} (This work)	K_{10} (Karinen et al. 2001)[174]
323	0.246	0.256
333	0.262	0.267
343	0.274	0.277
353	0.292	0.286

The molar enthalpy and entropy changes of reaction ($\Delta_r H^o_{10}$ and $\Delta_r S^o_{10}$) were calculated by assuming that the enthalpy change is constant over the temperature range, by means of Eq. 4.4.4 The case in which $\Delta_r H^o_{10}$ varies with temperature has not been considered because when the temperature range is small or the C^o_{pj} functions of the molecules are close to each other, as is the case between these C_4 dimers, the results are practically the same as for $\Delta_r H^o_{10}$ considered constant over the temperature range. From the experimental data linear regression, the following dependence of the equilibrium constant with temperature was found:

$$\ln K_5 = \left(\frac{-637.06 \pm 101.42}{T} \right) + \left(0.57 \pm 0.30 \right) \qquad (4.4.18)$$

Values of $\Delta_r H^o_{10}$ = (5.3±0.8) kJ/mol and $\Delta_r S^o_{10}$ = (4.7±2.5) J/(mol K) were obtained, with a correlation coefficient R^2 higher than 0.997. Slightly different values were found by Karinen et al. (2001b)[174], who reported experimental values of 3.51 kJ/mol for $\Delta_r H^o_{10}$ and 0.47 J/(mol K) for $\Delta_r S^o_{10}$. However, obtained values in this work are consistent with those determined experimentally by Parks et al. (1936)[190] who found values of $\Delta_r H^o_{10}$ = 4.65 kJ/mol and $\Delta_r S^o_{10}$ = 5.44 J/(mol K). Besides, Turner et al. (1958)[191] published an experimental value of 5.4 for the enthalpy change of reaction, nearby the same value obtained in this work. The similarity between results and the good fit obtained from experimental data for this isomerization reaction between trimethylpentenes enforce the reliability of the present study.

4.4.7 PARTIAL CONCLUSIONS

The thermodynamics of the involved reactions have been proven to be independent of the simultaneous process when activities are used for calculations. All four main chemical reactions in the ETBE and TAEE formation network have been found to be reversible and exothermic. Consequently, the amount of produced ethers at equilibrium decreases when temperature increases. As expected, no significant effect on the equilibrium state has been observed when using different catalysts, namely A-35, A-15 and CT-275.

The exothermicity of the etherification reactions (R1-R3) is higher than that of IA isomerization reaction (R4). ETBE formation (R1) was found to be the most exothermic reaction, followed by the TAEE formation from 2M1B (R2) and from 2M2B (R3). It can be explained by the stability of alkene involved in each reaction. Consequently, the higher the olefin size, the lower the equilibrium constant of the etherification reactions. For reactions R1, R2, R3 and R4, molar standard enthalpy changes of -36.3±7.2, -35.1±6.0, -25.5±3.0 and -9.7±3.8 kJ/mol were determined, respectively. Therefore, the more branched the olefin, the higher the exothermicity. The chemical equilibrium between the two IB dimers, TMP-1 and TMP-2, was also studied and a molar enthalpy change of reaction value of 5.3±0.8 kJ/mol was obtained.

There is an excellent agreement between the obtained molar standard enthalpies, entropies and Gibbs free energy changes of reactions with those quoted in open literature for the isolated ETBE and TAEE formation reactions. Nevertheless, from the small dispersion of the values, especially in theoretical and experimental equilibrium constants, more experimental work is needed in order to ascertain more reliable and precise data. Under this purpose, the standard molar enthalpies of formation for ETBE and TAEE were estimated from experimental data obtaining values of -351.5 and -372.3 kJ/mol, respectively.

4.4.8 CHAPTER NOTATION

a, b, c, d	temperature dependence parameters of thermodynamic functions
a_j, b_j, c_j, d_j	temperature dependence coefficients of heat capacity expression for compound j
a'_j	activity of compound j
C_{pj}^o	molar heat capacity of compound j in the liquid phase [J mol^{-1} K^{-1}]
$\Delta_f G_j^o$	liquid-phase standard molar free energy change of formation of compound j [kJ mol^{-1}]
$\Delta_f H_j^o$	liquid-phase standard molar enthalpy change of formation of compound j [kJ mol^{-1}]
$\Delta_r G_i^o$	standard Gibbs free energy change of reaction i in the liquid phase [kJ mol^{-1}]
$\Delta_r H_i^o$	standard molar enthalpy change of reaction i in the liquid phase [kJ mol^{-1}]
$\Delta_r S_i^o$	standard molar entropy change of reaction i in the liquid phase [J K^{-1} mol^{-1}]
I_H	van't Hoff integration constant [dimensionless]
I_K	Kirchoff integration constant [J mol^{-1}]
K_i	thermodynamic equilibrium constant of reaction i [dimensionless]
K_{xi}	equilibrium constant of reaction i based on molar fractions [dimensionless]
$K_{\gamma i}$	activity coefficients ratio of reaction i [dimensionless]
$K_{\Gamma i}$	Poynting correction factor of reaction i [dimensionless]
n	number of mole [mol]
P	pressure [bar]
R	gas constant, 8.31447 [J mol^{-1} K^{-1}]
$R°_{A/O}$	initial molar ratio alcohol to olefins
$R°_{C4/C5}$	initial molar ratio between C_4 and C_5 iso-olefins
S_j^o	absolute entropy of compound j [J K^{-1} mol^{-1}]
T	temperature [K]
t	time [min]
V_j	molar volume of compound j [L mol^{-1}]
W_{cat}	mass of dry catalyst [g]
X_j	relative conversion of reactant j
x_j	molar fraction of compound j

Greek letters

γ_j	activity coefficient of compound *j*
ν_{ji}	stoichiometric coefficient of compound *j* in reaction *i*

4.5 EFFECT OF WATER

An extended and revised version of this chapter was published as:

R. Soto, C. Fité, E. Ramírez, J. Tejero, F. Cunill. Effect of water addition on the simultaneous liquid-phase etherification of isobutene and isoamylenes with ethanol over Amberlyst™35. *Catal. Today.* **2015**; 256 (2): 336–346. http://dx.doi.org/10.1016/j.cattod.2014.12.031

4.5.1 INTRODUCTION

The use of bioethanol as reactant entails a potential source of water into etherification reactors, hence it is worthy to study the effect of water on the product distribution and on the activity performance of the catalyst, through the addition of known amounts of water to the initial reactant mixture. This effect has already been studied for the isolated ETBE and TAEE systems over acidic IER [37,49,91,121,162,192], and it was concluded that water affects the catalytic activity and selectivity towards desirable products, because water competes for the catalyst active sites with the main reactants, which reduces the number of available active sites for ether formation. Since water is highly polar, it promotes the swelling of catalyst, what improves the accessibility of reactants to inner active sites. Moreover, water can solvate the sulfonic group protons, what destroys the hydrogen bridge structure formed between them and diminishes their acid strength. Therefore, water presence induces lower reaction rates and favors side reactions of hydration of olefins. The aim of this work is to assess the influence of the initial water content on chemical equilibria, on byproducts formation and on reaction rates involved in the simultaneous etherification of IB and IA with EtOH over Amberlyst™35.

4.5.2 EXPERIMENTAL AND CALCULATIONS

The stirred tank batch reactor described in *Section 3.2.1* was used to carry out the experimental work. In the initial reactant mixture, the molar ratio alcohol to olefins ($R°_{A/O}$) and the molar ratio IB/IA ($R°_{C4/C5}$) were 0.5 and 1, respectively, for all the experimental runs. The working temperature was 353 K. These particular conditions were chosen because they favor the side reactions through which tertiary alcohols (TBA and TAA) and dimers are formed, in order to observe how water presence influences etherification, dimerization and hydration of olefins at the same time. Amounts of 0, 0.25, 0.5, 0.75 and 1 wt.% of water with respect to the total initial mixture were added. A dried catalyst mass of 4 g of A-35 was used in the commercial bead size distribution. Experiments lasted enough time to reach chemical equilibrium (360 min) and to assess the differences caused by the addition of water. Etherification rates, conversion, selectivity and yield at any instant were calculated as described in *Section 3.6.*

4.5.3 EFFECT OF WATER ON CHEMICAL EQUILIBRIA

As described in *Section 4.4*, reversible reactions reached a pseudo-equilibrium state in all the runs whereas dimerizations proceeded very slowly. This enables estimation of the equilibrium constants values for the main reactions (K_i), see Table 4.5.1. Experimental equilibrium constants were independent of the initial amount of water, as expected. This result is consistent with those

found in the syntheses of MTBE and ETBE in the presence of water [37]. Within the limits of the experimental error, estimated values are in good agreement with those determined at the same temperature in *Section 4.4*, where the initial content of water remained constant. Although water presence does not affect K_i values, it does affect the mixture composition at equilibrium since water competes with alcohols for the olefins.

Table 4.5.1. Equilibrium constants for etherification reactions R1-R4 at 353 K in the presence of different amounts of water. Errors of the mean values refer to 95% probability level.

Reaction	Water initial content [wt.%]					Average of values in *Section 4.4*
	0	0.25	0.5	0.75	1	
R1	13.8	13.5	13.1	13.9	12.9 ± 0.6	13.1 ± 1.2
R2	11.4	11.2	10.6	11.3	10.8 ± 0.5	9.6 ± 0.8
R3	1.1	1.1	1.0	1.1	1.1 ± 0.1	1.0 ± 0.1
R4	9.7	9.9	10.4	10.6	9.5 ± 0.5	9.5 ± 0.5

4.5.4 EFFECT OF WATER ON TERTIARY ALCOHOLS FORMATION

TBA and TAA formation (reactions R5-R7 in Fig. 4.1.1) was dependent on the initial amount of water and their concentration varied throughout the course of the experiments. TBA production was slightly faster than that of TAA. Hence, it can be concluded that IB is more reactive with water than IA. As mentioned, TBA and TAA reached chemical equilibria swiftly. It can be clearly seen in Fig. 4.5.1a (at t = 45 min) where the mole evolution of TBA is shown for the different runs. When the initial water contents were the highest, TBA production reached a maximum and afterwards decreased. This behavior is explained because adsorbed water reacts readily with the IB at the beginning of the experiment and then, the reverse reaction proceeded because IB was being consumed by competitive etherification and dimerization. This result is consistent with those found in a study on the formation of isopropyl *tert*-butyl ether in which several equilibrium reactions proceeded simultaneously [87]. The same explanation is acceptable for the case of TAA, where the performance was analogous to that observed for TBA in Fig. 4.5.1a but considering that TAA was always formed in less extent than TBA.

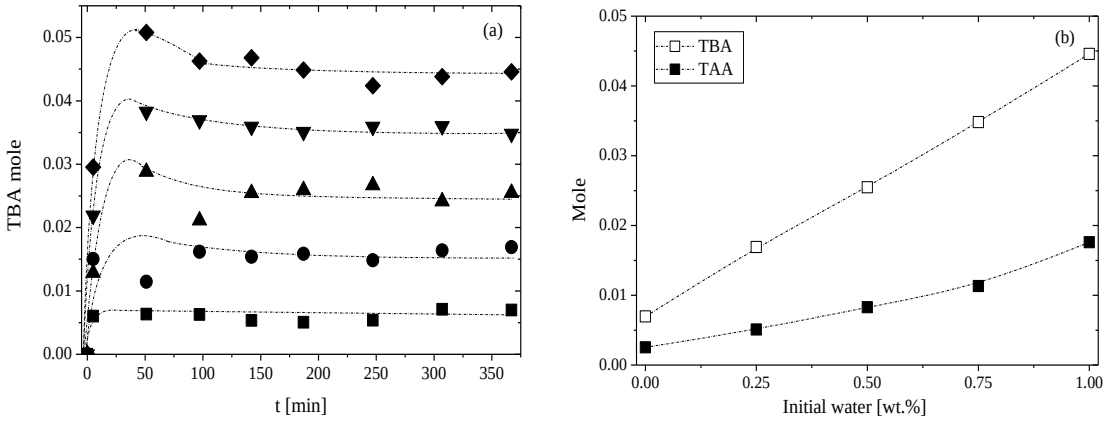

Figure 4.5.1. (a) Moles of TBA formed vs. reaction time at different initial water amounts. Amount of water: (■) 0 wt.%; (●) 0.25 wt.%; (▲) 0.5 wt.%; (▼) 0.75 wt.%; (◆) 1 wt.%. (b) Effect of initial water content on TBA and TAA formation (t = 360 min).

TBA was formed preferably and readily compared to TAA, in a molar ratio TBA to TAA of about 3. Thus it can be concluded that chemical equilibrium is more favorable to TBA

formation than to TAA. This conclusion is in agreement with the observed performance between olefins and EtOH in which ETBE production is favored thermodynamically rather than TAEE one. As can be seen in Fig. 4.5.1b, the increase of initial water content promoted both tertiary alcohols formation and, consequently, their final content increased. The small amount of tertiary alcohols formed in the absence of added water was a consequence of the remaining water within the resin after the pretreatment (tightly hydrogen-bonded to the $–SO_3H$ groups) and of the water content in EtOH used as reactant (< 0.02 wt.%). With the addition of 1 wt.% of water, the total number of moles of TBA and TAA increased significantly, from 0.01 to 0.06 (equivalent to a total tertiary alcohols molar fraction of 0.037).

4.5.5 EFFECT OF WATER FORMATION ON DIMERIZATION PRODUCTS

Since olefins are in stoichiometric excess ($R°_{A/O}$=0.5) and the working temperature is relatively high (353 K), irreversible formation of C_4 (R9 in Fig. 4.1.1) and C_5 dimers (R12 in Fig. 4.1.1) and thereof C_{4-5} codimers (R11 in Fig. 4.1.1) also takes place. It should be highlighted that obtained dimerization products could also be suitable gasoline additives by direct blending or after subsequent hydrogenation [29], which makes the study of these side reactions interesting. Dimerization and codimerization took place so slowly that the reversible reactions affected by the olefins consumption can be considered to be at pseudo-equilibrium state.

From the final reaction mixture, a sufficient amount of dimers was concentrated after successive distillations. All the C_4, some C_{4-5} and C_5 dimers have been identified by mass spectrometry. The most troublesome compounds to identify were C_{4-5} codimers and C_5 dimers due to the low amount detected and the wide variety of compounds formed. Only TMP-1 and TMP-2 were detected as C_4 dimers. The main C_{4-5} codimers and C_5 dimers that could be identified from the isomeric mixture and their estimated AKI indexes by means of the group contribution method described in Albahri (2003) [193] are depicted in Figs. 4.5.2 and 4.5.3, respectively. Concerning the detected C_5 dimers, more than 60% GC were branched hexenes. These results for C_5 dimers are in agreement with those found in studies on the IA dimerization over acidic ion-exchange resins [13,28]. Globally, nearby the 80% of the dimerization products could be identified by GC/MS. Neither trimers nor higher oligomers were detected in the present study, in agreement with literature data [31,37,49,121,125].

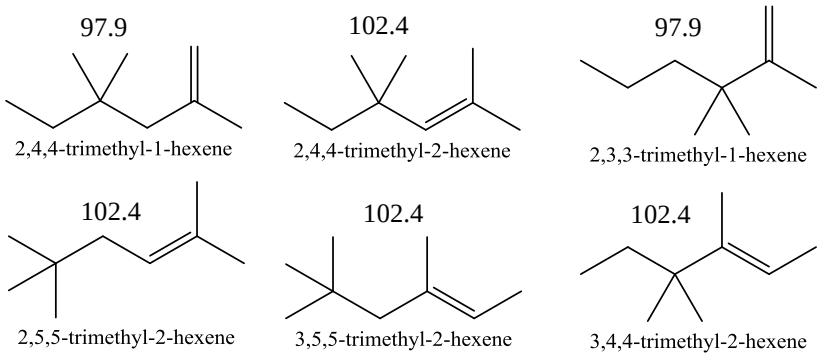

Figure 4.5.2. Identified C_{4-5} codimers by MS. Numbers are referred to the (RON+MON)/2 of molecules. Estimated as described in [193].

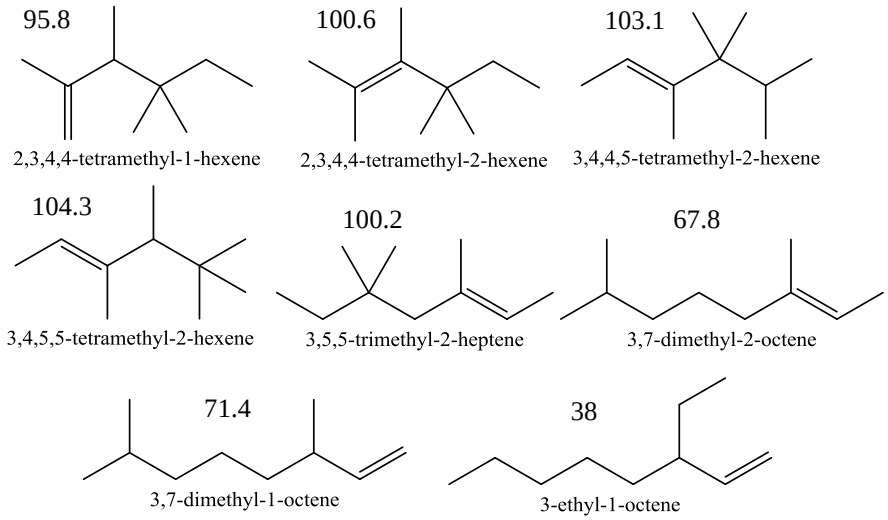

Figure 4.5.3. Identified C_5 dimers by MS. Numbers are referred to the (RON+MON)/2 of molecules. Estimated as described in [193].

Water was shown to influence dimerization reactions. In contrast to tertiary alcohols, increasing the initial water content decreased dimers formation with respect to the amount and reaction rate. In order to delve in this inhibitory effect over dimerization reactions, it is expedient to assess how the global amount of dimers varied along the experiments. Fig. 4.5.4a displays the mole profile evolution of C_4 dimers (TMP-1 and TMP-2 lumped together). The amount of dimers increased almost linearly with time in all the cases. It can be seen that water presence induced a strong inhibition over dimers formation. For $C_{4\text{-}5}$ codimers and C_5 dimers, the trends were very similar. This inhibitory effect was difficult to observe for C_5 dimers due to the low amount detected (Fig. 4.5.4b). The highest molar fraction of dimerization products (addition of C_4, $C_{4\text{-}5}$ and C_5) after 360 min was 0.035 and the lowest 0.003. The observed depletion in dimerization rates is a result of the competition between water, olefins and EtOH for the catalytic active sites, what hampers the reactions in which water is not a reactant, such as dimerization and etherification. Because of the preferential adsorption of H_2O and EtOH owing to their higher polarity, olefins are consumed to form mainly tertiary alcohols and ethers, especially at the beginning of the runs.

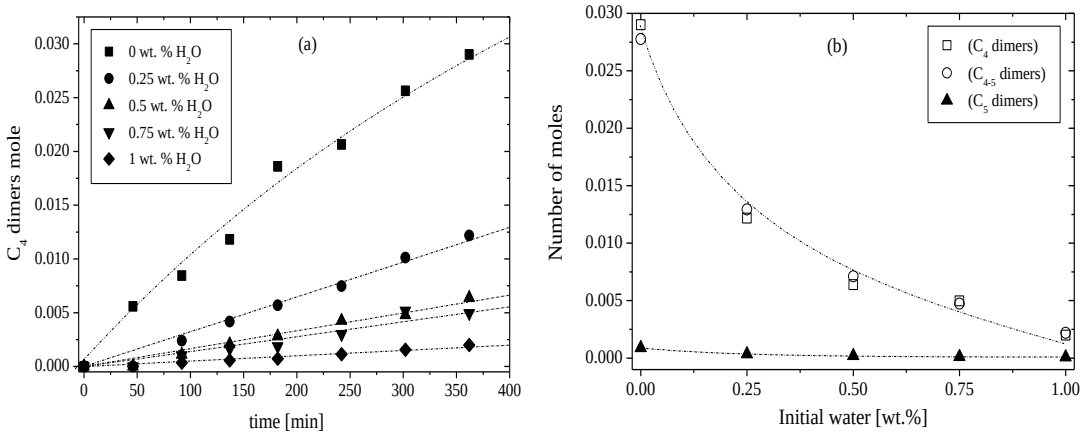

Figure 4.5.4. (a) Moles of IB dimers formed vs. reaction time at different initial water amounts. (b) Mole of dimerization products vs. initial water (wt.%), t = 360 min.

Focusing on dimers formation, the fact that the mole of C_4 dimers and $C_{4\text{-}5}$ codimers formed were very similar to each other and notably higher than those of C_5 dimers, suggests a competition between olefins for the active sites. Compared to IA, IB seems to adsorb preferentially on the active sites and consequently, its participation in dimerization reactions is higher. These results are in agreement with those obtained in the study of the adsorption equilibrium of IA, IB, EtOH and water [65]. IB and IA adsorption equilibrium constants values are quite different, especially at low temperatures. For instance, IB adsorption equilibrium constant over Amberlyst™15 is approximately five times higher than that of IA (2M1B and 2M2B) at 323 K, whereas at 373 K is only two times higher. It was also found that adsorption equilibrium constant of EtOH and MeOH are two orders of magnitude greater than those of IB and IA, which would explain the preferential initial formation of ethers over dimerization products. Nevertheless, water is known to have a higher affinity than EtOH to be adsorbed on acid sites of ion-exchange resins [166,192], which explains the quick initial formation of tertiary alcohols. The adsorption equilibrium constant of water is more than 3 times higher than that of EtOH [166]. Water, as the stronger nucleophile, is preferred in the competition for the active sites. The stronger nucleophilicity of water can be seen by comparison of the dielectric coefficients of water (78.5) and EtOH (24) [91].

4.5.6 EFFECT OF WATER ON EQUILIBRIUM CONVERSION, SELECTIVITY AND YIELD

Water affects both reactants conversion and selectivity toward ethers (main products). Fig. 4.5.5 plots reactants conversion after 360 min vs. the initial water content. It can be seen that the added amounts of water did not affect significantly the final reactants conversion by a compensating effect among the involved reactions. This is because water presence hindered ethers and dimers production while it enhanced tertiary alcohols formation, thus the obtained olefins conversion, specifically for IB, appeared to be approximately constant. Despite competitive adsorption between water and EtOH, X_{EtOH} showed to be quasi-independent of the initial water content with an almost constant value. This is explained by the stoichiometry of the focused etherification reactions, since EtOH is the limiting reactant at $R°_{A/O}$= 0.5. Globally, EtOH showed the highest final conversion (90%), followed by IB (78%) and IA (22%).

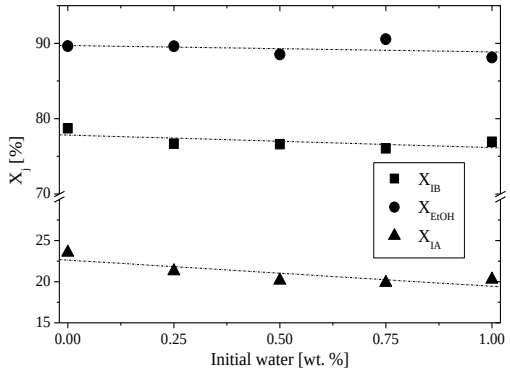

Figure 4.5.5. Reactants conversion vs. initially added water (wt.%) at t = 360 min.

In reaction systems in which several products can be formed from the same reactants mixture through a complex reaction network, selectivity is a metric of utmost importance. Figs. 4.5.6a and 4.5.6b plot the olefins selectivity at t = 360 min. S_{IB}^{TBA} and S_{IA}^{TAA} increased linearly with the initial water concentration, S_{IA}^{TAA} being slightly higher than S_{IB}^{TBA}. On the contrary, olefins selectivity toward dimerization products decreased on increasing the initial water content. Both

S_{IB}^{ETBE} and S_{IA}^{TAEE} presented a smooth maximum between 0.25 and 0.5 wt.% of initial water concentration as a consequence of the reactions shift. The inhibitory effect was more pronounced over dimerization than over etherification reactions and therefore, olefins selectivity to ethers rose from 0 to 0.5 wt.% of initial water. If the conditions of the experiments did not favor dimers formation in the absence of water ($R°_{A/O}$>1), the olefins selectivity to ethers would monotonically decrease when more water is initially present [37].

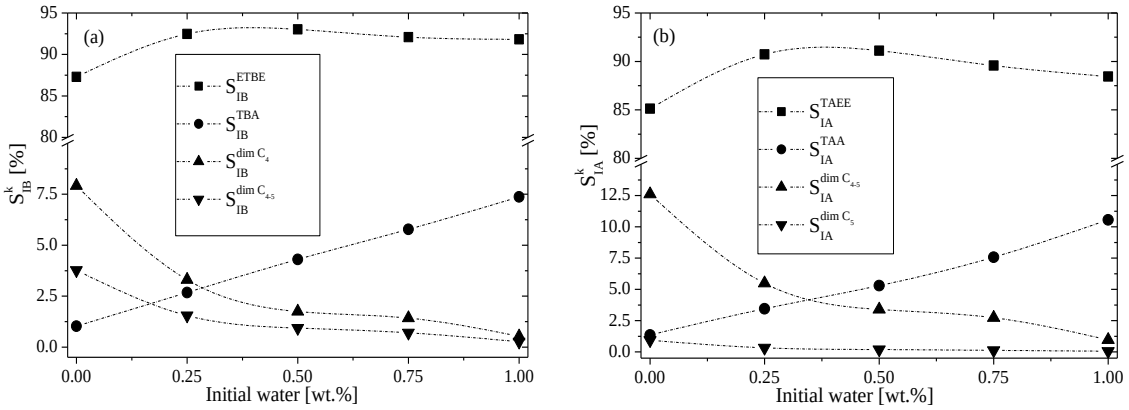

Figure 4.5.6. IB (a) and IA (b) selectivity toward products at t = 360 min.

Olefins yield to the corresponding products are depicted in Figs. 4.5.7a and 4.5.7b. Yields are directly related to conversion and selectivity (Eq. 3.3). Y_{IB}^{ETBE} remained almost constant, being slightly lower in the absence of water due to IB dimers formation. In the case of Y_{IA}^{TAEE}, that effect was not observed because IA consumption to form $C_{4\text{-}5}$ codimers and C_5 dimers was far lower compared to that of IB to form C_4 dimers and $C_{4\text{-}5}$ codimers. Y_{IA}^{TAEE} decreased on increasing the initial amount of water. Olefins yield to tertiary alcohols and dimers formation followed trends analogous to those observed for the selectivity. The average rise of the olefins yields toward tertiary alcohols in presence of 1 wt.% of initial water led to approximately 7 fold that observed in the absence of water.

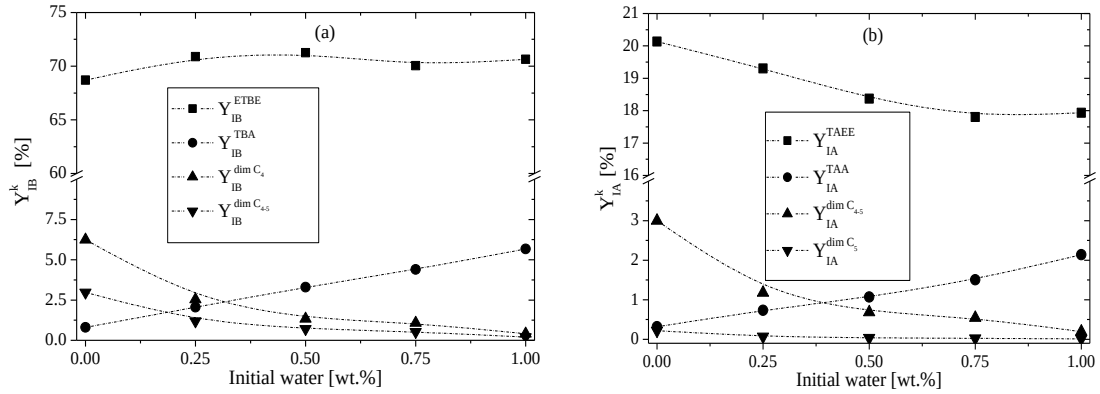

Figure 4.5.7. IB (a) and IA (b) yield toward products at t = 360 min.

The evolution of the olefins selectivity toward ethers is shown Figs. 4.5.8a and 4.5.8b. Observed trends for S_{IB}^{ETBE} and S_{IA}^{TAEE} were very similar along the experiments course and both decreased monotonically in the absence of water. The main by-products under this particular condition were dimers and since dimers content increased slowly and linearly with time, olefins selectivity to ethers followed an opposite trend. As more water was initially added, more tertiary

alcohols were quickly formed, thus S_{IB}^{ETBE} and S_{IA}^{TAEE} were initially lower (the first 50 min). In both cases, the selectivity showed a maximum between 50 and 120 min in the presence of water and afterwards, it decreased. It is related to the instant at which the amount of dimers became so significant that the olefins selectivity toward ethers decreased by irreversible consumption of IB and IA in dimerization reactions. It is observed that the maximum value of selectivity to ethers is reduced and delayed by increasing the initial water content.

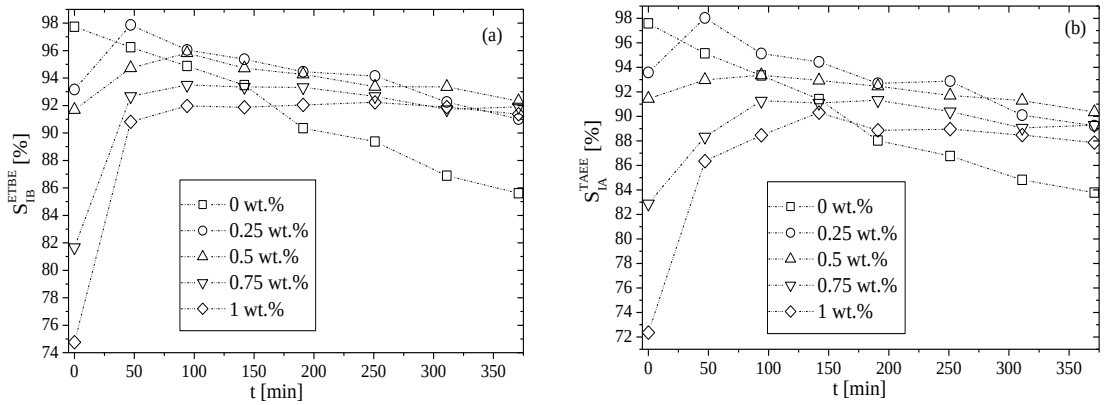

Figure 4.5.8. Dependence of the evolution of S_{IB}^{ETBE} (a) and S_{IA}^{TAEE} (b) on the initial water content. Each series correspond to the different mass fractions of initially added water.

Regarding products from ethanol, Fig. 4.5.9 displays the effect of the initial water content on EtOH selectivity and yield toward ETBE and TAEE. S_{EtOH}^{ETBE} and Y_{EtOH}^{ETBE} barely increased as more water was present in the initial reactant mixture, whereas S_{EtOH}^{TAEE} and Y_{EtOH}^{TAEE} followed an opposite trend. This is because in the presence of water, the foremost inhibited reactions are the C_4 and $C_{4\text{-}5}$ dimers formation, consequently a slightly higher amount of IB is available in the bulk phase to participate in ETBE formation. Since EtOH is the limiting reactant at $R°_{A/O}$=0.5, reacted moles of EtOH were very similar in all the runs and therefore its average conversion remained virtually constant, as shown in Fig. 4.5.5. It also explains the observed trends for EtOH yield toward ethers, since yield is obtained as the product of conversion and selectivity.

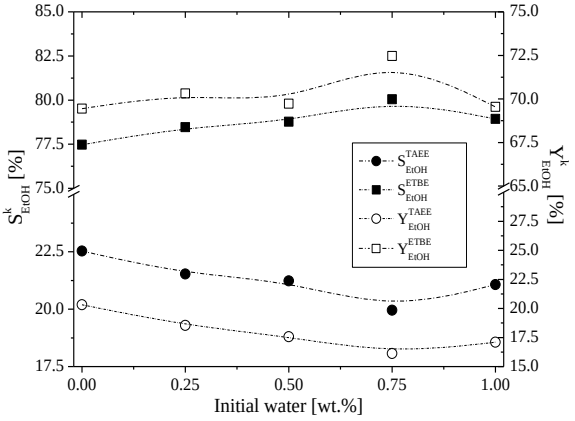

Figure 4.5.9. Ethanol selectivity (solid symbols, left Y axis) and yield (hollow symbols, right Y axis) toward products vs. the initial amount of water (wt.%) at t = 360 min.

4.5.7 EFFECT OF WATER ON CATALYTIC ACTIVITY

The inhibition of etherification reactions is stated as a reduction in the etherification rates, as occurred for dimerization reactions. Fig. 4.5.10a plots the initial reaction rates of ETBE and TAEE formation (r^0_{ETBE} and r^0_{TAEE}) versus the initial water concentration. As can be observed, r^0_{ETBE} and r^0_{TAEE} decreased substantially with the initial amount of water. For the purpose of assessing the evolution of experimental reaction rates, Fig. 4.5.10b plots the obtained r_{ETBE} and

r_{TAEE} versus the run time (in absence and in presence of a 1 wt.%) up to 100 min. For longer times, the plotted reaction rates become very low since the involved reactions almost reached the pseudo-equilibrium state. The initial presence of 1 wt.% of water produced a drastical reduction in both ETBE and TAEE formation rates. It should be noticed that reaction rate values presented in Fig. 4.5.10 are not probably intrinsic kinetic data due to the large size of the used resin particles. Accordingly, measured reaction rates could be highly influenced by internal diffusion of reactants and/or reaction products. This does not provide the intrinsic reaction rates, but rather the performance of the reactor producing simultaneously ETBE and TAEE in the presence of water.

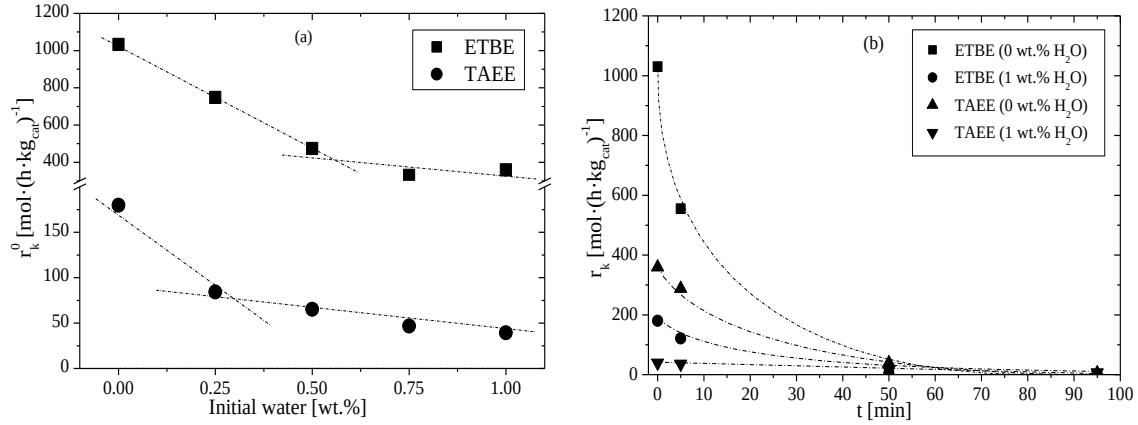

Figure 4.5.10. (a) Estimated r^0_{ETBE} and r^0_{TAEE} as a function of the initial water content. (b) Evolution of the estimated r_{ETBE} and r_{TAEE} at 0 and 1wt.% of initial water concentration.

A change in the slopes of the curves depicted in Fig 4.5.10a is observed. This change takes place at initial water content of about 0.55 and 0.35 wt.% for ETBE and TAEE, respectively. This water content corresponds to a value close to two molecules of water per $–SO_3H$ group for both ETBE and TAEE. According to the literature [103,106], two or more water molecules per sulfonic group produces the proton dissociation and induces a change in the reaction mechanism. The observed change in the slopes of r^0_k indicates that a change in the reaction mechanism must be taking place. At industrial scale, the ratio of two molecules of water per sulfonic group would be attained using EtOH containing 1.4 vol.% of water, which is far lower of the average water content of dry bioethanol [108], even considering the synthesis under stoichiometric conditions ($R°_{A/O}$=1). Thus, bioethanol could be used as raw material for the catalyst to work within the limits of general acid catalysis, with higher reaction rates, what reduces the needed size of the industrial reaction unit.

Figs. 4.5.11a and 4.5.11b depict how water affected production of both ETBE and TAEE until they reached the pseudo-equilibrium state. In all the cases ETBE production reached chemical equilibrium faster than TAEE what is consistent with the results found in the literature [123,131]. The inhibitory effect was more noticeable for TAEE formation, where the addition of 1 wt.% of water induced an important delay (almost 3 fold that in the absence of water) to reach equilibrium.

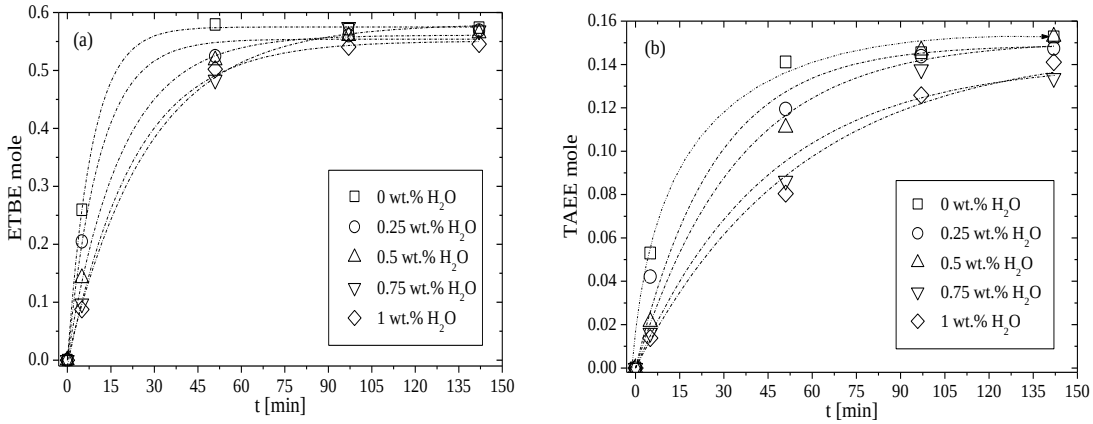

Figure 4.5.11. Mole evolution of ETBE (a) and TAEE (b) for different initial water content.

The depletion of etherification rates (inhibition) caused by water presence is attributed to the disruption of the $-SO_3H$ groups network. In addition, another influencing factor is the higher acidity of water compared to EtOH, which can produce a more basic solvated proton of lower activity [91]. Moreover, another important factor that can affect etherification rates is the accessibility. Water adsorption on the dry resin promotes swelling and therefore enhances accessibility toward inner active sites (mostly located in the resin gel phase), which should increase the reaction rates. In our reaction medium, the polarity decreased along the experiments due to the consumption of polar components, namely alcohol and water itself [195], and in the last stages of the runs (less polar conditions) significant changes in the reaction mechanism and selectivity should occur [80]. Therefore, both polarity and accessibility are expected to decrease throughout the runs, however, both are expected to increase with the initial addition of water and the EtOH used as reactant. As observed in Fig. 4.5.10a, r^0_{TAEE} and r^0_{ETBE} decreased on increasing the initial amount of water, thus it can be concluded that the inhibitory effect of water over etherification is more noticeable than the initial enhancement of accessibility. A possible reason for this phenomenon is the chemical nature of the catalyst (A-35). Since it is a macroreticular ion-exchange resin with a relatively high crosslinking degree, it could be that the swelling of the catalyst caused by the polar media was not significant due to the low flexibility of the polymeric matrix. Nevertheless, it has been stated that for relatively small molecules, such as IB, MeOH or methyl *tert*-butyl ether, the proportion of inaccessible active centers is negligible, even in the least swollen resins (the most cross-linked) [80]. As a consequence, the expected accessibility enhancement was not noticeable in the present study because the initial accessibility of the resin actives sites was very similar for all the experimental runs.

The relative difference of catalytic activity a_i for reaction i can be defined by Eq. 4.5.1, as the ratio between the initial reaction rate when a specific amount of water was added and the initial reaction rate in the absence of water.

$$a_i = \frac{r^0_{i,[H_2O]}}{r^0_{i,[H_2O]=0}} \qquad (4.5.1)$$

The value of a_{ETBE} in the presence of 1 wt.% of water is 0.36 and a_{TAEE} is 0.25. Thus, it can be concluded that the inhibitory effect of water is more significant for TAEE than for ETBE. It is also noteworthy that r^0_{ETBE} was always higher than r^0_{TAEE} both in absence and in presence of water (almost 6 fold). These rate differences are larger than those reported in open literature for isolated ETBE and TAEE syntheses. A possible explanation is due to the lower polarity of the

present reaction medium ($R°_{A/O}$=0.5) that makes the polarity change more noticeable as water is added. In these less polar conditions, the network of hydrogen bonds in which sulfonic groups are linked is mostly undisturbed and the undissociated groups are the actual catalytic species, thus the reaction mechanism is mostly concerted and quicker. This hypothesis is consistent with the results obtained focusing the effect of $R°_{A/O}$ on the kinetics of MTBE liquid-phase synthesis [195]. Both internal diffusion and competitive adsorption of IB and IA for the active sites also affect reaction rates. The easier diffusion and the preferential adsorption of IB with respect to IA due to its lower molecular size and larger adsorption equilibrium constant contribute to increase the difference between r^0_{ETBE} and r^0_{TAEE} found in this work, where both ethers are produced simultaneously.

4.5.8 PARTIAL CONCLUSIONS

Initial water presence does not affect the chemical equilibrium constants of involved reactions but it does affect the final composition. Increasing initial water concentration promotes both TBA and TAA formation. Furthermore, water drastically affects ethers formation: a 1wt.% of initial water leads to S^{TBA}_{IB} and S^{TAA}_{IA} of 7.6 % and 10.7%, respectively. The ensuing olefins yield toward tertiary alcohols when 1 wt.% of water is present is above 7 fold their values in absence of water.

The most important effects of water presence on the present system are the competition with reactants for the active sites and the inhibition of etherification and dimerization reactions. The effect of water over accessibility is not discernible under the experimental conditions. The inhibitory effect is more noticeable over dimerization reactions than over etherification ones. This fact is in reasonable agreement with the reported values of the adsorption equilibrium constants for the used chemical reactants over similar catalysts, which decreases in the order; water>ethanol>isobutene>isoamylenes. The observed drop in the catalytic activity for the formation reactions of ETBE and TAEE, when 1 wt.% of water was initially added, is 64% and 75% of their value in absence of water, respectively. Thus, TAEE synthesis is more affected by the presence of water than ETBE one.

Under experimental conditions, the sulfonic groups could be dissociated when more than 0.45 wt.% of water is added and the catalysis could be regarded as specific acid catalysis. Consequently, a change in kinetic mechanism should be expected. This fact can explain the depletion of r^0_k values observed for etherification reactions increasing the amount of water. As the average water content in dry bioethanol is far lower than this limit value, dry bioethanol could be used as reactant in the performed simultaneous synthesis to avoid sulfonic groups dissociation —working within the limits of general acid catalysis—. In fact, small amounts of water in the alcoholic feed could help to prevent the formation of oligomerization products in possible hot-spots of the catalytic reactor.

The small amount of tertiary alcohols formed when low amount of water (< 0.45 wt.%) is present is acceptable as a shortcoming, since both TBA and TAA are useful additives to gasoline and their use would produce some environmental benefits if they were blended with ethers (e.g. less aldehyde emissions). Finally, it is advisable to carry out experiments in a wider range of initial water content to ascertain the possible changes in kinetic mechanisms of ethers formation.

4.5.9 CHAPTER NOTATION

a_i	relative difference of catalytic activity for reaction *i* [dimensionless]
d_b	average particle diameter [mm]
K_i	thermodynamic equilibrium constant of reaction *i* [dimensionless]
$R°_{A/O}$	initial molar ratio alcohol to olefins
$R°_{C4/C5}$	initial molar ratio isobutene/isoamylenes
$r_i^0{}_{[H2O]}$	initial rate of reaction *i* in presence of initial water [$mol \cdot min^{-1} \cdot g_{cat}^{-1}$]
$r_i^0{}_{[H2O]=0}$	initial rate of reaction *i* in absence of initial water [$mol \cdot min^{-1} \cdot g_{cat}^{-1}$]
r_k	reaction rate of formation of product *k*
r_k^0	initial reaction rate of formation of product *k*
S_j^k	selectivity of reactant *j* toward product *k*
t	run time [min]
T	temperature [K]
T_{max}	maximum working temperature of catalyst [K]
X_j	conversion of reactant *j*
Y_j^k	yield of reactant *j* toward product *k*

Subscripts

i	reaction
j	reactant
k	product formed

Superscripts

0	initial (at t=0)

4.6 CATALYSTS SCREENING

An extended and revised version of this chapter is being prepared for submission to *Catal. Sci. Technol.* journal as: *R. Soto, C. Fité, E. Ramírez, M. Iborra and J. Tejero*. Catalytic activity dependence on morphological properties of acidic ion-exchange resins for the simultaneous ETBE and TAEE liquid-phase synthesis.

4.6.1 INTRODUCTION

Apart from the obvious relation with sulfonic groups concentration, the catalytic activity of a resin depends upon a combination of its morphological properties, which can vary substantially with the composition of the reaction medium. Catalytic activity is directly related to accessibility or ease of compounds to penetrate into the gel-phase and macroporous channels of the resin matrix. Accessibility to the inner resin active sites depends therefore on the nature of the resin backbone (polymeric matrix), and also on the reaction media in which the resin is immersed. Additionally, the combination of properties that influence the catalytic activity differ with the reaction system considered. In this study, a screening of fifteen sulfonic IER is performed for the simultaneous liquid-phase syntheses of ETBE and TAEE from pure olefins and EtOH. The main aim is to find out relationships between the resin physicochemical properties and the catalytic activity, as well as to study the accessibility of involved compounds.

4.6.2 EXPERIMENTAL AND CALCULATIONS

The stirred tank batch reactor described in *Section 3.2.1* was used to carry out the experimental work. Two different type of experiments were performed, volumetric swelling measurements and catalytic activity experiments. The following fifteen acidic IER were tested because they have a varied array of morphological properties: Amberlyst™15 (A-15), Amberlyst™16 (A-16), Amberlyst™35 (A-35), Amberlyst™36 (A-36), Amberlyst™39 (A-39), Amberlyst™40 (A-40), Amberlyst™45 (A-45), Amberlyst™46 (A-46), Amberlyst™48 (A-48), Amberlyst™DT (A-DT), Purolite®CT-124 (CT-124), Purolite®CT-175 (CT-175), Purolite®CT-275 (CT-275), Purolite®CT-482 (CT-482) and Purolite®MN-500 (MN-500). All IER were pretreated before the experiments in order to remove as much as possible the initial moisture following the same procedure described in *Section 3.1.3*. The maximum operating temperature was considered for choosing the conditions of the catalytic activity tests in order to preserve the thermal stability of the catalysts.

4.6.2.1 Volumetric swelling measurements

The degree of swelling of a resin immersed in different solvents can be quantified by means of the swelling ratio (*SR*), which can be defined as the ratio of the volume of swollen resin, in a particular solvent, to the volume of dry resin [77]. Graduated glass cylinders of 50 mL were used in these measurements conducted at room temperature (293 K). 35 mL of liquid were added to 10 mL of dried resin and after 24 h, *SR* was

determined for each combination of resin and solvent from the final volume of swollen polymer. The IER bead size distributions used for these runs were as commercially shipped.

4.6.2.2 Catalytic activity experiments

The selected operating conditions were close to those of industrial etherification processes: temperature of 335 K, and initial molar ratios of alcohol to olefins ($R°_{A/O}$) and between olefins ($R°_{C4/C5}$) equal to 1.1 and 1, respectively. The stirring speed was set to 600 rpm and the particle size range used was 0.25-0.4 mm in order to avoid the effects of external and internal mass resistances, respectively, as it will be further discussed in *Section 4.7*. The main physical properties of the catalyst used can be found in Table 3.1. The catalyst load (CL) varied from 0.5 to 2 g, depending on the different expected catalytic activity.

4.6.3 CHARACTERIZATION OF ION-EXCHANGE RESINS

As it was shown in Table 3.1, tested IER are all macroreticular, except CT-124, which is microporous, a full gel-type resin without permanent meso or macropores. A-35, A-36, A-40, A-48 and CT-275 are oversulfonated resins. A-15, A-16, A-39, CT-124 and CT-175 are conventionally sulfonated resins. A-45, A-DT and CT-482 are chlorinated and sulfonated resins. A-46 and MN-500 are surface sulfonated resins [196]. The limit of conventional sulfonation of styrenic resins is one sulfonic group per benzene ring [80], what approximately equates to an acid capacity of 4.5 eq $H^+ \cdot kg^{-1}$ in a resin with medium crosslinking degree [75]. In resins with such an acid capacity, the distribution of acid sites within the catalyst particle is nearly homogeneous, however, for resins with lower value of acid capacity, sulfonation is restricted to the outer layers since sulfonation proceeds from the external to internal layers of the particle [75], as seen in *Section 1.5.3*. A-39 is the resin with the lowest crosslinking degree of the macroporous resins evaluated presenting therefore a more flexible structure. On the contrary, MN-500 is a hyper-crosslinked resin and thus its structure is the stiffest among tested resins.

Fig. 4.6.1a shows the N_2 adsorption-desorption isotherms of A-35, CT-482, and CT-124 at 77 K, as examples of macroreticular (oversulfonated and sulfonated/chlorinated) and microporous types of IER. N_2 adsorption isotherms of macroporous resins are type II, typical of macroporous solids. In these isotherms the inflection point or knee is located near the saturation of the first adsorbed monolayer and with increasing relative pressure, second and higher layers are completed until the number of adsorbed layers becomes infinite [197]. Macroporous resins as A-35 or CT-482 generally show type H1 hysteresis corresponding to solids formed by aggregates of spherical particles [198]. Microporous materials as CT-124 show type I isotherms corresponding to gases adsorbing in microporous solids with pore sizes comparable to adsorbate molecular diameter. The pore volume for CT-124 is naught compared to those of A-35 or CT-482. Pore volume of CT-482 was less than a half of that of A-35. BJH analysis from desorption curve is shown in Fig. 4.6.1b for A-35, CT-124 and CT-482. Curves for A-35 and CT-482 show unimodal distribution in the meso and macroporous region with a maximum above 500-600 Å, in agreement with the literature [163]. CT-124 exhibited so low pore volume that these values can be associated with a high level of uncertainty.

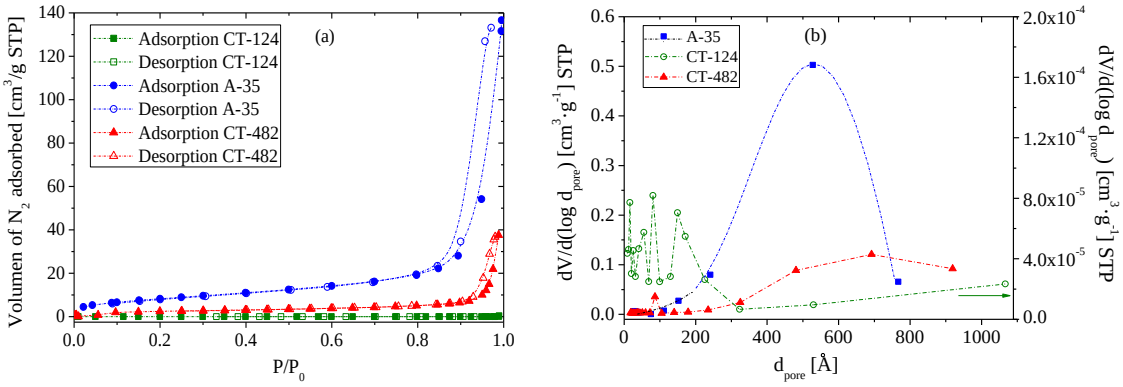

Figure 4.6.1. (a) Nitrogen adsorption-desorption isotherms at 77 K for A-35, CT-482 and CT-124. (b) Pore size distribution from N_2 desorption curve for A-35 and CT-482 (left Y axis), and CT-124 (right axis).

As it is well known, morphology of macroreticular resins can be modified as a result of swelling in polar media with the development of non-permanent meso and macropores. A reliable description of the actual pore structure in polar media can be obtained by means of the ISEC technique. The cylindrical pore model allows to characterize macro and mesopores (pore diameter and volume), but not to describe the spaces between polymer chains formed by aggregates and nodules swelling. The geometrical model developed by Ogston [81] gives a good approach of the three-dimensional network of swollen polymer describing micropores as spaces between randomly oriented rigid rods. This model also differentiates among zones of swollen gel-phase with different density of polymer chain concentration. The density of polymer chains is described as the total rod length per unit of volume. The distinctive parameter of this model is the specific volume of swollen polymer (V_{sp}) defined as the volume of free space plus the skeleton volume. From ISEC data, Ogston model enables the estimation of V_{sp} and also to distinguish gel zones of different density or characteristic polymer chain concentration. Particularly, for ISEC results in this study, V_{sp} has been modelled into 5 domains of polymer chains concentration of 0.1. 0.2, 0.4, 0.8 and 1.5 $nm \cdot nm^{-3}$ in which the spaces between chains are equivalent to pore diameters of 9.8, 4.3, 2.6, 1.5 and 1 nm, respectively [78]. The final ISEC output of the morphology of swollen resin consists of information on both, the distribution of "true pore" (meso and macropores) and the volume distribution of the differently dense gel fractions of the swollen polymer.

The main morphological properties obtained from adsorption-desorption of N_2 in dry polymer state at 77 K by BET method, and those obtained in swollen polymer state by ISEC method are presented in Table 4.6.1, where the values of polymer density obtained by He displacement are also included. As a rule of thumb, the higher the acid capacity, the higher the skeletal density of the polymer. With regards to the properties in dry state (Table 4.6.1), the hypercrosslinked resin MN-500 has the highest value (332 m^2g^{-1}) of BET surface area. Macroporous resins with high crosslinking degree showed also high values of BET surface area (from 20 to 60 m^2g^{-1}). The lowest values of BET surface area correspond to microporous resin CT-124 and the low crosslinked resin A-39. This confirms that gel-type resins do not show significant porous structure in dry state, and that crosslinking degree is directly related to the final catalyst BET surface area. With respect to the pore volumes in dry state, they ranged from $2.86 \cdot 10^{-4}$ to 0.64 cm^3g^{-1}, being MN-500 the resin with the largest pore volume. CT-124 and A-39 exhibited exiguous pore volumes, in agreement with the surface area results.

Table 4.6.1. Morphological properties of IER evaluated in dry and swollen states.

Catalyst	Skeletal density[a]	Dry state polymer (BET)[b]				Swollen state polymer (ISEC)[g]				
		Surface area[c]	Pore volume[d]	Pore diameter[e]	Porosity[f]	"True pores"			Gel phase	
	ρ	$S_{g,BET}$	$V_{pore,BET}$	$d_{pore,BET}$	θ_{BET}	$S_{g,ISEC}$	$V_{pore,ISEC}$	$d^e_{pore,ISEC}$	V_{sp}[h]	θ_{ISEC}[i]
	[g cm^{-3}]	[m^2 g^{-1}]	[cm^3 g^{-1}]	[nm]	[%]	[m^2 g^{-1}]	[cm^3 g^{-1}]	[nm]	[cm^3 g^{-1}]	[%]
A-15	1.416	42.0	0.33	31.2	31.7	156.9	0.63	16.1	0.77	49.5
A-16	1.401	1.7	0.01	30.8	1.8	149.3	0.38	10.3	1.13	52.8
A-35	1.542	34.0	0.21	24.7	24.5	198.9	0.72	14.5	0.61	51.3
A-36	1.567	21.0	0.14	27.2	18.3	146.5	0.33	9.1	1.03	53
A-39	1.417	0.1	$2.86\cdot10^{-4}$	12.7	0.0	56.0	0.16	11.1	1.62	60.3
A-40	1.431	0.2	$6.00\cdot10^{-4}$	10.9	0.1	11.0	0.13	45.5	0.44	–
A-45	1.466	49.0*	0.23	19.0*	25.4	220.2	0.52	9.5	0.97	54.4
A-46	1.137	57.4	0.26	18.3	23.0	186.0	0.48	10.3	0.52	12.3
A-48	1.538	33.8	0.25	29.5	27.7	186.0	0.57	12.3	0.62	45.3
A-DT	1.477	36.0*	0.20	22.0*	22.6	175.4	0.42	9.6	0.97	51.3
CT-124	1.420	0.1	$6.20\cdot10^{-4}$	35.7	0.1	0	0	0	1.90	62.9
CT-175	1.498	28.0	0.30	42.9	31.0	157.4	0.82	20.9	1.00	63.5
CT-275	1.506	20.3	0.38	74.4	36.2	209.4	0.77	14.7	0.81	57.9
CT-482	1.538	8.7	0.06	26.7	8.2	214.0	1.05	19.6	0.85	65.7
MN-500	1.539	332.0*	0.64*	152.0*	50.0	95.8	0.80	33.4	0.89	61.6

[a] Skeletal density. Measured by Helium displacement (Accupic 1330). [b] Samples dried at vacuum (10^{-4} mmHg, 110°C). [c] Brunauer-Emmett-Teller (BET) method. [d] Volume of N_2 adsorbed at relative pressure (P/P_0)=0.99. [e] $d_{pore,BET}= 4V_{pore,BET}/S_{g,BET}$ or $d_{pore,ISEC}= 4V_{pore,ISEC}/S_{g,ISEC}$. [f] $\theta_{BET}= V_{pore,BET}/V_{particle}=V_{pore,BET}/(V_{pore,BET}+1/\rho)$. [g] Measured with 0.2N aqueous solution of Na_2SO_4 as mobile phase except MN-500 where THF was used as mobile phase. [h] True volume of swollen polymer. [i] $\theta_{ISEC} =V_{pore,ISEC}/V_{particle}=(V_{pore,ISEC} +V_{sp}-1/\rho)/(V_{pore,ISEC} +V_{sp})$. *Manufacturer values.

The mean average pore diameter obtained for the studied resins in dry state is within the range 10.9–152 nm. Comparing conventionally sulfonated resins CT-175 and A-15 with their oversulfonated versions CT-275 and A-35, it is seen that the conventionally sulfonated ones present higher BET surface area than their oversulfonated versions.

Concerning the morphological properties obtained by ISEC (Table 4.6.1), V_{sp} values ranged from 0.44 to 1.9 cm^3g^{-1}. In agreement with volumetric swelling experiments, gel-type resin CT-124 and low crosslinked resin A-39 showed the highest values of V_{sp} confirming that swelling phenomenon is more relevant for gel-type resins. Generally, V_{sp} decreased on increasing crosslinking degree for macroreticular resins. "True pores" surface areas obtained by ISEC are notably larger than those obtained in dry state, as well as the pore volumes. This confirms that resins swelling in polar media affect not only the resins gel-phase but also the morphology of the permanent pores.

Comparing BET and ISEC values for A-16 and A-39, the absence of macropores in dry state is clear. However, new pores become detectable when swollen in aqueous media, with surface areas of 149 and 56 m^2g^{-1}, respectively. This enforces the abovementioned statement about the formation of new intermediate pores (meso and macropores) for macroporous resins in swollen state. On the other hand, neither meso nor macropores appeared in aqueous media for fully gel-type resin CT-124. Mean pore diameters of resins in swollen state are larger than those estimated in dry state, as expected from the higher pore volume in aqueous media. In addition, porosity values estimated from data in swollen state are generally larger than those estimated from data in dry state. Finally, results obtained for the resin A-40 in both dry and swollen state suggest an anomalous behavior of this resin. Since A-40 is a macroreticular resin with high crosslinking degree, the very low values of surface area exhibited in dry state are unusual. Moreover, the value of "true pores" surface area obtained from ISEC is closer to that expected

for a microporous resin. A possible explanation to this fact arises from the collapse of the resin structure during the pretreatment due to thermal creep and fatigue.

The polymer density zone distributions of the swollen gel-phase obtained by ISEC for the tested IER are shown in Fig. 4.6.2. As a whole, the densest polymer fraction (1.5 $nm \cdot nm^{-3}$) is generally the most frequent, particularly for macroreticular resins. Gel-type resin CT-124 and low crosslinked resin A-39 showed important contributions of the zones with medium density (0.4 and 0.8 $nm \cdot nm^{-3}$) to the total polymer volume in aqueous media. As it can be seen, the low polymer fraction volumes of MN-500 confirm the resistance of this resin to swelling according to its extremely high crosslinking degree (50%) and its ensuing stiff structure. Comparing conventionally sulfonated resins CT-175 and A-15 with their respective oversulfonated versions CT-275 and A-35, it can be observed that the former present larger contributions of the densest polymer zone to the total gel-phase volume of swollen polymer. However, A-16 and A-36 showed the opposite trend.

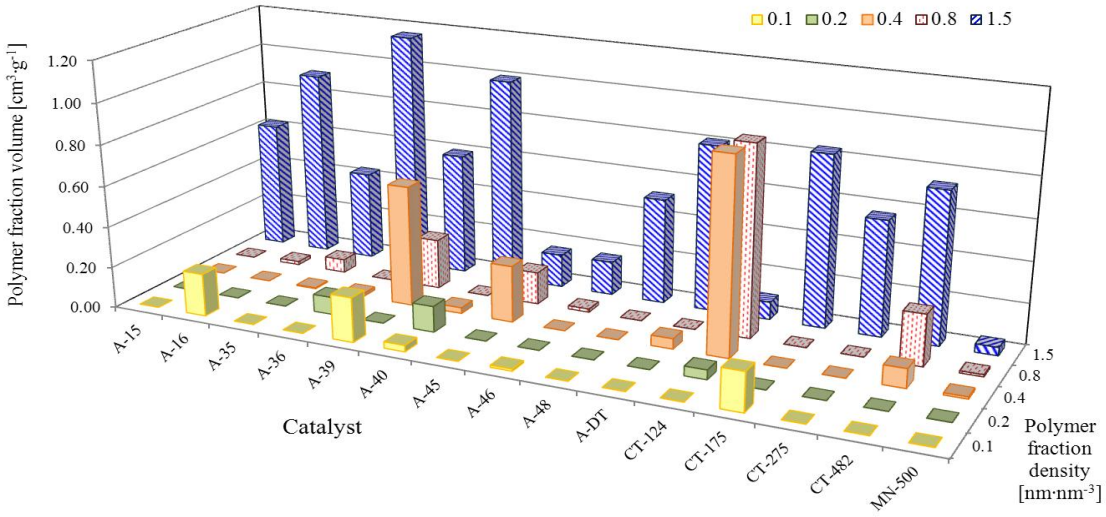

Figure 4.6.2. ISEC pattern of IER studied.

4.6.4 VOLUMETRIC SWELLING TESTS

The *SR* determined in different solvents and the dry bed densities for each IER are gathered in Table 4.6.2. Several factors are involved in the swelling phenomenon as the nature of the solvent (polar or non-polar), the resin crosslinking degree, the nature of the functional groups and its concentration [77]. All tested resins swelled in contact with solvents though in very different extent. In agreement with literature [76,77], water was found to be the solvent that produced the largest swelling for all IER. *SR* values obtained in water were slightly higher than those obtained with MeOH and EtOH, indicating that resins swelling in water and in C_1-C_2 alcohols are comparable. On the contrary, non-polar solvent (namely composed by ETBE and 2M2B) produced notably lower values of *SR* for all IER tested. It can be concluded therefore that the more polar the solvent the larger the swelling observed. The largest *SR* values were determined for CT-124 and A-39. As the crosslinking degree of A-39 is the lowest among macroporous resins evaluated and CT-124 is a gel-type resin, it can be inferred that the higher the crosslinking degree, the lower the swelling expected and thus the stiffer the resin structure.

Resins with very low acid capacity like A-46, swelled in a lesser extent that other resins with similar crosslinking degree but higher acid capacity (e.g. A-35 or A-48). Additionally, comparing conventionally sulfonated resins A-15 and CT-175 with their oversulfonated versions A-35 and CT-275, larger *SR* values are observed for the oversulfonated resins. Hence, the extent of swelling of a resin increases with the acid capacity, which can be explained by repulsion forces caused by extra electrostatic charges provided by an increase of sulfonic groups. Similar degree of swelling was observed for chlorinated resins (A-45, A-DT and CT-482) and macroreticular oversulfonated resin A-36. Finally, it is to be noted that laser diffraction technique is usually applied to measure accurately the diameter of particles swelled in diverse solvents. Nonetheless, *SR* data is especially valuable information for loading catalytic beds of industrial reactors, in which *SR* of commercial resins and bed density must be considered. It must be considered that the swelling of catalyst can exert extreme forces upon the reaction vessel and its internal structures. Pressures from swelling organic resins have been reported at nearly 690 bar [116], therefore it is easy to recognize the benefits of loading the catalytic beds in swollen state.

Table 4.6.2. Swelling ratio of IER in different solvents and dry resin bed density.

Catalyst	SR in solvents				Dry bed density [g mL^{-1}]
	Water	Ethanol	Methanol	Solvent [a]	
A-15	1.70	1.60	1.50	1.40	0.61
A-16	2.35	2.35	2.00	1.60	0.88
A-35	1.93	1.85	1.70	1.50	0.65
A-36	2.35	2.35	2.25	1.65	0.91
A-39	3.60	3.22	3.00	1.70	0.92
A-40	1.95	1.90	1.85	1.15	0.86
A-45	2.35	2.35	2.45	1.20	0.85
A-46	1.20	1.20	1.20	1.30	0.46
A-48	1.95	1.85	1.90	1.50	0.68
A-DT	2.30	2.40	2.00	1.15	0.91
CT-124	3.65±0.15	3.10	2.95	1.10	0.90
CT-175	1.70	1.65	1.60	1.40	0.54
CT-275	1.90	1.80	1.85	1.50	0.60
CT-482	2.25	2.10	2.10	1.15	1.10
MN-500	1.40	1.40	1.35	1.35	0.48

[a]Solvent composition (mol.%): IB (0.7), EtOH (0.1), 2M1B (3.0), 2M2B (58.8), ETBE (37.4)

4.6.5 CONVERSION, SELECTIVITY AND YIELD

As the experimental conditions of the present study were chosen to avoid olefins dimerization (bear in mind *Sections 4.3* and *4.5*), the product distribution obtained for all the runs is explained by the system of parallel reactions R1-R7 plotted in Fig. 4.1.1. Hydration reactions R5-R7 are a consequence of the remaining water content in the IER after pretreatment and the low water content of EtOH used as reactant.

Fig. 4.6.3 depicts the mole evolution profile obtained in a typical experiment, in this case for CT-175. All the tested IER were active for the simultaneous synthesis of ETBE and TAEE. According to initial concentrations and thermodynamics of involved reactions (as seen in *Section 4.4*), ETBE was the main product in all runs and its formation was faster than that of TAEE for all IER. The amount of tertiary alcohols formed was very similar for all IER and so low that etherification reactions can be considered to be non-affected by olefins hydration reactions. The molar fractions of TBA and TAA in these runs were always lower than 0.0033

and 0.0015, respectively. The trends in evolution of the reaction medium composition were similar for all tested resins.

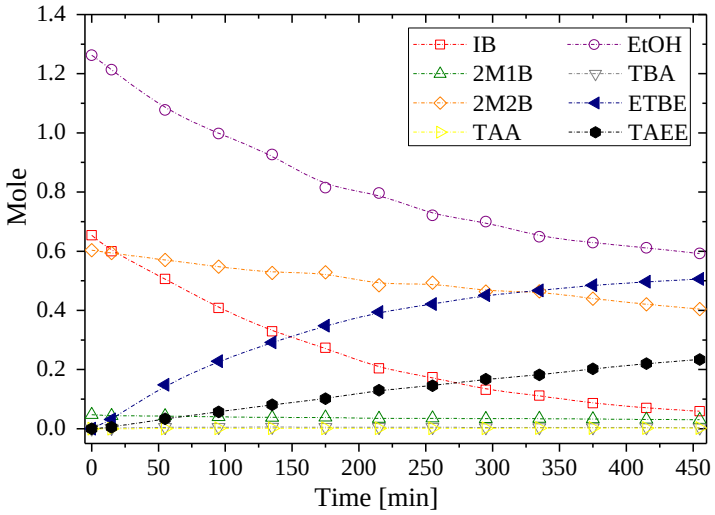

Figure 4.6.3. Mole evolution profile (1g of CT-175, T=335 K, $R°_{A/O}$=1.1 and $R°_{C4/C5}$=1)

Aiming to compare resins, Fig. 4.6.4 plots reactants conversion vs. contact time [$min \cdot g_{cat} \cdot (mol^0_{EtOH})^{-1}$] for all IER evaluated. IB was the reactant that reached the highest conversion level, being close to equilibrium conversion for the most active resins. X_{EtOH} was logically between X_{IB} and X_{IA}. The shape of reactants conversion profiles was very similar and three subgroups of resins are distinguished according to the activity level (high, medium and low), as clearly observed in Figs. 4.6.4a and 4.6.4b. High active resins were macroreticular oversulfonated and conventionally sulfonated resins (A-15, A-16, A-35, A-36, A-40, A-48, CT-175 and CT-275). Medium activity resins were chlorinated, gel-type and macroreticular with low crosslinking degree (A-39, A-45, A-DT, CT-124 and CT-482). Finally, surface sulfonated resins (A-46 and MN-500) showed the lowest activity level.

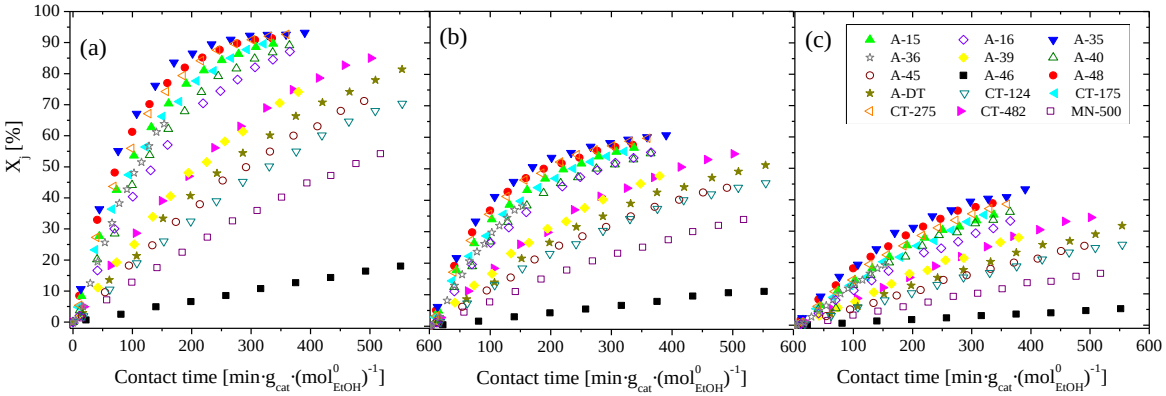

Figure 4.6.4. IB (a), EtOH (b) and IA (c) conversion vs. contact time for different resins at T=335 K, $R°_{A/O}$=1.1 and $R°_{C4/C5}$=1.

With respect to reactants selectivity toward products, S_{IB}^{ETBE} and S_{IA}^{TAEE} were larger than 99.7% for all tested resins. Neither olefins dimerization nor further oligomerization products were detected even for the most active catalyst at the end of the runs. Fig. 4.6.5a plots EtOH selectivities vs. X_{EtOH} for three resins, as representatives of highly, medium and low activity types described

before. The shape of this plot followed identical trends for the rest of resins. EtOH was far more selective toward ETBE than toward TAEE in the first steps of reaction for all IER, but this difference was progressively reduced with the course of reaction. Regarding reactants yield toward products, Fig. 4.6.5b depicts the yields profile obtained for CT-175. Reactants yield toward TAEE increased almost linearly with contact time. The olefins yield to tertiary alcohols was almost null. The shape of the yield evolution was very similar for the rest of IER, being always Y_{IB}^{ETBE} the highest yield reported. To compare data for all IER properly, Table 4.6.3 shows a summary of conversion and yield at the contact time 150 $min \cdot g_{cat} \cdot (mol^0_{EtOH})^{-1}$.

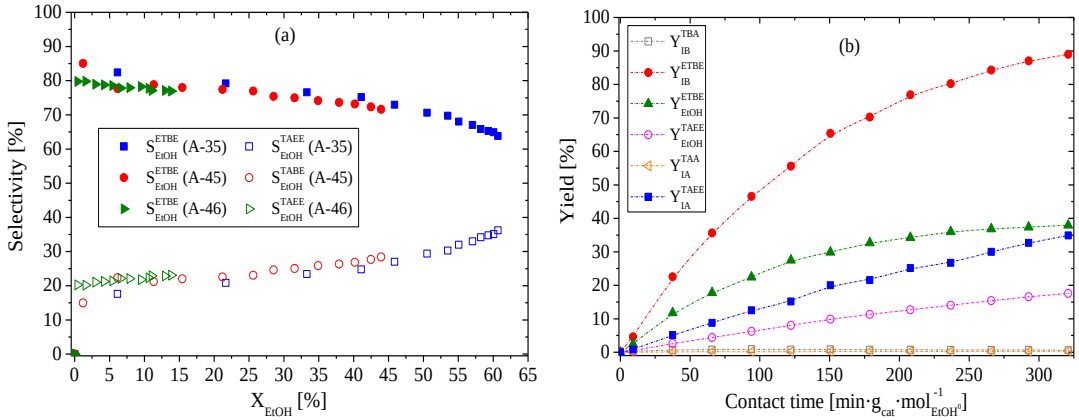

Figure 4.6.5. (a) EtOH selectivity vs. X_{EtOH} for A-35, A-45 and A-46. (b) Yield of reactants toward products vs. contact time (1g of CT-175 at T=335 K, $R°_{A/O}$=1.1 and $R°_{C4/C5}$=1).

Table 4.6.3. Conversion of reactants and yield to products (T= 335 K, $R°_{A/O}$=1.1 and $R°_{C4/C5}$=1) at a contact time of 150 [$min \cdot g_{cat} \cdot (mol^0_{EtOH})^{-1}$].

Catalyst	X_{IB}	X_{EtOH}	X_{IA}	Y_{IB}^{TBA}	Y_{IB}^{ETBE}	Y_{EtOH}^{ETBE}	Y_{EtOH}^{TAEE}	Y_{IA}^{TAA}	Y_{IA}^{TAEE}
A-15	68.4	37.2	21.4	0.2	68.1	28.1	10.4	0.1	23.3
A-16	56.0	33.3	17.1	0.4	55.5	26.9	9.7	0.1	16.8
A-35	78.3	48.5	25.5	0.4	78.0	33.7	13.3	0.3	25.0
A-36	62.5	37.5	18.6	0.3	62.2	28.1	9.4	0.1	18.6
A-39	39.0	23.1	12.6	0.5	38.3	18.8	6.4	0.1	11.2
A-40	60.2	38.0	18.4	1.1	57.2	26.8	11.3	0.3	15.6
A-45	30.5	19.4	7.9	0.3	30.0	14.0	4.0	0.1	7.7
A-46	4.9	3.1	1.4	0.1	4.9	2.5	0.7	0.0	1.4
A-48	75.7	45.2	26.0	0.7	72.9	32.5	12.1	0.2	21.9
A-DT	31.7	21.8	9.2	0.4	30.9	15.5	4.7	0.1	9.2
CT-124	24.1	17.5	10.0	0.4	25.7	13.5	3.9	0.1	9.8
CT-175	66.7	41.6	16.5	0.7	62.6	32.6	10.3	0.0	18.1
CT-275	70.7	45.3	19.5	0.4	74.2	33.2	11.6	0.1	21.4
CT-482	39.2	25.4	12.1	0.4	39.1	17.3	5.6	0.2	11.9
MN-500	18.8	10.1	4.7	0.6	18.1	10.0	2.5	0.1	4.7

4.6.6 ETHERIFICATION RATES AND TURN OVER FREQUENCIES

Initial turnover frequency (TOF^0_i) of the catalysts for both ether formations expressed as [$mol \cdot h^{-1} \cdot eq^{-1}$] were estimated as the quotient of r_k to the acid capacity. TOF is an interesting and widely used parameter in catalysis since it gives an idea of the mole converted per active site. Initial etherification rates were calculated from the slope of the mole evolution profiles by means of Eq. 3.4. Table 4.6.4 summarizes initial etherification

rates and TOF^0 obtained for each IER. As all IER were active in the present system, the relation between catalytic activity and sulfonic groups concentration is self-evident. However, there are more factors, of structural nature, as accessibility, that influence catalytic activity.

Table 4.6.4. Initial etherification rates and TOF^0 for the IER tested.

Catalyst	r^0_{ETBE} [mol·(h·kg)$^{-1}$]	r^0_{TAEE} [mol·(h·kg)$^{-1}$]	r^0_{ETBE} / r^0_{TAEE} [-]	TOF^0_{ETBE} [mol·(h·eq)$^{-1}$]	TOF^0_{TAEE} [mol·(h·eq)$^{-1}$]
A-15	223.30	47.89	4.66	46.42	9.96
A-16	149.41	34.80	4.29	31.13	7.25
A-35	299.53	70.14	4.27	55.88	13.09
A-36	153.47	38.37	4.00	28.42	7.11
A-39	87.25	24.27	3.60	18.14	5.05
A-40	161.51	39.30	4.11	31.06	7.56
A-45	63.00	16.55	3.81	17.28	4.54
A-46	10.18	3.21	3.17	11.70	3.69
A-48	276.05	62.93	4.39	49.12	11.20
A-DT	74.05	19.47	3.80	18.78	4.94
CT-124	58.97	16.44	3.59	11.79	3.29
CT-175	200.13	41.34	4.84	40.19	8.30
CT-275	249.97	51.69	4.84	46.55	9.62
CT-482	94.42	24.58	3.84	25.85	6.73
MN-500	39.71	10.68	3.72	14.71	3.96

As seen in Table 4.6.4, A-35 was the most active resin for the simultaneous synthesis of both ethers. On the contrary, A-46 was the least active resin. A special characteristic of A-46 is its low acid capacity since sulfonation is restricted to only the first outer few layers of styrene rings in the gel-phase. Globally, oversulfonated and conventionally sulfonated macroreticular IER (A-15, A-35, A-48, CT-175 and CT-275) reported the highest values of r^0_{ETBE} and r^0_{TAEE} (faster than 200 [mol·h^{-1}·kg^{-1}]). Gel-type resin CT-124 showed an activity level comparable to that of macroporous chlorinated resins with medium acid capacity (A-45 and A-DT) and higher than that of hyper-crosslinked resin MN-500. This result confirms that etherification reactions take place within the resins gel-phase, where most of the active sites are located, and that the main role of macropores is to provide channels that facilitate permeation of reactants and products to inner parts of the polymer. Such function of macropores is crucial for ETBE and TAEE reactions because the activity level of CT-124 is not comparable to that of macroreticular resins as A-15 or CT-175, despite having almost the same acid capacity. The increasing rank of activity obtained was: A-46 < MN-500 < CT-124 < A-45 < A-DT < A-39 < CT-482 < A-16 < A-36 < A-40 < CT-175 < A-15 < CT-275 < A-48 < A-35. This rank in terms of r^0_{ETBE} was maintained for r^0_{TAEE}, what indicates that the most active resins for ETBE formation are also the most active for TAEE synthesis. This is coherent due to the similar chemical nature of both etherification systems. The rate ratio r^0_{ETBE}/r^0_{TAEE} was about 4.4 for the high active resins, 3.8 for medium active resins and 3.4 for low active resins.

The obtained TOF^0 values for each resin, particularly for ETBE reaction, are larger than those typically reported in the dehydration of C_3-C_8 linear alcohols using the same catalysts [76,83,111], which can be due to clusters formation since the initial alcohol content, and therefore the effect of swelling, are larger in dehydration reaction systems. Generally, the etherification rates rank observed was maintained in terms of TOF values.

Nevertheless, TOF values for resin CT-124 were remarkably low, being almost the same of A-46, the resin with the lowest acid capacity evaluated. The absence of permanent pores in CT-124 resin influences therefore the relative efficiency of the active sites detrimentally. Despite having a relatively high acid capacity, the absence of macropores of CT-124 makes its active sites working at low efficiency, ascribed to accessibility limitations. The same explanation can be applied to the low TOF values obtained for A-39. With respect to the low TOF values obtained for MN-500, its very rigid structure impedes the swelling of microspheres and this could affect the diffusion of molecules and therefore accessibility of reactants to the gel-phase where active sites are located.

4.6.7 RELATIONS BETWEEN CATALYTIC ACTIVITY AND MORPHOLOGICAL PROPERTIES

The response surface methodology (RSM) was used to relate the catalytic activity with the catalyst physicochemical properties. The acid capacity and the catalyst properties from Table 4.6.1 (separately for those obtained in dry state from BET isotherms and those obtained in swollen polymer state from ISEC) were included as independent variables for the analysis. Because of the aforementioned anomalies obtained for A-40, it was decided to dismiss this resin for the analysis. The following second order polynomial form was used:

$$y = \beta_0 + \sum_{m=1}^{n} \beta_m z_m + \sum_{m=1}^{n} \beta_{mm} z_m^2 + \sum \sum_{l<m=2}^{n} \beta_{lm} z_l z_m \qquad \text{n=1,2,3…r} \qquad (4.6.1)$$

where z_1, z_2, …, z_k are the coded independent variables (catalysts properties from Tables 3.1 and 4.6.1), β_0, β_m, β_{mm} and β_{lm} are fitting parameters and, r^0_{ETBE} and r^0_{TAEE} are the fitted responses (y). A confidence level of 95% was used to assess the statistical significance of fitted polynomial models evaluated by the test of Fisher (F-value). The number of variables of Eq. 4.6.1 was reduced to the minimum statistically significant by means of the stepwise regression procedure [170] using the software Design-Expert 10. The significance level for each parameter to be either included or rejected from the final equation was evaluated by its *p*-value for a 95% of probability level (p=0.05). Because of the distribution of responses values, a transformation was necessary to correct the differences in variances (heteroscedasticity). The square root of the responses was used based on the results obtained from Box Cox power transformations method [199]. The analysis results in terms of coded variables are gathered in Table 4.6.5. The parity plot of experimental data vs. predicted values confirms the suitability of the fitted equations, and residuals plot confirms the randomness of the residuals for each model (Fig. 4.6.6).

Table 4.6.5. Parameters of the significant coded variables of the empirical models for initial etherification rates as a function of catalysts properties.

Terms	r^0_{ETBE}			r^0_{TAEE}		
	Coefficient	*p*-value	standard error	Coefficient	*p*-value	standard error
β_0	6.21	$1.42\cdot10^{-8}$	0.42	3.31	$4.64\cdot10^{-10}$	0.16
β_1 ($[H^+]$)	7.58	$1.31\cdot10^{-8}$	0.51	3.36	$3.01\cdot10^{-9}$	0.20
β_2 (V_{sp})	-4.15	$5.79\cdot10^{-6}$	0.51	-1.17	$3.13\cdot10^{-6}$	0.20
Adjusted R^2		0.95			0.96	
Model *F*-value		118.15			153.26	
Critical *F*-value		$3.62\cdot10^{-8}$			$9.29\cdot10^{-9}$	

Outcomes reveal that a lineal polynomial function with interactions fits satisfactorily to experimental data. The catalytic activity is correlated better with physicochemical and ISEC properties of the catalyst rather than with dry state properties, since nonsignificant correlation was found for catalytic activity with any dry state property. This is coherent because, as seen in volumetric swelling experiments and in agreement with the literature [77], IER swell similarly in EtOH and in water. Therefore, ISEC properties should be more representative of the actual working-state of the catalyst in the focused etherification reactions.

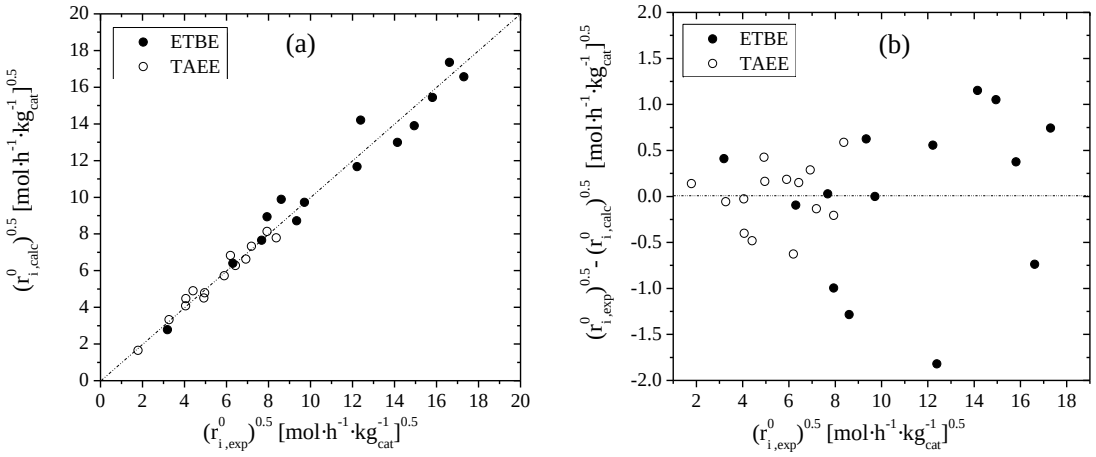

Figure 4.6.6. (a) Predicted etherification rates vs. experimental ones for ETBE and TAEE. (b) Residual plots for ETBE and TAEE reaction rates.

The analysis of variance (ANOVA) indicates that the proposed empirical models are adequate to express the actual relation between responses and significant variables with large values of adjusted R^2 (>0.95). Acid capacity and V_{sp} are the only significant variables in the proposed models for both r^0_{ETBE} and r^0_{TAEE}. This is logical since both ethers are produced from very similar reactions. The fitting goodness was slightly better for TAEE than for ETBE. The largest divergences in the fitting of empirical equations were found for initial etherification rates obtained on A-36 and A-DT. From empirical equations obtained in terms of non-coded variables (Eqs. 4.6.2 and 4.6.3), the positive values determined for the linear term of acid capacity and the negative ones for the volume of swollen polymer indicate that catalytic activity of IER is directly related to the ratio $[H^+]/V_{sp}$. Fig. 4.6.7 plots r^0_{ETBE} and r^0_{TAEE} versus the ratio $[H^+]/V_{sp}$, where a linear relationship is observed. Consequently, resins with high concentration of sulfonic groups and with low volume of swollen polymer are the best option for the simultaneous production of ETBE and TAEE. A high concentration of sulfonic groups in a reduced space can allow clusters formation or coordination of active sites that eventually favour etherification reactions. This result also enforces that crosslinking degree and macropores play a determinant role, since they make the permeation of molecules easier and thereby the ensuing accessibility to active sites. Examples of IER with such combination of features are those macroreticular oversulfonated with high crosslinking degree as A-35, A-48 and CT-275.

$$\left(r^0_{ETBE}\right)^{0.5} = (3.16 \pm 1.05) + (3.19 \pm 0.22)\cdot[H^+] - (6.03 \pm 0.74)\cdot V_{sp} \qquad (4.6.2)$$

$$\left(r^0_{TAEE}\right)^{0.5} = (1.72 \pm 0.41) + (1.42 \pm 0.08)\cdot[H^+] - (2.48 \pm 0.29)\cdot V_{sp} \qquad (4.6.3)$$

The relationship found (Eqs. 4.6.2 and 4.6.3) can be useful for designing new catalysts with a larger relation $[H^+]/V_{sp}$ with the aim of assess whether catalytic activity in etherification reactions can be increased. As sulfonation of the polymer is limited by the number of benzene rings, and V_{sp} depends on the crosslinking degree, the existence of a threshold or optimum value of $[H^+]/V_{sp}$ could be somehow expected.

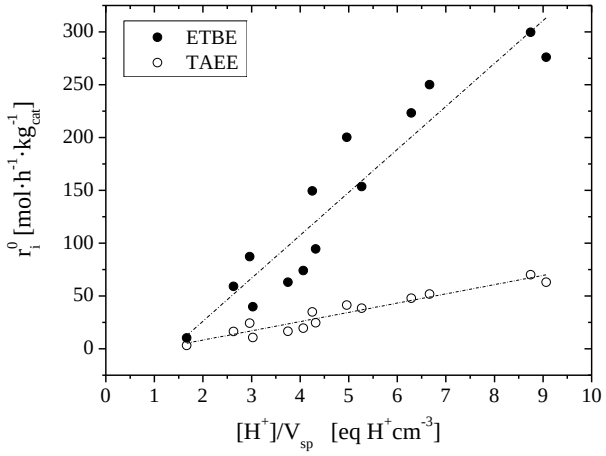

Figure 4.6.7. r^0_i vs. ratio of acid capacity to volume of swollen polymer.

As in the present reaction system the initial mixture is composed by EtOH and olefins ($R°_{A/O}$) = 1.1, the reaction mixture is undergoing a transition toward a less polar environment as reaction time increases, owing to EtOH consumption to form ethers (non-polar compounds). As a consequence, resins should experience some shrinking effect as reactions proceed. Catalytic activity has been measured as initial reaction rates, when the reaction medium is more polar. Therefore, IER are more swollen at initial reaction times, and ISEC properties should describe more reliably the initial actual catalyst working-state, in agreement with the results obtained. However, it can be inferred that resins do not swell in the same degree as it could be expected in pure water or pure EtOH. ISEC data provides information on the catalysts morphological properties when totally swelled in water and thus, the actual structural properties are somehow different in the present reaction system of lower polar nature. Nevertheless, it can be assumed that the specific volumes of swollen polymer described by ISEC maintain their relative identity despite the mentioned differences in the reaction media polarity. The good correlation found between catalytic activity and volume of swollen polymer enforces this assumption.

4.6.8 ACCESSIBILITY

As discussed, the largest contribution to the total reaction rate observed must come from the densest polymer domain, however, its relative efficiency may be influenced by limitations in accessibility or permeation of involved molecules. Accessibility can be defined as the maximum fraction of active sites that can be reached by a substrate molecule [104]. The catalytic activity of IER depends dramatically on both the nano-environment surrounding the active centres and their accessibility [80]. As mentioned in *Section 1.5.6*, several types of accessibility can be distinguished. Non-interaction accessibility is related to the morphology in an inert bulk phase, whereas interaction accessibility reflects the influence of the solvent and/or adsorbed molecules [104]. Accessibility to active sites is critically affected by the extent of swelling of the polymer in contact with the reaction medium for both macroreticular and gel-type resins. As a consequence of swelling, polymer chains separate from each other, what enhances the

accessibility to inner parts of the polymer network by making the pore channels wider. Accessibility to functional groups anchored in the polymer chains depends on the polymer morphology at micro and nanoscopic level. As stated for the IER studied, the primary role of macropores is to facilitate the contact between the molecules and the gel-phase, where the active sites are located, instead of providing active surface. Besides, the nature and amount of functional groups can also influence accessibility, which can be defined as a different type of interaction accessibility.

There are several methodologies to evaluate the different types of accessibility in an IER. In order to obtain non-interaction accessibility, the surface area ($S_{g,BET}$) measured by adsorption-desorption of N_2 is the method of choice [104]. The corresponding fraction of accessible functional groups ζ_N is proportional to the surface area per polymer skeletal density (ρ) according to Eq. 1.8. The values of ζ_N obtained for the resins evaluated are gathered in Table 4.6.6.

The largest ζ_N was obtained for MN-500 resin, as expected from its very high surface area. Values of ζ_N for A-15, A-35, A-48 and A-DT were similar, lower than those of A-46 and A-DT and slightly larger than those for CT-175, CT-275 and CT-482. Gel-type resin CT-124 and low crosslinked resin A-39 exhibited the lower ζ_N. This ranking of non-interaction accessibility is not directly related to the observed catalytic activity because it was measured during reaction and therefore accounts for the interactions caused by the bulk-phase. However, it defines a reference state that can be used to show the influence between adsorbate and adsorbent.

Table 4.6.6. Values of ζ_N obtained for the resins evaluated.

Resin	ζ_N [−]	Resin	ζ_N [−]
A-15	0.037	A-48	0.030
A-16	0.002	A-DT	0.035
A-35	0.031	CT-124	0.0001
A-36	0.019	CT-175	0.025
A-39	0.0001	CT-275	0.018
A-40	0.0002	CT-482	0.009
A-45	0.049	MN-500	0.376
A-46	0.078	–	–

Several procedures exist to assess the interaction accessibility or ease of penetration of molecules into a porous system. An approach of which part of a porous system is accessible to spherical molecules having the diameter d_m is given by the Ogston distribution coefficient (K_O) [110], which can be estimated by the expression:

$$K_O = \exp\left(-0.25\pi C\left(d_m + d_c\right)^2\right) \qquad (4.6.4)$$

where C is the chain density of a polymer domain and d_c is the diameter of rigid rods representing polymer chains (0.4 nm). K_O represents the relative amount of compound present in a zone of a particular density compared to the amount in the free solution. It takes values ranging from 0 (the molecule is fully excluded from the considered gel-phase zone) to 1 (indicating that the amount of a given molecule is the same as outside the gel-phase). As Eq. 4.6.4 considers spherical molecules, the molecular length can be a fair estimate of the effective size, d_m. The molecular length of compounds involved in the present reaction system was trigonometrically estimated through the atomic distances and the bond angles of molecules in their conformation of minimum energy using the software ChemBioOffice 2014. A detailed

description of the data used for the main involved species in the calculations can be found in *Appendix 7.9*.

Besides Ogston distribution coefficient, the comparison of random coil diameter (Φ_d) and the equivalent pore size of the different fractions of polymer chain density in the swollen polymer can also provide information about accessibility and permeability of compounds [111].

The random coil diameter (Φ_d) is a measure of the space filled by a molecule of molecular weight M_w (g mol^{-1}) and it can be computed by the empirical relation described by Eq. 4.6.5 [71]. Φ_d provides information about the spaces between polymer chains that a molecule needs to permeate through them without enthalpic interaction. It is accepted that such spaces between polymer chains should be at least 2.5 times the value of Φ_d to avoid permeation problems within the gel-phase.

$$\Phi_d = 0.02457(M_w)^{0.5882} \qquad (4.6.5)$$

Estimated values of molecular lengths, K_O and Φ_d for all the chemical species that were detected in this work are gathered in Table 4.6.7.

Table 4.6.7. Ogston distribution coefficients, K_O, in the different density zones of swollen polymer and random coil diameter, Φ_d, of olefins, alcohols and ethers considered.

Compound	Molecular length[a] [nm]	Polymer chain density [nm nm^{-3}]	0.1	0.2	0.4	0.8	1.5	Φ_d [nm]	$2.5\Phi_d$ [nm]
		Equivalent Pore diameter [nm]	9.8	4.3	2.6	1.5	1		
		M_w [g mol^{-1}]			K_O				
Water	0.15	18.02	0.98	0.95	0.91	0.83	0.70	0.13	0.34
IB	0.42	56.11	0.95	0.90	0.81	0.65	0.45	0.26	0.66
EtOH	0.39	46.07	0.95	0.91	0.82	0.67	0.48	0.23	0.58
2M1B	0.56	70.13	0.93	0.87	0.75	0.56	0.34	0.30	0.75
2M2B	0.51	70.13	0.94	0.88	0.77	0.60	0.38	0.30	0.75
TBA	0.42	74.12	0.95	0.90	0.81	0.65	0.45	0.31	0.77
TAA	0.54	88.15	0.93	0.87	0.76	0.57	0.35	0.34	0.86
ETBE	0.68	102.17	0.91	0.83	0.69	0.48	0.26	0.37	0.93
TAEE	0.68	116.20	0.91	0.83	0.70	0.48	0.26	0.40	1.01

[a]Estimated by ChemBioOffice 2014 Software (d_m).

K_O values indicate that all molecules would access to the swollen polymer matrix. Only ether molecules may present some impediment to permeate into the densest polymer zones. The relative amounts of ETBE and TAEE in 0.8 and 1.5 nm·nm^{-3} fractions are, respectively, a half and a quarter of those in the free solution. Even for the smallest molecules studied as EtOH and IB some permeation limitations are found in the densest domains. Consequently, ether formation in these areas could be affected by diffusional problems that reduce the efficiency of the active sites therein located. Regarding the equivalent pore size diameter of the swollen polymer zones, it is larger than estimated values of 2.5 Φ_d from Table 4.6.7, except in the densest zone (1.5 nm·nm^{-3}). This indicates that all molecules can penetrate in the swollen polymer and only the densest fraction could be somehow difficult to permeate for ETBE and TAEE, the biggest molecules of the reaction system. In other words, the diffusion coefficient of involved compounds, particularly ether molecules, sharply decreases in the densest zones of the swollen polymer.

Estimated data of random coil diameter and K_O values are in agreement. Both outcomes suggest that the relative efficiency of the densest polymer zones could be enhanced if the accessibility limitations estimated are overcome. As a whole, it is coherent that active sites located in those tough to reach areas present an efficiency affected by diffusional problems. The lower catalytic activity of resins with very large contributions of the densest area as A-36 and A-40 compared to that of A-35 is probably due to the mentioned accessibility limitations.

Finally, it is to be noted that morphological properties from ISEC data are obtained in conditions in which the sulfonic groups of the polymer have been modified by ionic-exchange with sodium ions of the mobile phase. Swelling and therefore accessibility are known to be influenced by the nature and amount of the functional groups (interaction accessibility) [104]. Consequently, measures of accessibility and morphological properties considering the interaction with functional groups (in situ) are strongly advisable for drawing more accurate conclusions. The complex and dynamic catalytic performance of IER can only be fully understood and properly modelled by using in situ characterization techniques that enable obtaining the catalysts structural properties under reaction conditions. In this sense, diffuse reflectance infrared Fourier transform (DRIFT) constitutes an example of in situ technique that gives information about adsorbed species and the active sites nature in working-state [64]. In addition, techniques that extract structural information of heterogeneous catalysts by analyzing their X-ray absorption spectrum are specially powerful when combined with specially designed in situ cells [200], for instance, X-ray Absorption Spectroscopy (XAS) and X-ray diffraction (XRD). The former includes both Extended X-Ray Absorption Fine Structure (EXAFS) and X-ray Absorption Near Edge Structure (XANES). XRD gives information on the well-ordered crystalline part of the catalysts whereas EXAFS is useful in the study of amorphous and microcrystalline structure of the catalysts being therefore complementing techniques. Further development of techniques that consider the catalyst as a dynamic entity under reaction conditions will be the key for developing new catalysts and toward the understanding of the mechanisms that occur on catalytic surfaces.

4.6.9 PARTIAL CONCLUSIONS

Swelling of a resin is influenced by the nature of the bulk phase and by the resin properties as crosslinking degree and acid capacity. Observed swelling in methanol and ethanol is comparable to that in water. All the tested resins are active and highly selective in the simultaneous synthesis of ETBE and TAEE. The outstanding values of reactants selectivity toward ethers obtained for all IER make the process industrially attractive as well as the selected experimental conditions suitable for the simultaneous production of ETBE and TAEE.

Macroreticular oversulfonated resins show the best performance in the present reaction system, among them Amberlyst™35 is the most active catalyst. RSM is used to obtain empirical equations that correlate the catalytic activity measured with the catalysts properties. The combination of acid capacity and swollen state properties correlate better with catalytic activity than structural properties in dry state. It is ascribed to the variation of the morphological properties caused by resin swelling in polar reaction media. Resins with high acid capacity and low volume of swollen polymer are the most suitable for the simultaneous production of ETBE and TAEE. Coordination of multiple active sites (clusters) can be the reason of the higher catalytic performance observed.

As for accessibility, Ogston model and random coil diameter approaches agree that the densest domain of 1.5 $nm \cdot nm^{-3}$ present permeation problems for ETBE and TAEE molecules. Even for smaller molecules some diffusional problems are expected. Consequently, the relative efficiency of active sites located in this fraction can be limited, affecting therefore the observed catalytic activity.

4.6.10 CHAPTER NOTATION

2M1B	2-methyl-1-butene
2M2B	2-methyl-2-butene
BET	Brunauer, Emmett and Teller analysis
BJH	Barrett, Joyner and Halenda analysis
C	chain density of a polymer domain [$nm \cdot nm^{-3}$]
d_c	diameter of rigid rods representing polymer chains [nm].
d_m	molecular length [nm]
d_{pore}	pore diameter [nm]
ETBE	ethyl *tert*-butyl ether
EtOH	ethanol
IB	isobutene
ISEC	Inverse Steric Exclusion Chromatography
K_O	Ogston coefficient [dimensionless]
M_w	molecular weight [g/mol]
n_k	mole of product *k* formed
r^0_i	initial intrinsic rate of reaction *i*, [mol $(kg_{cat} \cdot h)^{-1}$]
r_i	intrinsic rate of reaction *i*, [mol $(kg_{cat} \cdot h)^{-1}$]
$r_{i,n}$	rate contribution of polymer fraction *n* [mol $(kg_{cat} \cdot h)^{-1}$]
$R°_{A/O}$	initial ratio alcohol to olefins [dimensionless]
$R°_{C4/C5}$	initial ratio C_4 to C_5 olefins [dimensionless]
S_g	surface area determined by BET or ISEC [$m^2 \cdot g^{-1}$]
S_j^k	selectivity of reactant *j* toward product *k* [%]
Y_j^k	yield of reactant *j* toward product *k* [%]
SR	swelling ratio [dimensionless]
t	reaction time [min]
T	temperature [K]
TAA	*tert*-amyl alcohol
TAEE	*tert*-amyl ethyl ether
TBA	*tert*-butyl alcohol
TOF	turnover frequency of the catalyst [mol $(h \cdot eq[H^+])^{-1}$]
$TOF^0_{i,n}$	TOF of polymer fraction *n* for the reaction *i* [mol $(h \cdot eq[H^+])^{-1}$]
V_{pore}	pore volume determined by BET or ISEC [$cm^3 \cdot g^{-1}$]
V_{sp}	true volume of swollen polymer [$cm^3 \cdot g^{-1}$]
$V_{sp,n}$	specific volume of swollen polymer occupied by fraction *n* [$cm^3 \cdot g^{-1}$]
W_{cat}	catalyst mass in dry basis [g]
X_j	conversion of reactant *j* [%]
θ	porosity [%]
ρ	skeletal density [$g \cdot cm^{-3}$]
Φ_d	random coil diameter [nm]

4.7 KINETIC STUDY OVER AMBERLYST™35

A revised version of a part of this chapter was published as:

R. Soto, C. Fité, E. Ramírez, R. Bringué, F. Cunill. Kinetic modeling of the simultaneous etherification of ethanol with C_4 and C_5 olefins over Amberlyst™35 using model averaging. *Chem Eng. J.* **2017**; 307: 122–134. http://dx.doi.org/10.1016/j.cej.2016.08.038

4.7.1 INTRODUCTION

Mechanisms, kinetics and thermodynamics of the involved reactions determine the product distribution and, therefore, they are key factors for setting industrial operating conditions and understanding the catalytic behavior. To the best of our knowledge, there is a lack of information about detailed kinetic studies regarding the simultaneous production of tertiary ethers, and more specifically focused on the simultaneous production of ETBE and TAEE. Several kinetic modeling procedures coexist to describe a reaction system, among them response surface methodology (RSM) [169], power function models and mechanistic hyperbolic models are the most widely applied. The choice of the type of model is often reason for debate among the catalysis expert community [201–203] but generally, hyperbolic models are preferred for kinetic modeling because they provide more information.

Being statistically sound, the use of RSM in the early modeling provides one of the best empirical models that can be obtained [201]. Moreover, RSM provide an effective way to approach to a mechanistic model and numerous engineering advantages for the process design and economic standpoints. For instance, to obtain simpler expressions than those provided by hyperbolic models and equally able to predict reliable rate data. As a prospective analysis, the kinetic study of complex reaction systems can start by the application of RSM in order to draw some inferences about the significant variables that would be useful for the subsequent development of mechanistic reaction schemes [201]. Some parallelisms can thereby be drawn between the variables fitted in the analysis and their contribution to the classical models of heterogeneous catalysis based in the Langmuir-Hinshelwood-Hougen-Watson (LHHW) and Eley-Rideal (ER) formalisms [201,204]. Besides, power function models, based on Freundlich isotherm, can also describe solid catalyzed reactions. These models are very useful to extract conclusions about the kinetic pseudo-order of involved compounds.

Finally, kinetic hyperbolic models based on Langmuir isotherm provide maximum information related to kinetics and adsorption of involved compounds. Nevertheless, a wide array of models can be postulated for the same reaction system and the discrimination among plausible models can be arduous. In the search of the kinetic equations that describe experimental data, and due to the simultaneous occurrence of the involved chemical reactions, a considerably large number of combinations of kinetic expressions can be proposed. To make sure that a good kinetic model

candidate is not neglected, a systematic kinetic analysis should be the first step for fitting the experimental data. Then, model selection and model averaging can be applied to obtain a reliable kinetic model from a set of candidate models [205–210].

The aim of this work is to study the kinetics of the simultaneous liquid-phase synthesis of ETBE and TAEE from a pure iso-olefins feedstock and EtOH over Amberlyst™35 using different approaches for kinetic modeling. The main goals are to find the best kinetic model, to estimate the kinetic parameters, to extract mechanistic conclusions based on LHHW or ER formalisms, and to compare it with the isolated production of both ethers.

4.7.2 EXPERIMENTAL AND CALCULATIONS

The stirred tank batch reactor described in *Section 3.2.1* was used to carry out the isothermal experiments. The initial molar ratios of alcohol to olefins ($R^{o}_{A/O}$) and of IB to IA ($R^{o}_{C4/C5}$) were both varied from 0.5 to 2. The working temperature ranged from 323 to 353 K. A dry catalyst mass of 0.25, 0.4, 1 and 1.5 g of A-35 was used for kinetic experiments at 353, 343, 333 and 323 K, respectively. These catalyst loads allowed to obtain kinetic data with enough accuracy during the runs duration. All the preliminary experiments to evaluate the possible effect of mass transfer and catalyst load were conducted at the highest assayed temperature (353 K), where these effects are more noticeable.

Empirical models for initial etherification rates were obtained using the RSM. Coded values of the regressors (β) and the second order polynomial form with interaction terms (see Eq. 4.7.1) were used. The best empirical model for each reaction was chosen by means of the stepwise procedure among possible candidates. The significance level for each variable to be either included or rejected from the final equation was set to 0.05.

$$y = \beta_0 + \sum_{i=1}^{3} \beta_i z_i + \sum_{i=1}^{3} \beta_{ii} z_i^2 + \sum_{i=1}^{3} \sum_{j=1}^{2} \beta_{ij} z_i z_j \qquad (4.7.1)$$

Apart from RSM, initial reaction rates were fitted to the power function model described by Eq. 4.7.2, where x_A and x_O are respectively the alcohol and the corresponding olefin (isobutene or isoamylenes) molar fractions in the total reaction mixture; k_{Ai} and k_{Oi} are constants that can be related to the kinetic pseudo-order of each compound; and A'_i is the apparent pre-exponential factor (or simply the pre-factor).

$$r_i = A'_i \cdot e^{\frac{-Ea_i}{R \cdot T}} \cdot x_A^{k_{Ai}} x_O^{k_{Oi}} \qquad (4.7.2)$$

The calculations used for hyperbolic kinetic modeling are detailed through the *Section 4.7.6.3*.

4.7.3 EXTERNAL AND INTERNAL MASS TRANSFERS

In order to find out the experimental conditions for which the effects of internal and external mass transfers (IMT and EMT) can be neglected, a set of preliminary experiments was carried out at $R^{o}_{A/O}$=1, $R^{o}_{C4/C5}$=1, 353K, and using 1 g of pretreated A-35. The effect of IMT was evaluated for different ranges of particle size, obtained by crashing and sieving the catalyst. The

effect of EMT was tested by varying the stirring speed from 600 to 800 rpm, based on previous studies on isolated ETBE and TAEE syntheses [140,149,166]. Fig. 4.7.1 plots the initial etherification rates, where IMT and EMT effects are expected to be more noticeable, calculated for ETBE and TAEE as a function of the inverse of the average catalyst particle diameter ($1/d_p$) at different stirring speeds. As can be observed, mass transfer effects are negligible for particle size below 0.4 mm and stirring speed above 600 rpm. Consequently, a catalyst bead size of 0.25–0.4 mm and a stirring speed of 600 rpm have been used in the next stages of this study. The estimated effectiveness factors of commercial particles of A-35 (d_p=0.51mm) in ETBE and TAEE formation reactions at 353 K were 0.64 and 0.68, respectively.

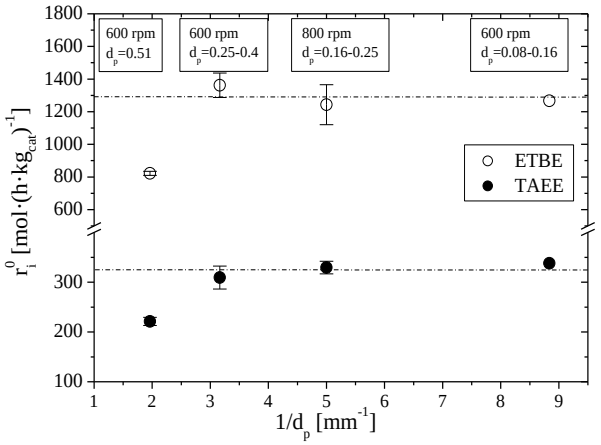

Figure 4.7.1. Effect of internal and external mass transfer. T=353 K, $R^{o}_{A/O}$=1, $R^{o}_{C4/C5}$=1, and 1g of A-35. Error bars refer to 95% confidence level.

4.7.4 EFFECT OF THE CATALYST LOAD

The effect of the catalyst load (CL) was also evaluated in preliminary experiments at $R^{o}_{A/O}$=1, $R^{o}_{C4/C5}$=1, 353K, 600 rpm, and using catalyst particle sizes of 0.25-0.4 mm. Assayed catalyst loads were 0.25, 1 and 2 g of dried A-35. Fig. 4.7.2 depicts the obtained reactants conversion for the different catalyst loads as a function of the standardized time, named as contact time, and used for comparative purposes. Since the obtained curves for different catalyst loads overlap, it can be concluded that the effect of CL up to 2 g of catalyst is negligible under the explored experimental conditions. Consequently, catalyst loads used for subsequent kinetic experiments were below 2 g, specifically 0.25, 0.4, 1, and 1.5 g at 353, 343, 333, and 323 K, respectively.

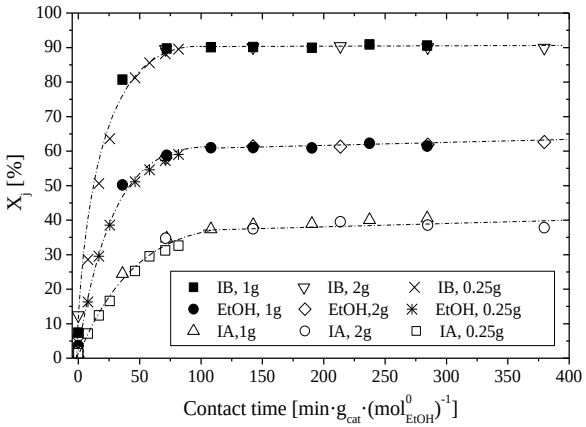

Figure 4.7.2. Evolution of the X_j with contact time for different catalyst loads. T=353 K, $R^{o}_{A/O}$=1, $R^{o}_{C4/C5}$=1, 600 rpm, d_p=0.25-0.4 mm. Dashed lines are guides to the eye.

4.7.5 MOLE EVOLUTION, CONVERSION AND SELECTIVITY PROFILES IN THE KINETIC EXPERIMENTS

As described in more detail in *Section 4.1*, some side reactions can take place in the simultaneous etherification of IB and IA with EtOH depending on temperature and initial reactants concentration. The experimental conditions of the present work were chosen to avoid the side reactions of olefins hydration and oligomerization. For this reason, only the system of parallel reactions depicted in Fig. 4.7.3 was evaluated for kinetic modeling.

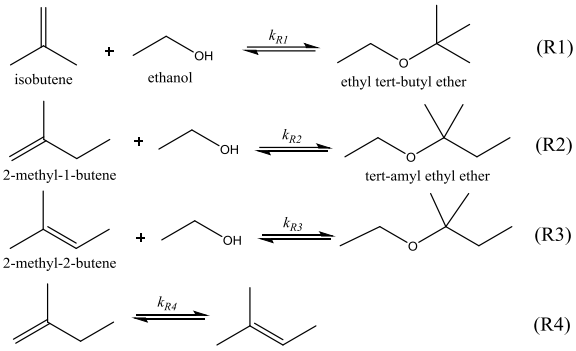

Figure 4.7.3. Main reactions considered for kinetic modeling.

A total set of 21 experiments (including replications) were carried out free of IMT, EMT and CL effects. Examples of the mole evolution profiles obtained under several experimental conditions are depicted in Fig. 4.7.4.

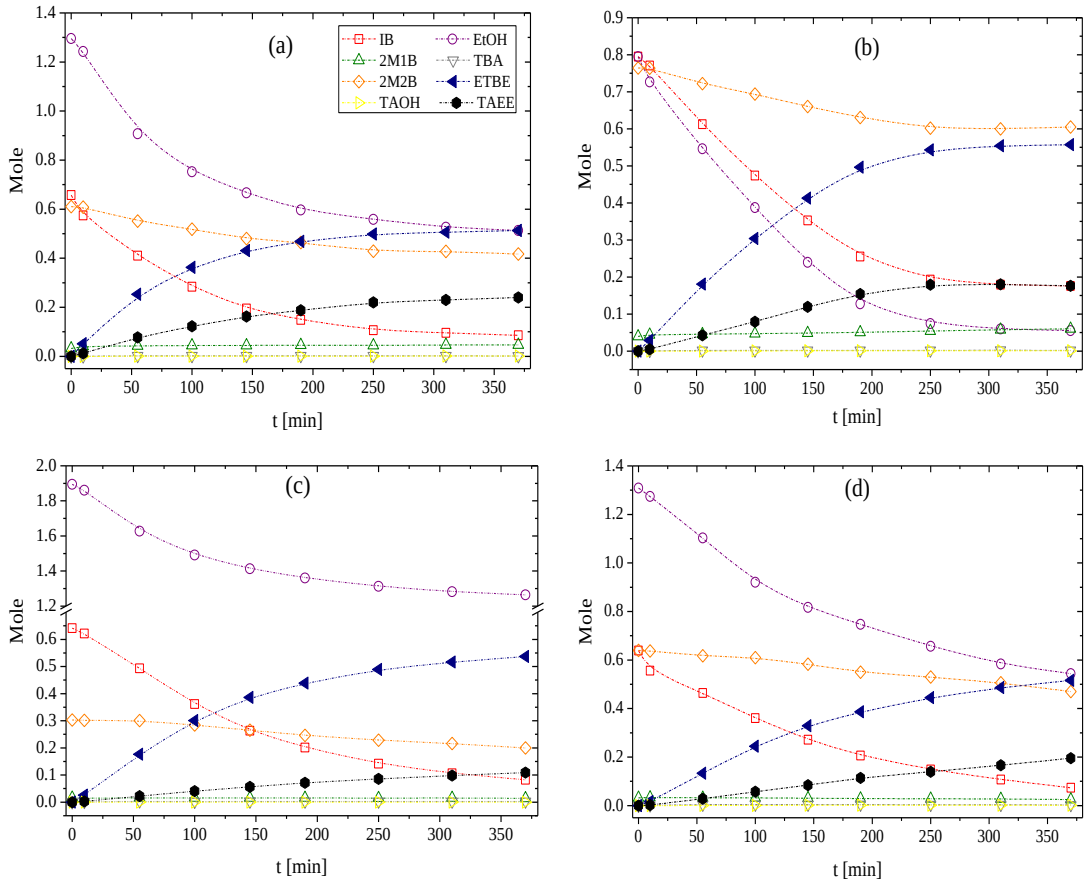

Figure 4.7.4. Experimental mole evolution obtained under different conditions: (a) T= 353.5 K, $R^{o}_{A/O}$=1, $R^{o}_{C4/C5}$=1, 0.29 g A-35; (b) T= 342.8 K, $R^{o}_{A/O}$=0.5, $R^{o}_{C4/C5}$=1, 0.41 g A-35; (c) T= 352.7 K, $R^{o}_{A/O}$=2, $R^{o}_{C4/C5}$=2, 0.27 g A-35; (d) T= 323.2 K, $R^{o}_{A/O}$=1, $R^{o}_{C4/C5}$=1, 1.54 g A-35. Dashed lines are guides to the eye.

In all runs, the amount of formed ETBE mole exceeded TAEE mole. As seen in *Section 4.5*, water inhibits etherification reactions and promote tertiary alcohols (TBA and TAA) formation, therefore special care was taken to minimize water sources: absolute dry EtOH was used as reactant, and the catalyst was dried under vacuum before its use. The amount of formed tertiary alcohols detected as the result of the remaining water content of the catalyst after pretreatment and the small water content in EtOH, was very low, the molar fractions of TBA and TAA being always lower than 0.003 and 0.001, respectively. Olefins dimers were formed only in the experiments at the highest explored temperature and initial stoichiometric excess of olefins, though in very low extent (molar fraction lower than 0.002). Therefore, it can be assumed that kinetic data for etherification reactions, obtained in a wide range of compositions and temperatures, were not affected by side reactions.

The evolution of reactants conversion vs. contact time for kinetic experiments at $R°_{A/O}=R°_{C4/C5}=1$ is plotted in Fig. 4.7.5. IB was the reactant that showed the highest level of conversion, followed by EtOH and finally, IA showed the lowest conversion. The higher the temperature explored, the steeper the fractional conversion profile.

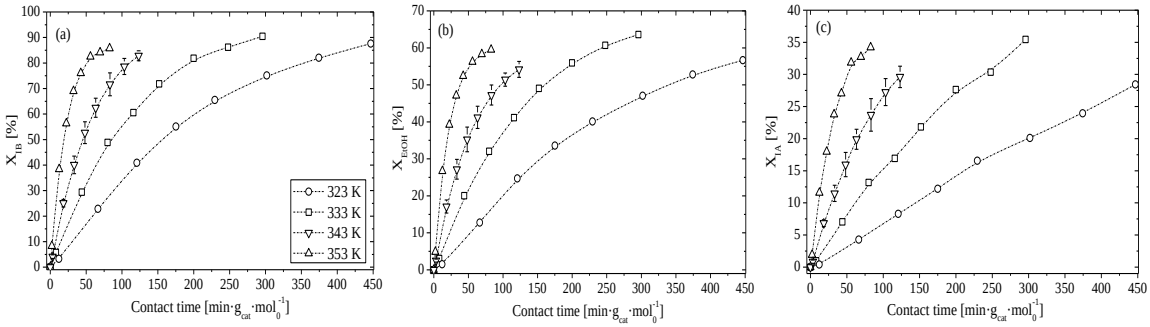

Figure 4.7.5. Reactants conversion vs. contact time for different temperatures at $R°_{A/O}=R°_{C4/C5}=1$. (a) IB, (b) EtOH and (c) IA. Error bars refer to a 95% of probability level.

Olefins selectivity toward their respective ethers were remarkably close to 100%, being the obtained values higher than 99.5% in most of the cases and never lower than 94%. For the sake of evaluating EtOH products, Fig. 4.7.6 illustrates EtOH selectivity vs. X_{EtOH}. It can be seen that curves showed a virtually equal shape at any temperature indicating that EtOH selectivity toward TAEE was increased as EtOH was consumed. Within the range explored, EtOH was notably more selective toward ETBE formation than toward TAEE formation at any rate.

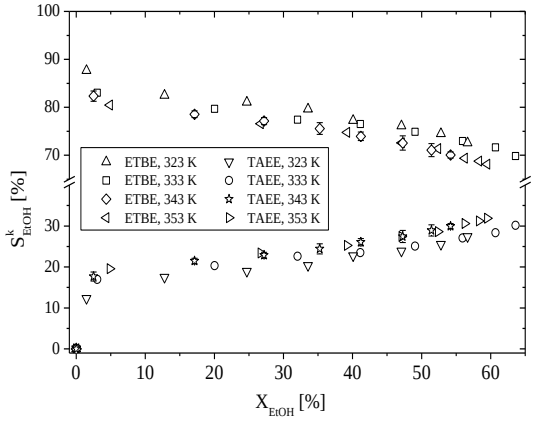

Figure 4.7.6. EtOH selectivity vs. EtOH conversion for different temperatures at $R°_{A/O}=R°_{C4/C5}=1$. Error bars are referred to a 95% of probability level.

4.7.6 KINETIC RESULTS

4.7.6.1 Experimental reaction rates

Initial reaction rates of reactants and products, estimated from Eq. 3.4, are gathered in Table 4.7.1. Initial etherification rates data obtained are in concordance with the experimental values determined for the isolated syntheses of ETBE and TAEE over similar catalysts [49,123,136]. As it can be seen, the lower the temperature, the lower the etherification rates obtained, as expected from the Arrhenius relationship. ETBE production took place readily compared to global formation of TAEE. At $R^o_{A/O}$=1 and $R^o_{C4/C5}$=1, the rate ratio r^0_{ETBE}/r^0_{TAEE} (Table 4.7.1) slightly decreased at increasing temperature, what indicates a higher activation energy for TAEE formation compared to ETBE formation. Estimated r^0_{TAEE} was generally higher than $-r^0_{2M2B}$. As for EtOH initial consumption rate, it is confirmed that it corresponds to the sum of initial formation rates of ETBE and TAEE ($-r^0_{EtOH} = r^0_{ETBE} + r^0_{TAEE}$) within the limits of the experimental error. Fig. 4.7.7 plots the evolution with time of the etherification rates obtained for several temperatures when $R^o_{A/O}$ and $R^o_{C4/C5}$ are both equal to unity.

Table 4.7.1. Experimental reaction rates.

T [K]	$R^o_{A/O}$	$R^o_{C4/C5}$	r^0_{EtOH} [mol·(kg$_{cat}$·h)$^{-1}$]	r^0_{2M2B} [mol·(kg$_{cat}$·h)$^{-1}$]	r^0_{ETBE} [mol·(kg$_{cat}$·h)$^{-1}$]	r^0_{TAEE} [mol·(kg$_{cat}$·h)$^{-1}$]	r^0_{ETBE}/r^0_{TAEE}
323.2	1.00	1.00	–153.9	–21.4	122.4	24.8	4.9
323.0	1.99	0.51	–63.1	–20.0	47.7	19.8	2.4
323.1	0.50	0.49	–125.7	–28.2	75.2	38.0	2.0
323.1	0.50	2.02	–265.3	–17.6	244.4	23.9	10.0
323.7	1.99	2.03	–172.8	–14.1	156.0	14.0	11.1
324.7	1.95	2.04	–192.7	–15.0	158.5	15.5	11.1
335.0	1.10	0.99	–379.4	–50.1	299.5	70.1	4.3
333.7	2.06	0.99	–278.5	–28.5	215.8	45.3	4.8
333.7	0.50	0.98	–619.9	–114.4	482.4	130.9	3.7
342.7	1.97	1.00	–522.0	–82.5	422.8	102.4	4.1
345.1	1.01	0.99	–744.6	–128.6	561.5	146.0	3.9
342.7	1.00	1.01	–650.6	–85.8	527.2	130.5	4.0
342.7	0.99	1.03	–660.6	–96.3	525.6	126.6	4.1
342.8	1.00	2.02	–709.5	–69.7	648.6	74.0	8.8
342.8	0.50	1.00	–928.9	–156.3	682.9	176.3	3.9
343.8	0.99	0.50	–627.0	–161.7	432.9	209.3	2.1
353.2	1.97	0.51	–742.4	–188.1	458.6	261.5	1.8
353.5	1.00	1.02	–1765.5	–285.6	1374.6	368.9	3.7
352.7	1.97	2.01	–1096.7	–76.8	946.2	105.7	9.0
352.8	0.50	2.04	–2486.5	–288.8	2207.8	251.4	8.8
353.8	0.50	0.50	–1807.9	–642.3	1126.6	618.1	1.8

Concerning the effect of EtOH concentration on etherification rates, alcohols, as water, present a moderator or even inhibitory effect at high concentrations on the syntheses of tertiary ethers [120,123]. It can be ascribed to a disruption of the catalyst sulfonic groups network caused by the adsorbed alcohol molecules, which results in a slower mechanism than a concerted mechanism by totally undissociated sulfonic groups. TAEE formation was slightly more affected by $R^o_{A/O}$ than ETBE, which is in concordance with the results obtained for water in *Section 4.5*. At constant $R^o_{C4/C5}$=1 and 343 K, the ratio r^0_{ETBE}/r^0_{TAEE} scarcely varied from 3.9 to 4.1 on increasing $R^o_{A/O}$ from 0.5 to 2 (Table 4.7.1). Focusing on the effect of olefins concentration on etherification rates at constant $R^o_{A/O}$, the higher the $R^o_{C4/C5}$, the higher the estimated r^0_{ETBE}. Accordingly, the analogous effect was observed between the initial IA

concentration and r^0_{TAEE}. Concerning the rate ratio r^0_{ETBE}/r^0_{TAEE} at 343 K and $R^o_{A/O}$=1, it decreased from 8.8 to 2.1 on decreasing $R^o_{C4/C5}$ from 2 to 0.5. These facts enforce the statement that olefins concentration presents a global positive kinetic order in etherification, whereas alcohol concentration presents a negative or close to zero kinetic order, in agreement with literature [120,136].

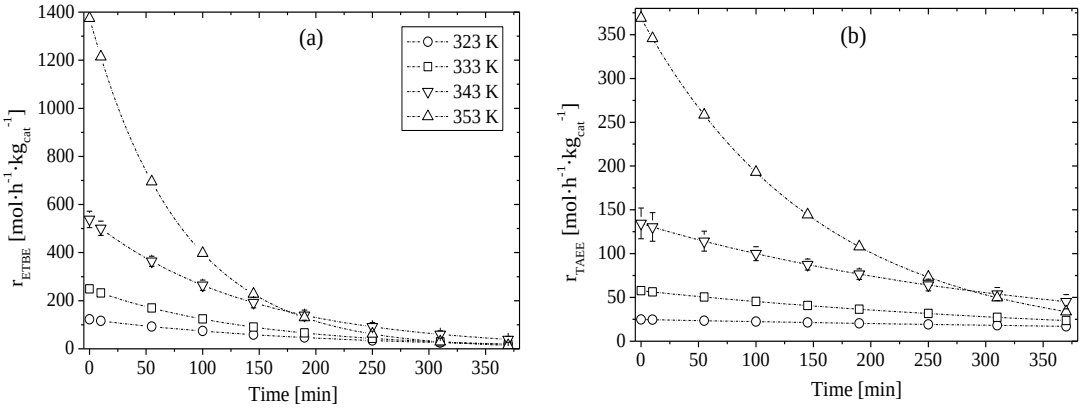

Figure 4.7.7. Evolution of (a) r_{ETBE} and (b) r_{TAEE} with temperature. $R^o_{A/O}$=1, $R^o_{C4/C5}$=1. Error bars refer to 95% confidence level for replicated experiments. Dashed lines are guides to the eye.

4.7.6.2 Empirical and power function kinetic modeling

Prior to model the kinetic results based on mechanistic approaches, initial reaction rates from Table 4.7.1 were modeled using power function laws and the RSM.

For obtaining the power function models (Eq. 4.7.2), the relative sum of squares (*RSS*) was used to minimize the differences between experimental and calculated initial reaction rates. Table 4.7.2 gathers the results obtained for the parameters in Eq. 4.7.2 and the associated error with their estimation. Fig. 4.7.8 show the parity plot between experimental and calculated values, where it can be seen that power function models fit experimental data in a remarkable good fashion.

Table 4.7.2. Estimated parameter values and associated standard error obtained in the power function modeling.

Parameter	ETBE	TAEE
$A_i \cdot 10^{-14}$ (mol·h^{-1}·kg^{-1})	2.08±0.06	1.10±0.03
$E'_{a,i}$ [kJ/mol]	72.15±0.08	73.41±0.08
$k_{A,i}$	-0.13±0.03	0.016±0.002
$k_{O,i}$	1.02±0.02	1.15±0.02
RSS	0.017	0.019
R^2	0.984	0.982

A_i values obtained, related to the pre-exponential factor with explicit kinetic meaning for each reaction, are comparable to those determined for the isolated synthesis of ETBE and TAEE in previous studies [48]. Concerning the values determined for the constants k_{xA} and k_{xO}, the pseudo kinetic order of alcohol in both etherification reactions is close to zero. Conversely, the kinetic pseudo-order of the olefins, IB and IA, is approximately the unity in the respective syntheses of ETBE and TAEE. Similar kinetic pseudo-orders were obtained in the isolated synthesis of TAEE from IA and EtOH [136] and in the addition of MeOH/BuOH to IB [120], which reinforce the results of this work.

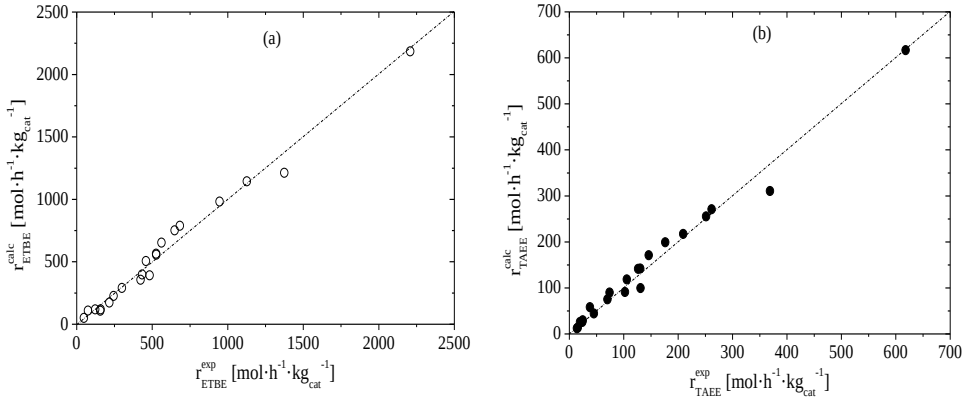

Figure 4.7.8. Calculated values vs. experimental values for: (a) r^0_{ETBE} and (b) r^0_{TAEE}.

Some parallelisms can be inferred from power function models in order to get information on the terms that a reliable mechanistic hyperbolic model should comprise. Zero kinetic pseudo-order with respect to one reactant means that such reactant should be included in both driving force and adsorption term of LHHW equations. Positive pseudo-orders represent that such compound should be included only in the driving force term and probably in the apparent kinetic constant. On the contrary, negative pseudo-orders mean that such compound should be included only in the adsorption term. Depending on the absolute value of the exponent obtained for the molar fraction of each compound we can draw some conclusions about the number of active sites and whether it is present in both the driving force term and the adsorption term of LHHW equations. Based on results from Table 4.7.2, IB concentration should be included only in the driving force term for ETBE mechanism and analogously IA should form part only in the driving force term for the mechanism proposed for TAEE formation. With respect to EtOH, the results obtained for both ethers suggest that it should be included in both the driving force and adsorption terms of the postulated mechanistic equations. Additionally, these kinetic pseudo-orders support the assumption that surface reaction is the rate-limiting step followed in most of kinetic studies [136].

Initial etherification rates obtained in the present work have also been modeled using the RSM. The working temperature, x_A and $x_{C4/C5}$ (molar fraction of IB in the olefins mixture) were chosen as the experimental variables to be included for the empirical modeling in order to center the experimental design. Other criteria such as fitting activities instead of concentrations could be used, but it was opted for modeling the raw data in order to obtain simple empirical equations able to predict rate data avoiding further transformation of experimental variables. The stepwise regression procedure [170] was used to reduce the number of variables from Eq. 4.7.1 to the minimum statistically significant. The significance of the parameters was evaluated by its *p*-value and the significance of the regression itself by means of the test of Fisher (F-value). The obtained empirical models comprise five variables and the intercept for both ETBE and TAEE. Table 4.7.3 shows the analysis results in terms of coded variables for the full second order polynomial and Table 4.7.4 the analogous results after removing of non-significant variables. The analysis of variance (ANOVA) revealed that these models were adequate to explain the response variation with large adjusted R^2 values of 0.981 and 0.986 for ETBE and TAEE, respectively. The experimental vs. predicted values parity graph also confirmed the goodness of the fitting and the graphical plotting of the residuals confirmed their randomness, see Fig. 4.7.9.

Table 4.7.3. Results obtained for the fitting of the second order polynomial in terms of coded variables before removing non-significant variables.

Terms	ETBE			TAEE		
	Coefficients	*p*-value	Error	Coefficients	*p*-value	Error
β_0	5.990	$5.7\cdot10^{-18}$	0.0558	4.5653	$1.21\cdot10^{-16}$	0.0562
β_1 (T)	1.1461	$2.01\cdot10^{-11}$	0.0423	1.2530	$8.24\cdot10^{-12}$	0.0426
β_2 (x_A)	-0.3414	$3.25\cdot10^{-6}$	0.0397	-0.38	$1.24\cdot10^{-6}$	0.04
β_3 ($x_{C4/C5}$)	0.4446	$5.28\cdot10^{-7}$	0.043	-0.3442	$6.93\cdot10^{-6}$	0.0433
β_{11} (T^2)	-0.0441	0.64	0.09	-0.0561	0.55	0.0911
β_{22} (x_A^2)	0.0282	0.71	0.0731	0.0413	0.56	0.0736
β_{33} ($x_{C4/C5}^2$)	-0.1612	0.07	0.081	-0.1691	0.03	0.0814
β_{12} ($T\cdot x_A$)	-0.0771	0.14	0.0487	0.0203	0.39	0.0491
β_{13} ($T\cdot x_{C4/C5}$)	-0.115	0.038	0.049	-0.1216	0.03	0.0489
β_{23} ($x_A\cdot x_{C4/C5}$)	0.00023	1	0.049	0.00076	0.88	0.04933
R^2 adjusted			0.979			0.983
Model F-value			106.53			134.46
Critical F-value			$2.1\cdot10^{-9}$			$5.94\cdot10^{-10}$

Table 4.7.4. Results obtained for the fitting of the second order polynomial in terms of coded variables after removing no significant terms by stepwise regression procedure.

Terms	ETBE			TAEE		
	Coefficient	*p*-value	Error	Coefficient	*p*-value	Error
β_0	5.9896	$6.07\cdot10^{-25}$	0.0418	4.5663	$1.76\cdot10^{-23}$	0.0399
β_1 (T)	1.1456	$1.5\cdot10^{-14}$	0.0397	1.2524	$2.02\cdot10^{-15}$	0.0379
β_2 (x_A)	-0.3369	$2.27\cdot10^{-7}$	0.0379	-0.3772	$2.83\cdot10^{-8}$	0.0361
β_3 ($x_{C4/C5}$)	0.4506	$1.47\cdot10^{-8}$	0.0411	-0.3396	$3.22\cdot10^{-7}$	0.0392
β_{13} ($T\cdot x_{C4/C5}$)	-0.1205	0.02	0.0464	-0.1254	0.013	0.0443
β_{33}($x^2_{C4/C5}$)	-0.1693	0.01	0.0604	-0.21235	0.002	0.058
R^2 adjusted	0.981			0.986		
Model F-value	206.64			290.88		
Critical F-value	$2.8\cdot10^{-13}$			$2.24\cdot10^{-14}$		

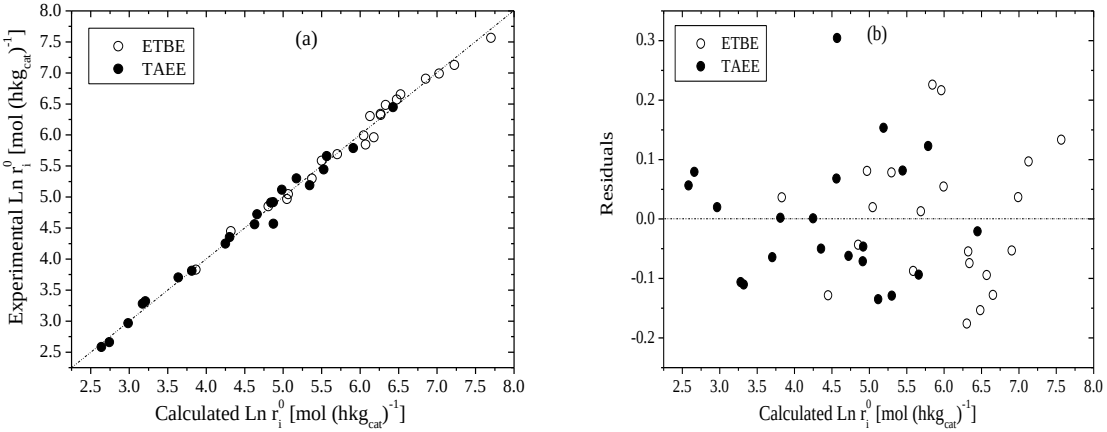

Figure 4.7.9. (a) Predicted values vs. experimental values for ln r^0_{ETBE} and ln r^0_{TAEE}.
(b) Residuals vs. predicted values of ln r^0_{ETBE} and ln r^0_{TAEE}.

Coded values from Table 4.7.4 are useful to compare the factor coefficients and identify their relative impact on the rate responses. The significant terms of the selected equations coincided for both ETBE and TAEE formation reactions (see Eqs. 4.7.3 and 4.7.4). That can be expected because both ethers are formed through similar chemical pathways. Results suggest a positive effect of the temperature (T), the molar fraction of the olefins mixture ($x_{C4/C5}$) and the alcohol (x_A), the quadratic effect of $x^2_{C4/C5}$ and the interaction effects of $T \cdot x_{C4/C5}$ and $T \cdot x_A$. The term $T \cdot x_A$ was significant only for ETBE formation. A sensitivity analysis revealed that the most important contributions to r^0_{ETBE} are caused by temperature and $x_{C4/C5}$ (in this order) whereas the main factor which decreases r^0_{ETBE} is x_A. Accordingly, r^0_{TAEE} is enhanced by temperature and notably decreased on increasing $x_{C4/C5}$ and x_A. The best model corresponds to an expression with the lowest number of terms in which all parameters and the regression itself are statistically significant within a 95% confidence level.

$$\ln r^0_{ETBE}\left[\text{mol}\cdot\left(\text{kg}_{cat}\cdot\text{h}\right)^{-1}\right] = -28.69 + 0.0973\cdot T - 1.98\cdot x_A + 23.89\cdot x_{C4/C5} - 0.0457\cdot T\cdot x_{C4/C5} - 5.78\cdot x^2_{C4/C5} \quad (4.7.3)$$

$$\ln r^0_{TAEE}\left[\text{mol}\cdot\left(\text{kg}_{cat}\cdot\text{h}\right)^{-1}\right] = -30.71 + 0.1051\cdot T - 2.22\cdot x_A + 21.37\cdot x_{C4/C5} - 0.0475\cdot T\cdot x_{C4/C5} - 7.25\cdot x^2_{C4/C5} \quad (4.7.4)$$

The goodness of the fitting is also illustrated in Fig. 4.7.10, where the experimental rate data are plotted together with the values obtained from empirical equations (surfaces). As it can be seen, the quality of the fitting was acceptable within the experimental range studied. Besides, it can be observed that the effect of x_A at lower temperatures is almost linear whereas at high temperatures the effect of x_A becomes exponential-like and more pronounced. The effect of $x_{C4/C5}$ on initial etherification rates is also more noticeable at high temperatures.

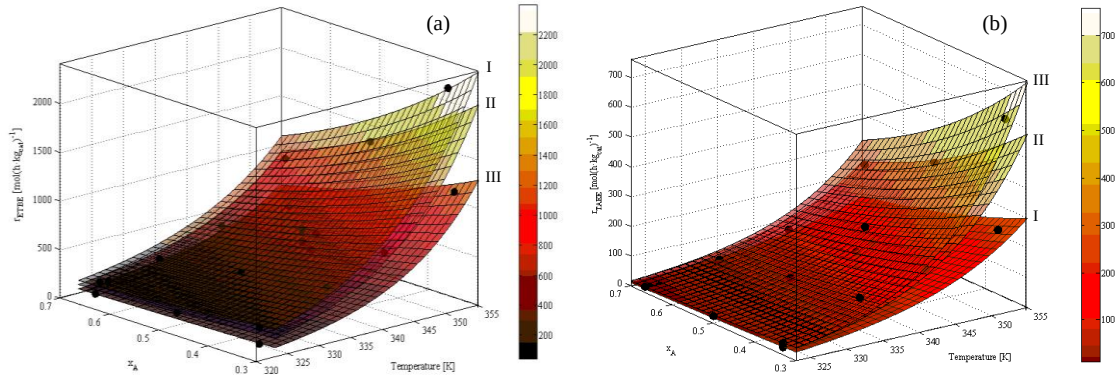

Figure 4.7.10. Experimental data (●) and response surfaces obtained for: (a) r^0_{ETBE} and (b) r^0_{TAEE}. I, II and III refer to the surface corresponding to $x_{C4/C5}$ values of 0.667, 0.500 and 0.333, respectively.

At this point, RSM is helpful to draw some kinetic inferences about the effect of reactants concentration in LHHW/ER-type rate equations. To stablish a parallelism between empirical equations obtained and classical formalisms of LHHW/RE a similar procedure to that outlined by Tejero et al. 1989 [211] was follow. Despite non-ideal systems are known to be described more reliably when concentrations are expressed in terms of activities of compounds, it was assumed that the qualitative effect of molar fractions will be the same of activities. Under differential conditions and far from equilibrium, a term with a positive sign represents an enhancing effect on the rate and therefore it is likely to be influencing the driving force term of a LHHW equation. On the contrary, a term with only negative sign has a decreasing effect on

the rate and it is foreseeable to influence the adsorption term in a LHHW equation. The evaluation of the interaction effects must be cautiously done since it can lead to misleading conclusions. For instance, for the evaluation of the overall effect of $x_{C4/C5}$, we considered the direct effect of the term $x_{C4/C5}$ and those related to the terms $T \cdot x_{C4/C5}$ and $x^2_{C4/C5}$ by means of a sensitivity analysis.

Following the described analysis procedure, the alcohol concentration showed to inhibit both etherification reactions. Therefore, the inclusion of the adsorption equilibrium constant of EtOH is expected in the adsorption term of LHHW/ER equations for both ETBE and TAEE formations. Moreover, an almost constant relation between x_A and etherification rates was revealed at low temperatures, which suggest a zero order with respect to the alcohol concentration, in agreement with the results obtained from power function modeling.

Concerning the global effect of $x_{C4/C5}$, r^0_{ETBE} increases on increasing $x_{C4/C5}$ while it produces the opposite effect on r^0_{TAEE}. Since active centers are chemically equivalent [106] it is assumed that adsorption of reactants is competitive. According to the above mentioned criteria, IB participation is expected in the driving force of LHHW equation for ETBE synthesis but also in the adsorption term. Since the quadratic effect of $x^2_{C4/C5}$ was significant for both ethers formation with a negative value, it can be concluded that IB, IA, ETBE or TAEE adsorption equilibrium constants presence in the adsorption term of LHHW/ER equations is expected to take into account the relative occupancy of active sites. That is to say, account for the active sites forming ETBE and those forming TAEE, in the simultaneous synthesis for both ethers.

Furthermore, adsorption is presumably taking place in more than one active center according to exponent value of $x_{C4/C5}$ in Eqs. 4.7.3 and 4.7.4. Thus, exponents higher than unity should be expected in the adsorption term of hyperbolic equations describing the simultaneous etherification system. These results are in agreement with some previous studies concerning the MTBE and ETBE formation from IB and MeOH or EtOH [123,211].

As partial conclusion from the results obtained from power function and RSM modeling, it can be inferred that both methodologies fitted excellently to experimental initial reaction rates. Such a smooth difference in the fitting goodness does not provide unbiased criteria to give priority to one of the modeling procedures obtained. Both RSM and power function models are able to describe the experimental reality and are a very useful tool for easily estimating the expected rates in the simultaneous synthesis of ETBE and TAEE. The kinetic inferences obtained from both methodologies can be helpful when selecting among plausible hyperbolic models. For instance, both methodologies suggest that alcohol concentration should be included in the adsorption term of mechanistic-based kinetic equations.

One major limitation of these modeling procedures is that they can be only applied trustingly within the assayed range of experimental conditions. Based on the obtained results, kinetic data obtained seem to be reliable to start the mechanistic modeling using equations based on the LHHW and RE formalisms. Mechanistic based models allow to obtain more information on adsorption equilibrium constants and adsorption related thermodynamic properties of the species showing significant adsorption. Moreover, hyperbolic models also provide more accurate information about kinetic coefficients and the possible mechanism occurring in the catalytic surface.

4.7.6.3 Mechanistic modeling

4.7.6.3.1 Kinetic equations

A systematic methodology for evaluating the fitting of the kinetic equations based on the LHHW and RE formalisms was applied to the present study. All kinetic expressions evaluated for each reaction *i* were constructed according to the general form described by Eq. 4.7.5. The kinetic term comprises the kinetic constant of reaction *i*, and it can include some adsorption equilibrium constant depending on the reaction mechanism; the driving force accounts for the distance to the chemical equilibrium; the adsorption term refers to the relative occupancy of the active sites by the adsorbed compounds; the resin-medium affinity term accounts for the interaction of the catalyst with the reaction medium; and *n* refers to the number of active sites or clusters of active sites that participate in the rate-controlling step of the proposed mechanism.

$$r_i = \frac{\{\text{Kinetic term}\}_i \cdot \{\text{Driving force}\}_i \cdot \{\text{Resin-medium affinity}\}}{\{\text{Adsorption term}\}^{n_i}} \tag{4.7.5}$$

In the LHHW and RE formalisms, the kinetic term corresponds to the product of the intrinsic kinetic constant, the total concentration of active sites and, depending on the mechanism, some adsorption equilibrium constants of the adsorbed species. All constants can be grouped in an apparent rate coefficient, k_i, for each reaction *i*.

The driving force of reaction *i*, is defined by Eq. 4.7.6, where a_j is the activity of compound *j*, ν_{ij} is the stoichiometric coefficient of the species *j* in reaction *i*, and K_i is the equilibrium constant of reaction *i*. Values of K_i have been taken from *Section 4.4*, see Eqs. 4.4.5–4.4.8.

$$\{\text{Driving force}\}_i = \left(\prod_{j=1}^{\text{reactants}} a_j^{\nu_{ij}} - \frac{\prod_{j=1}^{\text{products}} a_j^{\nu_{ij}}}{K_i} \right) \tag{4.7.6}$$

The adsorption of reactants and desorption of products was supposed to be fast compared to surface reaction. Hence, the surface reaction was assumed as the rate-determining step. The use of activities instead of concentrations for non-ideal reaction mixtures in mechanistic expressions has been widely accepted. Activities of involved compounds in the reaction medium were estimated by means of the UNIFAC-Dortmund predictive method [176–178].

The adsorption term accounts for the relative occupancy of the catalyst active centers by the different adsorbed species and, therefore, it should be the same irrespectively of the considered reaction *i*. This term is expressed by Eq. 4.7.7, where K_j is the liquid-phase adsorption equilibrium constant of compound *j*, a_j is the activity of compound *j*, and *S* is the number of adsorbed species. Since compound activities are those of the liquid bulk phase, adsorption equilibrium constants in the kinetic equations describe the global effect of both the actual surface adsorption equilibrium constant, and the possible partition or distribution of involved species between the bulk phase and within the catalyst pores. The parameter α takes the value of 1 or 0, depending on whether the fraction of unoccupied active sites is considered as significant or not, respectively. The exponent of the adsorption term n_i has been considered to be equal to 1, 2, or 3, since these are the more plausible values [148,180].

$$\{\text{Adsorption term}\} = \alpha + \sum_{j=1}^{S} K_j \cdot a_j \qquad (4.7.7)$$

An additional factor that can affect kinetics is the affinity between the reaction medium and the resin. As detailed in *Section 1.5*, A-35 consists of a flexible polymeric matrix where sulfonic groups are anchored. Since it is a non-rigid structure, its conformation can change depending on the physico-chemical nature and composition of the reaction medium, leading to different swelling degree along the reaction time, because the reaction medium composition progressively changes. A more open resin backbone can enhance accessibility to inner active sites, and therefore the global catalytic activity of resin beads. This effect should be included in the kinetic equation, splitted from the kinetic constant, which should not be composition dependent. The resin–medium affinity factor ψ, defined by the following expression, can account for this effect:

$$\{\text{Resin-medium affinity}\} = \psi = \exp\left(\frac{\overline{V_m}\ \phi_p^2}{RT} \left(\delta_m - \delta_p\right)^2 \right) \qquad (4.7.8)$$

The inclusion of ψ in the kinetic equation has been proved to enhance the prediction of the reaction rates for similar systems [49,144]. In Eq. 4.7.8, $\overline{V_m}$ is the mixture molar volume, estimated by the Hankinson-Brobst-Thomson (HBT) method [212], see *Appendix 7.10.1*. ϕ_p is the catalyst porosity in the reaction medium, whose value has been taken as 0.5132 for A-35, determined by Inverse Exclusion Steric Chromatography (ISEC) in water [151]. δ_m and δ_p are the Hildebrand solubility parameter of the liquid mixture and the catalyst, respectively. The value of δ_m depends on the reaction medium composition and temperature, and it can be calculated by means of the following expression [213] :

$$\delta_m = \sum_j \Phi_j \cdot \delta_j = \sum_j \Phi_j \sqrt{\frac{\Delta_v H_j^{\circ} - RT}{\overline{V_j}}} \qquad (4.7.9)$$

where Φ_j is the volume fraction of every compound *j* present in the reaction medium, with solubility parameter δ_j, $\Delta_v H^o_j$ is its molar enthalpy of vaporization, estimated at the run temperature by the methodology described in Yaws et al. [214], and $\overline{V_j}$ is its liquid molar volume in the medium, estimated by the HBT method.

It is to be noted that, in the search of the best kinetic equations, to include the possible case where the resin-medium interaction effect on kinetics is not significant, combinations with the term ψ equal to unity were also considered.

The estimated individual solubility parameters (δ_j) of involved compounds by means of Eq. 4.7.9 are depicted in Fig. 4.7.11a. These values are in good agreement with those determined by Fité et al. [144] and by Cruz et al. [107], for IB and EtOH, respectively. With respect to the liquid mixture, it was found that δ_m varied from 12.8 to 20.0 $MPa^{1/2}$ within the whole range of compositions for all the runs. As it can be observed in Fig. 4.7.11a, the variation of Hildebrand solubility parameter of compounds follows a virtually linear relationship with temperature. The changes of molar volumes of involved compounds ($\overline{V_j}$) in the range of

temperature explored are depicted in Fig. 4.7.11b. The molar volume of compounds increased with temperature. EtOH is the compound with the lowest molar volume in the present system whereas ETBE and TAEE are the compounds with the largest molar volumes. The molar volume of the reaction mixture ($\overline{V}_m$) was found to vary from 0.07 to 0.13 L mol^{-1} in all the experiments of this work.

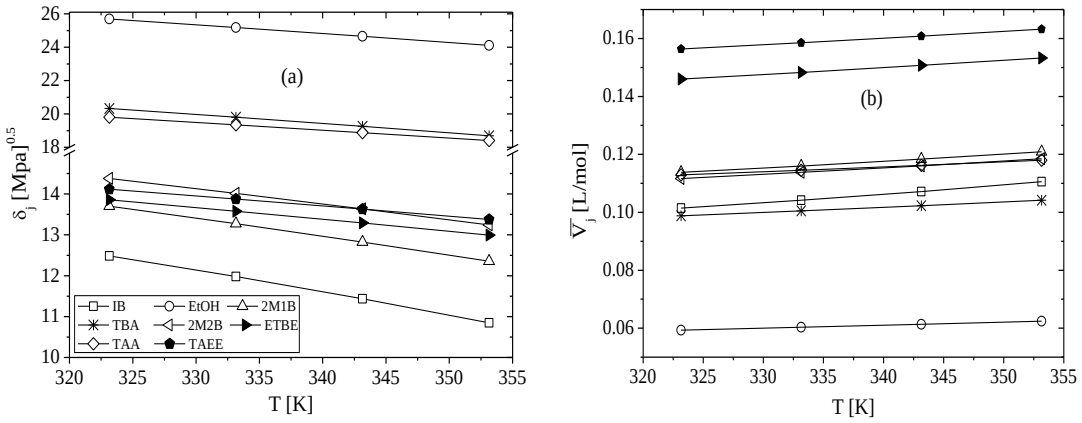

Figure 4.7.11. (a) Individual solubility parameter (δ_j) for involved compounds vs. temperature. (b) Variation of molar volume of involved compounds with temperature.

4.7.6.3.2 Temperature dependence of the parameters

The experimental runs have been carried out at different temperatures. Therefore, the parameters appearing in the kinetic equations have been expressed as a function of the temperature.

The adsorption equilibrium constant of species *j*, K_j, is expected to follow the van't Hoff equation. Accordingly, the relation indicated in Eq. 4.7.10 has been considered. Parameters $K_{1,j}$ and $K_{T,j}$ are directly related to the adsorption entropy, $\Delta_{ads}S°_j$, and enthalpy, $\Delta_{ads}H°_j$, of compound *j* onto the active sites of the catalyst, respectively. These thermodynamic properties have been considered as constant, because of the relatively narrow studied temperature range, and the large number of the fitted parameters in the kinetic equations, whose crosscorrelation would mask a possible temperature effect. The inverse of the mean temperature, $\overline{T}$, has been included to reduce the correlation between $K_{1,j}$ and $K_{T,j}$ in the fitting procedure, its value being 338.4 K.

$$K_j = \exp\left(\frac{\Delta_{ads}S°_j}{R} - \frac{\Delta_{ads}H°_j}{R}\left(\frac{1}{T} - \frac{1}{\overline{T}}\right)\right) = \exp\left(K_{1,j} + K_{T,j}\left(\frac{1}{T} - \frac{1}{\overline{T}}\right)\right) \qquad (4.7.10)$$

As for the kinetic term, k_i, by considering that the intrinsic kinetic constant follows the Arrhenius law and the temperature dependence of the equilibrium adsorption constants (Eq. 4.7.10), it can be expressed by Eq. 4.7.11. Again, the inverse of the mean temperature, $\overline{T}$, was included to reduce the correlation between $k_{1,i}$ and $k_{T,i}$.

$$k_i = \exp\left(k_{1,i} + k_{T,i}\left(\frac{1}{T} - \frac{1}{\overline{T}}\right)\right) \qquad (4.7.11)$$

In the resin-medium affinity term, the unknown parameter is the resin solubility parameter, δ_p. It has been reported that it follows a linear dependence with temperature in the assayed temperature range [14], and similarly to the solubility parameter dependency of pure species. Therefore, the following linear relation has been considered:

$$\delta_p = k_{D1} + k_{DT}\left(T - \overline{T}\right) \qquad (4.7.12)$$

Apart from using Eq. 4.7.12, the solubility parameter of Amberlyst™35 was also estimated at 298 K by means of the group contribution method described in Matsuura [215] with a result of 25.62 $MPa^{1/2}$. Then, it can be expected that EtOH should be the compound with the highest affinity for the resin since the difference (δ_{EtOH} - δ_p) is the smallest observed among all involved chemical species.

4.7.6.3.3 Proposed kinetic models

A kinetic model consists of a set of rate equations, being one per each reaction taking place, and consistent with the form indicated previously. Since reactions occur simultaneously on the same catalyst, the rate equations of a kinetic model have to present some common characteristics. The following assumptions have been applied for the different rate equations of a kinetic model:

i) For each reaction *i*, both parameters of the apparent kinetic constant, $k_{1,i}$ and $k_{T,i}$ (Eq. 4.7.11), have to be fitted, because the evolution of the reaction medium composition is highly temperature sensitive.

ii) The adsorption term is the same for all reactions, because it depends only on the reaction medium composition and temperature. The fraction of unoccupied sites could be significant (α=1) or not (α=0). The contribution of the adsorption of a given species *j* could be significant ($K_j \neq 0$) or non–significant (K_j=0); if significant, $K_{1,j} \neq 0$, and its temperature dependence could be relevant ($K_{T,j} \neq 0$) or not ($K_{T,j}$=0).

iii) The resin-medium affinity factor is the same for the kinetic equation of every reaction, because it would affect equally to catalyst activity. It could be significant ($\psi \neq 1$) or non-significant (ψ=1); if significant ($k_{D1} \neq 0$), the resin solubility parameter could be temperature sensitive ($k_{DT} \neq 0$) or non-sensitive (k_{DT}=0).

iv) Since the etherification reactions R1, R2, and R3 differ only on the olefin added to EtOH, the most plausible situation is that they proceed through the same mechanism, that is, the number of active sites participating in the rate-determining step, n_i, is the same. The isomerization reaction (R4) could involve a different number of active sites.

Consequently, the proposed kinetic models consist of all different combinations of equations 4.7.5 to 4.7.12 that fulfill the previous assumptions.

4.7.6.3.4 Multi-objective nonlinear least squares minimization

The estimation of the parameter values can be carried out by minimization of the sum of residual squares between experimental (r_i^{exp}) and calculated (r_i^{calc}) reaction rates for each

reaction *i* (RSS_i). The desired goal is to obtain a simultaneous good fit for all reactions, that is, to minimize all RSS_i. This constitutes a multi-objective optimization problem. The proposed objective function was the total weighted sum of residual squares (*TWRSS*) defined by Eq. 4.7.13, by selecting appropriate scalar weights, w_i.

$$TWRSS = \sum_{i=1}^{r} w_i \cdot RSS_i = \sum_{i=1}^{r} w_i \left(r_i^{\exp} - r_i^{calc} \right)^2 \qquad (4.7.13)$$

It can be difficult to discern how to set the weights for compensating the differences in individual objective function magnitudes (RSS_i), because measured reaction rates differ from one reaction to other. If w_i=1 is selected, that is equal importance for all responses, the obtained solution fits relatively better for large reaction rate values; if $w_i=1/(r_i^{exp})^2$, the procedure gives priority to the fitting of low reaction rates. However, if each objective function is divided by their respective maxima, objective functions are normalized between zero and one and then similar importance can be given to all objective functions minimized [216]. Consequently, the selected weights were $w_i=1/(r^{exp}{}_{i,max})^2$. A MATLAB script that applies the Levenberg-Marquardt method [217] was developed to estimate the kinetic parameters by minimizing *TWRSS*.

4.8.6.3.5 Criteria for model selection and model averaging

A suitable model has to predict accurately the experimental evolution of the composition of reaction medium in every single experimental run, all included parameters being relevant, and the estimated parameter values must present coherent thermodynamic and kinetic meaning. To discriminate among the different kinetic models, several criteria have been adopted, where a model is rejected if the fitted parameter values, or their estimated error, falls outside of a certain range. The considered ranges have been taken as very wide to be conservative, mainly to avoid the wrong rejection of a good candidate model, because the fit of reaction rates equations is a clearly nonlinear problem and, therefore, parameters can be highly crosscorrelated and non-normally distributed.

The first applied criterion was purely mathematic: models that present at least one fitted parameter with an estimated error larger than 3-fold its parameter value were directly rejected, because it indicates that the effect of the parameter is very likely non-significant. The parameter error value has been estimated as the square root of the diagonal elements from the covariance matrix of parameter estimates.

Parameters $K_{1,j}$ and $K_{T,j}$ are related to adsorption enthalpy and entropy of species *j* on the catalyst (Eq. 4.7.10). For a candidate model, their values, and taking into account the parameter uncertainty, have to be fulfill the Boudart rules [112,113]. These rules have been detailed in *Section 1.5.7*.

With respect to the apparent kinetic constant, the $k_{T,i}$ parameter (Eq. 4.7.11) is related to the apparent activation energy: $k_{T,i} = -E'_{a,i}/R$. Kinetic models where the obtained apparent activation energy for at least one reaction was either larger than 300 kJ/mol (an extremely large value for R1-R4 reactions [48]), or negative, were discarded.

The traditional approach to choose the best model is to select the one providing the highest prediction ability of experimental data with the lower number of parameters. But this approach

ignores uncertainty in model selection. Several models can describe experimental data satisfactorily and it is hard to discriminate among them to find the true model, because the models ranked in the group of best models are expected to be similar, and the experimental error can mask which is the true model. The concept of model averaging stems for the choice of a weighted average of the estimates obtained for the group of candidate models, as being more representative of the true values, rather than the choice of the particular estimates obtained for a selected model. The candidate models are those that present coherent thermodynamical meaning of the parameters and with lower deviation with respect experimental data. For this group composed of *M* candidate kinetic models, several criteria can be applied for model selection and averaging, such as the Akaike Information Criterion (AIC) and Bayesian Information Criterion (BIC) [205–210]. AIC and BIC are useful for penalizing overparameterized models. The Akaike Information Criterion (AIC) coefficient can be calculated for each model by the following equation [208]:

$$AIC = N \cdot \ln\left(\frac{TWRSS}{N}\right) + 2(p+1) + \frac{2(p+1)(p+2)}{N-p-2} \tag{4.7.14}$$

where N is the number of considered experimental values, and p is the number of parameters. In order to compare among candidate models, the delta AIC (Δ_m) and the Akaike weights (AW_m) for each model m are used:

$$\Delta_m = AIC_m - minAIC \tag{4.7.15}$$

$$AW_m = \frac{\exp(-\Delta_m/2)}{\sum_{m=1}^{M}\exp(-\Delta_m/2)} \tag{4.7.16}$$

where *minAIC* is the minimum value of the AIC for the set M of models selected.

The lower the Δ_m value, the more likely model m is the best model [208]. The Akaike weights indicate the probability of a model m to be the best among the group of M selected models. The sum of Akaike weights for the group of candidate models is equal to unity. Finally, natural model averaging [205,206,210] can be applied to the candidate models to calculate the weighted average of each parameter, θ, by means of the following equation:

$$\theta = \sum_{m=1}^{M} AW_m \theta_m \tag{4.7.17}$$

where θ_m is the value of the parameter estimate for model m from the group of M selected models.

4.7.6.3.6 Modeling results

Considering all the possible variations for each term of general Eq. 4.7.5, a total of 3,076 possible combinations (models) were obtained for each n (1, 2 or 3), which results in a total of 9,228 kinetic models. These combinations can be divided into two different sets or families of models: those that consider the fraction of free active sites significant (set I) and those that consider almost saturated the catalytic surface (set II). Table 4.7.5 shows the complete form of rate equations for these two sets. K'_k and k'_i for equations in set II are, in fact, K_k/K_j and k_i/K_j, respectively.

Table 4.7.5. General form of the considered reaction rate equations. Subscript *i* refer to the chemical reaction, and *j* and *k* to all chemical species adsorbed on the resin active sites.

Set	I	II
Rate equation	$r_i = \dfrac{k_i \left\{ Driving\ force \right\}_i \psi}{\left(1 + \sum_j K_j a_j \right)^n}$	$r_i = \dfrac{k'_i \left\{ Driving\ force \right\}_i \psi}{\left(a_j + \sum_{k \neq j} K'_k a_k \right)^n}$

It was found that the simultaneous fit of r_{R1}, r_{R2}, r_{R3} and r_{R4} was unachievable to perform, because of the extremely large error obtained for the estimates of the isoamylenes isomerization reaction (R4). This can be attributed to the proximity of the IA mixture to the isomerization equilibrium along the experimental runs. Therefore, the variation of the relative amounts between 2M1B and 2M2B during the runs was very low, what did not enable the simultaneous estimation of all the reactions studied. A similar drawback had been observed by Linnekoski et al. [91] and by Rihko et al. [90] in the kinetic modeling of the etherification of IA with EtOH and MeOH, respectively. Due to the low progress of the isomerization reaction, only r_{R1}, r_{R2} and r_{R3} were considered in the simultaneous fitting procedure. The results obtained after such decision confirmed the correct optimization and estimation of parameters for the fitted kinetic models.

It has been reported that the fraction of free active sites (α=1) is only relevant for alcohol molar fractions lower than 0.04 [48]. In the present work, EtOH concentration was higher. However, models from set I were not discarded to verify this assumption. Indeed, results showed that Boudart rules were not fulfilled for most of the models from set I, because positive values for the enthalpy of adsorption of involved compounds were obtained. Where Boudart rules were fulfilled, the values of *TWRSS* were considerably larger than those obtained for models from set II (α=0). As a consequence, it can be assumed that the fraction of unoccupied active sites is very low and, therefore, equations of set II are more appropriate to describe the reaction system. The obtained values of estimates for the first five ranked best models are gathered in Tables 4.7.6, 4.7.7 and 4.7.8 for *n*=1, 2 and 3, respectively. All models in these tables belong to set II equations, with the common characteristic that the first summand of the adsorption term, which is not accompanied by a parameter to be fitted, is the ethanol activity, a_{EtOH}. They provided a good fit, with thermodynamic coherence of the parameter estimates and with a low associated error. A more detailed compilation of the ranking of candidate models obtained for the different *n* evaluated and the parameters estimated is included in *Appendix 7.11*.

Table 4.7.6. Estimated parameter values for the first five best models ranked with *n*=1.

Model	$k'_{1,R1}$	$k'_{T,R1}$	$k'_{1,R2}$	$k'_{T,R2}$	$k'_{1,R3}$	$k'_{T,R3}$	k_{D1}	k_{DT}	$K'_{1,ETBE}$	$K'_{T,ETBE}$	$K'_{1,TAEE}$	$K'_{T,TAEE}$	TWRSS	AIC
203	6.46	–8954	6.93	–9457	4.59	–9775	23.71	–	0.53	–5139	–	–	0.26	–1193
500	6.47	–8958	7.01	–9781	4.55	–9583	23.68	–	0.41	–5610	–0.41	–	0.26	–1192
104	6.51	–8459	7.03	–7031	4.66	–9849	23.71	–	1.01	–	–	–	0.28	–1185
401	6.51	–8459	7.14	–7236	4.59	–9969	23.67	–	0.94	–	–0.42	–	0.28	–1183
105	6.44	–9119	6.95	–8020	4.59	–10366	24.26	–0.04	1.02	–	–	–	0.28	–1183

Table 4.7.7. Estimated parameter values for the first five best models ranked with *n*=2.

Model	$k'_{1,R1}$	$k'_{T,R1}$	$k'_{1,R2}$	$k'_{T,R2}$	$k'_{1,R3}$	$k'_{T,R3}$	k_{D1}	k_{DT}	$K'_{1,ETBE}$	$K'_{T,ETBE}$	$K'_{1,TAEE}$	$K'_{T,TAEE}$	TWRSS	AIC
203	6.42	–8795	6.96	–9035	4.49	–9725	21.18	–	–0.08	–4329	–	–	0.29	–1170
500	6.42	–8795	7.10	–9303	4.39	–9602	21.14	–	–0.24	–4852	–0.74	–	0.30	–1170
401	6.47	–8285	7.26	–6939	4.40	–10138	21.13	–	0.23	–	–0.76	–	0.31	–1160
104	6.47	–8292	7.11	–6674	4.53	–9845	21.17	–	0.34	–	–	–	0.32	–1159
402	6.45	–8497	7.23	–7231	4.38	–10298	21.40	–0.02	0.23	–	–0.75	–	0.31	–1158

Table 4.7.8. Estimated parameter values for the first five best models ranked with *n*=3.

Model	$k'_{1,R1}$	$k'_{T,R1}$	$k'_{1,R2}$	$k'_{T,R2}$	$k'_{1,R3}$	$k'_{T,R3}$	k_{D1}	k_{DT}	$K'_{1,ETBE}$	$K'_{T,ETBE}$	$K'_{1,TAEE}$	$K'_{T,TAEE}$	TWRSS	AIC
499	6.28	–9283	7.17	–9607	4.06	–9701	–	–	–0.59	–3849	–0.75	–	0.38	–1122
697	6.30	–9019	7.37	–8178	3.76	–11880	–	–	–0.23	–	–3.47	–25431	0.38	–1122
797	6.26	–8784	7.03	–10026	4.15	–8916	18.46	–	–0.23	–2156	–3.63	–25133	0.38	–1121
500	6.25	–8846	7.05	–9406	4.14	–9373	18.44	–	–0.39	–3709	–0.85	–	0.38	–1120
698	6.28	–8520	7.21	–8742	4.02	–9635	18.46	–	–0.06	–	–3.82	–28586	0.38	–1119

Globally, it can be seen that the values of *TWRSS* and *AIC* are similar for the best models with $n = 1$ and $n = 2$, and, therefore, it is difficult to discern which value of n is more appropriate. On the other side, models with $n = 3$ present notably larger values of *TWRSS* and *AIC*, what suggests that the participation of three active sites in the etherification reactions (R1 to R3) is not likely to occur.

From the analysis of the obtained results, some common features have been observed between the best models:

i) There is a coincidence of the form of best models for $n = 1$ and $n = 2$. They include the contribution of the same species in the adsorption term, the main differences being whether the temperature dependence of this contribution is significant or not. Moreover, the range of variation of the estimates obtained for different models was quite narrow, which is definitely a trustworthy sign of the reliability of the estimated values and the similarity of the best models, what supports the adequacy of the model averaging procedure.

ii) EtOH adsorption was significant in all best models. Since it appeared as the first summand of the adsorption term, the adsorption equilibrium constants of the rest of adsorbed species *j* are, in fact, $K'_j = K_j/K_{EtOH}$.

iii) ETBE adsorption was always significant, since $K'_{1,ETBE}$ appeared in all the best models, and its temperature dependent parameter, $K'_{T,ETBE}$, appeared in about the half of the best models. Therefore, K'_{ETBE} has been considered as temperature dependent.

iv) TAEE adsorption contributed in some of the candidate models, and its temperature dependent term was rarely significant. K'_{TAEE} has been considered as constant within the assayed temperature range.

v) Olefins (IB, 2M1B, and 2M2B) adsorption contribution did not appear in the best kinetic models, what indicates that their adsorption is negligible under the explored conditions.

vi) The solubility parameter of Amberlyst™35, δ_p, and hence the resin-medium affinity factor, ψ, was included in almost all best models, what indicates that the catalyst activity is affected by this interaction. Since its temperature dependent term (k_{DT}) was only significant in few candidate models, δ_p has been considered as constant within the assayed range of temperature. For models where k_{DT} was significant, its value was lower than 0.1 $MPa^{1/2}K^{-1}$, which is comparable with that determined in previous kinetic studies using a similar catalyst [144].

As a basis of the common features observed in the best models, the model averaging procedure has been applied to estimate the parameter values and their uncertainty in order to propose a reliable kinetic model. The results are gathered in Table 4.7.9.

Table 4.7.9. Mean values and standard error of the estimates, obtained after model averaging for n = 1, 2, and 3.

Parameter	n = 1	n = 2	n = 3
$k'_{1,R1}$	6.47 ± 0.02	6.42 ± 0.02	6.28 ± 0.02
$k'_{T,R1}$	–8950 ± 160	–8760 ± 170	–9000 ± 190
$k'_{1,R2}$	6.96 ± 0.04	7.05 ± 0.04	7.18 ± 0.03
$k'_{T,R2}$	–9520 ± 350	–9010 ± 340	–9150 ± 300
$k'_{1,R3}$	4.58 ± 0.03	4.42 ± 0.03	4.02 ± 0.04
$k'_{T,R3}$	–9720 ± 230	–9770 ± 270	–10150 ± 400
k_{D1}	23.71 ± 0.08	21.16 ± 0.12	–
$K'_{1,ETBE}$	0.50 ± 0.06	–0.12 ± 0.04	–0.35 ± 0.07
$K'_{T,ETBE}$	–5190 ± 480	–4560 ± 410	–3320 ± 440
$K'_{1,TAEE}$	–0.42 ± 0.53	–0.74 ± 0.30	–2.14 ± 0.30
TWRSS	0.26	0.29	0.40

As it can be seen, *TWRSS* values from model averaging almost match the lowest values for the best individual models with n=1, 2, and 3 (Tables 4.7.6, 4.7.7 and 4.7.8). The magnitude of fitted parameters and associated error obtained after model averaging are acceptable. Consequently, such estimated values can be considered as more representative of the true values than for an individual model, since they incorporate balanced information about the set of best selected models, and the model uncertainty has been also taken into account.

On one hand, lower similar values of *TWRSS* were obtained for n=1 and n=2, but there is not a clear evidence for discriminating between them beyond a doubt. On the other hand, in previous published studies, the proposed number of active sites for the isolated synthesis of ETBE and TAEE was typically 2 or 3 [48], that is, the participation of two active sites seems more feasible rather than only one. Finally, estimated values of K'_{ETBE} and K'_{TAEE} are lower for n=2 than for n=1, and generally lower that unity, as expected in a preferential adsorption of EtOH compared to ethers, because of its higher polarity [15]. Based upon these reasons, the averaged model with n=2 was selected as the more reliable for the present reaction system. Eqs. 4.7.18 and 4.7.19 are the finally proposed kinetic equations obtained for ETBE and TAEE formation. Fig. 4.7.12 shows the comparison of predicted vs experimental reaction rates from Eqs. 4.7.18 and 4.7.19. Figure 4.7.13 depicts the corresponding residuals distribution obtained showing a random distribution for TAEE whereas variance seems to increase with reaction rate for ETBE.

$$r_{ETBE} = r_{R1} = \frac{k'_{R1}\left(a_{IB}a_{EtOH} - a_{ETBE}/K_{R1}\right)\psi}{\left(a_{EtOH} + K'_{ETBE}\,a_{ETBE} + K'_{TAEE}\,a_{TAEE}\right)^2} \qquad (4.7.18)$$

$$r_{TAEE} = r_{R2} + r_{R3} = \frac{\left[k'_{R2}\left(a_{2M1B}a_{EtOH} - a_{TAEE}/K_{R2}\right) + k'_{R3}\left(a_{2M2B}a_{EtOH} - a_{TAEE}/K_{R3}\right)\right]\psi}{\left(a_{EtOH} + K'_{ETBE}\,a_{ETBE} + K'_{TAEE}\,a_{TAEE}\right)^2} \qquad (4.7.19)$$

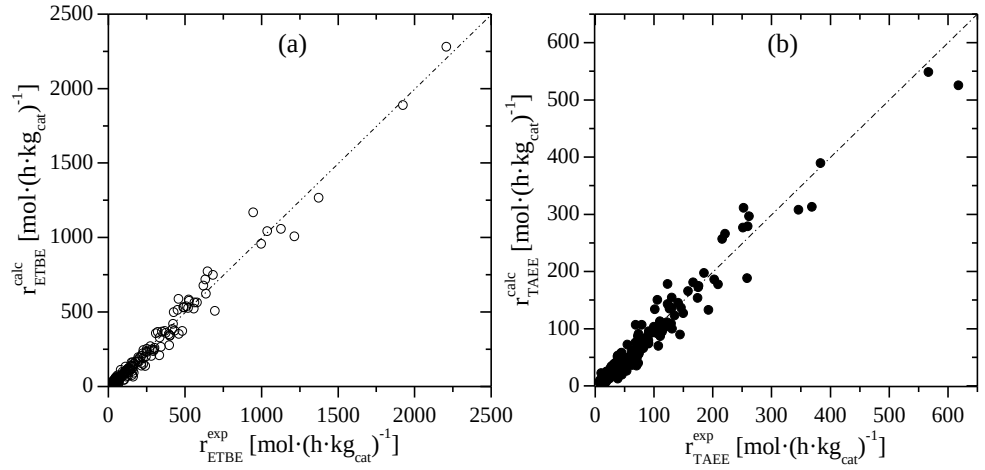

Figure 4.7.12. Comparison of experimental and predicted reaction rates using (a) Eq. 4.7.18, and (b) Eq. 4.7.19.

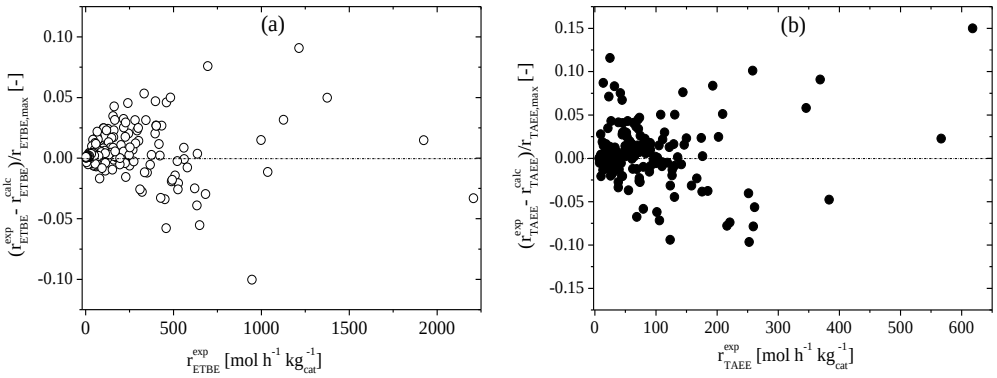

Figure 4.7.13. Residuals distribution for Eqs. 4.7.18 (a) and Eq. 4.7.19 (b).

Parameters appearing in the adsorption term, K'_j, are not the actual adsorption equilibrium constant of species *j*, but K_j/K_{EtOH} ratios. For ETBE, estimated K_{ETBE}/K_{EtOH} values ranged from 0.47 at 323 K to 1.55 at 353 K. Such increase suggests that ETBE adsorption is more sensitive to temperature, compared to EtOH adsorption. For TAEE, a constant value of 0.48 was obtained for K_{TAEE}/K_{EtOH} within the explored range of temperature. This value is very similar to that of ETBE at 323 K indicating that adsorption equilibrium constants of both ethers are comparable at low temperature. Some thermodynamic information can be obtained from the ratio of adsorption equilibrium constants, K'_j, according to Eq. 4.7.20. Estimated differences of adsorption enthalpies and entropies resulted in $(\Delta_{ads}H^o_{ETBE,(l)}-\Delta_{ads}H^o_{EtOH,(l)})$=37.9 kJ/mol, and $(\Delta_{ads}S^o_{ETBE,(l)}-\Delta_{ads}S^o_{EtOH,(l)})$= –0.97 J/(mol·K). These results indicate that EtOH adsorption is more exothermic than adsorption of ETBE and that the entropic loss for the adsorbed EtOH is larger than for the adsorbed ETBE. With respect to the adsorption Gibbs free energy difference between ETBE and EtOH $(\Delta_{ads}G^o_{ETBE,(l)}-\Delta_{ads}G^o_{EtOH,(l)})$ varied from 2.04 kJ/mol at 323 K to –1.29 kJ/mol at 353 K. With repect to TAEE and EtOH $(\Delta_{ads}G^o_{TAEE,(l)}-\Delta_{ads}G^o_{EtOH,(l)})$ varied from 1.98 kJ/mol at 323 K to 2.15 kJ/mol at 353 K. On one side, EtOH adsorption seems to be more favored than ETBE adsorption at low temperature, and less favored at high temperature, and, on the other, TAEE adsorption would be less favored than EtOH adsorption within the whole temperature range.

$$K_j' = \frac{K_j}{K_{EtOH}} = \exp\left(K'_{1,j} + K'_{T,j}\left(\frac{1}{T} - \frac{1}{\overline{T}}\right)\right) = \exp\left(\frac{\Delta_{ads}S^{\circ}_{j,(l)} - \Delta_{ads}S^{\circ}_{EtOH,(l)}}{R} - \frac{\Delta_{ads}H^{\circ}_{j,(l)} - \Delta_{ads}H^{\circ}_{EtOH,(l)}}{R}\left(\frac{1}{T} - \frac{1}{\overline{T}}\right)\right) = \quad (4.7.20)$$
$$= \exp\left(\frac{-\left(\Delta_{ads}G^{\circ}_{j,(l)} - \Delta_{ads}G^{\circ}_{EtOH,(l)}\right)}{R}\left(\frac{1}{T} - \frac{1}{\overline{T}}\right)\right)$$

With respect to the estimates of the resin solubility parameter, δ_p, they ranged from 17 to 30 $MPa^{1/2}$ for the whole set of candidate models. The value for the final averaged model (n=2) is 21.20±0.12 $MPa^{1/2}$ as a mean value within 323-353 K. This result is in good agreement with the constant value of 20.9±2.0 $MPa^{1/2}$ from 313 to 353K proposed by González [49] for A-35 in the isolated liquid-phase synthesis of ETBE, which gives reliability to the proposed kinetic models in this study. Finally, δ_p value is somehow low compared to that estimated by the group contribution method of Matsuura [215] (25.6 $MPa^{1/2}$) at 298 K but considering that this value is estimated at the reference temperature the observed difference is reasonable.

Once the final kinetic equations for R1, R2 and R3 (Eqs. 4.7.18 and 4.7.19) and their parameters were determined, the kinetic parameters of isoamylenes isomerization, R4, have been estimated. In that case, a separated non-linear least squares minimization was performed using the estimates previously obtained for n=2 (Table 4.7.9). The kinetic term k'_{R4} comprised the only two parameters to be estimated. It was found that optimization could be satisfactorily performed and the best results in terms of lower sum of squares indicated that one active site is involved in isoamylenes isomerization reaction, in accordance with a unimolecular reaction. The values obtained for the estimates $k'_{1,R4}$ and $k'_{T,R4}$ were 6.27 and –9199 K, respectively, and consequently an apparent activation energy of 76.5 kJ/mol. The proposed kinetic expression for the isoamylenes double bond isomerization is shown in Eq. 4.7.21. Although these obtained values are considered as approximate estimates, they are consistent with values quoted in previous studies [9, 29].

$$r_{2M2B} = r_{R4} - r_{R3} = \frac{\left[k'_{R4}(a_{2M1B} - a_{2M2B}/K_{R4}) - k'_{R3}(a_{2M2B}a_{EtOH} - a_{TAEE}/K_{R3})\right]\psi}{\left(a_{EtOH} + K'_{ETBE}\,a_{ETBE} + K'_{TAEE}\,a_{TAEE}\right)} \quad (4.7.21)$$

The values of apparent activation energies ($E'_{a,i}$) for reactions R1 to R4, and their associated standard error, obtained with the averaged model are gathered in Table 4.7.10, and compared with published values for the isolated synthesis of ETBE and TAEE over similar catalysts. In etherification reactions, $E'_{a,i}$ was found to increase as the exothermicity of reaction decreases, that is in the order R1< R2 < R3. $E'_{a,R1}$ is in good agreement with published values in the synthesis of ETBE over Amberlyst™15 by Ancillotti et al. [21], and over Amberlyst™35 by Gonzalez [49]. $E'_{a,R2}$ and $E'_{a,R3}$ are in reasonable agreement with those determined by Linnekoski et al. [140] in the synthesis of TAEE over Amberlyst™16. $E'_{a,R4}$ value is in fair agreement with the values of 72.9 and 91 kJ/mol for IA isomerization over Amberlyst™16 proposed by Linnekoski et al. [136,140]. Generally, published $E'_{a,i}$ values shown in Table 4.7.10, obtained with similar resins, are slightly higher than those obtained in this work, what indicates a lower temperature sensibility of A-35 compared to the other resins. A few values of $E'_{a,i}$ presented in Table 4.7.10 using resins with commercial bead size are rather low, within the range 40–55 kJ/mol, probably due to the presence of internal diffusion effects.

Table 4.7.10. Comparison of apparent activation energies obtained in this work with those previously reported for the isolated synthesis of ETBE and TAEE.

Reference	$E'_{a,i}$ [kJ/mol]			Catalyst	Bead size
	ETBE (R1)	TAEE (R2, R3)	Isomerization (R4)		
This work	72.8±1.4	74.9±2.8[a] 81.2±2.2[b]	76.5±7.2	Amberlyst™ 35	0.25–0.4 mm
Ancillotti et al. (1977) [21]	73.8	–	–	Amberlyst™ 15	Commercial
Fité et al. (1994) [123]	86.1	–	–	Bayer K–2631	< 0.1 mm
Solà et al. (1995) [148]	80.6	–	–	Bayer K–2631	0.063–0.16 mm
Umar et al.(2009) [163]	53.46	–	–	Purolite® CT–124	Commercial
Yang et al. (2000) [162]	79.45 43.69 84.11	–	–	Amberlyst™ 15 S–54 D–72	0.7 mm
González (2011) [49]	70.4±3.5	–	–	Amberlyst™ 35	0.25–0.4 mm
Linnekoski et al.(1997) [140]	–	76.8[a] 95.9[b]	72.9	Amberlyst™ 16	0.35–0.65 mm
Linnekoski et al.(1998) [91]	–	88.6	–	Amberlyst™ 16	< 0.65 mm
Linnekoski et al. (1999) [136]	–	87[a] 107[b]	91	Amberlyst™ 16	0.3–0.6 mm
Oktar et al.(1999) [124]	–	40.7[a] 73.6[b]	–	Amberlyst™ 15	Commercial
Aiouache and Goto (2003) [166]	–	74.0	–	Amberlyst™ 15	< 0.44 mm
Bozga et al.(2008) [145]	–	69.3±5.3	–	Amberlyst™ 35	Commercial
Boonthamtirawuti et al. (2009) [45]	–	103.1	–	Amberlyst™ 16	< 0.55 mm

[a] TAEE formation from 2M1B (R2). [b] TAEE formation from 2M2B (R3).

The apparent rate coefficient is related with the reactivity of olefins with EtOH. Fig. 4.7.14 shows the Arrhenius plot of the kinetic constant obtained for every reaction. Olefins reactivity in etherification with EtOH follows the order 2M1B>IB>2M2B, what indicates that a terminal double bond (α-position, 2M1B) reacts more readily than an internal double bond (β-position, 2M2B). Rihko et al. [89] also observed a higher reactivity for 2M1B than for 2M2B in the isolated etherification of IA with EtOH. Since both IA form the same carbocation, differences in their reactivity can be explained by an easier protonation of the terminal double bond due to a lower steric hindrance.

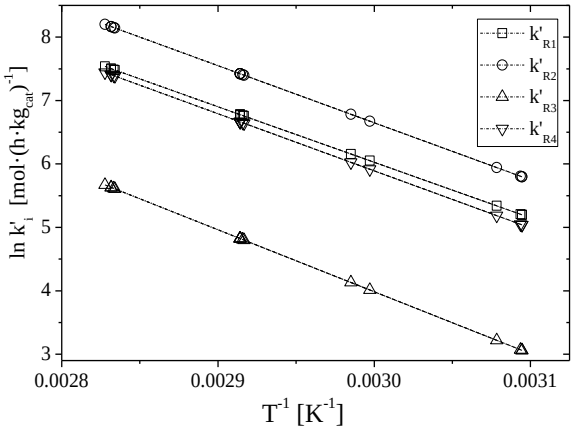

Figure 4.7.14. Arrhenius plot of kinetic terms for reactions R1, R2, R3 and R4.

Some outcomes about the reacting process are derived from kinetic equations 4.7.18, 4.7.19, and 4.7.21. The form of the driving force term indicates that the surface reaction is likely to be the rate determining step for all reactions. The inclusion of the ψ factor shows that the interaction between the reaction medium and the resin affects the catalytic activity. Species appearing in the adsorption term, namely EtOH, ETBE, and TAEE, are those adsorbed onto the catalytic active sites, and olefins do not adsorb in a significant extent. Finally, two active sites participate in the rate determining step, the surface reaction, in etherification reactions, and one active site in IA isomerization.

The proposed kinetic equations can come from either a LHHW o an ER mechanism. A LHHW mechanism involves that all species taking part in the surface reaction are adsorbed on the catalyst. In an ER mechanism at least one of the species is not adsorbed and it reacts directly from the reaction medium with other adsorbed species. Since alcohols are preferentially adsorbed on the active sites compared to olefins, as quoted in literature [65] and enforced by the results of this study, in case of the etherification through an ER mechanism it is more likely that olefins react directly from the reaction medium. This is not in contradiction that olefins adsorb on the resin, but more weakly, as seen that isomerization also occurs on the active sites. For comparable isolated etherification systems, Tejero et al. [195] and Françoise and Thyrion [139] suggested a transition from ER mechanisms to LHHW when the alcohol concentration become very low. Nonetheless, this transition of mechanisms is unexpected in the present work, because EtOH molar fraction was always higher than 0.04, and, therefore, an ER mechanism seems to be more reasonable.

In the reaction rate equations, the main difference between a LHHW and an ER mechanism is the form of the kinetic term. Considering the surface reaction between one molecule of alcohol and one molecule of olefin as the rate determining step, the corresponding kinetic term for a LHHW is expressed as $k_i=k^*_i\, K_{olefin}\, K_{alcohol}$, where k^*_i is the intrinsic kinetic constant, whereas for an ER mechanism it is $k_i=k^*_i\, K_{alcohol}$. Besides, for models that consider negligible the fraction of free active sites (set II), these kinetic terms vary depending upon the form of the adsorption term and the number of involved active sites. Hence, the kinetic terms of Eqs. 4.7.18 and 4.7.19 are expressed as: $k'_i=k^*_i\, K_{olefin}/K_{alcohol}$ for a LHHW mechanism or $k'_i=k^*_i/K_{alcohol}$ for an ER one. As a result, the true activation energies ($E_{a,i}$) of etherification reactions can be calculated from apparent activation energies ($E'_{a,i}$) and liquid-phase adsorption enthalpies ($\Delta_{ads}H^o_{j,(l)}$) of reactants as $E_{a,i} = E'_{a,i} - \Delta_{ads}H^o_{olefin,(l)} + \Delta_{ads}H^o_{alcohol,(l)}$ for a LHHW mechanism, or as $E_{a,i} = E'_{a,i} + \Delta_{ads}H^o_{alcohol,(l)}$ for an ER mechanism. If not available, liquid-phase adsorption enthalpy can be estimated from the sum of the gas-phase adsorption enthalpy ($\Delta_{ads}H^o_{j,(g)}$) and the enthalpy of vaporization of compound ($\Delta_v H^o_j$).

It is to be noted that an important lack of agreement between sources was found in the literature for thermodynamic adsorption properties of reactants. This divergence affects to the calculation of $E_{a,i}$. As no data were available for adsorption thermodynamic properties of EtOH and olefins on A-35, experimentally gas-phase determined values over Amberlyst™15, which is similar to Amberlyst™35 but with lower acid capacity, were used instead (Table 4.7.11). The resulting true activation energies estimated for LHHW or ER mechanisms, are gathered in Table 4.7.12.

The true activation energies values determined for the LHHW mechanism shown in Table 4.7.12 seem unlikely, since they are too high compared to values reported in the literature for isolated etherification of IB and IA with EtOH over similar catalysts [123,140]. So it can be concluded that an ER mechanism, in which adsorbed EtOH reacts with non-adsorbed olefins, is the most likely for the studied etherification reactions. The choice of an ER mechanism as the most feasible is in concordance with the results obtained from non-linear regression, which suggested one or two active sites as the most probable and with previous kinetic studies on the isolated etherification of isoalkenes with primary alcohols [123,142,195]. With respect to isoamylenes double bond isomerization reaction between the α- and the β-position of the alkenes [89], it follows an LHHW mechanism in which an adsorbed molecule of 2M1B (more reactive and less thermodynamically stable than 2M2B) adsorbs on one active site to form 2M2B.

Table 4.7.11. Vaporization, gas and liquid-phase adsorption enthalpies of reactants.

Compound	$\Delta_v H^o_j$ [kJ/mol]	$\Delta_{ads} H^o_{j,(g)}$ [kJ/mol]	$\Delta_{ads} H^o_{j,(l)}$ [kJ/mol]
IB	22.2[a]	–60.2[c]	–38
EtOH	42.3[b]	–43.5[c]	–1.2
2M1B	28.5[a]	–71.9[c]	–43.4
2M2B	28.4[a]	–76.9[c]	–48.5

[a]From National Institute of Standards and Technology (NIST) book [218]. [b]Average of 12 experimental values from NIST book. [c]Experimental values determined for A-15 [150].

Table 4.7.12. Activation energies estimated for etherification reactions.

Reaction	E'_a [kJ/mol]	E_a (LHHW) [kJ/mol]	E_a (ER) [kJ/mol]
R1	72.8	109.6	71.6
R2	74.9	117.1	73.7
R3	81.2	128.5	80.0

To sum up, taking into account the complexity of the studied system with three etherification reactions and one double bond isomerization that occur simultaneously, the proposed kinetic model can be considered as appropriate and reliable for describing the experimental runs. Results are coherent with previous studies on kinetics of isolated tertiary ether syntheses. Finally, additional experimental determination of liquid- and gas-phase adsorption thermodynamic properties of involved compounds on A-35 would provide valuable information for a categorical description of the actual reaction mechanisms and possible mechanism transition under different conditions.

4.7.7 PARTIAL CONCLUSIONS

The kinetics of the simultaneous etherification of IB and IA (2M1B and 2M2B) with EtOH catalyzed by Amberlyst™35 have been studied using different modeling approaches at 323-353K. Power function modeling and RSM are useful approaches that can be applied in the early modeling because they allow to draw some conclusions to be used in a subsequent mechanistic based modeling. Formation rate of ETBE is faster than global formation rate of TAEE. A large number of kinetic equations, expressed in terms of activities and based on the LHHW–ER formalism, have been systematically proposed and fitted to experimental data to obtain satisfactory kinetic models for the whole reaction network. Model selection and model averaging have been shown as a convenient technique to obtain a reliable kinetic model. The best obtained model in etherification stems for the surface reaction between one molecule of alcohol and one of olefin with the participation of two active sites. Adsorption of EtOH, ETBE and TAEE is significant, and the fraction of non-occupied sites is negligible. Obtained results

confirmed that adsorption of EtOH is stronger than that of olefins. EtOH is preferentially adsorbed rather than TAEE within the explored temperature and its adsorption is also favored compared to ETBE only at low temperatures. One active site participates in isoamylenes double bond isomerization. Apparent activation energies for ETBE formation from IB and EtOH, TAEE formation from 2M1B and EtOH, TAEE formation from 2M2B and EtOH, and isoamylenes double bond isomerization were 72.8±1.4, 74.9±2.8, 81.2±2.2 and, 76.5±7.2 kJ/mol, respectively. These values are in good agreement with those quoted in literature for the isolated ETBE and TAEE formation systems. 2M1B has been found to be more reactive with EtOH than 2M2B. From the estimated activation energies values, it has been found that an Eley-Rideal mechanism is more likely to occur than a LHHW mechanism in the etherification reactions.

4.7.8 CHAPTER NOTATION

$\Delta_{ads}G^o_j$	standard molar Gibbs free energy of adsorption of compound *j* [kJ·mol^{-1}]
$\Delta_{ads}H^o_j$	standard molar enthalpy of adsorption of compound *j* [kJ·mol^{-1}]
$\Delta_{ads}S^o_j$	standard molar entropy of adsorption of compound *j* [J·mol^{-1}·K^{-1}]
2M1B	2-methyl-1-butene
2M2B	2-methyl-2-butene
a_j	activity of chemical species *j*
*A*i	apparent preexponential factor of reaction *i*
AIC	Akaike Information Criterion coefficient
AW_m	Akaike weight of model *m*
DF	driving force
d_p	particle diameter [mm]
ETBE	ethyl *tert*-butyl ether
IA	isoamylenes
IB	isobutene
k_{Ai}	kinetic pseudo-order of alcohol in power function equation for reaction *i*
k_{Oi}	kinetic pseudo-order of olefins in power function equation for reaction *i*
k^*_i	kinetic coefficient of reaction *i* [mol·h^{-1}·kg$_{cat}^{-1}$]
k'_i	apparent rate coefficient of reaction *i* [mol·h^{-1}·kg$_{cat}^{-1}$]
k_i	rate coefficient of reaction *i* [mol·h^{-1}·kg$_{cat}^{-1}$]
K_i	equilibrium constant of reaction *i* [dimensionless]
K_j	liquid-phase adsorption equilibrium constant of compound *j* [dimensionless]
n	number of active sites or clusters of active sites participating in the rate limiting step
N	sample size, number of experimental points
p	number of parameters of the model
R	gas constant, 8.314472 J·mol^{-1}·K^{-1}
r^0_j	initial reaction rate of formation or consumption of compound *j* [mol·h^{-1}·kg$_{cat}^{-1}$]
r_j	reaction rate of formation or consumption of compound *j* [mol·h^{-1}·kg$_{cat}^{-1}$]
$R^o_{A/O}$	initial molar ratio of alcohol to olefins
$R^o_{C4/C5}$	initial molar ratio of isobutene to isoamylenes
RSM	response surface methodology
RSS	residual sum of squares
T	temperature [K]
TAA	*tert*-amyl alcohol
TAEE	*tert*-amyl ethyl ether

TBA	*tert*-butyl alcohol
TWRSS	total weighted residual sum of squares
x_A	alcohol molar fraction in the total reaction mixture
x_O	olefins molar fraction in the total reaction mixture
W_{cat}	catalyst mass in dry base [g]
w_i	weight assigned to each objective function

Greek letters

α	parameter that takes the value of either unity or zero.
Δ_m	delta of Akaike for model n
δ	Hildebrand solubility parameter [$MPa^{1/2}$]
ψ	resin-medium affinity factor [dimensionless]
θ	estimate value

Subscripts

(g)	gas-phase
(l)	liquid-phase
1	temperature independent term
i	reaction
j	chemical species
k	chemical compound different than *j*
m	number of model considered
p	related to the polymer (catalyst)
T	temperature dependent term
v	vaporization

Superscripts

0	Initial
M	set of candidate models
S	total number of compounds or species
exp	experimental
calc	calculated

4.8 ADSORPTION OF ALCOHOLS, OLEFINS AND ETHERS ON AMBERLYST™35

A revised version of a part of this chapter was published as:

R. Soto, N. Oktar, C. Fité, E. Ramírez, R. Bringué, J. Tejero. Adsorption of C_1-C_4 alcohols, C_4-C_5 isoolefins and their corresponding ethers over Amberlyst™35. *Chem. Eng. Technol*. **2017**; https://doi.org/10.1002/ceat.201600592

4.8.1 INTRODUCTION

As analyzed in *Section 4.7*, several kinetic studies have been focused so far on the syntheses of tertiary ethers using IER as catalysts [48,123,131,145]. Adsorption thermodynamic properties of compounds on IER are usually estimated from kinetic experiments by non-linear regression by assuming a certain kinetic model. Some spread in published estimated values is found. In fact, individual information on the adsorption of involved compounds cannot often be explicitly drawn due to the form of kinetic equations, which in most cases assume a catalytic surface saturated by reactants and products [49,85,219]. Experimental determination of adsorption related properties is of interest to contrast the non-linear regression outcomes and to reduce the number of variables in kinetic equations.

To date, experimental studies on adsorption of tertiary olefins, alcohols and ethers on IER, are scarce, particularly on A-35 [64,65,150]. Besides, data about effective diffusion coefficients on IER are rarely available. The present work aims to provide a detailed study about the adsorption of primary alcohols, olefins and ethers on A-35. Determination of adsorption equilibrium constants, heat of adsorption, macro− and micropore diffusion coefficients are the main goals.

4.8.2 EXPERIMENTAL AND CALCULATIONS

Liquid-phase adsorption experiments were carried out in the setup described in *Section 3.2.3* and gas-phase adsorption experiments were conducted in the setup described in *Section 3.2.4*. Fresh A-35 previously pretreated in commercial bead size distribution was used for all the runs. For gas-phase runs, the fixed bed consisted of 0.1 g of pretreated catalyst. The corresponding bed length was 0.012 m and a bed void fraction of ε_b=0.407 was estimated by means of the empirical correlation for spherical particles for which the ratio of tube diameter to particle diameter (d_t/d_p) ranges from 1.5 to 50 described in [220], see Eq. 4.8.1. d_t/d_p = 8.97 in this work.

$$\varepsilon_b = 0.390 + \frac{1.740}{\left(d_t / d_p + 1.140\right)^2} \qquad (4.8.1)$$

As for theory and calculations, similar procedures to those described by Doğu et al. [221] for liquid-phase batch adsorber and by Oktar et al. [65] for gas-phase packed bed adsorber were followed in this work. The species conservation equation for an adsorbed tracer (*j*), Eqs. 4.8.2 and 4.8.4, and the definition of the n^{th} moment ($m_{n,L}$ for liquid-phase and $m_{n,G}$ for gas-phase), Eqs. 4.8.3 and 4.8.5, depend on the adsorber flow model as follows [65,221,222]:

a) Perfectly mixed batch adsorber:

$$\frac{dC_j}{dt} = -\left(\frac{m_s}{\rho_p}\right)\left(\frac{3}{R_0}\right) D_a \left.\frac{\partial C_{j,a}}{\partial R}\right|_{R=R_0} \tag{4.8.2}$$

$$m_{n,L} = \int_0^\infty \left(\frac{C_j - C_{j,eq}}{C_{j,0} - C_{j,eq}}\right) t^n dt \tag{4.8.3}$$

b) Packed bed adsorber:

$$D_z \frac{\partial^2 C_j}{\partial z^2} - U_0 \frac{\partial C_j}{\partial z} - \frac{3(1-\varepsilon_b)}{R_0} D_a \left.\frac{\partial C_{j,a}}{\partial R}\right|_{R=R_0} = \varepsilon_b \frac{dC_j}{dt} \tag{4.8.4}$$

$$m_{n,G} = \int_0^\infty C_j t^n dt \tag{4.8.5}$$

Diffusing species within the macropores of macroreticular IER adsorb on the external surface of microspheres, and then adsorbed species penetrate into the microspheres by diffusion [221]. Such process may be modeled by considering adsorption of the external surface of the catalyst followed by diffusion of adsorbed species into the bead [65]. For this model, species conservation equations in the macropores for a batch and a packed bed adsorber are Eqs. 4.8.6 and 4.8.7, respectively. For both type of adsorbers, species conservation within the microspheres is expressed by Eq. 4.8.8.

$$\frac{D_a}{R^2}\frac{\partial}{\partial r}\left(R^2 \frac{\partial C_{j,a}}{\partial R}\right) - \frac{3}{r_0}\rho_p D_i \left.\frac{\partial q}{\partial r}\right|_{r=r_0} = \varepsilon_a \frac{\partial C_{j,a}}{\partial t} \tag{4.8.6}$$

$$\frac{D_a}{R^2}\frac{\partial}{\partial R}\left(R^2 \frac{\partial C_{j,a}}{\partial R}\right) - \left(\frac{3(1-\varepsilon_a)}{r_0}\right)\rho_p^* D_i \left.\frac{\partial q}{\partial r}\right|_{r=r_0} = \varepsilon_a \frac{\partial C_{j,a}}{\partial t} \tag{4.8.7}$$

$$\frac{D_i}{r^2}\frac{\partial}{\partial r}\left(r^2 \frac{\partial q}{\partial r}\right) = \frac{\partial q}{\partial t} \tag{4.8.8}$$

where

$$q\big|_{r=r_0} = K_j C_{j,a} \tag{4.8.9}$$

Partial differential Eqs. 4.8.6 to 4.8.8 can be solved in the Laplace domain [223]. The zeroth moment equation derived for the bidisperse system for the liquid-phase batch adsorber is eventually expressed by Eq. 4.8.10 [221].

$$m_{0,L} = \frac{\rho_p K'_{j,L}}{15\left(1+\frac{m_s}{\rho_p}\left(\varepsilon_a+\rho_p K'_{j,L}\right)\right)}\left(\frac{R_0^2}{D_a}+\frac{r_0^2}{D'_i}\right) \tag{4.8.10}$$

where $D'_i=D_i\rho_p K'_{j,L}$ is the effective microsphere diffusivity and $K'_{j,L}=q_m K_{j,L}$ is the apparent liquid-phase adsorption equilibrium constant. q_m is the maximum adsorption capacity.

Analogously, the moment equations for a packed bed adsorber (gas-phase) are expressed by Eqs. 4.8.11 and 4.8.12 [65,222]. The first absolute moment (μ_1) represents the time delay of the response curve and the second central moment (μ_2) represents the variance of the response peak.

$$\mu_1 = \frac{m_{1,G}}{m_{0,G}} = \frac{L\varepsilon_b}{U_0}\left[1+\frac{\left(1-\varepsilon_b\right)\varepsilon_a}{\varepsilon_b}\left(1+\frac{\rho_p K_{j,G}}{\varepsilon_a}\right)\right] \tag{4.8.11}$$

$$\mu_2 = \frac{m_{2,G}}{m_{0,G}} - \mu_1^2 = \frac{2L\varepsilon_b}{U_0}\left[\delta_d+\delta_f+\delta_a+\delta_i\right] \tag{4.8.12}$$

The gas-phase adsorption equilibrium constant of an adsorbing tracer ($K_{j,G}$) can be evaluated from μ_1, and effective diffusivities may be estimated from μ_2, which includes the contributions of axial dispersion (δ_d), film mass transfer (δ_f), macropore diffusion (δ_a), and micropore diffusion (δ_i) resistances. Such contributions are a function of $K_{j,G}$ and they can be expressed by Eqs. 4.8.13−4.8.16.

$$\delta_f = \frac{\left(1-\varepsilon_b\right)}{\varepsilon_b}\frac{R_0\varepsilon_a^2}{3k_f}\left(1+\frac{\rho_p K_{j,G}}{\varepsilon_a}\right)^2 \tag{4.8.13}$$

$$\delta_d = \frac{D_z\varepsilon_b}{U_0^2}\left[1+\frac{\left(1-\varepsilon_b\right)\varepsilon_a}{\varepsilon_b}\left(1+\frac{\rho_p K_{j,G}}{\varepsilon_a}\right)\right]^2 \tag{4.8.14}$$

$$\delta_a = \frac{\left(1-\varepsilon_b\right)}{\varepsilon_b}\frac{R_0^2\varepsilon_a^2}{15D_a}\left(1+\frac{\rho_p K_{j,G}}{\varepsilon_a}\right)^2 \tag{4.8.15}$$

$$\delta_i = \frac{\left(1-\varepsilon_b\right)}{\varepsilon_b}\frac{r_0^2}{15D_i}\rho_p K_{j,G} \tag{4.8.16}$$

Finally, the dimensionless parameter α, Eq. 4.8.17, characterizes the ratio of diffusion times in the macro and micropore regions [221,224]. For α >>1, micropore diffusion resistance may be neglected, and thus the bidisperse structure can be approximated to a monodispersed-like.

$$\alpha = \left(\frac{R_0}{r_0}\right)^2\left(\frac{D'_i}{D_a}\right) \tag{4.8.17}$$

4.8.3 CHARACTERIZATION OF AMBERLYST™35

The catalyst bead size distribution was determined by laser diffraction in air with an average particle diameter (D_0) of $531 \cdot 10^{-6}$ m, showing a quite narrow distribution: 422 μm (<10%), 466 μm (<25%), 531 μm (<50%), 619 μm (<75%), and 716 μm (<90%). Fig. 4.8.1 show the bead size distribution obtained for three samples of commercial A-35. Generally, the particle size does not play any role at all in the adsorption process, but the possible diffusion does present an effect on the rate at which the solid surface is filled.

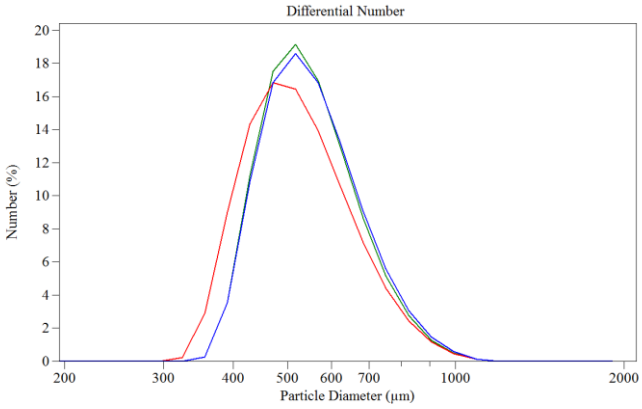

Figure 4.8.1. Bead size distribution of three different samples of A-35.

Mercury intrusion porosimetry and N_2 adsorption at 77 K (BET method) were applied to A-35, see Table 4.8.1. The values obtained are in coherence with those determined by Oktar et al. [65] for A-15 taking into account that the higher acid capacity of A-35 implies a lower surface area and pore volume. The surface area determined by nitrogen adsorption is notably smaller than that determined by mercury porosimetry what suggest than nitrogen could not penetrate into gelular microspheres at the liquid nitrogen temperature.

Table 4.8.1. Mercury intrusion porosimetry and BET results for A- 35.

Morphological Property	Hg intrusion	BET isotherm
Maximum pore volume [cm^3/g]	0.2662	0.211
Mean pore diameter [Å]	300.1	291.8
Surface Area [m^2/g]	52	34
Catalyst macroporosity (ε_a)[a] [%]	0.291	0.245
Apparent density[b] (ρ_p) [g/cm^3]	1.093	1.164

[a] $\varepsilon_a = V_{pore}/V_{particle} = V_g/(V_g+1/\rho)$. [b] $\rho_p = \rho(1-\varepsilon_a)$

Scanning Electron Microscope (SEM) was performed to commercial particles of A-35. From Fig. 4.8.2 it can be confirmed that the catalyst is formed by an aggregation of microspheres and therefore its consideration as a bidisperse catalyst (see Fig. 1.22) seems appropriate for the modeling of adsorption processes on A-35. Besides, the pretreatment of the catalyst caused fissures in the outer catalyst surface. This phenomenon was also observed by Guilera et al. [151] and it can be ascribed to the thermal pretreatment of the catalyst in order to remove moisture. From several images at the same magnification as Fig. 4.8.2d, an average microspheres diameter (d_0) of $3.11 \cdot 10^{-6}$ m was estimated from the measurement of 22 different microspheres. Besides, a mapping of electrons was carried out aiming to observe possible areas in which the concentration of sulfonic groups is different. However, such a technique only allowed to

determine and homogeneous and high concentration of sulfur elements in the resin particle. The mapping images are included in *Appendix 7.12*.

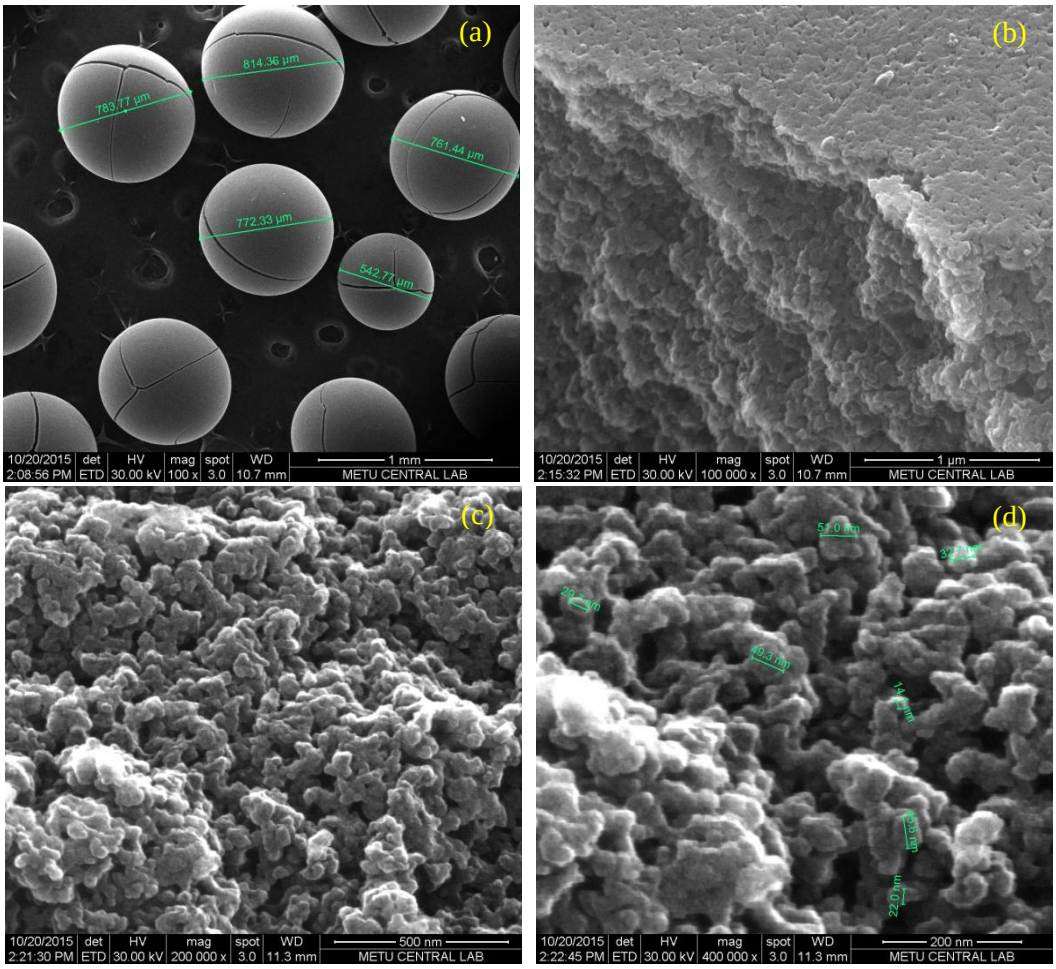

Figure 4.8.2. SEM images of pretreated A-35 particles at different magnifications: (a) Uncrashed particles at 100x. (b) Surface and inner face of a fracture at 100000x. (c) Inner face of a crashed particle at 200000x. (d) Inner face of a crashed particle at 400000x.

FTIR analysis of pyridine adsorption was performed on A-35. The total FTIR spectra obtained is shown in Fig. 4.8.3a. It can be seen that A-35 is a strongly sulfonated material since the sulfonation of a polystyrene copolymer produces two intense peaks 1219 and 1157 cm^{-1}, which correspond to the asymmetric and symmetric S=O stretching vibrations, respectively. Another strong absorbance attributed to the C−S stretching is detected at 1124 cm^{-1}. The characteristic intense peaks associated with the symmetric stretching of the $-SO_3H$ group and the in-plane bending of the para-substituted phenyl ring at 1030 and 1007 cm^{-1}, respectively, confirm the strong sulfonation of the material [225]. Furthermore, the broad and weak absorption band between 3600 and 3300 cm^{-1} indicates the presence of a significant number of −OH from the $-SO_3H$ groups. Some of the weak bands detected from 2500 to 3300 cm^{-1} could be overlapped −OH indicating carboxylic group presence since the O–H stretching vibration of hydrogenbonded dimers in which carboxylic acid exists is detected in this area.

Pyridine adsorption is often combined with in situ FTIR to assess the surface acidic properties of supports and catalysts [226]. The characteristic bands in the FTIR spectrum indicate whether pyridine is protonated through the nitrogen atom (by surface Brønsted acid sites) or bonded to

coordinative unsaturated sites (Lewis acids). Upon interaction with a Brønsted acid site, pyridine is protonated to a pyridinium ion and adsorbs with a characteristic band around 1545–1540 cm^{-1}. Interaction of pyridine with Lewis acid sites creates a coordinatively bonded pyridinium complex with a well-resolved band centered around 1452–1447 cm^{-1}. A band located around 1490 cm^{-1} is common to both adsorbed species. The A-35 FTIR spectra expansion in the area of interest is depicted in Fig. 4.8.3b. The acid sites of A-35 are mostly Brønsted type or Brønsted-Lewis since two well-defined bands were observed at 1544 and 1488 cm^{-1}, respectively. The presence of Lewis acid sites is discarded in A-35 since no bands appear in the specific region of the spectrum.

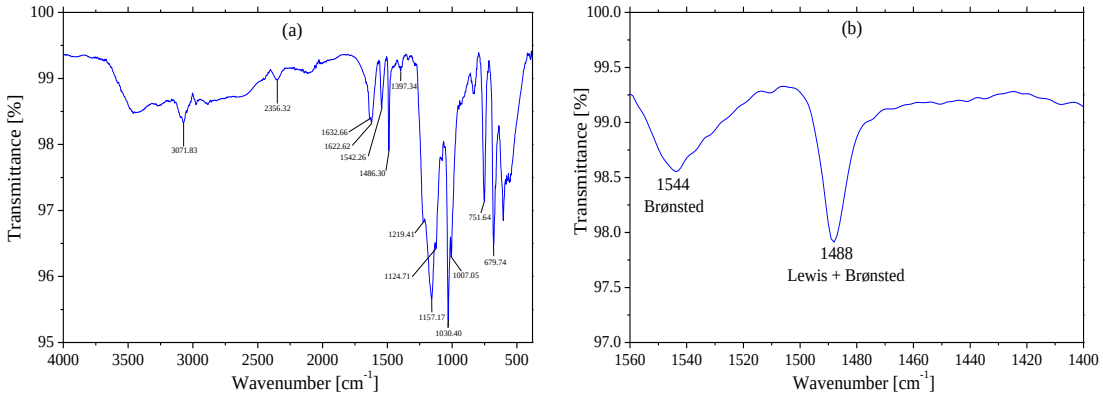

Figure 4.8.3. FTIR spectra of adsorbed pyridine over A-35 at 353 K.(a) Full spectra and (b) spectra expansion in the specific region for evaluating the acid sites nature.

TGA (*thermogravimetric analysis*) curves measure the variation of mass when a controlled variation of temperature is applied to a material. STDA curves (s*imultaneous difference thermal analysis*) measure the difference of temperature in the material (with respect to the reference temperature) that occur during the controlled variation of temperature, exothermic or endothermic effects in the material, in the same way as DSC technique (*differential scanning calorimetry*) measure differences of calorific power or heat. TGA and SDTA curves obtained for A-35 are plotted in Fig. 4.8.4.

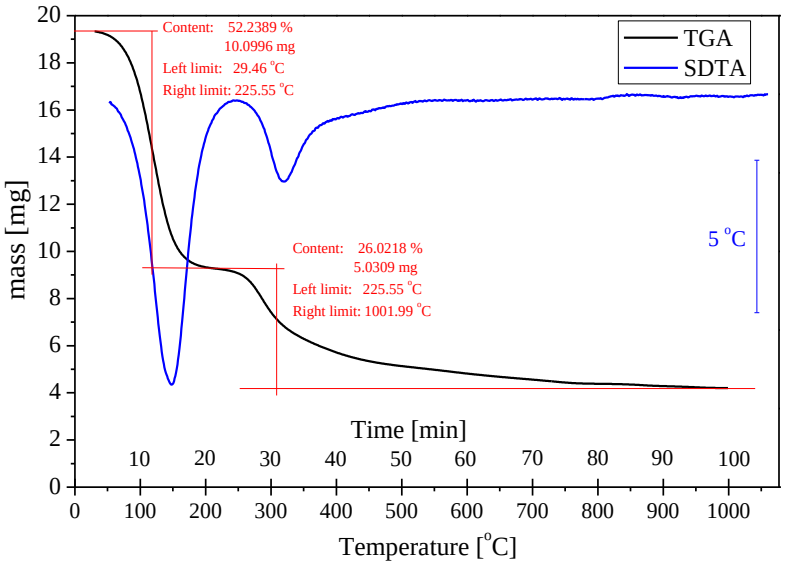

Figure 4.8.4. (–) TGA and (**–**) SDTA curves obtained for a commercial sample of A-35.

With regards to TGA curves, the first decreasing section is associated with the loss of humidity (drying) of the resin. As it can be observed, the initial moisture of the sample was around 50%. The second decreasing section of the TGA curve is related to desulfonation and to degradation of the polymeric matrix. Despite the differences between at which these two processes occur, TGA results overlap. This happens because the temperature at which the sulfonic groups are destroyed and the temperature at which the catalyst polymeric matrix starts to decompose are close to each other. Generally, the loss of mass between 250 and 350 °C can be associated to the desulfonation process whereas the last section from 420 °C can be related to the polymer destruction. Concerning SDTA curve, the endothermic process of drying can be appreciated around 100 °C. Due to the overlapping of results corresponding to the processes of desulfonation and destruction of the polymeric matrix, it is difficult to discern the limits between them. The polymer destruction depends on a series of morphological properties as crosslinking degree and morphology. Previous TGA analysis of non-functionalized polymeric matrix indicate that polymer destruction takes place from 420 °C.

4.8.4 LIQUID-PHASE ADSORPTION EXPERIMENTS

A preliminary run was performed at room temperature using *n*-hexane as solvent and *n*-heptane as tracer. Since concentration did not change with time in the batch adsorber, it is concluded that paraffins hardly adsorb on A-35. *n*-Heptane was chosen as the solvent, because its boiling point (372 K) is higher than that of *n*-hexane (342 K), and thus suitable for working in a temperature interval of 323–353 K. Special care was taken for the solubility of all tracers in *n*-heptane to assure a homogeneous liquid-phase in all the runs. In the case of very low concentrations of tracers, adsorption isotherms can be approximated by the Langmuir model [64], see Eq. 4.8.18.

$$\frac{q_{eq}}{q_m} = \frac{K_{j,L} C_{j,L}}{\left(1 + \sum_{j=1}^{S} K_{j,L} C_{j,L}\right)} \qquad (4.8.18)$$

where $q_{eq} = (C_{j,0}-C_{j,eq})/m_s$ is the adsorbed concentration at equilibrium and $m_s=m_{cat}/V_{T,L}$ is the mass of dry catalyst divided by the total volume of solid free liquid (solvent plus tracer). Linearization of Eq. 4.8.18 can provide adsorption equilibrium constant $K_{j,L}$ and the maximum adsorption capacity q_m at each temperature.

Liquid-phase adsorption experiments were conducted successfully only for C_1-C_4 alcohols and 2M2B. In an attempt to carry out this type of experiments with ethers, it was observed that reverse reactions of etherification took place leading to ethers decomposition into olefin and alcohol. Therefore, $K_{j,L}$ could not be experimentally determined for ethers. As expected, symmetric ethers from dehydration of C_1-C_4 primary alcohols were not detected, since such reactions usually take place at temperatures higher than 353 K [83,153]. Fig. 4.8.5 Shows examples of the obtained concentration decay curves.

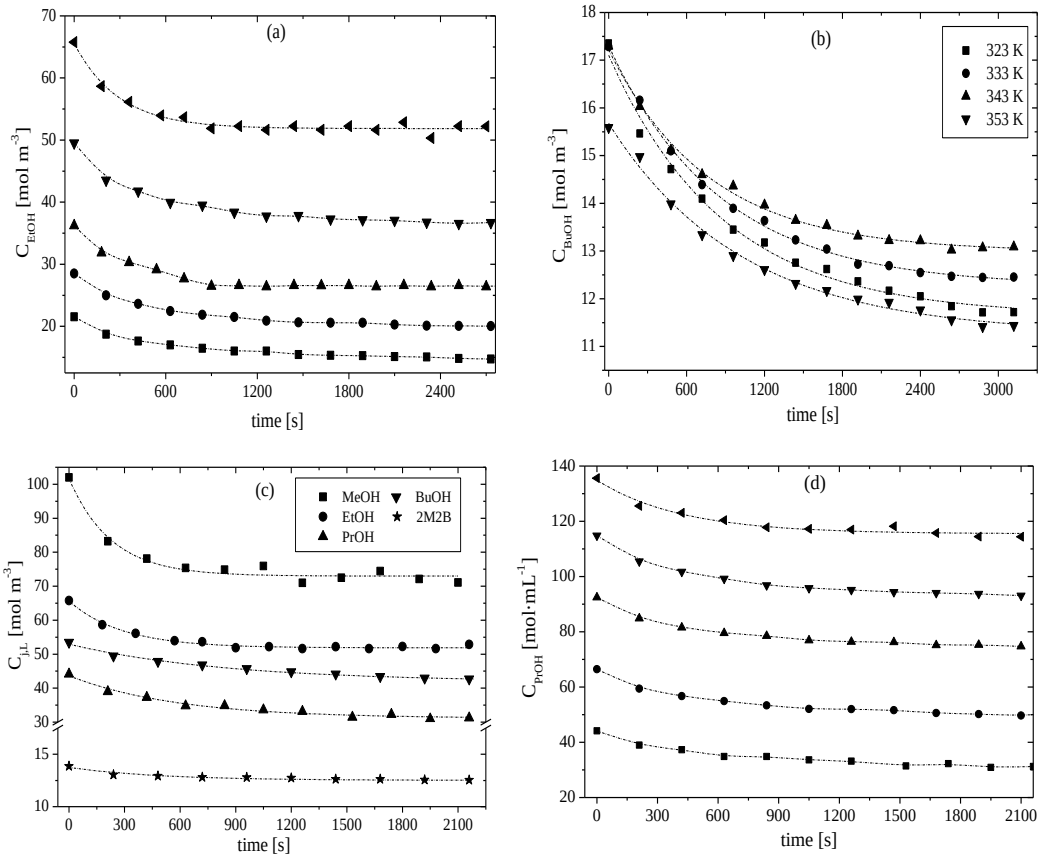

Figure 4.8.5. Concentration decay curves obtained for: (a) different initial concentrations of EtOH at 323 K, (b) BuOH at several temperatures, (c) different initial concentrations of MeOH, EtOH, PrOH, BuOH and 2M2B at 323K, and (d) different initial concentrations of PrOH at 323 K.

Concentration decay curves for each tracer at different temperatures revealed that alcohols adsorption was more significant in terms of $(C_{j,0}-C_{j,e})$ than that of 2M2B, what indicates a preferential adsorption of alcohols. MeOH and EtOH were adsorbed in higher extent than PrOH and BuOH. For the runs at 353 K with 2M2B, adsorption equilibrium was not reached after 2 h for any assayed concentration. It may be due to chemisorption of the olefin at high temperature as intermediate step for the olefin dimerization. Consequently, 2M2B adsorption was not studied at 353K. For the other cases, $K_{j,L}$ and $K'_{j,L}$ values were obtained at each temperature from the Langmuir type isotherms, see Fig. 4.8.6. All regression results are gathered in Table 4.8.2.

Generally, $K'_{j,L}$ decreased in the order MeOH>EtOH>PrOH>BuOH>2M2B. Molecular size can explain the decreasing trend of $K'_{j,L}$ as the number of carbon atoms of alcohol increased. The smaller the alcohol, the more accessible to inner active sites located in the densest polymer zones. Besides, the different polarity of alcohols, for which swelling of the polymeric matrix decreases in the same order, may present some influence. q_m and $K'_{j,L}$ values obtained for alcohols, especially for MeOH and EtOH, were found to be 2–5 fold higher than those of 2M2B. The obtained values are comparable to those determined for similar tracers over A-15 [64,221].

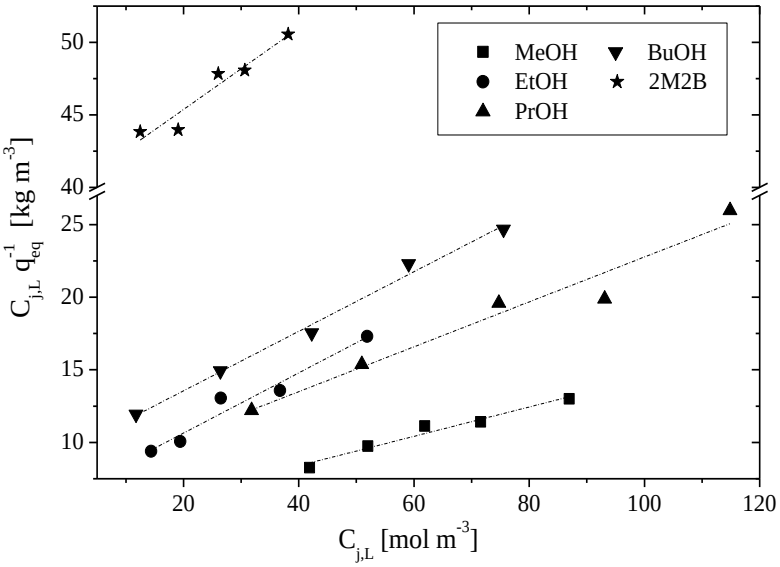

Figure 4.8.6. Example of linearization of liquid-phase adsorption isotherms on A-35 at 323 K.

Table 4.8.2. Liquid-phase adsorption equilibrium constants on A-35 and associated standard error.

Parameter	T [K]	MeOH	EtOH	PrOH	BuOH	2M2B
$K_{j,L}\cdot10^3$ [m^{3}mol^{-1}]	323	23.2 ± 3.8	31.9 ± 4.0	21.1 ± 4.4	21.67 ± 1.24	7.05 ± 0.21
	333	19.0 ± 2.6	28.6 ± 4.7	17.4 ± 2.5	15.37 ± 1.52	4.15 ± 0.13
	343	15.0 ± 3.4	25.2 ± 2.3	13.4 ± 2.1	13.78 ± 1.35	3.388 ± 0.028
	353	13.30 ± 1.10	20.56 ± 0.82	12.6 ± 2.4	10.59 ± 0.21	-
$K'_{j,L}\cdot10^3$ [m^{3}kg^{-1}]	323	229.8 ± 45.5	153.8 ± 26.6	136.8 ± 28.1	105.7 ± 8.3	25.2 ± 4.0
	333	187.2 ± 33.2	147.1 ± 34.7	119.1 ± 17.1	96.7 ± 15.5	31.4 ± 8.8
	343	152.7 ± 49.9	131.4 ± 18.0	98.5 ± 15.3	77.1 ± 13.2	21.3 ± 2.2
	353	167.3 ± 21.5	116.0 ± 8.1	91.4 ± 17.5	74.3 ± 3.2	-

$K'_{j,L}$ of alcohols and 2M2B decreased with temperature in the range investigated, as expected. In previous studies [64], it has been reported that $K_{j,L}$ increases with temperature above 334 K, what suggests chemisorption of EtOH on the active sites. However, such a behavior has not been observed for any of the alcohols used in this work. From the van't Hoff equation (Eq. 4.8.19), the liquid-phase adsorption enthalpy ($\Delta_{ads}H°_{j,L}$) and entropy ($\Delta_{ads}S°_{j,L}$) can be obtained, see Fig. 4.8.7. These values are gathered in Table 4.8.3. The dimensionless adsorption equilibrium constants ($K^*_{j,L}$) used for van't Hoff plots were obtained by transformation of values from Table 4.8.2 using Eq. 4.8.20. The total concentration C_0 was assumed to be equal to that of *n*-heptane, since tracers were highly diluted. The activity coefficients of the species, γ_j, were calculated at every temperature by means of the UNIFAC-Dortmund method [176,177].

$$\ln K^*_{j,L} = \frac{-\Delta_{ads}H^o_{j,L}}{RT} + \frac{\Delta_{ads}S^o_{j,L}}{R} \qquad (4.8.19)$$

$$K^*_{j,L} = \frac{K_{j,L}C_0}{\gamma_j} \qquad (4.8.20)$$

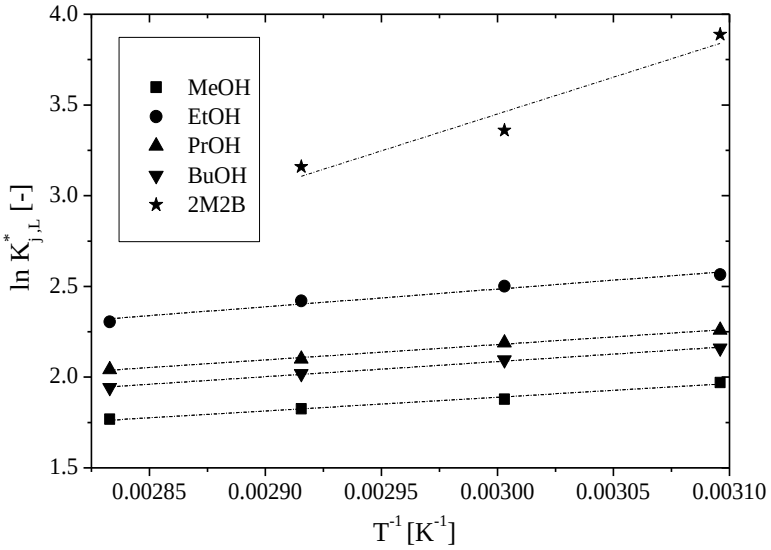

Figure 4.8.7. van't Hoff plot for tracers used in liquid-phase adsorption experiments on A-35.

Table 4.8.3. Liquid-phase adsorption thermodynamic properties and associated standard error when available.

Tracer	$\Delta_{ads}H_{j,L}$ (This work) [kJmol^{-1}]	$\Delta_{ads}S_{j,L}$ (This work) [J(molK)$^{-1}$]	$S°_{j,L}$ [J(molK)$^{-1}$]	Δ_vH_j [kJmol^{-1}]	$\Delta_{ads}H_{j,G}$ [kJmol^{-1}]	$\Delta_{ads}H_{j,L}$ [kJmol^{-1}]
MeOH	-6.3 ± 0.5	-3.2 ± 1.5	127.19[a]	37[f]	-39.7[h]	-2.7[i]
EtOH	-8.1 ± 0.9	-3.7 ± 2.8	159.86[b]	41.3[f]	-43.5[h]	-2.2[i]
PrOH	-7.0 ± 0.3	-2.9 ± 1.0	192.80[c]	44.7[f]	-50.5[h]	-5.8[i]
BuOH	-6.9 ± 0.3	-3.4 ± 1.0	225.73[d]	50.1[f]	–	–
2M2B	-33.7 ± 8.1	-72.5 ± 24.5	251.2[e]	28.4[g]	-76.9[h]	-48.5[i]

Data from the National Institute of Standards and Technology (NIST) Book: [a][227], [b][228], [c][229], [d][230], [e][231]. [f][218], [g][232], [h][150], [i]Estimated from gas-phase data and enthalpy of vaporization of compounds (Δ_vH_j) as: $\Delta_{ads}H_{j,L}=\Delta_vH_j+\Delta_{ads}H_{j,G}$.

The obtained $\Delta_{ads}H°_{j,L}$ values were very similar for alcohols and also similar to the value of -6.36 kJmol^{-1} determined by Limbeck et al. (2001) [233] for water adsorption on a strongly acidic cation exchange resin. Their low values indicate weak temperature dependence of adsorption equilibrium constants. This is in good agreement with the results obtained in *Section 4.7* in the kinetic modeling by non-linear regression. On the contrary, $\Delta_{ads}H°_{2M2B,L}$ and $\Delta_{ads}S°_{2M2B,L}$ were notably larger than those of alcohols. These unexpected large values could be attributed to chemisorption of the olefin, since isomerization reaction is expected to be significant within the explored temperature range. The fulfillment of the Boudart rules [112,113] was checked to assess the thermodynamic consistency of estimated data. The rules that can be applied to IER are detailed in *Section 1.5.7*. Those values use for comparison purposes are gathered in Table 4.8.3. As seen, the obtained $\Delta_{ads}H_{j,L}$ values are in reasonable agreement with those estimated from gas-phase studies on A-15 [150].

4.8.5 GAS-PHASE ADSORPTION EXPERIMENTS

Pulse-response experiments were performed for PrOH, BuOH, IB, 2M1B, 2M2B, MTBE, ETBE, PTBE, BTBE and TAEE. The first moment showed a linear dependence on space time (LU_0^{-1}) at different temperatures with R^2 values ranging from 0.94 to 0.99 for all the tracers.

Alcohols response peaks presented very long tails to the right (positive skew), taking about 5-10 h to obtain the whole peak. Response peaks for olefins and ethers presented also positive skew, though 1 or 2 h were typically enough for total elution. This fact clearly indicates a strong interaction of alcohols in the packed bed resulting in very high retention times. Typical results obtained for first absolute moments are depicted in Fig. 4.8.8. Responses with long tails suggest important contribution of diffusion phenomena to the second absolute moment.

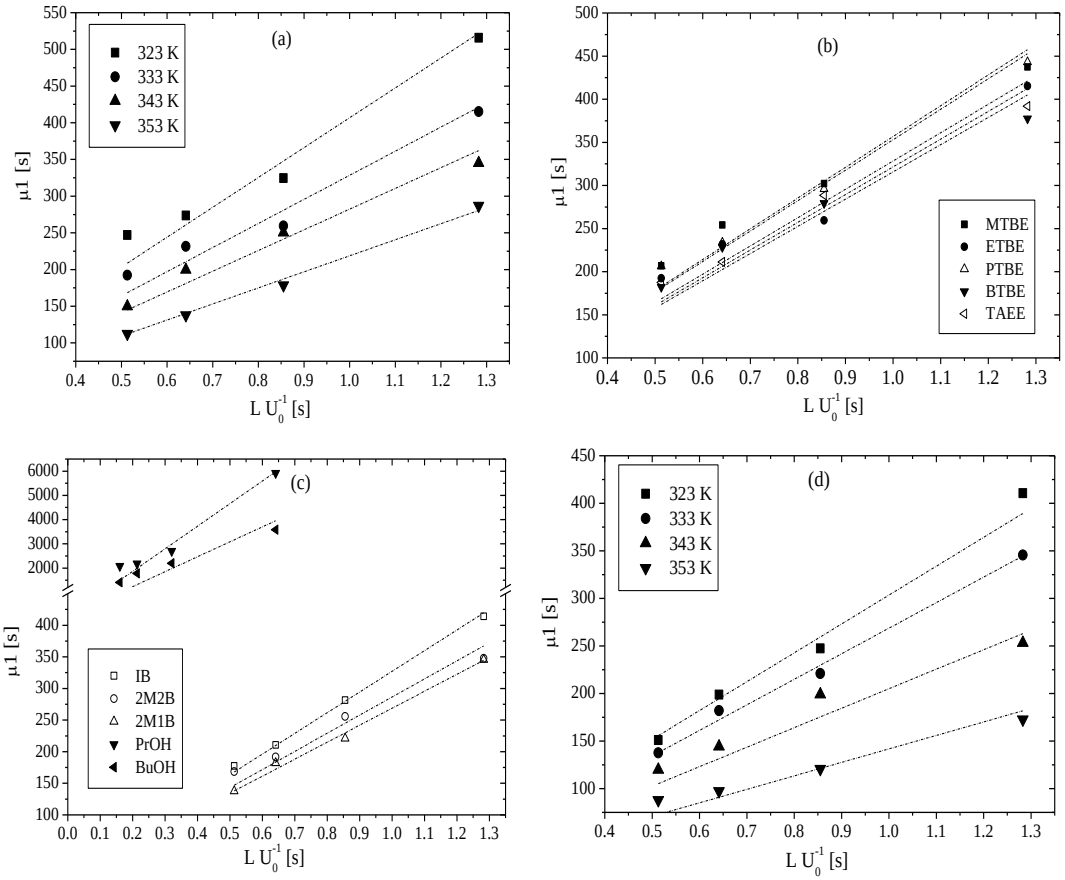

Figure 4.8.8. First absolute moment data obtained for: (a) ETBE at different temperatures, (b) ethers at 333 K. (c) IB, 2M1B, 2M2B, PrOH and BuOH at 333K, and (d) 2M1B at different temperatures.

$\rho_p K_{j,G}$ values obtained from the slopes (passing from the origin) of linear relations μ_1 vs. $L\ U_0^{-1}$ are gathered in Table 4.8.4. When gas-phase adsorption data could not be obtained, they were estimated from liquid-phase values following the procedure described elsewhere [64,234]. As it can be seen, very similar values of $\rho_p K_{j,G}$ were obtained for MTBE, ETBE, PTBE and TAEE, and slightly lower for BTBE. With respect to olefins, $\rho_p K_{2M1B,G}$ and $\rho_p K_{2M2B,G}$ were similar and slightly lower than $\rho_p K_{IB,G}$, whose values are very similar to those of ethers. This suggests that IB is more prone to be adsorbed on the resin than isoamylenes. Among 2M1B and 2M2B, the former presented slightly lower values of $\rho_p K_{j,G}$. Such preferential adsorption of IB is in concordance with results of *Sections 4.5* and *4.7*. Generally, it can be concluded that adsorption equilibrium constants of olefins and ethers are of the same order of magnitude, implying comparable adsorption. $\rho_p K_{j,G}$ of alcohols were about two order of magnitude larger than those of olefins and ethers, showing a preferential adsorption, in agreement with literature [65]. As for the liquid-phase case, this fact can be explained by the formation of hydrogen bonds between the $-SO_3H$ network of active sites and the hydroxyl group of alcohols and by the swelling induced by alcohols that favors adsorption. Differences between experimental $\rho_p K_{j,G}$ and those from liquid phase data could be due to a different swelling in liquid- and gas-phase experiments.

The estimated gas-phase apparent heat of adsorption ($\Delta_{ads}H^{o}_{j,G}$) from van't Hoff equation for all tracers, see Table 4.8.4, are in reasonable agreement with those determined over A-15 [65]. As a whole, adsorption of alcohols was more exothermic than those of olefins and the corresponding ethers. 2M1B adsorption was slightly more exothermic than that of 2M2B. Generally, obtained $\Delta_{ads}H^{o}_{j,G}$ were notably larger than $\Delta_{ads}H^{o}_{j,L}$, indicating that adsorption process in gas-phase is more temperature dependent. Globally, the obtained $\rho_p K_{j,G}$ and $\Delta_{ads}H^{o}_{j,G}$ values are in reasonable agreement with those obtained for these tracers over A-15 [65].

Table 4.8.4. Adsorption equilibrium constants ($\rho_p K_{j,G}$) and apparent heat of adsorption obtained in gas-phase from 323 to 353 K over A-35.

	$\rho_p K_{j,G}$ [-]				$\Delta_{ads}H^{o}_{j,G}$
Tracer	323 K	333 K	343 K	353 K	[kJmol^{-1}]
MTBE	169.3	147.6	114.1	90.2	-20.3 ± 2.1
ETBE	168.4	135.8	116.7	90.3	-19.1 ± 1.5
PTBE	168.5	146.1	116.7	86.9	-20.9 ± 2.7
BTBE	139.3	130.6	102.6	69.8	-21.8 ± 5.2
2M1B	125.5	111.0	87.8	58.4	-21.7 ± 1.1
2M2B	136.8	118.4	106.0	72.1	-19.1 ± 4.5
TAEE	162.9	133.0	105.4	82.0	-23.8 ± 4.7
IB	168.8	135.3	112.6	66.8	-27.9 ± 5.9
MeOH	3485.1[a]	2341.5 [a]	1619.2 [a]	1392.7 [a]	-29.7 ± 3.4
EtOH	4775.5 [a]	3666.9 [a]	2697.5 [a]	1984.2 [a]	-27.9 ±1.2
PrOH	13399.5[a]	8658.9[a]	5508.4[a] 8576.0	3983.0[a] 3868.4	-38.9 ± 1.4
BuOH	28877.7[a]	18784.9[a]	10594.3[a] 5888.1	7973.8[a] 2556.9	-41.8 ± 2.4

[a]Estimated from liquid-phase values through thermodynamic relations.

Empty tube experiments were performed for BuOH, TAEE and 2M2B to assess the possible contributions to the moments caused by dead volumes in the setup. Such contributions were estimated as lower than 1% for μ_2 and less than 5% for μ_1, therefore no corrections were applied to calculated moments. Decomposition of ethers was expected in gas-phase runs, but only the tracer peak was observed in the signals. It can be explained by the short contact time with the packed bed adsorber compared to the batch adsorber [65], and by the fact that gas-phase reaction rates are around 25 times slower than in the liquid-phase [123].

4.8.6 DIFFUSION RESISTANCES

4.8.6.1 Gas-phase diffusivities

As for the second central moments (Eq. 4.8.12), the contributions of δ_d, δ_f, δ_a and δ_i have been evaluated. If adsorption and desorption within porous particles is sufficiently rapid and strong, the concentration profile within the particle may be asymmetric, which can lead to significant contribution of axial dispersion arising from the transport through the porous solid. The axial dispersion coefficient D_z in the packed bed was estimated by means of Eq. 4.8.21, as Wakao proposed for porous particles [62], where υ is the kinematic viscosity (the ratio of dynamic viscosity to gas-phase density of tracers), and D_v is the gas-phase molecular diffusivity of the tracers in the carrier gas. Dynamic viscosity has been estimated by means of the corresponding states method, accounting for correction factors for polarity of compounds as described by Lucas [212]. Critical properties for viscosity calculations have been estimated from Joback method [212]. Gas-phase densities have been calculated from the Redlich-Kwong Equation for

real gases, but ideal-gases law can also be safely used, since deviations from ideal behavior have been found to be lower than 0.8% for all tracers and temperatures. D_v values have been estimated following the Chapman and Enskog equations (see *Appendices 7.10.2* and *7.10.3*) and the method described by Fuller [212]. The contribution of δ_d to μ_2 varied from 1 to 5%.

$$\frac{D_z}{2\upsilon R_0} = \frac{20}{\varepsilon_b}\left(\frac{D_\upsilon}{2\upsilon R_0}\right) + \frac{1}{2} = \frac{20}{ReSc} + \frac{1}{2} \tag{4.8.21}$$

The film mass transfer coefficient (k_f) has been estimated by Eq. 4.8.22 [63]. The values range was from 6 to 23 m s^{-1}. The contribution of δ_f to μ_2 was negligible, less than 0.001 %.

$$\left(\frac{2k_f R_0}{D_v}\right) = 1.15\left(\frac{v}{D_v}\right)^{1/3}\left(\frac{2R_0U_0}{v}\right)^{1/2} \tag{4.8.22}$$

Macropore gas-phase diffusion coefficient (D_a) is a function of the Knudsen diffusion coefficient (D_T) and it can be calculated through Eq. 4.8.23. D_T has been estimated by Eq. 4.8.24 as described by Smith [235]. The tortuosity factor ($\tau=1/\varepsilon_a$) for A-35 has been estimated as 4.1. D_a values varied from $8\cdot10^{-8}$ to $3.6\cdot10^{-7}$ m^2s^{-1} for all tracers. The final contribution of δ_a to the μ_2 was less than 7%.

$$D_a = \frac{\varepsilon_a D_T}{\tau} \tag{4.8.23}$$

$$D_T = 9700 r_a\left(\frac{T}{M_j}\right)^{\frac{1}{2}} \tag{4.8.24}$$

Once μ_2, δ_d, δ_f and δ_a were known, δ_i was calculated and micropore diffusivities (D_i) have been estimated using the r_0 value determined by SEM. D_i obtained values have been of the order 10^{-20}–10^{-21} m^2s^{-1}. Contributions of δ_i to μ_2 were larger than 85%, hence important micropore diffusion limitations occur in commercial particles of A-35. Obtained D_a and D_i values are reasonable, since D_i is usually smaller than D_a [224]. Typical values obtained from μ_2 analysis for evaluated tracers are gathered in Table 4.8.5. Finally, the obtained α values in gas-phase ranged from 0.005 to 0.05, what indicates that both macro and micropore diffusion resistances are significant and they cannot be neglected. Obtained values are in agreement with those reported for A-15 [65], but micropore diffusion resistance has resulted to be more significant on A-35.

Table 4.8.5. Second central moment analysis for some tracers at 353 K and $L\cdot U_0^{-1}$= 0.64 s.

Tracer	μ_1 [s]	μ_2 [s^2]	k_f [m s^{-1}]	$D_T\cdot10^6$ [m^2 s^{-1}]	$D_a\cdot10^7$ [m^2 s^{-1}]	$D_i\cdot10^{20}$ [m^2 s^{-1}]	$\frac{D_i}{r_0^2}\cdot10^5$ [s^{-1}]	$\frac{R_0^2}{D_a}+\frac{r_0^2}{D_i(\rho_p K)}$ [s]	$\frac{R_0^2}{D_a}$ [s]	α [–]
MTBE	150.79	46219	10.47	2.29	1.39	2.41	9.98	111.68	0.51	0.005
ETBE	137.73	37675	10.18	1.98	1.20	2.97	12.3	90.69	0.59	0.007
PTBE	141.47	47733	9.96	1.74	1.05	2.25	9.31	124.32	0.67	0.005
BTBE	89.30	10029	9.78	1.55	0.94	8.78	36.3	40.21	0.75	0.019
2M1B	97.36	6991	10.56	2.88	1.74	10.5	43.3	39.97	0.40	0.010
2M2B	119.94	13685	10.45	2.88	1.74	6.57	27.2	51.46	0.40	0.008
TAEE	123.91	29037	9.98	1.74	1.05	3.51	14.5	84.82	0.67	0.008
IB	120.11	26956	10.87	3.60	2.18	3.06	12.6	118.75	0.32	0.003
PrOH	5915.86	11924709	11.03	3.36	2.03	0.42	1.74	15.21	0.35	0.023
BuOH	3583.56	11329494	10.91	2.73	1.65	0.28	1.17	33.72	0.43	0.013

4.8.6.2 Liquid-phase diffusivities

Dimensionless concentration profiles, $(C_j-C_{j,eq})/(C_{j,0}-C_{j,eq})$ vs. time, were built and the area under these curves, the zeroth moments (Eq. 4.8.3), was used to estimate liquid-phase effective diffusion coefficients. The obtained $m_{0,L}$ values ranged between 250-800s for alcohols and 500-2000s for 2M2B. R_0^2/D_a and $r_0^2/D_i^{'}$ terms in Eq. 4.8.10 are the characteristic times of diffusion in the macropores and within the gel-like microspheres. D_a values are expected to be different in liquid- and gas-phase, but D_i is expected to be the same, since it occurs by strong interactions of the adsorbed molecules and the catalyst matrix by forming hydrogen bonds with the catalyst $–SO_3H$ groups [221]. The parameter α in liquid-phase, which ranged from 30 to 150, has been estimated by $D_i^{'}$ values shown in Table 4.8.5. Micropore diffusion was the most relevant contribution to the diffusion times ($R_0^2/D_a + r_0^2/D_i^{'}$) for gas-phase adsorption (Table 4.8.5). However, obtained α values indicate that micropore diffusion resistance is much smaller than macropore diffusion resistance in liquid-phase. This result is supported by those obtained for A-15 [221,236], where it was found that the efficiency of the catalyst operating in liquid-phase reactions is mainly due to the process occurring in the macropores since the efficiency in the gel microspheres is unity [237]. As a consequence, Eqs. 4.8.6 and 4.8.10 can be rewritten as Eqs. 4.8.25 and 4.8.26, respectively.

$$\frac{D_a}{R^2}\frac{\partial}{\partial R}\left(R^2\frac{\partial q}{\partial R}\right)=\frac{\partial q}{\partial t} \tag{4.8.25}$$

$$m_{0,L}=\frac{R_0^2}{15D_a\left(1+\frac{m_s}{\rho_p}\left(\varepsilon_A+\rho_p K_{j,L}^{'}\right)\right)} \tag{4.8.26}$$

D_a can be estimated once the values of $m_{0,L}$ and $K'_{j,L}$ are known. Table 4.8.6 summarizes some typical values obtained for the different tracers evaluated in the liquid-phase. Generally, D_a values for alcohols were larger than those obtained for 2M2B. This result can be ascribed to resin swelling caused by alcohols, which eventually favors diffusion of adsorbing species after the widening of the catalyst pores. Among alcohols, slightly higher D_a values were obtained for MeOH and EtOH that can be related to the molecular size, since the smaller the molecule the easier the diffusion through the catalyst macropores. Although D_a values are expected to increase with temperature and tracer concentration, no clear trends have been observed for the explored range. D_a values estimated on A-35 are lower than those on A-15 in the presence of the same tracers [221]. This is coherent, since A-35 is the oversulfonated version of A-15. The larger amount of sulfonic groups of A-35 resulted in a denser structure through which adsorbing species had found more hindrances to diffuse. The smaller surface area, pore volume and diameter obtained by BET analysis for A-35 compared to A-15 enforced this conclusion [19]. Liquid-phase macropore diffusion times (R_0^2/D_a) calculated from Table 4.8.6 ranged from 550 to 1000 s, being about 10 times larger than micropore diffusion times ($r_0^2/D_i^{'}$), which confirms the higher importance of macropore diffusion resistance in liquid-phase. Possible differences in the extent of swelling of microspheres in gas- and liquid-phase experiments could have some effect on the diffusion times within the gel-like microspheres. Nonetheless, such differences were not expected to be significant in the present system because the high dilution of tracers explored.

Table 4.8.6. Diffusivities of tracers evaluated in the liquid-phase.

Tracer	T [K]	$C_{j,e}$ [molm^{-3}]	$D_a \cdot 10^{12}$ [m^{2}s^{-1}]
MeOH	323	41.87	11.08
	333	50.78	11.10
	343	59.25	9.68
	353	71.13	12.41
EtOH	323	26.50	11.32
	333	19.94	7.48
	343	26.24	12.29
	353	37.34	9.44
PrOH	323	74.72	8.87
	333	33.85	9.38
	343	33.25	6.98
	353	92.66	9.12
BuOH	323	59.07	7.68
	333	44.17	7.62
	343	44.54	9.15
	353	77.21	8.57
2M2B	323	38.16	1.99
	333	37.70	1.71
	343	36.62	2.05
	353	10.78	2.56

The effect that resin swelling in different solvents can exert on the morphological properties and therefore on effective diffusion coefficients is also crucial, since porosity, pore size, particle radius and microspheres radius can change significantly. The more polar the solvent, the larger the swelling expected. Nonetheless, in very dilute systems, as in the present study, this effect is less noticeable and therefore the approximation of constant morphological properties, determined in dry state by BET technique, can be considered accurate enough for calculations. Since obtained values were in concordance with previous studies over a similar catalyst, diffusion data presented in this work are considered as reliable. In non-diluted systems in which resin is more swollen such consideration will not be appropriated and other characterization techniques as ISEC would be more suitable.

Furthermore, adsorption must be taken into account as a complex process in which several species are competing for the active sites. As previously demonstrated, adsorption equilibrium constants of olefins increase when the catalyst is previously pretreated with alcohols [65], indicating that the adsorption of one tracer influences the adsorption of others. This presents a remarkable effect on estimated diffusion coefficients, apart from possible effects of varying liquid-phase concentrations.

4.8.7 PARTIAL CONCLUSIONS

Liquid- and gas-phase adsorption of C_1-C_4 alcohols, C_4-C_5 iso-olefins and tertiary ethers obtained thereof has been studied on Amberlyst™35 in the temperature range from 323 to 353K. Adsorption equilibrium constants of olefins and ethers are similar, and notably lower than those of alcohols. Obtained liquid-phase adsorption enthalpy indicates that alcohols adsorption had relied less on temperature whereas the larger values for 2M2B had suggested chemisorption of the olefin as intermediate step of isomerization reaction. The moment technique has been used to assess the effective diffusion coefficients of adsorbing species. Macropore resistance has been found to be more significant than diffusion within the gel-like microspheres in liquid-phase, while both macro and micropore diffusion are significant in gas-phase. Diffusion and adsorption are influenced not only by the molecular size of adsorbing species, but also by swelling caused by alcohols.

4.8.8 CHAPTER NOTATION

$\Delta_{ads}H^o_j$ standard molar heat of adsorption of compound *j* [kJ mol^{-1}]
$\Delta_v Hj$ enthalpy of vaporization of compound j [kJ mol^{-1}]
$\Delta_{ads}S^o_j$ standard molar entropy change of adsorption of compound *j* [J(mol K)$^{-1}$]
ΔS^o_j standard molar entropy of formation of compound *j* [J(mol K)$^{-1}$]

C_0 total concentration of species [mol m^{-3}]
C_j tracer concentration equation in the bulk phase (liquid or gas) [mol L^{-1}]
$C_{j,0}$ initial concentration of tracer in the liquid-phase [mol m^{-3}]
$C_{j,a}$ tracer concentration equation in the macropores [mol m^{-3}]
$C_{j,e}$ equilibrium concentration of tracer in the liquid-phase [mol m^{-3}]
D_0 average diameter of catalyst particles [m]
d_0 average microsphere diameter [m]
D_a effective macropore diffusion coefficient [$m^2 s^{-1}$]
D_i' effective microsphere diffusion coefficient [$m^2 s^{-1}$]
D_T Knudsen diffusion coefficient [$m^2 s^{-1}$]
D_z axial dispersion coefficient [$m^2 s^{-1}$]
D_υ molecular diffusivity of tracers in the carrier gas [$m^2 s^{-1}$]
K^*_j dimensionless adsorption equilibrium constant of compound *j* [–]
K'_j apparent adsorption equilibrium constant of compound *j* [$m^3 kg^{-1}$]
k_f film mass transfer coefficient [m s^{-1}]
K_j adsorption equilibrium constant of compound *j* [$m^3 mol^{-1}$]
L packed bed length [m]
M_j molecular weight of compound *j* [kg mol^{-1}]
m_n n^{th} moment [–]
m_s ratio of catalyst dry mass to total volume of liquid (solvent plus tracer) [kg L^{-1}]
q adsorbed concentration [mol kg^{-1}]
q_{eq} adsorbed concentration at equilibrium [mol kg^{-1}]
q_m maximum adsorption capacity (at saturation) [mol kg^{-1}]
r_0 average microsphere radius [m]
R_0 average radius of catalyst particles [m]
Re Reynolds number [dimensionless]
r_a macropore radius [m]
T temperature [K]
t time [s]
U_0 linear velocity [m s^{-1}]

Greek symbols

ε_a macroporosity of the catalyst [dimensionless]
ε_b bed void fraction [dimensionless]
ρ_p catalyst apparent density [kgm^{-3}]
υ kinematic viscosity [$m^2 s^{-1}$]
α parameter for macro- and micro-pore diffusion times ratio [dimensionless]
γ_j activity coefficient of a species j [dimensionless]
τ macropore tortuosity factor [dimensionless]
μ_1 first absolute moment [s]
μ_2 second central moment [s^2]

Subscripts

G gas-phase
L liquid-phase
ads adsorption
n number of moment evaluated

4.9 DEACTIVATION OF ION-EXCHANGE RESINS BY ACETONITRILE

A revised version of this chapter is being prepared by *R. Soto, C. Fité, E. Ramírez, J. Tejero* & *F. Cunill* for submission to *Appl. Catal., A* journal under the title: Deactivation of acidic ion-exchange resins by acetonitrile in the simultaneous liquid-phase syntheses of ethyl *tert*-butyl ether and *tert*-amyl ether.

4.9.1 INTRODUCTION

A fundamental basis of process intensification and integration relies on the catalyst lifespan and how to make the catalytic beads in industrial reactors longer lasting [238] to enhance production indexes as kg product/kg catalyst. While catalyst deactivation is inevitable for most processes, some of its immediate and drastic consequences may be avoided, postponed, or even reversed [239]. Catalyst lifespan is, after yield and selectivity, the most important catalytic feature when selecting a catalyst for an industrial process. Consequently, sound studies on the causes of catalyst deactivation can generate remarkable benefits. Unfortunately, catalyst deactivation studies are limited and the literature related to catalyst lifespan is very scarce, particularly those referred to ion-exchange resins [118,119].

The most prominent poison in MTBE and ETBE plants is ACN, with typical concentrations up to 2000 ppm the recycle streams to the reaction unit [116]. Experimental studies on the effect of ACN presence on etherification plants are barely found [118,119,240] and while some authors support that deactivation proceed through direct hydrolysis, others consider that alcoholysis is the prevalent deactivation mechanism [119]. Deactivation by ACN in the synthesis of TAEE has not been studied to the best to our knowledge. The present work aims to study the effect of ACN presence in the ethanol feed stream on the simultaneous liquid-phase production of ETBE and TAEE using acidic ion-exchange resins. The determination of the deactivation mechanism and the involved kinetic parameters are also goals to achieve.

4.9.2 EXPERIMENTAL AND CALCULATIONS

The setup described in *Section 3.2.2* was used in all the runs of the present section. Most of the experiments were carried out using Amberlyst™35 as catalyst. Purolite®CT-275 was also used to compare deactivation process on both ion-exchange resins. Both acidic ion-exchange resins are macroporous and oversulfonated and they show a high level of activity in the simultaneous ETBE and TAEE formation (see *Section 4.6*). The main physicochemical and structural properties of both catalysts are detailed in Tables 3.1 and 4.6.1. According to the results obtained in *Section 4.7*, the catalysts particle size range used was 0.25–0.4 mm to avoid the effects of internal mass transfer.

The catalyst bed consisted of resin homogeneously diluted with inert silicon carbide. The inert was used to keep the bed isothermal, and also to assure good contact between reactants and catalyst avoiding back-mixing and channeling. The dilution ratio (DR) of inert mass to catalyst load in the bed was varied from 10 to 330, depending on the temperature. These DR range is usually small enough to avoid the effects of excessive dilution on reaction rates caused by the distribution of inert and catalyst particles in the bed [241]. The used catalyst loads allowed to work under differential regime, what is to say at very low conversion levels (X_{IB}<10% in the present work). Under these conditions, the reactor can be considered isothermal and therefore reaction rate is practically constant along the reactor. Consequently, the measure of the conversion evolution at the reactor outlet is related to the activity level and the activity decay can be evaluated at known conditions.

As for the experimental procedure, initially, the three reactants reservoirs were filled respectively with an equimolar mixture of olefins (IB and IA), EtOH and EtOH containing ACN. ACN concentration in the EtOH feed stream was varied in the range 500–4000 ppm. Though these concentrations are higher than those typically found in etherification plants, they were chosen to observe significant activity decay during the runs duration. The water content in the poisoned EtOH stream was varied from 1000 to 5000 ppm to study its inhibitory effect from a kinetic standpoint and to assess the effect of water in the deactivation process, since water can also act as reactant in deactivation reactions [117]. Then the reactor was filled with the mixture of catalyst and inert and it was connected to the setup. Afterwards, pressure, temperature and pump flows were set in the PID controlling software. Pressure was always set to 17 bar to widely exceed the mixture vapor pressure at the highest temperature explored and to impel the reactants and products mixture through the piping to the analysis system avoiding the pressure drops of the setup elements. The temperature was varied from 313 to 353 K. HPLC pump flow rate used for EtOH or poisoned EtOH was set to 0.831 mL/min. When the desired reactor temperature was reached, the flow of the second HPLC pump was set to 1.28 mL/min and the mixture of IB and IA was fed to the reactor inlet stream. These flows were adjusted for an initial alcohol to olefins molar ratio of $R^{\circ}_{A/O}$=1.1 and an initial olefins molar ratio of $R^{\circ}_{C4/C5}$=1. Besides, the total inlet mass flow rate was 87 g/h, which corresponds to a WHSV ranging from 400 to 2000 h^{-1}, depending on the catalyst load used, which is sufficiently high to avoid the effects of external mass transfer, according to literature [19,118].

The reactor outlet composition was analyzed inline. When the system reached the steady state (constant reactions rates), the feed stream of EtOH was immediately switched to poisoned EtOH by means of a three ways valve. That moment was considered as the initial time of the deactivation experiments. Samples from the reactor outlet were analyzed periodically (approximately each 11 min). The typical deactivation runs duration was 4h.

Etherification rates were calculated by Eq. 3.5 from the corresponding olefin (IB or IA) consumption in the reactor at steady state, since no side reactions were detected. By plotting the Arrhenius equation, apparent activation energies of ETBE and TAEE formation reactions were estimated from Eq. 4.9.1:

$$\ln r_i^0 \cong \ln A - \left(\frac{Ea'_i}{RT} \right) \qquad (4.9.1)$$

where r_i^0 is the reaction rate measured at steady state and A is related to the apparent reaction pre-exponential factor.

Catalyst activity was calculated as the ratio of the measured ETBE or TAEE formation rate at any instant (r_j^t) to that obtained at steady state (r_j^0), in the absence of poison, as follows:

$$a_j^t = \frac{r_j^t}{r_j^0} \qquad (4.9.2)$$

In order to assess the reproducibility of experiments, experimental uncertainty was estimated from rate data at steady state. Standard errors associated with the determination of experimental etherification rates were lower than 4% at 353 K and lower than 2% at 333 K. Therefore, experiments were assumed as reproducible and reliable.

4.9.3 DESCRIPTION OF THE REACTION SYSTEM

In addition to the expected reactions involved in the simultaneous etherification of IB and IA with EtOH in absence of poisons that are described in Fig. 4.1.1 (*Section 4.1*), some additional reactions are derived from the presence of ACN in the feed. ACN is a weak base and it adsorbs on the resin active sites. The interaction of diffused adsorption of ACN is of prevailing acid-base nature. Two different deactivation mechanisms of the catalyst sulfonic groups can occur as a result of the presence of ACN in the feed streams [116]: i) direct hydrolysis (Fig. 4.9.1) and, ii) alcoholysis followed by hydrolysis (Fig. 4.9.2), also known as Pinner reaction. In the former, ACN reacts with water to form acetamide, which in turn reacts with another water molecule to form ammonia and acetic acid. In the Pinner reaction, adsorbed ACN reacts with EtOH to produce an unstable intermediate (salt of imido ester) that subsequently undergoes hydrolysis with a molecule of water to produce ethyl acetate and ammonia. For both mechanisms, ammonia is the final chemical species that neutralize the active sites.

It is to be noticed that hydrolysis reaction rate is much faster than alcoholysis, in spite of the low water content present compared to that of EtOH [117]. Acetamide, ammonium acetate, acetic acid and ethyl acetate were not detected in any run, which is ascribed to their adsorption on active sites that eventually causes neutralization, according to literature [119]. ACN was always detected at the reactor outlet though in lower concentrations than those fed to the reactor.

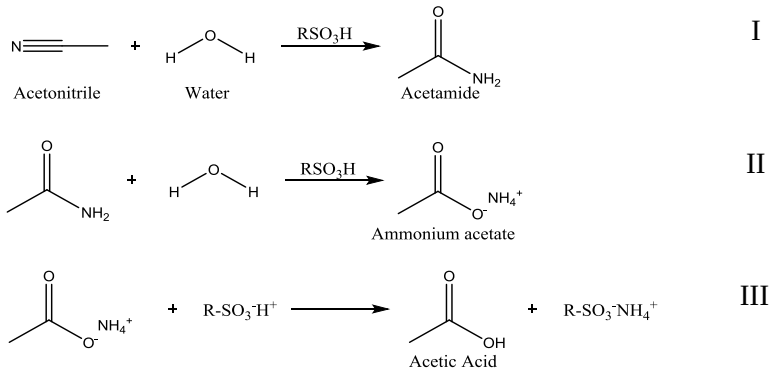

Figure 4.9.1. Direct hydrolysis mechanism.

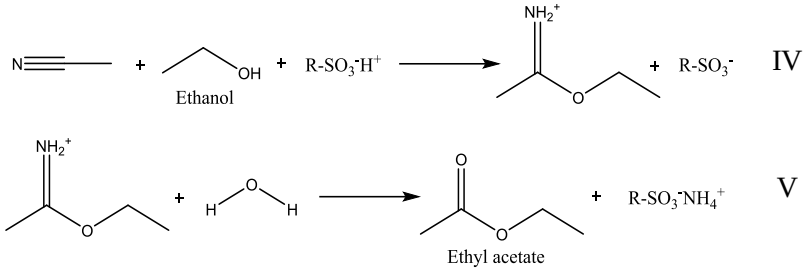

Figure 4.9.2. Alcoholysis mechanism (Pinner reaction).

4.9.4 STEADY STATE ETHERIFICATION RATES AND WATER INHIBITION MODELING

Experimental etherification rates for all tested experimental conditions are gathered in Table 4.9.1, whence several inferences can be drawn. Firstly, the higher the temperature the faster the etherification rates at steady state, as expected. Secondly, the higher the initial water content in the EtOH stream the lower the reaction rate obtained at steady state. This fact was expected since the inhibitory effect of water on etherification reactions has been already observed in other studies [37] and also in *Section 4.5*. Finally, both ETBE and TAEE formation rates were faster on A-35 than on CT-275. This result is in good agreement with previous studies regarding similar etherification reactions on several ion-exchange resins [19] and also with the results obtained in a batch reactor in *Section 4.6*. The different catalytic activity of A-35 and CT-275 must be attributed to the slightly higher acid capacity of A-35, rather than to a higher acid strength of the active sites, since the enthalpy of ammonia adsorption on both resins was found to be identical (113 ± 3 kJ/mol) [34].

Table 4.9.1. Etherification rates obtained at different experimental conditions.

Catalyst	T [K]	C_{H2O} [ppm]	C_{ACN} [ppm]	r^0_{ETBE} [mol (h kg_{cat})$^{-1}$]	r^0_{TAEE} [mol (h kg_{cat})$^{-1}$]
A-35	353	1000	2300	855.4	147.3
A-35	353	1000	500	911.2	161.1
A-35	333	1000	1100	200.3	29.5
A-35	353	1000	4000	814.6	139.3
A-35	333	1000	3100	196.9	28.8
A-35	313	1000	4000	38.3	5.1
A-35	333	5000	3100	155.9	20.5
A-35	333	3000	3100	163.3	20.9
CT-275	333	1000	3100	148.4	24.6
A-35	333	1500	3100	189.5	27.5

From Eq. 4.9.1, Arrhenius plot of experimental etherification rates, see Fig. 4.9.3, allowed the estimation of apparent activation energies on A-35 as 72.5 ± 3.8 and 80.6 ± 6.3 kJ/mol for ETBE and TAEE, respectively. These apparent activation energies and rate values from Table 4.9.1 are in good agreement with those determined in *Section 4.7* considering that the lower water content in these runs was 1000 ppm and also with those previously obtained for the isolated formation of these ethers [123,131]. Such outcome enforces the reliability of the steady state values obtained prior to start the deactivation experiments.

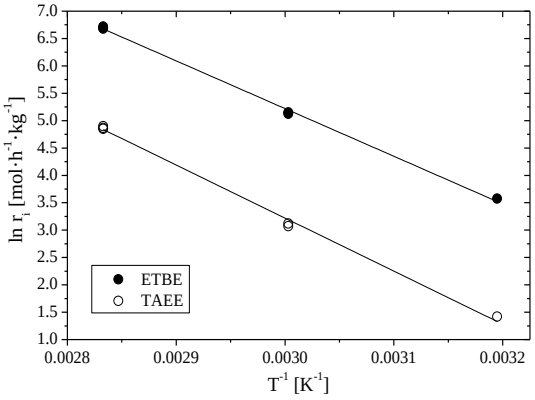

Figure 4.9.3. Arrhenius plot of reactions rates obtained at steady state and different temperatures over A-35. $R^{o}_{A/O}$=1.1 and $R^{o}_{C4/C5}$=1.

From reaction rates obtained at steady state for different water contents in the EtOH feed stream, the inhibition process caused by water can be assessed. Several mathematical expressions were evaluated based on previously proposed models regarding the inhibitory effect of water, see Table 4.9.2. Nonlinear regression was performed to estimate the parameters in such expressions by minimizing the residual sum of squares (RSS) between experimental and calculated r/r^0 values at different initial water concentrations.

The values of r^0 correspond to the global rate of EtOH consumption obtained in the absence of extra water and it was calculated as $-r_{EtOH} = r_{ETBE} + r_{TAEE}$ by means of the kinetic expressions determined in *Section 4.7* as 258.15 mol(h kg_{cat})$^{-1}$. r_{EtOH} was used since EtOH is the common reactant for both etherification reactions, which allows to evaluate the inhibitory effect of water through the estimation of the adsorption equilibrium constant of water (K_w) as a singular value. Nonetheless, it is to be noted that the inhibitory effect of water has been shown to affect differently to ETBE and TAEE formation reactions, as seen in *Section 4.5*, which is probably due morphological reasons arising from the different accessibility of active sites.

Table 4.9.2. Modeling results for the inhibition caused by water.

Model	Expression type	RSS	Parameter value	Literature	
I[c]	$\left(\frac{r}{r^0}\right)=\exp\left(-K_w\cdot a_w\right)$	0.0018	K_w=12.48	-	[h]K_w=10.92
II[a,d]	$\left(\frac{r}{r^0}\right)=\frac{1}{1+K_w\cdot\sqrt{a_w}}$	0.005	K_w=2.17	[d] K_w=2.43	[h]K_w=39.01
III[a,e]	$\left(\frac{r}{r^0}\right)=\frac{1}{1+K_w\cdot a_w}$	0.0009	K_w=14.82	[e]K_w=0.659 L/mol	[h]K_w=19.51
IV[b,f]	$\left(\frac{r}{r^0}\right)=\exp\left(-K_w\cdot\left(a_w\right)^{\frac{1}{\alpha}}\right)$	0.0008	K_w=3.52 α=1.43	[f]K_w=0.88 [f]α=10.75	[h]K_w=3.30 [h]α=0.58
V[a,g]	$\left(\frac{r}{r^0}\right)=\frac{1}{1+K_w\cdot a_w^2}$	0.018	K_w=542.4	-	-

[a] Derived from the Langmuir isotherm. [b] Derived from the Freundlich isotherm. [c] Exponential-like model. [d] From Limbeck et al. (2001)[233] at 383–393 K. [e] From Yang et al. (1998) [242]. [f] From Du Toit et al. (2004)[243] within 353–408k on Amberlyst™16. [g]From Baba & Ono (1986) [244]. [h] From Gonzalez (2011) [49] at 333 K and $R°_{A/O}$=1 on A-35.

The results show that Freundlich based model is more accurate than Langmuir based ones for the prediction of the inhibitory effect caused by water, in agreement with literature [243]. However, Langmuir-type model III also reported reliable results and could be used within the assayed range of water concentrations. Even exponential-like model I fits relatively well to the

experimental data. The worst fit was found for models II and V. Fig. 4.9.4 plots the r/r^0 vs. the activity of water (calculated using UNIFAC-Dortmund method) for all the evaluated models.

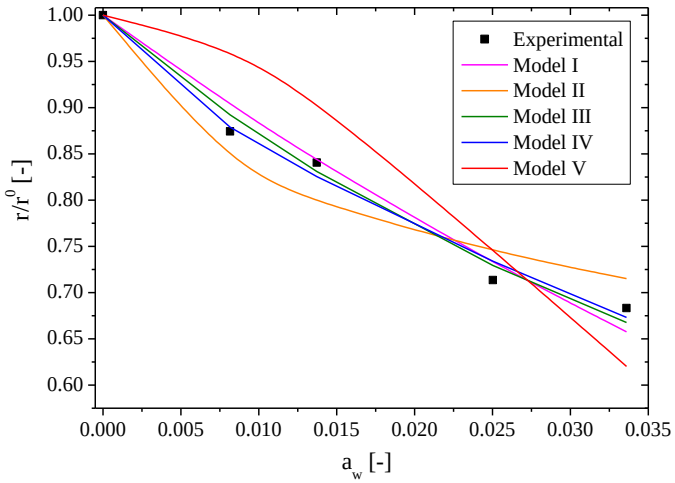

Figure 4.9.4. r/r^0 vs. the activity of water for all the evaluated models.

4.9.5 EFFECT OF ACN CONCENTRATION

Due to the different chemical effects that some species will show in the present study, it is important to distinguish between poisons and inhibitors. Poisons are usually substances showing a strong and typically irreversible interaction with the active sites, whereas inhibitors show a generally weak and reversible interaction [245]. Though some authors have classified water as deactivator (poison) for etherification reactions on IER, its consideration as inhibitor is more frequent and appropriate owing to the reversible nature of its adsorption. Concerning ACN, it is a poison since it originates a series of reactions that eventually deactivate the catalyst active sites irreversibly.

The effect of ACN concentration on the catalytic activity decay is plotted in Fig. 4.9.5. All the curves showed a similar trend where two different zones can be observed. The first period corresponds to about the first 30 min of the runs, where an initial increase of activity is observed. The extent of the increase depended on the temperature, the ACN concentration and the water content. Such phenomenon could be explained by the consumption of the water adsorbed on the resin active sites through the hydrolysis reaction with ACN. As it has been stated before, water can be adsorbed (hydrogen bonded) on up to three active sites. When ACN reaches the catalytic bed, adsorbed water is consumed by reactions I, II and V (see Fig. 4.9.1). Consequently, some additional active sites would become available, which would increase the catalytic activity as observed in the initial period. Besides, the extent of the initial increase of activity is related to the concentration of acetonitrile, being more noticeable at low concentrations. It is explained by the catalyst deactivation rate which is proportional to the concentration of deactivating agent. For high ACN concentrations, deactivation proceeded so fast that initial increase of activity was undetectable. That first initial increase of activity was also observed at low ACN concentrations in a previous study on the deactivation by basic compounds in the synthesis of ETBE [118]. The second period is a monotonically exponential-like decay of catalytic activity. As more ammonia is being produced from reactions III and V (see Fig. 4.9.2), more active sites are neutralized what indeed, reduces the catalytic activity.

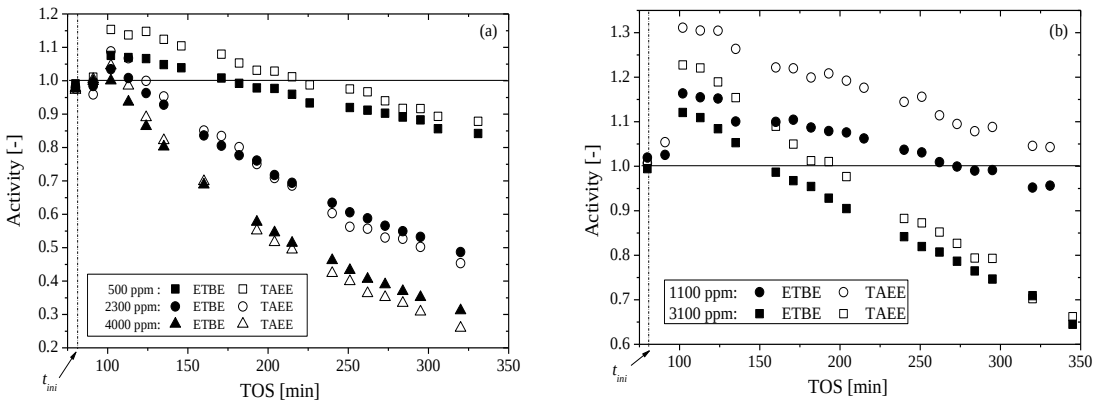

Figure 4.9.5. Relative activity decay for ETBE and TAEE formation rate over Amberlyst™35 vs. Time on Stream (TOS) at different ACN concentrations (ppm) in the alcohol feed at (a)T=353K and (b)T=333 K. $R°_{A/O}$=1.1 and $R°_{C4/C5}$=1. t_{ini} refers to the TOS at which ACN was added to the inlet stream.

The higher the initial concentration of ACN the steeper the activity decay observed. As it can be seen in Fig. 4.9.5, complete catalyst deactivation was not observed for any poison concentration explored after 4 h of experiment. It has been reported that at saturation conditions in steady state, up to 6 g of acetonitrile can be adsorbed in 100 g of dry resin [117]. This limit was not reached in any of the experiments in the present work. The shape of activity decay curves obtained was almost linear for the lowest ACN concentration, whereas it followed and exponential-like decay profile for higher poison concentrations, what is consistent with a slower deactivation rate. With respect to activity of etherification reactions, TAEE formation was slightly more affected by ACN than ETBE. This suggests that neutralization progresses from outer to inner layers of the resin. Therefore, active sites located in the inner parts of the catalyst, with a lower accessibility for TAEE formation than for ETBE formation, were preferentially yielding ETBE.

4.9.6 EFFECT OF TEMPERATURE

The effect of temperature on the deactivation process was studied at a constant poison concentration of 4000 ppm, see Fig. 4.9.6. As expected from Arrhenius law, the higher the temperature the higher the deactivation rate. As mentioned, the initial increase of activity was less noticeable as temperature increased due to faster deactivation rates. After 4 h of deactivation experiment, the final level of activity at 313 K was four times larger than that observed at 353 K. As a result, a lower reaction temperature in the etherification unit would be beneficial, since it slows down both hydrolysis and alcoholysis reaction rates and therefore it would contribute to increase the catalyst lifespan.

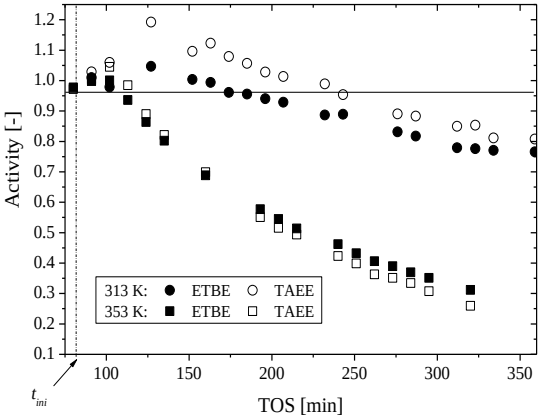

Figure 4.9.6. Activity profiles observed at 4000 ppm of ACN at different temperatures and $R°_{A/O}$=1.1 and $R°_{C4/C5}$=1. t_{ini} refers to the TOS at which ACN was added to the inlet stream.

4.9.7 ACTIVITY DECAY OBSERVED FOR DIFFERENT CATALYSTS

Fig. 4.9.7 shows the catalytic activity decay curves obtained for A-35 and CT-275 under the same experimental conditions. Deactivation proceeded faster on A-35 than on CT-275, which could be explained by the larger pore diameter of CT-275, with its inner active sites more accessible than those of A-35. If deactivation occurs from outer to inner layers of the resin, after external active sites have been neutralized only inner sulfonic groups are still active for etherification and therefore their accessibility influences the etherification rates observed. The initial increase of activity was more significant on A-35. This is probably due to the slightly higher acid capacity of A-35, which in turn, resulted in a higher amount of available active sites after consumption of water in ammonia forming reactions.

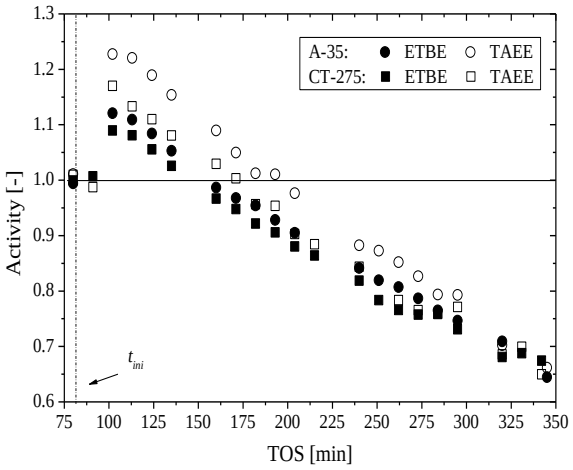

Figure 4.9.7. Activity profiles observed for A-35 and CT 275 at [ACN]= 3100 ppm, 333 K, $R^o_{A/O}$=1.1 and $R^o_{C4/C5}$=1. t_{ini} refers to the TOS at which ACN was added to the inlet stream.

4.9.8 EFFECT OF INITIAL WATER CONTENT

Since water acts as reactant in the deactivation reactions involved with ACN, its effects on deactivation was studied at different water concentrations, while keeping constant temperature and ACN concentration. Fig. 4.9.8 depicts the activity profiles obtained, where it can be clearly seen that the initial increase of activity depends on the water entering the reactor bed. The lower the initial water content, the more significant the initial increase of activity. In addition, the deactivation rate observed was faster in absence of extra added water. This could be due to important competition between ACN and water for the active sites, since water is inhibiting also the ammonia forming reactions, and it suggests a negative or close to zero order of water in deactivation reactions.

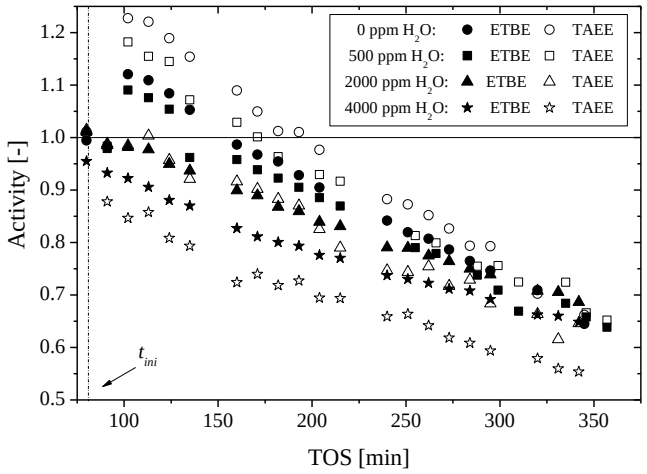

Figure 4.9.8. Activity decay curves obtained for different water concentrations at 333 K and [ACN]=3100 ppm, $R^o_{A/O}$=1.1 and $R^o_{C4/C5}$=1.

4.9.9 KINETIC MODELING OF THE DEACTIVATION PROCESS BY ACN

Deactivation via poisoning in the feed streams can be modeled by means of several approaches. According to the concept of separability coined by Szepe and Levenspiel described in [245], the reaction rate equation can be separated in two terms: a kinetic dependency (time independent) and an activity dependence (time dependent). As a way of example, taking the expression for ETBE formation in its simultaneous synthesis with TAEE obtained in *Section 4.7*, combined with the concept of separability defined, r_{ETBE} in a deactivating environment can be expressed as follows:

$$r_{ETBE} = \frac{k'_{R1}\left(a_{IB}a_{EtOH} - a_{ETBE}/K_{R1}\right)\psi}{\left(a_{EtOH} + K'_{ETBE}\,a_{ETBE} + K'_{TAEE}\,a_{TAEE}\right)^2}\,a(t) \qquad (4.9.3)$$

where *a(t)* is the relative catalyst activity and the rest of parameters are detailed in *Section 4.7*. Analogous expressions can be derived for TAEE formation reactions.

The fraction of active sites that are available for adsorption is essentially the activity *a(t)* and time dependence can be expressed by Eq. 4.9.4. Several activity decay expressions for poisoning can be found in the literature, among them the most typically used are linear-, exponential- or hyperbolic-like, referred to as zero, first or second deactivation order laws [115], respectively. However, deactivation order for poisoning are typically 0 or 1 [246]. It was found that a first order kinetic law, Eq. 4.9.5, fits better the experimental results. An example of the regression obtained in plotted in Fig. 4.9.9a. Two assumptions were taken into account to perform the regressions: i) since an initial increase of activity was observed, activity values were renormalized between 0 and 1 by assigning the unity to the maximum activity reached in the first period, ii) k'_d values were calculated from the activities obtained from $-r_{EtOH}$ since k'_d represents the relative rate at which active sites become inactive. Concerning the assumption ii), it was observed that deactivation progressed slightly differently for ETBE and TAEE, which was ascribed to the different accessibility of the still available active sites for ETBE or TAEE formation. However, such a difference was lower than 5% for most of the cases evaluated due to the similar chemical nature of both etherification systems.

$$-\frac{da}{dt} = a(t)\cdot k'_d \qquad (4.9.4)$$

$$\ln\frac{a^0}{a^t} = k'_d \cdot t \qquad (4.9.5)$$

The values of k'_d obtained for all the experiments are gathered in Table 4.9.3, their associated error were always lower than 5 % under a 95% of confidence level. It was found that k'_d values were dependent on the poison concentration in a proportional trend ($k'_d = k^*_d\, C_{ACN}$), which allowed the determination of the process deactivation kinetic constant (k^*_d). From Arrhenius plot of k^*_d values determined at each temperature, see Fig. 4.9.9b, the apparent activation energy for the deactivation process was estimated as 30.7 ± 2.6 kJ/mol. To the best to our knowledge, activation energy for the process of ACN poisoning on A-35 has not been reported in the literature, therefore comparison could not be made. Since activation energies of etherification reactions studied are about 2.5 times larger than activation energy of the global deactivation process, special care must be taken into account when choosing the optimum temperature for

the simultaneous process. High temperatures would increase both etherification and deactivation reactions rate, but at the expense of lower equilibrium conversion and therefore lower yield to ethers. On the contrary, low reaction rates would be beneficial to slow down the deactivation process. However, etherification reactions would be more affected by these lower temperatures since they present higher activation energy. As seen in Figs. 4.9.1 and 4.9.2, both deactivation pathways (alcoholysis and direct hydrolysis) need water as reagent to form the intermediates that eventually would be converted into ammonia adsorbed on the active sites. Therefore, the first important consideration to mitigate the effects of deactivation by ACN would be to avoid the entrance of uncontrolled sources of water to etherification reactors.

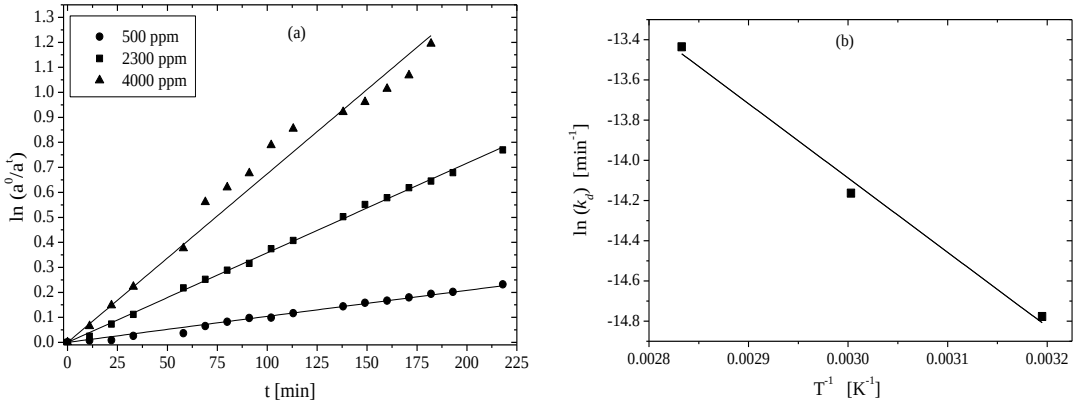

Figure 4.9.9. (a) Example of a first law deactivation order fitting for ETBE and TAEE activities obtained at 353 K and different ACN concentrations. (b) Arrhenius plot of deactivation kinetic constant obtained at different temperatures.

Table 4.9.3. Apparent deactivation kinetic constants obtained at different experimental conditions. Errors are referred to a 95% of confidence level.

Catalyst	T [K]	C_{H2O} [ppm]	C_{ACN} [ppm]	$k'_d \cdot 10^3$ [min^{-1}]
A-35	353	0	2300	3.58 ± 0.04
A-35	353	0	500	1.11 ± 0.03
A-35	333	0	1100	0.88 ± 0.03
A-35	353	0	4000	5.68 ± 0.12
A-35	333	0	3100	2.15 ± 0.046
A-35	313	0	4000	1.53 ± 0.051
A-35	333	4000	3100	1.56 ± 0.042
A-35	333	2000	3100	1.52 ± 0.019
A-35	333	500	3100	2.18±0.12
CT-275	333	0	3100	2.12 ± 0.044

The comparison of experimentally determined activities and those calculated from Eq. 4.9.4 is depicted in Fig. 4.9.10a, where it can be seen that a first order deactivation law fits satisfactorily well the experimental data of the present work. Several types of poisoning can be distinguished when plotting the activity versus poison concentration curve at a fixed time [239]. Poisoning can be selective, non-selective or antiselective. Fig 4.9.10b shows that ACN poisoning follows a selective poisoning typical pattern. This involves preferential adsorption of the poison on the

most active sites at low concentrations, which implies that not all actives sites in the catalyst are identical. In other words, acid sites with higher acid strength are neutralized first [245], therefore the first steps of the neutralization process are essential since it implies the deactivation of the most active sites and therefore the most important loss of catalytic activity.

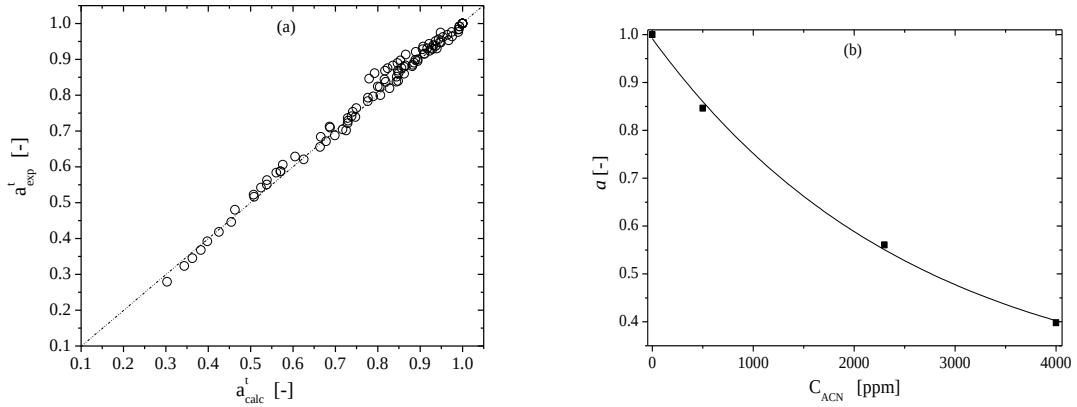

Figure 4.9.10. (a) Parity plot of experimental and calculated activities. (b) Activity vs. poison concentration pattern.

Finally, although catalyst deactivation is inevitable for etherification processes, a solution for mitigating the related problems due to ACN presence in the etherification reactor relies in the pretreatment of the olefin feedstock by water wash (scrubber). However, it should be noted that water wash cannot remove amines higher than methylamines and it is not very effective removing nitriles higher than ACN, as PPN [117,240]. Another technique that has been pointed out as efficient for reducing nitriles in C_4 and C_5 cuts from FCC units is the simultaneous selective hydrogenation of the diolefins and nitriles present in such streams [240].

4.9.10 PARTIAL CONCLUSIONS

The deactivating effect of ACN on the active sites of macroporous ion-exchange resins has been studied in the simultaneous synthesis of ETBE and TAEE from ethanol and pure olefins feedstock. Two different periods are observed as deactivation progresses: an initial increase of activity followed by a monotonically exponential-like first order decay of activity. The initial increase of activity has been proven to be related to the initial water content, being enhanced at low water concentrations in the EtOH feed. The inhibitory effect of water has been assessed and a Freundlich-type model is more reliable to predict the occupation of active sites by water that eventually inhibits both etherification reactions.

The deactivation of the catalyst is enhanced at high temperatures and high ACN concentrations. ACN presence in the feed hampers similarly the synthesis of both ethers, but TAEE synthesis is slightly more sensitive to deactivation by ACN than ETBE synthesis. Deactivation by ACN follows a first order kinetics. Arrhenius plot of apparent deactivation kinetic constants obtained allowed the estimation of the apparent activation energy for the neutralization process as 30.7 ± 2.6 kJ/mol. Finally, the extent of deactivation is very similar for both assayed catalysts, although CT-275 resulted slightly more resistant toward ACN neutralization than A-35. Finally, it is to be highlighted that a low reaction temperature in the etherification reactor substantially reduces both hydrolysis and alcoholysis reaction rates, and avoids the possible alcohol dehydration with ensuing undesired formation of water.

4.9.11 CHAPTER NOTATION

2M1B 2-methyl-1-butene
2M2B 2-methyl-2-butene
a_0 initial activity [dimensionless]
ACN acetonitrile
a_t activity at time *t* [dimensionless]
a_w activity coefficient of water [dimensionless]
E'_a activation energy [kJ/mol]
ETBE ethyl *tert*-butyl ether
EtOH ethanol
k'_d kinetic constant [min^{-1}]
$R°_{A/O}$ initial molar ratio of alcohol to olefins
$R°_{C4/C5}$ initial molar ratio of isobutene to isoamylenes
RSS residual sum of squares
r_i^0 rate of reaction i in the absence of poison or inhibitor
r_i^t rate of reaction *i* [$mol(h\ kg_{cat})^{-1}$]
r_j^0 rate of formation or consumption of compound *j* in the absence of poison or inhibitor
r_j^t rate of formation or consumption of compound *j* [$mol(h\ kg_{cat})^{-1}$]
T temperature [K]
t time [min]
TAEE *tert*-amyl ethyl ether

5. GENERAL CONCLUSIONS AND FUTURE PROSPECTIVE WORK

5.1 GENERAL CONCLUSIONS

According to the objectives established in *Section 2* and the results discussed through *Section 4*, the following general conclusions can be drawn:

- The Green Metric Analysis shows that the simultaneous etherification of the correspondent tertiary olefins (IB and IA) with EtOH to produce ETBE and TAEE at 333 K is greener than their synthesis from the correspondent tertiary alcohols (TBA or TAA) and EtOH. A simulated continuous process based on the reaction-distillation configuration allows to reduce the main drawback of the process which is the low IA conversion. It constitutes an evaluation and approach to the process feasibility with a promising industrial prospective.

- Within the range of experimental conditions studied ($R°_{A/O}$=0.5-2, $R°_{C4/C5}$0.5-2 and T=323-353 K), equilibrium conversion of IB, IA and EtOH ranges from 69.8 to 97.9%, from 17 to 65.6% and from 32.3 to 97.0%, respectively. Olefins equilibrium conversion increases with $R°_{A/O}$ but at the expense of lower X_{EtOH}. Increasing $R°_{C4/C5}$ slightly increases X_{EtOH} and favors ETBE formation over TAEE one. The simultaneous etherification process is a feasible technique to convert up to 65% of the environmentally troublesome isoamylenes and entails large EtOH use as raw material. Olefins selectivity to ethers is remarkably high, which is certainty desirable from an industrial standpoint. Increasing temperature promotes formation of both tertiary alcohols and dimerization products whereas increasing $R°_{A/O}$ shows an opposite effect on the formation of both side products. $R°_{A/O}$ is therefore an important control variable to avoid side reactions. The effect of IB concentration is a critical factor toward dimers formation at high temperatures. The experimental yield data have been empirically modeled and optimized showing that experimental conditions that maximize the simultaneous production of both ETBE and TAEE are $R°_{A/O}$=0.86, $R°_{C4/C5}$=0.5 and a temperature of 323 K in the presence of a 1 wt.% of water.

- Etherification reactions of IB and IA with EtOH, as well as IA isomerization are reversible and exothermic. Hence, the amount of produced ethers at equilibrium decreases with temperature. As expected, no significant effect on the equilibrium composition has been observed when using different catalysts, namely A-35, A-15 and CT-275. ETBE formation (R1) is the most exothermic reaction, followed by the TAEE formation from 2M1B (R2) and from 2M2B (R3). The exothermicity of the etherification reactions (R1-R3) is higher than that of IA isomerization reaction (R4). Reaction equilibrium constants decrease in the order $K_{R1}>K_{R2}>K_{R4}>K_{R3}$. The more branched the olefin, the higher the exothermicity since for reactions R1, R2, R3 and R4, molar standard enthalpy changes of -36.3±7.2, -35.1±6.0, -25.5±3.0 and -9.7±3.8 kJ mol^{-1} are determined, respectively. The molar enthalpy change of reaction determined for the chemical equilibrium between TMP-1 and TMP-2 is 5.3±0.8 kJ mol^{-1}. From experimental data, the estimated standard molar enthalpies of formation for ETBE and TAEE are -351.5 and -372.3 kJ mol^{-1}, respectively.

- Initial water presence in the reaction system does not change the chemical equilibrium constants of involved reactions but it does affect the final composition of the mixture. Increasing initial water concentration promotes both TBA and TAA formation and increases the olefins selectivity of tertiary olefins drastically. The most important effects of water presence on the present system are the competition with reactants for the active sites and the

inhibition of etherification and dimerization reactions. The inhibitory effect is more noticeable over dimerization reactions than over etherification ones. The observed drop in the catalytic activity for the formation reactions of ETBE and TAEE, when 1 wt.% of water was initially added, is 64% and 75% of their value in absence of water, respectively. Thus, TAEE synthesis is more affected by the presence of water than ETBE one. When more than 0.45 wt.% of water is initially added, the catalysis could be regarded as specific acid catalysis and a change in kinetic mechanism is expected. As the average water content in dry bioethanol is far lower than this limit value, dry bioethanol could be used as reactant in the performed simultaneous synthesis avoiding sulfonic groups dissociation and such a small water content could help to prevent the formation of oligomerization products in possible hot-spots of the catalytic reactor.

- The resins swelling is influenced by the nature and composition of the bulk phase and by the resin properties as crosslinking degree and acid capacity. Resins swell similarly in alcohols and water. All resins evaluated are active and highly selective in the simultaneous synthesis of ETBE and TAEE. The resins catalytic activity observed increases in the order: A-46 < MN-500 < CT-124 < A-45 < A-DT < A-39 < CT-482 < A-16 < A-36 < A-40 < CT-175 < A-15 < CT-275 < A-48 < A-35. Macroreticular oversulfonated resins show the best performance in the present reaction system, among them Amberlyst™35 is the most active catalyst. RSM is used to obtain empirical equations that correlate the catalytic activity measured with the catalysts properties. The combination of acid capacity and swollen state properties correlate better with catalytic activity than structural properties in dry state. It is ascribed to the variation of the morphological properties caused by resin swelling in polar reaction media. Resins with high acid capacity and low volume of swollen polymer are the most suitable for the present reaction system. The resins densest gel-phase domain of 1.5 $nm \cdot nm^{-3}$ present permeation problems for ETBE and TAEE molecules. Even for smaller molecules some diffusional problems are expected.

- Concerning the kinetic study performed, initial reaction rates have been satisfactorily modeled using the RSM and power function models. Olefins concentration has a positive kinetic order on etherification rates whereas EtOH concentration shows a negative or close to zero order. Formation rate of ETBE is faster than global formation rate of TAEE. 2M1B has been found to be more reactive with EtOH than 2M2B. A systematic kinetic fitting along with model selection and averaging has been applied in order to find out a reliable kinetic model based on the LHHW–ER formalisms. The best model obtained stems for the surface reaction between one molecule of alcohol and one of olefin with the participation of two active sites. Adsorption of EtOH, ETBE and TAEE is significant, and the fraction of non-occupied sites is negligible. Results suggest that adsorption of EtOH is stronger than that of olefins. One active site participates in isoamylenes double bond isomerization. The final kinetic models obtained for ETBE and TAEE formation reactions and, isoamylenes isomerization reaction are:

$$r_{ETBE} = r_{R1} = \frac{k'_{R1}\left(a_{IB}a_{EtOH} - a_{ETBE}/K_{R1}\right)\psi}{\left(a_{EtOH} + K'_{ETBE}\,a_{ETBE} + K'_{TAEE}\,a_{TAEE}\right)^2}$$

$$r_{TAEE} = r_{R2} + r_{R3} = \frac{\left[k'_{R2}\left(a_{2M1B}a_{EtOH} - a_{TAEE}/K_{R2}\right) + k'_{R3}\left(a_{2M2B}a_{EtOH} - a_{TAEE}/K_{R3}\right)\right]\psi}{\left(a_{EtOH} + K'_{ETBE}\,a_{ETBE} + K'_{TAEE}\,a_{TAEE}\right)^2}$$

$$r_{2M2B} = r_{R4} - r_{R3} = \frac{\left[k'_{R4}(a_{2M1B} - a_{2M2B}/K_{R4}) - k'_{R3}(a_{2M2B}a_{EtOH} - a_{TAEE}/K_{R3})\right]\psi}{\left(a_{EtOH} + K'_{ETBE}\,a_{ETBE} + K'_{TAEE}\,a_{TAEE}\right)}$$

Estimated apparent activation energies for ETBE formation from IB and EtOH, TAEE formation from 2M1B and EtOH, TAEE formation from 2M2B and EtOH, and isoamylenes double bond isomerization are 72.8±1.4, 74.9±2.8, 81.2±2.2 and, 76.5±7.2 kJ mol^{-1}, respectively. These values are in good agreement with those quoted in literature for the isolated ETBE and TAEE formation systems. Based on these values, an Eley-Rideal mechanism has been found to be more likely to occur than a LHHW mechanism in the etherification reactions.

- Regarding the adsorption study of C_1-C_4 alcohols, C_4-C_5 iso-olefins and tertiary ethers obtained thereof on Amberlyst™35, adsorption equilibrium constants of olefins and ethers are similar, and notably lower than those of alcohols. Obtained liquid-phase adsorption enthalpy indicates that alcohols adsorption had relied less on temperature whereas the larger values for 2M2B had suggested chemisorption of the olefin as intermediate step of isomerization reaction. The moment technique has been used to assess the effective diffusion coefficients of adsorbing species. Macropore resistance has been found to be more significant than diffusion within the gel-like microspheres in liquid-phase, while both macro and micropore diffusion are significant in gas-phase. Diffusion and adsorption are influenced not only by the molecular size of adsorbing species, but also by swelling caused by alcohols. The obtained effective macropore diffusion coefficients are in the range 10^{-12}-10^{-13} m^2 s^{-1} for liquid-phase and in the range 10^{-6}-10^{-7} m^2 s^{-1} for gas-phase. Effective micropore diffusion coefficients are in the range 10^{-20}-10^{-21} m^2 s^{-1}.

- Deactivation of ion-exchange resins by ACN has been studied in the simultaneous synthesis of ETBE and TAEE. ACN concentration was varied in the range 500-4000 ppm in the presence of different amounts of water (1000-5000 ppm) within the temperature range 313 to 353 K. Two different periods have been observed as deactivation progresses: an initial increase of activity followed by a monotonically exponential-like first order decay of activity. The initial increase of activity has been proven to be related to the initial water content. The inhibitory effect of water has been assessed and a Freundlich-type model is more reliable to predict the occupation of active sites by water that eventually inhibit both etherification reactions. The catalyst deactivation rate increases with temperature and ACN concentration. ACN presence in the feed hampers similarly the synthesis of both ethers, but TAEE synthesis is slightly more sensitive to deactivation by ACN than ETBE synthesis. Catalytic activity decay has been found to follow a first order kinetics. The estimated apparent activation energy for the neutralization process is 30.7 ± 2.6 kJ mol^{-1}. Finally, the extent of deactivation is very similar for both assayed catalysts, but CT-275 resulted slightly more resistant toward ACN neutralization than A-35.

As the main general conclusion, the simultaneous synthesis of ETBE and TAEE could be carried out in the same reaction unit at mild temperatures, and Amberlyst™35 would be the most promising catalyst for the process. Such versatile process can overcome some of the environmental drawbacks of current gasoline. For instance, the troublesome isoamylenes content can be reduced by a 50%. Such technology can be implemented at short term, avoiding drastical changes in current etherification plants and remaining fully compatible with actual vehicles, which at the end, makes the process a real and interesting possibility for refiners.

5.2 FUTURE PROSPECTIVE WORK

The following recommendations are suggested for continuing the research developed in the present thesis:

- To study the simultaneous synthesis of ETBE and TAEE in a reactive distillation setup in order to find out the main advantages and drawbacks of such configuration since it is and industrially attractive alternative.

- To extend the product distribution and kinetic studies using real or synthetic C_4 and C_5 fractions in order to determine the main differences with respect to the use of pure olefins as reactants and to approach actual industrial conditions for the feed streams.

- Since propionitrile (PPN) can be a potential deactivating agent contained in the C_5 stream from refineries, it is advisable to study the deactivating effect of this species in order to figure out the effect that it can exert when ACN and PPN are simultaneously fed to a catalytic bed.

- To study the simultaneous etherification of IB and IA with EtOH and BuOH since these two alcohols can be obtained from biomass and thus the ethers obtained thereof are bioethers that can fulfill the future legislation limitations. At the same time, such an etherification system makes the versatility and flexibility of the process unit larger since it can be adapted to several production targets depending on the refineries need or stream supplying.

- To study the inhibitory effect of water in a wider range of concentrations in order to delve in the switch of mechanisms taking place that eventually determine the observed catalytic activity.

- To perform adsorption studies of water, because such studies are rarely found in the literature in spite of the great importance of water in etherification reactions and in processes catalyzed by ion-exchange resins. Likewise, to make wider the adsorption studies by using different catalysts in order to correlate adsorption equilibrium constants and state functions with morphological properties of the ion-exchange resins.

6. REFERENCES, LIST OF TABLES AND FIGURES

6.1 REFERENCES

[1] L. T. Molina, M. J. Molina. Air quality impacts: local and global concern. *Springer Netherlands* **(2002)** 1–19.

[2] http://www.eia.gov. Website of U. S. Energy Information Administration. Accesed on March, **2016**.

[3] J. Burri, R. Crockett, R. Hany, D. Rentsch. Gasoline composition determined by 1H NMR spectroscopy. *Fuel*. 83 **(2004)** 187–193.

[4] R. da Silva, R. Cataluña, E. W. de Menezes, D. Samios, C. M. S. Piatnicki. Effect of additives on the antiknock properties and Reid vapor pressure of gasoline. *Fuel*. 84 **(2005)** 951–959.

[5] M. Lebreton. Hot and cold fuel volatility indexes of French cars: a cooperative study by the GFC Volatility Group. SAE Tech. Pap. 841386 **(1984)**.

[6] J. S. Gaffney, N. A. Marley. The impacts of combustion emissions on air quality and climate - from coal to biofuels and beyond. *Atmos. Environ.* 43 **(2009)** 23–36.

[7] K. L. Rock, T. de Cardenas, L. Fornoff. C5 olefins. The new refinery challenge. *Fuel Reformul*. 2 **(1992)** 42–48.

[8] D. A. Keyworth, T. A. Reid. Higher ethers coud provide blending benefits. *Fuel Reformul*. 1 **(1992)** 56–57.

[9] K. Schädlich, P. Schug, J. Fabri, W. Dabelstein, A. Reglitzky, K. Schädlich, P. Schug, J. Fabri, W. Dabelstein, A. Reglitzky. Octane Enhancers, in: *Ullmann's Encyclopedia of Industrial Chemistry*. Wiley-VCH Verlag GmbH & Co. KGaA, Weinheim, Germany, **2003**.

[10] R. Reuter, J. Benson, V. Burns, R. Gorse, A. M. Hochhauser, W. Koehl, L. Painter, B. Rippon, J. Rutherford. Effects of oxygenated fuels and RVP on automotive emissions – auto/oil air quality improvement program. SAE Tech. Pap. 920326 **(1992)** 391–412.

[11] M. Al-Hasan. Effect of ethanol–unleaded gasoline blends on engine performance and exhaust emission. *Energy Convers. Manag.* 44 **(2003)** 1547–1561.

[12] A. Arteconi, A. Mazzarini, G. Nicola. Emissions from ethers and organic carbonate fuel additives: a review. *Water, Air, Soil Pollut.* 221 **(2011)** 405–423.

[13] T. Higgins and P. Steiner. *Study on relative CO_2 savings comparing ethanol and TAEE as a gasoline component*. Hart energy consulting, **2010**.

[14] E. W. de Menezes, R. da Silva, R. Cataluña, R. J. C. Ortega. Effect of ethers and ether/ethanol additives on the physicochemical properties of diesel fuel and on engine tests. *Fuel*. 85 **(2006)** 815–822.

[15] S. Radhakrishnan, J. Franken, J. A. Martens. Selective synthesis of 2-ethoxy alkanes through ethoxylation of 1-alkenes with bioethanol over zeolite beta catalyst in a liquid phase continuous process. *Green Chem*. 14 **(2012)** 1475-1479.

[16] L. R. Lynd, J. H. Cushman, R. J. Nichols, C. E. Wyman. Fuel ethanol from cellulosic biomass. *Science.* 251 **(1991)** 1318–1323.

[17] R. Cascone. Biobutanol-a replacement for bioethanol?. *Chem. Eng. Prog*. 108 **(2008)** 54–59.

[18] T. Doğu, D. Varisli. Alcohols as Alternatives to Petroleum for Environmentally Clean Fuels and Petrochemicals. *Turkish J. Chem*. 31 **(2007)** 551–567.

[19] J. H. Badia, C. Fité, R. Bringué, E. Ramírez, M. Iborra. Relevant properties for catalytic activity of sulfonic ion-exchange resins in etherification of isobutene with linear primary alcohols. *J. Ind. Eng. Chem*. 42 **(2016)** 36–45.

[20] J. H. Badia, C. Fité, R. Bringué, M. Iborra, F. Cunill. Catalytic Activity and Accessibility of Acidic Ion-Exchange Resins in Liquid Phase Etherification Reactions. *Top. Catal*. 58 **(2015)** 919–932.

[21] F. Ancillotti, M. Mauri, E. Pescarollo. Ion-exchange resin catalyzed addition of alcohols to olefins. *J. Catal*. 46 **(1977)** 49–57.

[22] P. Kitchaiya, R. Datta. Ethers from Ethanol. 2. Reaction Equilibria of Simultaneous *tert*-Amyl Ethyl Ether Synthesis and Isoamylene Isomerization. *Ind. Eng. Chem. Res*. 34 **(1995)** 1092–1101.

[23] R. K. Niven. Ethanol in gasoline: environmental impacts and sustainability review article. *Renew. Sustain. Energy Rev*. 9 **(2005)** 535–555.

[24] D. Pimentel, T. Patzek, G. Cecil. Ethanol production: energy, economic, and environmental losses. *Rev. Environ. Contam. Toxicol.* **(2007)** 25–41.

[25] W. Kiatkittipong, P. Thipsunet, S. Goto, C. Chaisuk, P. Praserthdam, S. Assabumrungrat. Simultaneous enhancement of ethanol supplement in gasoline and its quality improvement. *Fuel Process. Technol*. 89 **(2008)** 1365–1370.

[26] R. Cataluña, R. da Silva, E. W. de Menezes, R. B. Ivanov. Specific consumption of liquid biofuels in gasoline fuelled engines. *Fuel*. 87 **(2008)** 3362–3368.

[27] W. J. Piel. Expanding refinery technology leads to new ether potential. *Fuel Reformul*. 6 **(1992)** 34–40.

[28] H. L. Brockwell, P. R. Sarathy, R. Trotta. Synthesize ethers. *Hydrocarb. Process*. 70 **(1991)** 133–141.

[29] V. J. Cruz, J. F. Izquierdo, F. Cunill, J. Tejero, M. Iborra, C. Fité, R. Bringué. Los diisoamilenos como aditivos de las gasolinas. *Ing. Química*. 436 **(2006)** 100–107.

[30] A. S. Hamadi. Selective Additives for Improvement of Gasoline Octane Number. *Tikrit J. Eng. Sci*. 17 **(2010)** 22–35.

[31] J. H. Badia, C. Fité, R. Bringué, E. Ramírez, F. Cunill. Byproducts formation in the ethyl *tert*-butyl ether (ETBE) synthesis reaction on macroreticular acid ion-exchange resins. *Appl. Catal. A Gen*. 468 **(2013)** 384–394.

[32] J. R. Peterson. Alkylate is key for cleaner burning gasoline. *Natl. Meet. Am. Chem. Soc.* Leawood 41 **(1996)** 916–921.

[33] B. E. Poling, R. C. Reid, J. M. Prausnitz. *The properties of gases and liquids*. 4th ed. Mc Graw Hill, New York, **1987**.

[34] J. H. Badia. *Synthesis of ethers as oxygenated additives for the gasoline pool*. PhD thesis. University of Barcelona, **2016**.

[35] http://biofuel.org.uk/bioalcohols.html. Biofuels - Types of Biofuels - Bioalcohols. Accesed on November, **2016**.

[36] K. L. Rock, M. Korpelshoek. Increasing refinery biofuels production. *PTQ Catal*. 13 **(2008)** 45–50.

[37] F. Cunill, M. Vila, J. F. Izquierdo, M. Iborra, J. Tejero. Effect of water presence on methyl *tert*-butyl ether and ethyl *tert*-butyl ether liquid-phase syntheses. *Ind. Eng. Chem. Res*. 32 **(1993)** 564–569.

[38] M. Marchionna, M. di Girolamo, R. Patrini. Light olefins dimerization to high quality gasoline components. *Catal. Today*. 65 **(2001)** 397–403.

[39] M. L. Honkela, A.O.I. Krause. Influence of polar components in the dimerization of isobutene. *Catal. Lett*. 87 **(2003)** 113–119.

[40] M. Granollers, J. F. Izquierdo, F. Cunill. General effect of macroreticular acidic ion-exchange resins on 2-methyl-1-butene and 2-methyl-2-butene mixture oligomerization.

Appl. Catal. A Gen. 436 **(2012)** 163–171.

[41] A. Chauvel, G. Lefebvre. *Petrochemical Processes. Synthesis-gas derivatives and major hydrocarbons*. 2nd ed. Editions Technip, Paris, **1989**.

[42] M. M. Sharma. Some novel aspects of cationic ion-exchange resins as catalysts. *React. Funct. Polym*. 26 **(1995)** 3–23.

[43] K. Hauge, E. Bergene, D. Chen, G. R. Fredriksen, A. Holmen. Oligomerization of isobutene over solid acid catalysts. *Catal. Today*. 100 **(2005)** 463–466.

[44] F. E. Ahmed. Toxicology and human health effects following exposure to oxygenated or reformulated gasoline. *Toxicol. Lett*. 123 **(2001)** 89–113.

[45] O. Boonthamtirawuti, W. Kiatkittipong, A. Arpornwichanop, P. Praserthdam, S. Assabumrungrat. Kinetics of liquid phase synthesis of *tert*-amyl ethyl ether from *tert*-amyl alcohol and ethanol over Amberlyst 16. *J. Ind. Eng. Chem*. 15 **(2009)** 451–457.

[46] http://www.efoa.eu. European Fuel Oxygenates Association (EFOA) - Home. Accessed on January, **2017**.

[47] K. F. Yee, A. R. Mohamed, S. H. Tan. A review on the evolution of ethyl *tert*-butyl ether (ETBE) and its future prospects. *Renew. Sustain. Energy Rev*. 22 **(2013)** 604–620.

[48] H. Hamid, M. A. Ali. *Handbook of MTBE and other gasoline oxygenates*. 1st ed. Marcel Dekker, Inc., Mew York, **2004**.

[49] R. González. *Performance of Amberlyst™35 in the synthesis of ETBE from ethanol and C4 cuts*. PhD thesis. University of Barcelona, **2011**.

[50] M. Vila, F. Cunill, J. F. Izquierdo, J. González, A. Hernández. The role of by-products formation in methyl *tert*-butyl ether synthesis catalyzed by a macroporous acidic resin. *Appl. Catal. A Gen*. 117 **(1994)** L99–L108.

[51] A. O. I. Krause, L. G. Hammarström. Etherification of isoamylenes with methanol. *Appl. Catal*. 30 **(1987)** 313–324.

[52] M. N. Petre. The potential environmental benefits of utilising oxy-compounds as additives in gasoline, a laboratory based study. *Environ. Heal. Issues Pract.* **(2012)** 147–176.

[53] M. N. Petre, P. Rosca, R. Dragomir. The effect of bio-ethers on the volatility properties of oxygenated gasoline. *Rev. Chim.* 62 **(2011)** 567–574.

[54] D. J. C. Constable, A. D. Curzons, V. L. Cunningham. Metrics to 'green' chemistry-which are the best?. *Green Chem*. 4 **(2002)** 521–527.

[55] A. D. Curzons, D. N. Mortimer, D. J. C. Constable, V. L. Cunningham. So you think your process is green, how do you know? – Using principles of sustainability to determine what is green – a corporate perspective. *Green Chem*. 3 **(2001)** 1–6.

[56] R. A. Sheldon. Fundamentals of green chemistry: efficiency in reaction design. *Chem. Soc. Rev*. 41 **(2012)** 1437–1451.

[57] J. Lima-Ramos, P. Tufvesson, J. M. Woodley. Application of environmental and economic metrics to guide the development of biocatalytic processes. *Green Process. Synth*. 3 **(2014)** 195–213.

[58] J. Andraos. *The Algebra of Organic Synthesis: Green Metrics, Design Strategy, Route Selection, and Optimization*. 1st ed. CRC press, New York, **2012**.

[59] P. Tundo, P. Anastas, D. S. Black, J. Breen, T. J. Collins, S. Memoli, J. Miyamoto, M. Polyakoff, W. Tumas. Synthetic pathways and processes in green chemistry. Introductory overview. *Pure Appl. Chem*. 72 **(2000)** 1207–1228.

[60] T.W. Evans, K.R. Edlund. Tertiary alkyl ethers preparation and properties. *Ind. Eng. Chem*. 28 **(1936)** 1186–1188.

[61] O. Levenspiel. *Chemical reaction engineering*. 3rd ed. Wiley-Eastern Limited, New York, **1999**.

[62] D. M. Ruthven. *Principles of adsorption and adsorption processes*. 1st ed. John Wiley & Sons, New York, **1984**.

[63] J. J. Carberry. *Chemical and catalytic reaction engineering*. 1st ed. Dover Publications Inc., New York Courier Corporation, **2001**.

[64] T. Doğu, N. Boz, E. Aydin, N. Oktar, K. Mürtezaoğlu, G. Doğu. DRIFT studies for the reaction and adsorption of alcohols and isobutylene on acidic resin catalysts and the mechanism of ETBE and MTBE synthesis. *Ind. Eng. Chem. Res*. 15 **(2001)** 5044–5051.

[65] N. Oktar, K. Mürtezaoğlu, G. Doğu, T. Doğu. Dynamic analysis of adsorption equilibrium and rate parameters of reactants and products in MTBE, ETBE and TAME production. *Can. J. Chem. Eng*. 77 **(1999)** 406–412.

[66] G. Doğu, C. Ercan. Dynamic analysis of adsorption on bidisperse porous catalysts. *Can. J. Chem. Eng*. 61 **(1983)** 660–664.

[67] N. Hashimoto, J. M. Smith. Diffusion in bidisperse porous catalyst pellets. *Ind. Eng. Chem. Fundam*. 13 **(1974)** 115–120.

[68] C. E. Harland. *Ion exchange: theory and practice*. 2nd ed. The Royal Society of Chemistry, Cambridge, **1994**.

[69] B. M. Antunes, A. E. Rodrigues, Z. Lin, I. Portugal, C. M. Silva. Alkenes oligomerization with resin catalysts. *Fuel Process. Technol*. 138 **(2015)** 86–99.

[70] K. Jeřábek, L. Hanková, A. Revillon. Functional polymers prepared from p-styrenesulfonyl chloride as the functional monomer. *Ind. Eng. Chem. Res*. 34 **(1995)** 2598–2604.

[71] R. L. Albright. Porous polymers as an anchor for catalysis. *React. Polym. Ion Exch. Sorbents*. 4 **(1986)** 155–174.

[72] N. G. Polyanskii, V. K. Sapozhnikov. New advances in catalysis by ion-exchange resins. *Russ. Chem. Rev*. 46 **(1977)** 226–245.

[73] R. Bringué. *Thermally stable ion-exchange resins as catalysts for the liquid-phase dehydration of 1-pentanol to di-n-pentyl ether*. PhD thesis. University of Barcelona, **2007**.

[74] S. Fisher, R. Kunin. Routine exchange capacity determinations of ion exchange resins. *Anal. Chem*. 27 **(1955)** 1191–1194.

[75] U. Kunz, C. Altwicker, U. Limbeck, U. Hoffmann. Improvement of active site accessibility of resin catalysts by polymer/carrier composites: development and characterisation of monolithic catalytic chromatographic reactors. *J. Mol. Catal. A Chem*. 177 **(2001)** 21–32.

[76] C. Casas, R. Bringué, E. Ramírez, M. Iborra, J. Tejero. Liquid-phase dehydration of 1-octanol, 1-hexanol and 1-pentanol to linear symmetrical ethers over ion exchange resins. *Appl. Catal. A Gen*. 396 **(2011)** 129–139.

[77] E. Van de Steene, J. de Clerq, J. W. Thybaut. Kinetic study of acetic acid esterification with methanol catalyzed by gel and macroporous resins. *J. Ion Exch*. 25 **(2014)** 234–241.

[78] J. Guilera, E. Ramírez, C. Fité, J. Tejero, F. Cunill. Synthesis of ethyl hexyl ether over acidic ion-exchange resins for cleaner diesel fuel. *Catal. Sci. Technol*. 5 **(2015)** 2238–2250.

[79] S. Sterchele, P. Centomo, M. Zecca, L. Hanková, K. Jeřábek. Dry- and swollen-state morphology of novel high surface area polymers. *Microporous Mesoporous Mater*. 185 **(2014)** 26–29.

[80] B. Corain, M. Zecca, K. Jeřábek. Catalysis and polymer networks – the role of morphology and molecular accessibility. *J. Mol. Catal. A Chem*. 177 **(2001)** 3–20. [81] A. G. Ogston. The spaces ina uniform random suspension of fibres. *Trans. Faraday Soc*. 54 **(1958)** 1754–1757.

[82] G. Gelbard. Organic synthesis by catalysis with ion-exchange resins. *Ind. Eng. Chem. Res.* 44 **(2005)** 8468–8498.

[83] M. A. Pérez, R. Bringué, M. Iborra, J. Tejero, F. Cunill. Ion exchange resins as catalysts for the liquid-phase dehydration of 1-butanol to di-n-butyl ether. *Appl. Catal. A Gen.* 482 **(2014)** 38–48.

[84] R. Bringué, J. Tejero, J. F. Izquierdo, C. Fité, F. Cunill. Experimental study of the chemical equilibria in the liquid-phase dehydration of 1-pentanol to di- n -pentyl ether. *Ind. Eng. Chem. Res*. 46 **(2007)** 6865–6872.

[85] J. Guilera, R. Bringué, E. Ramírez, C. Fité, J. Tejero. Kinetic study of ethyl octyl ether formation from ethanol and 1-octanol on Amberlyst 70. *AIChE J*. 60 **(2014)** 2918–2928.

[86] C. Fité, J. Tejero, M. Iborra, F. Cunill, J. F. Izquierdo, D. Parra. The effect of the reaction medium on the kinetics of the liquid-phase addition of methanol to isobutene. *Appl. Catal. A Gen*. 169 **(1998)** 165–177.

[87] J. Tejero, A. Calderón, F. Cunill, J. F. Izquierdo, M. Iborra. The formation of byproducts in the reaction of synthesis of isopropyl *tert*-butyl ether from isopropyl alcohol and isobutene on an acidic macroporous copolymer. *React. Funct. Polym*. 33 **(1997)** 201–209.

[88] R. S. Karinen, J. A. Linnekoski, A. O. I. Krause. Etherification of C5 and C8 alkenes with C1 to C4 alcohols. *Catal. Lett*. 76 **(2001)** 81–87.

[89] L. K. Rihko, A. O. I. Krause. Reactivity of isoamylenes with ethanol. *Appl. Catal. A Gen*. 101 **(1993)** 283–295.

[90] L. K. Rihko, P.K. Kiviranta-Pääkkönen, A.O. I. Krause. Kinetic model for the etherification of isoamylenes with methanol. *Ind. Eng. Chem. Res*. 36 **(1997)** 614–621.

[91] J. A. Linnekoski, A. O. I. Krause, L. K. Struckmann. Etherification and hydration of isoamylenes with ion exchange resin. *Appl. Catal. A Gen*. 170 **(1998)** 117–126.

[92] A. Delion. Hydration of isopentenes in an acetone environment over ion-exchange resin: thermodynamic and kinetic analysis. *J. Catal*. 103 **(1987)** 177–187.

[93] K. F. Yee, E. P. Ng, A. R. Mohamed, F. Adam, S. H. Tan. Functionalized multi-walled carbon nanotubes as heterogeneous lewis acid catalysts in the etherification reaction of *tert*-butyl alcohol and ethanol. *Chem. Eng. Commun*. 203 **(2016)** 1385–1394.

[94] P. Rechnia, A. Malaika, M. Kozłowski. Synthesis of *tert*-amyl methyl ether (TAME) over modified activated carbon catalysts. *Fuel*. 154 **(2015)** 338–345.

[95] L. Degirmenci, N. Oktar, G. Doğu. Activated carbon supported silicotungstic acid catalysts for ethyl-*tert*-butyl ether synthesis. *AIChE J*. 57 **(2011)** 3171–3181.

[96] W. Kiatkittipong, S. Wongsakulphasatch, N. Tintan, N. Laosiripojana, P. Praserthdam, S. Assabumrungrat. Gasoline upgrading by self-etherification with ethanol on modified beta-zeolite. *Fuel Process. Technol*. 92 **(2011)** 1999–2004.

[97] F. Collignon, G. Poncelet. Comparative vapor phase synthesis of ETBE from ethanol and isobutene over different acid zeolites. *J. Catal*. 202 **(2001)** 68–77.

[98] N. V. Vlasenko, Y. N. Kochkin, A. M. Puziy. Liquid phase synthesis of ethyl-*tert*-butyl ether: The relationship between acid, adsorption and catalytic properties of zeolite catalysts. *J. Mol. Catal. A Chem*. 253 **(2006)** 192–197.

[99] W. Kiatkittipong, K. Yoothongkham, C. Chaisuk, P. Praserthdam, S. Goto, S. Assabumrungrat. Self-etherification process for cleaner fuel production. *Catal. Lett*. 128

(2009) 154–163.

[100] G. Ertl, H. Knozinger, F. Schuth, J. Weitkamp. *Handbook of heterogeneous catalysis*. 2nd ed. Wiley-VCH, New York, **2008**.

[101] B. C. Gates, W. Rodriguez. General and specific acid catalysis in sulfonic acid resin. *J. Catal*. 31 **(1973)** 27–31.

[102] G. Zundel. *Hydration and intermolecular interaction: infrared investigations with polyelectrolyte membranes*. 1st ed. Academic Press, New York, **1969**.

[103] B. C. Gates, L. N. Johanson. The dehydration of methanol and ethanol catalyzed by polystyrene sulfonate resins. *J. Catal*. 14 **(1969)** 69–76.

[104] C. Buttersack. Accesibility and catalytic activity of sulphonic acid ion-exchange resins in different solvents. *React. Polym*. 10 **(1989)** 143–164.

[105] J. Tejero, F. Cunill, S. Manzano. Influence of water on the gas-phase decomposition of methyl *tert*-butyl ether catalysed by a macroporous ion-exchange resin. *Appl. Catal.* 38 **(1988)** 327–340.

[106] R. Thornton, B. C. Gates. Catalysis by matrix-bound sulfonic acid groups: olefin and paraffin formation from butyl alcohols. *J. Catal*. 34 **(1974)** 275–287.

[107] V. J. Cruz, R. Bringué, F. Cunill, J. F. Izquierdo, J. Tejero, M. Iborra, C. Fité. Conversion, selectivity and kinetics of the liquid-phase dimerisation of isoamylenes in the presence of C1 to C5 alcohols catalysed by a macroporous ion-exchange resin. *J. Catal*. 238 **(2006)** 330–341.

[108] C. Berlanga, M. V. Biezma, J. Fernández. Revisión y estado del arte de la corrosividad del etanol y sus mezclas con gasolina. *Rev. Metal*. 47 **(2012)** 507–518.

[109] E. Gnansounou, A. Dauriat. Ethanol fuel from biomass: a review. *J. Sci. Ind. Res.* 64 **(2005)** 809–821.

[110] K. Jeřábek. Characterization of swollen polymer gels using size exclusion chromatography. *Anal. Chem*. 57 **(1985)** 1598–1602.

[111] R. Bringué, E. Ramírez, M. Iborra, J. Tejero, F. Cunill. Influence of acid ion-exchange resins morphology in a swollen state on the synthesis of ethyl octyl ether from ethanol and 1-octanol. *J. Catal*. 304 **(2013)** 7–21.

[112] M. Boudart. Kinetics and Mechanism of Catalytic Reactions. *Ind. Chim. Belge*. 23 **(1958)** 383.

[113] M. Boudart, D. E. Mears, M. A. Vannice. Kinetics of heterogeneous catalytic reactions. *Ind. Chim. Belge*. 32 **(1967)** 281–284.

[114] S. K. Ihm, J. H. Ahn, Y. D. Jo. Interaction of reaction and mass transfer in ion-exchange resin catalysts. *Ind. Eng. Chem. Res*. 35 **(1996)** 2946–2954.

[115] H. S. Fogler. *Elements of chemical reaction engineering*. 3rd ed. Prentice-Hall International, Inc., New Jersey, **2009**.

[116] C. R. Marston. Improve etherification plan efficiency and safety. *Fuel Reformul*. 4 **(1994)** 42–46.

[117] R. Trotta, E. Pescarollo, M. Hyland, S. Bertollli. Consider the advantages of water cooled reactors for ether production from refinery feedstocks. *Fuel Reformul*. 4 **(1994)** 40–45.

[118] R. González, C. Fité, F. Cunill, K. D. Topp, R. Olsen. Deactivation of ion exchange catalysts by acetonitrile and methylamine. *Top. Catal*. 54 **(2011)** 1054–1062.

[119] M. Quiroga, M. Rosa Capeletti, N. Fígoli, U. Sedran. Catalyst deactivation by acetonitrile in MTBE synthesis. *Appl. Catal. A Gen.* 177 **(1999)** 37–42.

[120] F. Ancillotti, M. M. Mauri, E. Pescarollo, L. Romagnoni. Mechanisms in the reaction

between olefins and alcohols catalyzed by ion exchange resins. *J. Mol. Catal*. 4 **(1978)** 37–48.

[121] A. Fitó. *Equilibrium of simultaneous tert-amyl ethyl ether and tert-amyl alcohol formation reactions*. PhD thesis. Helsinki University of Technology, **2008**.

[122] C. Gómez, F. Cunill, M. Iborra, F. Izquierdo, J. Tejero. Experimental study of the simultaneous synthesis of methyl *tert*-butyl ether and ethyl *tert*-butyl ether in liquid phase. *Ind. Eng. Chem. Res*. 36 **(1997)** 4756–4762.

[123] C. Fité, M. Iborra, J. Tejero, J. F. Izquierdo, F. Cunill. Kinetics of the liquid-phase synthesis of ethyl *tert*-butyl ether (ETBE). *Ind. Eng. Chem. Res.* 33 **(1994)** 581–591.

[124] N. Oktar, K. Mürtezaoğlu, G. Doğu, I. Gönderten, T. Doğu. Etherification rates of 2-methyl-2-butene and 2-methyl-1-butene with ethanol for environmentally clean gasoline production. *J. Chem. Technol. Biotechnol.* 161 **(1999)** 155–161.

[125] V. J. Cruz, J. F. Izquierdo, F. Cunill, J. Tejero, M. Iborra, C. Fité. Acid ion-exchange resins catalysts for the liquid-phase dimerization/etherification of isoamylenes in methanol or ethanol presence. *React. Funct. Polym.* 65 **(2005)** 149–160.

[126] M. Iborra, J. Tejero, M. El-Fassi, F. Cunill, J.F. Izquierdo, C. Fité. Experimental study of the liquid-phase simultaneous syntheses of methyl *tert*-butyl ether (MTBE) and *tert*-butyl alcohol (TBA). *Ind. Eng. Chem. Res*. 41 **(2002)** 5359–5365.

[127] J. F. Izquierdo, F. Cunill, M. Vila, M. Iborra, J. Tejero. Equilibrium constants for methyl *tert*-butyl ether and ethyl *tert*-butyl ether liquid-phase syntheses using C4 olefinic cut. *Ind. Eng. Chem. Res.* 33 **(1994)** 2830–2835.

[128] W. Mao, X. Wang, H. Wang, H. Chang, X. Zhang, J. Han. Thermodynamic and kinetic study of *tert*-amyl methyl ether (TAME) synthesis. *Chem. Eng. Process. Process Intensif.* 47 **(2008)** 761–769.

[129] I. Muja, A. Toma, D. C. Popescu, I. Ivanescu, V. Stanistean. Thermodynamic study of the methanol addition to isoamylen. *Chem. Eng. Process. Process Intensif.* 44 **(2005)** 645–651.

[130] L. K. Rihko, A. O. I. Krause. Kinetics of heterogeneously catalyzed *tert*-amyl methyl ether reactions in the liquid phase. *Ind. Eng. Chem. Res.* 34 **(1995)** 1172–1180.

[131] J. A. Linnekoski, A. O. I. Krause, L. K. Rihko. Kinetics of the heterogeneously catalyzed formation of *tert*-amyl ethyl ether. *Ind. Eng. Chem. Res.* 36 **(1997)** 310–316.

[132] J. A. Serda, J. F. Izquierdo, J. Tejero, F. Cunill, M. Iborra. Equilibrium and thermodynamics for 2-methyl-2-methoxybutane liquid-phase decomposition. *Thermochim. Acta*. 259 **(1995)** 111–120.

[133] L. Solà, M. A. Pericàs, F. Cunill, J. F. Izquierdo. A comparative thermodynamic and kinetic study of the reaction between olefins and light alcohols leading to branched ethers. Reaction calorimetry study of the formation of *tert*-amyl methyl ether (TAME) and *tert*-butyl isopropyl ether (IPTBE). *Ind. Eng. Chem. Res*. 36 **(1997)** 2012–2018.

[134] F. H. Syed, C. Egleston, R. Datta. *tert*-Amyl methyl ether (TAME). Thermodynamic analysis of reaction equilibria in the liquid phase. *J. Chem. Eng. Data*. 45 **(2000)** 319–323.

[135] K. L. Jensen, R. Datta. Ethers from Ethanol. 1. Equilibrium thermodynamic analysis of the liquid-phase ethyl *tert*-butyl ether reaction (ETBE). *Ind. Eng. Chem. Res*. 34 **(1995)** 392–399.

[136] J. A. Linnekoski, P. Kiviranta-Pääkkönen, A. O. I. Krause, L.K. Rihko-Struckmann. Simultaneous isomerization and etherification of isoamylenes. *Ind. Eng. Chem. Res*. 38 **(1999)** 4563–4570.

[137] L. K. Rihko, J. A. Linnekoski, A. O. I. Krause. Reaction equilibria in the synthesis of 2-

methoxy-2-methylbutane and 2-ethoxy-2-methylbutane in the liquid phase. *J. Chem. Eng. Data*. 39 **(1994)** 700–704.

[138] K. G. Sharonov, A. M. Rozhnov, A. Korol'kov, S. Y. Karaseva, E. A. Miroshnichenko, L. I. Korchatova. Enthalpies of formation of 2-methyl-2-ethoxypropane and 2-ethyl-2-ethoxypropane from equilibrium measurements. *J. Chem. Thermodyn*. 27 **(1995)** 751–753.

[139] O. Françoisse, F. C. Thyrion. Kinetics and mechanism of ethyl *tert*-butyl ether liquid-phase synthesis. *Chem. Eng. Process. Process Intensif*. 30 **(1991)** 141–149.

[140] J. A. Linnekoski, A. O. I. Krause. Kinetics of the heterogeneously catalyzed formation of *tert* -amyl ethyl ether. *Ind. Eng. Chem. Res*. 36 **(1997)** 310–316.

[141] T. Zhang, K. Jensen, P. Kitchaiya, C. Phillips, R. Datta. Liquid-phase synthesis of ethanol-derived mixed tertiary alkyl ethyl ethers in an isothermal integral packed-bed reactor. *Ind. Eng. Chem. Res*. 36 **(1997)** 4586–4594.

[142] L. K. Rihko-Struckmann, P. V Latostenmaa, A. O. I. Krause. Interaction between the reaction medium and an ion-exchange resin catalyst in the etherification of isoamylenes. *J. Mol. Catal. A Chem*. 177 **(2001)** 41–47.

[143] M. S. Caceci. Estimating error limits in parametric curve fitting. *Anal. Chem*. 61 **(1989)** 2324–2327.

[144] C. Fité, J. Tejero, M. Iborra, F. Cunill, J. F. Izquierdo. Enhancing MTBE rate equation by considering reaction medium influence. *AIChE J*. 44 **(1998)** 2273–2279.

[145] G. Bozga, A. Motelica, R. Dima, V. Plesu, A. Toma, C. Simion: Evaluation of published kinetic models for *tert*-amyl ethyl ether synthesis. *Chem. Eng. Process. Process Intensif*. 47 **(2008)** 2247–2255.

[146] K. Sundmacher, R. S. Zhang, U. Hoffmann. Mass transfer effects on kinetics of nonideal liquid phase ethyl*tert*-butyl ether formation. *Chem. Eng. Technol*. 18 **(1995)** 269–277.

[147] K. Jensen, R. Datta, Ethers from Ethanol. 7. Transition-state theory analysis of the kinetics of liquid-phase ethyl *tert*-butyl ether synthesis reaction. *Submitt. Publ. to Ind. Eng. Chem. Res.* **(1997)**.

[148] L. Solà, M. A. Pericàs, F. Cunill, J. Tejero. Thermodynamic and kinetic studies of the liquid phase synthesis of *tert*-butyl ethyl ether using a reaction calorimeter. *Ind. Eng. Chem. Res*. 34 **(1995)** 3718–3725.

[149] M. Umar, A. R. Saleemi, S. Qaiser. Synthesis of ethyl *tert*-butyl ether with *tert*-butyl alcohol and ethanol on various ion exchange resin catalysts. *Catal. Commun*. 9 **(2008)** 721–727.

[150] P. Słomkiewicz. Determination of the adsorption equilibrium of alcohols and alkenes on a sulphonated styrene–divinylbenzene copolymer. *Adsorpt. Sci. Technol*. 24 **(2006)** 239–256.

[151] J. Guilera. *Ethyl octyl ether synthesis from 1-octanol and ethanol or diethyl carbonate on acidic ion-exchange resins*. PhD thesis. University of Barcelona, **2013**.

[152] K. Jeřábek. Determination of pore volume distribution from size exclusion chromatography data. *Anal. Chem*. 57 **(1985)** 1595–1597.

[153] P. Kiviranta-Pääkkönen, L. K. Struckmann, J. A. Linnekoski, A.O. I. Krause. Dehydration of the alcohol in the etherification of isoamylenes with methanol and ethanol. *Ind. Eng. Chem. Res*. 37 **(1998)** 18–24.

[154] J. Andraos, M. Sayed. On the use of "green" metrics in the undergraduate organic chemistry lecture and lab to assess the mass efficiency of organic reactions. *J. Chem. Educ*. 84 **(2007)** 1004–1010.

[155] J. Andraos. Unification of reaction metrics for green chemistry II: evaluation of named

organic reactions and application to reaction discovery. *Org. Process Res. Dev*. 9 **(2005)** 404–431.

[156] R. A. Sheldon. The E Factor: fifteen years on. *Green Chem*. 9 **(2007)** 1273–1283.

[157] J. Andraos. Global green chemistry metrics analysis algorithm and spreadsheets: evaluation of the material efficiency performances of synthesis plans for oseltamivir phosphate (Tamiflu) as a test case. *Org. Process Res. Dev*. 13 **(2008)** 161–185.

[158] J. Andraos. A database tool for process chemists and chemical engineers to gauge the material and synthetic efficiencies of synthesis plans to industrially important targets. *Pure Appl. Chem*. 83 **(2011)** 1361–1378.

[159] J. Andraos. Unification of reaction metrics for green chemistry: applications to reaction analysis. *Org. Process Res. Dev*. 9 **(2005)** 149–163.

[160] M. Vila, F. Cunill, J.F. Izquierdo, J. Tejero, M. Iborra. Equilibrium constants for ethyl *tert*-butyl ether liquid phase sinthesis. *Chem. Eng. Commun*. 124 **(1993)** 223–232.

[161] B. L. Yang, S. Goto. Pervaporation with reactive distillation for the production of ethyl *tert*-butyl ether. *Sep. Sci. Technol*. 32 **(1997)** 971–981.

[162] B. L. Yang, S. B. Yang, R. Yao. Synthesis of ethyl *tert*-butyl ether from *tert*-butyl alcohol and ethanol on strong acid cation-exchange resins. *React. Funct. Polym*. 44 **(2000)** 167–175.

[163] M. Umar, D. Patel, B. Saha. Kinetic studies of liquid phase ethyl *tert*-butyl ether (ETBE) synthesis using macroporous and gelular ion exchange resin catalysts. *Chem. Eng. Sci*. 64 **(2009)** 4424–4432.

[164] N. Boz, T. Doğu. Reflux-recycle-reactor for high yield and selectivity in TAME and TAEE production. *AIChE J*. 51 **(2005)** 631–640.

[165] D. Varisli, T. Doğu. Simultaneous production of *tert*-amyl ethyl ether and *tert*-amyl alcohol from isoamylene-ethanol-water mixtures in a batch-reactive distillation column. *Ind. Eng. Chem. Res*. 44 **(2005)** 5227–5232.

[166] F. Aiouache, S. Goto. Sorption effect on kinetics of etherification of *tert*-amyl alcohol and ethanol. *Chem. Eng. Sci*. 58 **(2003)** 2065–2077.

[167] M. G. Sneesby, M. O. Tadé, R. Datta. *tert*-Butyl ethers - a comparison of properties, synthesis techniques and operating conditions for high conversions. *Dev. Chem. Eng. Miner. Process*. 3 **(2008)** 89–116.

[168] R. L. Mason, R. F. Gunst, J. L. Hess. *Statistical design and analysis of experiments: with applications to engineering and science*. 2nd ed. John Wiley & Sons, New York, **2003**.

[169] R. H. Myers, D. C. Montgomery, C. M. Anderson-Cook. *Response surface methodology: process and product optimization using designed experiments*. 3rd ed. John Wiley & Sons, New York, **2009**.

[170] N. Draper, H. Smith. *Applied regression analysis*. 2nd ed. John Wiley & Sons, New York, **1981**.

[171] A. I. Khuri and J. A. Cornell. *Response surfaces: designs and analyses*. 1st ed. M. Dekker, New York, **1987**.

[172] E. C. Harrington. The desirability function. *Ind. Qual. Control*. 21 **(1965)** 494–498.

[173] G. Derringer, R. Suich. Simultaneous Optimization of Several Response Variables. *J. Qual. Technol*. 12 **(1980)** 214–219.

[174] R. S. Karinen, M. S. Lylykangas, A. O. I. Krause. Reaction equilibrium in the isomerization of 2,4,4-trimethyl pentenes. *Ind. Eng. Chem. Res*. 40 **(2001)** 1011–1015.

[175] T. W. G. Solomons, C. B. Fryhle. *Organic chemistry*. 9th ed. John Wiley & Sons, New York, **2000**.

[176] J. Gmehling, J. Li, M. Schiller, A modified UNIFAC model. 2. Present parameter matrix and results for different thermodynamic properties. *Ind. Eng. Chem. Res*. 32 **(1993)** 178–193.

[177] J. Gmehling, J. Lohmann, A. Jakob, J. Li, R. Joh. A Modified UNIFAC (Dortmund) Model. 3. Revision and Extension. *Ind. Eng. Chem. Res*. 37 **(1998)** 4876–4882.

[178] J. Lohmann, R. Joh, J. Gmehling. From UNIFAC to Modified UNIFAC (Dortmund). *Ind. Eng. Chem. Res*. 40 **(2001)** 957–964.

[179] U. Weidlich, J. Gmehling. A modified UNIFAC model. 1. Prediction of VLE, hE, and gamma.infin. *Ind. Eng. Chem. Res*. 26 **(1987)** 1372–1381.

[180] M. V. Ferreira, J. M. Loureiro. Number of actives sites in TAME synthesis: mechanism and kinetic modeling. *Ind. Eng. Chem. Res*. 43 **(2004)** 5156–5165.

[181] R. W. Gallant. *Physical properties of hydrocarbons*. 1st ed. Gulf Publishing Co., vol. 1, Houston, **1993**.

[182] M. Zábranský, Z. Kolská, V. Růžička, E.S. Domalski, M. Zabransky, Z. Kolska, J. R. Vlastimil, E.S. Domalski. Heat capacity of liquids: critical review and recommended values. Supplement II. *J. Phys. Chem. Ref. Data*. 39 **(2010)** 013103-1–013103-404.

[183] C. L. Yaws. *Thermodynamic and physical property data*. 1st ed. Gulf Publishing Co., Houston, **1992**.

[184] TRC Thermodynamic Tables. Thermodynamics Research Center, The Texas A&M University System, College Station, vol. 5, **(1986)** 6090–6091.

[185] V. J. Cruz, J. F. Izquierdo, F. Cunill, J. Tejero, M. Iborra, C. Fité, R. Bringué. Kinetic modelling of the liquid-phase dimerization of isoamylenes on Amberlyst 35. *React. Funct. Polym*. 67 **(2007)** 210–224.

[186] M. M. Abbott, J.M. Smith, H. C. van Ness. *Introduction to chemical engineering thermodynamics*. 7th ed. Mc Graw Hill, Boston, **2001**.

[187] S. P. Verevkin. Thermochemistry of branched ethers: experimental study of chemical equilibrium in the reacting system of *tert*-amyl alkyl ether synthesis. *J. Chem. Eng. Data*. 49 **(2004)** 576–581.

[188] T. Zhang, R. Datta, Ethers from ethanol. 5. Equilibria a n d kinetics of the coupled reaction network of synthesis. *Chem. Eng. Sci*. 51 **(1996)** 649–661.

[189] S. P. Verevkin. Improved Benson increments for the estimation of standard enthalpies of formation and enthalpies of vaporization of alkyl ethers, acetals, ketals. and ortho esters. *J. Chem. Eng. Data*. 47 **(2002)** 1071–1097.

[190] G. S. Parks, S. S. Todd, C. H. Shomate. Thermal data on organic compounds. XVII. Some heat capacity, entropy and free energy data for five higher olefins. *J. Am. Chem. Soc*. 58 **(1936)** 2505–2508.

[191] R. B. Turner, D. E. Nettleton, M. Perelman. Heats of hydrogenation. VI. Heats of hydrogenation of some substituted ethylenes. *J. Am. Chem. Soc*. 80 **(1958)** 1430–1433.

[192] L. Degirmenci, N. Oktar, G. Doğu. Product distributions in ethyl *tert*-butyl ether synthesis over different solid acid catalysts. *Ind. Eng. Chem. Res*. 48 **(2009)** 2566–2576.

[193] T. A. Albahri. Structural group contribution method for predicting the octane number of pure hydrocarbon liquids. *Ind. Eng. Chem. Res*. 42 **(2003)** 657–662.

[194] N. F. Shah, M. M. Sharma. Dimerization of isoamylene: ion exchange resin and acid-treated clay as catalysts. *React. Polym*. 19 **(1993)** 181–190.

[195] J. Tejero, F. Cunill, J. F. Izquierdo, M. Iborra, C. Fité, D. Parra. Scope and limitations of mechanistic inferences from kinetic studies on acidic macroporous resins. The MTBE liquid-phase synthesis case. *Appl. Catal. A Gen*. 134 **(1996)** 21–36.

[196] M. Granollers. *Liquid-phase oligomerization of isoamylenes over solid acid catalysts*. PhD thesis, University of Barcelona, **2012**.

[197] S. Lowell, J.E. Shields. *Powder Surface Area and Porosity*. 2nd ed. Chapman and Hall, Dordrecht, **1984**.

[198] G. Leofanti, M. Padovan, G. Tozzola, B. Venturelli. Surface area and pore texture of catalysts. *Catal. Today*. 41 **(1998)** 207–219.

[199] G. E. P. Box, D. R. Cox. An Analysis of Transformations. *J. R. Stat. Soc. Ser*. B. 26 **(1964)** 211–252.

[200] J. D. Grunwaldt, B. S. Clausen. Combining XRD and EXAFS with on-line catalytic studies for in situ characterization of catalysts. *Top. Catal*. 18 **(2002)** 37–43.

[201] J. R. Kittrell, J. Erjavec. Response surface methods in heterogeneous kinetic modeling. *Ind. Eng. Chem. Process Des. Dev*. 7 **(1968)** 321–327.

[202] M. Boudart. Classical catalytic kinetics: a placebo or the real thing?. *Ind. Eng. Chem. Fundam*. 25 **(1986)** 656–658.

[203] H. Hofmann. Industrial process kinetics and parameter estimation. *Chem. React. Eng*. 8 **(1970)** 519–534.

[204] J. R. Kittrell, W. G. Hunter, C. C. Watson. Nonlinear least squares analysis of catalytic rate models. *AIChE J*. 11 **(1965)** 1051–1057.

[205] F. E. Turkheimer, R. Hinz, V. J. Cunningham. On the undecidability among kinetic models, from model selection to model averaging. 23 **(2003)** 490–498.

[206] L. Wasserman. Bayesian model selection and model averaging. *J. Math. Psychol*. 44 **(2000)** 92–107.

[207] J. A. Hoeting, D. Madigan, A. E. Raftery, C. T. Volinsky. Bayesian model averaging: a tutorial . *Stat. Sci*. 14 **(1999)** 382–417.

[208] G. Glatting, P. Kletting, S. N. Reske, K. Hohl, C. Ring. Choosing the optimal fit function: comparison of the Akaike information criterion and the F-test. *Med. Phys*. 34 **(2007)** 4285–4292.

[209] K. P. Burnham, D. R. Anderson. *Model selection and multimodel inference: A practical information-theoretic approach*. 2nd ed. Springer Science, New York, **2003**.

[210] M. R. E. Symonds, A. Moussalli. A brief guide to model selection, multimodel inference and model averaging in behavioural ecology using Akaike's information criterion. *Behav. Ecol. Sociobiol*. 65 **(2010)** 13–21.

[211] J. Tejero, F. Cunill, J. F. Izquierdo. Vapor-phase addition of methanol to isobutene on a macroporous resin. A kinetic study. *Ind. Eng. Chem. Res*. 28 **(1989)** 1269–1277.

[212] B. E. Poiling, J. M. Prausnitz, J. P. O' Connell. *The properties of gases and liquids*. 5th ed. Mc Graw Hill, New York, **2004**.

[213] C. Reichardt. *Solvents and solvent effects in organic chemistry*. 3rd ed. Willey-VCH, Weinheim, **2003**.

[214] C. L. Yaws. *Thermophysical properties of chemicals and hydrocarbons*. 2nd ed. Elsevier Science, Oxford, **2014**.

[215] T. Matsuura. *Synthetic Membranes and Membrane Separation Processes*. 1st ed. CRC Press Inc., Boca Raton, FL, **1993**.

[216] R. T. Marler, J. S. Arora. The weighted sum method for multi-objective optimization: new insights. *Struct. Multidiscip. Optim.* 41 **(2009)** 853–862.

[217] G. Puxty, M. Maeder, K. Hungerbühler. Tutorial on the fitting of kinetics models to multivariate spectroscopic measurements with non-linear least-squares regression. *Chemom. Intell. Lab. Syst*. 81 **(2006)** 149–164.

[218] R. M. Stephenson, S. Malanowski. *Handbook of the thermodynamics of organic compounds*. 1st ed. Elsevier Science, New York, **1987**.

[219] M. A. Pérez-Maciá, R. Bringué, M. Iborra, J. Tejero, F. Cunill. Kinetic study of 1-butanol dehydration to di- *n* -butyl ether over Amberlyst 70. *AIChE J*. 62 **(2016)** 180–194.

[220] F. Benyahia, K. E. O'Neill. Enhanced voidage correlations for packed beds of various particle shapes and sizes. *Part. Sci. Technol*. 23 **(2005)** 169–177.

[221] T. Doğu, E. Aydin, N. Boz, K. Murtezaoğlu, G. Doğu. Diffusion resistances and contribution of surface diffusion in TAME and TAEE production using Amberlyst-15. *Int. J. Chem. React. Eng*. 1 **(2002)** 1–10.

[222] K. Kawazoe, M. Suzuki, K. Chihara. Chromatographsc study of diffusion in molecular-sieving carbon. *J. Chem. Eng. Japan*. 7 **(1974)** 151–157.

[223] T. Furusawa, M. Suzuki. Moment analysis of concentration decay in a batch adsorption vessel. *J. Chem. Eng. Japan*. 8 **(1975)** 119–122.

[224] T. Doğu. Diffusion and reaction in catalyst pellets with bidisperse pore size distribution. *Ind. Eng. Chem. Res*. 37 **(1998)** 2158–2171.

[225] F. Mü, C. A. Ferreira, L. Franco, J. Puiggalí, C. Alema, E. Armelin. New sulfonated polystyrene and styrene−ethylene/butylene−styrene block copolymers for applications in electrodialysis. *J. Phys. Chem. B*. 116 **(2012)** 11767–11779.

[226] D. Li, P. Bui, H.Y. Zhao, S.T. Oyama, T. Dou, Z.H. Shen. Rake mechanism for the deoxygenation of ethanol over a supported Ni_2P/SiO_2 catalyst. *J. Catal*. 290 **(2012)** 1–12.

[227] H. G. Carlson, E. F. Westrum Jr. Methanol: heat capacity, enthalpies of transition and melting, and thermodynamic properties from 5–300 K. *J. Chem. Phys*. 54 **(1971)** 1464–1471.

[228] O. Haida, H. Suga, S. Seki. Calorimetric study of the glassy state XII. Plural glass-transition phenomena of ethanol. *J. Chem. Thermodyn*. 9 **(1977)** 1133–1148.

[229] J. F. Counsell, E. B. Lees, J. F. Martin. Thermodynamic properties of organic oxygen compounds. Part XIX. Low-temperature heat capacity and entropy of propan-1-ol, 2-methylpropan-1-ol, and pentan-1-ol. *J. Chem. Soc. A Inorganic, Phys. Theor*. 1 **(1968)** 1819–1823.

[230] J. F. Counsell, J. L. Hales, J. F. Martin. Thermodynamic properties of organic oxygen compounds. Part 16-Butyl alcohol. *Trans. Faraday Soc*. 61 **(1965)** 1869–1875.

[231] J. Chao, K. R. Hall, J. Yao. Thermodynamic properties of simple alkenes. *Thermochim. Acta*. 64 **(1983)** 285–303.

[232] V. Majer, V. Svoboda, H. V. Kehiaian. *Enthalpies of vaporization of organic compounds: a critical review and data compilation*. 1st ed. Blackwell Scientific, Oxford, **1985**.

[233] U. Limbeck, C. Altwicker, U. Kunz, U. Hoffmann. Rate expression for THF synthesis on acidic ion exchange resin. *Chem. Eng. Sci*. 56 **(2001)** 2171–2178.

[234] L. Boulicaut, S. Brandani, D. M. Ruthven. Liquid phase sorption and diffusion of branched and cyclic hydrocarbons in silicalite. *Microporous Mesoporous Mater*. 25 **(1998)** 81–93.

[235] J. M. Smith. *Chemical engineering kinetics*. 3rd ed. Mc Graw Hill, New York, **1981**.

[236] R. M. Quinta-Ferreira, C.A. Almeida-Costa, A. E. Rodrigues. Heterogeneous models of tubular reactors packed with ion-exchange resins: simulation of the MTBE synthesis. *Ind. Eng. Chem. Res*. 35 **(1996)** 3827–3841.

[237] A. Rehfinger, U. Hoffmann. Kinetics of methyl tertiary butyl ether liquid phase synthesis

catalyzed by ion exchange resin—II. Macropore diffusion of methanol as rate-controlling step. *Chem. Eng. Sci*. 45 **(1990)** 1619–1626.

[238] S. Becht, R. Franke, A. Geißelmann, H. Hahn. An industrial view of process intensification. *Chem. Eng. Process. Process Intensif*. 48 **(2009)** 329–332.

[239] C. H. Bartholomew. Mechanisms of catalyst deactivation. *Appl. Catal. A Gen*. 212 **(2001)** 17–60.

[240] M. Ramírez-Corredores, Z. Hernández, J. Guerra, R. Alvarez, J. Medina. Options for nitriles removal from C4–C5 cuts. *Fuel Process. Technol*. 81 **(2003)** 143–154.

[241] C. van den Bleek, K. van der Wielle, P. J. van den Berg. The effect of dilution on the degree of conversion in fixed bed catalytic reactors. *Chem. Eng. Sci*. 24 **(1969)** 681–694.

[242] B. L. Yang, M. Maeda, S. Goto. Kinetics of liquid phase synthesis of *tert*-amyl methyl ether from *tert*-amyl alcohol and methanol catalyzed by ion exchange resin. *Int. J. Chem. Kinet*. 30 **(1998)** 137–143.

[243] E. du Toit, W. Nicol. The rate inhibiting effect of water as a product on reactions catalysed by cation exchange resins: formation of mesityl oxide from acetone as case study. *Appl. Catal. A Gen*. 277 **(2004)** 219–225.

[244] T. Baba, Y. Ono. Kinetic studies in liquid phase dehydration-cyclization of 1,4-butanediol to tetrahydrofuran with heteropoly acids. *J. Mol. Catal*. 37 **(1986)** 317–326.

[245] P. Forzatti. Catalyst deactivation. *Catal. Today*. 52 **(1999)** 165–181.

[246] C. H. Bartholomew, R. J. Farranto. *Fundamental of industrial catalytic processes*. 2nd ed. John Wiley & Sons, New Jersey, **2006**.

[247] C. L. Yaws. *Handbook of Thermodynamic Properties for Hydrocarbons and Chemicals*. 1st ed. Elsevier Science, Oxford, **2009**.

6.2 LIST OF TABLES

6.3 LIST OF FIGURES

7. APPENDICES

7.1 GASOLINE ANALYSIS BY GC/MS

Table 7.1.1. Composition of a typical gasoline from a petrol station in Barcelona (Spain). Year 2016. Determined by GC/MS.

Peak	R. T. (min)	Crom. Area (%)	Compound	Type	Peak	R. T. (min)	Crom. Area (%)	Compound	Type
1	5.209	0.152	isobutane	P	55	19.196	0.056	6-methyl-1-heptene	O
2	5.389	0.304	1-butene	O	56	19.359	0.653	2-methylheptane	P
3	5.47	0.38	butane	P	57	19.477	0.261	4-methylheptane	P
4	5.555	0.158	cis-2-butene	O	58	19.672	0.096	3,4-dimethylhexane	P
5	5.701	0.099	2-butene/2methyl-1-propene	O	59	19.932	0.879	3-methylheptane	P
6	5.83	0.737	ethanol	OH	60	20.27	0.485	1,3-dimethylcyclohexane (cis)	P
7	6.099	0.028	3-methyl-1-butene	O	61	20.407	0.192	1,4-dimethylcyclohexane (trans)	P
8	6.374	6.543	2-methyl-butane (isopentane)	P	62	20.88	0.066	1,1-dimethylcyclohexane	P
9	6.612	0.099	1-pentene	O	63	21.034	0.144	1-ethyl-3-methylcyclopentane (trans)	P
10	6.733	0.267	2-methyl-1-butene (2M1B)	O	64	21.206	0.128	1-ethyl-3-methylcyclopentane (cis)	P
11	6.827	2.939	pentane	P	65	21.304	0.107	1-ethyl-2-methylcyclopentane	P
12	6.962	0.715	trans-2-pentene	O	66	21.516	0.053	5,7-dimethyl-1,6-octadiene	O
13	7.048	0.064	tert-butyl alcohol (TBA)	OH	67	21.787	0.147	1,2-dimethylcyclohexane	P
14	7.139	0.151	cis-2-pentene	O	68	21.915	0.692	Octane	P
15	7.249	0.715	2-methyl-2-butene (2M2B)	O	69	22.305	0.228	1,3-dimethylcyclohexane (trans)	P
16	7.661	4.999	2,2-dimethylbutane	P	70	22.83	0.054	butylcyclopentane	P
17	8.154	0.946	cyclopentene	O	71	23.821	0.05	hexylpentyl ether	E
18	8.507	1.515	2,3-dimethylbutane	P	72	24.328	0.118	propylcyclopentane	P
19	8.614	2.899	2-methylpentane (isohexane)	P	73	24.547	0.184	ethylcyclohexane	P
20	9.107	1.216	3-methylpentane	P	74	24.867	0.085	3,5-dimethylheptane	P
21	9.256	0.073	2-methyl-1-pentene	O	75	24.976	0.108	1,1,3-trimethylcyclohexane	P
22	9.717	0.945	hexane	P	76	25.906	3.353	ethylbenzene	A
23	9.882	0.075	2-hexene	O	77	26.198	0.08	1,2,4-trimethylcyclohexane	P
24	9.973	0.069	3-methyl-2-pentene	O	78	26.601	12.042	m-xylene/p-xylene	A
25	10.148	0.078	2-ethyl-1,3-butadiene	O	79	27.202	0.269	4-methyloctane	P
26	10.284	0.049	trans-2-methyl-1,3-pentadiene	O	80	27.777	0.167	3-ethyloctane	P
27	10.417	8.747	ethyl *tert*-butyl ether (ETBE)	E	81	28.482	4.636	o-xylene/p-xylene	A
28	10.764	0.054	2,2-dimethylpentane	P	82	28.891	0.053	hexylcyclopentane	P
29	10.934	0.534	methylcyclopentane	P	83	29.086	0.092	1-ethyl-3-methylcyclohexane	P
30	11.024	0.106	2,4-dimethylpentane	P	84	30.057	0.154	nonane	P

Table 7.1.1. Composition of a typical gasoline from a petrol station in Barcelona (Spain). Year 2016. Determined by GC/MS. Continued.

31	11.865	0.045	ethyl *sec*-butyl ether (ESBE)	E	85	31.186	0.127	m-ethyltoluene	A
32	12.065	0.888	benzene	A	86	33.645	0.455	propylbenzene	A
33	12.318	0.134	3,3-dimethylpentane	P	87	34.248	1.722	p-ethyltoluene	A
34	12.585	0.559	ciclohexane	P	88	34.426	0.835	o-ethyltoluene	A
35	12.905	1.415	2-methylhexane	P	89	34.895	0.847	1,3,5-trimethylbenzene	A
36	13.053	0.495	2,3-dimethylpentane	P	90	35.734	0.584	1,2,3-trimethylbenzene	A
37	13.286	0.058	1,1-dimethylcyclopentane	P	91	36.968	3.297	1,2,4-trimethylbenzene	A
38	13.403	1.786	3-methylhexane	P	92	39.257	0.544	1,3,3-trimethylbenzene	A
39	13.862	0.284	1,3-dimethylcyclopentane (trans)	P	93	40.21	0.527	indane	A
40	14.019	0.43	1,3-dimethylcyclopentane (cis)	P	94	41.46	0.055	1,4-diethylbenzene	A
41	14.197	0.445	1,2-dimethylcyclopentane (cis)	P	95	41.673	0.118	m-propyltoluene	A
42	14.814	1.698	n-heptane	P	96	41.994	0.083	o-propyltoluene	A
43	15.404	0.038	4-methyl-2-hexene	O	97	42.202	0.143	1,2-dimethyl-4-ethylbenzene	A
44	15.552	0.08	2,4,4-trimethyl-1-pentene (TMP1)	O	98	42.957	0.051	1-methyl-4-propylbenzene (p-ethyltoluene)	A
45	16.292	1.198	methylcyclohexane	P	99	43.741	0.079	1-ethyl-2,4-dimethylbenzene	A
46	16.437	0.118	1,1,3-trimethylcyclopentane	P	100	43.893	0.075	Cymene	A
47	16.935	0.144	2,5-dimethylhexane	P	101	44.378	0.158	1-ethyl-3,5-dimethylbenzene	A
48	17.079	0.517	2,4-dimethylhexane	P	102	45.898	0.314	octahydro-4,7-methano-1H indene	O
49	17.595	0.239	1,2,4-trimethylcyclopentane	P	103	46.946	0.087	1,2,3,4-tetramethylbenzene	A
50	18.092	0.118	1,2,3-trimethylcyclopentane	P	104	47.213	0.142	1,2,4,5-tetramethylbenzene	A
51	18.273	0.129	1-(ethenyloxy)-3-methyl-butane= vinylisopentyl ether	E	105	48.564	0.047	3,4-dimethylstyrene	A
52	18.587	17.118	Toluene	A	106	49.343	0.05	2,6-dimethylstyrene	A
53	18.983	0.172	2,3-dimethylhexane	P	107	49.654	0.065	1,3,8-p-menthatriene	A
54	19.106	0.045	3-ethyl-2-methylpentane	P	108	51.627	0.112	Naphtalene	N

Table 7.1.2. Analysis Parameters for gasoline composition determination. Apparatus: Agilent 6890 Gas Chromatograph system coupled to 5973N Mass Selective Detector

GC		MS	
Column	HP PONA 50mx0.2mmx0.5mm	Quadrupole Temperature	150 °C
Column oven temperature	40 °C (1 min) → (2 °C min^{-1})→150 °C (10 min)	Ion source Temperature 200 °C	200 °C
Vaporization Chamber temperature	250 °C	Data sampling time	1 min to 66 min
Injection mode	split	Adquisition mode	Scan
Carrier gas	Helium	Mass Range	m/z 20 to 500
Pressure	0.942 bar	Event time	66 min
Flow	1.7 mL min^{-1}	Gain Factor	1
Linear velocity	47 cm/sec		
Split Ratio	300:1		
Injection quantity	2mL		

7.2 EXAMPLES OF PROCESS CONTROL GRAPHS FOR THE PID CONTROLLER

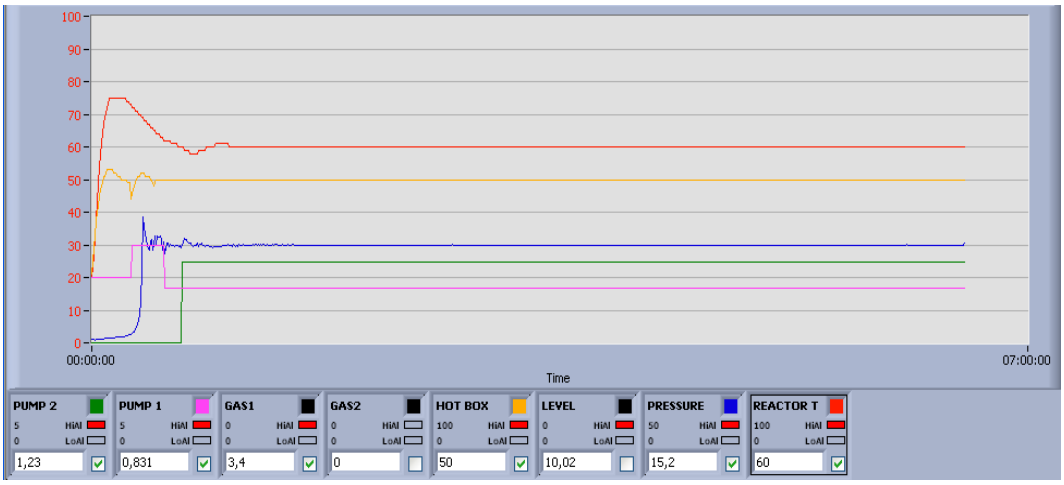

Figure 7.2.1. Diagram for process variables values during a typical run.

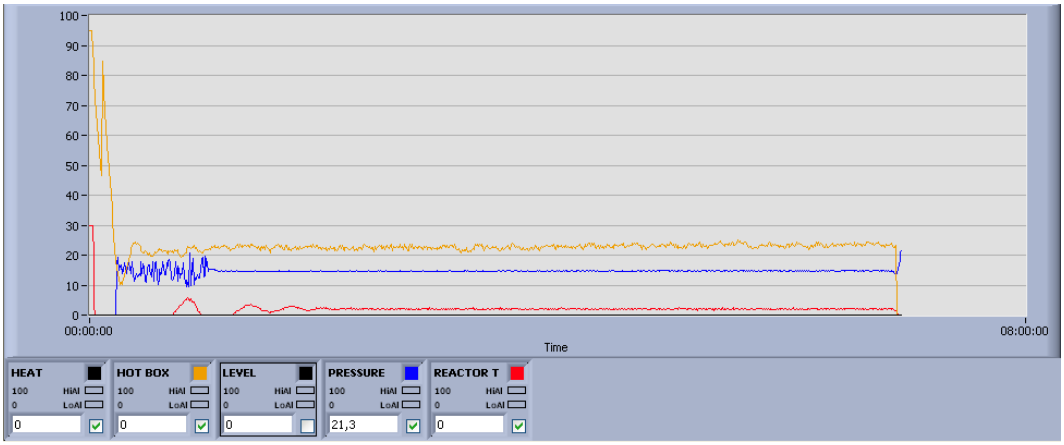

Figure 7.2.2. Diagram for output controllers during a typical run.

7.3. ANALYTICAL DATA AND MASS SPECTRA OF COMPOUNDS

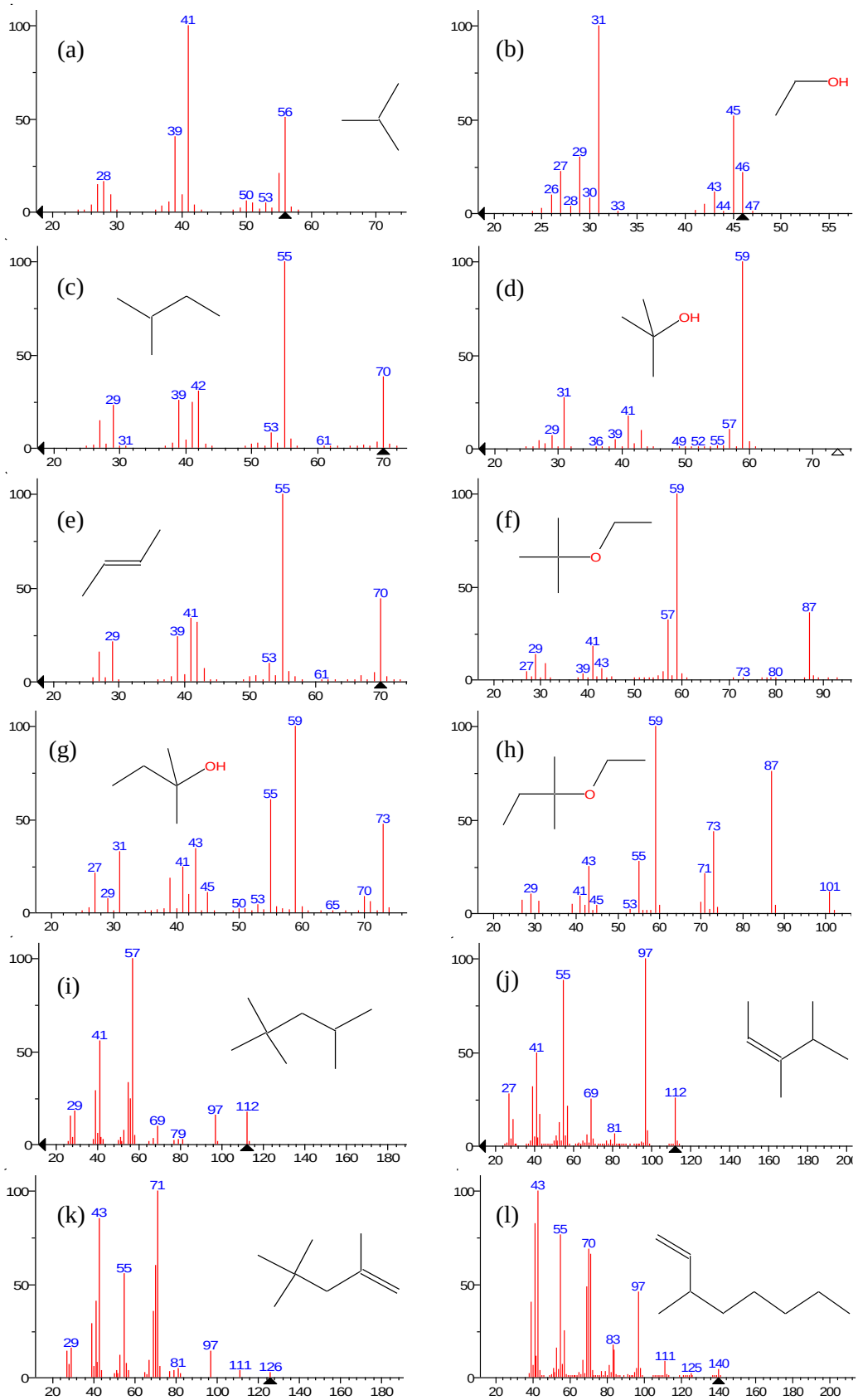

Figure 7.3.1. Mass spectra of: (a) 2-methyl-1-propene, (b) ethanol, (c) 2-methyl-1-butene, (d) *tert*-butyl alcohol, (e) 2-methyl-2-butene, (f) ethyl *tert*-butyl ether, (g) *tert*-amyl alcohol, (h) *tert*-amyl ethyl ether, (i) 2,4,4-trymethyl-1-pentene, (j) 2,4,4-trymethyl-2- pentene, (k) 2,4,4-trymethyl-1-hexene, and (l) 1.3,7-dimethyl-1-octene.

Table 7.3.1. Average linear velocities of compounds obtained with the chromatographic method described in *Section 3.3*.

Compound	Tr (min)	Average linear velocity [m/s]
IB	6.3	0.133
EtOH	7.0	0.119
2M1B	8.5	0.098
DEE	8.8	0.094
TBA	9.1	0.092
2M2B	9.4	0.089
ETBE	13.5	0.062
TAA	13.9	0.060
TMP-1	17.7	0.047
TAEE	18.1	0.046
TM2-P	18.3	0.046
Dimers $_{C4-C5}$	20.8	0.041
Dimers $_{C5}$	22.3	0.037

7.4 SYSTEM CALIBRATIONS

7.4.1 CALIBRATION OF THE GC/MS

The chromatographic area obtained for each species during experiment series was divided by the chromatographic area of 2M2B. In order to transform the areas in mass responses the following calculation procedure was applied, using the calibration curves shown above:

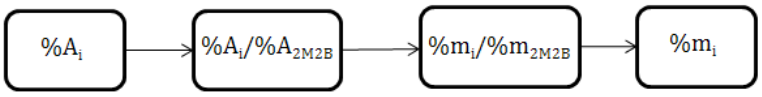

It is known that:

$$\sum_{j=1}^{S} \%M_j = 1 \qquad (7.4.1.1)$$

Since by means of the calibration curves obtained the terms $\%m_i/\%m_{2M2B}$ are known, the $\%m_{2M2B}$ can be obtained from:

$$\sum_{j=1}^{S} \frac{\%M_j}{\%M_{2M2B}} = \frac{1}{\%M_{2M2B}} \qquad (7.4.1.2)$$

Once $\%M_{2M2B}$ was obtained, the mass percentage of each species ($\%M_j$) was as follows:

$$\%M_j = \frac{\%M_j}{\%M_{2M2B}} \cdot \%M_{2M2B} \qquad (7.4.1.3)$$

The following calibration curves were obtained for the calibration of the GC/MS system used in the experiments carried out in the batch reactor. They were used to transform the responses ($\%A_j/\%A_{2M2B}$) into ($\%M_j/\%M_{2M2B}$).

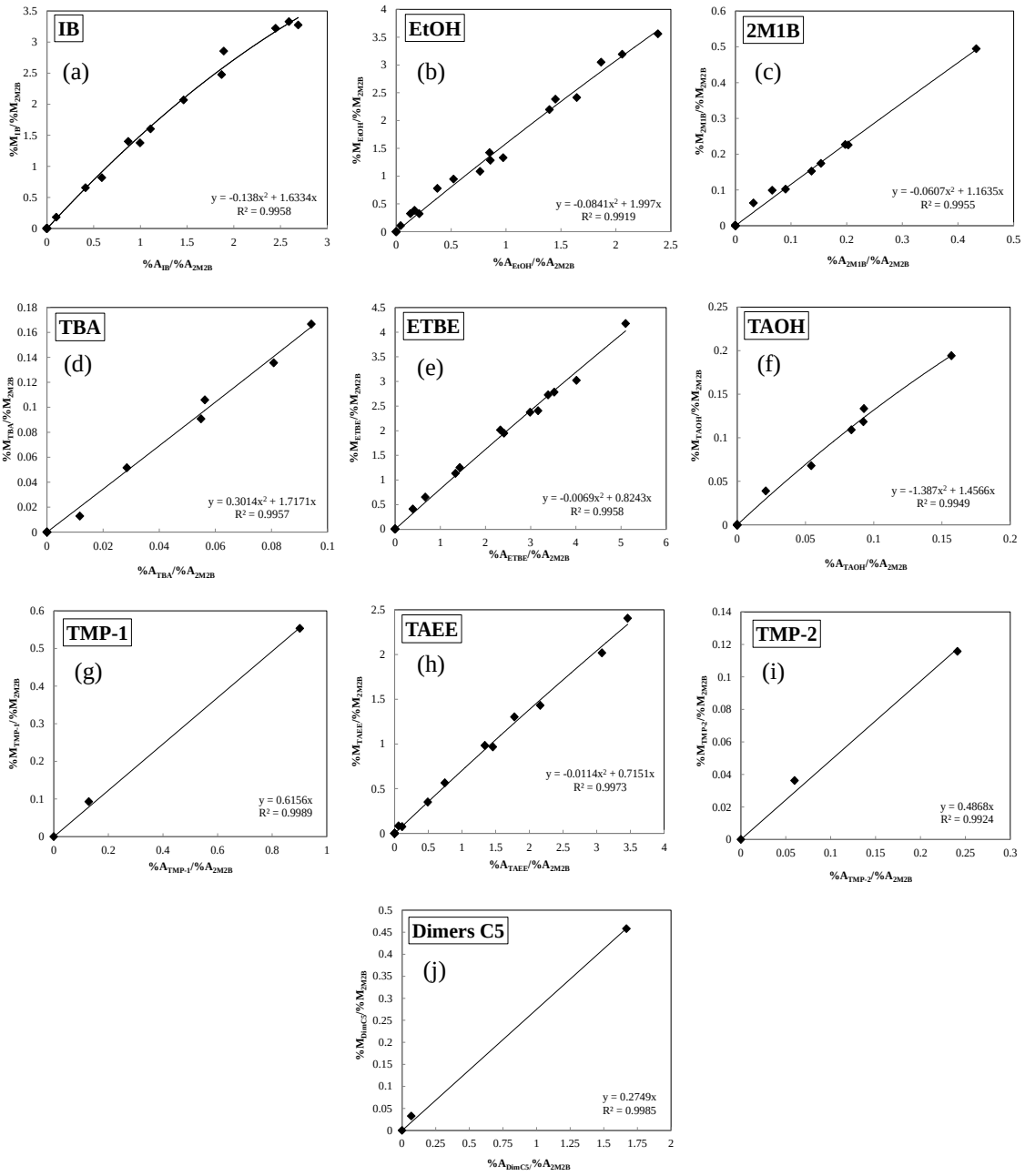

Figure 7.4.1. Calibration curves obtained for the GC/MS system described Figure 3.2.1. (a) isobutene, (b) ethanol, (c) 2-methyl-1-butene, (d) *tert*-butyl alcohol, (e) ethyl *tert*-butyl ether, (f) *tert*-amyl alcohol, (g) 2,4,4-trymethyl-1-pentene, (h) *tert*-amyl ethyl ether, (i) 2,4,4-trymethyl-2-pentene, and (j) Dimers C_5.

7.4.2 CALIBRATION OF THE GC CONNECTED TO THE FIXED BED REACTOR

The following calibration curves were obtained for the GC connected to the fixed bed catalytic reactor:

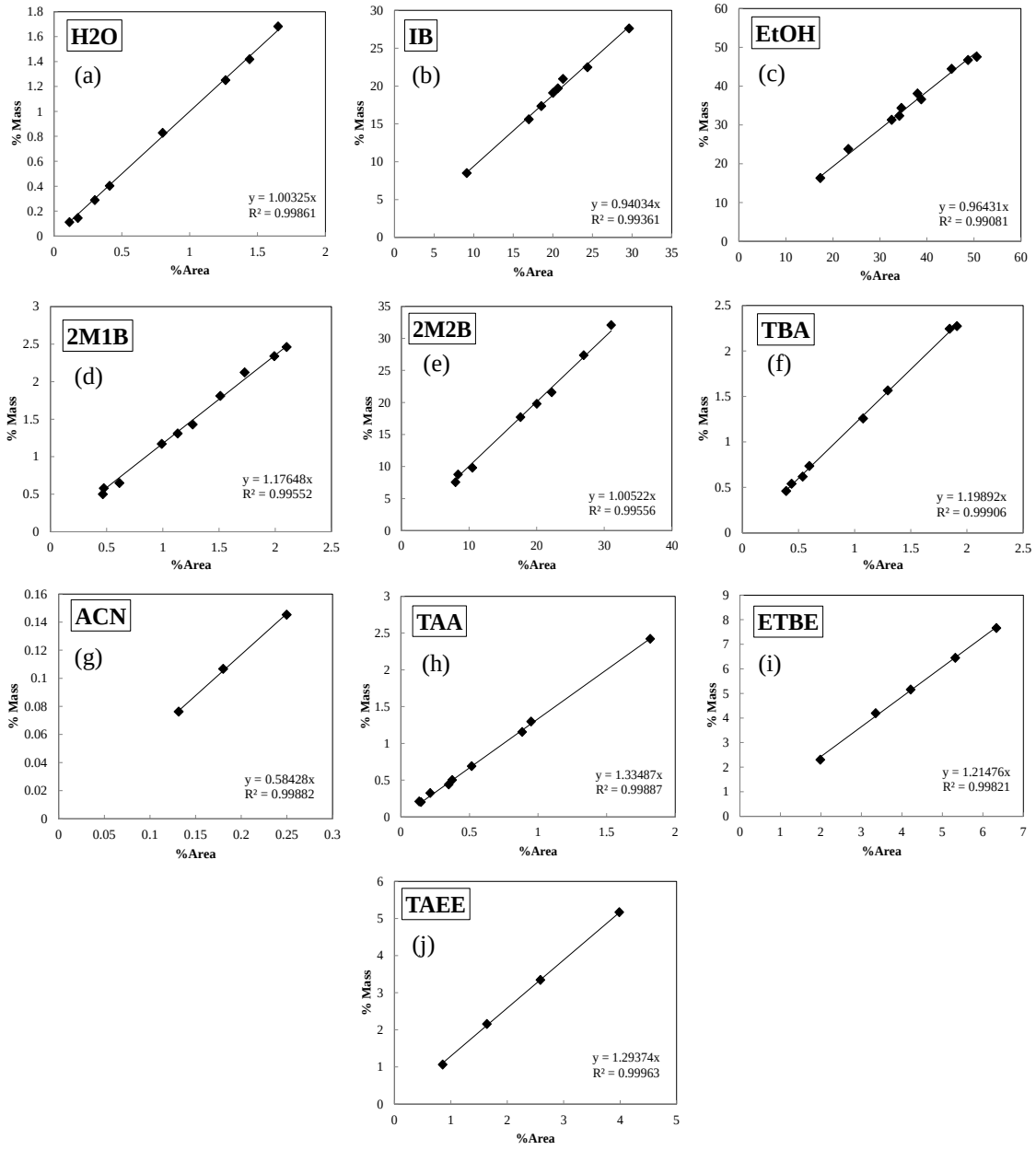

Figure 7.4.2. Calibration curves obtained for the GC system described Figure 3.2.2. (a) water, (b) isobutene, (c) ethanol, (d) 2-methyl-1-butene, (e) 2-methyl-2-butene, (f) *tert*-butyl alcohol, (g) acetonitrile, (h) *tert*-amyl alcohol, (i) ethtyl *tert*-butyl ether, and (j) *tert*-amyl ethyl ether.

7.4.3 CALIBRATION OF HPLC PUMPS

As for the calibration of the HPLC pumps used for feeding the fixed bed catalytic reactor, the following data was obtained:

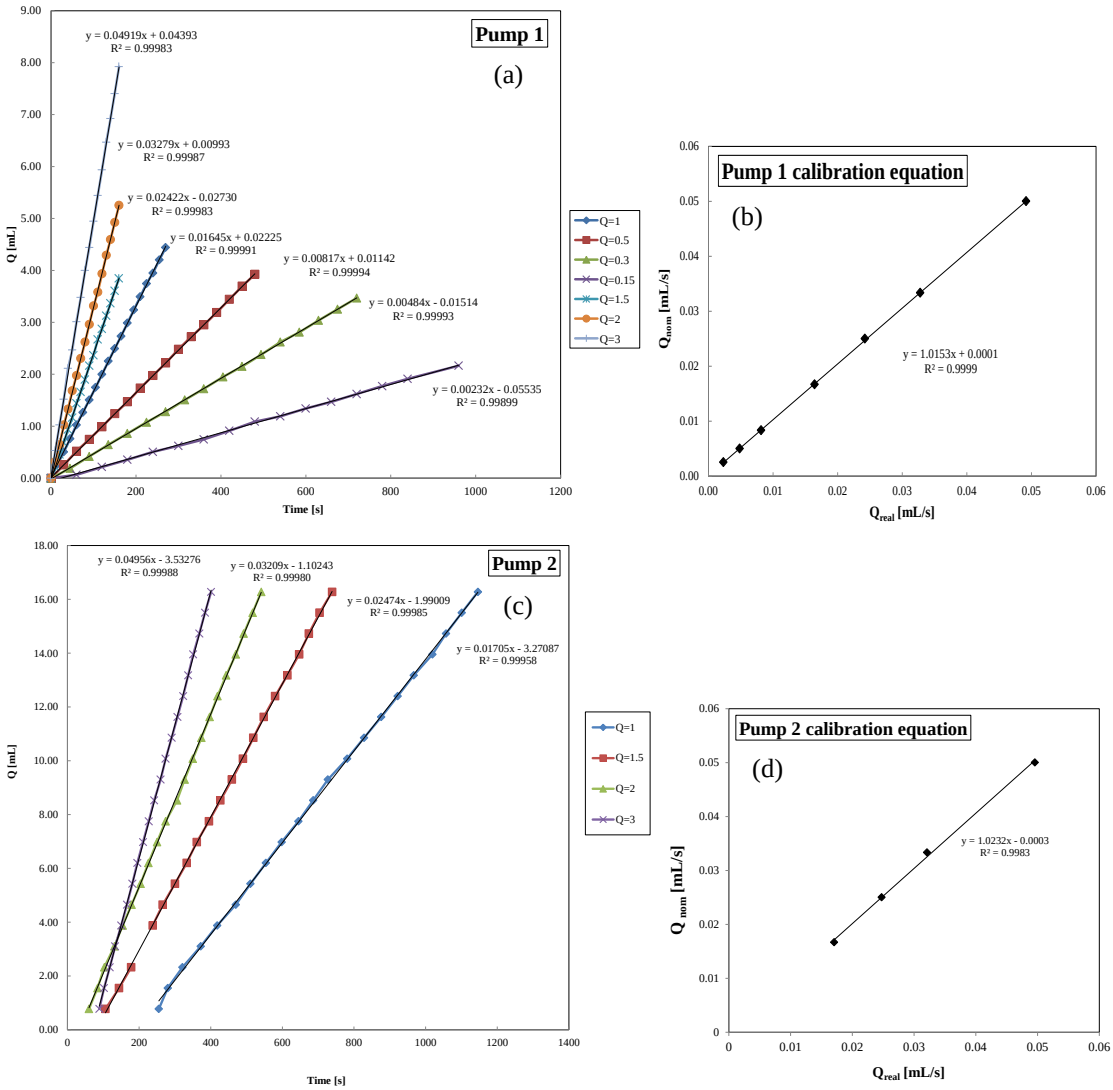

Figure 7.4.3. (a) Volume vs. time curve obtained for Pump 1 at different volumetric flows. (b) nominal vs. real volumetric flow curve for Pump 1. (c) Volume vs. time curve obtained for Pump 2 at different volumetric flows. (d) nominal vs. real volumetric flow curve for Pump 2.

7.4.4 CALIBRATION OF THE GC FOR LIQUID-PHASE ADSORPTION EXPERIMENTS

For the calibration of the GC response for each of the mixtures of *n*-heptane and tracers, several diluted mixtures with different known volumes of tracer (A) and *n*-heptane (B) were prepared and injected to the GC. The following calculation procedure was followed.

The molar fraction (x_A) of the component *A* in a binary mixture of *A* and *B* species can be defined as:

$$x_A = \frac{A_A \cdot \beta_A}{A_B \cdot \beta_B + A_A \cdot \beta_A} = \frac{\frac{A_A \cdot \beta_A}{A_B \cdot \beta_B}}{\frac{A_B \cdot \beta_B}{A_B \cdot \beta_B} + \frac{A_A \cdot \beta_A}{A_B \cdot \beta_B}} \qquad (7.4.4.1)$$

where A_i is the chromatographic area of component i and β_i is the individual system calibration factor for the component i.

The calibration factor of the component i (α_i) in the binary mixture can be defined as:

$$\alpha_A = \frac{\beta_A}{\beta_B} \qquad (7.4.4.2)$$

Therefore, Eq. 7.4.4.1 can be rewritten as a function of (α_i) as:

$$x_A = \frac{\frac{A_A}{A_B}\alpha_A}{1 + \frac{A_A}{A_B}\alpha_A} \qquad (7.4.4.3)$$

Finally, the calibration factor of the species A can be obtained as:

$$\alpha_A = \frac{x_A}{\frac{A_A}{A_B}(1 - x_A)} \qquad (7.4.4.4)$$

The relation between the ratio of molar fractions and volumetric fractions in the binary mixture of liquids can be expressed as:

$$\frac{x_A}{x_B} = \frac{y_A}{y_B}\frac{\frac{\rho_A}{MW_A}}{\frac{\rho_B}{MW_B}} \qquad (7.4.4.5)$$

Since $x_A + x_B = 1$, the molar fraction of B, can be expressed as:

$$\frac{1}{1 + \frac{x_A}{x_B}} = x_B \qquad (7.4.4.6)$$

Once x_B is known, x_A can be easily obtained ($x_A = 1 - x_B$). Then (α_i) can be computed from Eq. 7.4.4.4. Table 7.4.1 gathers the average of the calibration factors obtained for each pair of solvent and tracer.

Table 7.4.1. Calibration factors obtained for tracers evaluated in liquid-phase adsorption experiments.

Component	Calibration factor (α_i)
Methanol	9.68 ± 0.67
Ethanol	3.82 ± 0.1
Propanol	2.85 ± 0.04
Butanol	2.03 ± 0.05
2-methyl-2-butene	2.17 ± 0.11

7.5 CALCULATIONS FOR GREEN METRIC ANALYSIS

7.5.1 DATA USED FOR CALCULATIONS IN EACH PLAN ANALYZED

The input and output data used for the calculations in the Green Metric Analysis (*Section 4.2*) are gathered in Table 7.5.1. Such data is based on the results and information provided in the corresponding references.

Table 7.5.1. Data used for the calculation of main parameters in the Green Metric Analysis.

Case studied	Catalyst mass [g]	Component	Initial [g]	Final [g]
Françoisse and Thryrion [139]	10.0	IB	100.8	-
		EtOH	82.8	-
		ETBE	0	160.8
		Solvents	209.6	209.6
Vila et al. [160]	10.0	IB	114.2	-
		EtOH	92.8	-
		ETBE	0	187.31
Yang and Goto [161]	13.0	TBA	148	-
		EtOH	184	-
		ETBE	0	178.5
Yang et al. [162]	10.0	TBA	74	-
		EtOH	86	-
		ETBE	0	53.1
Umar et al. [163]	19.7	TBA	175.0	-
		EtOH	217.6	-
		ETBE	0	94.1
Rihko et al. [137]	1	IA	34.1	-
		EtOH	22.4	-
		TAEE	0	31.2
Boz and Doğu [164]	60	IA	776.7	-
		EtOH	4593.4	-
		TAEE	0	643.5
Boonthamtirawuti et al. [45]	2	TAA	52.8	-
		EtOH	27.6	-
		TAEE	0	21.7
Varisli and Doğu [165]	20	IA	456.4	-
		EtOH	4973.5	-
		TAEE	0	642.9
Aiouiache and Goto [166]	1	TAA	88	-
		EtOH	46	-
		TAEE	0	25.4

7.5.2 CHOOSING THE OPTIMUM COLUMN

Several simulations were preformed to select the column finally presented in *Section 4.2.4*. The parameters varied were the recycling flow, ethanol molar fraction in the product (ether) stream, molar fraction of ETBE in the recycling stream, recycling ratio, reboiler and condenser temperatures, and number of column trays (see Fig. 7.5.1).

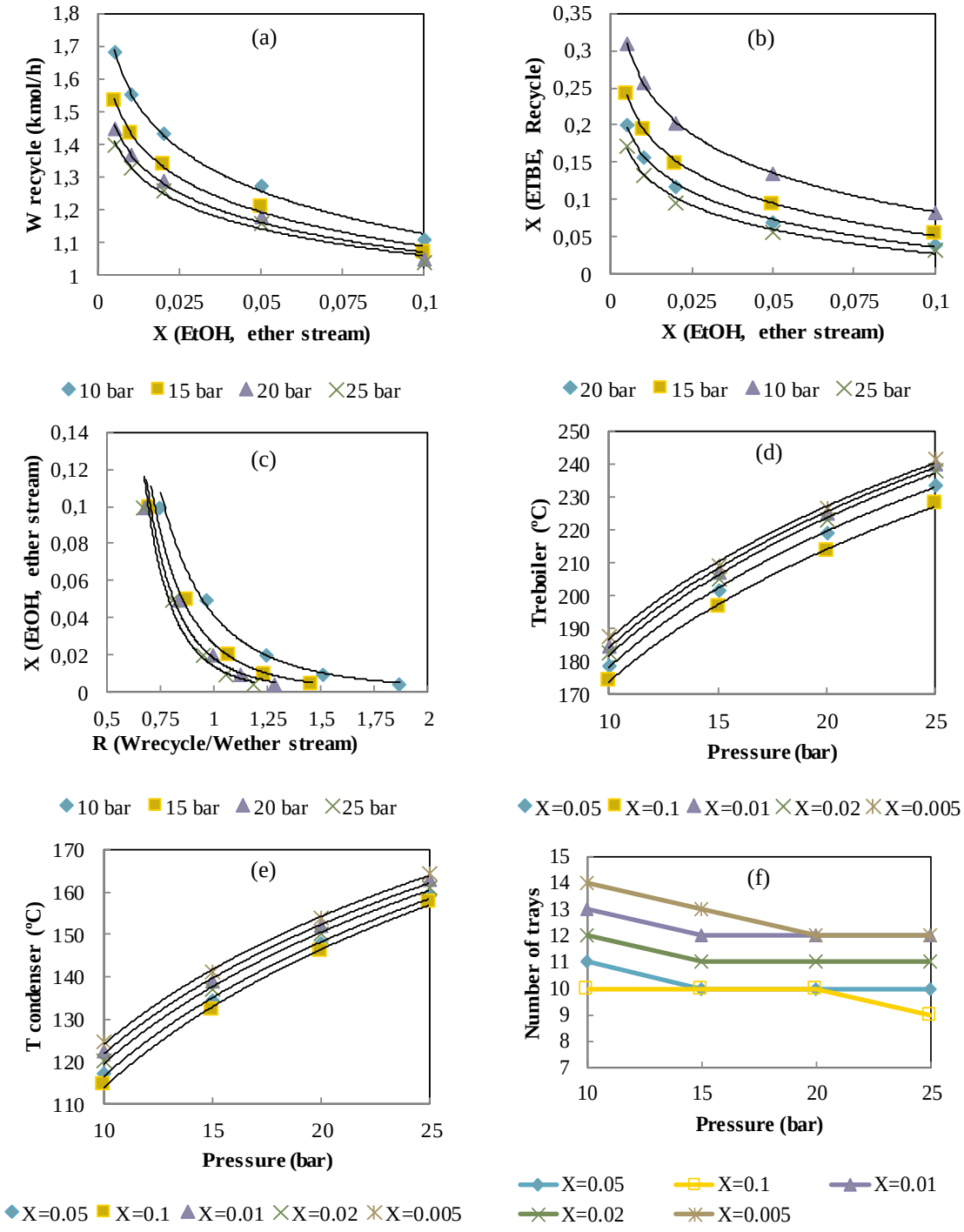

Figure 7.5.1. (a) Molar flow recycled vs. EtOH molar fraction in product stream. (b) ETBE molar fraction in recycled stream vs. ethanol molar fraction in product stream. (c) EtOH molar fraction in product stream vs. recycling ratio. (d) Reboiler temperature vs. column pressure. (e) Condenser temperature vs. column pressure. (f) Number of column trays vs. column pressure.

7.6 MODELING OF EXPERIMENTAL YIELD DATA OF *SECTION 4.3*

The data used for the modeling of experimental etherification yields in *Section 4.3* are included in Table 7.6.1.

Table 7.6.1. Experimental yield data empirically modeled. Errors refer to a 95% probability level for the replicated experiments.

$R_{C4/C5}$	$R_{A/O}$	T (K)	Y_{IA}^{TAEE}	Y_{IB}^{ETBE}	Y_{EtOH}^{TAEE}	Y_{EtOH}^{ETBE}
0.5	0.5	323	31.06	85.47	43.47	49.40
0.5	0.5	333	29.15	84.62	41.14	49.97
0.5	0.5	343	23.91	80.00	33.48	50.22
0.5	0.5	353	21.91	74.46	32.27	50.78
0.5	1	323	51.94	93.78	37.24	37.69
0.5	1	333	47.17	91.90	33.91	36.83
0.5	1	343	42.42	89.09	30.59	28.38
0.5	1	353	36.75	84.91	26.99	29.67
0.5	2	323	60.87	90.65	22.21	15.71
0.5	2	333	55.60	89.96	20.51	15.30
0.5	2	343	49.17	90.25	17.89	15.00
0.5	2	353	46.60	91.92	16.38	15.93
1	0.5	323	22.50	76.72	23.65	72.77
1	0.5	333	20.94	74.40	22.17	72.47
1	0.5	343	18.37	70.03	19.71	72.04
1	0.5	353	16.81	61.61	18.33	71.11
1	1	323	49.74±3.84	91.30±1.55	27.85±0.62	45.69±2.26
1	1	333	44.82±3.21	89.28±1.63	25.26±0.36	44.99±1.73
1	1	343	39.46±2.22	86.02±1.22	22.20±0.44	42.10±2.60
1	1	353	32.34±0.73	80.66±0.39	19.49±0.91	42.00±2.4
1	2	323	61.70	93.06	17.26	24.05
1	2	333	55.83	91.87	15.91	23.88
1	2	343	49.21	89.24	13.12	22.66
1	2	353	39.44	86.35	12.78	25.75
2	0.5	323	16.70	63.50	11.44	85.45
2	0.5	333	15.96	62.80	10.35	85.60
2	0.5	343	14.95	62.01	10.48	83.87
2	0.5	353	13.43	60.13	9.86	80.28
2	1	323	50.18	91.35	19.02	58.27
2	1	333	45.21	88.92	17.14	55.81
2	1	343	37.44	87.94	14.61	62.08
2	1	353	33.53	82.57	12.32	57.29
2	2	323	61.08	91.49	11.62	31.94
2	2	333	56.58	90.20	10.47	30.47
2	2	343	47.70	87.97	9.15	31.67
2	2	353	44.16	86.64	7.87	31.19

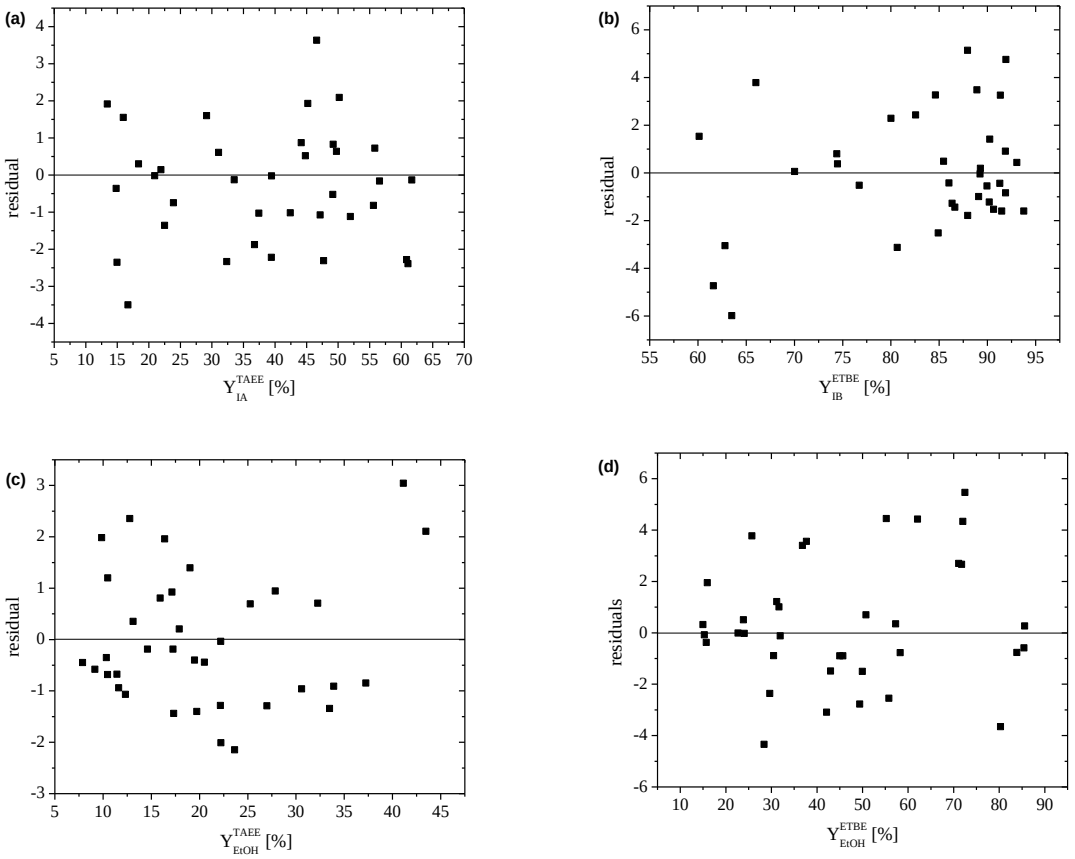

Figure 7.6.1. Residuals plots obtained for the modeled yield data in *Section 4.3* at all assayed temperature and initial composition.

7.7 UNIFAC-DORTMUND PREDICTIVE METHOD

In the modified UNIFAC (Dortmund) model, as in the original UNIFAC model, the activity coefficient is the sum of a combinatorial and a residual part:

$$\ln \gamma_i = \ln \gamma_i^C + \ln \gamma_i^R \qquad (7.7.1)$$

The combinatorial part was changed in an empirical way to make it possible to deal with compounds very different in size:

$$\ln \gamma_i^C = 1 - V_i' + \ln V_i' - 5q_i\left(1 - \frac{V_i}{F_i} + \ln\left(\frac{V_i}{F_i}\right)\right) \qquad (7.7.2)$$

The parameter V'_i can be calculated by using the relative van der Waals volumes R_k of the different groups.

$$V_i' = \frac{r_i^{3/4}}{\sum_j x_j r_j^{3/4}} \qquad (7.7.3)$$

All other parameters are calculated in the same way as for the original UNIFAC model; i.e.

$$V_i = \frac{r_i}{\sum_j x_j r_j} \qquad (7.7.4)$$

$$r_i = \sum \upsilon_k^{(i)} R_k \qquad (7.7.5)$$

$$F_i = \frac{q_i}{\sum_j x_j q_j} \tag{7.7.6}$$

$$q_i = \sum \upsilon_k^{(i)} Q_k \tag{7.7.8}$$

The residual part can be obtained by using the following relations:

$$\ln \gamma_i^R = \sum_k \upsilon_k^{(i)} \left(\ln \Gamma_k - \ln \Gamma_k^{(i)} \right) \tag{7.7.9}$$

$$\ln \Gamma_k = Q_k \left(1 - \ln \left(\sum_m \theta_m \Psi_{mk} \right) - \sum_m \frac{\theta_m \Psi_{km}}{\sum_n \theta_n \Psi_{nm}} \right) \tag{7.7.10}$$

whereby the group area fraction θ_m, and group mole fraction X_m, are given by the following equations:

$$\theta_m = \frac{Q_m X_m}{\sum_n Q_n X_n} \tag{7.7.11}$$

$$X_m = \frac{\sum_j \upsilon_m^{(j)} x_j}{\sum_j \sum_n \upsilon_n^{(j)} x_j} \tag{7.7.12}$$

In comparison to the original UNIFAC method, only the van der Waals properties were changed slightly, at the same time temperature-dependent parameters were introduced to permit a better description of the real behavior (activity coefficients) as a function of temperature.

$$\Psi_{nm} = \exp\left(-\frac{a_{nm} + b_{nm} T + c_{nm} T^2}{T} \right) \tag{7.7.13}$$

For the present system, the involved compounds comprised the subgroups gathered in Table X. For the case of C_4-C_5 codimers and C_5 dimers, 3-ethyl-3-heptene and 3-ethyl-3-octene were respectively chosen as representative molecules of all compounds detected.

Table 7.7.1. Subgroups used for involved molecules in UNIFAC-Dortmund predictive method.

Compound	Subgroup[a]							
	1	2	4	7	8	14	25	82
Isobutene	2	0	0	1	0	0	0	0
EtOH	1	1	0	0	0	1	0	0
2M1B	2	1	0	1	0	0	0	0
TBA	3	0	1	0	0	0	0	1
2M2B	3	0	0	0	1	0	0	0
ETBE	4	0	1	0	0	0	1	0
TAA	3	1	1	0	0	0	0	2
TMP-1	4	1	1	1	0	0	0	0
TAEE	4	1	1	0	0	0	1	0
TMP-2	5	0	1	0	1	0	0	0
3-ethyl-3-heptene	3	1	0	0	1	0	0	0
3-ethyl-3-octene	3	5	0	0	1	0	0	0

[a]Subgroup code. 1:CH3, 2: −CH2−, 4:>C<, 7:CH2=C, 8:CH=C, 14:OH(*p*), 25:O−CH2, 82:OH(*t*).

7.8 THERMODYNAMIC DATA OBTAINED

7.8.1 EXPERIMENTAL REACTION EQUILIBRIUM CONSTANTS

Table 7.8.1. Experimental equilibrium constants K_{xi}, $K_{\gamma i}$ and K_i at different temperatures and initial molar ratios. Standard errors at $R_{A/O}$=1 and $R_{C4/C5}$=1 were obtained from replicated experiments.

T [K] (catalyst)	$R_{A/O}$	$R_{C4/C5}$	K_{x1}	K_{x2}	K_{x3}	K_{x4}	$K_{\gamma 1}$	$K_{\gamma 2}$	$K_{\gamma 3}$	$K_{\gamma 4}$	K_1	K_2	K_3	K_4
323 (A-35)	0.5	0.5	236.0	183.3	14.6	12.5	0.183	0.176	0.174	1.013	43.2	32.2	2.5	12.7
	0.5	1	208.5	170.2	14.7	11.6	0.181	0.174	0.171	1.014	37.7	29.5	2.5	11.8
	0.5	2	194.6	183.1	15.1	12.1	0.178	0.170	0.168	1.014	34.6	31.2	2.5	12.3
	1	0.5	132.6	79.5	6.6	12.1	0.344	0.330	0.325	1.015	45.6	26.2	2.2	12.2
	1	1	120.0	77.6	5.7	13.7	0.373	0.357	0.352	1.015	44.8±4.1	27.8±2.1	2.0±0.1	13.9±0.3
	1	2	106.5	89.5	6.2	14.4	0.368	0.353	0.347	1.017	39.2	31.6	2.2	14.6
	2	0.5	70.8	45.5	3.5	13.0	0.620	0.596	0.593	1.006	43.9	27.1	2.1	13.0
	2	1	82.4	50.4	3.6	14.0	0.616	0.592	0.588	1.007	50.8	29.9	2.1	14.1
	2	2	60.5	47.9	3.7	12.9	0.621	0.597	0.592	1.007	37.6	28.6	2.2	13.0
333 (A-35)	0.5	0.5	173.5	127.4	11.0	11.6	0.199	0.191	0.188	1.013	34.5	24.3	2.1	11.8
	0.5	1	118.8	100.5	9.5	10.5	0.196	0.188	0.185	1.014	23.3	18.9	1.8	10.7
	0.5	2	123.5	114.0	10.2	11.2	0.189	0.182	0.179	1.015	23.4	20.7	1.8	11.3
	1	0.5	85.0	54.0	4.9	11.1	0.366	0.351	0.346	1.015	31.1	19.0	1.7	11.2
	1	1	72.5	50.7	4.2	12.1	0.391	0.375	0.369	1.015	28.3±1.6	19.0±0.9	1.6±0.1	12.2±0.2
	1	2	63.6	55.5	4.5	12.4	0.395	0.379	0.373	1.017	25.1	21.0	1.7	12.6
	2	0.5	49.1	32.4	2.8	11.6	0.626	0.602	0.599	1.005	30.7	19.5	1.7	11.7
	2	1	54.7	34.7	2.8	12.3	0.618	0.594	0.590	1.007	33.8	20.6	1.7	12.3
	2	2	40.4	35.2	2.9	12.0	0.630	0.606	0.602	1.007	25.5	21.3	1.8	12.0
343 (A-35)	0.5	0.5	109.2	80.2	7.1	11.3	0.218	0.209	0.206	1.014	23.8	16.8	1.5	11.4
	0.5	1	80.4	68.5	6.7	10.3	0.215	0.206	0.203	1.015	17.3	14.1	1.4	10.4
	0.5	2	90.9	84.4	7.7	10.9	0.221	0.212	0.209	1.017	20.0	17.2	1.6	10.9
	1	0.5	54.4	31.5	3.1	10.3	0.432	0.415	0.409	1.013	23.5	13.1	1.3	10.4
	1	1	42.3	31.1	3.0	10.3	0.422	0.405	0.399	1.015	17.9±0.6	12.6±0.5	1.2±0.1	10.5±0.2
	1	2	44.0	40.5	3.8	10.7	0.354	0.340	0.334	1.019	15.6	13.8	1.3	10.9
	2	0.5	37.8	21.4	2.1	10.4	0.630	0.606	0.604	1.004	23.8	13.0	1.3	10.4
	2	1	35.0	23.5	2.1	11.3	0.636	0.611	0.608	1.005	22.2	14.4	1.3	11.4
	2	2	28.7	24.6	2.1	11.8	0.624	0.600	0.596	1.007	17.9	14.7	1.2	11.9
353 (A-35)	0.5	0.5	55.2	41.1	4.6	9.0	0.247	0.237	0.234	1.014	13.6	9.8	1.1	9.1
	0.5	1	49.5	39.9	4.8	8.3	0.225	0.216	0.213	1.015	11.2	8.6	1.0	8.4
	0.5	2	51.1	45.4	4.7	9.7	0.238	0.229	0.225	1.016	12.2	10.4	1.1	9.8
	1	0.5	32.7	21.3	2.4	9.0	0.438	0.421	0.416	1.013	14.3	9.0	1.0	9.1
	1	1	26.4	20.7	2.3	9.1	0.419	0.403	0.397	1.015	11.1±0.1	8.3±0.1	0.9±0.01	9.3±0.2
	1	2	32.0	27.8	2.7	10.5	0.418	0.402	0.395	1.019	13.4	11.2	1.1	10.7
	2	0.5	25.6	17.4	1.8	9.9	0.630	0.606	0.604	1.004	16.1	10.6	1.1	10.0
	2	1	20.4	14.4	1.6	9.4	0.600	0.577	0.573	1.007	12.2	8.3	0.9	9.4
	2	2	21.8	17.2	1.7	9.9	0.628	0.604	0.600	1.007	13.2	10.4	1.0	9.9
353 (CT-275)	0.5	1	55.2	46.1	5.2	8.8	0.235	0.225	0.222	1.015	13.0	10.4	1.2	8.9
353 (A-15)	0.5	1	58.8	50.0	5.6	8.9	0.234	0.224	0.221	1.016	13.7	11.1	1.2	9.0

7.8.2 POYNTING CORRECTION FACTORS FOR PRESSURE

Values of Poynting correction factors estimated at each temperature for evaluating the effect of pressure on reaction equilibrium constants experimentally determined are shown in Table 7.8.2.

Table 7.8.2. Estimated values of Poynting correction factors for reactions R1-R4 in the range of temperature explored.

T [K]	$K_{\Gamma i}$			
	R1	R2	R3	R4
323.15	0.999896	0.999882	0.999897	0.999985
333.15	0.999889	0.999878	0.999893	0.999985
343.15	0.999881	0.999874	0.999890	0.999985
353.15	0.999872	0.999870	0.999885	0.999984

7.9 ESTIMATION OF MOLECULAR LENGTHS USING CHEMBIOOFFICE 2014

The molecular lengths of involved molecules were measured by trigonometric relations in the conformation of minimum energy. The longest of the dimensions, high, width or depth was chosen as the length for subsequent calculations concerning accessibility. The data used are presented below and a summary of the calculated dimensions can be found in Table 7.9.10.

Table 7.9.1. Angles and distance for isobutene molecule.

Distances	Å	Angles	[°/Å]	Angles	[°/Å]
C(1)-H(6)	1.1	H(12)-C(4)-H(11)	108.812	H(7)-C(3)-C(2)	110
C(1)-H(1)	1.1	H(12)-C(4)-H(10)	109	H(6)-C(1)-H(1)	119.749
C(2)-C(1)	1.337	H(12)-C(4)-C(2)	110	H(6)-C(1)-C(2)	119.749
C(3)-H(9)	1.113	H(11)-C(4)-H(10)	109	H(1)-C(1)-C(2)	120.5
C(3)-H(8)	1.113	H(11)-C(4)-C(2)	110	C(4)-C(2)-C(3)	115.983
C(3)-H(7)	1.113	H(10)-C(4)-C(2)	110	C(4)-C(2)-C(1)	122.007
C(4)-H(12)	1.113	H(9)-C(3)-H(8)	108.812	C(3)-C(2)-C(1)	122.008
C(4)-H(11)	1.113	H(9)-C(3)-H(7)	109		
C(4)-C(2)	1.497	H(9)-C(3)-C(2)	110		
C(2)-C(3)	1.497	H(8)-C(3)-H(7)	109		
C(4)-H(10)	1.113	H(8)-C(3)-C(2)	110		

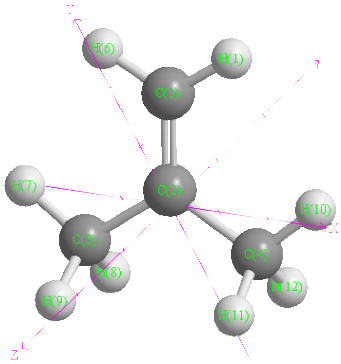

Table 7.9.2. Angles and distance for 2-methyl-2-butene molecule.

Distances	Å	Angles	[°/Å]	Angles	[°/Å]
C(5)-H(15)	1.113	H(15)-C(5)-H(14)	109.359	C(4)-C(3)-C(2)	125.934
C(5)-H(14)	1.113	H(15)-C(5)-H(13)	107.188	C(5)-C(2)-C(3)	122.75
C(5)-H(13)	1.113	H(15)-C(5)-C(2)	110.644	C(5)-C(2)-C(1)	115.792
C(4)-H(12)	1.114	H(14)-C(5)-H(13)	107.19	C(3)-C(2)-C(1)	121.458
C(4)-H(11)	1.114	H(14)-C(5)-C(2)	110.642	H(8)-C(1)-H(7)	108.609
C(4)-H(10)	1.111	H(13)-C(5)-C(2)	111.685	H(8)-C(1)-H(6)	107.524
C(3)-H(9)	1.104	H(12)-C(4)-H(11)	108.248	H(8)-C(1)-C(2)	110.074
C(1)-H(8)	1.114	H(12)-C(4)-H(10)	107.542	H(7)-C(1)-H(6)	107.524
C(1)-H(7)	1.114	H(12)-C(4)-C(3)	109.851	H(7)-C(1)-C(2)	110.073
C(1)-H(6)	1.113	H(11)-C(4)-H(10)	107.541	H(6)-C(1)-C(2)	112.9
C(2)-C(5)	1.509	H(11)-C(4)-C(3)	109.85		
C(3)-C(4)	1.506	H(10)-C(4)-C(3)	113.639		
C(2)-C(3)	1.345	H(9)-C(3)-C(4)	115.337		
C(1)-C(2)	1.51	H(9)-C(3)-C(2)	118.728		

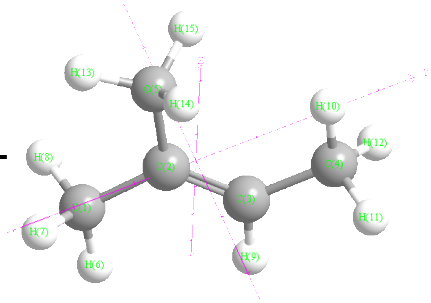

Table 7.9.3. Angles and distance for 2-methyl-1-butene molecule.

Distances	Å	Angles	[°/Å]	Angles	[°/Å]
C(5)-H(15)	1.113	H(15)-C(5)-H(14)	108.449	H(9)-C(3)-C(2)	107.786
C(5)-H(14)	1.113	H(15)-C(5)-H(13)	107.509	H(8)-C(3)-C(4)	108.465
C(5)-H(13)	1.113	H(15)-C(5)-C(2)	110.222	H(8)-C(3)-C(2)	107.786
C(4)-H(12)	1.114	H(14)-C(5)-H(13)	107.509	C(4)-C(3)-C(2)	116.628
C(4)-H(11)	1.114	H(14)-C(5)-C(2)	110.222	C(5)-C(2)-C(3)	114.964
C(4)-H(10)	1.115	H(13)-C(5)-C(2)	112.781	C(5)-C(2)-C(1)	120.95
C(3)-H(9)	1.116	H(12)-C(4)-H(11)	108.817	C(3)-C(2)-C(1)	124.086
C(3)-H(8)	1.116	H(12)-C(4)-H(10)	106.997	H(7)-C(1)-H(6)	116.225
C(1)-H(7)	1.098	H(12)-C(4)-C(3)	111.577	H(7)-C(1)-C(2)	122.713
C(1)-H(6)	1.1	H(11)-C(4)-H(10)	106.997	H(6)-C(1)-C(2)	121.062
C(2)-C(5)	1.511	H(11)-C(4)-C(3)	111.576		
C(3)-C(4)	1.534	H(10)-C(4)-C(3)	110.662		
C(2)-C(3)	1.514	H(9)-C(3)-H(8)	107.359		
C(1)-C(2)	1.343	H(9)-C(3)-C(4)	108.464		

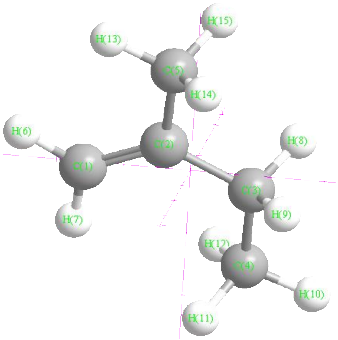

Table 7.9.4. Angles and distance for *tert*-butyl alcohol molecule.

Distances	Å	Angles	[°/Å]	Angles	[°/Å]
O(5)-Lp(17)	0.601	Lp(17)-O(5)-Lp(16)	112.719	H(10)-C(3)-C(1)	111.294
O(5)-Lp(16)	0.601	Lp(17)-O(5)-H(15)	103.921	H(9)-C(3)-C(1)	111.204
O(5)-H(15)	0.96	Lp(17)-O(5)-C(1)	113.024	H(8)-C(2)-H(7)	107.75
C(4)-H(14)	1.114	Lp(16)-O(5)-H(15)	103.931	H(8)-C(2)-H(6)	107.745
C(4)-H(13)	1.114	Lp(16)-O(5)-C(1)	113.032	H(8)-C(2)-C(1)	111.109
C(4)-H(12)	1.114	H(15)-O(5)-C(1)	109.33	H(7)-C(2)-H(6)	107.537
C(3)-H(11)	1.114	H(14)-C(4)-H(13)	107.75	H(7)-C(2)-C(1)	111.263
C(3)-H(10)	1.114	H(14)-C(4)-H(12)	107.769	H(6)-C(2)-C(1)	111.26
C(3)-H(9)	1.114	H(14)-C(4)-C(1)	111.121	O(5)-C(1)-C(4)	108.048
C(2)-H(8)	1.114	H(13)-C(4)-H(12)	107.527	O(5)-C(1)-C(3)	108.051
C(2)-H(7)	1.114	H(13)-C(4)-C(1)	111.295	O(5)-C(1)-C(2)	108.13
C(2)-H(6)	1.114	H(12)-C(4)-C(1)	111.203	C(4)-C(1)-C(3)	110.916
C(1)-O(5)	1.404	H(11)-C(3)-H(10)	107.745	C(4)-C(1)-C(2)	110.785
C(1)-C(3)	1.529	H(11)-C(3)-H(9)	107.773	C(3)-C(1)-C(2)	110.787
C(1)-C(4)	1.529	H(11)-C(3)-C(1)	111.117		
C(1)-C(2)	1.529	H(10)-C(3)-H(9)	107.532		

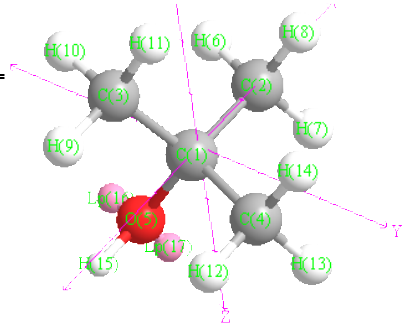

Table 7.9.5. Angles and distance for *tert*-amyl alcohol molecule.

Distances	Å	Angles	[º/Å]	Angles	[º/Å]
O(6)-Lp(20)	0.601	Lp(20)-O(6)-Lp(19)	112.684	H(11)-C(3)-H(9)	106.958
O(6)-Lp(19)	0.601	Lp(20)-O(6)-H(18)	103.856	H(11)-C(3)-C(2)	111.867
O(6)-H(18)	0.96	Lp(20)-O(6)-C(1)	113.075	H(10)-C(3)-H(9)	106.982
C(5)-H(17)	1.113	Lp(19)-O(6)-H(18)	103.849	H(10)-C(3)-C(2)	111.878
C(5)-H(16)	1.114	Lp(19)-O(6)-C(1)	113.07	H(9)-C(3)-C(2)	110.629
C(5)-H(15)	1.114	H(18)-O(6)-C(1)	109.407	H(8)-C(2)-H(7)	106.379
C(4)-H(14)	1.113	H(17)-C(5)-H(16)	107.955	H(8)-C(2)-C(3)	108.416
C(4)-H(13)	1.114	H(17)-C(5)-H(15)	107.027	H(8)-C(2)-C(1)	108.874
C(4)-H(12)	1.114	H(17)-C(5)-C(1)	111.78	H(7)-C(2)-C(3)	108.361
C(3)-H(11)	1.113	H(16)-C(5)-H(15)	107.486	H(7)-C(2)-C(1)	108.885
C(3)-H(10)	1.113	H(16)-C(5)-C(1)	111.325	C(3)-C(2)-C(1)	115.545
C(3)-H(9)	1.115	H(15)-C(5)-C(1)	111.052	O(6)-C(1)-C(5)	107.148
C(2)-H(8)	1.117	H(14)-C(4)-H(13)	107.942	O(6)-C(1)-C(4)	107.145
C(2)-H(7)	1.117	H(14)-C(4)-H(12)	107.034	O(6)-C(1)-C(2)	107.154
C(1)-O(6)	1.406	H(14)-C(4)-C(1)	111.786	C(5)-C(1)-C(4)	110.545
C(1)-C(4)	1.53	H(13)-C(4)-H(12)	107.476	C(5)-C(1)-C(2)	112.275
C(1)-C(5)	1.53	H(13)-C(4)-C(1)	111.332	C(4)-C(1)-C(2)	112.246
C(2)-C(3)	1.535	H(12)-C(4)-C(1)	111.053		
C(1)-C(2)	1.536	H(11)-C(3)-H(10)	108.278		

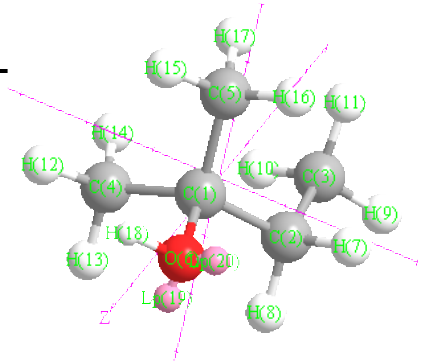

Table 7.9.6. Angles and distance for ethanol molecule.

Distances	Å	Angles	[º/Å]	Angles	[º/Å]
O(3)-Lp(2)	0.601	Lp(2)-O(3)-Lp(1)	112.699	H(6)-C(2)-H(8)	107.841
O(3)-Lp(1)	0.601	Lp(2)-O(3)-C(1)	113.057	H(7)-C(2)-H(8)	108.007
C(1)-C(2)	1.523	Lp(2)-O(3)-H(9)	103.936	C(2)-C(1)-O(3)	109.520
C(1)-O(3)	1.413	Lp(1)-O(3)-C(1)	113.053	C(2)-C(1)-H(4)	111.441
C(1)-H(4)	1.113	Lp(1)-O(3)-H(9)	103.925	C(2)-C(1)-H(5)	111.446
C(1)-H(5)	1.113	C(1)-O(3)-H(9)	109.280	O(3)-C(1)-H(4)	107.576
C(2)-H(6)	1.114	C(1)-C(2)-H(6)	110.848	O(3)-C(1)-H(5)	107.579
C(2)-H(7)	1.114	C(1)-C(2)-H(7)	111.081	H(4)-C(1)-H(5)	109.127
C(2)-H(8)	1.114	C(1)-C(2)-H(8)	111.078		
O(3)-H(9)	0.960	H(6)-C(2)-H(7)	107.844		

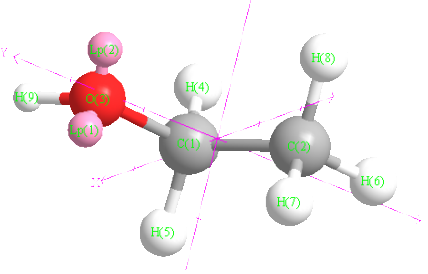

Table 7.9.7. Angles and distance for ethyl *tert*-butyl ether molecule.

Distances	Å	Angles	[°/Å]	Angles	[°/Å]
O(1)-Lp(23)	0.601	H(21)-C(7)-H(20)	107.909	H(12)-C(4)-C(2)	111.407
O(1)-Lp(22)	0.601	H(21)-C(7)-H(19)	107.725	H(11)-C(4)-C(2)	110.892
C(7)-H(21)	1.114	H(21)-C(7)-C(6)	111.11	H(10)-C(3)-H(9)	107.387
C(7)-H(20)	1.114	H(20)-C(7)-H(19)	107.745	H(10)-C(3)-H(8)	107.427
C(7)-H(19)	1.114	H(20)-C(7)-C(6)	111.147	H(10)-C(3)-C(2)	111.255
C(6)-H(18)	1.113	H(19)-C(7)-C(6)	111.048	H(9)-C(3)-H(8)	107.422
C(6)-H(17)	1.112	H(18)-C(6)-H(17)	110.019	H(9)-C(3)-C(2)	111.843
C(5)-H(16)	1.114	H(18)-C(6)-C(7)	108.745	H(8)-C(3)-C(2)	111.28
C(5)-H(15)	1.114	H(18)-C(6)-O(1)	110.205	C(5)-C(2)-C(4)	110.867
C(5)-H(14)	1.112	H(17)-C(6)-C(7)	108.933	C(5)-C(2)-C(3)	108.411
C(4)-H(13)	1.112	H(17)-C(6)-O(1)	110.543	C(5)-C(2)-O(1)	112.076
C(4)-H(12)	1.114	C(7)-C(6)-O(1)	108.347	C(4)-C(2)-C(3)	108.269
C(4)-H(11)	1.114	H(16)-C(5)-H(15)	107.476	C(4)-C(2)-O(1)	111.564
C(3)-H(10)	1.114	H(16)-C(5)-H(14)	108.289	C(3)-C(2)-O(1)	105.388
C(3)-H(9)	1.113	H(16)-C(5)-C(2)	111.435	Lp(23)-O(1)-Lp(22)	126.339
C(3)-H(8)	1.114	H(15)-C(5)-H(14)	105.97	Lp(23)-O(1)-C(6)	103.71
O(1)-C(6)	1.406	H(15)-C(5)-C(2)	110.865	Lp(23)-O(1)-C(2)	103.718
C(6)-C(7)	1.527	H(14)-C(5)-C(2)	112.525	Lp(22)-O(1)-C(6)	103.766
O(1)-C(2)	1.401	H(13)-C(4)-H(12)	108.089	Lp(22)-O(1)-C(2)	103.702
C(2)-C(4)	1.534	H(13)-C(4)-H(11)	105.956	C(6)-O(1)-C(2)	116.578
C(2)-C(5)	1.534	H(13)-C(4)-C(2)	112.698		
C(2)-C(3)	1.539	H(12)-C(4)-H(11)	107.511		

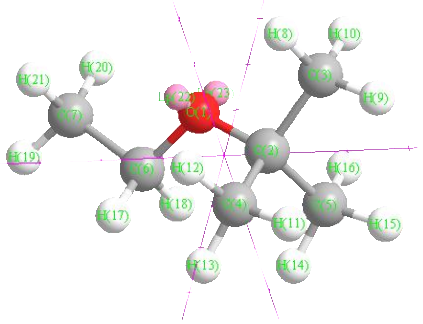

Table 7.9.8. Angles and distance for water molecule.

Distances	Å	Angles	[°/Å]
O(2)-Lp(5)	0.6	Lp(5)-O(2)-Lp(4)	110.558
O(2)-Lp(4)	0.6	Lp(5)-O(2)-H(3)	110.489
O(2)-H(3)	0.942	Lp(5)-O(2)-H(1)	110.489
H(1)-O(2)	0.942	Lp(4)-O(2)-H(3)	110.49
		Lp(4)-O(2)-H(1)	110.49
		H(3)-O(2)-H(1)	104.161

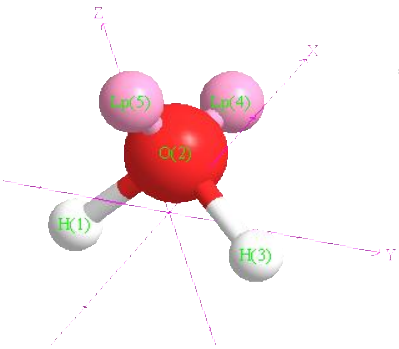

Table 7.9.9. Angles and distance for *tert*-amyl ethyl ether molecule.

Distances	Å	Angles	[°/Å]	Angles	[°/Å]
O(1)-Lp(26)	0.601	H(24)-C(8)-H(23)	107.503	O(1)-C(4)-C(8)	111.544
O(1)-Lp(25)	0.601	H(24)-C(8)-H(22)	108.007	O(1)-C(4)-C(5)	105.903
C(8)-H(24)	1.114	H(24)-C(8)-C(4)	111.53	C(7)-C(4)-C(8)	109.977
C(8)-H(23)	1.114	H(23)-C(8)-H(22)	105.783	C(7)-C(4)-C(5)	109.889
C(8)-H(22)	1.112	H(23)-C(8)-C(4)	110.961	C(8)-C(4)-C(5)	107.805
C(7)-H(21)	1.112	H(22)-C(8)-C(4)	112.748	H(13)-C(3)-H(12)	107.898
C(7)-H(20)	1.113	H(21)-C(7)-H(20)	107.368	H(13)-C(3)-H(11)	107.742
C(7)-H(19)	1.113	H(21)-C(7)-H(19)	105.982	H(13)-C(3)-C(2)	111.107
C(6)-H(18)	1.113	H(21)-C(7)-C(4)	112.46	H(12)-C(3)-H(11)	107.755
C(6)-H(17)	1.113	H(20)-C(7)-H(19)	107.774	H(12)-C(3)-C(2)	111.132
C(6)-H(16)	1.115	H(20)-C(7)-C(4)	112.007	H(11)-C(3)-C(2)	111.05
C(5)-H(15)	1.117	H(19)-C(7)-C(4)	110.934	H(10)-C(2)-H(9)	110.056
C(5)-H(14)	1.116	H(18)-C(6)-H(17)	108.159	H(10)-C(2)-O(1)	110.276
C(3)-H(13)	1.114	H(18)-C(6)-H(16)	106.886	H(10)-C(2)-C(3)	108.746
C(3)-H(12)	1.114	H(18)-C(6)-C(5)	111.883	H(9)-C(2)-O(1)	110.524
C(3)-H(11)	1.114	H(17)-C(6)-H(16)	107.187	H(9)-C(2)-C(3)	108.905
C(2)-H(10)	1.113	H(17)-C(6)-C(5)	111.8	O(1)-C(2)-C(3)	108.282
C(2)-H(9)	1.112	H(16)-C(6)-C(5)	110.682	Lp(26)-O(1)-Lp(25)	126.402
O(1)-C(4)	1.401	H(15)-C(5)-H(14)	106.391	Lp(26)-O(1)-C(4)	103.619
C(4)-C(7)	1.535	H(15)-C(5)-C(6)	108.029	Lp(26)-O(1)-C(2)	103.496
C(4)-C(8)	1.537	H(15)-C(5)-C(4)	108.851	Lp(25)-O(1)-C(4)	103.77
C(5)-C(6)	1.536	H(14)-C(5)-C(6)	108.33	Lp(25)-O(1)-C(2)	103.82
C(4)-C(5)	1.545	H(14)-C(5)-C(4)	109.753	C(4)-O(1)-C(2)	116.742
O(1)-C(2)	1.406	C(6)-C(5)-C(4)	115.125		
C(2)-C(3)	1.527	O(1)-C(4)-C(7)	111.572		

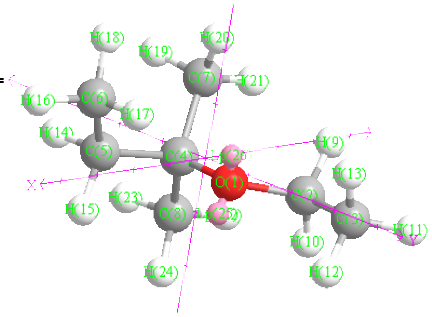

Table 7.9.10. Summary of the estimated dimensions of involved molecules.

Compound	Width (Å)	High (Å)	Depth (Å)
Water	1.486	0.921	0.986
IB	4.222	3.337	1.810
EtOH	3.945	2.239	1.814
2M1B	5.603	3.392	1.812
2M2B	5.073	3.697	1.816
TBA	4.214	3.718	4.211
TAA	5.388	3.073	4.210
ETBE	6.769	3.090	4.222
TAEE	6.757	4.255	4.412

7.10 METHODS USED FOR PROPERTIES ESTIMATION

7.10.1 HILDEBRAND SOLUBILITY PARAMETER AND MOLAR VOLUME OF A LIQUID MIXTURE

For a multicomponent system, the Hildebrand solubility parameter of the mixture can be estimated by means of:

$$\delta_m = \sum_i \Phi_i \cdot \delta_i \qquad (7.10.1.1)$$

where Φi is the volumetric fraction of compound *i* in the mixture, and considering that volumes are additive, it can be calculated by means of the following expression:

$$\Phi_i = \frac{x_i \cdot \frac{M_i}{\rho_i}}{\sum_j x_j \cdot \frac{M_j}{\rho_j}} \qquad (7.10.1.2)$$

where M_i and ρ_i are the molecular weight and the density at the corresponding temperature of compound *i*, respectively.

For the calculation of the individual solubility parameter (δ_i) the following expression is suggested [215]:

$$\delta_i = \sqrt{\frac{\Delta H_{v,i} - RT}{\overline{V}_i}} \qquad (7.10.1.3)$$

where $\overline{V}_i$ is the molar volume of compound *i* [m^3 Kg^{-1}] and $\Delta H_{v,i}$ is the enthalpy of vaporization of pure compound *i* [kJ mol^{-1}].

To calculate the liquid molar volume at the explored temperatures, the extension of the Hankinson-Brohst-Thomson (HBT) method was used [33]. The following expressions were used for the calculation of the saturated densities or molar volumes of liquids:

$$\frac{V_s}{V^*} = V_R^{(0)} \left[1 - \omega_{SRK} V_R^{(\delta)} \right] \qquad (7.10.1.4)$$

$$V_R^{(0)} = 1 + a\left(1 - T_r\right)^{1/3} + b\left(1 - T_r\right)^{2/3} + c\left(1 - T_r\right) + d\left(1 - T_r\right)^{4/3} \qquad (7.10.1.5)$$

for $0.25 < T_r < 0.95$

$$V_R^{(\delta)} = \left[e + fT_r + gT_r^2 + hT_r^3 \right] / \left(T_r - 1.00001 \right) \qquad (7.10.1.6)$$

for $0.25 < T_r < 1$

The values of constants *a* through *h* in Eqs. 7.10.1.4−7.10.1.6 are:

a: -1.52816	b: 1.43907	c: -0.81446	d: 0.190454
e: -0.296123	f: 0.386914	g: -0.0427258	h: -0.0480645

V^* is a pure component characteristic volume generally within 1−4% of the critical volume and ω_{SRK} is the acentric factor which forces the Soave equation to give the best fit of existing vapor pressure data. Values of V^* and ω_{SRK} can be found in [33]. If the value of V^* is not available, it can be estimated by means of the Eq. 7.10.1.6. If the value of ω_{SRK} is not available, the acentric factor (ω) must be used instead since the resulting error will be often less than 1%.

$$V^* = \frac{RT_c}{P_c}\left(a + b\omega_{SRK} + c\omega_{SRK}^2\right) \qquad (7.10.1.6)$$

Finally, to estimate the compressed liquid volume the following expression was used:

$$V = V_s\left(1 - c\cdot\ln\frac{\beta + P}{\beta + P_{v,i}}\right) \qquad (7.10.1.7)$$

where the saturated liquid volume V_s at the vapor pressure P_v should be calculated from Eq. 7.10.1.4. β and c are obtained from:

$$\beta / P_c = 1 - a\left(1 - T_r\right)^{1/3} + b\left(1 - T_r\right)^{2/3} + d\left(1 - T_r\right) + e\left(1 - T_r\right)^{4/3} \qquad (7.10.1.8)$$

$$e = \exp\left(f + \omega_{SRK} + h\omega_{SRK}^2\right) \qquad (7.10.1.9)$$

$$c = j + k\omega_{SRK} \qquad (7.10.1.10)$$

The constants a through k for Eqs. 7.9.1.4-7.9.1.7 are:

a: -9.070217	b: 62.45326	d: -135.1102	f: 4.79594
g: 0.250047	h: 1.14188	j: 0.0861488	k: 0.0344483

Reduced temperature (T_r) was calculated as T/T_c. The vapor pressure of pure compounds at each temperature ($P_{v,i}$) was estimated by the Antoine equation (Eq. 7.10.1.11).

$$\ln P_{v,i} = A - \frac{B}{T + C} \qquad (7.10.1.11)$$

when values of constants A,B, and C for Eq. 7.10.1.11 were not available, the Gomez-Thodos equations [33] were used instead:

$$\ln P_{v,i} = \beta\left[\frac{1}{T_r^m} - 1\right] + \gamma\left[T_r^7 - 1\right] \qquad (7.10.1.12)$$

where the constants β, γ and m are calculated through the expression of the reduced normal boiling point (T_{br}) as:

$$\gamma = ah + b\beta \qquad (7.10.1.13)$$

$$a = \frac{1-1/T_{b_r}}{T_{b_r}^7 - 1} \quad (7.10.1.14)$$

$$a = \frac{1-1/T_{b_r}^m}{T_{b_r}^7 - 1} \quad (7.10.1.15)$$

$$h = T_{b_r} \frac{\ln\left(P_c/1.01325\right)}{1-T_{b_r}} \quad (7.10.1.16)$$

Values of P_c, T_c, V^* and ω_{SRK} estimated following the described procedure are gathered in Table 7.10.1.

Table 7.10.1. Estimated values of P_c, T_c, V^* and ω_{SRK}.

Property	Compound							
	IB	EtOH	2M1B	TBA	2M2B	ETBE	TAOH	TAEE
P_c [bar]	40	61.4	34.5	39.7	34.5	29.34	39.5	26.54
T_c [K]	417.9	513.9	465	506.2	470	509.4	545	542.46
V^* [L mol^{-1}]	0.2369	0.1752	0.2887	0.2876	0.2883	0.394	0.3313	0.442
ω_{SRK}	0.1959	0.6378	0.2355	0.6134	0.2852	0.2891	0.5007	0.3613

Finally, the estimated density of compounds, molar volumes, enthalpies of vaporization and individual solubility parameters at the assayed temperatures were estimated following the methodology described in Yaws 2009 [247]. The obtained vales are gathered in Table 7.10.2.

Table 7.10.2. Molar volume, enthalpy of vaporization, density and individual solubility parameters of involved compounds at the assayed temperatures.

Property	Temperature [K]	Compound							
		IB	EtOH	2M1B	TBA	2M2B	ETBE	TAOH	TAEE
δ_i [MPa$^{1/2}$]	323.15	12.485	25.695	13.704	20.330	14.378	13.857	19.798	14.119
	333.15	11.979	25.182	13.272	19.799	14.015	13.578	19.342	13.877
	343.15	11.436	24.656	12.822	19.254	13.637	13.290	18.875	13.630
	353,15	10.848	24.115	12.353	18.694	13.243	12.994	18.399	13.377
ρ_i [g cm^{-3}]	323,15	0.556	0.764	0.617	0.755	0.629	0.710	0.781	0.724
	333,15	0.541	0.754	0.605	0.743	0.617	0.700	0.771	0.715
	343,15	0.526	0.744	0.593	0.731	0.605	0.689	0.761	0.706
	353,15	0.509	0.734	0.580	0.719	0.592	0.679	0.750	0.697
$\overline{V}_i$ [L mol^{-1}]	323,15	0.101	0.059	0.114	0.099	0.112	0.146	0.113	0.156
	333,15	0.104	0.060	0.116	0.100	0.114	0.148	0.115	0.159
	343.15	0.107	0.061	0.118	0.102	0.116	0.151	0.116	0.161
	353.15	0.111	0.062	0.121	0.104	0.118	0.153	0.118	0.163
$\Delta H_{v,i}$ [kJ mol^{-1}]	323.15	18.499	41.845	24.053	25.769	30.721	33.856	43.521	46.946
	333.15	17.714	41.008	23.198	25.117	30.108	33.302	42.162	45.613
	343.15	16.869	40.142	22.310	24.434	29.474	32.732	40.767	44.256
	353.15	15.953	39.244	21.384	23.717	28.816	32.145	39.335	42.874

7.10.2 ESTIMATION OF KINEMATIC AND DYNAMIC VISCOSITIES

Prior to calculate the viscosities at different temperatures. The critical properties of involved compounds and dipole moments (μ) were obtained. Table 7.10.3 summarizes the data used for subsequent calculations that either can be found in Poiling et al. [212] or was obtained by means of the Joback method described in [212].

Table 7.10.3. Estimated properties necessary for subsequent viscosity calculations.

Component	Properties								
	Tc [K]	Pc [bar]	Pc [N m^{-2}]	Vc [cm^3 mol^{-1}]	μ [dB]	Zc[a]	Tb [K]	ω[b]	MW [g mol^{-1}]
MeOH	512.6	81.0	8097000	118.0	1.7	0.224	337.7	0.565	32.04
EtOH	513.9	61.5	6148000	167.0	1.7	0.240	351.8	0.649	46.07
1-PrOH	536.8	51.8	5175000	219.0	1.7	0.254	370.9	0.629	60.10
1-BuOH	563.1	44.2	4423000	275.0	1.8	0.260	390.9	0.590	74.12
MTBE	496.4	33.7	3370000	322.5	1.2	0.263	328.3	0.269	88.15
ETBE	509.4	29.3	2934000	394.0	1.2[c]	0.273	345.0	0.289	102.18
PTBE	553.9	28.1	2805408	434.5	1.2[c]	0.265	378.8	0.329	116.20
BTBE	576.1	25.4	2540485	490.5	1.2[c]	0.260	401.6	0.386	130.23
TAEE	542.5	26.5	2654000	442.0	1.2[c]	0.260	375.0	0.361	116.20
2M1B	465.0	34.5	3450000	286.5	0.5	0.256	304.1	0.236	70.13
2M2B	470.0	38.6	3860000	292.0	0.5	0.288	311.7	0.244	70.13
IB	417.9	40.0	4000000	238.8	0.5	0.275	266.2	0.199	56.11
TBA	506.2	39.7	3973000	275.0	1.7	0.260	355.5	0.613	74.12
TAA	545.0	37.9	3790000	323.0	1.9	0.270	375.2	0.478	88.15

[a] Zc is the vapor/liquid critical compressibility factor estimated as Z_c=0.291-0.080ω. [b] ω is the acentric factor. [c] As dipole moment (μ) of C_1-C_4 alcohols is identical, an also those of IB and 2M1B, the dipole moments of ethers have been assumed to be the same of that of MTBE and the dipole moment of 2M2B equal to that of 2M1B.

The particular form of the corresponding state methods equation defined by Lucas et al. [212] for the estimation of dynamic viscosities at different temperatures is:

$$\eta\xi = \left[0.807T_r^{0.618} - 0.357\exp{-\left(0.449T_r\right)} + 0.34\exp\left(4.058T_r\right) + 0.018\right]F_P^0 F_Q^0 \qquad (7.10.2.1)$$

where η is the dynamic viscosity [μP], ξ has the units of [μP^{-1}] or inverse viscosity and it is defined by Eq. 7.10.2.2, *Tr* is the reduced temperature, and F^0_p and F^0_Q are correction factors to account for polarity or quantum effects.

$$\xi = 0.176\left(\frac{T_c}{MW^3 P_c^4}\right)^{1/6} \qquad (7.10.2.2)$$

where T_c is in [K], P_c is in [bar] and MW in [g mol^{-1}].

To obtain F^0_p a reduced dipole moment (μ_r) in [dB] is required. It can be obtained by means of Eq. 7.10.2.3.

$$\mu_r = 52.46\left(\frac{\mu^2 P_c}{T_c^2}\right) \qquad (7.10.2.3)$$

Then, F^0_p values can be found depending of the value of μ_r as:

$$\begin{aligned} F_P^0 &= 1 && 0 \le \mu_r < 0.022 \\ F_P^0 &= 1 + 30.55\left(0.292 - Z_c\right)^{1.72} && 0.022 \le \mu_r < 0.075 \\ F_P^0 &= 1 + 30.55\left(0.292 - Z_c\right)^{1.72}\left|0.96 + 0.1\left(T_r - 0.7\right)\right| && 0.075 \le \mu_r \end{aligned} \qquad (7.10.2.4)$$

The factor F^0_Q is only used for quantum gases, in other cases F^0_Q =1.

Examples of the estimated values of η at 343 K are gathered in Table 7.10.4.

Table 7.10.4. Parameters estimated for the calculation of dynamic viscosity of involved compounds at 343 K.

	Parameter						
Component	ξ [μP^{-1}]	Tr	ηξ	F^0_p	F^0_q	μ_r	η [μP]
MeOH	0.0047	0.6691	0.5273	1.2999	1	0.0467	112.2049
EtOH	0.0047	0.6674	0.4812	1.1890	1	0.0353	102.1309
1-PrOH	0.0047	0.6390	0.4301	1.1102	1	0.0272	92.2724
1-BuOH	0.0047	0.6092	0.3995	1.0820	1	0.0237	85.0539
MTBE	0.0051	0.6910	0.4190	1	1	0.0103	82.8765
ETBE	0.0052	0.6733	0.4083	1	1	0.0085	78.9299
PTBE	0.0051	0.6192	0.3753	1	1	0.0069	74.0565
BTBE	0.0051	0.5954	0.3608	1	1	0.0058	70.0927
TAEE	0.0052	0.6323	0.3833	1	1	0.0068	73.1403
2M1B	0.0055	0.7376	0.4473	1	1	0.0021	81.0457
2M2B	0.0051	0.7298	0.4426	1	1	0.0023	86.2628
IB	0.0055	0.8208	0.4975	1	1	0.0030	90.5662
TBA	0.0050	0.6776	0.4446	1.0820	1	0.0235	89.6896
TAA	0.0047	0.6294	0.3979	1.0431	1	0.0242	83.8009

Finally, the kinematic viscosity of compounds can be estimated as the ratio of dynamic viscosity to gas density of compounds. Estimation of gas density of compounds is detailed in *Appendix 7.10.3.*

7.10.3 ESTIMATION OF GAS DENSITIES OF COMPOUNDS

Gas densities of involved compounds was calculated by means of the Redlich-Kwong equation (Eq. 7.10.3.1).

$$RT = P\left(V_m - b\right) + \frac{a}{V_m\left(V_m + b\right)T^{1/2}}\left(V_m - b\right) \tag{7.10.3.1}$$

where V_m is the molar volume (V/n) and, a and b are empirical parameters, which are not the same of the van der Waals equation. These parameters are determined as:

$$a = 0.4275\frac{R^2 T_c^{2.5}}{P_c} \tag{7.10.3.2}$$

$$b = 0.0867\frac{RT_c}{P_c} \tag{7.10.3.3}$$

The gas density values obtained for the different tracers evaluated are gathered in Table 7.10. 5.

Table 7.10.5. Gas-phase density of evaluated compounds

Compound	a	b	Gas density [g L^{-1}]			
			323 K	333 K	343 K	353 K
MeOH	214.3392	0.0456	1.2068	1.1709	1.1365	1.1053
EtOH	284.0531	0.0603	1.7342	1.6820	1.6322	1.5845
1-PrOH	376.2487	0.0748	2.2610	2.1891	2.1282	2.0652
1-BuOH	496.0724	0.0918	2.7876	2.7014	2.6251	2.5524
MTBE	475.1646	0.1062	3.3124	3.2104	3.1166	3.0268
ETBE	582.2129	0.1252	3.8361	3.7372	3.6239	3.5210
PTBE	750.8843	0.1423	4.3615	4.2213	4.0979	3.9862
BTBE	914.5617	0.1635	4.8826	4.7374	4.6139	4.4787
TAEE	753.2046	0.1473	4.3606	4.2206	4.0972	3.9856
2M1B	394.1921	0.0972	2.6365	2.5595	2.4872	2.4167
2M2B	361.8695	0.0878	2.6374	2.5603	2.4880	2.4175
IB	260.3248	0.0753	2.1111	2.0479	1.9905	1.9367
TBA	423.2557	0.0918	2.7876	2.7014	2.6251	2.5524
TAA	533.6379	0.1037	3.3127	3.2107	3.1168	3.0271

7.11 SUMMARY OF CANDIDATE KINETIC MODELS OBTAINED

A more detailed summary of the first fifteen candidate best models obtained for *n*=1, *n*=2 and *n*=3 described in *Section 4.7* is presented in Tables 7.11.1, 7.11.2 and 7.11.3. Such values were used for model averaging.

Table 7.11.1. Estimated parameter values for the first fifteen best models ranked with *n*=1.

Model	$k'_{1,R1}$	$k'_{T,R1}$	$k'_{1,R2}$	$k'_{T,R2}$	$k'_{1,R3}$	$k'_{T,R3}$	k_{D1}	k_{DT}	$K'_{1,ETBE}$	$K'_{T,ETBE}$	$K'_{1,TAEE}$	$K'_{T,TAEE}$	TWRSS	AIC
203	6.46	-8954	6.93	-9457	4.59	-9775	23.71	-	0.53	-5139	-	-	0.26	-1193
Error	*0.3%*	*1.7%*	*0.6%*	*3.8%*	*0.5%*	*2.3%*	*0.3%*	*-*	*10%*	*9%*	*-*	*-*		
500	6.47	-8958	7.01	-9781	4.55	-9583	23.68	-	0.41	-5610	-0.41	-	0.26	-1192
Error	*0.3%*	*1.7%*	*0.5%*	*3.3%*	*0.6%*	*2.6%*	*0.3%*	*-*	*14%*	*9%*	*128%*	*-*		
104	6.51	-8459	7.03	-7031	4.66	-9849	23.71	-	1.01	-	-	-	0.28	-1185
Error	*0.3%*	*1.9%*	*0.6%*	*6.2%*	*0.5%*	*2.2%*	*0.3%*	*-*	*5%*	*-*	*-*	*-*		
401	6.51	-8459	7.14	-7236	4.59	-9969	23.67	-	0.94	-	-0.42	-	0.28	-1183
Error	*0.3%*	*1.9%*	*0.6%*	*5.4%*	*0.5%*	*2.3%*	*0.3%*	*-*	*6%*	*-*	*131%*	*-*		
105	6.44	-9119	6.95	-8020	4.59	-10366	24.26	-0.04	1.02	-	-	-	0.28	-1183
Error	*0.3%*	*1.7%*	*0.6%*	*5.3%*	*0.5%*	*2.1%*	*0.3%*	*14.1%*	*5%*	*-*	*-*	*-*		
402	6.44	-9154	7.05	-8252	4.52	-10501	24.26	-0.05	0.94	-	-0.39	-	0.27	-1182
Error	*0.3%*	*1.7%*	*0.6%*	*4.6%*	*0.6%*	*2.2%*	*0.3%*	*13.5%*	*6%*	*-*	*138%*	*-*		
599	6.59	-9031	7.66	-11322	3.97	-7108	22.10	-	-	-	1.31	-7085	0.43	-1102
Error	*0.3%*	*2.2%*	*0.3%*	*2.0%*	*2.3%*	*12.6%*	*0.6%*	*-*	*-*	*-*	*6%*	*9%*		
302	6.63	-8553	7.79	-8876	3.97	-10486	22.07	-	-	-	1.97	-	0.45	-1095
Error	*0.3%*	*2.4%*	*0.4%*	*3.0%*	*1.7%*	*5.9%*	*0.6%*	*-*	*-*	*-*	*4%*	*-*		
303	6.51	-9745	7.57	-11156	4.06	-9084	23.29	-0.09	-	-	1.99	-	0.45	-1094
Error	*0.3%*	*2.1%*	*0.4%*	*2.3%*	*1.7%*	*7.4%*	*0.5%*	*10.3%*	*-*	*-*	*4%*	*-*		
697	6.82	-10093	7.93	-11633	4.11	-6436	-	-	-0.43	-	-1.06	-18811	0.73	-1002
Error	*0.4%*	*2.6%*	*0.4%*	*2.5%*	*3.4%*	*22.5%*	*-*	*-*	*67%*	*-*	*19%*	*9%*		
598	6.80	-10116	8.04	-11478	3.57	-5669	-	-	-	-	0.49	-9701	0.75	-1001
Error	*0.4%*	*2.7%*	*0.4%*	*2.3%*	*7.1%*	*46.9%*	*-*	*-*	*-*	*-*	*27%*	*12%*		
499	6.82	-10139	7.94	-10816	4.14	-8532	-	-	-2.12	-16624	0.85	-	0.74	-1000
Error	*0.4%*	*2.6%*	*0.4%*	*2.9%*	*2.8%*	*13.1%*	*-*	*-*	*13%*	*13%*	*27%*	*-*		
796	6.82	-10169	7.92	-11618	4.08	-6978	-	-	-0.70	-3247	-0.75	-15952	0.73	-1000
Error	*0.4%*	*2.6%*	*0.4%*	*2.5%*	*3.4%*	*20.1%*	*-*	*-*	*41%*	*86%*	*28%*	*11%*		
400	6.85	-9795	8.03	-9443	4.07	-10677	-	-	-0.44	-	0.85	-	0.75	-1000
Error	*0.4%*	*2.7%*	*0.4%*	*3.5%*	*2.5%*	*8.7%*	*-*	*-*	*68%*	*-*	*27%*	*-*		
301	6.84	-9736	8.12	-9704	3.67	-10701	-	-	-	-	1.41	-	0.77	-998
Error	*0.4%*	*2.8%*	*0.4%*	*3.1%*	*4.2%*	*13.1%*	*-*	*-*	*-*	*-*	*10%*	*-*		

Table 7.11.2. Estimated parameter values for the first fifteen best models ranked with *n*=2.

Model	$k'_{1,R1}$	$k'_{T,R1}$	$k'_{1,R2}$	$k'_{T,R2}$	$k'_{1,R3}$	$k'_{T,R3}$	k_{D1}	k_{DT}	$K'_{1,ETBE}$	$K'_{T,ETBE}$	$K'_{1,TAEE}$	$K'_{T,TAEE}$	TWRSS	AIC
203	6.42	-8795	6.96	-9035	4.49	-9726	21.18	-	-0.08	-4329	-	-	0.29	-1170
Error	*0%*	*2%*	*1%*	*4%*	*1%*	*3%*	*1%*	*-*	*57%*	*9%*	*-*	*-*		
500	6.42	-8795	7.10	-9303	4.39	-9602	21.14	-	-0.24	-4852	-0.74	-	0.30	-1170
Error	*0%*	*2%*	*0%*	*3%*	*1%*	*3%*	*1%*	*-*	*20%*	*9%*	*42%*	*-*		
401	6.47	-8285	7.26	-6939	4.40	-10138	21.13	-	0.23	-	-0.76	-	0.31	-1160
Error	*0%*	*2%*	*1%*	*5%*	*1%*	*3%*	*1%*	*-*	*21%*	*-*	*43%*	*-*		
104	6.47	-8292	7.11	-6674	4.53	-9845	21.17	-	0.34	-	-	-	0.32	-1159
Error	*0%*	*2%*	*1%*	*6%*	*1%*	*2%*	*1%*	*-*	*13%*	*-*	*-*	*-*		
402	6.45	-8497	7.23	-7231	4.38	-10298	21.40	-	0.23	-	-0.75	-	0.31	-1158
Error	*0%*	*2%*	*1%*	*5%*	*1%*	*3%*	*1%*	*43%*	*21%*	*-*	*43%*	*-*		
105	6.44	-8505	7.08	-6983	4.51	-10011	21.44	-0.02	0.34	-	-	-	0.32	-1157
Error	*0%*	*2%*	*1%*	*6%*	*1%*	*2%*	*1%*	*43%*	*13%*	*-*	*-*	*-*		
697	6.58	-9405	7.75	-8283	3.73	-13632	-	-	-0.31	-	-2.45	-20743	0.46	-1089
Error	*0%*	*2%*	*0%*	*3%*	*2%*	*4%*	*-*	*-*	*29%*	*-*	*8%*	*8%*		
499	6.56	-9622	7.65	-8833	3.96	-12162	-	-	-0.95	-6459	-0.25	-	0.46	-1089
Error	*0%*	*2%*	*0%*	*3%*	*1%*	*4%*	*-*	*-*	*10%*	*-13%*	*90%*	*-*		
796	6.56	-9601	7.44	-11188	4.30	-8222	-	-	-0.59	-3111	-1.85	-15065	0.45	-1088
Error	*0%*	*2%*	*0%*	*2%*	*1%*	*7%*	*-*	*-*	*15%*	*27%*	*12%*	*12%*		
202	6.56	-9640	7.41	-8745	4.35	-11166	-	-	-0.52	-4788	-	-	0.47	-1086
Error	*0%*	*2%*	*1%*	*4%*	*1%*	*3%*	*-*	*-*	*14%*	*14%*	*-*	*-*		
400	6.60	-9214	7.70	-7676	4.03	-12198	-	-	-0.30	-	-0.31	-	0.47	-1085
Error	*0%*	*2%*	*0%*	*4%*	*1%*	*4%*	*-*	*-*	*31%*	*-*	*78%*	*-*		
103	6.60	-9238	7.51	-7204	4.38	-11333	-	-	-0.06	-	-	-	0.49	-1083
Error	*0%*	*2%*	*1%*	*6%*	*1%*	*3%*	*-*	*-*	*120%*	*-*	*-*	*-*		
599	6.51	-8925	7.79	-10702	3.17	-6410	18.61	-	-	-	0.79	-6251	0.61	-1037
Error	*0%*	*3%*	*0%*	*2%*	*7%*	*37%*	*2%*	*-*	*-*	*-*	*8%*	*9%*		
302	6.56	-8363	7.93	-8555	3.02	-12926	18.52	-	-	-	1.38	-	0.64	-1029
Error	*0%*	*3%*	*0%*	*3%*	*5%*	*10%*	*2%*	*-*	*-*	*-*	*5%*	*-*		
303	6.49	-9083	7.77	-10122	3.44	-8561	20.07	-0.12	-	-	1.39	-	0.64	-1028
Error	*0%*	*3%*	*0%*	*3%*	*4%*	*17%*	*1%*	*19%*	*-*	*-*	*5%*	*-*		

Table 7.11.3. Estimated parameter values for the first fifteen best models ranked with *n*=3.

Model	$k'_{1,R1}$	$k'_{T,R1}$	$k'_{1,R2}$	$k'_{T,R2}$	$k'_{1,R3}$	$k'_{T,R3}$	k_{D1}	k_{DT}	$K'_{1,2M1B}$	$K'_{T,2M1B}$	$K'_{1,ETBE}$	$K'_{T,ETBE}$	$K'_{1,TAEE}$	$K'_{T,TAEE}$	TWRSS	AIC
499	6.28	-9283	7.17	-9607	4.06	-9701	-	-	-	-	-0.59	-3849	-0.75	-	0.38	-1122
Error	*0%*	*2%*	*0%*	*3%*	*1%*	*4%*	*-*	*-*	*-*	*-*	*8%*	*12%*	*29%*	*-*		
697	6.30	-9019	7.37	-8178	3.76	-11880	-	-	-	-	-0.23	-	-3.47	-25431	0.38	-1122
Error	*0%*	*2%*	*0%*	*3%*	*1%*	*4%*	*-*	*-*	*-*	*-*	*21%*	*-*	*5%*	*6%*		
797	6.26	-8784	7.03	-10026	4.15	-8916	18.46	-	-	-	-0.23	-2156	-3.63	-25133	0.38	-1121
Error	*0%*	*2%*	*0%*	*3%*	*1%*	*4%*	*1%*	*-*	*-*	*-*	*18%*	*19%*	*6%*	*7%*		
500	6.25	-8846	7.05	-9405	4.14	-9373	18.44	-	-	-	-0.39	-3709	-0.85	-	0.38	-1120
Error	*0%*	*2%*	*0%*	*3%*	*1%*	*4%*	*1%*	*-*	*-*	*-*	*11%*	*11%*	*29%*	*-*		
698	6.28	-8520	7.21	-8742	4.02	-9635	18.46	-	-	-	-0.06	-	-3.82	-28586	0.38	-1119
Error	*0%*	*2%*	*0%*	*3%*	*1%*	*4%*	*1%*	*-*	*-*	*-*	*75%*	*-*	*5%*	*5%*		
202	6.28	-9307	6.99	-9327	4.24	-9899	-	-	-	-	-0.39	-3419	-	-	0.40	-1118
Error	*0%*	*2%*	*1%*	*4%*	*1%*	*3%*	*-*	*-*	*-*	*-*	*11%*	*12%*	*-*	*-*		
203	6.26	-8860	6.89	-9222	4.28	-9499	18.49	-	-	-	-0.23	-3398	-	-	0.39	-1117
Error	*0%*	*2%*	*1%*	*4%*	*1%*	*3%*	*1%*	*-*	*-*	*-*	*17%*	*11%*	*-*	*-*		
218	6.29	-8793	7.03	-9228	4.23	-9601	18.65	-	-0.74	-	-0.23	-3386	-	-	0.39	-1116
Error	*0%*	*2%*	*1%*	*4%*	*1%*	*4%*	*1%*	*-*	*36%*	*-*	*17%*	*11%*	*-*	*-*		
400	6.32	-8848	7.35	-7375	3.94	-11283	-	-	-	-	-0.22	-	-0.77	-	0.40	-1114
Error	*0%*	*2%*	*0%*	*4%*	*1%*	*3%*	*-*	*-*	*-*	*-*	*23%*	*-*	*29%*	*-*		
230	6.32	-8486	7.12	-8290	4.21	-9775	18.67	-	-0.18	5668	-0.26	-3619	-	-	0.39	-1114
Error	*0%*	*2%*	*1%*	*4%*	*1%*	*3%*	*1%*	*-*	*131%*	*43%*	*16%*	*10%*	*-*	*-*		
401	6.30	-8366	7.22	-7312	4.11	-10095	18.44	-	-	-	-0.03	-	-0.85	-	0.41	-1110
Error	*0%*	*2%*	*1%*	*5%*	*1%*	*3%*	*1%*	*-*	*-*	*-*	*151%*	*-*	*30%*	*-*		
103	6.32	-8875	7.17	-7099	4.20	-10542	-	-	-	-	-0.06	-	-	-	0.42	-1110
Error	*0%*	*2%*	*1%*	*6%*	*1%*	*3%*	*0*	*-*	*-*	*-*	*74%*	*-*	*-*	*-*		
402	6.28	-8568	7.18	-7663	4.11	-10152	-	-0.04	-	-	-0.03	-	-0.85	-	0.41	-1108
Error	*0%*	*2%*	*1%*	*5%*	*1%*	*3%*	*1%*	*43%*	*-*	*-*	*159%*	*-*	*30%*	*-*		
118	6.33	-8869	7.21	-7104	4.18	-10656	-	-	-2.22	-	-0.06	-	-	-	0.42	-1108
Error	*0%*	*2%*	*1%*	*5%*	*1%*	*3%*	*-*	*-*	*52%*	*-*	*70%*	*-*	*-*	*-*		
416	6.30	-8358	7.23	-7312	4.11	-10130	18.46	-	-2.76	-	-0.03	-	-0.88	-	0.41	-1108
Error	*0%*	*2%*	*1%*	*5%*	*1%*	*4%*	*1%*	*-*	*73%*	*-*	*174%*	*-*	*30%*	*-*		

7.12 MAPPING OF ELEMENTS ON FRESH AMBERLYST™35

The following images were obtained in the mapping of elements applied to the catalyst in *Section 4.8*.

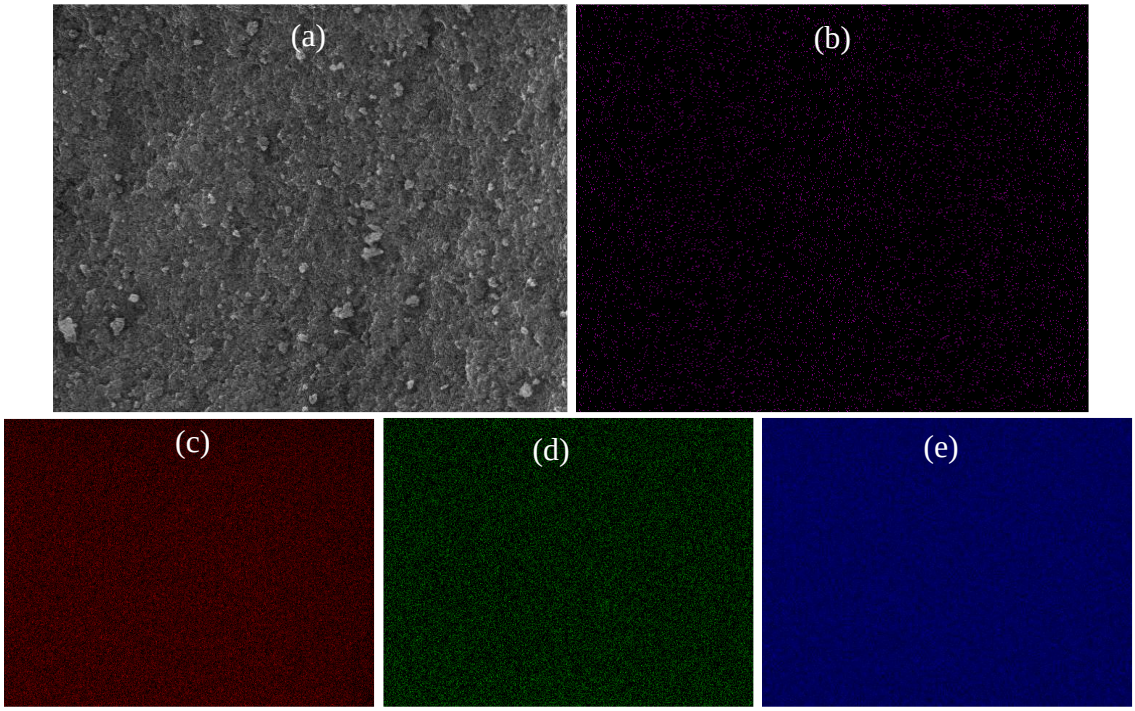

Figure 7.12.1. Images obtained in the mapping of elements applied in a fresh particle of Amberlyst™35. (a) Surface of resin where the mapping was performed. (b) Gold particles distribution from the coating. (c) Oxygen elements distribution. (d) Carbon elements distribution. (e) Sulfur elements distribution.

8. SUMMARY IN SPANISH

8.1. INTRODUCCIÓN

8.1.1 PETRÓLEO Y SOCIEDAD

En la actualidad, un elevado porcentaje del consumo global de energía proviene del petróleo. Esta cantidad oscila desde un 32% en Europa hasta un 53% en Oriente Medio. El consumo global de petróleo ha aumentado continuamente en los últimos años, y también el consumo de derivados del petróleo usados para el transporte, principalmente gasolina y diésel. Este aumento de consumo ha ido acompañado inevitablemente de un aumento en las emisiones a la atmósfera de compuestos contaminantes provenientes de la combustión de hidrocarburos. En consecuencia, se ha generado una alarma a escala global ya que la calidad del aire está deteriorándose profundamente, especialmente en las grandes ciudades, como Paris, México o Tokio, dónde los niveles de contaminación han alcanzado records históricos [1,2].

Los principales contaminantes emitidos por la combustión de gasolina y diésel son el monóxido de carbono (CO), dióxido de carbono (CO_2), material particulado, óxidos de nitrógeno (NO_x's) y compuestos orgánicos volátiles (COV's). Es importante resaltar que, aunque la combustión de diésel produce un 15% menos de CO_2, implica unas emisiones cuatro veces mayores de NO_x's y veintidós veces mayores de material particulado. Las emisiones de partículas sólidas son especialmente peligrosas porque la mayor parte de ellas son carcinogénicas y se acumulan en el sistema respiratorio de animales y humanos. Además, actúan como catalizadores en reacciones de formación de contaminantes secundarios muy peligrosos como pueden ser los peroxiacetilnitratos (PAN's) [4,5]. Por ende, se espera que el uso de gasolina gane relevancia en los próximos años, especialmente en zonas como Europa, en las que la tendencia ha sido usar mayoritariamente vehículos de tipo diésel. En efecto, algunas de las grandes ciudades europeas como Paris se están planteando prohibir la circulación de vehículos diésel para el 2020.

Con el objetivo de contrarrestar los efectos detrimentales sobre el medio ambiente provenientes de la quema de combustibles fósiles, en los últimos años se están desarrollando tecnologías que permitan utilizar fuentes de energía renovables para el transporte. Uno de los ejemplos en los que se está invirtiendo más esfuerzo es el coche eléctrico. Sin embargo, y desde un punto de vista realista, esta tecnología está aún lejos de implantarse socialmente a un coste razonable y de forma eficiente desde un punto de vista energético, autonomía de los vehículos, puntos de carga, etc. Además, es obvio que la flota de vehículos actual no puede desaparecer de forma repentina. Por lo tanto, una optimización o mejora de los combustibles fósiles, proporcionándoles un carácter medioambientalmente más limpio y que sean, a su vez, compatibles con los motores de los vehículos actuales constituye una solución más plausible a corto y medio plazo.

En ese sentido, la legislación es cada vez más estricta con respecto a la composición de diésel y gasolinas, así como con la proveniencia de sus componentes, la cual se incentiva que sea de fuentes de energías renovables. Las directivas europeas 2009/28/EC, 2009/30/EC y 2015/1513/EC establecen las principales líneas de actuación para reducir las emisiones de gases de efecto invernadero producidos por el uso de gasolina y diésel en los próximos años, a la vez que promueven el uso de fuentes de energía renovables. Por ejemplo, entre otras medidas, se limita la presión de vapor de una gasolina a 60 kPa, el contenido de olefinas en un 18 %vol., el de etanol en un 10 %vol., el de éteres con cinco o más átomos de carbono en un 22 %vol., y el contenido en oxígeno en un 3.7 %m. También se marca que para el 2020, al menos un 20% de la energía utilizada para el transporte debe tener un origen renovable.

8.1.2 REFORMULACIÓN DE GASOLINAS

Uno de los componentes más perjudiciales de las gasolinas son las olefinas reactivas de la fracción C_5, también conocidas como isoamilenos (IA), 2-metil-1-buteno (2M1B) y 2-metil-2-buteno (2M2B). El potencial relativo de formación de ozono troposférico de un componente de la gasolina (P_{OF}) se puede calcular como el producto de su presión de vapor, su reactividad atmosférica y su distribución en volumen. Como se puede observar en la Figura 8.1, las olefinas C_5 son las que están presentes en mayor cantidad en volumen en una gasolina, también poseen la mayor reactividad atmosférica y presión de vapor. Por lo tanto, son las olefinas con mayor potencial de formación de ozono troposférico (alrededor del 90% del total de una gasolina). En consecuencia, la reducción del contenido de isoamilenos en una gasolina es medioambientalmente recomendable. Para ello, coexisten varias alternativas, por ejemplo, eterificación, alquilación u oligomerización [7].

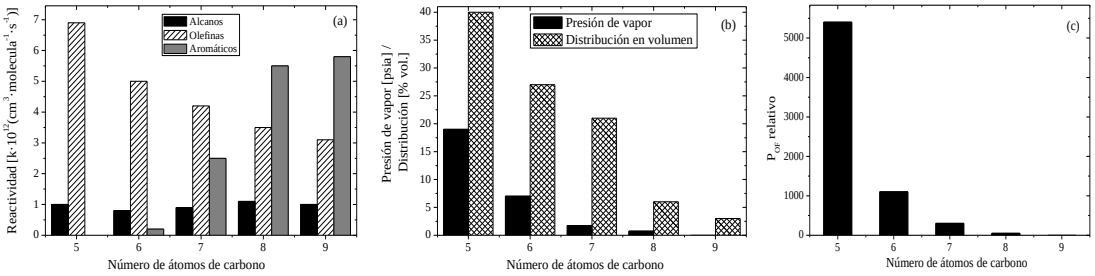

Figura 8.1. Relación entre el número de carbonos y (a) reactividad atmosférica de alcanos, olefinas y aromáticos, (b) presión de vapor y distribución en volumen de olefinas y, (c) potencial relativo de formación de ozono troposférico de las olefinas de una gasolina. Fuente de datos [7].

Dentro de los compuestos oxigenados, éteres y alcoholes han sido elegidos como los principales compuestos para ser usados como aditivos de gasolinas [9]. Entre los alcoholes, el más utilizado ha sido el etanol (EtOH) ya que este puede obtenerse mediante la fermentación de biomasa, como maíz, trigo e incluso residuos vegetales. Además, alcoholes más pesados como el butanol están considerándose como aditivos apropiados para gasolinas ya que también pueden obtenerse por fermentación de biomasa [17]. Dentro de los éteres, las opciones más plausibles son el metil *terc*-butil éter (MTBE), etil *terc*-butil éter (ETBE), *terc*-amil metil éter (TAME) y *terc*-amil etil éter (TAEE). El uso de éteres se ha favorecido ya que el *blending* directo de etanol, el llamado "gasohol" presenta algunas desventajas. Por ejemplo, mayor presión de vapor de la mezcla a causa de la formación de azeótropos, posibilidad de introducir agua en el sistema, menor contenido energético, menor entalpía de combustión y mayor riesgo de corrosión de equipos. Además, las emisiones evaporativas y de tubo de escape de la quema de gasohol son normalmente mayores. Incluso el consumo específico de un motor que funciona con gasohol es alrededor del 40% superior a aquel inducido por éteres terciarios como el ETBE y el TAEE. Finalmente, el alto contenido en oxígeno del etanol puede promover la formación de NO_x's o limitar la cantidad de aditivo a usar para no superar los niveles legislados [25,26]. Por lo tanto, un mejor uso del etanol o bioetanol, es incorporarlo al diésel como ésteres de ácidos grasos o a la gasolina reformulada en forma de ETBE o TAEE.

Con respecto a los éteres, aunque el MTBE es actualmente el éter que más se produce a escala global, algunas de sus propiedades, principalmente su solubilidad en agua, le otorgan un potencial contaminante de aguas subterráneas, lo que ha causado su prohibición en muchos estados, como en California [44]. Además, el metanol (MeOH) y, por tanto, sus éteres derivados

MTBE y TAME, provienen del gas natural, contribuyendo por tanto al calentamiento global [45]. Por causa de estas razones, los éteres provenientes del etanol y, por consiguiente, considerados bioéteres (ETBE y TAEE), son las alternativas más atractivas desde un punto de vista medioambiental y de eficiencia energética. Estos éteres también tienen usos eficientes cómo disolventes para aceites, pinturas y tintes, lo que les otorga un mayor valor añadido debido a su amplio rango de aplicaciones [15].

Además de éteres y alcoholes primarios, otros compuestos son interesantes como aditivos de las gasolinas. Por ejemplo, los alcoholes terciarios *terc*-butil alcohol (TBA) y *terc*-amil alcohol (TAA) son una alternativa interesante ya que presentan una baja volatilidad, una baja reactividad atmosférica y pueden reducir las emisiones de aldehídos producidas de la quema de éteres [37]. Por otra parte, los dímeros hidrogenados de isobuteno (IB) e IA son interesantes aditivos ya que poseen un elevado índice de octano [38]. Un resumen de las propiedades más relevantes de todos los compuestos introducidos hasta el momento se encuentra en la Tabla 8.1.

Tabla 8.1. Propiedades relevantes de algunos potenciales aditivos para gasolina [17,18,27–35].

Compuesto	(RON+MON)/2	Solubilidad en agua [mg/L agua]	Contenido oxígeno [wt.%]	bRVP [psi]	b_p [K]	Reactividad[a]
MTBE	110	48.500	18,2	8	328	2,6
ETBE	112	26.000	15,7	4	345	8,1
TAME	105	20.000	15,7	2	361	7,9
TAEE	100	4.000	13,8	2	375	-
PTBE	100,5	-	13,8	-	379[e]	-
BTBE	81[b]	-	12,2	-	402[e]	-
Metanol	116	∞	50	60	338	1
Etanol	115	∞	34,8	18	351	3,4
Propanol	108	∞	26,7	-	371	-
Butanol	87	73.000	21,6	6,4	391	-
IB	Low	388	0	66	266	55
2M2B	91	190	0	15	304	85
2M1B	92	130	0	19	312	70
TBA	101	∞	21,6	10	356	1,1
TAA	97[c]	120.000	18,2	0,32[d]	375	-
TMP-1 and TMP-2	~100	0	0	1,56[d]	375	-
Dímero C_5 hidrogenado	95	-	0	0.5	420	-

[a]Constante de velocidad de reacción de hidroxilo: k· 10^{12} $cm^3 \cdot molecula^{-1} \cdot s^{-1}$. [b]Como (RON+MON)/2 no está disponible, el MON se da en su lugar. [c]Como (RON+MON)/2 no está disponible, el RON se da en su lugar. [d]Como la presión de vapor Reid de la mezcla no está disponible, la presión de vapor a 293 K se da en su lugar. [e]Estimada mediante el método de Joback.

8.1.3 MARCO DE PRODUCCIÓN DE ÉTERES TERCIARIOS

Existen varias rutas químicas y procesos para sintetizar éteres terciarios. A modo general, las dos principales vías químicas son: i) la reacción entre olefinas terciarias y alcoholes primarios, y ii) la reacción de deshidratación entre un alcohol terciario y un alcohol primario. Para ambas rutas químicas se utilizan catalizadores ácidos, principalmente resinas ácidas de intercambio iónico [47]. MTBE y ETBE suelen producirse haciendo reaccionar IB con MeOH o EtOH, respectivamente. La Figura 8.2 ilustra un diagrama de flujo de una planta convencional de producción de MTBE o ETBE. Análogamente, la reacción de los IA con estos dos alcoholes da lugar a TAME o TAEE. En Europa, gran parte de las plantas de MTBE se han renovado para producir ETBE. De igual manera, se espera que, en los próximos años, muchas de las plantas de

TAME cambien a operar con el TAEE como principal objetivo de producción con vistas a cumplir con la cada vez más exigente legislación.

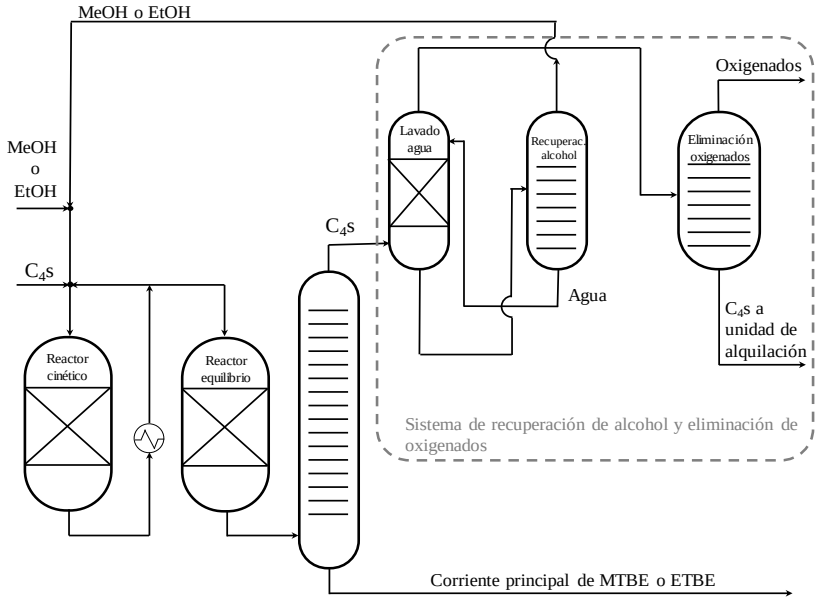

Figura 8.2. Proceso convencional de producción de MTBE o ETBE con unidad integrada de recuperación de alcohol y sistema de eliminación de oxigenados. Adaptado de [48].

Por otra parte, las plantas de eterificación pueden tener diferentes configuraciones. Por lo general, el núcleo de ellas es el reactor de eterificación, habitualmente un reactor de lecho fijo, sin embargo, otras tecnologías como la destilación resultan también interesantes. El alimento al reactor de eterificación típicamente consta de una corriente olefínica, C_4 o C_5 proveniente de las unidades de craqueo fluido catalítico o del craqueo con vapor, FCC o SC por sus siglas en inglés, respectivamente.

Dependiendo de la tecnología, las plantas de MTBE se pueden integrar con las de TAME, y análogamente una planta de ETBE con TAEE, aunque hasta el momento, estas configuraciones no se han implementado a nivel industrial y han sido poco estudiadas. Una unidad de eterificación simultánea para producir ETBE y TAEE implica varias ventajas como pueden ser [46]: i) versatilidad del proceso para adaptar la producción dependiendo de los suministros olefinicos de la refinería, ii) integración de dos procesos a nivel industrial con el consecuente ahorro en costes de instalación, mantenimiento y de operación, iii) posibilidad de utilizar grandes cantidades de etanol y reducir el contenido de las problemáticas olefinas reactivas de la fracción C_5 al mismo tiempo, y iv) evitar la separación de las corrientes C_4 y C_5 de FCC o SC que en muchas refinerías se obtienen como una corriente mixta. La Figura 8.3 representa un posible esquema de producción industrial simultanea de ETBE y TAEE.

Una metodología útil para escoger la ruta química y configuración de unidades más apropiada es el Green Metric Analysis (GMA) de un proceso [12,13]. Mediante GMA se pueden comparar varios procesos considerados, utilizando para ello parámetros normalizados que miden la eficiencia desde un punto medioambiental de cada etapa. Es, por tanto, una herramienta fundamental para la toma de decisiones en el diseño de procesos y a la hora de mejorar y optimizar procesos ya existentes. Hasta el momento hay una falta de este tipo de análisis a las diferentes opciones que emergen al considerar la producción de éteres como ETBE y TAEE.

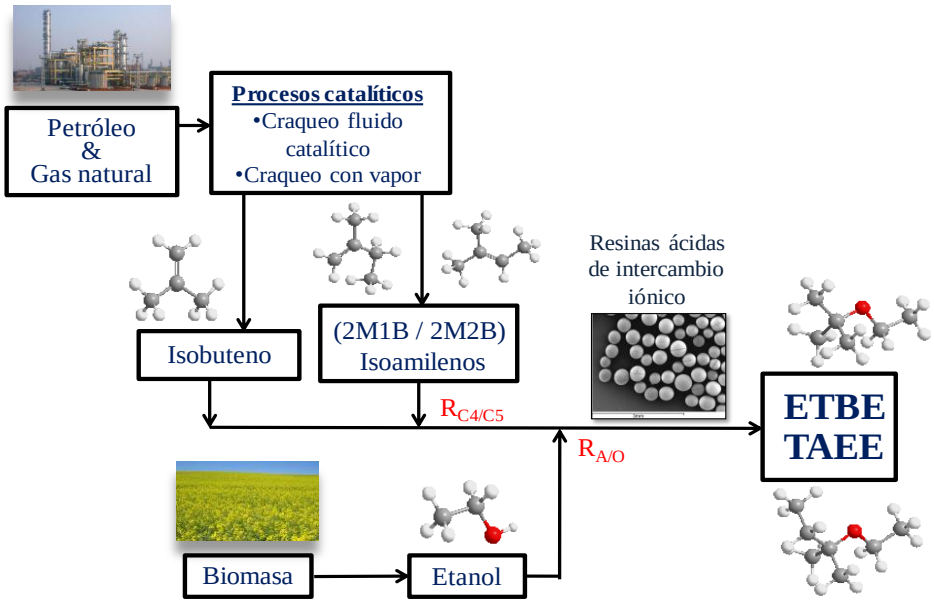

Figura 8.3. Representación esquemática de una posible ruta industrial para la producción simultánea de ETBE y TAEE.$R_{A/O}$= razón molar entre alcohol y olefinas. $R_{C4/C5}$=razón molar entre IB y IA.

8.1.4 RESINAS DE POLIESTIRENO-DIVINILBENCENO COMO CATALIZADOR

Las resinas de intercambio iónico (IER por sus siglas en inglés) son materiales orgánicos sólidos compuestos por una matriz polimérica que conforma una estructura tridimensional porosa de carácter hidrofóbico en la que los grupos funcionales son anclados o soportados. Uno de los tipos más comunes de IER son las resinas de poliestireno-divinilbenceno (PS-DVB). Este tipo de resinas se sintetizan por la copolimerización de estireno y divinilbenceno, siendo este último el agente de entrecruzamiento. Es una reacción exotérmica que tiene lugar en suspensión acuosa dónde los monómeros mezclados (inmiscibles) se dispersan como gotas esféricas a través del medio de reacción resultando en la formación de partículas esféricas individuales [68]. Dependiendo de la aplicación prevista, los grupos funcionales que finalmente se añaden a la matriz polimérica y que otorgan actividad catalítica pueden ser de carácter ácido, básico, redox o incluso complejos metálicos [69]. Las IER se funcionalizan típicamente con ácido sulfúrico entre 90 y 140 °C. Los grupos sulfónicos (–SO_3H) resultan ser los grupos funcionales incorporados a la matriz de la resina. La Figura 8.4 ilustra la síntesis de este tipo de catalizadores y su estructura final.

Existen dos grandes tipos de IER, las resinas macroporosas o macroreticulares y las resinas microporosas o tipo gel. Las primeras consisten en largos aglomerados de micropartículas tipo gel, que se adhieren juntas formando porosidad permanente (macro y mesoporos). Las segundas son una celda cerrada, habitualmente llamada fase gel en la que no hay porosidad permanente a parte de los microporos que tienen lugar entre cadenas de polímero [71]. El porcentaje de agente de entrecruzamiento usado en la copolimerización determina que finalmente la resina sea de uno u otro tipo. Este tipo de catalizadores no exhiben un único tamaño de poro, sino que se obtiene una distribución de tamaños de poro que puede determinarse mediante algunas técnicas analíticas como la adsorción-desorción de N_2 a 77 K (método BET).

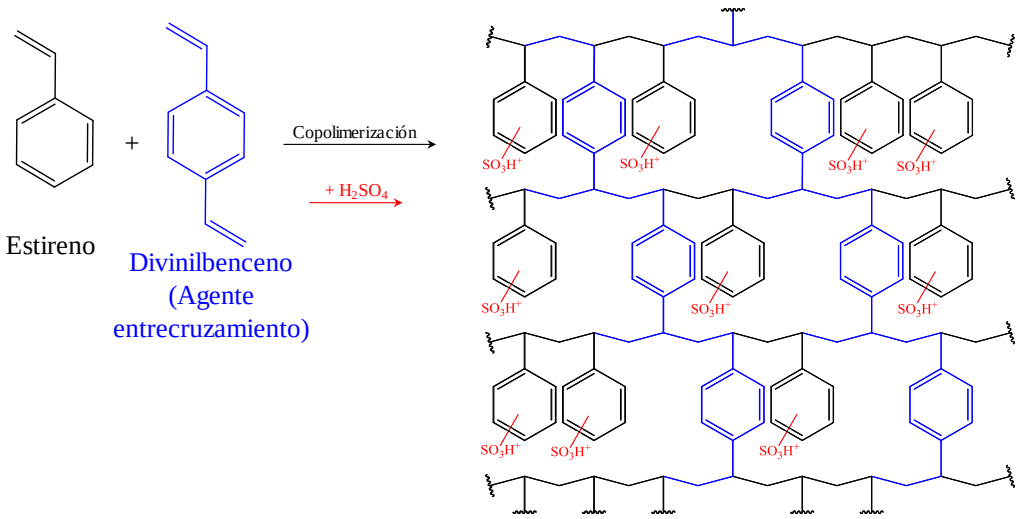

Figura 8.4. Representación esquemática de la síntesis y estructura final de las resinas ácidas de intercambio iónico PS-DVB.

Son muchas las propiedades de las IER que se pueden determinar mediante diferentes técnicas analíticas y que, en mayor o menor medida, determinan su comportamiento catalítico y morfología interna [74]. Entre todas ellas, se pueden destacar las siguientes:

- **Grado de funcionalización.** Representa el porcentaje de anillos aromáticos funcionalizados.

- **Capacidad de intercambio iónico.** Se define como el número de grupos funcionales que la resina es capaz de introducir en reacciones de intercambio iónico. Habitualmente se mide como meq[H^+] por unidad de masa y se puede determinar mediante valoración frente a una base standard [74].

- **Grado de entrecruzamiento.** Indica el porcentaje en peso de agente de entrecruzamiento con respecto al peso total de monómeros. Generalmente, la rigidez y resistencia mecánica de una resina aumentan con el grado de entrecruzamiento.

- **Grado de hinchamiento.** Como es bien sabido, las resinas de intercambio iónico se hinchan en presencia de disolventes polares como son el agua y los alcoholes primarios. A causa del hinchamiento las propiedades morfológicas se ven seriamente afectadas. La tendencia de una resina a hincharse está relacionada con la naturaleza y cantidad de grupos funcionales, grado de entrecruzamiento, la temperatura y la naturaleza química del solvente en el que se encuentran inmersas [77]. El grado de hinchamiento y cómo este afecta a las propiedades morfológicas de la resina se pueden determinar mediante la técnica de cromatografía inversa por exclusión estérica (ISEC).

- **Área superficial o específica (S_g).** Es el área superficial total (externa más poros) de la partícula por unidad de masa. Se suele determinar en condiciones de polímero seco mediante adsorción-desorción de N_2 a 77K.

- **Estabilidad.** Se diferencian la estabilidad química, térmica y mecánica del sólido. Un buen catalizador ha de contar con todas ellas antes de ser utilizado industrialmente.

- **Volumen de poros (V_g) y distribución.** Es el volumen total de poros por gramo de sólido. En cuanto a la distribución, en función del diámetro de poro (d_{pore}) se distinguen: micro (< 2 nm), meso (2 nm < dpore < 50 nm) y macroporos (> 50 nm).

- **Porosidad (θ).** Está relacionada con los huecos que quedan entre las cadenas de polímero que forman la resina.

- **Densidad o densidad de esqueleto (ρ_p).** Se define como el peso de resina seca por unidad de volumen y se puede determinar en un picnómetro de Helio. La densidad de esqueleto solo considera el volumen ocupado por el sólido y no los poros.

- **Diámetro de partícula.** Cuando se sintetizan IER se obtiene una distribución de tamaños de partícula, normalmente de tipo Gaussiana. Se puede determinar mediante difracción de rayos láser en diferentes medios.

- **Contenido de humedad.** A causa de la naturaleza hidrofílica de los grupos funcionales, las resinas tienden a atrapar agua en su estructura. Se define como el porcentaje de agua en el peso total de una resina hidratada.

Dentro de las principales aplicaciones de las resinas de intercambio iónico como catalizadores destacan la oligomerización de olefinas C_3-C_8 [38], deshidratación de alcoholes para producir éteres simétricos [76,83–85], eterificación de olefinas terciarias con alcoholes primarios [20,86–90], hidratación de olefinas terciarias para formar alcoholes terciarios [91,92], formación de alquil fenoles mediante alquilación de fenoles y reacciones de condensación, por ejemplo la formación de bisfenol A partir de fenol y acetona, reacciones de esterificación entre ácidos y alcoholes, hidrólisis de éteres y ésteres, síntesis de hidroximetilfurfural (HMF), producción de metil isobutil cetona (MIBK), síntesis de tetrahidrofurano (THF), reacciones del silvano con aldehídos y cómo soportes para enzimas.

8.1.5 DESACTIVACIÓN DE RESINAS ÁCIDAS DE INTERCAMBIO IÓNICO

La desactivación de catalizadores o su tiempo de vida útil es, después de la selectividad, la característica más importante para un proceso dado. Desactivación puede definirse como la disminución de la concentración sitios activos accesibles para reacción. El cambio de catalizador en procesos industriales implica, en la mayor parte de ocasiones, la parada de la planta, lo que aumenta los costes de operación [115,116]. A pesar de la vital importancia de este campo de estudio, la mayoría de estudios en catálisis heterogénea carecen del estudio de las causas y mecanismos de desactivación de los catalizadores empleados.

Existen varios tipos de desactivación que pueden afectar a una resina ácida de intercambio iónico. Entre los más importantes, destacan: la sinterización, la desulfonación, estrés térmico, decrosslinking de la matriz, desactivación por deposición y la desactivación por envenenamiento. El envenenamiento o neutralización de los centros ácidos de una resina a causa de la presencia de impurezas de tipo básico en las corrientes de alimento a reactores industriales es el tipo de desactivación que afecta con más frecuencia y en mayor magnitud a los reactores de eterificación en las plantas de ETBE y MTBE actuales.

Dentro de los diferentes mecanismos de neutralización, se distinguen la neutralización de tipo flujo en pistón y la neutralización de tipo difuso. La primera tiene lugar cuando un catión básico fuerte como el sodio reacciona con los grupos sulfónicos del catalizador. Este tipo de neutralización comienza en la entrada del reactor y avanza lentamente a lo largo de toda la longitud del lecho [115,116]. A medida que la desactivación progresa, la neutralización en flujo en pistón resulta en un acortamiento del lecho catalítico activo. La neutralización difusa tiene lugar cuando un compuesto básico débil como una amida alcanza el lecho catalítico. Estos compuestos básicos débiles no neutralizan directamente, sino que van reaccionando con los grupos sulfónicos, desactivándolos uniformemente a lo largo de toda la longitud de lecho catalítico. Ejemplos de neutralizazores de tipo flujo en pistón son sales, aminas y otras bases de Lewis y Brønsted. La Figura 8.5 ilustra el comportamiento de un reactor catalítico para ambos casos de neutralización. Ejemplos de neutralizadores de tipo difuso son el acetonitrilo (ACN), propionitrilo (PPN) y otros nitrilos, dimetilformamida, dimetilsulfóxido y el sulfuro de hidrógeno (H_2S).

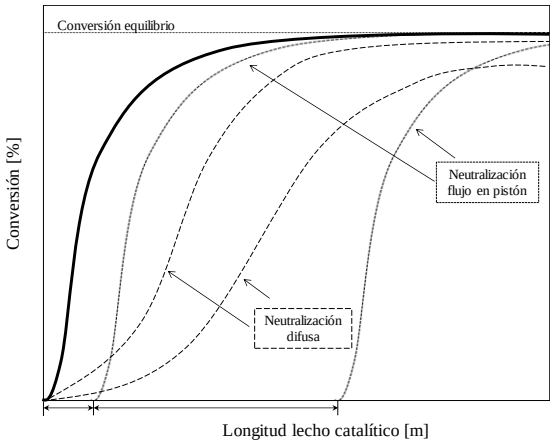

Figure 8.5. Funcionamiento de un reactor tubular afectado por neutralización de tipo flujo en pistón (⋯) o tipo difusa (---). Comportamiento de un reactor ideal sin desactivación (**—**). Adaptado de [117].

El más importante de los desactivantes anteriormente descritos y que afecta a las plantas de producción de ETBE y MTBE es el ACN. Las concentraciones típicas de ACN en las corrientes de hidrocarburos provenientes de FCC llega hasta las 2.000 ppm [116]. Con respecto a las plantas de producción de TAME, el PPN es el neutralizador más prominente [48]. Debido al efecto detrimental del ACN en las plantas de eterificación, la desactivación de resinas ácidas causada por esta base débil ha sido estudiada previamente [117–119]. En el mecanismo de desactivación por ACN el primer paso es la adsorción de esta base débil de forma difusa a lo largo del lecho catalítico. El segundo paso es la reacción del ACN adsorbido con agua, alcohol o un ión carbonio mediante alguno de los siguientes mecanismos [115,116].

a) **Hidrólisis directa.** El ACN adsorbido reacciona con agua para formar una amida que, a su vez, reacciona con otra molécula de agua para formar ácido acético y amoníaco, que finalmente neutraliza los grupos sulfónicos.

b) **Alcohólisis seguida de hidrólisis.** El ACN adsorbido reacciona con una molécula de alcohol (Pinner síntesis) para formar un intermedio inestable, una sal de imido éster, que a su vez sufre hidrólisis con una molécula de agua para formar el correspondiente alquil acetato y amoníaco, que neutraliza los centros ácidos.

c) **Reacción de Ritter.** El ACN adsorbido reacciona con un ión carbonio para formar otras aminas que neutralizan los centros activos mediante el mecanismo flujo en pistón.

8.1.6 FUNDAMENTOS DE CATÁLISIS HETEROGÉNEA

El tipo más común de catálisis heterogénea es aquel en el que los reactantes en fase fluida, gas o líquida, se ponen en contacto con un catalizador sólido. La Figura 8.6 ilustra uno de los modelos físicos más utilizados en el que se pueden distinguir las siguientes etapas:

I) Transferencia externa de materia (TEM) de los reactantes desde la fase fluida a la superficie externa del catalizador a través de la película externa.
II) Transferencia interna de materia (TIM) o difusión de los reactantes a través de los poros del catalizador.
III) Adsorción de los reactantes en los centros activos.
IV) Reacción química entre las especies adsorbidas o entre las especies adsorbidas y aquellas de la fase fluida. Los productos de reacción adsorbidos se obtienen en esta etapa.
V) Desorción de los productos de reacción.
VI) TIM o difusión de los productos a través de los poros del catalizador hasta la superficie externa del mismo.
VII) TEM de los productos desde la superficie externa del catalizador hacía la fase fluida a través de la película externa.

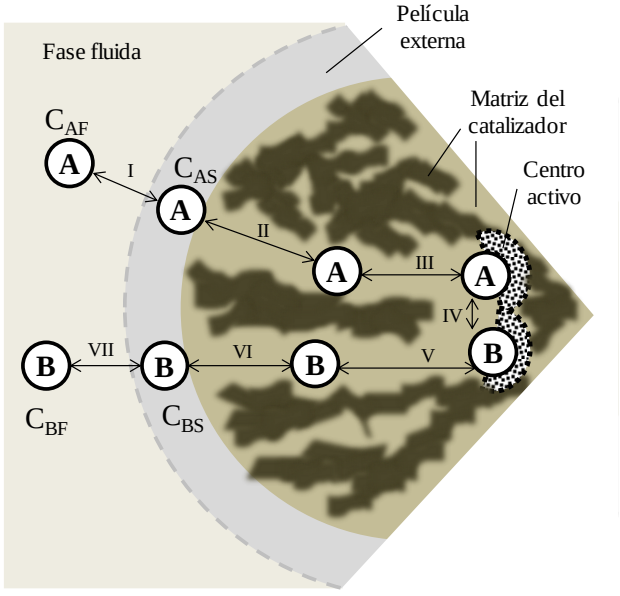

Figure 8.6. Etapas del proceso catalítico heterogéneo para la reacción A ⇄ B en un sólido poroso.

En el modelo descrito las etapas III, IV y V son de naturaleza química, mientras las etapas I, II, VI y VII son de naturaleza física e incluyen los efectos de las TEM y TIM. En un modelo cinético propuesto, tiene que considerarse que las etapas I, III, IV, V y VII tienen lugar en serie mientras que las etapas II y VI tienen lugar en serie-paralelo con las anteriores.

Con respecto a la adsorción y desorción de reactantes, este es un fenómeno complejo. El proceso de adsorción puede definirse como como el incremento en la concentración de una

sustancia en la interfaz de un condensado y una capa líquida o gaseosa debido a la operación de las fuerzas de superficie (IUPAC). Es por tanto un fenómeno de superficie y crea una película de adsorbato en la superficie del adsorbente. La adsorción puede ser física o química. La adsorción física implica fuerzas intermoleculares débiles, mientras que la quimisorción implica la formación de enlaces entre la molécula de adsorbato y la superficie del catalizador [62]. Ambos procesos son de naturaleza exotérmica y aunque las definiciones previas son útiles desde un punto de vista conceptual, en ocasiones es difícil diferenciar inequívocamente qué tipo de adsorción tiene lugar. La Tabla 8.2 resume algunas de las principales características de ambos procesos.

Tabla 8.2. Características específicas de los diferentes tipos de adsorción.

Adsorción física	Quimisorción
• Bajo calor de adsorción (<2 o 3 veces el calor latente de vaporización)	• Alto calor de adsorción (>2 o 3 veces el calor latente de vaporización)
• No específica	• Altamente específica
• Monocapa o multicapa	• Monocapa únicamente
• No disociación de las especies adsorbidas	• Puede implicar disociación
• Sólo significativa a temperaturas relativamente bajas	• Posible en un amplio rango de temperaturas
• Rápida, no-activada, reversible	• Activada, puede ser lenta e irreversible
• No hay transferencia de electrones aunque puede haber polarización del adsorbato	• Con transferencia de electrones que lleva a la formación de enlaces entre adsorbato y adsorbente

Con respecto a las etapas de transferencia de materia (TEM y TIM), habitualmente un modelo cinético propuesto suele determinarse en condiciones en las que estas etapas no sean las controlantes de la velocidad de reacción. En la película externa que rodea a la partícula de catalizador tienen lugar perfiles de concentración y de temperatura. Estos perfiles deben considerarse cuando se diseñan reactores catalíticos. De forma análoga, mientras que la reacción química tiene lugar en los sitios activos, la difusión de reactantes y productos también afecta a la velocidad de reacción observada a causa del fenómeno conocido como TIM. El estudio del efecto de la TEM depende del tipo de reactor considerado. Considerando un reactor discontinuo tanque agitado, los efectos son inversamente proporcionales a la velocidad de agitación. Si se considera un reactor de lecho fijo, los efectos de la TEM en la velocidad de reacción observada se reducen a medida que la velocidad espacial aumenta. Con respecto al estudio de la TIM, se acepta, generalmente, que los posibles efectos derivados disminuyen a medida que disminuye el tamaño de partícula del catalizador sólido. Los procesos catalizados por resinas ácidas de intercambio iónico en tamaño de partícula comercial suelen ser un ejemplo de reacciones en las que la influencia de la TIM es considerable.

Finalmente, con respecto a la etapa de reacción química, es habitualmente considerada como la etapa controlante de la velocidad de reacción. La cinética de formación de éteres terciarios sobre resinas ácidas de intercambio iónico se ha modelado generalmente utilizando los mecanismos clásicos de catálisis heterogénea descritos por Langmuir-Hinshelwood-Hougen-Watson (LHHW) y Eley-Rideal (ER). En un mecanismo del tipo LHHW, todos los reactantes se adsorben en los centros activos y reaccionan entre ellos para producir los productos de reacción adsorbidos. En un mecanismo del tipo ER, al menos uno de los reactantes se adsorbe en los centros activos del catalizador y reacciona con una molécula presente en la fase fluida para formar el producto de reacción adsorbido.

8.1.7 ESTADO DEL ARTE EN LAS SÍNTESIS DE ETBE Y TAEE

Hasta el momento, numerosos estudios se han centrado en la eterificación de alquenos terciarios con alcoholes [21,88,96,120]. Con respecto al ETBE y al TAEE se han realizado numerosos avances en sus síntesis aisladas con respecto a la distribución de productos, el efecto del agua en el sistema de reacción, relaciones entre actividad y propiedades del catalizador empleado, la termodinámica y cinética de las reacciones implicadas y, en menor medida, sobre el efecto desactivante de compuestos básicos en la síntesis de ETBE. No obstante, es difícil encontrar información concerniente a las conversiones de equilibrio en estos sistemas. Se ha estudiado el efecto del agua en ambos sistemas concluyendo que el agua favorece la formación de alcoholes terciarios y afecta a las reacciones de eterificación como un inhibidor. Con respecto a la distribución de productos, un exceso de alcohol en la mezcla inicial puede promover la formación de dietil éter a altas temperaturas. Por el contrario, un exceso de olefinas en la mezcla inicial puede dar lugar a la formación de dímeros. Con respecto a la termodinámica, se ha determinado que las reacciones implicadas son todas exotérmicas y las constantes de equilibrio de las mismas se pueden encontrar en la literatura [22,89,91,121,122,127,129,135–138].

Con respecto a la cinética de las reacciones implicadas, Fité el. [123], sugirió un mecanismo ER para la síntesis de ETBE a partir de IB y EtOH. Françoisse y Thyrion [139] propusieron un cambio de mecanismo dependiendo de la concentración inicial de EtOH en la síntesis de ETBE. Linnekoski y Krause [131] propusieron un mecanismo del tipo LHHW en la síntesis de TAEE a partir de IA y EtOH. Además, se han logrado progresos en referencia a la influencia del medio de reacción en la cinética, determinación de constantes de equilibrio de adsorción y funciones de estado termodinámicas del proceso de adsorción. Las Tablas 8.3, 8.4 y 8.5 resumen los principales modelos cinéticos propuestos hasta el momento.

Tabla 8.3. Modelos cinéticos publicados para la síntesis de ETBE.

Referencia	Ecuación	Catalizador
Françoisse y Thyrion (1991) [139]	$r_{\mathrm{ETBE}} = k\left[c_{\mathrm{IB}} - \alpha\frac{c_{\mathrm{ETBE}}}{c_{\mathrm{EtOH}}} + \frac{\beta\left(c_{\mathrm{IB}}c_{\mathrm{EtOH}} - \alpha c_{\mathrm{ETBE}}\right)}{c_{\mathrm{IB}} + Fc_{\mathrm{EtOH}}^2 + c_{\mathrm{ETBE}}}\right]$	Amberlyst™15
Fité & col. (1994)[123]	$r_{\mathrm{ETBE}} = k\left(\frac{a_{\mathrm{IB}}a_{\mathrm{EtOH}} - a_{\mathrm{ETBE}}/K}{a_{\mathrm{EtOH}}^3}\right)$	Lewatit K2631
Sundmacher & col. (1995)[146]	$r_{\mathrm{ETBE}} = k\left(\frac{a_{\mathrm{IB}}}{a_{\mathrm{EtOH}}} - \frac{1}{K_a}\frac{a_{\mathrm{ETBE}}}{a_{\mathrm{EtOH}}^2}\right)$	Amberlyst™15
Jensen y Datta [147]	$r_{\mathrm{ETBE}} = k\frac{a_{\mathrm{EtOH}}^2\left[a_{\mathrm{IB}} - a_{\mathrm{ETBE}}/(Ka_{\mathrm{EtOH}})\right]}{\left(1 + K_{\mathrm{EtOH}}a_{\mathrm{EtOH}}\right)^3}$	Amberlyst™15
Solà & col. (1995)[148]	$r_{\mathrm{ETBE}} = k\left(\frac{a_{\mathrm{IB}}a_{\mathrm{EtOH}} - a_{\mathrm{ETBE}}/K}{a_{\mathrm{EtOH}}^2}\right)$	Lewatit K2631
González (2011) [49]	$r_{\mathrm{ETBE}} = \frac{k\left(a_{\mathrm{IB}}a_{\mathrm{EtOH}} - a_{\mathrm{ETBE}}/K\right)\exp\left(\frac{\overline{V}_{\mathrm{M}}\phi_P^2}{RT}\left(\delta_{\mathrm{M}} - \delta_{\mathrm{P}}\right)\right)}{\left(a_{\mathrm{H2O}} + K_{\mathrm{IB}}a_{\mathrm{IB}} + K_{\mathrm{ETBE}}a_{\mathrm{ETBE}} + K_{\text{1-butene}}a_{\text{1-butene}}\right)^2}$	Amberlyst™35
Badia (2016) [34]	$r_{\mathrm{ETBE}} = \frac{k\left(a_{\mathrm{IB}}a_{\mathrm{EtOH}} - a_{\mathrm{ETBE}}/K\right)\exp\left(\frac{\overline{V}_{\mathrm{M}}\phi_P^2}{RT}\left(\delta_{\mathrm{M}} - \delta_{\mathrm{P}}\right)^2\right)}{\left(a_{\mathrm{EtOH}} + K_{\mathrm{BuOH}}a_{\mathrm{BuOH}} + K_{\mathrm{ETBE}}a_{\mathrm{ETBE}}\right)}$	Amberlyst™35

Tabla 8.4. Modelos cinéticos publicados para la síntesis de TAEE.

Referencia	Ecuación	Catalizador
Zhang & col. (1997) [141]	$r_{\mathrm{TAEE}} = k\,\frac{a_{\mathrm{EtOH}}^2\left[a_{iC5} - a_{\mathrm{TAEE}}/(Ka_{\mathrm{EtOH}})\right]}{\left(1+K_{\mathrm{EtOH}}a_{\mathrm{EtOH}}\right)^3}$	Amberlyst™15
Linnekoski & col. (1997) [131]	$r_{\mathrm{TAEE}} = \frac{k_1^{'}\left(a_{\mathrm{EtOH}}a_{\mathrm{2M1B}} - a_{\mathrm{TAEE}}/K_{e1}\right)}{\left(1+K_{\mathrm{EtOH}}a_{\mathrm{EtOH}}\right)^2} + \frac{k_3^{'}\left(a_{\mathrm{EtOH}}a_{\mathrm{2M2B}} - a_{\mathrm{TAEE}}/K_{e2}\right)}{\left(1+K_{\mathrm{EtOH}}a_{\mathrm{EtOH}}\right)^2}$	Amberlyst™16
Linnekoski & col. (1998) [91]	$r_{\mathrm{TAEE}} = \frac{k^{'}\left(a_{\mathrm{olef}}a_{\mathrm{EtOH}} - a_{\mathrm{TAEE}}/K_{e\mathrm{TAEE}}\right)}{\left(1+K_{\mathrm{EtOH}}a_{\mathrm{EtOH}} + K_{\mathrm{water}}a_{\mathrm{water}} + K_{\mathrm{TAOH}}a_{\mathrm{TAOH}} + K_{\mathrm{TAEE}}a_{\mathrm{TAEE}} + K_{\mathrm{olef}}a_{\mathrm{olef}}\right)^2}$	Amberlyst™16
Linnekoski & col. (1999) [136]	$r_{\mathrm{TAEE}} = \frac{k_1^{'}\left(a_{\mathrm{EtOH}}a_{\mathrm{2M1B}} - a_{\mathrm{TAEE}}/K_{e1}\right)}{\left(K_0^{'}\left(a_{\mathrm{2M2B}}+a_{\mathrm{2M1B}}\right)+a_{\mathrm{TAEE}}\right)\left(1+K_{\mathrm{EtOH}}a_{\mathrm{EtOH}}\right)} + \frac{k_3^{'}\left(a_{\mathrm{EtOH}}a_{\mathrm{2M2B}} - a_{\mathrm{TAEE}}/K_{e2}\right)}{\left(K_0^{'}\left(a_{\mathrm{2M2B}}+a_{\mathrm{2M1B}}\right)+a_{\mathrm{TAEE}}\right)\left(1+K_{\mathrm{EtOH}}a_{\mathrm{EtOH}}\right)}$	Amberlyst™16
Oktar & col. (1999)[124]	$r_{\mathrm{TAEE}} = 17.34\exp\left(-\frac{4899}{T}\right)C_{\mathrm{2M1B}}^{0.93} + 5.6\cdot10^5\exp\left(-\frac{8850}{T}\right)C_{\mathrm{2M2B}}^{0.69}$ [molg^{-1}s^{-1}]	Amberlyst™15
Bozga & col. (2008)[145]	$r_{\mathrm{TAEE}} = \frac{k\left(a_{\mathrm{EtOH}}a_{\mathrm{IA}} - a_{\mathrm{TAEE}}/K\right)}{\left(1+K_{\mathrm{EtOH}}a_{\mathrm{EtOH}}\right)^2}$	Amberlyst™35

Tabla 8.5. Modelos cinéticos publicados para la reacción de isomerización de doble enlace entre IA.

Referencia	Ecuación	Catalizador
Zhang & col. (1997)[141]	$r_{\mathrm{ISOM}} = \frac{\left(a_{\mathrm{2M1B}} - a_{\mathrm{2M2B}}/K_3\right)}{\left(1+K_{\mathrm{EtOH}}a_{\mathrm{EtOH}}\right)^2}$	Amberlyst™15
Linnekoski & col. (1997) [131]	$r_{\mathrm{2M1B}} = -\frac{k_1^{'}\left(a_{\mathrm{EtOH}}a_{\mathrm{2M1B}} - a_{\mathrm{TAEE}}/K_{e1}\right)}{\left(1+K_{\mathrm{EtOH}}a_{\mathrm{EtOH}}\right)^2} - \frac{k_5^{'}\left(a_{\mathrm{2M1B}} - a_{\mathrm{2M2B}}/K_{e3}\right)}{\left(1+K_{\mathrm{EtOH}}a_{\mathrm{EtOH}}\right)}$	Amberlyst™16
Linnekoski & col. (1999) [136]	$r_{\mathrm{ISOM}} = \frac{k_5^{'}\left(a_{\mathrm{2M1B}} - a_{\mathrm{2M2B}}/K_{e3}\right)}{\left(K_0^{'}\left(a_{\mathrm{2M2B}}+a_{\mathrm{2M1B}}\right)+a_{\mathrm{TAEE}}\right)}$	Amberlyst™16

En las últimas décadas, nuevos procesos de producción simultánea de varios éteres están siendo considerados y podrían ser una realidad industrial en un futuro no muy lejano. Entre ellos, la síntesis simultánea de ETBE y TAEE es una de las alternativas más interesantes, como ya se ha mencionado en la *Sección 8.1.3*. Sin embargo, hay una carencia de estudios relativos a la distribución de productos, el efecto del agua en el sistema de reacción, los posibles modelos cinéticos que describen el sistema simultaneo, los catalizadores más apropiados, el efecto de agente desactivadores en las corrientes de alimento y sobre la termodinámica del proceso de adsorción de las especies implicadas. La presente tesis doctoral tiene como objetivo elucidar información en estos aspectos a la vez que estudiar la viabilidad del proceso simultáneo.

8.2 EXPERIMENTAL

8.2.1 CATALIZADORES

La Tabla 8.6 resume las principales propiedades físicas de los catalizadores utilizados en los experimentos de las diferentes secciones de la presente tesis. Todos los catalizadores son resinas ácidas de intercambio iónico. En concreto: Amberlyst™15 (A-15), Amberlyst™16 (A-16), Amberlyst™35 (A-35), Amberlyst™36 (A-36), Amberlyst™39 (A-39), Amberlyst™40 (A-40), Amberlyst™45 (A-45), Amberlyst™46 (A-46), Amberlyst™48 (A-48), Amberlyst™DT (A-DT), Purolite®CT-124 (CT-124), Purolite®CT-175 (CT-175), Purolite®CT-275 (CT-275), Purolite®CT-482 (CT-482) and Purolite®MN-500 (MN-500).

Tabla 8.6. Principales propiedades físicas de los catalizadores evaluados.

Catalizador	Tipo	Capacidad ácida [eq $H^+ \cdot kg^{-1}$] [a]	DVB [%][b]	Diámetro de partícula, d_b [mm][c]	Humedad [%]	Max. T. de operación [°C]	Tipo de sulfonación[d]
A-15	macro	4,81	20	0,74	50	120	C
A-16	macro	4,80	12	0,6–0,85	52–57	120	C
A-35	macro	5,36	20	0,51	55	150	O
A-36	macro	5,40	15	0,63	55	150	O
A-39	macro	4,81	8	0,54	60–66	130	C
A-40	macro	5,20	alto	0,58–0,80	44–53	140	O
A-45	macro	3,65	medio	0,58–0,75	49–54	170	S/Cl
A-46	macro	0,87	alto	0,78	26–36	120	S
A-48	macro	5,62	alto	0,95	49–56	–	O
A-DT	macro	3,94	medio	0,58–0,75	49–54	170	S/Cl
CT-482	macro	3,65	bajo	0,81	48–58	190	S/Cl
CT-124	micro	5,00	4	0,77	63	130	C
CT-175	macro	4,98	alto	0,94	55	145	C
CT-275	macro	5,37	alto	0,75	55	145	O
MN-500	macro	2,70	hiper	0,5–1	52–57	130	S

[a] Valoración frente a base estándar. [b] Clasificación del grado de entrecruzamiento: bajo (7-12%); medio (12-17%); alto (17-25%); hiper (50%). [c] Determinado por difracción de láser en aire (Beckman Coulter LS particle size analyzer) o valores del fabricante (rango). [d] Convencionalmente sulfonadas (C), sobresulfonadas (O), sulfonadas en superficie (S) y, sulfonada/clorada (S/Cl).

Con el objetivo de eliminar al máximo la humedad inicial de los catalizadores y evitar así la entrada al sistema de reacción de cantidades no controladas de agua, todos los catalizadores fueron pretratados antes de los experimentos siguiendo el mismo protocolo experimental. En primer lugar, se secaron durante 3h en una estufa a presión atmosférica a 383 K y posteriormente durante 15 h en una estufa de vacío a 383 K. El contenido residual de agua tras este pretratamiento se midió por valoración Karl Fisher para varias muestras de A-35 con un resultado medio de menos de 3,5 % $g_{agua} \cdot g_{cata}^{-1}$. Se asumió que el contenido de humedad para el resto de resinas fue del mismo orden de magnitud.

Cuando la dilución del lecho catalítico fue necesaria para asegurar el régimen diferencial de operación en el reactor de lecho fijo, es decir, para obtener un lecho isotermo y conversiones inferiores al 10 %, se utilizó carburo de silicio en tamaño de partícula similar al de los catalizadores empleados. Ya se ha demostrado anteriormente que el carburo de silicio es inerte en las reacciones de eterificación [19].

8.2.2 INSTALACIONES EXPERIMENTALES UTILIZADAS

Los experimentos referidos en las *Secciones 4.2−4.7* fueron realizados en la instalación experimental representada en la Figura 8.7 y que se compone principalmente del sistema de inyección de reactantes, el reactor, el baño termostático y el sistema de análisis. El reactor discontinuo de tanque agitado (200 mL) está equipado con un agitador magnético de seis palas y fue operado en modo isotermo. Una salida del reactor está directamente conectada al sistema de análisis, el cual está compuesto por un cromatógrafo de gases acoplado a un detector selectivo de masas. Una descripción más detallada se puede encontrar en [125].

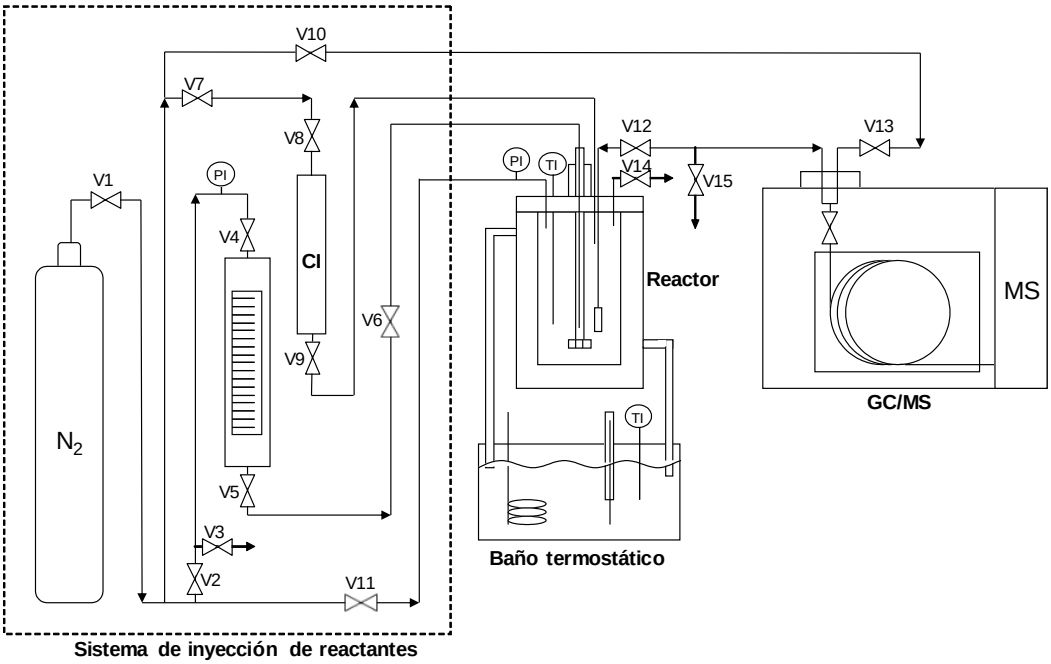

Figure 8.7. Esquema detallado de la instalación experimental. V1-V15: Válvulas. GC/MS: Cromatógrafo de gases / Espectrómetro de masas. CI: Inyector de catalizador. PI: Indicador de presión (Manómetro). TI: Indicador de temperatura (NiCr/NiAl Termopar).

Los experimentos correspondientes a la *Sección 4.9* se realizaron en un reactor de lecho fijo (Process Integral Development Eng&Tech S.L., Madrid, Spain), ver Figura 8.8. El reactor de acero inoxidable (180 mm x 16.5 mm i.d) se emplaza dentro de una camisa térmica eléctrica y cuenta con un termopar en el lecho para el control de la temperatura. Las tuberías situadas después de las bombas HPLC de inyección de reactantes y el reactor están también emplazados dentro de un habitáculo aislado (Hot box) que cuenta con un horno de convección forzada para controlar la temperatura. La salida del reactor está conectada a un cromatógrafo de gases. El sistema está equipado con un control de tipo PID que permite monitorizar y controlar las temperaturas, presión y flujo de las bombas en cada momento. Los parámetros de control utilizados para alcanzar el estado estacionario se muestran en la Tabla 8.7.

Tabla 8.7. Valor de los parámetros para el controlador PID.

Parámetro de control	Banda proporcional [%] (P)	Tiempo integral [s] (I)	Tiempo derivative [s] (D)
Presión sistema	50	50	0
Temperatura reactor	60	400	60
Temperatura Hot Box	16	120	20

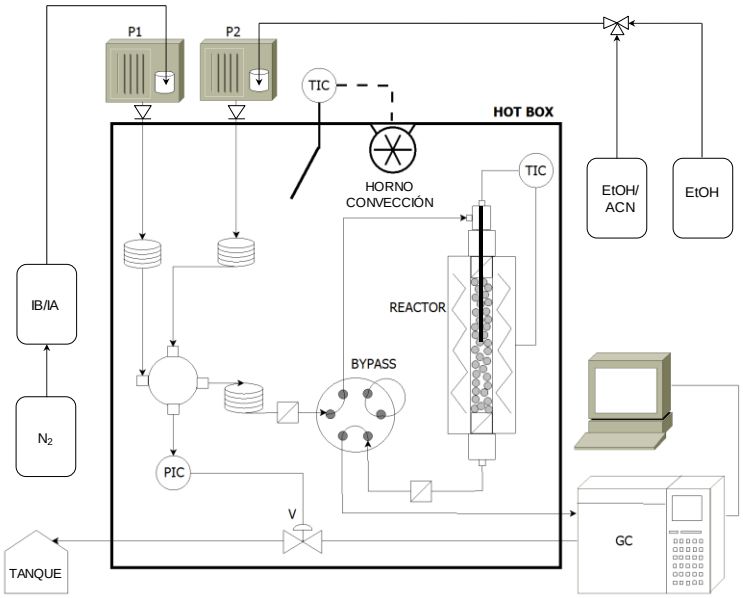

Figure 8.8. Instalación experimental usada en los experimentos de desactivación. P1-P2: Bombas HPLC. TIC: Indicador y controlador de temperatura. PIC: Indicador y controlador de presión. GC: Cromatógrafo de gases.

Con respecto a los experimentos de adsorción de la *Sección 4.8*, se realizaron en instalaciones experimentales análogas a las descritas en Doğu & col. [221] para fase líquida y en Oktar & col. [65] para fase gas.

Además de las instalaciones descritas, se utilizaron las siguientes técnicas y aparatos auxiliares: adsorción-desorción de N_2 a 77 K, porosimetría por intrusión de mercurio, cromatografía inversa por exclusión de tamaño (ISEC), microscopía electrónica de barrido (SEM), análisis termogravimétrico (TGA), espectroscopía infrarroja por transformada de Fourier (FTIR), picnómetro de Helio, difracción de laser en aire, columnas de destilación, Karl Fisher, y estufas.

8.2.3 CÁLCULOS

En todos los experimentos, la conversión de reactantes, selectividad y rendimiento se calcularon mediante las ecuaciones 8.1–8.3. La velocidad de formación de un compuesto se calculó mediante la expresión 8.4 en el caso de un reactor discontinuo y mediante la ecuación 8.5 para el reactor de lecho fijo.

$$X_j = \frac{\text{moles de } j \text{ reaccionados}}{\text{moles iniciales de } j} \tag{8.1}$$

$$S_j^k = \frac{\text{moles de } k \text{ producidos}}{\text{moles de } j \text{ reaccionados}} \tag{8.2}$$

$$Y_j^k = X_j \cdot S_j^k \tag{8.3}$$

$$r_k^t = \frac{1}{W_{cat}} \left[\frac{dn_k}{dt} \right]_{t=t} \tag{8.4}$$

$$\mathrm{r_{éter}} = \frac{F_{\mathrm{olef}}^0 \left(X_{\mathrm{olef,entrada}} - X_{\mathrm{olef,salida}} \right)}{W_{\mathrm{cat}}} \tag{8.5}$$

8.3 RESULTADOS

8.3.1 DESCRIPCIÓN DEL SISTEMA DE REACCIÓN

Tras varios experimentos preliminares a varias temperaturas y diversas concentraciones iniciales de reactantes, se pudieron identificar por espectrometría de masas los principales compuestos que pueden formarse en el sistema de reacción partiendo de una mezcla de isoamilenos, isobuteno y etanol como reactantes. La Figura 8.9 muestra el esquema de posibles reacciones propuesto y que da lugar a la formación de todos los productos detectados.

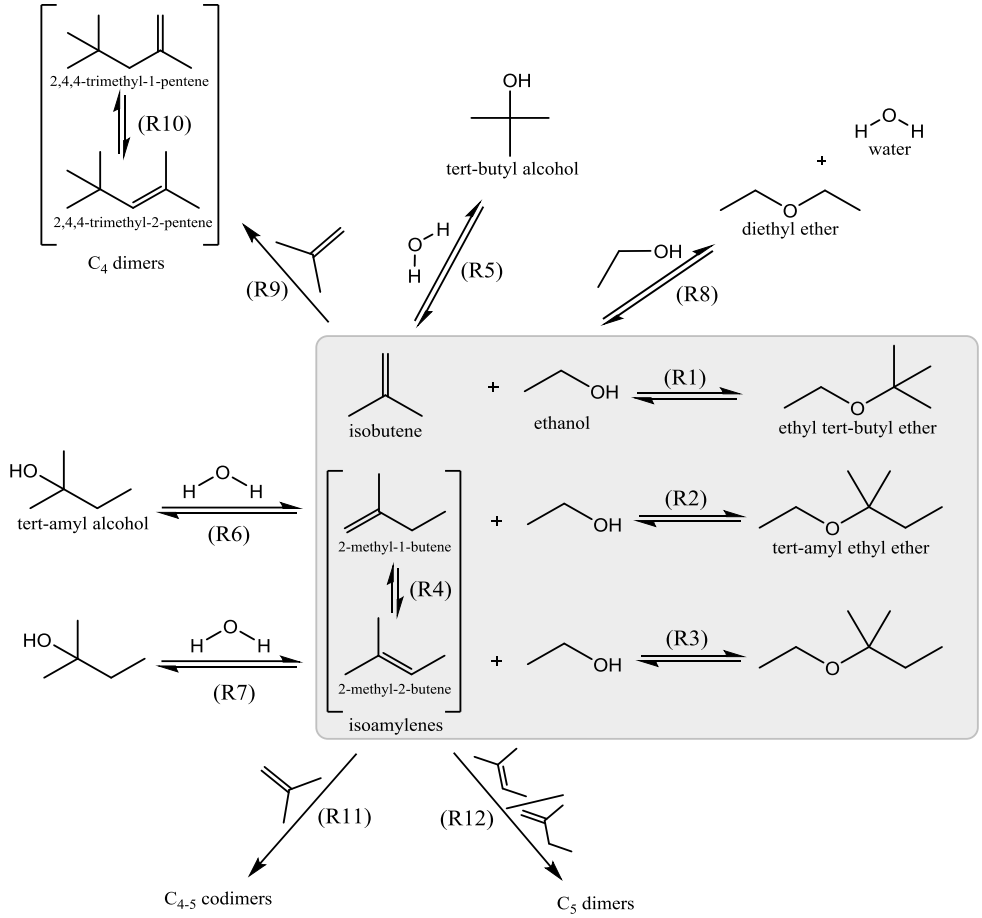

Figura 8.9. Esquema de reacción completo. El área coloreada de gris comprende las reacciones principales a través de las cuales se forman los éteres estudiados (ETBE y TAEE).

La reacción R1 es la eterificación de IB con EtOH para producir ETBE. R2 y R3 son las reacciones de eterificación de 2M1B y 2M2B con EtOH, respectivamente, que dan lugar a la formación de TAEE. La reacción R4 es la reacción de isomerización de doble enlace entre ambos isoamilenos. R5, R6 y R7 son las reacciones de hidratación de IB, 2M1B y 2M2B que dan lugar a la formación de *terc*-butil alcohol (TBA) y *terc*-amil alcohol (TAA). R9 es la reacción de dimerización de IB que produce 2,4,4-trimetil-1-penteno (TMP-1) y 2,4,4-trimetil-2-penteno (TMP-2). R10 es la reacción de isomerización entre ambos trimetilpentenos. R11 es la dimerización entre IB y IA para formar dímeros $C_{4\text{-}5}$ y R12 la dimerización entre dos moléculas de IA para formar dímeros C_5. A partir de las reacciones R11 y R12 pueden formarse una gran variedad de compuestos con 9 y 10 átomos de carbono, respectivamente.

8.3.2 GREEN METRIC ANALYSIS DEL SISTEMA DE REACCIÓN

Mediante Green Metric Análisis (GMA) se analizaron varias rutas de producción de ETBE y TAEE, así como varios dispositivos experimentales. Los parámetros evaluados en este análisis se describen a continuación. La economía atómica (AE) que mide cuantos de los átomos de los reactantes forman parte de la estructura de la molécula de producto final. El rendimiento (yield) de reactantes a productos. La eficiencia másica de la reacción (RME) que considera el rendimiento, las masas de reactantes y producto implicadas y las cantidades molares de reactantes. El factor estequiométrico (SF) que considera el uso de reactantes en exceso. El parámetro de recuperación de masa (MRP) que considera el uso de otros materiales como solventes u otros materiales usados en el lavado, purificación, etc. Todos estos parámetros están normalizados entre cero y uno. El vector de magnitud (VMR) es la suma cuadrática de los cinco parámetros anteriormente descritos. El factor medioambiental (E_{factor}) expresa la razón másica entre los residuos y el producto formados. Finalmente, la eficiencia en masa de carbono (CME) que se define como el porcentaje de carbono en los reactantes que forma parte de la molécula de producto. La Tabla 8.8 resume los valores obtenidos para los diferentes procesos evaluados separadamente para ETBE y TAEE con el objetivo de poder comprar apropiadamente.

Tabla 8.8. Resumen de los valores obtenidos en el GMA de los procesos evaluados. Todos los valores hacen referencia a la situación de no recuperación.

Caso	Plan	Catalizador	T [K]	Instalación	AE	Yield	1/SF	RME	MRP	VMR	E_{total}	CME [%]
ETBE	Este estudio	Amberlyst™35	333	Reactor discontinuo	1	0,94	0,97	0,82	0,89	0,93	0,23	92,4
	Françoisse y Thyrion. (1991) [139]	Amberlyst™15	333	Reactor discontinuo	1	0,88	1	0,40	0,46	0,79	1,51	87,6
	Vila & col. (1993) [160]	Bayer K-2431	333	Reactor discontinuo	1	0,91	0,99	0,86	0,95	0,95	0,16	90,4
	Yang y Goto. (1997) [161]	Amberlyst™15	343	Destilación reactiva y pervaporación	0,85	0,88	0,72	0,52	0,96	0,80	0,93	65,6
	Yang & col. (2000) [162]	S-54	338	Reactor discontinuo	0,85	0,52	1	0,41	0,92	0,78	1,45	52,0
	Umar & col. (2009) [163]	CT-124	343	Reactor discontinuo	0,85	0,39	0,72	0,23	0,95	0,69	3,38	29,3
TAEE	Este estudio	Amberlyst™35	333	Reactor discontinuo	1	0,53	0,97	0,47	0,90	0,81	1,13	52,4
	Rihko & col. (1994) [137]	Amberlyst™16	333	Reactor discontinuo	1	0,55	1	0,54	0,98	0,84	0,84	55,2
	Boz y Dogu. (2005) [164]	Amberlyst™15	377	Destilación reac. discontin.	1	0,50	0,24	0,12	0,99	0,68	7,44	15,2
	Boonthamtirawuti & col. (2009) [45]	Amberlyst™16	353	Reactor semicontinuo	0,87	0,31	1	0,26	0,98	0,76	2,79	31,2
	Varisli y Dogu. (2005) [165]	Amberlyst™16	383	Destilación reac. discontin.	1	0,85	0,14	0,12	1	0,74	7,45	15,6
	Aiouache y Goto. (2003) [166]	Amberlyst™15	353	Reactor discontinuo	0,87	0,22	1	0,19	0,99	0,75	4,32	21,9

Con respecto a la formación de ETBE, la ruta óptima de las evaluadas se basa en la síntesis a partir de IB y EtOH en condiciones estequiométricas en un reactor discontinuo de tanque agitado. Obviamente el uso de disolventes disminuye MRP y RME y conlleva a un aumento de los costes del proceso. La síntesis de ETBE a partir de EtOH y TBA implica la formación de agua y por tanto menor rendimiento, AE, RME. Además, esta ruta promueve la formación de posibles azeótropos lo que incrementa la dificultad de separación del éter formado. La destilación reactiva permite obtener un mayor rendimiento, sin embargo, requiere un exceso de

EtOH lo que conlleva a menor RME y SF. Con respecto a la formación de TAEE, su síntesis a partir de IA y EtOH en un reactor discontinuo de tanque agitado resulta ser la ruta óptima, análogamente a lo obtenido para el caso del ETBE. No obstante, la producción de TAEE es menos favorable en términos de rendimiento. La síntesis de TAEE a partir de EtOH y TAA es menos favorable en términos de rendimiento, RME, y AE a causa de la formación de agua. La destilación reactiva permite mejorar considerablemente el rendimiento, pero el exceso de EtOH necesario repercute en detrimento de RME y SF.

Se puede concluir que la ruta óptima de producción de ETBE y TAEE es a partir de una mezcla estequiométrica de olefinas y EtOH y que el proceso en simultáneo no implica diferencias significativas a los procesos de producción aislados, por tanto, su viabilidad es factible. La principal limitación es el bajo rendimiento del sistema del TAEE a causa de la menor conversión de equilibrio de los isoamilenos. Con el objetivo de mejorar este inconveniente se diseñó un proceso en continuo, basado en la tecnología conocida como reacción con destilación. La Figura 8.10 muestra el diagrama de flujo del proceso propuesto.

La columna de destilación consta de diez platos de separación, siendo el último plato el óptimo para la alimentación, un condensador parcial y un condensador total. El diámetro de plato obtenido es de 0,55 m (altura total 5,5 m). La razón de reflujo externa se fijó en 3 y la razón mínima de reflujo obtenida fue de 0,203. Las temperaturas del condensador y la caldera son 410,4 K y 473,6 K respectivamente. La presión de la columna es 1,5 Mapa para evitar las limitaciones de separación por la mezcla azeotrópica de éteres y alcoholes a menores presiones, pese a que ello implica aumentar los requerimientos energéticos de la columna.

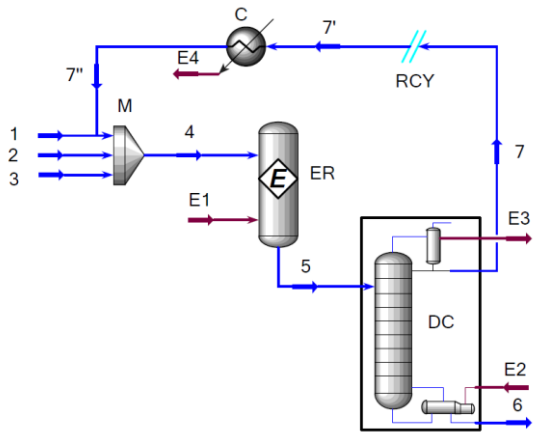

Figure 8.10. Diagrama de flujo del proceso simulado para la producción simultánea de ETBE y TAEE. (1—7'') Corrientes materiales. (E1—E4) Corrientes de energía. (M) Mezclador. (ER) Reactor de equilibrio. (DC) Columna de destilación. (RCY) Corriente de reciclo. (C) Refrigerador.

La configuración propuesta permite obtener una corriente de éteres al 95 %mol., siendo el resto EtOH, y podría incluso usarse para blending directo con gasolinas base. Un 20 %mol. del ETBE producido se ha de recircular al reactor, pero dado que más del 80 %mol. del ETBE y más de 99,9 %mol. del TAEE producidos se obtienen en la corriente 6, el proceso se considera viable. El proceso simulado permite aumentar la conversión de reactantes hasta un 97.4 % mejorando, sin duda, las principales limitaciones observadas en el GMA inicial. La Tabla 8.9 incluye los valores del GMA del proceso simulado. Como se puede observar hay una mejora significativa de los parámetros del proceso evaluados.

Tabla 8.9. Valores obtenidos en el GMA del proceso en continúo simulado.

Caso\Parámetro	AE	Yield	1/SF	RME	MRP	VMR	E-total	CME (%)
ETBE	1	1	0,96	0,92	0,96	0,97	0,08	97,3
TAEE	1	1	0,94	0,88	0,94	0,95	0,13	95,61

8.3.3 CONVERSIÓN DE EQUILIBRIO, SELECTIVIDAD Y OPTIMIZACIÓN DE RENDIMIENTOS SOBRE AMBERLYST™35

Se realizaron experimentos de equilibrio a varias concentraciones iniciales y temperaturas. Como puede observarse en la Figura 8.11, las conversiones de equilibrio disminuyen al aumentar la temperatura, como es de esperar para reacciones exotérmicas. El IB fue la especie que mostró mayor nivel de conversión, seguida del EtOH y finalmente los IA, que mostraron la conversión más baja. Globalmente, las conversiones de reactantes oscilaron entre 69,8 y 97,9 %, 17,0 y 65,6 % y, 32,3 y 97,0 % para IB, IA, y EtOH, respectivamente.

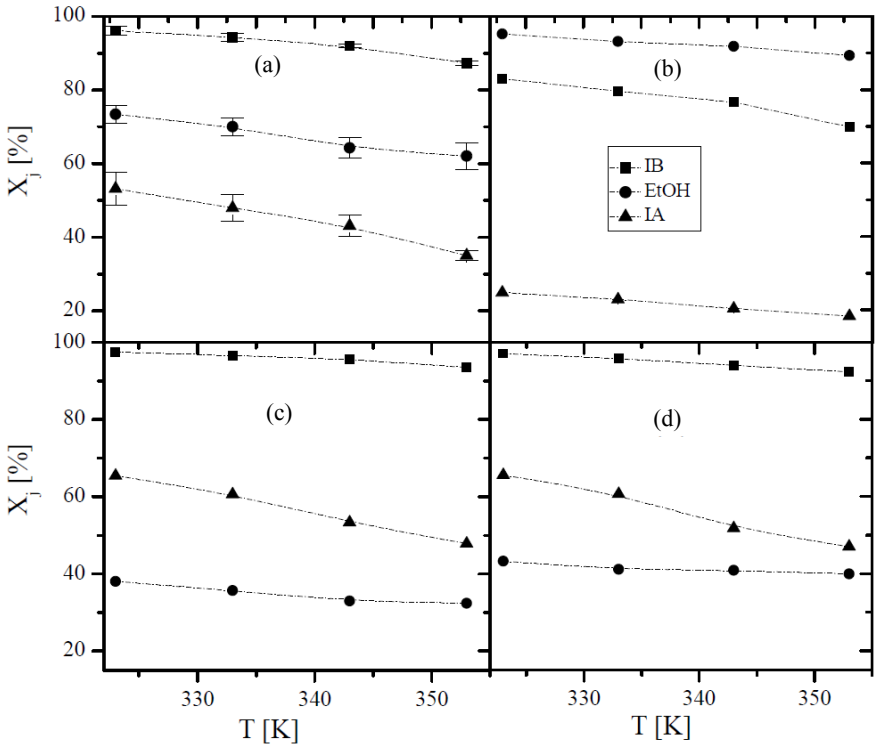

Figura 8.11. Conversión de equilibrio de reactantes frente a temperatura. (a) $R°_{A/O}$=$R°_{C4/C5}$=1. (b) $R°_{A/O}$=0.5, $R°_{C4/C5}$=1. (c) $R°_{A/O}$=2, $R°_{C4/C5}$=0.5. (d) $R°_{A/O}$=$R°_{C4/C5}$=2. Las barras de error están referidas a un intervalo de confianza del 95 %.

Con respecto al efecto del $R°_{A/O}$ en las conversiones de equilibrio, X_{EtOH} disminuye a medida que $R°_{A/O}$ aumenta, mientras que la conversión de equilibrio de olefinas es mayor cuanto mayor es $R°_{A/O}$. Con respecto al efecto de $R°_{C4/C5}$ en las conversiones de equilibrio, este fue menos pronunciado que los de la temperatura y $R°_{A/O}$. En general, a mayor $R°_{C4/C5}$ mayor X_{EtOH} pero menor conversión de equilibrio de olefinas. Por otra parte, la selectividad hacía los éteres correspondientes fue siempre superior al 90 % en cualquiera de las condiciones experimentales exploradas lo que es, sin duda, un aliciente para el proceso desde un punto vista industrial.

En lo que refiere a la formación de subproductos, se formaron siempre más moles de TBA que de TAA en cualquier condición. No obstante, S_{IA}^{TAA} fue mayor que S_{IB}^{TBA} en todos los casos. La selectividad de olefinas a alcoholes terciarios siempre estuvo por debajo del 13 %. La formación de alcoholes terciarios aumentó con la temperatura pese a ser reacciones exotérmicas debido a la presencia de eterificaciones simultáneamente y disminuyó con $R°_{A/O}$. Un aumento de $R°_{C4/C5}$ favorece la formación de TBA mientras que disminuye la de TAA.

En cuanto a la dimerización de las olefinas, estas reacciones solamente fueron significativas a las temperaturas más altas exploradas (343 y 353 K) y en exceso de olefinas en la mezcla inicial ($R°_{A/O}$=0,5). Una descripción más detallada sobre la estructura de estos dímeros se hará en la *Sección 8.3.5*. En general, la formación de dímeros tuvo lugar lentamente y casi linealmente con el tiempo de reacción. La cantidad de dímeros de IB (TMP-1 y TMP-2) fue muy similar a la de dímeros $C_{4\text{-}5}$, lo que sugiere una adsorción preferencial del IB comparado con los IA. La mayor cantidad de dímeros se obtuvo a 353 K, $R°_{A/O}$ =0.5 y $R°_{C4/C5}$ =2.

A partir de las conversiones de equilibrio y las selectividades obtenidas se calcularon los rendimientos a éteres en equilibrio en todo el rango de condiciones experimentales explorado. Posteriormente, se utilizó la metodología de las superficies de respuesta para obtener expresiones empíricas que permitieran modelizar los rendimientos en la situación de equilibrio químico. Se utilizó un polinomio de segundo grado con interacciones en el modelado y una regresión por pasos para obtener ecuaciones con el mínimo número de variables estadísticamente significativas (p<0,05). Un ejemplo de las superficies resultantes se muestra en la Figura 8.12. Las expresiones polinómicas obtenidas para los rendimientos fueron:

$$Y_{IA}^{TAEE} = -50.12 + 0.094 \cdot T + 663.21 \cdot x_A - 115.37 \cdot x_{C4} - 225.36 \cdot x_A^2 + 52.92 \cdot x_{C4}^2 - 1.15 \cdot T \cdot x_A + 95.11 \cdot x_A \cdot x_{C4} \quad (8.6)$$

$$Y_{IB}^{ETBE} = 235.77 - 0.559 \cdot T + 27.53 \cdot x_A - 95.68 \cdot x_{C4} - 245.07 \cdot x_A^2 + 0.588 \cdot T \cdot x_A + 147.62 \cdot x_A \cdot x_{C4} \quad (8.7)$$

$$Y_{EtOH}^{TAEE} = 235.91 - 0.512 \cdot T + 86.35 \cdot x_A - 354.02 \cdot x_{C4} - 190.52 \cdot x_A^2 + 33.93 \cdot x_{C4}^2 + 0.556 \cdot T \cdot x_{C4} + 158.27 \cdot x_A \cdot x_{C4} \quad (8.8)$$

$$Y_{EtOH}^{ETBE} = 59.15 - 0.07 \cdot T - 54.665 \cdot x_A + 155.2 \cdot x_{C4} - 160.88 \cdot x_A \cdot x_{C4} \quad (8.9)$$

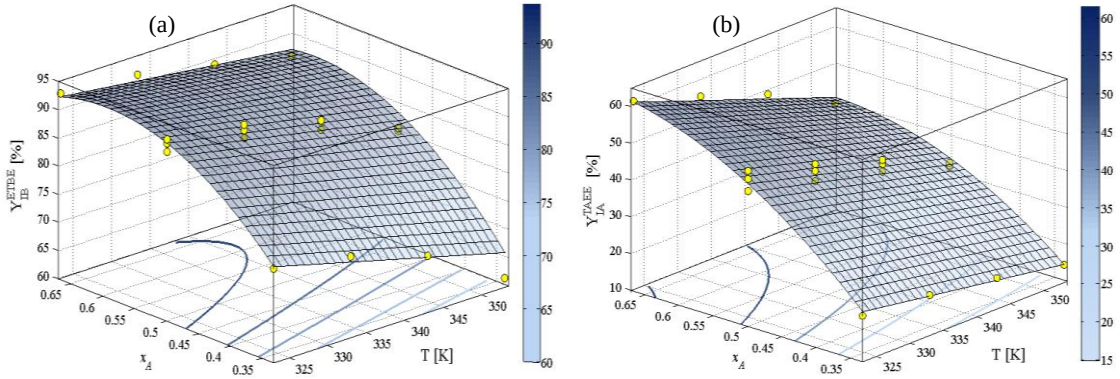

Figura 8.12. (a) Superficie de respuesta para Y_{IB}^{ETBE} vs. x_A y T a x_{C4}=0,5. (b) Superficie de respuesta para Y_{IA}^{TAEE} vs. x_A y T a x_{C4}=0,5. Los símbolos (○) marcan los valores experimentales.

Las ecuaciones obtenidas ajustaron satisfactoriamente los valores experimentales ($R^2_{ajustado}$>0.93). A continuación, se utilizó la metodología de la superposición de los contornos de las superficies obtenidas y la función de deseabilidad con el objetivo de encontrar las condiciones experimentales que maximizan simultáneamente todos los rendimientos a éteres. Las condiciones óptimas obtenidas y los valores óptimos de rendimientos se incluyen en la Tabla 8.10. Estos valores tienen en cuenta la presencia de 1 %m. de agua en la mezcla inicial.

Tabla 8.10. Deseabilidades individuales ($d_n(Y_n(z))$), deseabilidad global $D(x)$ y rendimientos a éteres en las condiciones óptimas.

T [K]	x_A	x_{C4}	$d(Y_{EtOH}^{TAEE})$	$d(Y_{IA}^{TAEE})$	$d(Y_{IB}^{ETBE})$	$d(Y_{EtOH}^{ETBE})$	$D(x)$	Y_{EtOH}^{TAEE}	Y_{IA}^{TAEE}	Y_{IB}^{ETBE}	Y_{EtOH}^{ETBE}
323	0,462	0,333	0,92	0,79	1	0,45	0,76	39,8	49,0	94,2	38,2

8.3.4 EQUILIBRIO QUÍMICO Y ANÁLISIS TERMODINÁMICO

A partir de las concentraciones de equilibrio obtenidas en la sección anterior se calcularon las constantes de equilibrio, ver ecuación 8.10, de las principales reacciones implicadas (R1-R4 en la Figura 8.9). Para ello se estimaron las actividades mediante el método UNIFAC-Dortmund ya que el sistema es fuertemente no ideal debido a la presencia de EtOH. Los valores de constantes de equilibrio obtenidas y aquellas determinadas previamente en otros estudios para las mismas reacciones se muestran en las Tablas 8.11 y 8.12.

$$K_i \equiv \prod_{j=1}^{s} (a'_j)_{ei}^{\nu_j} = \left(\prod_{j=1}^{s} (\gamma_j)_e^{\nu_j} \right)_i \left(\prod_{j=1}^{s} (x_j)_e^{\nu_j} \right)_i \equiv K_{\gamma_i} K_{x_i} \qquad (8.10)$$

Tabla 8.11. Constantes de equilibrio experimentales para la reacción de formación de ETBE (R1) y comparación con los valores de la literatura.

	T [K]	Este trabajo	Françoise y Thyrion (1991) [139]	Vila & col. (1993) [160]	Cunill & col. (1993) [37]	Izquierdo & col. (1994) [127]	Jensen y Datta (1995) [135]	Gómez & col. (1997) [122]	Teóricas
K_1	323	41,9 ± 3,9	46	42,1	41,5	40±7	44	34,3±0,4	54,6
	333	28,4 ± 3,3	26	26,4	26,8	26±3	27	22,3±1	36,7
	343	20,2 ± 2,5	16	18,4	18,1	18±1	17	17,1±1,8	25,3
	353	13,1 ± 1,2	11,5	12,8	12,6	13±2	11	11,3±0,7	17,7

Tabla 8.12. Constantes de equilibrio experimentales para las reacciones de formación de TAEE (R2 and R3) y para la reacción de isomerización de isoamilenos (R4), y comparación con los valores de la literatura.

	T [K]	Este trabajo	Rihko & col. (1994)[137]	Kitchaiya y Datta (1995)[22]	Cruz & col. (2007) [185]	Fitó y Linnekoski (2008) [121]	Teóricas
K_2	323	29,3 ± 1,6	24,8±1,5	30,6	-	31,1	36,7
	333	20,5 ± 1,3	17,4±1,1	20,8	20,6	20,9	25,0
	343	14,4 ± 1,3	11,3±0,8	14,7	-	14,5	17,4
	353	9,6 ± 0,8	8,3±0,6	-	8	-	12,4
K_3	323	2,3 ± 0,2	2,2±0,1	2,6	-	2,6	3,4
	333	1,7 ± 0,1	1,7±0,1	1,9	2,1	1,9	2,5
	343	1,3 ± 0,1	1,2±0,1	1,5	-	1,5	1,8
	353	1,0 ± 0,1	1,0±0,1	-	1,2	-	1,4
K_4	323	13,1 ± 0,7	11±0,4	11,9	-	12	11,0
	333	11,8 ± 0,5	10,2±0,4	10,9	-	10,9	10,2
	343	10,9 ± 0,5	9,3±0,4	10	-	10,0	9,5
	353	9,5 ± 0,5	8,6±0,4	-	-	-	8,8

Se puede observar que los valores obtenidos en este estudio son comparables a la literatura, por tanto, se descarta algún posible efecto del sistema simultáneo sobre las constantes de equilibrio. R1 es la reacción con mayor constante de equilibrio, seguida de R2 y R4. Por último, R3 es la reacción con menor valor de constante de equilibrio. Cabe destacar que del sistema R2-R4 sólo dos reacciones son estequiométricamente independientes, por tanto: $K_2=K_3 \cdot K_4$. Además, se evaluó el posible efecto de la presión de trabajo sobre las constantes de equilibrio obtenidas a

través del factor de Poynting y resultó ser despreciable. Por otra parte, la dependencia de las constantes de equilibrio con la temperatura es:

$$\ln K_i = \frac{-\Delta_r G_i^o}{RT} = \frac{-\Delta_r H_i^o}{RT} + \frac{\Delta_r S_i^o}{R} \tag{8.11}$$

Llegados a este punto, se consideraron dos posibles casos: i) $\Delta_r H_i^o$ constante con la temperatura ($\Delta_r H_i^o \neq f(T)$), y ii) $\Delta_r H_i^o$ varía con la temperatura ($\Delta_r H_i^o = f(T)$). Mediante representación de van't Hoff se obtuvieron las propiedades termodinámicas de reacción para ambos casos. Los valores obtenidos se resumen en la Tabla 8.13. Como la variación de la entalpía de reacción en el rango de temperatura explorado no fue significativa, se puede considerar constante. Por tanto, las ecuaciones 8.12–8.15 indican la variación con la temperatura de las constantes de equilibrio de las reacciones.

Tabla 8.13. Resumen de las propiedades termodinámicas obtenidas a 298 K y comparación con los valores de la literatura. Los errores se refieren a un intervalo de confianza del 95%.

Reacción	Propiedad	Caso $\Delta_r H_i^o \neq f(T)$	Caso $\Delta_r H_i^o = f(T)$	Teóricas	Literatura			
R1	$\Delta_r H°_1$ [kJ/mol]	-36,3±7,2	-35,0±6,7	-35,6	-34,8 ±1,3 [a]	-35,5±2 [b]	-36±2 [c]	-44,3 [d]
	$\Delta_r S°_1$ [J/(mol K)]	-81,3±21,4	-77,1±20,0	-76,9	-77,3±0,6 [a]	-82,4±6 [b]	-	-
	$\Delta_r G°_1$ [kJ/mol]	-12,1±4,5	-12,0±6,7	-12,7	11,8±1,3 [a]	-	-	-
R2	$\Delta_r H°_2$ [kJ/mol]	-35,1±6,0	-33,8±5,5	-34,4	-33,6 [e]	-35,2±5,8 [f]	-34,5 [g]	-
	$\Delta_r S°_2$ [J/(mol K)]	-80,3±17,9	-76,1±16,3	-76,5	-75,4 [e]	-82,3±17,3 [f]	-80,1 [g]	-
	$\Delta_r G°_2$ [kJ/mol]	-11,1±2,7	-11,1±5,5	-11,6	-11,1 [e]	-10,7 [e]	-10,6 [g]	-
R3	$\Delta_r H°_3$ [kJ/mol]	-25,5±3,0	-24,4±2,5	-27,3	-24,2 [e]	-27,3±6,7 [f]	-27 [g]	-27,7±0,8 [h]
	$\Delta_r S°_3$ [J/(mol K)]	-72,1±8,8	-68,6±7,4	-74,5	-67 [e]	-77,8±19,8 [f]	-76,5 [g]	-
	$\Delta_r G°_3$ [kJ/mol]	-4,0±4,7	-4,0±2,5	-5,1	-4,1 [e]	-4,1 [f]	-4,2 [g]	-
R4	$\Delta_r H°_4$ [kJ/mol]	-9,7±3,8	-9,5±3,8	-7,1	-9,16 [e]	-8±1,4 [f]	-8,8±2,7 [i]	-9,5 [j]
	$\Delta_r S°_4$ [J/(mol K)]	-8,6±11,3	-8,0±11,2	-2,0	-7,48 [e]	-4,7±4,2 [f]	-4,1±7,8 [i]	-10±6,6 [k]
	$\Delta_r G°_4$ [kJ/mol]	-7,1±2,5	-7,1±3,8	-6,5	-6,93 [e]	-6,6 [f]	-7,1±11,7 [k]	-6,8 [j]

[a] Vila & col. (1993)[160]; [b] Sharonov & col. (1995)[138]; [c] Gómez & col. (1997)[122]; [d] Françoisse y Thyrion (1991)[139]; [e] Kitchaiya y Datta (1995)[22]; [f] Rihko & col. (1994)[137]; [g] Linnekoski & col. (1999)[136]; [h] Verevkin (2004)[187]; [i] Ferreira y Loureiro (2004)[180]; [j] Syed & col. (2000)[134]; [k] Mao & col. (2008)[128].

$$\ln K_1 = \left(\frac{4370,52 \pm 868,01}{T}\right) - \left(9,77 \pm 2,57\right) \tag{8.12}$$

$$\ln K_2 = \left(\frac{4218,21 \pm 726,33}{T}\right) - \left(9,66 \pm 2,15\right) \tag{8.13}$$

$$\ln K_3 = \left(\frac{3068,08 \pm 357,38}{T}\right) - \left(8,67 \pm 1,06\right) \tag{8.14}$$

$$\ln K_4 = \left(\frac{1168,30 \pm 459,28}{T}\right) - \left(1,04 \pm 1,36\right) \tag{8.15}$$

Finalmente, se estudió también el equilibrio químico de la isomerización entre TMP-1 y TMP-2, oscilando las constantes de equilibrio entre 0,246 y 0,292 entre 323 y 353 K. La entalpía de reacción obtenida fue de 5,3 ± 0,8 kJ/mol y la entropía de 4,7 ± 2,5 J/(mol K).

8.3.5 EFECTO DEL AGUA

Se estudió el efecto del agua en la mezcla inicial de reactantes sobre el sistema de reacción ya que la utilización de EtOH seco es industrialmente inviable debido a su elevado coste. Los experimentos se realizaron en condiciones en las que se favorecieran además las reacciones de dimerización de olefinas (T=353 K y $R°_{A/O}$=0,5) con el objetivo de estudiar simultáneamente las principales reacciones secundarias. Se añadieron cantidades controladas (0–1 %m.) de agua a la mezcla inicial de reactantes. Como en todos los experimentos se alcanzó un estado de pseudoequilibrio químico, se calcularon también las constantes de equilibrio de las reacciones implicadas, ver Tabla 8.14. Concluyendo que la presencia de diferentes cantidades de agua no afecta a las constantes de equilibrio de las reacciones de eterificación implicadas.

Tabla 8.14. Constantes de equilibrio de las reacciones R1-R4 a 353 K en presencia de diferentes cantidades de agua. Los errores se refieren a un 95% de intervalo de confianza.

Reacción	Contenido inicial de agua [%m.]					Valores medios en la *Sección 8.3.4*
	0	0,25	0,5	0,75	1	
R1	13,8	13,5	13,1	13,9	12,9 ± 0,6	13,1 ± 1,2
R2	11,4	11,2	10,6	11,3	10,8 ± 0,5	9,6 ± 0,8
R3	1,1	1,1	1,0	1,1	1,1 ± 0,1	1,0 ± 0,1
R4	9,7	9,9	10,4	10,6	9,5 ± 0,5	9,5 ± 0,5

La adición de diferentes cantidades de agua tuvo varios efectos observables sobre el sistema de reacción. Por un lado, a medida que la cantidad inicial de agua era mayor también lo eran las cantidades formadas de alcoholes terciarios (TBA y TAA) al final de los experimentos, ver Figura 8.13a. Por otra parte, a medida que la cantidad de agua aumentó menor fue la formación de los productos de dimerización de las olefinas, ver Figura 8.13b. Por tanto, se puede concluir que el agua presenta un efecto inhibidor sobre las reacciones de dimerización, muy probablemente causado por la competencia entre moléculas por adsorberse en los centros activos.

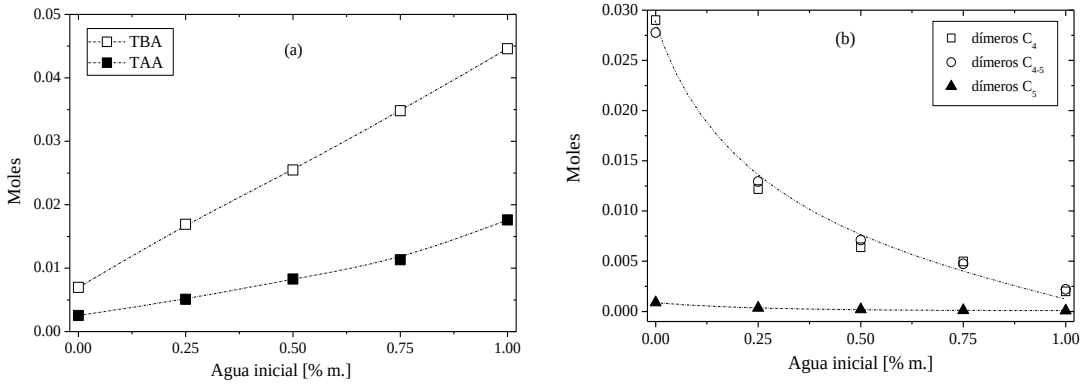

Figure 8.13. (a) Moles de TBA y TAA formados a diferentes cantidades de agua (t=360 min). (a) Moles de diferentes dímeros formados a diferentes cantidades de agua (t=360 min).

A partir de la mezcla de reacción obtenida de los experimentos se pudo concentrar suficiente cantidad de dímeros y mediante sucesivas destilaciones se pudo separar una cantidad significativa que permitiese su análisis mediante espectrometría de masas. Los únicos dímeros de IB detectados fueron TMP-1 y TMP-2 mientras que se obtuvieron variedad de compuestos representativos de los codímeros C_{4-5} y dímeros C_5, ver Figura 8.14. Estos compuestos son interesantes ya que tienen elevados índices de octano y tras su hidrogenación podrían ser eficientes aditivos para gasolina.

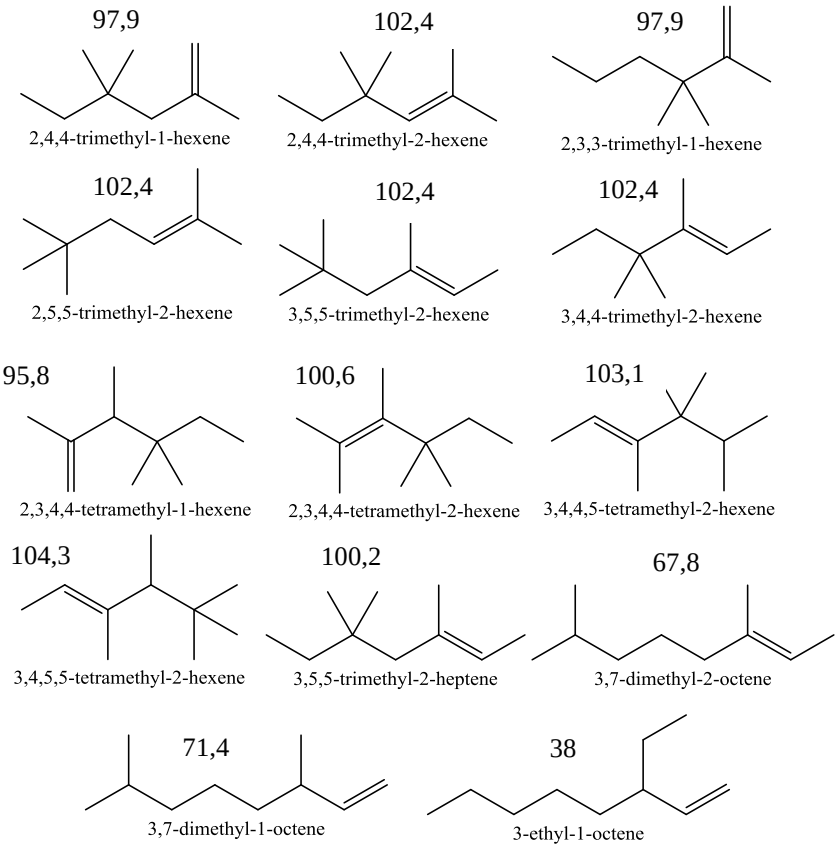

Figura 8.14. Codímeros $C_{4\text{-}5}$ y dímeros C_5 identificados por MS. Los números se refieren al índice antidetonante (RON+MON)/2 de las moléculas. Estimado según [193].

Finalmente, el agua también resultó inhibir las reacciones de eterificación ya que la velocidad de formación de ETBE y TAEE fue menor a mayor cantidad de agua inicial, ver Figura 8.15. Con respecto a las velocidades iniciales de formación de ambos éteres, cuando el contenido inicial de agua supera el 0,45 %m. aproximadamente, se aprecia un cambio en la pendiente, Figura 8.15a, y que se atribuye a un cambio de mecanismo. Superando esta cantidad de agua hay más de dos moléculas de agua por centro activo lo que provoca la disociación de grupos sulfónicos y que, por tanto, se pase de un mecanismo concertado (catálisis heterogénea) a catálisis específica (quasihomogénea).

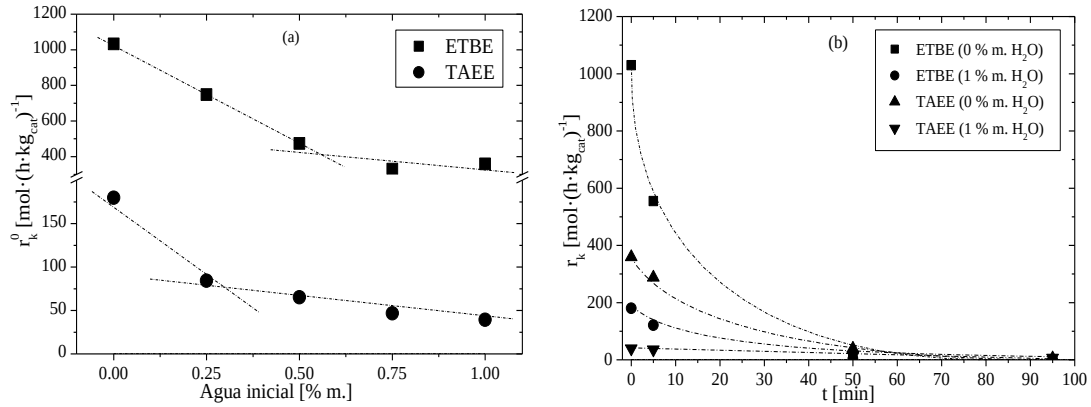

Figura 8.15. (a) r^0_{ETBE} y r^0_{TAEE} estimadas frente al contenido inicial de agua. (b) Evolución de r_{ETBE} y r_{TAEE} a 0 y 1 %m. de concentración inicial de agua.

8.3.6 SCREENING DE CATALIZADORES

Se aplicaron las técnicas de adsorción-desorción de N_2 a 77 K, ISEC y picnómetro de He a todas las resinas incluidas en la Tabla 8.6. Los principales resultados obtenidos de la caracterización se muestran en la Tabla 8.15. Además, la Figura 8.16 muestra el patrón ISEC de la fase gel de las resinas estudiadas.

Tabla 8.15. Propiedades morfológicas de las resinas evaluadas en estado seco e hinchado.

Catalizador	Densidad esqueleto[a]	Polímero seco (BET)[b]				Polímero hinchado (ISEC)[g]				
		Area superf.[c]	Volumen poro[d]	Diámetro poro[e]	Porosidad[f]	"Poros reales"			Fase gel	
	ρ	$S_{g,BET}$	$V_{pore,BET}$	$d_{pore,BET}$	θ_{BET}	$S_{g,ISEC}$	$V_{pore,ISEC}$	$d^e_{pore,ISEC}$	$V_{sp}{}^h$	$\theta_{ISEC}{}^i$
	[g cm^{-3}]	[m^2 g^{-1}]	[cm^3 g^{-1}]	[nm]	[%]	[m^2 g^{-1}]	[cm^3 g^{-1}]	[nm]	[cm^3 g^{-1}]	[%]
A-15	1,416	42,0	0,33	31,2	31,7	156,9	0,63	16,1	0,77	49,5
A-16	1,401	1,7	0,01	30,8	1,8	149,3	0,38	10,3	1,13	52,8
A-35	1,542	34,0	0,21	24,7	24,5	198,9	0,72	14,5	0,61	51,3
A-36	1,567	21,0	0,14	27,2	18,3	146,5	0,33	9,1	1,03	53
A-39	1,417	0,1	$2{,}86\cdot10^{-4}$	12,7	0,0	56,0	0,16	11,1	1,62	60,3
A-40	1,431	0,2	$6{,}00\cdot10^{-4}$	10,9	0,1	11,0	0,13	45,5	0,44	–
A-45	1,466	49,0*	0,23	19,0*	25,4	220,2	0,52	9,5	0,97	54,4
A-46	1,137	57,4	0,26	18,3	23,0	186,0	0,48	10,3	0,52	12,3
A-48	1,538	33,8	0,25	29,5	27,7	186,0	0,57	12,3	0,62	45,3
A-DT	1,477	36,0*	0,20	22,0*	22,6	175,4	0,42	9,6	0,97	51,3
CT-124	1,420	0,1	$6{,}20\cdot10^{-4}$	35,7	0,1	0	0	0	1,90	62,9
CT-175	1,498	28,0	0,30	42,9	31,0	157,4	0,82	20,9	1,00	63,5
CT-275	1,506	20,3	0,38	74,4	36,2	209,4	0,77	14,7	0,81	57,9
CT-482	1,538	8,7	0,06	26,7	8,2	214,0	1,05	19,6	0,85	65,7
MN-500	1,539	332,0*	0,64*	152,0*	50,0	95,8	0,80	33,4	0,89	61,6

[a] Densidad de esqueleto. Medida por desplazamiento de Helio (Accupic 1330). [b] Muestras secadas al vacío (10^{-4} mmHg, 110°C). [c] Método Brunauer-Emmett-Teller (BET). [d] Volumen de N_2 adsorbido a presión relativa $(P/P_0)=0.99$. [e] $d_{pore,BET}= 4V_{pore,BET}/S_{g,BET}$ or $d_{pore,ISEC}= 4V_{pore,ISEC}/S_{g,ISEC}$. [f] $\theta_{BET}= V_{pore,BET}/V_{particle}=V_{pore,BET}/(V_{pore,BET}+1/\rho)$. [g] Medido en solución acuosa 0.2N de Na_2SO_4 como fase móvil excepto MN-500 dónde THF se usó como fase móvil. [h] Volumen real de polímero hinchado. [i] $\theta_{ISEC} =V_{pore,ISEC}/V_{particle}=(V_{pore,ISEC} +V_{sp}-1/\rho)/(V_{pore,ISEC} +V_{sp})$. *Valores del fabricante.

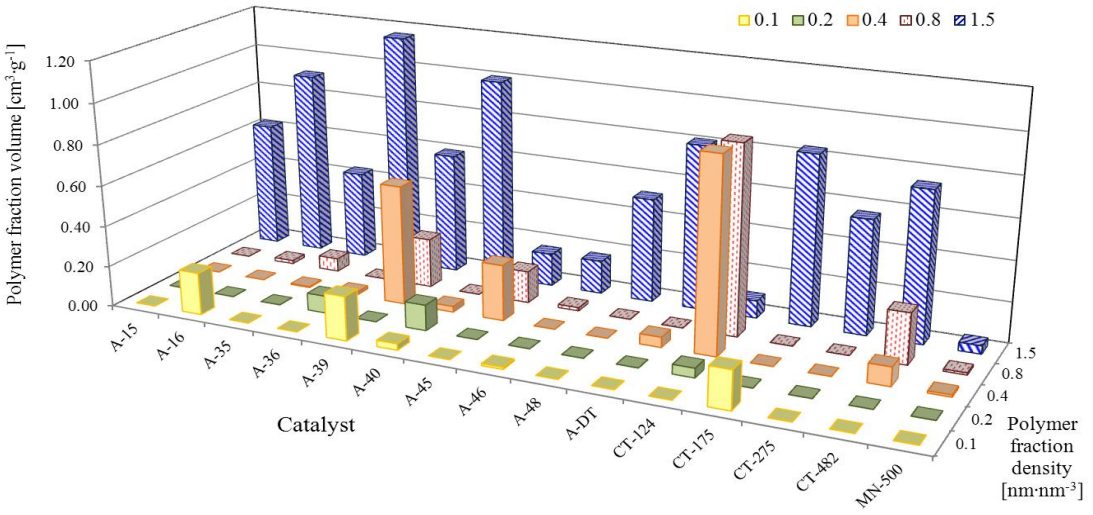

Figura 8.16. Patrón ISEC de la fase gel de las resinas estudiadas.

Se puede observar que, en general, el área superficial, volumen de poro y porosidad de las resinas es mayor en condiciones de polímero hinchado. Por otra parte, la fracción de polímero que mayor contribución tiene sobre la fase gel es aquella de mayor densidad 1,5 nm nm^{-3}.

Además, se realizaron medidas del hinchamiento volumétrico en diferentes medios utilizando tubos de ensayo graduados. La Tabla 8.16 recoge los valores de la razón de hinchamiento obtenida para las diferentes resinas. Todas las resinas evaluadas se hincharon en contacto con los diferentes medios. El hinchamiento en agua fue ligeramente superior, aunque similar, a aquel obtenido en MeOH y EtOH. El hinchamiento en el solvente no polar fue considerablemente inferior. Las resinas con bajo %DVB fueron las que más se hincharon, siendo la resina tipo gel CT-124 la resina que mayor hinchamiento mostró, seguida de A-39. Por el contrario, la resina que menos se hinchó fue MN-500 debido a su elevado contenido en DVB (50%) y, por consiguiente, su rígida estructura.

Tabla 8.16. Razón de hinchamiento en diferentes medios y densidad de lecho seco para las diferentes resinas estudiadas.

Catalizador	SR en diferentes medios				Densidad de lecho seco [g mL^{-1}]
	Agua	Etanol	Metanol	Solvente [a]	
A-15	1,70	1,60	1,50	1,40	0,61
A-16	2,35	2,35	2,00	1,60	0,88
A-35	1,93	1,85	1,70	1,50	0,65
A-36	2,35	2,35	2,25	1,65	0,91
A-39	3,60	3,22	3,00	1,70	0,92
A-40	1,95	1,90	1,85	1,15	0,86
A-45	2,35	2,35	2,45	1,20	0,85
A-46	1,20	1,20	1,20	1,30	0,46
A-48	1,95	1,85	1,90	1,50	0,68
A-DT	2,30	2,40	2,00	1,15	0,91
CT-124	3,65±0,15	3,10	2,95	1,10	0,90
CT-175	1,70	1,65	1,60	1,40	0,54
CT-275	1,90	1,80	1,85	1,50	0,60
CT-482	2,25	2,10	2,10	1,15	1,10
MN-500	1,40	1,40	1,35	1,35	0,48

[a]Composición del solvente (% mol.): IB (0,7), EtOH (0,1), 2M1B (3,0), 2M2B (58,8), ETBE (37,4)

Con respecto a los experimentos realizados para evaluar la actividad catalítica, todas las resinas resultaron activas en las reacciones de eterificación implicadas. En ninguno de los experimentos se llegó a alcanzar el equilibrio químico, aunque estuvo cerca con las resinas más activas. El perfil de conversión de reactantes obtenido se representa en la Figura 8.17. Se pueden distinguir, ver Figura 8.17a, tres tipos de resinas: aquellas que reflejaron una elevada actividad, las de actividad media y las que mostraron un bajo nivel de actividad. Las resinas que mayor actividad mostraron fueron aquellas macroreticulares y sobresulfonadas o convencionalmente sulfonadas. En cuanto a las velocidades de reacción iniciales obtenidas para cada resina, la Figura 8.18 las representa de forma ordenada, en la que puede verse que A-35 fue la resina con mayor actividad.

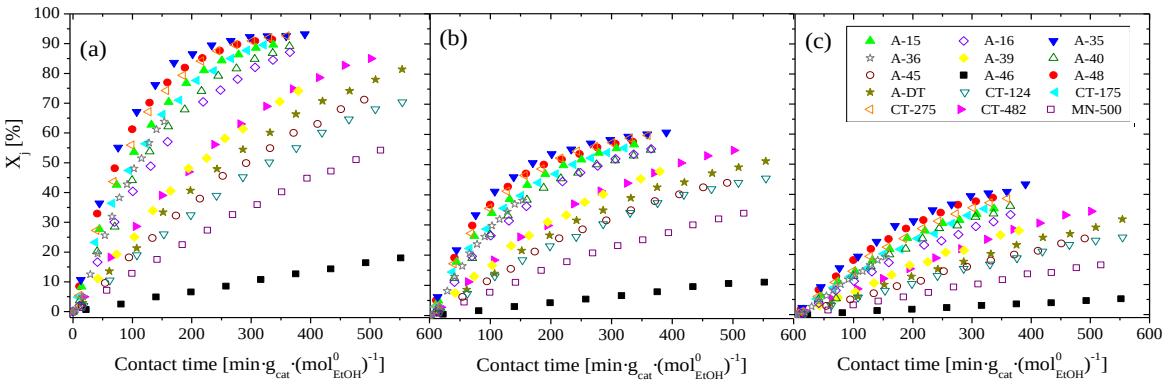

Figura 8.17. IB (a), EtOH (b) and IA (c) Conversión vs. tiempo de contacto para diferentes resinas a T=335 K, $R°_{A/O}$=1,1 and $R°_{C4/C5}$=1.

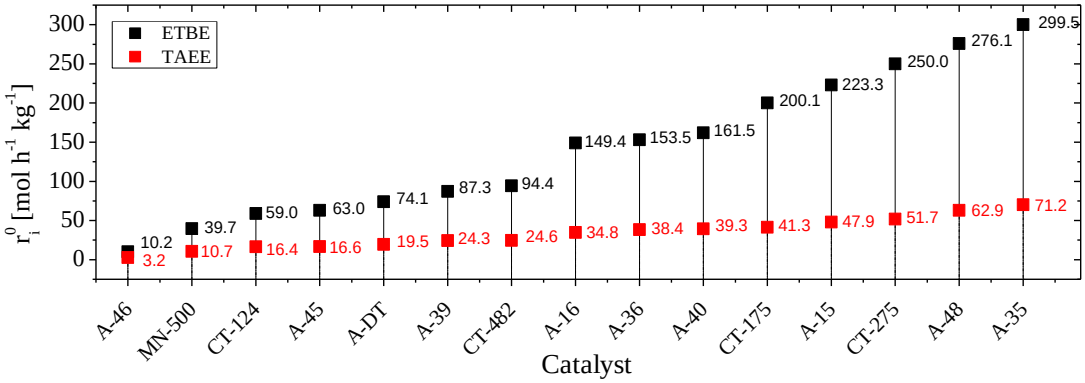

Figura 8.18. Velocidades iniciales de formación de ETBE y TAEE obtenidas para diferentes resinas a T=335 K, $R°_{A/O}$=1,1 and $R°_{C4/C5}$=1.

Se utilizó la metodología de las superficies de respuesta para evaluar la relación entre la actividad catalítica y las propiedades de las resinas. Se utilizaron como variables dependientes las propiedades de la Tabla 8.15 y como variables independientes las velocidades iniciales de eterificación obtenidas. Resultó que las propiedades que mejor describen la actividad catalítica son la combinación de capacidad ácida y el volumen de polímero hinchado determinado por ISEC. Esto es coherente ya que, en el presente sistema de reacción, en el cual hay una importante cantidad de alcohol se espera que las resinas estén hinchadas de una forma similar a la que estarían en agua (ISEC). Las ecuaciones 8.16 y 8.17 son las expresiones empíricas obtenidas de las que se deduce que resinas con elevada capacidad ácida y poco volumen de polímero hinchado son las más aptas para la producción simultánea de ETBE y TAEE.

$$\left(r^0_{ETBE}\right)^{0.5} = (3{,}16 \pm 1{,}05) + (3{,}19 \pm 0{,}22)\cdot[H^+] - (6{,}03 \pm 0{,}74)\cdot V_{sp} \qquad (8.16)$$

$$\left(r^0_{TAEE}\right)^{0.5} = (1{,}72 \pm 0{,}41) + (1{,}42 \pm 0{,}08)\cdot[H^+] - (2{,}48 \pm 0{,}29)\cdot V_{sp} \qquad (8.17)$$

Finalmente, se evaluó la accesibilidad de las moléculas implicadas a las zonas de diferente densidad de la fase gel, dónde la mayor parte de los centros ácidos están localizados. Para ello, se utilizó el coeficiente de distribución de Ogston y el diámetro cinético o *random coil diameter*. Ambas teorías coinciden en que las zonas de mayor densidad (1,5 y 0,8 nm nm^{-3}) son de difícil acceso, especialmente para ETBE y TAEE, las moléculas de mayor tamaño en este estudio. Esto puede conllevar problemas de difusión de los productos en los poros del catalizador y afectar, por ende, considerablemente a la velocidad de reacción observada.

Tabla 8.17. Coeficientes de distribución de Ogston, K_O, en las zonas de polímero hinchado de diferente densidad y random coil diameter, Φ_d, de olefinas, alcoholes y éteres considerados.

Compuesto	Longitud molecular [nm]	Densidad cadena de polímero [nm nm^{-3}]	0,1	0,2	0,4	0,8	1,5	Φ_d [nm]	2.5Φ_d [nm]
		Diámetro de poro equivalente [nm]	9,8	4,3	2,6	1,5	1		
		M_w [g mol^{-1}]			K_O				
Agua	0,15	18,02	0,98	0,95	0,91	0,83	0,70	0,13	0,34
IB	0,42	56,11	0,95	0,90	0,81	0,65	0,45	0,26	0,66
EtOH	0,39	46,07	0,95	0,91	0,82	0,67	0,48	0,23	0,58
2M1B	0,56	70,13	0,93	0,87	0,75	0,56	0,34	0,30	0,75
2M2B	0,51	70,13	0,94	0,88	0,77	0,60	0,38	0,30	0,75
TBA	0,42	74,12	0,95	0,90	0,81	0,65	0,45	0,31	0,77
TAA	0,54	88,15	0,93	0,87	0,76	0,57	0,35	0,34	0,86
ETBE	0,68	102,17	0,91	0,83	0,69	0,48	0,26	0,37	0,93
TAEE	0,68	116,20	0,91	0,83	0,70	0,48	0,26	0,40	1,01

8.3.7 ESTUDIO CINÉTICO SOBRE AMBERLYST™35

Primeramente, se llevaron a cabo una serie de experimentos preliminares para determinar las condiciones en las que los efectos de la TEM, TIM y de la carga de catalizador fuesen despreciables. Se dedujo de ellos que el efecto de la carga de catalizador es despreciable hasta 2g, que los efectos de la TIM son negligibles utilizando partículas de diámetro inferior a 0.4 mm y que los efectos de la TEM no son significativos a velocidades de agitación superiores a 600 rpm. En estas condiciones, se realizaron 21 experimentos a varias concentraciones iniciales y temperaturas. La Figura 8.18 muestra un ejemplo de los perfiles molares obtenidos.

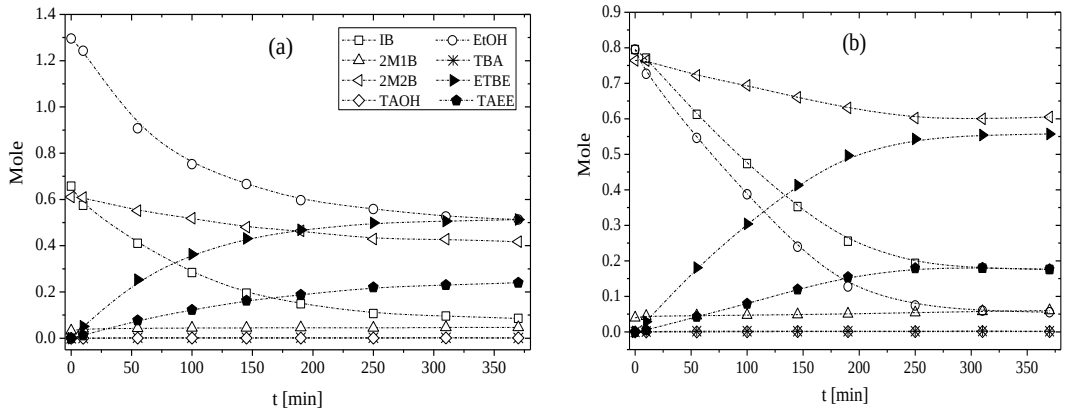

Figura 8.18. Evolución del número de moles obtenida a: (a) T= 353,5 K, $R^{o}_{A/O}$=1, $R^{o}_{C4/C5}$=1, 0,29 g de A-35; (b) T= 342.8 K, $R^{o}_{A/O}$=0,5, $R^{o}_{C4/C5}$=1. 0,41 g de A-35

Una vez calculadas las velocidades de reacción en cada instante se procedió realizar diferentes tipos de ajustes con el objetivo de modelar la cinética del sistema de reacción. Las velocidades de reacción iniciales calculadas en las condiciones experimentales exploradas se incluyen en la Tabla 8.18.

Tabla 8.18. Velocidades de reacción experimentales.

T [K]	$R^{o}_{A/O}$	$R^{o}_{C4/C5}$	r^{0}_{EtOH} [mol·(kg$_{cat}$·h)$^{-1}$]	r^{0}_{2M2B} [mol·(kg$_{cat}$·h)$^{-1}$]	r^{0}_{ETBE} [mol·(kg$_{cat}$·h)$^{-1}$]	r^{0}_{TAEE} [mol·(kg$_{cat}$·h)$^{-1}$]	$r^{0}_{ETBE}/r^{0}_{TAEE}$
323,2	1,00	1,00	–153,9	–21,4	122,4	24,8	4,9
323,0	1,99	0,51	–63,1	–20,0	47,7	19,8	2,4
323,1	0,50	0,49	–125,7	–28,2	75,2	38,0	2,0
323,1	0,50	2,02	–265,3	–17,6	244,4	23,9	10,0
323,7	1,99	2,03	–172,8	–14,1	156,0	14,0	11,1
324,7	1,95	2,04	–192,7	–15,0	158,5	15,5	11,1
335,0	1,10	0,99	–379,4	–50,1	299,5	70,1	4,3
333,7	2,06	0,99	–278,5	–28,5	215,8	45,3	4,8
333,7	0,50	0,98	–619,9	–114,4	482,4	130,9	3,7
342,7	1,97	1,00	–522,0	–82,5	422,8	102,4	4,1
345,1	1,01	0,99	–744,6	–128,6	561,5	146,0	3,9
342,7	1,00	1,01	–650,6	–85,8	527,2	130,5	4,0
342,7	0,99	1,03	–660,6	–96,3	525,6	126,6	4,1
342,8	1,00	2,02	–709,5	–69,7	648,6	74,0	8,8
342,8	0,50	1,00	–928,9	–156,3	682,9	176,3	3,9
343,8	0,99	0,50	–627,0	–161,7	432,9	209,3	2,1
353,2	1,97	0,51	–742,4	–188,1	458,6	261,5	1,8
353,5	1,00	1,02	–1765,5	–285,6	1374,6	368,9	3,7
352,7	1,97	2,01	–1096,7	–76,8	946,2	105,7	9,0
352,8	0,50	2,04	–2486,5	–288,8	2207,8	251,4	8,8
353,8	0,50	0,50	–1807,9	–642,3	1126,6	618,1	1,8

En primer lugar, se procedió a ajustar las velocidades iniciales de reacción a una función exponencial que permitiera obtener información del pseudoorden de reacción de los reactantes y de las energías de activación aparentes del sistema. Las ecuaciones obtenidas fueron las siguientes:

$$r_{ETBE} = 2,08 \cdot e^{\left(\frac{-72,15}{R \cdot T}\right)} \cdot x_A^{-0,13} x_O^{1,02} \qquad (8.18)$$

$$r_{TAEE} = 1,10 \cdot e^{\left(\frac{-73,41}{R \cdot T}\right)} \cdot x_A^{0,016} x_O^{1,15} \qquad (8.19)$$

De estas ecuaciones se desprende que la energía de activación aparente del sistema de formación de TAEE es ligeramente superior a la del ETBE. Además, para ambos sistemas el pseudoorden cinético del alcohol es cercano a cero mientras que el de las olefinas es positivo y cercano a la unidad. A partir de estos resultados se pueden extraer paralelismos útiles con vistas a formular modelos hiperbólicos. Por ejemplo, la concentración de alcohol debería incluirse en ambos, numerador y denominador mientras que la concentración de las olefinas correspondientes parece formar parte solo del numerador en modelos hiperbólicos.

Además de funciones potenciales, se utilizó la metodología de las superficies de respuesta para obtener ecuaciones empíricas que permitieran modelizar las velocidades de reacción iniciales con respecto a la temperatura y fracciones molares de reactantes. Un ejemplo de las superficies obtenidas se representa en la Figura 8.19. Las ecuaciones empíricas obtenidas son:

$$\ln r^0_{ETBE} = -28,69 + 0,0973 \cdot T - 1,98 \cdot x_A + 23,89 \cdot x_{C4/C5} - 0,0457 \cdot T \cdot x_{C4/C5} - 5,78 \cdot x^2_{C4/C5} \qquad (8.20)$$

$$\ln r^0_{TAEE} = -30,71 + 0,1051 \cdot T - 2,22 \cdot x_A + 21,37 \cdot x_{C4/C5} - 0,0475 \cdot T \cdot x_{C4/C5} - 7,25 \cdot x^2_{C4/C5} \qquad (8.21)$$

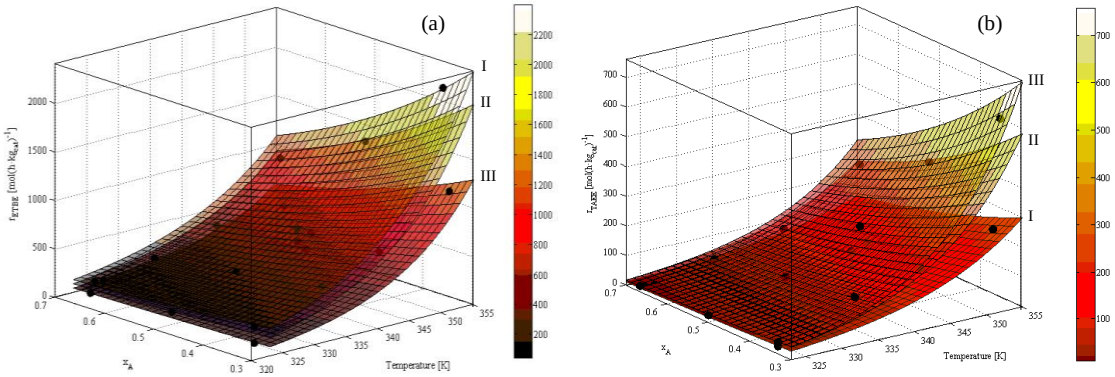

Figure 8.19. Datos experimentales (●) y superficies de respuestas obtenidas para: (a) r^0_{ETBE} y (b) r^0_{TAEE}. I, II y III se refieren a las superficies que corresponden a valores de $x_{C4/C5}$ de 0.666, 0.5 y 0.333, respectivamente.

Análogamente, algunos paralelismos se pueden extraer de las ecuaciones empíricas obtenidas. De acuerdo con los signos de los diferentes términos, la concentración de alcohol inhibe las reacciones de eterificación y, por tanto, debería de incluirse en el denominador de modelos hiperbólicos. Siguiendo el mismo criterio, el IB se espera que esté en la fuerza impulsora de la ecuación de formación del ETBE. Como aparecen términos cuadráticos es también de esperar que haya exponentes mayores a uno en el término de adsorción de un modelo hiperbólico plausible. En resumen, tanto las funciones potenciales como las polinómicas obtenidas ajustan bien a las velocidades iniciales experimentales y aportan información útil sobre ecuaciones a postular basadas en los modelos clásicos LHHW y ER.

Con el fin de obtener información más detallada sobre la cinética de las reacciones implicadas, se procedió a un análisis sistemático de 9.228 modelos cinéticos basados en los mecanismos de LHHW y ER. Para ello, se creó un script de Matlab que permitiese minimizar las diferencias entre las velocidades experimentales y calculadas para todas las reacciones implicadas simultáneamente. Posteriormente, con el set de modelos candidatos se procedió a hacer una selección y aplicar la metodología de "model averaging" [205–210] con el fin de obtener un promedio ponderado de los valores estimados en los mejores modelos para cada parámetro, en lugar de tomar aquello de un único modelo como los valores reales. Los valores finales obtenidos para los parámetros se resumen en la Tabla 8.19. Se dedujo en base a los resultados obtenidos y a la información disponible sobre las constantes de adsorción de las especies implicadas que el mecanismo más plausible considera que dos centros activos intervienen en la etapa determinante de la velocidad de reacción. Además, la adsorción de olefinas resultó ser no significativa comparada con aquella de EtOH y los éteres implicados. Finalmente, la inclusión de un término que considere la interacción entre el catalizador y el medio de reacción en cada instante resultó también ser significativa. Por lo tanto, los modelos cinéticos finalmente obtenidos son las ecuaciones 8.22-8.24.

Tabla 8.19. Valores promedio y error estándar de los parámetros estimados y obtenidos tras el *model averaging* para n = 1, 2, y 3.

Parámetro	$k'_{1,R1}$	$k'_{T,R1}$	$k'_{1,R2}$	$k'_{T,R2}$	$k'_{1,R3}$	$k'_{T,R3}$	k_{D1}	$K'_{1,ETBE}$	$K'_{T,ETBE}$	$K'_{1,TAEE}$	*TWRSS*
n = 1	6,47	–8950	6,96	–9520	4,58	–9720	23,71	0,50	–5190	–0,42	0,26
	± 0,02	*± 160*	*± 0,04*	*± 350*	*± 0,03*	*± 230*	*± 0,08*	*± 0,06*	*± 480*	*± 0,53*	
n = 2	6,42	–8760	7,05	–9010	4,42	–9770	21,16	–0,12	–4560	–0,74	0,29
	± 0,02	*± 170*	*± 0,04*	*± 340*	*± 0,03*	*± 270*	*± 0,12*	*± 0,04*	*± 410*	*± 0,30*	
n = 3	6,28	–9000	7,18	–9150	4,02	–10150	–	–0,35	–3320	–2,14	0,4
	± 0,02	*± 190*	*± 0,03*	*± 300*	*± 0,04*	*± 400*		*± 0,07*	*± 440*	*± 0,30*	

$$r_{ETBE} = r_{R1} = \frac{k'_{R1}\left(a_{IB}a_{EtOH} - a_{ETBE}/K_{R1}\right)\psi}{\left(a_{EtOH} + K'_{ETBE}\,a_{ETBE} + K'_{TAEE}\,a_{TAEE}\right)^2} \tag{8.22}$$

$$r_{TAEE} = r_{R2} + r_{R3} = \frac{\left[k'_{R2}\left(a_{2M1B}a_{EtOH} - a_{TAEE}/K_{R2}\right) + k'_{R3}\left(a_{2M2B}a_{EtOH} - a_{TAEE}/K_{R3}\right)\right]\psi}{\left(a_{EtOH} + K'_{ETBE}\,a_{ETBE} + K'_{TAEE}\,a_{TAEE}\right)^2} \tag{8.23}$$

$$r_{2M2B} = r_{R4} - r_{R3} = \frac{\left[k'_{R4}(a_{2M1B} - a_{2M2B}/K_{R4}) - k'_{R3}(a_{2M2B}a_{EtOH} - a_{TAEE}/K_{R3})\right]\psi}{\left(a_{EtOH} + K'_{ETBE}\,a_{ETBE} + K'_{TAEE}\,a_{TAEE}\right)} \tag{8.24}$$

Las energías de activación aparentes obtenidas para las reacciones R1-R4 fueron 72,8 ± 1,4, 74,9 ± 2,8, 81,2 ± 2,2 y 76,5 ± 7,2 kJ mol^{-1}. Estos valores son comparables a los reportados previamente en la literatura para los sistemas aislados de eterificación utilizando catalizadores similares. A partir de las constantes cinéticas obtenidas se concluyó que las olefinas con el doble enlace localizado en un carbono terminal son más reactivas con EtOH. A partir de las energías de activación aparentes se pudieron calcular las energías de activación reales para un modelo del tipo LHHW y un modelo del tipo ER. Las energías de activación reales para las reacciones R1-R3 según un mecanismo del tipo LHHW resultaron poco probables ya que eran demasiado altas para reacciones de eterificación. Por tanto, se infirió que un mecanismo del tipo ER es el más probable. Las energías de activación reales obtenidas para las reacciones R1-R3 fueron de 71,6, 73,7 y 80,0 kJ mol^{-1}, respectivamente.

8.3.8 ADSORCIÓN DE ALCOHOLES, OLEFINAS Y ÉTERES SOBRE AMBERLYST™35

Se realizaron experimentos de adsorción en fase líquida y en fase gas para los alcoholes C_1-C_4, las isolefinas C_4-C_5 y los éteres correspondientes con el objetivo de encontrar las constantes de equilibrio de adsorción y parámetros termodinámicos de adsorción de estos compuestos sobre A-35. Además, se realizaron imágenes SEM de A-35, porosimetría por intrusión de mercurio, difracción de láser en aire, FTIR y TGA con el objetivo de obtener información sobre la morfología de la resina, sus propiedades texturales y estructurales.

La Figura 8.20 muestra las imágenes obtenidas por SEM de A-35 a diferentes aumentos. Se puede observar que está formada por un agregado de micropartículas (fase gel) que da lugar a pososidad permanente (zonas más oscuras), por lo tanto, puede considerarse como un catalizador bidisperso. Con respecto al espectro FTIR obtenido, permitió determinar la naturaleza de los centros activos de A-35, siendo estos de tipo Brønsted o Brønsted Lewis.

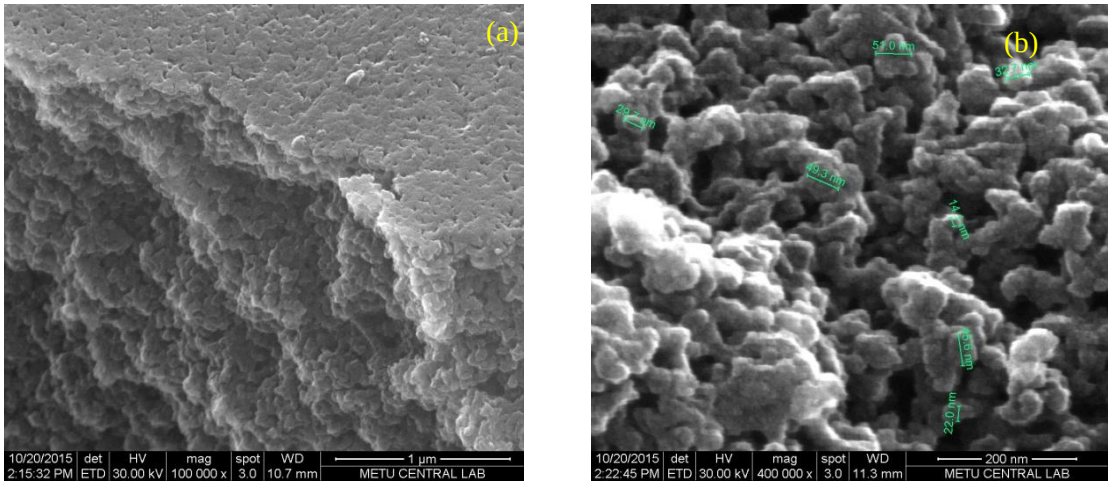

Figura 8.20. Imágenes SEM de A-35 pretratada a diferentes aumentos: (a) Superficie y cara interna de una fractura a 100000x. (b) Cara interna de una partícula fracturada a 400000x.

Con respecto a los experimentos en fase líquida, la Tabla 8.20 resume los valores de las constantes de adsorción ($K_{j,L}$) obtenidas para las especies estudiadas. En general los valores de $K_{j,L}$ disminuyeron en el orden MeOH>EtOH>PrOH>BuOH>2M2B. En el caso de los alcoholes esta tendencia puede explicarse por el tamaño molecular de los mismos. Se deduce también que los alcoholes se adsorben preferencialmente en comparación con las olefinas a cualquier temperatura, ya que los valores de $K_{j,L}$ para MeOH y EOH son de 2 a 5 veces mayores que los de 2M2B. Los valores obtenidos son coherentes con los determinados en la literatura sobre A-15.

Tabla 8.20. Constantes de equilibrio de adsorción en fase líquida sobre A-35 y su error asociado.

Parámetro	T [K]	MeOH	EtOH	PrOH	BuOH	2M2B
$K_{j,L} \cdot 10^3$ [m^3mol^{-1}]	323	23,2 ± 3,8	31,9 ± 4,0	21,1 ± 4,4	21,67 ± 1,24	7,05 ± 0,21
	333	19,0 ± 2,6	28,6 ± 4,7	17,4 ± 2,5	15,37 ± 1,52	4,15 ± 0,13
	343	15,0 ± 3,4	25,2 ± 2,3	13,4 ± 2,1	13,78 ± 1,35	3,388 ± 0,028
	353	13,30 ± 1,10	20,56 ± 0,82	12,6 ± 2,4	10,59 ± 0,21	-
$K'_{j,L} \cdot 10^3$ [m^3kg^{-1}]	323	229,8 ± 45,5	153,8 ± 26,6	136,8 ± 28,1	105,7 ± 8,3	25,2 ± 4,0
	333	187,2 ± 33,2	147,1 ± 34,7	119,1 ± 17,1	96,7 ± 15,5	31,4 ± 8,8
	343	152,7 ± 49,9	131,4 ± 18,0	98,5 ± 15,3	77,1 ± 13,2	21,3 ± 2,2
	353	167,3 ± 21,5	116,0 ± 8,1	91,4 ± 17,5	74,3 ± 3,2	-

Mediante la representación de van't Hoff se determinaron la entalpía y entropía de adsorción de las especies a partir de las constantes de equilibrio. Los valores obtenidos se resumen en la Tabla 8.21. Se deduce que la adsorción de alcoholes es poco sensible a la temperatura. El valor relativamente alto de $\Delta_{ads}H_{2M2B,L}$ se puede deber a la quimisorción como etapa previa a las reacciones de isomerización y dimerización. El cumplimiento de las reglas de Boudart [112,113] garantiza la coherencia termodinámica de los valores obtenidos.

Tabla 8.21. Propiedades termodinámicas en fase líquida y error estimado.

Tracer	$\Delta_{ads}H_{j,L}$ (This work) [kJmol^{-1}]	$\Delta_{ads}S_{j,L}$ (This work) [J(molK)$^{-1}$]	$S°_{j,L}$ [J(molK)$^{-1}$]	Δ_vH_j [kJmol^{-1}]	$\Delta_{ads}H_{j,G}$ [kJmol^{-1}]	$\Delta_{ads}H_{j,L}$ [kJmol^{-1}]
MeOH	-6,3 ± 0,5	-3,2 ± 1,5	127,19[a]	37[f]	-39,7[h]	-2,7[i]
EtOH	-8,1 ± 0,9	-3,7 ± 2,8	159,86[b]	41,3[f]	-43,5[h]	-2,2[i]
PrOH	-7,0 ± 0,3	-2,9 ± 1,0	192,80[c]	44,7[f]	-50,5[h]	-5,8[i]
BuOH	-6,9 ± 0,3	-3,4 ± 1,0	225,73[d]	50,1[f]	–	–
2M2B	-33,7 ± 8,1	-72,5 ± 24,5	251,2[e]	28,4[g]	-76,9[h]	-48,5[i]

Datos del National Institute of Standards and Technology (NIST) Book: [a][227], [b][228], [c][229], [d][230], [e][231]. [f][218], [g][232], [h][150], [i]Estimados a partir de datos en fase gas y la entalpía de vaporización (Δ_vH_j) como: $\Delta_{ads}H_{j,L} = \Delta_vH_j + \Delta_{ads}H_{j,G}$.

Con respecto a los experimentos en fase gas, la Tabla 8.22 recoge los valores de constantes termodinámicas y calores de adsorción obtenidos para los compuestos estudiados. Se puede observar que las constantes de equilibrio de adsorción de los alcoholes son alrededor de dos ordenes de magnitud superiores a las de olefinas y éteres. La adsorción de olefinas y éteres resultó ser de una magnitud comparable. Con respecto a los calores de adsorción, los valores obtenidos para los alcoholes resultaron ser más altos que en fase líquida, lo que implica una mayor sensibilidad con la temperatura del proceso de adsorción en fase gas.

Tabla 8.22. Constantes de equilibrio de adsorción en fase gas ($\rho_pK_{j,G}$) y calores de adsorción aparentes obtenidos entre 323 y 353 K sobre A-35.

	$\rho_pK_{j,G}$ [-]				$\Delta_{ads}H°_{j,G}$
Especie	323 K	333 K	343 K	353 K	[kJmol^{-1}]
MTBE	169,3	147,6	114,1	90,2	-20,3 ± 2,1
ETBE	168,4	135,8	116,7	90,3	-19,1 ± 1,5
PTBE	168,5	146,1	116,7	86,9	-20,9 ± 2,7
BTBE	139,3	130,6	102,6	69,8	-21,8 ± 5,2
2M1B	125,5	111,0	87,8	58,4	-21,7 ± 1,1
2M2B	136,8	118,4	106,0	72,1	-19,1 ± 4,5
TAEE	162,9	133,0	105,4	82,0	-23,8 ± 4,7
IB	168,8	135,3	112,6	66,8	-27,9 ± 5,9
MeOH	3485,1[a]	2341,5[a]	1619,2[a]	1392,7[a]	-29,7 ± 3,4
EtOH	4775,5[a]	3666,9[a]	2697,5[a]	1984,2[a]	-27,9 ±1,2
PrOH	13399,5[a]	8658,9[a]	5508,4[a] 8576,0	3983,0[a] 3868,4	-38,9 ± 1,4
BuOH	28877,7[a]	18784,9[a]	10594,3[a] 5888,1	7973,8[a] 2556,9	-41,8 ± 2,4

[a]Estimados a partir de los valores en fase líquida mediante relaciones termodinámicas.

Mediante la técnica de los momentos [64–67] se pudieron estimar los coeficientes de difusión efectiva de las especies en los macroporos en fase líquida y en fase gas, oscilando respecivamente entre 10^{-12}–10^{-13} m^2 s^{-1}, y entre 10^{-6}–10^{-7} m^2 s^{-1}. Los coeficientes de difusión efectiva en los microporos son idénticos en fase líquida y gas variando entre 10^{-20} y 10^{-21} m^2 s^{-1}.

8.3.9 DESACTIVACIÓN DE RESINAS ÁCIDAS DE INTERCAMBIO IÓNICO POR ACETONITRILO

Se estudió el efecto desactivante del ACN en el sistema en un reactor de lecho fijo operado en régimen diferencial. El rango de concentraciones de ACN estudiadas fue 0-5000 ppm en la corriente de EtOH. También se estudió el efecto del agua en el rango 0-4000 ppm ya que, además de inhibir las reacciones de eterificación, actúa como reactante en las reacciones de desactivación implicadas. Además de las reacciones descritas en la *Sección 8.3.1*, las reacciones de la Figura 8.21 tienen lugar. I, II y III se corresponden con el mecanismo de hidrólisis directa y las reacciones IV y V corresponden al mecanismo de alcohólisis. En ambos mecanismos el amoníaco es la especie química formada que acaba desactivando los centros ácidos.

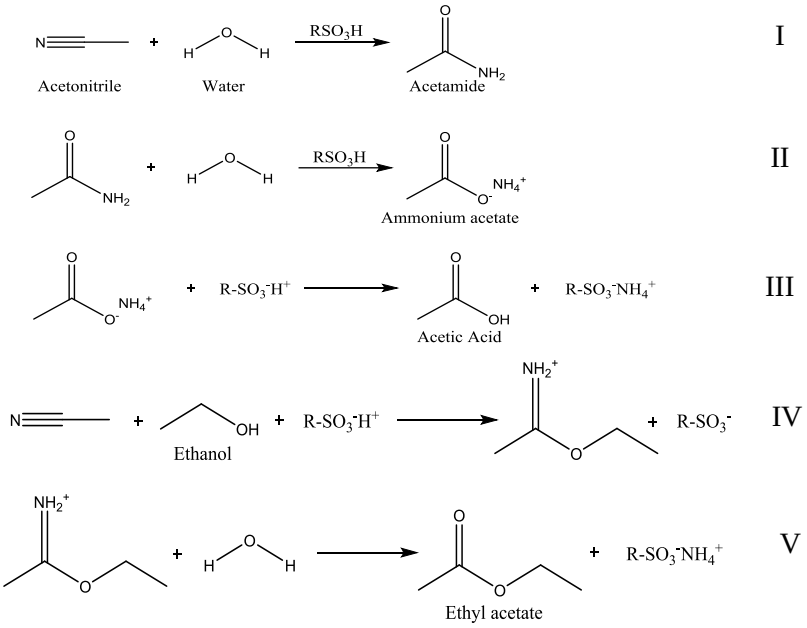

Figura 8.21. Reacciones que tienen lugar en la desactivación por acetonitrilo.

El efecto desactivante provocado por el acetonitrilo se vio favorecido a mayor concentración de ACN y por la temperatura. La Figura 8.22 muestras ejemplos de los perfiles obtenidos en los experimentos. En ningún caso se llegó a la desactivación total del catalizador.

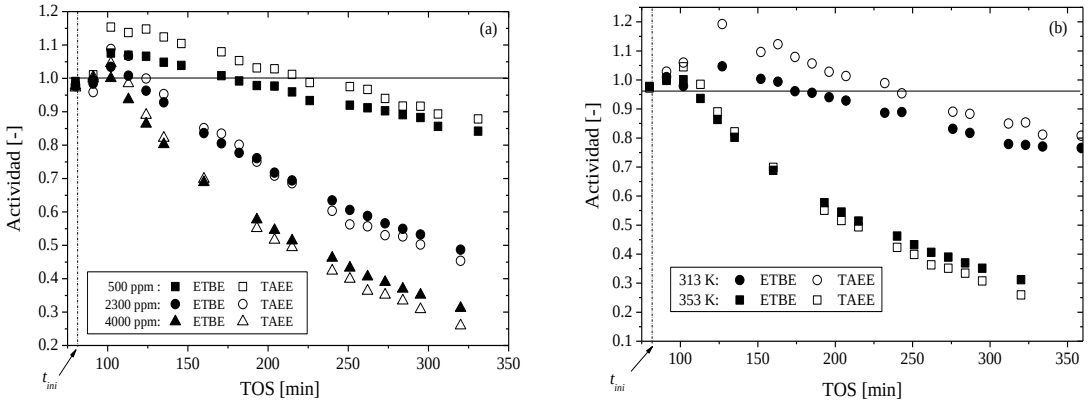

Figura 8.22. Caída relativa de actividad catalítica para las velocidades de formación de ETBE y TAEE sobre Amberlyst™35 vs. time on stream (TOS) a: (a) diferentes concentraciones de ACN en la corriente de alimento de EtOH y T=353K y, (b) diferentes temperaturas y 4000 ppm de ACN. $R°_{A/O}$=1,1 and $R°_{C4/C5}$=1. t_{ini} se refiere al TOS en el que el ACN se añadió al alimento.

Se pueden observar dos periodos en los experimentos realizados. Un aumento inicial de actividad atribuible al consumo del agua adsorbida en los centros activos en las reacciones de desactivación, seguido de una caída monótona de actividad con un perfil tipo exponencial. La desactivación afectó ligeramente más a la formación de TAEE que a la de ETBE. En cuanto a los catalizadores empleados, A-35 y CT-275, aunque la diferencia no es muy significativa, el proceso de desactivación fue ligeramente más rápido en A-35. Por otra parte, mediante la representación de la actividad frente a la concentración de ACN a diferentes TOS se pudo determinar que la desactivación por ACN se corresponde con un envenenamiento de tipo selectivo. Es decir, no todos los centros activos se desactivan por igual, sino que aquellos más ácidos son neutralizados primero.

Con los datos de actividad (r/r_0) obtenidos se realizó un ajuste cinético de la desactivación resultando que una expresión de primer orden del tipo $da/dt=k'_d \cdot a(t)$ se ajusta satisfactoriamente a los datos obtenidos en el rango de condiciones explorado, ver Figura 8.23a. Se determinó que las constantes cinéticas aparentes obtenidas dependen de la concentración de ACN en la forma $k'_d = k_d \cdot$[ACN], de dónde se pudieron obtener las constantes cinéticas reales k_d. A partir de las constantes cinéticas obtenidas y mediante la expresión de Arrhenius, ver Figura 8.23b, se obtuvo una energía de activación de 30,73 ± 2,59 kJ mol^{-1}. Por otra parte, con los valores de velocidad obtenidos en estado estacionario (antes de alimentar ACN) se estimaron unas energías de activación aparentes para los sistemas de formación d ETBE y TAEE de 72,5 ± 3,8 y 80,6 ± 6,3 kJ mol^{-1}. Estos valores son muy similares a los obtenidos en la *Sección 8.3.7* en un reactor discontinuo.

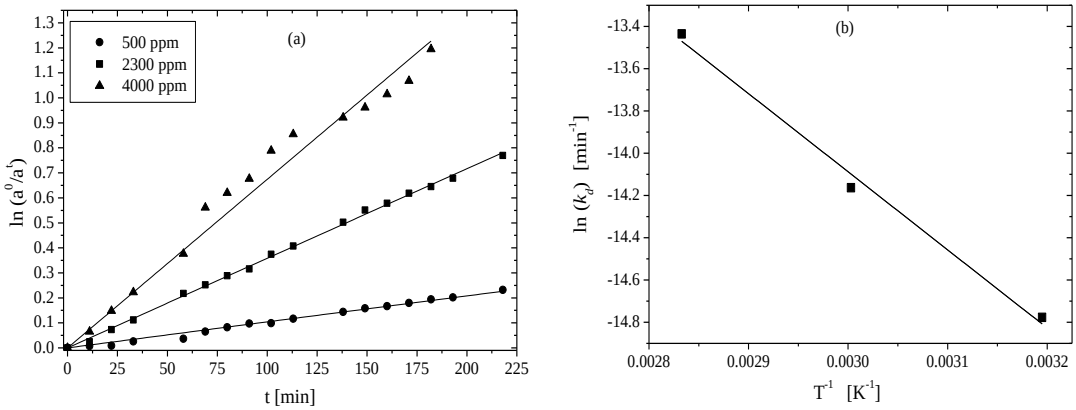

Figura 8.23. (a) Ejemplo de del ajuste a una desactivación de primer orden para las actividades obtenidas a 353 K conjuntamente para ETBE y TAEE a 353 K y diferentes concentraciones de ACN. (b) Gráfico de Arrhenius de las constantes cinéticas obtenidas a diferentes temperaturas.

En cuanto al efecto del agua en el sistema de reacción. Se observó que el incremento inicial de actividad está influenciado por la cantidad de agua, la concentración de ACN y la temperatura. Lógicamente, a mayores concentraciones de agua en la corriente de alimento EtOH, se alcanzaron menores velocidades de formación de éteres a causa del efecto inhibidor causado por componentes polares. Se profundizó en el modelo de inhibición y se ajustaron los datos obtenidos a diferentes modelos propuestos en la literatura. Se obtuvo que una expresión basada en el modelo Freundlich, ecuación 8.25, se ajusta mejor a los datos experimentales. Los valores de K_w y α obtenidos fueron 0,88 y 10,75, respectivamente.

$$\left(\frac{r}{r^0}\right) = \exp\left(-K_w \cdot \left(a_w\right)^{\frac{1}{\alpha}}\right) \qquad (8.25)$$

8.3.10 CONCLUSIONES GENERALES

A partir del Green Metric Analysis se ha podido confirmar que la ruta más eficiente para la producción simultánea de ETBE y TAEE es a partir de isobuteno, isoamilenos y etanol partiendo de una relación estequiométrica de reactantes. El inconveniente de la baja conversión de equilibrio de los isoamilenos puede resolverse mediante la tecnología de reacción más destilación.

El proceso en simultáneo permite convertir hasta el 65% de las olefinas problemáticas de la fracción C_5 en TAEE. Globalmente, las conversiones de equilibrio de reactantes oscilaron entre 69,8 y 97,9 %, 17,0 y 65,6 % y, 32,3 y 97,0 % para IB, IA, y EtOH, respectivamente. La selectividad de las olefinas a los éteres correspondientes es superior al 90 % en las condiciones estudiadas y el etanol es más selectivo hacia la producción de ETBE. La presencia de agua en el sistema favorece la formación de alcoholes terciarios e inhibe las reacciones de eterificación. Cuando hay presente más de un 0,45 %m. de agua en el sistema tiene lugar un cambio en el mecanismo de reacción atribuible a la disociación de los centros ácidos.

Las principales reacciones R1-R4 son exotérmicas. Las constantes de equilibrio de las reacciones decrecen en el orden $K_{R1}>K_{R2}>K_{R4}>K_{R3}$. Las entalpías estándar de las reacciones implicadas obtenidas son -36,3 ± 7,2, -35,1 ± 6,0, -25,5 ±3,0 y -9,7 ± 3,8 kJ mol^{-1}. La entalpía de reacción para la isomerización entre TMP-1 y TMP-2 obtenida es de 5,3 ± 0,8 kJ mol^{-1}.

El hinchamiento de las resinas evaluadas es similar en agua, etanol y metanol y significativamente mayor del observado en un medio no polar. La actividad catalítica de las resinas evaluadas aumenta en el orden: A-46 < MN-500 < CT-124 < A-45 < A-DT < A-39 < CT-482 < A-16 < A-36 < A-40 < CT-175 < A-15 < CT-275 < A-48 < A-35. Las resinas macroreticulares y sobresulfonadas muestran el mejor nivel de actividad catalítica, la cual está relacionada con el cociente entre capacidad ácida y volumen de polímero hinchado. Los dominios más densos de la fase gel presentan limitaciones de accesibilidad que pueden influir en la permeación de los compuestos y, por tanto, en la velocidad de reacción observada.

El pseudoorden cinético con el que las olefinas intervienen en las reacciones de eterificación estudiadas es positivo y próximo a cero mientras que el alcohol presenta un peudoorden negativo o cercano a cero. Las energías de activación aparentes estimadas para las principales reacciones R1-R4 son 72,8±1,4, 74,9±2,8, 81,2±2,2 y, 76,5±7,2 kJ mol^{-1}, respectivamente. Los modelos cinéticos finalmente encontrados y que describen el sistema de reacción son:

$$r_{ETBE} = r_{R1} = \frac{k'_{R1}\left(a_{IB}a_{EtOH} - a_{ETBE}/K_{R1}\right)\psi}{\left(a_{EtOH} + K'_{ETBE}\,a_{ETBE} + K'_{TAEE}\,a_{TAEE}\right)^2}$$

$$r_{TAEE} = r_{R2} + r_{R3} = \frac{\left[k'_{R2}\left(a_{2M1B}a_{EtOH} - a_{TAEE}/K_{R2}\right) + k'_{R3}\left(a_{2M2B}a_{EtOH} - a_{TAEE}/K_{R3}\right)\right]\psi}{\left(a_{EtOH} + K'_{ETBE}\,a_{ETBE} + K'_{TAEE}\,a_{TAEE}\right)^2}$$

$$r_{2M2B} = r_{R4} - r_{R3} = \frac{\left[k'_{R4}(a_{2M1B} - a_{2M2B}/K_{R4}) - k'_{R3}(a_{2M2B}a_{EtOH} - a_{TAEE}/K_{R3})\right]\psi}{\left(a_{EtOH} + K'_{ETBE}\,a_{ETBE} + K'_{TAEE}\,a_{TAEE}\right)}$$

Finalmente, el mecanismo más probable en las reacciones de eterificación estudiadas es del tipo Eley-Rideal.

Las constantes de equilibrio de adsorción determinadas sobre A-35 indican que la adsorción de alcoholes es más significativa que la de éteres y olefinas, mostrando estas dos últimas especies una adsorción de magnitud comparable. Las entalpías de adsorción obtenidas en fase líquida reflejan que la adsorción de alcoholes depende menos de la temperatura que la de 2M2B, lo que puede atribuirse a la quimisorción de la olefina como etapa previa en las reacciones de isomerización y dimerización. La resistencia a la difusión en los macroporos es más significante que aquella en los microporos en fase líquida, mientras que en fase gas ambas resistencias son significativas y han de ser consideradas. El proceso de adsorción en fase gas es más sensible a cambios de temperatura que en fase líquida. Por último, los coeficientes de difusión efectiva de las especies en los macroporos en fase líquida y en fase gas, oscilan respecivamente entre 10^{-12}-10^{-13} m^2 s^{-1} y, entre 10^{-6}–10^{-7} m^2 s^{-1}. Los coeficientes de difusión efectiva en los microporos son idénticos en fase líquida y gas variando entre 10^{-20} y 10^{-21} m^2 s^{-1}.

En cuanto a la desactivación de resinas ácidas causada por la presencia de acetonitrilo en el sistema de reacción, sus efectos son incrementados a mayores concentraciones de veneno y con la temperatura. Se han observado dos periodos en el proceso de desactivación, un aumento inicial de actividad atribuible al consumo de agua previamente adsorbida en las reacciones de desactivación, seguido de una caída monótona de actividad con perfil exponencial. El progreso de desactivación es muy similar en A-35 y en CT-275, aunque ligeramente más acentuado sobre A-35. Una ley primer orden permite explicar satisfactoriamente la cinética de la desactivación, cuya energía de activación estimada es de 30,73 ± 2,9 kJ mol^{-1}.

ACKNOWLEDGEMENT

First, I want to show all my gratitude to my father, Rodrigo Soto Tortosa, and to my mother, L. Encarnación López Mora. You both have given me the life, the education, the values and the courage for facing my challenges. Also to my sister, Rosa Mª Soto, and to my brother, Fernando Soto, for all the things that we have shared and for supporting me.

Second, I sincerely acknowledge to my supervisors, Dr. Carles Fité Piquer and Dr. Eliana Ramírez Rangel. They listened to me and they supported me when necessary during these years. Besides, they provided me knowledge and wisdom to cope with the PhD. Likewise, I want to show my heartily gratitude to the rest of the members of the Catalysis and Applied Kinetics research group, Prof. Fidel Cunill, Prof. Javier Tejero, Prof. Montserrat Iborra and Dr. Roger Bringué. I have had the opportunity of learning how to work in a research group, how to be a part of a team that push together for what we love, science. You all have given me very valuable lessons. Now, you all are a part of me. I would like also to express my gratefulness to the teachers that I had during the Chemical Engineering degree at the University of Málaga.

Besides, I thank to Middle East Technical University, Ankara, for performing the SEM images and to Gazi University, Ankara, for providing the installations and resources to perform the experimental work of the adsorption studies. Finally, I gratefully acknowledge Prof. Dr. Nuray Oktar, Prof. Dr. T. Doğu and Prof. Dr. G. Doğu for their help, kindness and valuable contributions during my predoctoral stay in Ankara.

The author is grateful to Rohm & Haas France SAS (The Dow Chemical Company) and Purolite Company Int. for providing the ion–exchange resins used in the present thesis. I also would like to express my gratefulness to Dr. Karel Jeřábek from Institute of Chemical Process Fundamentals (Prague, Czech Republic) for ISEC morphological analysis of the resins.

An important part of this acknowledgement is devoted to GUISOBA, as the third member of such a nice team, I sincerely thank to Dr. Jordi Hug Badia Córcoles and to Dr. Jordi Guilera Sala for all the interesting conversations, motivation, support, help and good moments that we have shared. I hope to find a place for working all together in the future.

Special Thanks Mª Dolores Ruiz Perea for all the help, support and motivation received during the PhD duration. Also thanks to Ms. Christina Zitello for revising the English of the contributions. I am also grateful to Ms. Laura González Saladich for helping me with the cover and for giving me support and advice with the artwork. Also thanks to Antonio Sotomayor Sola for being to me the friend that everyone should find.

At last but not least, I also acknowledge to all the lab mates that I have had during this period either in Barcelona or in Ankara for all the good moments we shared together and for their help. Dr. Carlos Casas, Dr. Mª Angeles Perez, Dr. Hüseyin Arbag, Nurbanu, Birce, Melike and to the undergraduate students that worked with me, Marta Allemany, Andres Granda and Alberto Fernández.

Finally, I want to say thanks to all the people that have believed in me, who, in any way or another, have given me support, love and happiness.